FRONTIERS IN SYNAPTIC NEUROSCIENCE - EDITOR'S PICK 2021

EDITED BY: P. Jesper Sjöström
PUBLISHED IN: Frontiers in Synaptic Neuroscience

frontiers Research Topics

ISSN 1664-8714
ISBN 978-2-88971-065-2
DOI 10.3389/978-2-88971-065-2

About Frontiers

Frontiers is more than just an open-access publisher of scholarly articles: it is a pioneering approach to the world of academia, radically improving the way scholarly research is managed. The grand vision of Frontiers is a world where all people have an equal opportunity to seek, share and generate knowledge. Frontiers provides immediate and permanent online open access to all its publications, but this alone is not enough to realize our grand goals.

Frontiers Journal Series

The Frontiers Journal Series is a multi-tier and interdisciplinary set of open-access, online journals, promising a paradigm shift from the current review, selection and dissemination processes in academic publishing. All Frontiers journals are driven by researchers for researchers; therefore, they constitute a service to the scholarly community. At the same time, the Frontiers Journal Series operates on a revolutionary invention, the tiered publishing system, initially addressing specific communities of scholars, and gradually climbing up to broader public understanding, thus serving the interests of the lay society, too.

Dedication to Quality

Each Frontiers article is a landmark of the highest quality, thanks to genuinely collaborative interactions between authors and review editors, who include some of the world's best academicians. Research must be certified by peers before entering a stream of knowledge that may eventually reach the public - and shape society; therefore, Frontiers only applies the most rigorous and unbiased reviews.
Frontiers revolutionizes research publishing by freely delivering the most outstanding research, evaluated with no bias from both the academic and social point of view. By applying the most advanced information technologies, Frontiers is catapulting scholarly publishing into a new generation.

What are Frontiers Research Topics?

Frontiers Research Topics are very popular trademarks of the Frontiers Journals Series: they are collections of at least ten articles, all centered on a particular subject. With their unique mix of varied contributions from Original Research to Review Articles, Frontiers Research Topics unify the most influential researchers, the latest key findings and historical advances in a hot research area! Find out more on how to host your own Frontiers Research Topic or contribute to one as an author by contacting the Frontiers Editorial Office: frontiersin.org/about/contact

FRONTIERS IN SYNAPTIC NEUROSCIENCE - EDITOR'S PICK 2021

Topic Editor:
P. Jesper Sjöström, McGill University, Canada

Citation: Sjöström, P. J., ed. (2021). Frontiers in Synaptic Neuroscience - Editor's Pick 2021. Lausanne: Frontiers Media SA. doi: 10.3389/978-2-88971-065-2

Table of Contents

frontiers
in Synaptic Neuroscience

REVIEW
published: 09 April 2019
doi: 10.3389/fnsyn.2019.00010

Control of Long-Term Plasticity by Glutamate Transporters

Silvana Valtcheva*[*†] and Laurent Venance[*]

Dynamics and Pathophysiology of Neuronal Networks Team, Center for Interdisciplinary Research in Biology (CIRB), Collège de France, CNRS UMR7241/INSERM U1050, Paris, France

Activity-dependent long-term changes in synaptic strength constitute key elements for learning and memory formation. Long-term plasticity can be induced *in vivo* and *ex vivo* by various physiologically relevant activity patterns. Depending on their temporal statistics, such patterns can induce long-lasting changes in the synaptic weight by potentiating or depressing synaptic transmission. At excitatory synapses, glutamate uptake operated by excitatory amino acid transporters (EAATs) has a critical role in regulating the strength and the extent of receptor activation by afferent activity. EAATs tightly control synaptic transmission and glutamate spillover. EAATs activity can, therefore, determine the polarity and magnitude of long-term plasticity by regulating the spatiotemporal profile of the glutamate transients and thus, the glutamate access to pre- and postsynaptic receptors. Here, we summarize compelling evidence that EAATs regulate various forms of long-term synaptic plasticity and the consequences of such regulation for behavioral output. We speculate that experience-dependent plasticity of EAATs levels can determine the sensitivity of synapses to frequency- or time-dependent plasticity paradigms. We propose that EAATs contribute to the gating of relevant inputs eligible to induce long-term plasticity and thereby select the operating learning rules that match the physiological function of the synapse adapted to the behavioral context.

Keywords: synaptic plasiticty, excitatory amino acid transporters, glutamate uptake, astrocytes, spike-timing dependent plasticity, neuro-glia crosstalk, glutamate spillover

Edited by:
Clive R. Bramham,
University of Bergen, Norway

Reviewed by:
Michel Baudry,
Western University of Health Sciences, United States
Vidar Jensen,
University of Oslo, Norway

****Correspondence:***
Silvana Valtcheva
silvana.valtcheva@nyumc.org
Laurent Venance
laurent.venance@college-de-france.fr

[†]Present address:
Silvana Valtcheva,
Departments of Otolaryngology, Neuroscience and Physiology, Skirball Institute, Neuroscience Institute, New York University School of Medicine, New York, NY, United States

Received: *18 December 2018*
Accepted: *12 March 2019*
Published: *09 April 2019*

Citation:
Valtcheva S and Venance L (2019) Control of Long-Term Plasticity by Glutamate Transporters. Front. Synaptic Neurosci. 11:10. doi: 10.3389/fnsyn.2019.00010

INTRODUCTION

Information processing at central synapses is governed by two main neural coding strategies: integration and coincidence detection, which rely on the rate- and spike-time coding, respectively (deCharms and Zador, 2000; Brette, 2015). Accordingly, the ability of synapses to undergo long-term changes in synaptic weight have been investigated *in vivo* and *ex vivo* using two main types of cell conditioning paradigms: rate-based and spike-timing-based protocols (Malenka and Bear, 2004; Sjöström et al., 2008; Feldman, 2012). The induction of long-term potentiation (LTP) or depression (LTD), following different cell conditioning paradigms, is assessed by the relative change in the magnitude of postsynaptic responses. The induction of long-term synaptic plasticity at glutamatergic synapses requires the activation of presynaptic and postsynaptic glutamate receptors, situated at synaptic, perisynaptic and extrasynaptic sites (Asztely et al., 1997; Bergles and Jahr, 1997; Bergles et al., 1997; Min et al., 1998; Rusakov and Kullmann, 1998; Lehre and Rusakov, 2002; Zheng et al., 2008; **Figure 1**). The timing of activation of glutamate receptors is expected to be proportional to their distance from the presynaptic release site (Attwell and Gibb, 2005). There is a critical role of glutamate diffusion in determining the balance of receptor activation. High-affinity membrane glutamate transporters (also named excitatory amino acid transporters, EAATs)

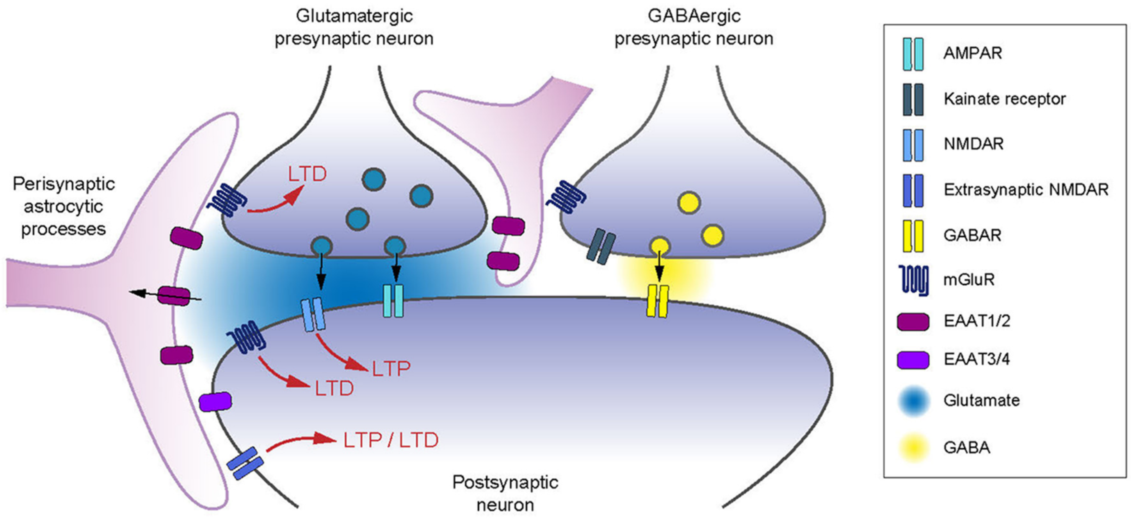

FIGURE 1 | Excitatory amino acid transporters (EAATs) control of receptors involved in long-term synaptic plasticity. EAATs control the activation of pre- and postsynaptic glutamate receptors, as well as the spread of glutamate to neighboring inhibitory neurons. EAAT2 controls the induction of long-term plasticity relying on presynaptic (Omrani et al., 2009) and postsynaptic mGluRs (Brasnjo and Otis, 2001; Valtcheva and Venance, 2016) and postsynaptic NMDARs (Katagiri et al., 2001; Massey et al., 2004; Wong et al., 2007; Scimemi et al., 2009; Valtcheva and Venance, 2016). Astrocytic coverage of neurons controls the activation of presynaptic type-III mGluRs or kainate receptors on GABAergic terminals (Piet et al., 2004; Bonfardin et al., 2010).

control the degree to which glutamate receptors located in the perisynaptic space or outside the synaptic cleft are activated following each release event (Bergles et al., 1997; Min et al., 1998; Zheng et al., 2008; Vandenberg and Ryan, 2013). The glutamate uptake process is electrogenic and is driven by the ion gradients of K^+ and Na^+ (Zerangue and Kavanaugh, 1996; Levy et al., 1998; Owe et al., 2006). EAATs have similar affinities for glutamate as glutamate receptors (Arriza et al., 1994) and their transport cycle is slow relative to the time course of glutamate in the synaptic cleft (Clements et al., 1992; Wadiche et al., 1995; Bergles and Jahr, 1998). Therefore, the main role of EAATs is to terminate the glutamate transient by primary acting as glutamate buffers followed by active transport. While during sparse activation of synapses, glutamate is likely cleared from the synaptic cleft by diffusion instead of active transport (Helassa et al., 2018), EAATs appear as key players for plasticity induction by controlling the spatiotemporal activation of glutamatergic receptors during episodes of high neuronal activity.

EAATs are constituted by five subtypes, named EAAT1-5 (Danbolt, 2001). EAAT type-1 (EAAT1) and type-2 (EAAT2) are mainly expressed in glial cells. EAAT1 is mostly expressed by Bergmann glia cells but is also found in other brain regions (Arriza et al., 1994; Rothstein et al., 1994; Chaudhry et al., 1995; Lehre et al., 1995; Wadiche and Kavanaugh, 1998). EAAT2 is specifically expressed in perisynaptic astrocytic processes ensheathing synaptic complexes, but not in astrocytic cell bodies (Danbolt et al., 1992; Rothstein et al., 1994; Lehre et al., 1995; Furuta et al., 1997; Levy et al., 1998; Minelli et al., 2001; Holmseth et al., 2009). EAAT2 can also be found in some excitatory neurons in hippocampus and cortex but its physiological role remains uncertain based on its distribution (not concentrated at synapses) and its low level of expression (∼10% of astrocytic EAAT2; Chen et al., 2004; Furness et al., 2008; Melone et al., 2009, 2011; Petr et al., 2015; Danbolt et al., 2016; Rimmele and Rosenberg, 2016). EAAT type-3 (EAAT3) and EAAT type-4 (EAAT4) are found in neurons at postsynaptic sites (Rothstein et al., 1994; Fairman et al., 1995; Lehre et al., 1995; Furuta et al., 1997; Conti et al., 1998). EAAT4 is expressed by cerebellar Purkinje cells in particular on extrasynaptic sites (Tanaka et al., 1997; Dehnes et al., 1998). Finally, EAAT type-5 (EAAT5) is expressed in the photoreceptors, bipolar and amacrine cells of the retina and has been suggested to mainly act as glutamate-activated chloride channel to control the excitability of retinal neurons (Eliasof and Jahr, 1996; Arriza et al., 1997; Veruki et al., 2006; Schneider et al., 2014).

Numerous studies have shown that both astrocytic and neuronal EAATs regulate the output of activity-dependent long-term synaptic plasticity triggered by different cell conditioning paradigms. Pharmacological or genetic alteration of EAATs activity can either facilitate or impair rate-based synaptic plasticity (Brasnjo and Otis, 2001; Katagiri et al., 2001; Massey et al., 2004; Wang et al., 2006; Wong et al., 2007; Omrani et al., 2009; Bellini et al., 2018). Spike-timing-based cell-conditioning paradigms such as spike-timing-dependent plasticity (STDP) reveal subtler multidimensional regulation of synaptic plasticity by EAATs. STDP is a Hebbian synaptic learning rule accounting for experience-dependent changes in neural networks (Sjöström et al., 2008; Feldman, 2012), which depends on pre- and post-synaptic activity. Besides the change in synaptic weight, STDP rules are described by the permissive temporal window (Δt_{STDP}) for plasticity expression. If pre- and post-synaptic activity occur at Δt_{STDP} beyond a few tens of milliseconds, it does not generally trigger long-term synaptic efficacy changes, and, therefore, these events are considered as uncorrelated. Altering glutamate uptake by up- or downregulation of the astrocytic EAAT2 has an effect on both STDP expression and the temporal range of its permissive window (Valtcheva and Venance, 2016).

Here, we review recent findings on the control of long-term synaptic plasticity by EAATs and we discuss how alterations of glutamate transport affect behavior. Finally, we focus on the physiological regulation of EAATs by different forms of experience and speculate on how this might shape the sensitivity of synapses to undergo different forms of long-term plasticity.

EAATs CONTROL OF LONG-TERM SYNAPTIC PLASTICITY DEPENDS ON THE CELL CONDITIONING PARADIGM

EAATs exert differential control on long-term synaptic plasticity depending on the cell conditioning paradigm, i.e., rate- vs. spike-timing protocols. EAATs regulate the expression and magnitude of rate-based synaptic plasticity, whereas EAATs control the expression and the temporal window of spike-timing-based synaptic plasticity.

Pharmacological or genetic targeting of EAATs alters the magnitude of plasticity induced with rate-based protocols such as low- and high-frequency stimulation (LFS and HFS, respectively) or theta-burst stimulation (TBS; **Figures 2**, **3**; **Table 1**). Inhibition of glutamate uptake with bath application of threo-β-benzyloxyaspartic acid (TBOA), a broad-spectrum non-transportable EAATs blocker, or with *trans*-4-carboxy-L-proline (t-PDC), a transportable inhibitor, promotes LFS-LTD in layer II/III of perirhinal cortex of adult rats while no plasticity is observed in control conditions (Massey et al., 2004; **Figure 3A**). Similarly, TBOA bath application in acute brain slices or intracerebroventricular infusion *in vivo* also promotes LFS-LTD in the CA1 region of the hippocampus of adult rats, while no plasticity is observed after LFS in control conditions *in vivo* and *ex vivo* (Wong et al., 2007; **Figure 3A**). Blockade of glutamate transport with TBOA also increases single-cell LTD magnitude in cerebellar Purkinje cells in juvenile rats, triggered by HFS of the parallel fibers paired with Purkinje cell depolarization (Brasnjo and Otis, 2001; **Figures 2A**, **3A**). Genetic deletion of astrocytic EAAT2 results in impaired HFS-LTP, but has no effect on LFS-LTD, in brain slices of the stratum radiatum of mice (Katagiri et al., 2001; **Figures 2B**, **3A**). Pharmacological blockade with the EAAT2 specific inhibitor dihydrokainic acid (DHK) decreases TBS-LTP magnitude of C-fiber evoked field potentials in the spinal dorsal horn of anesthetized rats (Wang et al., 2006; **Figure 3A**). TBS-LTP in the hippocampal CA1 region is impaired in mice lacking neuronal EAAT3 (Scimemi et al., 2009; **Figure 3A**). Overexpression of EAAT2 protein levels *via* i.p. treatment with the beta-lactam antibiotic ceftriaxone (Rothstein et al., 2005) prevents the expression of LFS-LTD and decreases the magnitude of HFS-LTP at the hippocampal mossy fibers-CA3 synapse (Omrani et al., 2009; **Figures 2D**, **3B**).

Exploring STDP expression with specific pharmacological targeting of EAAT2 glutamate uptake uncovers that together with its control over plasticity magnitude, EAAT2 tightly regulates the temporal window for plasticity induction in the rat dorsolateral striatum (Valtcheva and Venance, 2016; **Figures 2C**, **3C**; **Table 1**). Indeed, specific pharmacological blockade of EAAT2 (with DHK or WAY-213,613) during the STDP induction protocol results in a broadening of the permissive window for plasticity expression at corticostriatal synapses. Inhibition of EAAT2 promotes the expression of spike-timing-dependent LTD (t-LTD) or spike-timing-dependent LTP (t-LTP) at temporal intervals, where no plasticity is observed under control conditions (beyond $\Delta t_{STDP} = \pm 30$ ms for 1 Hz pairings). Upon EAAT2 inhibition, plasticity expression does not follow STDP rule, as a non-timing-dependent LTP can be triggered by uncorrelated events (randomized pre-post and post-pre pairings) or even unpaired activity (postsynaptic activation alone). EAAT2 inhibition reveals an overlap between non-timing-dependent LTP and LTD triggered by the recruitment of GABAergic networks at a narrow temporal window ($-70 < \Delta t_{STDP} < +70$ ms; Valtcheva and Venance, 2016). On the contrary, overexpression of EAAT2 following chronic ceftriaxone treatment of rats results in a lack of STDP at corticostriatal synapses (Valtcheva and Venance, 2016; **Figures 2E**, **3D**). Therefore, EAAT2 control the expression of spike-timing-based plasticity but also acts as a selector for Hebbian vs. non-Hebbian plasticity.

HOW EAATs CONTROL LONG-TERM PLASTICITY

EAATs regulate the expression of both rate- and spike-timing-based long-term plasticity by several mechanisms. EAATs control the extent of activation of receptors present in synaptic and peri-/extrasynaptic compartments, or on neighboring neurons, by controlling the temporal and spatial profile of the glutamate transient (Tong and Jahr, 1994; Brasnjo and Otis, 2001; Clark and Cull-Candy, 2002; Dzubay and Otis, 2002; Reichelt and Knöpfel, 2002; Attwell and Gibb, 2005; Tzingounis and Wadiche, 2007; Chalifoux and Carter, 2011). Synaptically released glutamate diffuses out of the synaptic cleft and binds to NMDARs and mGluRs in the peri- or extrasynaptic membrane or at neighboring synapses (Kullmann et al., 1996; Barbour and Häusser, 1997; Scanziani et al., 1997; Kullmann and Asztely, 1998; Szapiro and Barbour, 2007). The extent of such extrasynaptic actions is regulated by the high-affinity glutamate uptake operated mainly by EAAT2 (Asztely et al., 1997; Bergles and Jahr, 1997; Min et al., 1998; Rusakov and Kullmann, 1998; Lehre and Rusakov, 2002; Zheng et al., 2008). EAAT2 rapidly reduces the free concentration of glutamate but part of the content of the exocytosis of presynaptic vesicles binds to glutamatergic receptors situated in the immediate perisynaptic space (Rusakov and Kullmann, 1998; Zheng et al., 2008). Moreover, sustained episodes of high-frequency presynaptic activity delay glutamate clearance by astrocytes and allow prolonged activation of NMDARs (Armbruster et al., 2016). Finally, diffusion of EAAT2 on the astrocytic membrane is crucial for the glutamate buffering function of EAAT2, thus

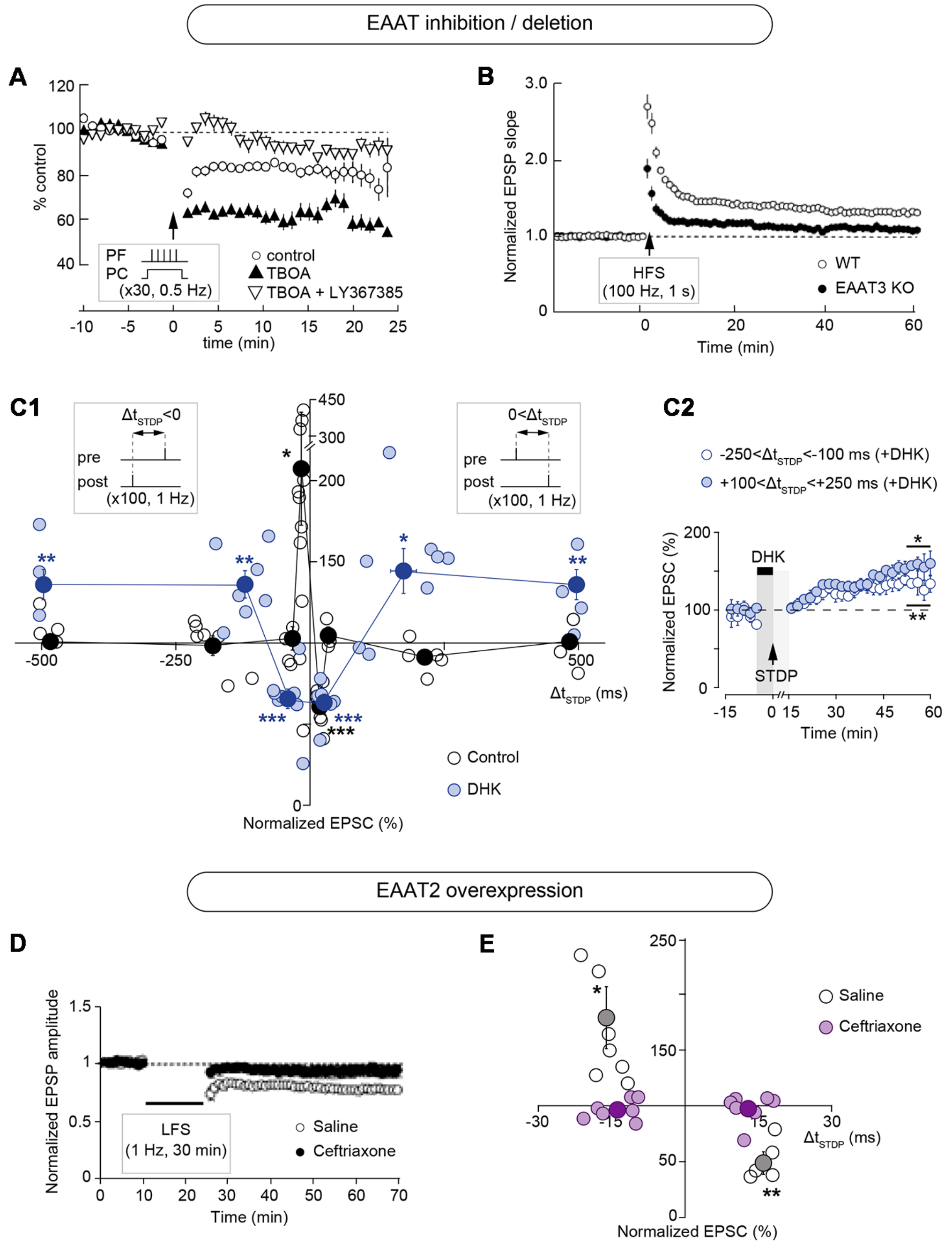

FIGURE 2 | Modulation of long-term synaptic plasticity by EAATs. **(A)** Pharmacological inhibition of EAATs by the broad-spectrum non-transportable blocker threo-β-benzyloxyaspartic acid (TBOA) increases the magnitude of long-term depression (LTD) in cerebellar Purkinje cells, triggered by high frequency stimulation (HFS) of the parallel fibers (five pulses at 100 Hz) paired with Purkinje cell depolarization (0 mV for 50 ms) repeated at 0.5 Hz for 1 min. This LTD is mGluR1-dependent since it is inhibited by LY367385. Adapted with permission from Brasnjo and Otis (2001). **(B)** Genetic deletion of EAAT2 decreases the amplitude of HFS-induced long-term potentiation (LTP) in the stratum radiatum region of the hippocampus. Adapted with permission from Katagiri et al. (2001). **(C)** Specific pharmacological blockade of EAAT2 with dihydrokainic acid (DHK) results in a broadening of the permissive window for spike-timing dependent plasticity (STDP) expression at corticostriatal synapses. Inhibition of EAAT2 results in t-LTD or t-LTP at temporal intervals where no plasticity is observed under control conditions (beyond $\Delta t_{STDP} = \pm 30$ ms). **(C1)** Time window (Δt_{STDP}) for long-term synaptic strength for post-pre and pre-post pairings. **(C2)** Averaged time-course of experiments with transient blockade of EAAT2 with bath-application of DHK for post-pre and pre-post pairings beyond $\Delta t_{STDP} = \pm 100$ ms. Adapted with permission from Valtcheva and Venance (2016). **(D)** Overexpression of EAAT2 by chronic ceftriaxone treatment prevents the expression of low frequency stimulation (LFS)-induced LTD at the hippocampal mossy fibers-CA3 synapse. Adapted with permission from Omrani et al. (2009). **(E)** STDP time window (Δt_{STDP}) for long-term synaptic strength for post-pre and pre-post pairings showing that overexpression of EAAT2 by chronic ceftriaxone treatment prevents the expression of STDP at corticostriatal synapses. Adapted with permission from Valtcheva and Venance (2016). $^{*}p < 0.05$; $^{**}p < 0.01$; $^{***}p < 0.001$.

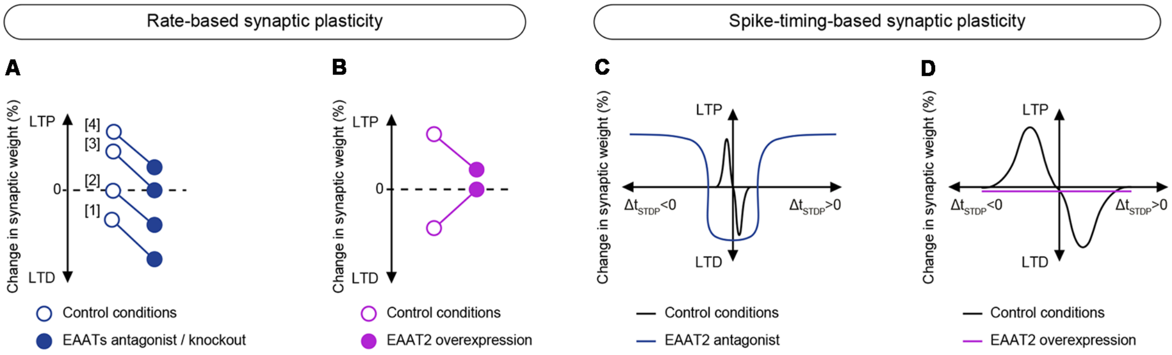

FIGURE 3 | Effects of EAATs modulation on long-term plasticity. **(A,B)** Effects of EAATs regulation on rate-based plasticity. **(A)** Downregulation of EAATs by pharmacological inhibition or genetic knock-out (closed circles) results in a lower threshold for LTD induction and a higher threshold for LTP induction using rate-based plasticity paradigms compared to control conditions (open circles). Pharmacological inhibition of EAATs: (1) increases LTD magnitude (Brasnjo and Otis, 2001); (2) promotes LTD (Massey et al., 2004; Wong et al., 2007); (3) prevents LTP induction (Wang et al., 2006). Genetic knock-out of EAATs; and (4) decreases LTP amplitude (Katagiri et al., 2001; Scimemi et al., 2009). **(B)** Upregulation of EAATs by chronic ceftriaxone treatment (closed circles) prevents the expression of LFS-induced LTD and decreases the amplitude of HFS-induced LTP compared to control conditions (open circles; Omrani et al., 2009). **(C,D)** Effects of EAATs regulation on spike-timing-based plasticity. **(C)** Downregulation of EAAT2 by pharmacological inhibition with DHK results in a broadening of the permissive window (Δt_{STDP}) for plasticity expression (Valtcheva and Venance, 2016). **(D)** Upregulation of EAATs by chronic ceftriaxone treatment prevents the expression of STDP (Valtcheva and Venance, 2016).

allowing the transporter to relocate between synaptic and peri-/extrasynaptic sites (Murphy-Royal et al., 2015). There is a critical role of glutamate diffusion in determining the balance of receptor activation and EAATs control the degree to which receptors located outside the cleft are activated following each release event (Bergles et al., 1997; Min et al., 1998; Zheng et al., 2008).

EAATs Control the Activation of Receptors Involved in Long-Term Plasticity

Up- or down-regulation of glutamate uptake can have a profound effect on plasticity expression or magnitude. Increase in EAATs density would increase the buffering capacity for glutamate and decrease glutamate receptor stimulation as EAATs compete for the extracellular glutamate with NMDARs and mGluRs located in the peri- or extrasynaptic space (Bergles et al., 2002; Tzingounis and Wadiche, 2007; **Figure 1**). Increasing glutamate clearance can also reduce synaptic receptor activation (Min et al., 1998). In contrast, downregulation of EAATs should allow extended binding of glutamate to its receptors (**Figure 1**).

Up-regulation of EAAT2, with ceftriaxone (Rothstein et al., 2005), prevents LFS-LTD and decreases the magnitude of HFS-LTP at the hippocampal mossy fibers-CA3 synapse (Omrani et al., 2009; **Figures 2D**, **3C**). The effect on LFS-LTD can be explained by the enhanced glutamate clearance resulting from EAAT2 up-regulation, thus limiting the activation of perisynaptic mGluRs which are responsible for LFS-LTD induction at the mossy fibers-CA3 synapse (Kobayashi et al., 1996; Yokoi et al., 1996). Indeed, bath-applied DHK during LFS rescues LTD in ceftriaxone-treated animals, by promoting glutamate accumulation and mGluRs activation (Omrani et al., 2009). Likewise, reduced glutamate access to presynaptic kainate receptors, which mediates HFS-LTP at the mossy the fibers-CA3 synapse (Schmitz et al., 2003) might account for the reduction in HFS-LTP magnitude. A similar mechanism is likely involved in the loss of striatal t-LTD and t-LTP expression after EAAT2 up-regulation with ceftriaxone treatment (Valtcheva and Venance, 2016; **Figures 2E**, **3D**). At corticostriatal synapses in the dorsolateral striatum, t-LTD is mGluR-mediated and t-LTP depends on NMDARs (Fino et al., 2010; Evans et al., 2012), and these receptors are located within but also outside the synaptic cleft (Baude et al., 1993; Paoletti et al., 2013). Therefore, EAAT2 overexpression may limit the activation of receptors responsible for STDP induction and impair the detection of correlated synaptic activity.

EAATs inhibition by TBOA increases the magnitude of associative mGluR-dependent LTD at cerebellar parallel fiber-Purkinje cell synapse by enhancing mGluRs transmission (Brasnjo and Otis, 2001; **Figures 2A**, **3A**). Specific pharmacological blockade of EAAT2 with intrathecal infusion of DHK in the spinal dorsal horn decreases HFS-LTP magnitude at lower doses of DHK and precludes LTP expression at higher doses (Wang et al., 2006; **Figure 3A**). LTP of unmyelinated C-fibers onto spinal dorsal horn neurons synapse relies on NMDARs activation (Randić et al., 1993). Therefore, continuous EAAT2 blockade (*via* intrathecal DHK infusion) and subsequent glutamate accumulation may result in excessive NMDAR stimulation, neuronal depolarization and subsequent increase in intracellular Ca^{2+} concentration, which would hinder further LTP induction. Similarly, genetic deletion of either astrocytic EAAT2 (Katagiri et al., 2001) or neuronal EAAT3 (Scimemi et al., 2009) impairs HFS-LTP in the hippocampus, most likely due to the chronic activation of NMDARs (**Figure 3A**). In knock-out mice for either EAAT2 or EAAT3 (Katagiri et al., 2001), glutamatergic transmission is increased, which may lead to enhanced stimulation of NMDARs, therefore precluding the ability of synapses to further potentiate.

TABLE 1 | Effect of excitatory amino acid transporters (EAATs) down- or up-regulation on rate-based and spike-timing-based synaptic plasticity.

Reference	Structure/synapse	Manipulation/drug	Recording	Brain slice cutting conditions	Plasticity paradigm	Effect on plasticity
Downregulation						
Brasnjo and Otis (2001)	Cerebellum, parallel fiber-Purkinje neurons	TBOA, bath-application	*Ex vivo*, whole-cell, EPSCs	Ice-cold (4°C) ACSF	HFS + postsynaptic depolarization	Increases LTD magnitude
Katagiri et al. (2001)	Hippocampus stratum radiatum	Knock-out	*Ex vivo*, extracellular, fEPSPs	ice-cold (4°C) ACSF	HFS and LFS	Decreases HFS-LTP magnitude; no effect on LFS-LTD
Massey et al. (2004)	Perirhinal cortex, layer II/III pyramidal neurons	TBOA, bath-application	*Ex vivo*, extracellular, fEPSPs	Ice-cold (4°C) ACSF	HFS and LFS	Promotes LFS-LTD induction
Tsvetkov et al. (2004)	Cortex-/Thalamus-Lateral amygdala pyramidal neurons	DHK, bath-application	*Ex vivo*, whole-cell, EPSCs	*	LFS	Promotes heterosynaptic LFS-LTP plasticity of unpaired input
Wang et al. (2006)	C-fibers-spinal dorsal horn	DHK, *in vivo* intrathecal administration	*In vivo*, extracellular, fEPSPs	N/A	HFS	Decreases HFS-LTP amplitude
Wong et al. (2007)	Hippocampus Schaffer collateral-CA1	TBOA, *ex vivo* bath-application or *in vivo* intraventricular infusion	*Ex vivo* and *in vivo*, extracellular, fEPSPs	Ice-cold (4°C) ACSF	HFS and LFS	Promotes LFS-LTD induction
Scimemi et al. (2009)	Hippocampus CA1	knock-out	*Ex vivo*, extracellular, fEPSPs	Ice-cold (4°C) ACSF	TBS and LFS	Impaires TBS-LTP
Valtcheva and Venance (2016)	Somatosensory cortex- dorsolateral striatum output neurons	DHK or WAY-213,613, bath-application	*Ex vivo*, whole-cell, EPSCs	Ice-cold (4°C) ACSF	STDP	Induces non-Hebbian LTP Induces heterosynaptic LTD
Overexpression						
Omrani et al. (2009)	Hippocampus Mossy fiber-CA3 Hippocampus Schaffer collateral-CA1	Ceftriaxone, i.p. injection	*Ex vivo*, extracellular, fEPSPs	Ice-cold (4°C) ACSF	HFS and LFS	MF-CA3: impairs LFS-LTD and decreases magnitude of HFS-LTP Schaffer collateral-CA1: no effecton HFS-LTP magnitude
Valtcheva and Venance (2016)	Somatosensory cortex- dorsolateral striatum output neurons	Ceftriaxone, i.p. injection	*Ex vivo*, whole-cell, EPSCs	Ice-cold (4°C) ACSF	STDP	Occludes t-LTP and t-LTD

**Not mentioned in the Methods; N/A, not applicable.*

Distinct natural expression patterns of EAATs also affect plasticity expression in different regions. Indeed, Purkinje cells in the cerebellar vermis express lower levels of EAAT4 and exhibit mGluR-dependent LFS-LTD at the parallel fiber-Purkinje cell synapse. In contrast, LFS-LTD is absent in the cerebellar flocculus where EAAT4 is highly expressed, which might decrease the extent of mGluRs recruitment during HFS (Wadiche and Jahr, 2005).

EAATs Prevent the Expression of Aberrant Plasticity

EAATs control the extent of glutamate spillover and the access of glutamate to receptors located at the peri- and extrasynaptic sites (**Figure 1**). Although EAATs are not overwhelmed by physiological activity, a total synaptic isolation is not reached (Asztely et al., 1997; Diamond and Jahr, 1997, 2000). Receptors that are typically not recruited by glutamate release under afferent stimulation in control conditions, can become key actors of long-term plasticity when glutamate uptake is altered (Tzingounis and Wadiche, 2007). Therefore, physiological or pathological down-regulation of EAATs has a permissive role for the expression of different forms of long-term plasticity (Massey et al., 2004; Wong et al., 2007; Aida et al., 2015; Valtcheva and Venance, 2016). EAATs prevent the expression of aberrant plasticity that is absent in physiological conditions but can be revealed when EAATs are blocked. Both rate- (Massey et al., 2004; Wong et al., 2007) and spike-timing-based (Valtcheva and Venance, 2016) paradigms which fail to induce changes in synaptic strength in control conditions *in vivo* and *ex vivo*, can promote long-term plasticity when glutamate uptake is impaired.

Pharmacological inhibition of all EAAT subtypes by TBOA in the perirhinal cortex (Massey et al., 2004) and in the CA1 region of the hippocampus (Wong et al., 2007) has a permissive role for the expression of *in vivo* and *ex vivo* LFS-LTD, mediated by NMDARs containing the GluN2B-subunit (**Figure 3A**). In the dorsolateral striatum, specific EAAT2 inhibition by DHK (or WAY-213,613) disrupts the temporal contingency between pre- and postsynaptic activity, which is required for STDP expression (Valtcheva and Venance, 2016; **Figures 2C**, **3C**). The sharp sensitivity to the timing of synaptic inputs of striatal STDP is erased in conditions of EAAT2 blockade when DHK (or WAY-213,613) is applied exclusively during the STDP protocol. This promotes the expression of a non-timing-dependent LTP mediated by GluN2B-NMDARs which is can also be induced by uncorrelated pre- and postsynaptic events. This non-timing-dependent LTP is absent in control conditions when EAAT2 activity is intact.

EAATs Ensure Synaptic Independence

Astrocytic EAAT2 is of crucial importance for limiting glutamate spillover to neighboring synapses, and therefore tightly controlling both cooperation and synaptic independence (Arnth-Jensen et al., 2002; Huang et al., 2004; Scimemi et al., 2004; Attwell and Gibb, 2005; Tzingounis and Wadiche, 2007; **Figure 1**). High-affinity NMDARs and mGluRs, located on peri- or extrasynaptic sites (Baude et al., 1993; Paoletti et al., 2013), or on neighboring neurons, mediate most of the glutamatergic spillover responses and their activation is limited by active astrocytic glutamate uptake (Kullmann and Asztely, 1998; Diamond and Jahr, 2000; Huang and Bergles, 2004; Coddington et al., 2013). Therefore, inhibition of EAAT2 favors synaptic crosstalk by the recruitment of neighboring neurons (Huang et al., 2004), or *via* the loss of specificity of afferent inputs (Arnth-Jensen et al., 2002; Scimemi et al., 2004).

EAAT2 blockade results in heterosynaptic LTP in the lateral amygdala (Tsvetkov et al., 2004). LTP at both cortical and thalamic synapses onto pyramidal cells in the lateral amygdala depends on NMDAR activation (Huang and Kandel, 1998; Bauer et al., 2002; Tsvetkov et al., 2002, 2004). Specific pharmacological blockade of EAAT2 with DHK leads to the loss of input specificity in the lateral amygdala, most likely by promoting intersynaptic crosstalk between cortical and thalamic inputs onto pyramidal cells (Tsvetkov et al., 2004). Glutamate spillover may also recruit neighboring interneurons and their activation can impact long-term plasticity expression of principal cells. Indeed, specific blockade of EAAT2 with DHK results in an increased inhibitory drive from GABAergic microcircuits in the striatum (Valtcheva and Venance, 2016). Suprathreshold activation of GABAergic interneurons by cortical stimulation masks the expression of non-timing-dependent LTP of striatal output neurons. In these conditions, enhanced inhibitory transmission promotes the expression of GABA-dependent LTD, instead of postsynaptic NMDAR-mediated LTP, at a narrow temporal window. As a result, postsynaptic NMDAR-mediated LTP is expressed only at a larger temporal window, when the cortical stimulation occurs far from the postsynaptic spike and thus the strong inhibitory drive does not interfere with postsynaptic LTP expression (Valtcheva and Venance, 2016; **Figures 2C**, **3C**).

EAATs Set the Balance Between LTP and LTD

Interestingly, in many cases of rate-based synaptic plasticity EAATs downregulation by either genetic or pharmacological manipulations leads to a reduction of LTP magnitude or occludes its expression (Katagiri et al., 2001; Wang et al., 2006; Scimemi et al., 2009) and promotes LTD (Brasnjo and Otis, 2001; Massey et al., 2004; Wong et al., 2007; **Figure 3A**). Therefore, blockade of glutamate transport may alter the balance between LTP and LTD (Katagiri et al., 2001; Scimemi et al., 2009) by reducing LTP magnitude and promoting LTD. Imposing a bias towards synaptic depression in conditions when EAAT activity is downregulated, may result from a shift in the modification threshold for plasticity induction (Cooper and Bear, 2012) by lowering LTD threshold and increasing LTP threshold (**Figure 3A**). When synaptic glutamate spillover is chronically enhanced and levels of ambient glutamate are thus increased, LTP induction can also be damped by plasticity saturation (Katagiri et al., 2001; Scimemi et al., 2009). In contrast, promoting glutamate spillover can facilitate glutamate access to extrasynaptic glutamate receptors and thus lower LTD threshold (Massey et al., 2004; Wong et al., 2007). It is worthy of note that increasing the frequency of afferent stimulation in control conditions can induce LTD (**Figure 3**), thus mimicking the effects of EAATs inhibition (Massey et al., 2004). A subtle balance between LTP and LTD should be of crucial importance for optimal memory storage in neural networks and altering glutamate uptake can have profound consequences for learning and memory.

In contrast to the effects triggered by inhibition of glutamate uptake, EAAT2 overexpression with ceftriaxone tends to suppress plasticity expression by altering both LTP and LTD (Omrani et al., 2009; Valtcheva and Venance, 2016; **Figures 3B,D**). It would be appealing to explore if increasing the frequency of afferent activation could overcome enhanced glutamate uptake by promoting an increased glutamate spillover and, therefore, restoring plasticity.

CONSEQUENCES OF EAATs ALTERATION ON BEHAVIOR

Because EAAT activity controls synaptic plasticity, glutamate uptake is expected to play an essential role in learning and shaping behavior. Although making a causal direct link between molecular impairment with behavioral changes is challenging, we review in this chapter studies correlating the effect of EAATs alterations to behavioral outputs.

In vivo chronic blockade of EAAT2 by DHK infusion in the central nucleus of the amygdala induces anxiety (John et al., 2015). This anxiogenic effect could arise from disrupted input specificity in amygdala networks, processing both fear and reward cues, due to enhanced glutamate spillover (Janak and Tye, 2015). Similarly, specific blockade of EAAT2 leads to the loss of specificity of cortical and thalamic inputs onto pyramidal cells in the lateral amygdala, resulting in heterosynaptic LTP of the unpaired input (cortical or thalamic; Tsvetkov et al., 2004). Fear conditioning has been shown to strengthen cortical inputs to the lateral amygdala (Tsvetkov et al., 2002). Therefore heterosynaptic LTP of these inputs following EAAT2 downregulation might impair fear memory formation. The proper functioning of other types of glutamate transporters might also be involved in fear memory formation as mice lacking EAAT3 exhibit decreased freezing behavior following fear conditioning (Wang et al., 2014).

EAATs impairment has consequences on social interactions, reward processing and motivation. EAAT1 knock-out mice exhibit poor nesting behavior and decreased sociability measured by the time spent sniffing an unfamiliar mouse during free social interaction (Karlsson et al., 2009). EAATs blockade in the basolateral amygdala decreases social interactions (Lee et al., 2007). In addition, blocking EAAT2 by *in vivo* DHK infusion in the ventral tegmental area, decreases response to electrical self-stimulation in the medial forebrain bundle (Herberg and Rose, 1990), suggesting that astrocytic glutamate uptake also controls brain reward circuitry. Astrocytic ablation by the gliotoxin L-alpha-aminoadipic acid in the prelimbic part of the prefrontal cortex results in both decreased motivation and increased anxiety (Banasr and Duman, 2008). It is important to note, however, that bulk ablation of astrocytes results not only in decreased levels of astrocytic EAAT2 but it can also impair other astrocytic functions such as gliotransmission and metabolic support, and may result in structural changes of synapses. *In vivo* EAAT2 blockade by DHK in the infralimbic part of the prefrontal cortex (John et al., 2012) or intracerebroventricular infusion of DHK (Bechtholt-Gompf et al., 2010) results in depressive-like behaviors and anhedonia, which are translated by a reduction in motivation and reward-seeking. Interestingly, these effects are prevented by EAAT2 up-regulation following ceftriaxone treatment (Mineur et al., 2007).

In contrast, *in vivo* infusion of DHK in the infralimbic part of the prefrontal cortex reduced despair and anxiety (Gasull-Camós et al., 2017). These effects were not observed when DHK was infused in the prelimbic part of the prefrontal cortex. The effect of increased glutamatergic tone, following DHK infusion, might either stimulate local serotoninergic release or increase the transmission of prefrontal inputs to brainstem serotoninergic neurons and subsequently trigger serotonin release in the infralimbic cortex, thus suppressing anxiety. The molecular pathways and synaptic plasticity mechanisms underlying these phenotypes remain to be determined.

The effects of EAAT2 overexpression on hippocampal learning are complex. EAAT2 overexpression by ceftriaxone impairs LTD and reduces LTP magnitude at the mossy fiber-CA3 synapses (Omrani et al., 2009). Ceftriaxone-treated rats or mice display impaired novel object recognition (Matos-Ocasio et al., 2014; Tian et al., 2019), whereas ceftriaxone administration in mice has no effect on spatial memory (Karaman et al., 2013). Inhibition of EAATs with TBOA facilitates hippocampal LTD induction *in vivo* and *ex vivo*, and disrupts spatial memory retrieval in mice (Wong et al., 2007). CA1 hippocampal LTP is also impaired in knock-out mice for either EAAT2 or EAAT3 (Katagiri et al., 2001; Scimemi et al., 2009), although spatial orientation in the Morris water maze when tested in EAAT3-deficient mice remains unaffected (Peghini et al., 1997).

In vivo intrathecal administration of the specific EAAT2 inhibitor DHK impairs LTP of evoked field potentials at C-fiber in the spinal dorsal horn, induced by tetanic stimulation of the sciatic nerve (Wang et al., 2006), and induces spontaneous nociceptive behaviors (Liaw et al., 2005). In addition, an intrathecal infusion of the broad-band EAAT inhibitor TBOA leads to hypersensitivity in response to thermal and mechanical stimuli (Liaw et al., 2005).

Variations in glutamate uptake also affect locomotion. EAAT3 deficient mice display normal motor coordination assessed by rotarod task but a decreased spontaneous locomotion in an open field (Peghini et al., 1997). In contrast, an increased spontaneous locomotion is observed in ceftriaxone-treated rats (Bellesi et al., 2012). Knock-out mice for EAAT1 exhibit motor discoordination in rotarod task (Watase et al., 1998), novelty-induced locomotor hyperactivity measured as an increase in distance traveled during exposure to an open field, and impaired sensory-motor gating translated by reduced acoustic startle response (Karlsson et al., 2008, 2009).

Finally, an inducible astrocytic EAAT2 deletion leads to pathological repetitive behaviors and glutamatergic overactivity (used as a proxy for LTP) in the dorsal striatum

(Aida et al., 2015). This is the first study aiming at linking behavior with the effect of EAAT2 downregulation on synaptic plasticity. This spurious plasticity in EAAT2 knock-out mice is likely induced by excessive glutamate spillover as it is dependent on extrasynaptic NMDARs activation. Moreover, the repetitive behavior was diminished by memantine, an extrasynaptic NMDAR antagonist (Aida et al., 2015).

PHYSIOLOGICAL VARIATION OF EAATs LEVELS

Variations in Glial Coverage and EAATs Expression Across Synapses

Perisynaptic astrocytic processes expressing EAAT1 and EAAT2 are found in all brain regions but the degree of astrocytic coverage is region-specific and the proportion of synapses surrounded by processes can be highly variable within the same structure (Bernardinelli et al., 2014a; Medvedev et al., 2014; Heller and Rusakov, 2015; Khakh and Sofroniew, 2015; Gavrilov et al., 2018). Astrocytic enwrapment of synapses controls the spatial distribution of EAATs and thus their efficiency to uptake glutamate (Oliet et al., 2001; Boudaba et al., 2003; Genoud et al., 2006).

An example of non-uniform distribution of perisynaptic astrocytic processes within the same structure is found in the cerebellum and hippocampus. Climbing fiber–Purkinje cell synapse is extensively enwrapped by astrocytic processes, whereas mossy fiber-granule cell layer synapses (mainly Golgi cells) in the cerebellar vermis are moderately surrounded by astrocytic processes (Xu-Friedman et al., 2001; Xu-Friedman and Regehr, 2003). Mossy fiber-granule cell layer synapses display both rate-based plasticity and STDP depending on the input frequency (D'Errico et al., 2009; Sgritta et al., 2017). Rate-dependent LTD and LTP are induced with LFS ($\leq$1 Hz) and HFS ($>$50 Hz), respectively, while the frequency range for STDP induction is restricted at the mid-frequency range (6–10 Hz; D'Errico et al., 2009; Sgritta et al., 2017). In the hippocampus, CA3 synapses have lower glial coverage compared with CA1 synapses (Derouiche and Frotscher, 1991; Rollenhagen et al., 2007). Interestingly, upregulation of EAAT2 by ceftriaxone prevents LFS-LTP at mossy fiber-CA3 synapses but not at Schaffer collateral-CA1 (Omrani et al., 2009). LTP at CA3 synapses is mediated by presynaptic kainate receptors (Schmitz et al., 2003), which are particularly sensitive to synaptic glutamate levels (Min et al., 1998), whereas LTP at Schaffer collateral-CA1 depends on postsynaptic NMDARs (Nicoll and Malenka, 1995). Therefore, increasing glutamate uptake *via* EAAT2 upregulation selectively alters HFS-LTP at mossy fiber-CA3 synapses (Omrani et al., 2009).

EAAT density can also differ across similar synapses within the same structure. Purkinje cells in the flocculus express higher levels of EAAT4 than Purkinje cells in the vermis and the regional differences in neuronal transporter density affect the expression of parallel fiber-Purkinje cell LFS-LTD (Wadiche and Jahr, 2005). Interestingly, the rules for induction of Purkinje cell LTD also differ between these two regions. In the vermis, both LFS of parallel fibers and input-timing-dependent stimulation of parallel and climbing fibers result in LFS-LTD and t-LTD, respectively (Wadiche and Jahr, 2005; Safo and Regehr, 2008; Suvrathan et al., 2016). In contrast, Purkinje cells of the flocculus exhibit t-LTD but not LFS-LTD (Wadiche and Jahr, 2005; Suvrathan et al., 2016), suggesting that high EAATs levels might disfavor the expression of rate-based plasticity. Lower EAAT4 expression in the vermis may allow both rate-based and spike-timing-based LTD at Purkinje cells, whereas higher levels of EAAT4 in the flocculus may prevent LFS-LTD, but allow t-LTD to occur at larger temporal intervals (Δt_{STDP} = 120 ms; Suvrathan et al., 2016). This may favor the association of non-coincident inputs occurring with a longer delay than the decay time of transporter currents resulting from parallel fiber stimulation (Wadiche and Jahr, 2005; Suvrathan et al., 2016).

Plasticity of Glial Coverage and EAATs Expression

Astrocytic enwrapment of neurons controlling glutamate clearance exhibits structural plasticity in response to neuronal activity and can be modulated by experience. The density of astrocytic processes is increased in the layer II/III of the visual cortex of rats which were reared in an enriched environment with new toys and increased social interactions (Jones et al., 1996). Another type of sensory experience such as prolonged whisker stimulation increases the astrocytic enwrapment of synapses and EAAT2 expression in the sensory cortex (Genoud et al., 2006). Interestingly, following whisker stimulation, the motility of astrocytic endfeets is increased specifically in the corresponding whisker barrel while stimulation of the surrounding whisker fails to induce such effect (Bernardinelli et al., 2014b). Negative experience like stress alters hippocampal EAAT2 expression with a biphasic profile: acute stress, *via* tail shock, downregulates EAAT2 levels (Yang et al., 2005), whereas chronic restraint stress upregulates EAAT2 (Reagan et al., 2004). Different learning paradigms can also trigger structural plasticity of astrocytes and EAATs expression. Motor-skill learning induces glial hypertrophy in the molecular layer of cerebellum leading to a greater volume of glia per Purkinje cell, possibly limiting glutamate spillover (Anderson et al., 1994). Similarly, voluntary free exercise on a running wheel for 3 weeks results in increased ramification and more complex morphology of astrocytic processes in the globus pallidus of mice. These changes are correlated with sustained physical exercise since they disappear after a resting period of additional 3 weeks (Tatsumi et al., 2016). Contextual fear conditioning increases the rate of glutamate uptake and EAAT3 membrane expression in the hippocampal CA1 region (Levenson et al., 2002). This suggests that increased glial ensheathment of synapses and upregulation of glutamate uptake may be especially important for counterbalancing the increased synaptic efficacy and maintaining the synaptic strength following experience-dependent potentiation. Indeed, hippocampal LTP is associated with an increase in the astrocytic coverage of pre- and postsynaptic elements (Lushnikova et al., 2009), an increase in the EAAT3- and EAAT2-dependent glutamate uptake during the early and late phase of LTP, respectively, and EAAT3 translocation from the cytosol to the plasma membrane (Diamond et al., 1998; Lüscher et al., 1998; Levenson et al., 2002; Kawamura et al., 2004; Pita-Almenar et al., 2005, 2006). In addition, LTP-induced astrocytic group-I mGluR-dependent potentiation of EAAT2 glutamate uptake, as well as membrane insertion of EAAT1, has been reported (Shen and Linden, 2005; Devaraju et al., 2013).

Decrease in the glial enwrapment of synapses onto oxytocinergic neurons in the hypothalamus of female rats occurs with the transition to motherhood during the lactation period and these changes are reversed in post-lactating animals (Theodosis and Poulain, 1993). This results in an increase in the tonic glutamate concentration likely due to altered glutamate clearance (Oliet et al., 2001). This, in turn, decreases the probability of glutamate release by activation of presynaptic type-III mGluRs mediated by glutamate spillover (Oliet et al., 2001). Similar retraction of astrocytic endfeet occurs with chronic dehydration when rats drink hypertonic saline for several days (Perlmutter et al., 1985; Chapman et al., 1986), which results in a decreased expression of EAAT2 and activation of presynaptic type-III mGluRs (Boudaba et al., 2003). Increased tonic glutamate concentration activates postsynaptic GluN2B-NMDARs and increases neuronal excitability and firing frequency of hypothalamic neurons (Fleming et al., 2011; Naskar and Stern, 2014). Interestingly, both HFS-LTP and LFS-LTD induced in the hypothalamus of female rats are NMDAR-dependent (Panatier et al., 2006a) and, therefore, might be sensitive to changes in glutamate uptake triggered by astrocytic structural plasticity. The switch in the threshold for plasticity induction in lactating rats is attributed to a decreased GluN2B-NMDARs activation caused by a deficiency in D-serine signaling (Panatier et al., 2006b). An alternative mechanism could be that the retraction of astrocytes and increased glutamate uptake may serve as a high-pass filter, increasing HFS-LTP threshold by prioritizing high-frequency afferent inputs.

Physiological fluctuations in the glial coverage of neurons can occur in a cyclic manner. Indeed, in the arcuate hypothalamic nucleus, the density of astrocyte cell bodies and processes revealed an increased on the afternoon of proestrus and on the morning of estrus compared to other phases of the oestrous cycle. This structural plasticity is dependent on estradiol and absent in ovariectomized rats (Garcia-Segura et al., 1994). Neurons in the suprachiasmatic hypothalamic nucleus undergo rhythmic ultrastructural rearrangements in their astrocytic coverage over the circadian cycle (Lavialle et al., 2001; Becquet et al., 2008). Importantly, this structural plasticity is synapse-specific. At nighttime, the glial coverage of neurons expressing the vasoactive intestinal peptide increases, whereas the glial coverage of arginine vasopressin-expressing neurons decreases (Becquet et al., 2008). Glutamate uptake is crucial in the regulation of neuronal circadian oscillations (Brancaccio et al., 2017). Sleep deprivation induces upregulation of EAAT1 and increased glial coverage in the prefrontal cortex (Bellesi et al., 2015). In contrast, sleep deprivation has a synapse-specific effect in the lateral hypothalamus as it decreases EAAT2 expression around wake-promoting orexin neurons, while it increases EAAT2 around sleep-promoting melanin-concentrating hormone neurons (Briggs et al., 2018). In conclusion, EAATs exert a tight control of endogenous rhythms by regulating the degree of coordination between neurons and most likely by setting the threshold for synaptic plasticity induction.

It should be taken into consideration that some experimental conditions can affect glial coverage and thus synaptic plasticity. Indeed, acute brain slice preparation and incubation methods (**Table 1**) may alter the ultrastructure of the neuropil (Bourne et al., 2007; Bourne and Harris, 2012; Harris and Bourne, 2012) and likely the morphology of the fine astrocytic processes, which in turn could affect long-term synaptic plasticity expression. Exposure to ice-cold artificial cerebrospinal fluid (ACSF) has been reported to induce synaptogenesis and increase in spine density in acute hippocampal slices, which can be prevented if slices are prepared at room temperature (Bourne et al., 2007; Bourne and Harris, 2012). Similarly, incubation of acute hippocampal slices in submerged chamber results in a loss or retraction of astrocytic process but can be prevented if slices are incubated in an interface chamber (Harris and Bourne, 2012).

CONCLUSIONS AND FUTURE DIRECTIONS

Here, we reviewed studies evidencing that the subtle equilibrium between the localization and density of EAATs, together with the glial coverage of neurons, shapes not only excitatory transmission but also long-term synaptic plasticity, thus impacting on learning and memory. Interestingly, baseline GABAergic is not affected by the decrease in the astrocytic enwrapment of neurons and increased levels of ambient glutamate. Indeed, resting glutamate concentrations are not sufficient to tonically activate type-III mGluRs located on GABAergic terminals in the hypothalamus of lactating rats (Piet et al., 2004). However, the evoked inhibitory transmission is decreased when glutamatergic terminals are activated. This results in intersynaptic crosstalk and activation of presynaptic type-III mGluRs (Piet et al., 2004), or kainate receptors (Bonfardin et al., 2010) on GABAergic terminals (**Figure 1**). It remains to determine whether, in addition to glutamatergic synaptic plasticity (**Figure 3**), EAATs also control long-term synaptic plasticity of GABAergic inputs. Physiological fluctuations (Theodosis and Poulain, 1993; Garcia-Segura et al., 1994; Becquet et al., 2008; Briggs et al., 2018) and regional differences (Wadiche and Jahr, 2005) in the glial coverage of neurons and EAATs levels might thus regulate the balance between synaptic excitation and inhibition and shape excitatory and inhibitory synaptic plasticity (Vogels et al., 2013).

Increase in the glial coverage of neurons together with EAATs expression and/or proximity to presynaptic release sites would limit glutamate access to receptors involved in synaptic plasticity (Omrani et al., 2009; Valtcheva and Venance, 2016), thus increasing the threshold for plasticity induction and preventing synaptic crosstalk. Indeed, protrusion of astrocytic processes increases EAAT2 activity, without altering EAAT2 expression, and decreases the magnitude of HFS-LTP at Schaffer collateral-CA synapses (Pannasch et al., 2014). EAAT2 might differentially control synaptic plasticity depending on the type of postsynaptic neuron. Interestingly, synaptic glutamatergic tone is higher around inhibitory neurons compared to excitatory neurons in the prefrontal cortex likely caused by a difference in the density or activity of EAAT2 (Yao et al., 2018). Therefore long-term synaptic plasticity of inhibitory neurons (Kullmann and Lamsa, 2007; Fino and Venance, 2011) might be particularly sensitive to upregulation of glutamate uptake.

Under weak glial coverage of neurons (Perlmutter et al., 1985; Theodosis and Poulain, 1993; Becquet et al., 2008), the ambient glutamatergic tone is high due to decreased glutamate uptake (Oliet et al., 2001). This may cause synapses to become less sensitive to the precise timing of pre- and post-synaptic spikes, thus inducing a switch from spike-timing- to rate-coding. In this scenario, only high-frequency trains of presynaptic activity would be successful in inducing long-term synaptic plasticity. EAATs expression and their proximity to the synapse may, therefore, serve as a metaplastic mechanism to influence activity-dependent plasticity induction. Adjusting neuronal computations by EAATs may be important for synapses to adapt to different physiological demands (during sleep/wake cycle, circadian cycle, estrous cycle, lactation).

The question of whether individual neurons encode and process information by using precise spike timings, thus, working as coincidence detectors, or spike rates, thus, working as temporal integrators, has been debated (deCharms and Zador, 2000). Both mechanisms generally coexist in the same neuron. In the prefrontal cortex, depending on the synaptic inputs to layer V pyramidal neurons, dendrites behave either as temporal integrators or as coincident detectors (Dembrow et al., 2015). Neurons in the subthalamic nucleus operate by combining integration and coincidence detection depending on the ongoing presynaptic activity (Farries et al., 2010). Theoretical work has shown that cortical pyramidal neurons are capable of operating in a continuum between temporal integration and coincidence detection, depending on the characteristics of the synaptic inputs (Rudolph and Destexhe, 2003). Here, we hypothesize that EAATs levels, their distribution and/or astrocytic enwrapment of neurons may define if neurons operate in a rate- or spike-timing-based manner.

Future advances in *in vivo* two-photon imaging would allow chronic (hours or days) monitoring of astrocytic processes across different physiological states. This will make possible to image the motility of perisynaptic astrocytic endfeets around fluorescently-tagged spines of identified neuronal populations. Simultaneous monitoring of astrocytic structural rearrangements and dendritic spine remodeling of specific neuronal types will help establish a model of their dynamic relationship during learning, sensory stimulation and physiological rhythms. Perisynaptic astrocytic endfeets are highly dynamic *in vivo* (Bernardinelli et al., 2014b), and coupling *in vivo* imaging of astrocytes with *in vivo* whole-cell recordings of individual neurons would allow correlating astrocytic structural rearrangement and synaptic transmission and plasticity.

Genetic and pharmacological approaches have proved the crucial involvement of EAATs in synaptic plasticity. However, these tools do not provide information about the dynamics of EAATs activity at fast timescale, which may be essential for regulating the activation of synaptic and extrasynaptic glutamate receptors and thus shaping different forms of plasticity. With the rise of new tools allowing photocontrol of protein activity (Kramer et al., 2013; Durand-de Cuttoli et al., 2018) and high-speed glutamate imaging *via* the intensity-based glutamate-sensing fluorescent reporter iGluSnFR and its fast variants (Marvin et al., 2013; Parsons et al., 2016; Helassa et al., 2018), it would be possible to manipulate EAATs activity at a millisecond timescale and monitor the time course of glutamate in coordination with pre- and postsynaptic activity. An important advance of optical methods compared to biochemical assays in measuring glutamate transport is that the time course of evoked fluorescent responses reflects transporter-mediated uptake as well as glutamate diffusion. Another crucial factor is that genetically encoded sensors can be driven under the control of a specific promoter allowing measurement of glutamate sensed at the plasma membrane of neurons, compared to glutamate responses at the astrocytic membrane measured by astrocytic transporter currents. With these powerful tools, it would be particularly interesting to explore whether EAATs activity and astrocytic coverage of synapses across different brain regions tune the sensitivity of synapses to rate- and/or STDP paradigms (Wadiche and Jahr, 2005; Suvrathan et al., 2016).

AUTHOR CONTRIBUTIONS

SV and LV wrote the review article, have edited and corrected the manuscript. SV did the figures and the table.

FUNDING

This work was supported by Université de Recherche Paris-Sciences-et-Lettres (PSL).

REFERENCES

Aida, T., Yoshida, J., Nomura, M., Tanimura, A., Iino, Y., Soma, M., et al. (2015). Astroglial glutamate transporter deficiency increases synaptic excitability and leads to pathological repetitive behaviors in mice. *Neuropsychopharmacology* 40, 1569–1579. doi: 10.1038/npp.2015.26

Anderson, B. J., Li, X., Alcantara, A. A., Isaacs, K. R., Black, J. E., and Greenough, W. T. (1994). Glial hypertrophy is associated with synaptogenesis following motor-skill learning, but not with angiogenesis following exercise. *Glia* 80, 73–80. doi: 10.1002/glia.440110110

Armbruster, M., Hanson, E., and Dulla, C. G. (2016). Glutamate clearance is locally modulated by presynaptic neuronal activity in the cerebral cortex. *J. Neurosci.* 36, 10404–10415. doi: 10.1523/JNEUROSCI.2066-16.2016

Arnth-Jensen, N., Jabaudon, D., and Scanziani, M. (2002). Cooperation between independent hippocampal synapses is controlled by glutamate uptake. *Nat. Neurosci.* 5, 325–331. doi: 10.1038/nn825

Arriza, J. L., Eliasof, S., Kavanaugh, M. P., and Amara, S. G. (1997). Excitatory amino acid transporter 5, a retinal glutamate transporter coupled to a chloride conductance. *Proc. Natl. Acad. Sci. U S A* 94, 4155–4160. doi: 10.1073/pnas.94.8.4155

Arriza, J. L., Fairman, W. A., Wadiche, I., Murdoch, G. H., Kavanaugh, P., and Amara, S. G. (1994). Functional comparisons of three glutamate cloned from human motor cortex transporter. *J. Neurosci.* 14, 5559–5569. doi: 10.1523/JNEUROSCI.14-09-05559.1994

Asztely, F., Erdemli, G., and Kullmann, D. M. (1997). Extrasynaptic glutamate spillover in the hippocampus: dependence on temperature and the role of active glutamate uptake. *Neuron* 18, 281–293. doi: 10.1016/s0896-6273(00)80268-8

Attwell, D., and Gibb, A. (2005). Neuroenergetics and the kinetic design of excitatory synapses. *Nat. Rev. Neurosci.* 6, 841–849. doi: 10.1038/nrn1784

Banasr, M., and Duman, R. S. (2008). Glial loss in the prefrontal cortex is sufficient to induce depressive-like behaviors. *Biol. Psychiatry* 64, 863–870. doi: 10.1016/j.biopsych.2008.06.008

Barbour, B., and Häusser, M. (1997). Intersynaptic diffusion of neurotransmitter. *Trends Neurosci.* 20, 377–384.

Baude, A., Nusser, Z., Roberts, J. D. B., Mulvihill, E., Jeffrey Mcllhinney, R. A., and Somogyi, P. (1993). The metabotropic glutamate receptor (mGluR1 α) is concentrated at perisynaptic membrane of neuronal subpopulations as detected by immunogold reaction. *Neuron* 11, 771–787. doi: 10.1016/0896-6273(93)90086-7

Bauer, E. P., Schafe, G. E., and LeDoux, J. E. (2002). NMDA receptors and L-type voltage-gated calcium channels contribute to long-term potentiation and different components of fear memory formation in the lateral amygdala. *J. Neurosci.* 22, 5239–5249. doi: 10.1523/JNEUROSCI.22-12-05239.2002

Bechtholt-Gompf, A. J., Walther, H. V., Adams, M. A., Carlezon, W. A. Jr., Öngür, D., and Cohen, B. M. (2010). Blockade of astrocytic glutamate uptake in rats induces signs of anhedonia and impaired spatial memory. *Neuropsychopharmacology* 35, 2049–2059. doi: 10.1038/npp.2010.74

Becquet, D., Girardet, C., Guillaumond, F., François-Bellan, A., and Bosler, O. (2008). Ultrastructural plasticity in the rat suprachiasmatic nucleus. *Glia* 56, 294–305. doi: 10.1002/glia.20613

Bellesi, M., de Vivo, L., Tononi, G., and Cirelli, C. (2015). Effects of sleep and wake on astrocytes: clues from molecular and ultrastructural studies. *BMC Biol.* 13:66. doi: 10.1186/s12915-015-0176-7

Bellesi, M., Vyazovskiy, V. V., Tononi, G., Cirelli, C., and Conti, F. (2012). Reduction of EEG theta power and changes in motor activity in rats treated with ceftriaxone. *PLoS One* 7:e34139. doi: 10.1371/journal.pone.0034139

Bellini, S., Fleming, K. E., De, M., McCauley, J. P., Petroccione, M. A., D'Brant, L. Y., et al. (2018). Neuronal glutamate transporters control dopaminergic signaling and compulsive behaviors. *J. Neurosci.* 38, 937–961. doi: 10.1523/JNEUROSCI.1906-17.2017

Bergles, D. E., Dzubay, J. A., and Jahr, C. E. (1997). Glutamate transporter currents in bergmann glial cells follow the time course of extrasynaptic glutamate. *Proc. Natl. Acad. Sci. U S A* 94, 14821–14825. doi: 10.1073/pnas.94.26.14821

Bergles, D. E., and Jahr, C. E. (1997). Synaptic activation of glutamate transporters in hippocampal astrocytes. *Neuron* 19, 1297–1308. doi: 10.1016/s0896-6273(00)80420-1

Bergles, D. E., and Jahr, C. E. (1998). Glial contribution to glutamate uptake at Schaffer collateral-commissural synapses in the hippocampus. *J. Neurosci.* 18, 7709–7716. doi: 10.1523/JNEUROSCI.18-19-07709.1998

Bergles, D. E., Tzingounis, A. V., and Jahr, C. E. (2002). Comparison of coupled and uncoupled currents during glutamate uptake by GLT-1 transporters. *J. Neurosci.* 22, 10153–10162. doi: 10.1523/JNEUROSCI.22-23-10153.2002

Bernardinelli, Y., Muller, D., and Nikonenko, I. (2014a). Review article astrocyte-synapse structural plasticity. *Neural Plast.* 2014:232105. doi: 10.1155/2014/232105

Bernardinelli, Y., Randall, J., Janett, E., Nikonenko, I., König, S., Jones, E. V., et al. (2014b). Activity-dependent structural plasticity of perisynaptic astrocytic domains promotes excitatory synapse stability. *Curr. Biol.* 24, 1679–1688. doi: 10.1016/j.cub.2014.06.025

Bonfardin, V. D. J., Fossat, P., Theodosis, D. T., and Oliet, S. H. R. (2010). Glia-dependent switch of kainate receptor presynaptic action. *J. Neurosci.* 30, 985–995. doi: 10.1523/JNEUROSCI.3389-09.2010

Boudaba, C., Linn, D. M., Halmos, K. C., and Tasker, J. G. (2003). Increased tonic activation of presynaptic metabotropic glutamate receptors in the rat supraoptic nucleus following chronic dehydration. *J. Physiol.* 551, 815–823. doi: 10.1113/jphysiol.2003.042739

Bourne, J. N., and Harris, K. M. (2012). Coordination of size and number of excitatory and inhibitory synapses results in a balanced. *Hippocampus* 21, 354–373. doi: 10.1002/hipo.20768

Bourne, J. N., Kirov, S. A., Sorra, K. E., and Harris, K. M. (2007). Warmer preparation of hippocampal slices prevents synapse proliferation that might obscure LTP-related structural plasticity. *Neuropharmacology* 52, 55–59. doi: 10.1016/j.neuropharm.2006.06.020

Brancaccio, M., Patton, A. P., Chesham, J. E., Maywood, E. S., Hastings, M. H., Brancaccio, M., et al. (2017). Astrocytes control circadian timekeeping in the suprachiasmatic nucleus via glutamatergic signaling. *Neuron* 93, 1420.e5–1435.e5. doi: 10.1016/j.neuron.2017.02.030

Brasnjo, G., and Otis, T. S. (2001). Neuronal glutamate transporters control activation of postsynaptic metabotropic glutamate receptors and influence cerebellar long-term depression. *Neuron* 31, 607–616. doi: 10.1016/s0896-6273(01)00377-4

Brette, R. (2015). Philosophy of the spike: rate-based vs. spike-based theories of the brain. *Front. Syst. Neurosci.* 9:151. doi: 10.3389/fnsys.2015.00151

Briggs, C., Hirasawa, M., and Semba, K. (2018). Sleep deprivation distinctly alters glutamate transporter 1 apposition and excitatory transmission to orexin and MCH neurons. *J. Neurosci.* 38, 2505–2518. doi: 10.1523/JNEUROSCI.2179-17.2018

Chalifoux, J. R., and Carter, A. G. (2011). Glutamate spillover promotes the generation of NMDA spikes. *J. Neurosci.* 31, 16435–16446. doi: 10.1523/JNEUROSCI.2777-11.2011

Chapman, D., Theodosis, D., Montagnese, C., Poulain, D., and Morris, J. (1986). Osmotic stimulation causes structural plasticity of neurone-glia relationships of the oxytocin but not vasopressin secreting neurones in the hypothalamic supraoptic nucleus. *Neuroscience* 17, 679–686. doi: 10.1016/0306-4522(86)90039-4

Chaudhry, F. A., Lehre, K. P., van Lookeren Campagne, M., Ottersen, O. P., Danbolt, N. C., and Storm-Mathisen, J. (1995). Glutamate transporters in glial plasma membranes: highly differentiated localizations revealed by quantitative ultrastructural immunocytochemistry. *Neuron* 15, 711–720. doi: 10.1016/0896-6273(95)90158-2

Chen, W., Mahadomrongkul, V., Berger, U. V., Bassan, M., DeSilva, T., Tanaka, K., et al. (2004). The glutamate transporter GLT1a is expressed in excitatory axon terminals of mature hippocampal neurons. *J. Neurosci.* 24, 1136–1148. doi: 10.1523/JNEUROSCI.1586-03.2004

Clark, B. A., and Cull-Candy, S. G. (2002). Activity-dependent recruitment of extrasynaptic NMDA receptor activation at an AMPA receptor-only synapse. *J. Neurosci.* 22, 4428–4436. doi: 10.1523/JNEUROSCI.22-11-04428.2002

Clements, J. D., Lester, R. A., Tong, G., Jahr, C. E., and Westbrook, G. L. (1992). The time course of glutamate in the synaptic cleft. *Science* 258, 1498–1501. doi: 10.1126/science.1359647

Coddington, L., Rudolph, S., Vande Lune, P., Overstreet-Wadiche, L., and Wadiche, J. (2013). Spillover-mediated feedforward inhibition functionally segregates interneuron activity. *Neuron* 78, 1050–1062. doi: 10.1016/j.neuron.2013.04.019

Conti, F., Debiasi, S., Minelli, A., Jeffrey, D., and Melone, M. (1998). EAAC1, a high-affinity glutamate tranporter, is localized to astrocytes and GABAergic neurons besides pyramidal cells in the rat cerebral cortex. *Cereb. Cortex* 8, 108–116. doi: 10.1093/cercor/8.2.108

Cooper, L. N., and Bear, M. F. (2012). The BCM theory of synapse modification at 30: interaction of theory with experiment. *Nat. Rev. Neurosci.* 13, 798–810. doi: 10.1038/nrn3353

D'Errico, A., Prestori, F., and D'Angelo, E. (2009). Differential induction of bidirectional long-term changes in neurotransmitter release by frequency-coded patterns at the cerebellar input. *J. Physiol.* 587, 5843–5857. doi: 10.1113/jphysiol.2009.177162

Danbolt, N. C. (2001). Glutamate uptake. *Prog. Neurobiol.* 65, 1–105. doi: 10.1016/S0301-0082(00)00067-8

Danbolt, N. C., Furness, D. N., and Zhou, Y. (2016). Neuronal vs. glial glutamate uptake: resolving the conundrum. *Neurochem. Int.* 98, 29–45. doi: 10.1016/j.neuint.2016.05.009

Danbolt, N. C., Storm-Mathisen, J., and Kanner, B. I. (1992). An [Na^+ + K^+] coupled L-glutamate transporter purified from rat brain is located in glial cell processes. *Neuroscience* 51, 295–310. doi: 10.1016/0306-4522(92)90316-t deCharms, R. C., and Zador, A. (2000). Neural representation and the cortical code. *Annu. Rev. Neurosci.* 24, 1193–1216. doi: 10.1146/annurev.neuro.23.1.613

Dehnes, Y., Chaudhry, F. A., Ullensvang, K., Lehre, K. P., Storm-Mathisen, J., and Danbolt, N. C. (1998). The glutamate transporter EAAT4 in rat cerebellar Purkinje cells: a glutamate-gated chloride channel concentrated near the synapse in parts of the dendritic membrane facing astroglia. *J. Neurosci.* 18, 3606–3619. doi: 10.1523/JNEUROSCI.18-10-03606.1998

Dembrow, N. C., Zemelman, B. V., and Johnston, D. (2015). Temporal dynamics of L5 dendrites in medial prefrontal cortex regulate integration versus coincidence detection of afferent inputs. *J. Neurosci.* 35, 4501–4514. doi: 10.1523/JNEUROSCI.4673-14.2015

Derouiche, A., and Frotscher, M. (1991). Astroglial processes around identified glutamatergic synapses contain glutamine synthetase: evidence for transmitter degradation. *Brain Res.* 552, 346–350. doi: 10.1016/0006-8993(91)90103-3

Devaraju, P., Sun, M.-Y., Myers, T. L., Lauderdale, K., and Fiacco, T. A. (2013). Astrocytic group I mGluR-dependent potentiation of astrocytic glutamate and potassium uptake. *J. Neurophysiol.* 109, 2404–2414. doi: 10.1152/jn.00517.2012

Diamond, J. S., Bergles, D. E., and Jahr, C. E. (1998). Glutamate release monitored with astrocyte transporter currents during LTP. *Neuron* 21, 425–433. doi: 10.1016/s0896-6273(00)80551-6

Diamond, J. S., and Jahr, C. E. (1997). Transporters buffer synaptically released glutamate on a submillisecond time scale. *J. Neurosci.* 17, 4672–4687. doi: 10.1523/JNEUROSCI.17-12-04672.1997

Diamond, J. S., and Jahr, C. E. (2000). Synaptically released glutamate does not overwhelm transporters on hippocampal astrocytes during high-frequency stimulation. *J. Neurophysiol.* 83, 2835–2843. doi: 10.1152/jn.2000.83.5.2835

Durand-de Cuttoli, R., Mondoloni, S., Marti, F., Lemoine, D., Nguyen, C., Naudé, U., et al. (2018). Manipulating midbrain dopamine neurons and reward-related behaviors with light- controllable nicotinic acetylcholine receptors. *Elife* 7:e37487. doi: 10.7554/elife.37487

Dzubay, J. A., and Otis, T. S. (2002). Climbing fiber activation of metabotropic glutamate receptors on cerebellar purkinje neurons. *Neuron* 36, 1159–1167. doi: 10.1016/s0896-6273(02)01052-8

Eliasof, S., and Jahr, C. E. (1996). Retinal glial cell glutamate transporter is coupled to an anionic conductance. *Proc. Natl. Acad. Sci. U S A* 93, 4153–4158. doi: 10.1073/pnas.93.9.4153

Evans, R. C., Morera-Herreras, T., Cui, Y., Du, K., Sheehan, T., Kotaleski, J. H., et al. (2012). The effects of NMDA subunit composition on calcium influx and spike timing-dependent plasticity in striatal medium spiny neurons. *PLoS Comput. Biol.* 8:e1002493. doi: 10.1371/journal.pcbi.1002493

Fairman, W. A., Vandenberg, R. J., Arriza, J. L., Kavanaugh, M. P., and Amara, S. G. (1995). An excitatory amino-acid transporter with properties of a ligand-gated chloride channel. *Nature* 375, 599–603. doi: 10.1038/375599a0

Farries, M. A., Kita, H., and Wilson, C. J. (2010). Dynamic spike threshold and zero membrane slope conductance shape the response of subthalamic neurons to cortical input. *J. Neurosci.* 30, 13180–13191. doi: 10.1523/JNEUROSCI.1909-10.2010

Feldman, D. E. (2012). The spike-timing dependence of plasticity. *Neuron* 75, 556–571. doi: 10.1016/j.neuron.2012.08.001

Fino, E., Paillé, V., Cui, Y., Morera-Herreras, T., Deniau, J.-M., and Venance, L. (2010). Distinct coincidence detectors govern the corticostriatal spike timing-dependent plasticity. *J. Physiol.* 588, 3045–3062. doi: 10.1113/jphysiol.2010.188466

Fino, E., and Venance, L. (2011). Spike-timing dependent plasticity in striatal interneurons. *Neuropharmacology* 60, 780–788. doi: 10.1016/j.neuropharm.2011.01.023

Fleming, T. M., Scott, V., Naskar, K., Joe, N., Brown, C. H., and Stern, J. E. (2011). State-dependent changes in astrocyte regulation of extrasynaptic NMDA receptor signalling in neurosecretory neurons. *J. Physiol.* 589, 3929–3941. doi: 10.1113/jphysiol.2011.207340

Furness, D. N., Dehnes, Y., Akhtar, A. Q., Rossi, D. J., Hamann, M., Grutle, N. J., et al. (2008). A quantitative assessment of glutamate uptake into hippocampal synaptic terminals and astrocytes: new insights into a neuronal role for excitatory amino acid transporter 2 (EAAT2). *Neuroscience* 157, 80–94. doi: 10.1016/j.neuroscience.2008.08.043

Furuta, A., Rothstein, J. D., and Martin, L. J. (1997). Glutamate transporter protein subtypes are expressed differentially during rat CNS development. *J. Neurosci.* 17, 8363–8375. doi: 10.1523/JNEUROSCI.17-21-08363.1997

Garcia-Segura, L. M., Luquín, S., Párducz, A., and Naftolin, F. (1994). Gonadal hormone regulation of glial fibrillary acidic protein immunoreactivity and glial ultrastructure in the rat neuroendocrine hypothalamus. *Glia* 10, 59–69. doi: 10.1002/glia.440100108

Gasull-Camós, J., Tarrés-Gatius, M., Artigas, F., and Castañé, A. (2017). Glial GLT-1 blockade in infralimbic cortex as a new strategy to evoke rapid antidepressant-like effects in rats. *Transl. Psychiatry* 7:e1038. doi: 10.1038/tp.2017.7

Gavrilov, N., Golyagina, I., Brazhe, A., Scimemi, A., Turlapov, V., and Semyanov, A. (2018). Astrocytic coverage of dendritic spines, dendritic shafts, and axonal boutons in hippocampal neuropil. *Front. Cell. Neurosci.* 12:248. doi: 10.3389/fncel.2018.00248

Genoud, C., Quairiaux, C., Steiner, P., Hirling, H., Welker, E., and Knott, G. W. (2006). Plasticity of astrocytic coverage and glutamate transporter expression in adult mouse cortex. *PLoS Biol.* 4:e343. doi: 10.1371/journal.pbio.0040343

Harris, J. N., and Bourne, K. M. (2012). Nanoscale analysis of structural synaptic plasticity. *Curr. Opin. Neurobiol.* 22, 372–382. doi: 10.1016/j.conb.2011.10.019

Helassa, N., Dürst, C. D., Coates, C., Kerruth, S., Arif, U., Schulze, C., et al. (2018). Ultrafast glutamate sensors resolve high-frequency release at Schaffer collateral synapses. *Proc. Natl. Acad. Sci. U S A* 115, 5594–5599. doi: 10.1073/pnas.1720648115

Heller, J. P., and Rusakov, D. A. (2015). Morphological plasticity of astroglia: understanding synaptic microenvironment. *Glia* 63, 2133–2151. doi: 10.1002/glia.22821

Herberg, L. J., and Rose, I. C. (1990). Excitatory amino acid pathways in brain-stimulation reward. *Behav. Brain Res.* 39, 230–239. doi: 10.1016/0166-4328(90)90029-e

Holmseth, S., Scott, H. A., Real, K., Lehre, K. P., Leergaard, T. B., Bjaalie, J. G., et al. (2009). The concentrations and distributions of three C-terminal variants of the GLT1 (EAAT2; slc1a2) glutamate transporter protein in rat brain tissue suggest differential regulation. *Neuroscience* 162, 1055–1071. doi: 10.1016/j.neuroscience.2009.03.048

Huang, Y. H., and Bergles, D. E. (2004). Glutamate transporters bring competition to the synapse. *Curr. Opin. Neurobiol.* 14, 346–352. doi: 10.1016/j.conb.2004.05.007

Huang, Y. Y., and Kandel, E. R. (1998). Postsynaptic induction and PKA-dependent expression of LTP in the lateral amygdala. *Neuron* 21, 169–178. doi: 10.1016/s0896-6273(00)80524-3

Huang, Y. H., Sinha, S. R., Tanaka, K., Rothstein, J. D., and Bergles, D. E. (2004). Glutamate receptor-mediated excitation of hippocampal interneurons. *J. Neurosci.* 24, 4551–4559. doi: 10.1523/JNEUROSCI.5217-03.2004

Janak, P. H., and Tye, K. M. (2015). From circuits to behaviour in the amygdala. *Nature* 517, 284–292. doi: 10.1038/nature14188

John, C. S., Smith, K. L., Van't Veer, A., Gompf, H. S., Carlezon, W. A. Jr., Cohen, B. M., et al. (2012). Blockade of astrocytic glutamate uptake in the prefrontal cortex induces anhedonia. *Neuropsychopharmacology* 37, 2467–2475. doi: 10.1038/npp.2012.105

John, C. S., Sypek, E. I., Carlezon, W. A., Cohen, B. M., Öngür, D., and Bechtholt, A. J. (2015). Blockade of the GLT-1 transporter in the central nucleus of the amygdala induces both anxiety and depressive-like symptoms. *Neuropsychopharmacology* 40, 1700–1708. doi: 10.1038/npp.2015.16

Jones, T. A., Hawrylak, N., and Greenough, W. T. (1996). Rapid laminar-dependent changes in GFAP immunoreactive astrocytes in the visual cortex of rats reared in a complex environment. *Psychoneuroendocrinology* 21, 189–201. doi: 10.1016/0306-4530(95)00041-0

Karaman, I., Kizilay-Ozfidan, G., Karadag, C. H., and Ulugol, A. (2013). Lack of effect of ceftriaxone, a GLT-1 transporter activator, on spatial memory in mice. *Pharmacol. Biochem. Behav.* 108, 61–65. doi: 10.1016/j.pbb.2013.04.013

Karlsson, R. M., Tanaka, K., Heilig, M., and Holmes, A. (2008). Loss of glial glutamate and aspartate transporter (excitatory amino acid transporter 1) causes locomotor hyperactivity and exaggerated responses to psychotomimetics: rescue by haloperidol and metabotropic glutamate 2/3 agonist. *Biol. Psychiatry* 64, 810–814. doi: 10.1016/j.biopsych.2008.05.001

Karlsson, R. M., Tanaka, K., Saksida, L. M., Bussey, T. J., Heilig, M., and Holmes, A. (2009). Assessment of glutamate transporter GLAST (EAAT1)-deficient mice for phenotypes relevant to the negative and executive/cognitive symptoms of schizophrenia. *Neuropsychopharmacology* 34, 1578–1589. doi: 10.1038/npp.2008.215

Katagiri, H., Tanaka, K., and Manabe, T. (2001). Requirement of appropriate glutamate concentrations in the synaptic cleft for hippocampal LTP induction. *Eur. J. Neurosci.* 14, 547–553. doi: 10.1046/j.0953-816x.2001.01664.x

Kawamura, Y., Manita, S., Nakamura, T., Inoue, M., Kudo, Y., and Miyakawa, H. (2004). Glutamate release increases during mossy-CA3 LTP but not during Schaffer-CA1 LTP. *Eur. J. Neurosci.* 19, 1591–1600. doi: 10.1111/j.1460-9568.2004.03258.x

Khakh, B. S., and Sofroniew, M. V. (2015). Diversity of astrocyte functions and phenotypes in neural circuits. *Nat. Neurosci.* 18, 942–952. doi: 10.1038/nn.4043

Kobayashi, K., Manabe, T., and Takahashi, T. (1996). Presynaptic long-term depression at the hippocampal mossy fiber—CA3 synapse. *Science* 273, 648–650. doi: 10.1126/science.273.5275.648

Kramer, R. H., Mourot, A., and Adesnik, H. (2013). Optogenetic pharmacology for control of native neuronal signaling proteins. *Nat. Neurosci.* 16, 816–823. doi: 10.1038/nn.3424

Kullmann, D. M., and Asztely, F. (1998). Extrasynaptic glutamate spillover in the hippocampus: evidence and implications. *Trends Neurosci.* 21, 8–14. doi: 10.1016/s0166-2236(97)01150-8

Kullmann, D. M., Erdemli, G., and Asztély, F. (1996). LTP of AMPA and NMDA receptor-mediated signals: evidence for presynaptic expression and extrasynaptic glutamate spill-over. *Neuron* 17, 461–474. doi: 10.1016/s0896-6273(00)80178-6

Kullmann, D. M., and Lamsa, K. P. (2007). Long-term synaptic plasticity in hippocampal interneurons. *Nat. Rev. Neurosci.* 8, 687–699. doi: 10.1038/nrn2207

Lavialle, M., Begue, A., Papillon, C., and Vilaplana, J. (2001). Modifications of retinal afferent activity induce changes in astroglial plasticity in the hamster circadian clock. *Glia* 100, 88–100. doi: 10.1002/glia.1044

Lee, Y., Gaskins, D., Anand, A., and Shekhar, A. (2007). Glia mechanisms in mood regulation: a novel model of mood disorders. *Psychopharmacology* 191, 55–65. doi: 10.1007/s00213-006-0652-4

Lehre, K. P., Levy, L. M., Storm-mathisen, J., Ottersen, O. P., and Danbolt, N. C. (1995). Differential expression of two glial glutamate transporters in the rat brain: quantitative and lmmunocytochemical observations. *J. Neurosci.* 15, 1835–1853. doi: 10.1523/JNEUROSCI.15-03-01835.1995

Lehre, K. P., and Rusakov, D. A. (2002). Asymmetry of glia near central synapses favors presynaptically directed glutamate escape. *Biophys. J.* 83, 125–134. doi: 10.1016/s0006-3495(02)75154-0

Levenson, J., Weeber, E., Selcher, J. C., Kategaya, L. S., Sweatt, J. D., and Eskin, A. (2002). Long-term potentiation and contextual fear conditioning increase neuronal glutamate uptake. *Nat. Neurosci.* 5, 155–161. doi: 10.1038/nn791

Levy, L. M., Warr, O., and Attwell, D. (1998). Stoichiometry of the glial glutamate transporter GLT-1 expressed inducibly in a Chinese hamster ovary cell line selected for low endogenous Na^+-dependent glutamate uptake. *J. Neurosci.* 18, 9620–9628. doi: 10.1523/JNEUROSCI.18-23-09620.1998

Liaw, W., Stephens, R. L. Jr., Binns, B. C., Chu, Y., Sepkuty, J. P., Johns, R. A., et al. (2005). Spinal glutamate uptake is critical for maintaining normal sensory transmission in rat spinal cord. *Pain* 115, 60–70. doi: 10.1016/j.pain.2005.02.006

Lüscher, C., Malenka, R. C., and Nicoll, R. A. (1998). Monitoring glutamate release during LTP with glial transporter currents. *Neuron* 21, 435–441. doi: 10.1016/s0896-6273(00)80552-8

Lushnikova, I., Skibo, G., Muller, D., and Nikonenko, I. (2009). Synaptic potentiation induces increased glial coverage of excitatory synapses in CA1 hippocampus. *Hippocampus* 19, 753–762. doi: 10.1002/hipo.20551

Malenka, R. C., and Bear, M. F. (2004). LTP and LTD: an embarrassment of riches. *Neuron* 44, 5–21. doi: 10.1016/j.neuron.2004.09.012

Marvin, J., Borghuis, B., Tian, L., Cichon, J., Harnett, M., Akerboom, J., et al. (2013). An optimized fluorescent probe for visualizing glutamate neurotransmission. *Nat. Methods* 2, 162–170. doi: 10.1038/nmeth.2333

Massey, P. V., Johnson, B. E., Moult, P. R., Auberson, Y. P., Brown, M. W., Molnar, E., et al. (2004). Differential roles of NR2A and NR2B-containing NMDA receptors in cortical long-term potentiation and long-term depression. *J. Neurosci.* 24, 7821–7828. doi: 10.1523/JNEUROSCI.1697-04.2004

Matos-Ocasio, F., Hernández-López, A., and Thompson, K. J. (2014). Ceftriaxone, a GLT-1 transporter activator, disrupts hippocampal learning in rats. *Pharmacol. Biochem. Behav.* 122, 118–121. doi: 10.1016/j.pbb.2014.03.011

Medvedev, N., Popov, V., Henneberger, C., Kraev, I., Rusakov, D. A., and Stewart, M. G. (2014). Glia selectively approach synapses on thin dendritic spines. *Philos. Trans. R. Soc. B Biol. Sci.* 369:20140047. doi: 10.1098/rstb.2014.0047

Melone, M., Bellesi, M., and Conti, F. (2009). Synaptic localization of GLT-1a in the rat somatic sensory cortex. *Glia* 57, 108–117. doi: 10.1002/glia.20744

Melone, M., Bellesi, M., Ducati, A., Iacoangeli, M., and Conti, F. (2011). Cellular and synaptic localization of EAAT2a in human cerebral cortex. *Front. Neuroanat.* 4:151. doi: 10.3389/fnana.2010.00151

Min, M., Rusakov, D. A., and Kullmann, D. M. (1998). Activation of AMPA, kainate, and metabotropic receptors at hippocampal mossy fiber synapses: role of glutamate diffusion. *Neuron* 21, 561–570. doi: 10.1016/s0896-6273(00)80566-8

Minelli, A., Barbaresi, P., Reimer, R. J., Edwards, R. H., and Conti, F. (2001). The glial glutamate transporter GLT-1 is localized both in the vicinity of and at distance from axon terminals in the rat cerebral cortex. *Neuroscience* 108, 51–59. doi: 10.1016/s0306-4522(01)00375-x

Mineur, Y. S., Picciotto, M. R., and Sanacora, G. (2007). Antidepressant-like effects of ceftriaxone in male C57BL/6J mice. *Biol. Psychiatry* 61, 250–252. doi: 10.1016/j.biopsych.2006.04.037

Murphy-Royal, C., Dupuis, J. P., Varela, J. A., Panatier, A., Pinson, B., Baufreton, J., et al. (2015). Surface diffusion of astrocytic glutamate transporters shapes synaptic transmission. *Nat. Neurosci.* 18, 219–226. doi: 10.1038/nn.3901

Naskar, K., and Stern, J. E. (2014). A functional coupling between extrasynaptic NMDA receptors and A-type K^+ channels under astrocyte control regulates hypothalamic neurosecretory neuronal activity. *J. Physiol.* 592, 2813–2827. doi: 10.1113/jphysiol.2014.270793

Nicoll, R., and Malenka, R. (1995). Contrasting properties of two forms of long-term potentiation in the hippocampus. *Nature* 377, 115–118. doi: 10.1038/377115a0

Oliet, S. H., Piet, R., and Poulain, D. A. (2001). Control of glutamate clearance and synaptic efficacy by glial coverage of neurons. *Science* 292, 923–926. doi: 10.1126/science.1059162

Omrani, A., Melone, M., Bellesi, M., Safiulina, V., Aida, T., Tanaka, K., et al. (2009). Up-regulation of GLT-1 severely impairs LTD at mossy fibre-CA3 synapses. *J. Physiol.* 587, 4575–4588. doi: 10.1113/jphysiol.2009.177881

Owe, S. G., Marcaggi, P., and Attwell, D. (2006). The ionic stoichiometry of the GLAST glutamate transporter in salamander retinal glia. *J. Physiol.* 577, 591–599. doi: 10.1113/jphysiol.2006.116830

Panatier, A., Gentles, S. J., Bourque, C. W., and Oliet, S. H. R. (2006a). Activity-dependent synaptic plasticity in the supraoptic nucleus of the rat hypothalamus. *J. Physiol.* 573, 711–721. doi: 10.1113/jphysiol.2006.109447

Panatier, A., Theodosis, D. T., Mothet, J., Touquet, B., Pollegioni, L., Poulain, D. A., et al. (2006b). Glia-derived D-serine controls NMDA receptor activity and synaptic memory. *Cell* 125, 775–784. doi: 10.1016/j.cell.2006.02.051

Pannasch, U., Freche, D., Dallérac, G., Ghézali, G., Escartin, C., Ezan, P., et al. (2014). Connexin 30 sets synaptic strength by controlling astroglial synapse invasion. *Nat. Neurosci.* 17, 549–558. doi: 10.1038/nn.3662

Paoletti, P., Bellone, C., and Zhou, Q. (2013). NMDA receptor subunit diversity: impact on receptor properties, synaptic plasticity and disease. *Nat. Rev. Neurosci.* 14, 383–400. doi: 10.1038/nrn3504

Parsons, M. P., Vanni, M. P., Woodard, C. L., Kang, R., Murphy, T. H., and Raymond, L. A. (2016). Real-time imaging of glutamate clearance reveals normal striatal uptake in Huntington disease mouse models. *Nat. Commun.* 7:11251. doi: 10.1038/ncomms11251

Peghini, P., Janzen, J., and Stoffel, W. (1997). Glutamate transporter EAAC-1-deficient mice develop dicarboxylic aminoaciduria and behavioral abnormalities but no neurodegeneration. *EMBO J.* 16, 3822–3832. doi: 10.1093/emboj/16.13.3822

Perlmutter, L. S., Tweedle, C. D., and Hatton, G. I. (1985). Neuronal/glial plasticity in the supraoptic dendritic zone in response to acute and chronic dehydration. *Brain Res.* 361, 225–232. doi: 10.1016/0006-8993(85)91293-4

Petr, G. T., Sun, Y., Frederick, X. N. M., Zhou, Y., Dhamne, S. C., Hameed, X. M. Q., et al. (2015). Conditional deletion of the glutamate transporter GLT-1 reveals that astrocytic GLT-1 protects against fatal epilepsy while neuronal GLT-1 contributes significantly to glutamate uptake into synaptosomes. *J. Neurosci.* 35, 5187–5201. doi: 10.1523/jneurosci.4255-14.2015

Piet, R., Vargová, L., Syková, E., Poulain, D. A., and Oliet, S. H. R. (2004). Physiological contribution of the astrocytic environment of neurons to intersynaptic crosstalk. *Proc. Natl. Acad. Sci. U S A* 101, 2151–2155. doi: 10.1073/pnas.0308408100

Pita-Almenar, J. D., Collado, M. S., Colbert, C. M., and Eskin, A. (2006). Different mechanisms exist for the plasticity of glutamate reuptake during early long-term potentiation (LTP) and late LTP. *J. Neurosci.* 26, 10461–11071. doi: 10.1523/jneurosci.2579-06.2006

Pita-Almenar, J. D., Zou, S., Colbert, C. M., and Eskin, A. (2005). Relationship between increase in astrocytic GLT-1 glutamate transport and late-LTP. *Learn. Mem.* 19, 615–626. doi: 10.1101/lm.023259.111

Randić, M., Jiang, M. C., and Cerne, R. (1993). Long-term potentiation and long-term depression of primary afferent neurotransmission in the rat spinal cord. *J. Neurosci.* 13, 5228–5241. doi: 10.1523/jneurosci.13-12-05228.1993

Reagan, L. P., Rosell, D. R., Wood, G. E., Spedding, M., Mun, C., Rothstein, J., et al. (2004). Chronic restraint stress up-regulates GLT-1 mRNA and protein expression in the rat hippocampus: reversal by tianeptine. *Proc. Natl. Acad. Sci. U S A* 101, 2179–2184. doi: 10.1073/pnas.0307294101

Reichelt, W., and Knöpfel, T. (2002). Glutamate uptake controls expression of a slow postsynaptic current mediated by mGluRs in cerebellar Purkinje cells. *J. Neurophysiol.* 87, 1974–1980. doi: 10.1152/jn.00704.2001

Rimmele, T. S., and Rosenberg, P. A. (2016). GLT-1: the elusive presynaptic glutamate transporter. *Neurochem. Int.* 98, 19–28. doi: 10.1016/j.neuint.2016.04.010

Rollenhagen, A., Sätzler, K., Rodríguez, E. P., Jonas, P., Frotscher, M., and Lübke, J. H. R. (2007). Structural determinants of transmission at large hippocampal mossy fiber synapses. *J. Neurosci.* 27, 10434–10444. doi: 10.1523/JNEUROSCI.1946-07.2007

Rothstein, J. D., Levey, A. I., Dykes-hoberg, M., Jin, L., Wu, D., Nash, N., et al. (1994). localization of neuronal and glial glutamate transporters. *Neuron* 13, 713–725. doi: 10.1016/0896-6273(94)90038-8

Rothstein, J. D., Patel, S., Regan, M. R., Haenggeli, C., Huang, Y. H., Bergles, D. E., et al. (2005). Beta-lactam antibiotics offer neuroprotection by increasing glutamate transporter expression. *Nature* 433, 73–77. doi: 10.1038/nature03180

Rudolph, M., and Destexhe, A. (2003). Tuning neocortical pyramidal neurons between integrators. *J. Comput. Neurosci.* 14, 239–251. doi: 10.1023/A:1023245625896

Rusakov, D. A., and Kullmann, D. M. (1998). Extrasynaptic glutamate diffusion in the hippocampus: ultrastructural constraints, uptake, and receptor activation. *J. Neurosci.* 18, 3158–3170. doi: 10.1523/jneurosci.18-09-03158.1998

Safo, P., and Regehr, W. G. (2008). Timing dependence of the induction of cerebellar LTD patrick. *Neuropharmacology* 54, 213–218. doi: 10.1016/j.neuropharm.2007.05.029

Scanziani, M., Salin, P., Vogt, K., Malenka, R., and Nicoll, R. (1997). Use-dependent increases in glutamate concentration activate presynaptic metabotropic glutamate receptors. *Nature* 385, 630–634. doi: 10.1038/385630a0

Schmitz, D., Mellor, J., Breustedt, J., and Nicoll, R. A. (2003). Presynaptic kainate receptors impart an associative property to hippocampal mossy fiber long-term potentiation. *Nat. Neurosci.* 6, 1058–1063. doi: 10.1038/nn1116

Schneider, N., Cordeiro, S., Machtens, J. P., Braams, S., Rauen, T., and Fahlke, C. (2014). Functional properties of the retinal glutamate transporters GLT-1c and EAAT 5. *J. Biol. Chem.* 289, 1815–1824. doi: 10.1074/jbc.m113.517177

Scimemi, A., Fine, A., Kullmann, D. M., and Rusakov, D. A. (2004). NR2B-containing receptors mediate cross talk among hippocampal synapses. *J. Neurosci.* 24, 4767–4777. doi: 10.1523/jneurosci.0364-04.2004

Scimemi, A., Tian, H., and Diamond, J. S. (2009). Neuronal transporters regulate glutamate clearance, NMDA receptor activation, and synaptic plasticity in the hippocampus. *J. Neurosci.* 29, 14581–14595. doi: 10.1523/jneurosci.4845-09.2009

Sgritta, M., Prestori, F., and D'Angelo, E. (2017). Hebbian spike-timing dependent plasticity at the cerebellar input stage. *J. Neurosci.* 37, 2809–2823. doi: 10.1523/jneurosci.2079-16.2016

Shen, Y., and Linden, D. J. (2005). Long-term potentiation of neuronal glutamate transporters. *Neuron* 46, 715–722. doi: 10.1016/j.neuron.2005.04.033

Sjöström, P. J., Rancz, A., Roth, A., and Häusser, M. (2008). Dendritic excitability and synaptic plasticity. *Physiol. Rev.* 88, 769–840. doi: 10.1152/physrev.00016.2007

Suvrathan, A., Payne, H. L., and Raymond, J. L. (2016). Timing rules for synaptic plasticity matched to behavioral function. *Neuron* 92, 959–967. doi: 10.1016/j.neuron.2016.10.022

Szapiro, G., and Barbour, B. (2007). Multiple climbing fibers signal to molecular layer interneurons exclusively via glutamate spillover. *Nat. Neurosci.* 10, 735–742. doi: 10.1038/nn1907

Tanaka, J., Ichikawa, R., Watanabe, M., Tanaka, K., and Inoue, Y. (1997). Extra-junctional localization of glutamate transporter EAAT4 at excitatory Purkinje cell synapses. *Neuroreport* 8, 2461–2464. doi: 10.1097/00001756-199707280-00010

Tatsumi, K., Okuda, H., Morita-Takemura, S., Tanaka, T., Isonishi, A., Shinjo, T., et al. (2016). Voluntary exercise induces astrocytic structural plasticity in the globus pallidus. *Front. Cell. Neurosci.* 10:165. doi: 10.3389/fncel.2016.00165

Theodosis, D. T., and Poulain, D. A. (1993). Activity-dependent neuronal-glial and synaptic plasticity in the adult mammalian hypothalamus. *Neuroscience* 57, 501–535. doi: 10.1016/0306-4522(93)90002-w

Tian, S.-W., Yu, X.-D., Cen, L., and Xiao, Z.-Y. (2019). Glutamate transporter GLT1 inhibitor dihydrokainic acid impairs novel object recognition memory performance in mice. *Physiol. Behav.* 199, 28–32. doi: 10.1016/j.physbeh.2018.10.019

Tong, G., and Jahr, E. (1994). Block of glutamate transporters potentiates synaptic excitation. *Neuron* 13, 1195–1203. doi: 10.1016/0896-6273(94)90057-4

Tsvetkov, E., Carlezon, W. A., Benes, F. M., Kandel, E. R., and Bolshakov, V. Y. (2002). Fear conditioning occludes LTP-induced presynaptic enhancement of synaptic transmission in the cortical pathway to the lateral amygdala. *Neuron* 34, 289–300. doi: 10.1016/s0896-6273(02)00645-1

Tsvetkov, E., Shin, R. M., and Bolshakov, V. Y. (2004). Glutamate uptake determines pathway specificity of long-term potentiation in the neural circuitry of fear conditioning. *Neuron* 41, 139–151. doi: 10.1016/s0896-6273(03)00800-6

Tzingounis, A. V., and Wadiche, J. I. (2007). Glutamate transporters: confining runaway excitation by shaping synaptic transmission. *Nat. Rev. Neurosci.* 8, 935–947. doi: 10.1038/nrn2274

Valtcheva, S., and Venance, L. (2016). Astrocytes gate Hebbian synaptic plasticity in the striatum. *Nat. Commun.* 7:13845. doi: 10.1038/ncomms13845

Vandenberg, R. J., and Ryan, R. M. (2013). Mechanisms of glutamate transport. *Physiol. Rev.* 93, 1621–1657. doi: 10.1152/physrev.00007.2013

Veruki, M. L., Mørkve, S. H., and Hartveit, E. (2006). Activation of a presynaptic glutamate transporter regulates synaptic transmission through electrical signaling. *Nat. Neurosci.* 9, 1388–1396. doi: 10.1038/nn1793

Vogels, T. P., Froemke, R. C., Doyon, N., Gilson, M., Haas, J. S., Liu, R., et al. (2013). Inhibitory synaptic plasticity: spike timing-dependence and putative network function. *Front. Neural Circuits* 7:119. doi: 10.3389/fncir.2013.00119

Wadiche, J. I., Amara, S. G., and Kavanaugh, M. P. (1995). Ion fluxes associated with excitatory amino acid transport. *Neuron* 15, 721–728. doi: 10.1016/0896-6273(95)90159-0

Wadiche, J. I., and Jahr, C. E. (2005). Patterned expression of Purkinje cell glutamate transporters controls synaptic plasticity. *Nat. Neurosci.* 8, 1329–1334. doi: 10.1038/nn1539

Wadiche, J. I., and Kavanaugh, M. P. (1998). Macroscopic and microscopic properties of a cloned glutamate transporter/chloride channel. *J. Neurosci.* 18, 7650–7661. doi: 10.1523/jneurosci.18-19-07650.1998

Wang, Z., Park, S. H., Zhao, H., Peng, S., and Zuo, Z. (2014). A critical role of glutamate transporter type 3 in the learning and memory of mice. *Neurobiol. Learn. Mem.* 114, 70–80. doi: 10.1016/j.nlm.2014.04.012

Wang, Z.-Y., Zhang, Y.-Q., and Zhao, Z.-Q. (2006). Inhibition of tetanically sciatic stimulation-induced LTP of spinal neurons and Fos expression by disrupting glutamate transporter GLT- 1. *Neuropharmacology* 51, 764–772. doi: 10.1016/j.neuropharm.2006.05.024

Watase, K., Hashimoto, K., Kano, M., Yamada, K., Watanabe, M., Inoue, Y., et al. (1998). Motor discoordination and increased susceptibility to cerebellar injury in GLAST mutant mice. *Eur. J. Neurosci.* 10, 976–988. doi: 10.1046/j.1460-9568.1998.00108.x

Wong, T. P., Howland, J. G., Robillard, J. M., Ge, Y., Yu, W., Titterness, A. K., et al. (2007). Hippocampal long-term depression mediates acute stress-induced spatial memory retrieval impairment. *Proc. Natl. Acad. Sci. U S A* 104, 11471–11476. doi: 10.1073/pnas.0702308104

Xu-Friedman, M. A., Harris, K. M., and Regehr, W. G. (2001). Three-dimensional comparison of ultrastructural characteristics at depressing and facilitating synapses onto cerebellar purkinje cells. *J. Neurosci.* 21, 6666–6672. doi: 10.1523/JNEUROSCI.21-17-06666.2001

Xu-Friedman, M. A., and Regehr, W. G. (2003). Ultrastructural contributions to desensitization at cerebellar mossy fiber to granule cell synapses. *J. Neurosci.* 23, 2182–2192. doi: 10.1523/jneurosci.23-06-02182.2003

Yang, C.-H., Huang, C.-C., and Hsu, K.-S. (2005). Behavioral stress enhances hippocampal CA1 long-term depression through the blockade of the glutamate uptake. *J. Neurosci.* 25, 4288–4293. doi: 10.1523/jneurosci.0406-05.2005

Yao, L., Grand, T., Hanson, J., Paoletti, P., and Zhou, Q. (2018). Higher ambient synaptic glutamate at inhibitory versus excitatory neurons differentially impacts NMDA receptor activity. *Nat. Commun.* 9:4000. doi: 10.1038/s41467-018-06512-7

Yokoi, M., Kobayashi, K., Manabe, T., Takahashi, T., Sakaguchi, I., Katsuura, G., et al. (1996). Impairment of hippocampal mossy fiber LTD in mice lacking mGluR2. *Science* 273, 645–647. doi: 10.1126/science.273.5275.645

Zerangue, N., and Kavanaugh, M. P. (1996). Flux coupling in a neuronal glutamate transporter. *Nature* 383, 634–637. doi: 10.1038/383634a0

Zheng, K., Scimemi, A., and Rusakov, D. A. (2008). Receptor actions of synaptically released glutamate: the role of transporters on the scale from nanometers to microns. *Biophys. J.* 95, 4584–4596. doi: 10.1529/biophysj.108.129874

Conflict of Interest Statement: The authors declare that the research was conducted in the absence of any commercial or financial relationships that could be construed as a potential conflict of interest.

frontiers
in Synaptic Neuroscience

ORIGINAL RESEARCH
published: 14 May 2019
doi: 10.3389/fnsyn.2019.00014

Major Contribution of Somatostatin-Expressing Interneurons and Cannabinoid Receptors to Increased GABA Synaptic Activity in the Striatum of Huntington's Disease Mice

Sandra M. Holley, Laurie Galvan, Talia Kamdjou, Ashley Dong, Michael S. Levine and Carlos Cepeda*

Intellectual and Developmental Disabilities Research Center, Department of Psychiatry and Biobehavioral Sciences, Jane and Terry Semel Institute for Neuroscience and Human Behavior, Brain Research Institute, University of California, Los Angeles, Los Angeles, CA, United States

OPEN ACCESS

Edited by:
Laurent Venance,
INSERM U1050 Centre Interdisciplinaire de Recherche en Biologie, France

Reviewed by:
Giuseppe Sciamanna,
University of Rome Tor Vergata, Italy
Atsuo Fukuda,
Hamamatsu University School of Medicine, Japan

***Correspondence:**
Carlos Cepeda
ccepeda@mednet.ucla.edu

Received: *27 January 2019*
Accepted: *23 April 2019*
Published: *14 May 2019*

Citation:
Holley SM, Galvan L, Kamdjou T, Dong A, Levine MS and Cepeda C (2019) Major Contribution of Somatostatin-Expressing Interneurons and Cannabinoid Receptors to Increased GABA Synaptic Activity in the Striatum of Huntington's Disease Mice. Front. Synaptic Neurosci. 11:14. doi: 10.3389/fnsyn.2019.00014

Huntington's disease (HD) is a heritable neurological disorder that affects cognitive and motor performance in patients carrying the mutated *huntingtin (HTT)* gene. In mouse models of HD, previous reports showed a significant increase in spontaneous GABA_A receptor-mediated synaptic activity in striatal spiny projection neurons (SPNs). In this study, using optogenetics and slice electrophysiology, we examined the contribution of γ-aminobutyric acid (GABA)-ergic parvalbumin (PV)- and somatostatin (SOM)-expressing interneurons to the increase in GABA neurotransmission using the Q175 (heterozygote) mouse model of HD. Patch clamp recordings in voltage-clamp mode were performed on SPNs from brain slices of presymptomatic (2 months) and symptomatic (8 and 12 months) Q175 mice and wildtype (WT) littermates. While inhibitory postsynaptic currents (IPSCs) evoked in SPNs following optical activation of PV- and SOM-expressing interneurons differed in amplitude, no genotype-dependent differences were observed at all ages from both interneuron types; however, responses evoked by either type were found to have faster kinetics in symptomatic mice. Since SOM-expressing interneurons are constitutively active in striatal brain slices, we then examined the effects of acutely silencing these neurons in symptomatic mice with enhanced *Natronomonas pharaonis* halorhodopsin (eNpHR). Optically silencing SOM-expressing interneurons resulted in a greater decrease in the frequency of spontaneous IPSCs (sIPSCs) in a subset of SPNs from Q175 mice compared to WTs, suggesting that SOM-expressing interneurons are the main contributors to the overall increased GABA synaptic activity in HD SPNs.

Abbreviations: ACSF, artificial cerebrospinal fluid; AMPA, α-amino-3-hydroxy-5-methyl-4-isoxazolepropionic acid; CAG, cytosine–adenine–guanine; CaMKII, Ca^{2+}/calmodulin-dependent protein kinase II; CB1, cannabinoid receptor type 1; ChR2, channelrhodopsin-2; D1, dopamine D1 receptor type; eNpHR, enhanced *Natronomonas pharaonis* halorhodopsin; FSI, fast-spiking interneuron; GABA, γ-aminobutyric acid; HD, Huntington's disease; LTS, low-threshold spiking (interneuron); NMDA, N-methyl-D-aspartate; NOS, nitric oxide synthase; NPY, neuropeptide-Y; PV, parvalbumin; EPSC, excitatory postsynaptic current; IPSC, inhibitory postsynaptic current; SOM, somatostatin; SPN, spiny projection neuron; WT, wildtype.

Additionally, the effects of activating $GABA_B$ and cannabinoid (CB1) receptors were investigated to determine whether these receptors were involved in modulating interneuron-specific GABA synaptic transmission and if this modulation differed in HD mice. When selectively activating PV- and SOM-expressing interneurons in the presence of the CB1 receptor agonist WIN-55,212, the magnitudes of the evoked IPSCs in SPNs decreased for both interneuron types although this change was less prominent in symptomatic Q175 SPNs during SOM-expressing interneuron activation. Overall, these findings show that dysfunction of SOM-expressing interneurons contributes to the increased GABA synaptic activity found in HD mouse models and that dysregulation of the endocannabinoid system may contribute to this effect.

Keywords: striatum, Huntington's disease (HD), GABA interneurons, CB1 receptors, electrophysiology, optogenetics

INTRODUCTION

Huntington's disease (HD) is a fatal autosomal dominant genetic disorder caused by an unstable expansion of cytosine–adenine–guanine (CAG) repeats in exon 1 of the *huntingtin (HTT)* gene (MacDonald et al., 1993). Individuals affected with HD exhibit symptoms such as loss of motor coordination, cognitive impairment and psychiatric disturbances that progress in severity with age (Walker, 2007; Bates et al., 2015; Snowden, 2017). The main neuropathological feature of HD is atrophy of the striatum, as well as the cerebral cortex, hippocampus, thalamus, hypothalamus and cerebellum (Waldvogel et al., 2015). In the striatum, there is massive degeneration and loss of spiny projection neurons (SPNs), the main cell type involved in relaying integrated information from the cortex and thalamus to output structures of the basal ganglia (Albin et al., 1990).

SPNs are γ-aminobutyric acid (GABA)-ergic cells that represent over 90% of all striatal neurons and form labyrinthine connections with other SPNs and striatal interneurons (reviewed by Bolam et al., 2000; Chuhma et al., 2011). The remaining cell types in the striatum are interneurons that modulate intra-striatal communication in addition to SPN output. While SPN degeneration and loss are abundant in early and late stages of HD, other striatal cells also are affected. In symptomatic HD patients and mouse models, the number of GABAergic parvalbumin (PV)-expressing interneurons is decreased and their dendritic arborization is greatly diminished (Reiner et al., 2013; Simmons et al., 2013; Paldino et al., 2017; Holley et al., 2019). Furthermore, while large cholinergic and GABAergic somatostatin (SOM)-expressing interneurons appear to be spared in HD, both types of interneurons display altered physiology in symptomatic HD mice (Holley et al., 2015, 2019; Tanimura et al., 2016). These disease-related dysfunctions in individual cell populations add stress on striatal microcircuits leading to altered striatal output generally associated with abnormal movements.

GABA-releasing interneurons make up about 5% of all striatal cells and one of their primary roles is to modulate SPN output. Recent reports show that the diversity of striatal GABAergic interneurons is greater than previously thought (reviewed by Tepper et al., 2018). There are three main types, low-threshold spiking (LTS) interneurons, which are SOM-, neuropeptide Y (NPY)-, and nitric oxide synthase (NOS)-expressing, fast-spiking (FS) PV-expressing interneurons and calretinin-expressing interneurons. All but the latter have been characterized in brains of healthy and HD mice (Tepper et al., 2010; Cepeda et al., 2013; Holley et al., 2019). Fast-spiking interneurons (FSIs) display fast-firing properties and mediate feed-forward inhibition, while the LTS interneurons fire spontaneously at lower frequencies and, in addition to GABA, they release neuromodulators that may have neuroprotective attributes (Kumar, 2008; Rajput et al., 2011).

There is growing evidence that GABA neurotransmission is abnormal in animal models of HD (Cepeda et al., 2004, 2010; Centonze et al., 2005; Andre et al., 2011; Dvorzhak et al., 2013; Indersmitten et al., 2015; Hsu et al., 2018). Further studies from our laboratory demonstrated alterations in intrinsic and synaptic properties in both FSIs and LTS interneurons which may contribute to the increased striatal GABA transmission (Cepeda et al., 2013; Holley et al., 2019). While there are multiple sources of GABA inhibition in the striatum of HD model mice, the underlying mechanisms are not well understood. In an attempt to elucidate the key cell type(s) involved in increased inhibition we used optogenetics to selectively manipulate (activate or inhibit) PV- or SOM-expressing interneurons in the Q175 mouse model of HD to determine how evoked responses and spontaneous GABA synaptic activity in SPNs are altered throughout disease progression. In addition, we investigated whether activation of $GABA_B$ and endocannabinoid-dependent signaling affects interneuron-specific inhibitory synaptic transmission in SPNs and whether these signaling pathways are altered in HD mice.

MATERIALS AND METHODS

Mice

Experimental procedures were performed in accordance with the United States Public Health Service Guide for Care and Use of Laboratory Animals and were approved by the Institutional Animal Care and Use Committee at the University of California Los Angeles (UCLA). All mice were obtained from our breeding colonies and every effort was made to minimize pain, discomfort, and the number of mice used. Animal housing conditions were maintained under a standard 12 h light/dark cycle (light cycle starting at 6 AM and ending at 6 PM) and at a temperature of 20–26°C. The animals had *ad libitum* access to food and water. Total numbers of mice used for all experiments were 105 wildtype (WT; 63 males, 42 females) and 111 heterozygous Q175 mice (50 males, 61 females). In order to limit the number of mice used, wherever feasible, multiple experiments were performed using brain slices from the same mouse. In all experiments mice were examined at presymptomatic (2–3 month; mean age 81 ± 2 and 80 ± 2 days for WT and Q175, respectively) and fully symptomatic (10.5–15 month; mean age 408 ± 5 and 413 ± 5 days for WT and Q175, respectively) stages. In selected experiments, a third group was added (8–9 month; mean age 265 ± 3 days for both WT and Q175). Mice from this latter group are also symptomatic but the phenotype is not as severe as in older mice (Heikkinen et al., 2012). For optogenetic experiments involving PV- and SOM-expressing interneurons, heterozygous Q175 mice (CHDI, Inc.) were crossed with homozygous PV- or SOM-Cre mice (B6.129P2-Pvalb$^{tm1(cre)Arbr}$/J, RRID:IMSR_JAX:008069 and Sst$^{tm2.1(cre)Zjh}$/J, RRID:IMSR_JAX:013044, The Jackson Laboratory) to produce heterozygote Q175 mice with Cre expression in PV- or SOM-expressing interneurons. To examine differential inputs to direct and indirect pathway neurons, Drd1a-tdTomato mice [B6.Cg-Tg(Drd1a-tdTomato)6Calak/J, RRID:IMSR_JAX:016204, The Jackson Laboratory] were crossed with heterozygous Q175 mice to produce mice with D1 cells labeled with tdTomato. Additionally, 17 R6/2 mice (11 males, six females) and 14 WT littermates (six males, eight females) from our colony were used in selected experiments. For these mice, WT male C57BL/6xCBA mice were crossed with WT female C57BL/6xCBA mice that had transplanted R6/2 ovaries [B6CBA-Tg(HDexon1)62Gpb/3J, RRID:IMSR_JAX:006494, The Jackson Laboratory]. For experiments investigating alterations in SPN responses induced by activation of dopamine receptor-expressing (D1)-SPNs, we crossed WT and Q175 mice with D1-Cre mice [B6.FVB(Cg)-Tg(Drd1-cre)EY262Gsat/Mmucd, RRID:MMRRC_030989-UCD]. Genotyping was performed using PCR of DNA obtained from tail samples, once at weaning and again following use to confirm the genotype. CAG repeat lengths were determined for breeders and for experimental animals by Laragen (Culver City, CA, USA). For Q175 mice, CAG repeats were 184.8 ± 1.4 (range 160–215) and for R6/2 mice, repeats were 158.1 ± 1.7 (range 144–165). Both male and female mice were used for all experiments. We observed no consistent differences between sexes and the data were pooled.

Surgery

Animals were anesthetized with isoflurane and burr holes were drilled into the skull at the injection sites. For experiments involving the activation or silencing of striatal interneurons AAV2/1-EF1a-DIO-hChR2(H134R)-eYFP or AAV2/1-EF1a-DIO-eNpHR3.0-eYFP (University of Iowa Viral Vector Core Facility, Iowa City, IA or UNC Vector Core, Chapel Hill, NC, USA) was stereotactically injected bilaterally into the dorsolateral striata. The stereotaxic injection coordinates were (relative to Bregma): AP +1.0, ML ± 2.0, and DV −3.3 mm from the surface of the brain. For each AAV (titer 1.2–3.0 × 10^{12} vg/ml), a total of 1.0 μl (per hemisphere) was injected at a rate of 0.2 μl/min into WT and Q175 PV- or SOM-Cre mice. For selective activation of cortical (M1) inputs, mice were injected unilaterally at two sites (0.25 μl each) with AAV-CaMKII-hChR2(H134R)-eYFP (University of Iowa Viral Vector Core Facility, Iowa City, IA or UNC Vector Core, Chapel Hill, NC, USA) at a rate of 0.1 μl/min. Coordinates for cortical injections were (relative to Bregma): AP +1.7, ML ± 1.5, DV −1.2 and −0.5 mm from the surface of the brain. After each AAV injection (titer UNC 3.0–5.0 × 10^{12} vg/ml), the needle remained in place for 5–7 min before retraction in order to avoid vector backflow. Mice were sacrificed for electrophysiological and experiments ∼4–6 weeks post-injection to ensure sufficient opsin expression.

Brain Slice Electrophysiology

Mice were deeply anesthetized with isoflurane and perfused transcardially with an ice-cold, high sucrose-based solution containing (in mM): 26 $NaHCO_3$, 1.25 NaH_2PO_4, 208 sucrose, 10 glucose, 2.5 KCl, 1.3 $MgCl_2$, 8 $MgSO_4$. Mice were decapitated, brains dissected out and immediately placed in the oxygenated slicing solution. Coronal or sagittal slices (300 μm) were cut and transferred to an incubating chamber containing artificial cerebrospinal fluid (ACSF; in mM): 130 NaCl, 3 KCl, 1.25 NaH_2PO_4, 26 $NaHCO_3$, 2 $MgCl_2$, 2 $CaCl_2$, and 10 glucose oxygenated with 95% O_2–5% CO_2 (pH 7.2–7.4, osmolality 290–310 mOsm/L, 32–34°C). Slices were allowed to recover for an additional 30 min at room temperature. Brain slice recordings were limited to the dorsolateral region of the striatum and all recordings were performed at room temperature using upright microscopes (Olympus BX51WI or BX61WI) equipped with differential interference contrast optics and fluorescence imaging (QIACAM fast 1394 monochromatic camera with Q-Capture Pro software, QImaging). Whole-cell patch clamp recordings in voltage- and current-clamp modes were obtained using a MultiClamp 700B Amplifier (Molecular Devices) and the pCLAMP 10.3 or 10.5 acquisition software. The patch pipette (3–5 MΩ resistance) contained a cesium (Cs)-based internal solution (in mM): 125 Cs-methanesulfonate, 4 NaCl, 1 $MgCl_2$, 5 MgATP, 9 EGTA, 8 HEPES, 1 GTP-Tris, 10 phosphocreatine, and 0.1 leupeptin (pH 7.2 with CsOH, 270–280 mOsm) for voltage-clamp recordings or a K-gluconate-based solution containing (in mM): 112.5 K-gluconate, 4 NaCl, 17.5 KCl, 0.5 $CaCl_2$, 1 $MgCl_2$, 5 ATP (K^+ salt), 1 NaGTP, 5 EGTA, 10 HEPES, pH 7.2 (270–280 mOsm/L) for current-clamp recordings. All internal electrode solutions contained 0.2% biocytin for subsequent immunodetection and identification of recorded cells. In experiments where evoked excitatory postsynaptic currents (EPSCs) were recorded in SPNs following optical activation of cortical inputs, QX 314 Cl^-

(4 mM) was included in the internal pipette solution to block activity-dependent Na^+ channels. After breaking through the membrane, cell properties (capacitance, input resistance, decay time constant) were recorded in voltage-clamp mode while holding the membrane potential at −70 mV. Resting membrane potentials were recorded in current-clamp mode. Data were omitted if electrode access resistance exceeded 30 MΩ.

For optogenetic experiments, PV- or SOM-expressing interneurons or D1 receptor-expressing SPNs were activated with a single light pulse (470 nm, 0.5 ms, 3 mW, CoolLED) delivered through the epifluorescence illumination pathway using Chroma Technologies filter cubes. Evoked inhibitory postsynaptic currents (IPSCs) in response to optical activation were recorded in voltage-clamp mode, at a holding potential of +10 mV and in the presence of 2,3-Dioxo-6-nitro-1,2,3,4-tetrahydrobenzo[f]quinoxaline-7-sulfonamide (NBQX, 10 μM) and DL-2-Amino-5-phosphonopentanoic acid (APV, 50 μM) to block α-amino-3-hydroxy-5-methyl-4-isoxazolepropionic acid (AMPA) and N-methyl-D-aspartate (NMDA) receptors, respectively. In some cells, 10 μM bicuculline (BIC) was applied to block optically-evoked IPSC responses, confirming they were due to activation of $GABA_A$ receptors. In our recording conditions, based on the Cl^- concentration in the internal solution and the addition of NBQX/APV in the bath, the E_{Cl} was -55.0 ± 1.6 mV ($n = 8$). For stimulation of channelrhodopsin (ChR2)-expressing corticostriatal projections in decorticated coronal slices, a single light pulse (470 nm, 1 ms, 5 mW) was delivered and evoked EPSCs were recorded in SPNs while holding the membrane at −70 mV and in the presence of BIC (10 μM). For experiments where SOM-expressing interneurons were silenced with optical activation of enhanced *Natronomonas pharaonis* halorhodopsin (eNpHR), yellow light (585 nm, 1 mW) was applied at various durations through the microscope objective. Recordings of spontaneous IPSCs (sIPSCs) were obtained from SPNs (60 s) prior to and (60 s) during yellow light illumination at a holding potential of +10 mV and in the presence of NBQX (10 μM) and APV (50 μM).

Following recordings, brain slices were fixed in 4% PFA for 24 h. Slices were then washed with 0.1 M PBS, permeabilized with 1% Triton overnight at 4°C, and incubated for 2 h with Alexa 594 conjugated streptavidin (1:1,000, ThermoFisher Scientific, Waltham, MA, USA) at room temperature. Fluorescent images from both recorded cells and eYFP-expressing terminals were obtained using a Zeiss confocal ApoTome equipped with 40× and 63× objectives.

The following drug reagents were obtained from Tocris Bioscience/Bio-Techne (Minneapolis, MN, USA): BIC, NBQX, APV, QX314 Cl^-, the cannabinoid type 1 (CB1) receptor agonist WIN 55,212-2 and the antagonist, AM 251. All drug stocks were made using double-distilled H_2O except for WIN 55,212-2 and AM 251 which were dissolved in DMSO. The final concentration of DMSO in recording bath solutions did not exceed 0.05%, a concentration that when tested in a few cells did not significantly alter cell membrane or evoked response properties following prolonged exposure (20 min).

Analyses and Statistics

Analyses of optically-evoked postsynaptic responses were performed using the Clampfit 10.3 or 10.5 software (Molecular Devices). Evoked response peak amplitudes were calculated by measuring the difference between the highest absolute value point of the response and average baseline. Response areas were calculated using an integral function available in the Clampfit software that measures the area under the response curve relative to baseline. Decay times were calculated by measuring the time (in ms) the response took to decay from 90% to 10% of the peak amplitude (Parievsky et al., 2017). In addition, adjusted decay times and time constants were assessed by first normalizing the amplitudes of optically-evoked IPSCs or EPSCs amplitudes to the maximal WT response amplitude for each group (see **Supplementary Material**). For all optically-evoked responses, 3–6 sweeps were recorded and averaged (30 s inter-sweep interval). sIPSCs were analyzed off-line using the automatic threshold detection protocol within the Mini Analysis Program version 6.0 (Synaptosoft) and subsequently checked manually for accuracy. The threshold amplitude for the detection of an event (10 pA) was set 3× above the root mean square background noise level (max ~3 pA at $V_{\text{hold}} = +10$ mV). All statistical analyses were performed using SigmaPlot 13.0 software. Differences between group means were assessed with appropriate Student's *t*-tests (unpaired) or Fisher exact tests for proportions, and appropriately designed analyses of variance (two-way ANOVAs, followed by Holm-Sidak or Bonferroni *post hoc* tests). Values in figures, tables and text are presented as mean ± SEM. Differences were considered statistically significant if $p < 0.05$ and are indicated with asterisks in the figures ($^*p < 0.05$, $^{**}p < 0.01$, $^{***}p < 0.001$, $^{****}p < 0.0001$).

RESULTS

Expression and Activation of Channelrhodopsin in Striatal GABAergic Interneurons

ChR2 was selectively expressed in striatal PV- and SOM-expressing interneurons by stereotactically injecting a Cre-dependent AAV-ChR2-eYFP into WT and Q175 mice crossed with PV- and SOM-Cre mice, respectively (**Figures 1A,C**). Recordings from eYFP positive cells in PV-Cre (**Figure 1B1**) and SOM-Cre (**Figure 1D1**) mice showed distinct electrophysiological properties as previously reported (Tepper et al., 2010; Holley et al., 2019). Compared with SOM-expressing interneurons, PV-expressing interneurons were more hyperpolarized at rest, and displayed suprathreshold firing frequencies of 50–100 Hz. In contrast, SOM-expressing interneurons exhibited increased membrane input resistances, more depolarized resting membrane potentials, and fired spontaneously at frequencies between 1–10 Hz. After a brief pulse of blue light (0.5 ms, 470 nm), both PV- and SOM-expressing interneurons fired a single action potential as shown in current- (**Figures 1B2,D2**) and voltage-clamp recordings (**Figures 1B3,D3**). Thus, utilizing specific Cre-reporter mice combined with optogenetics, we were able to effectively activate

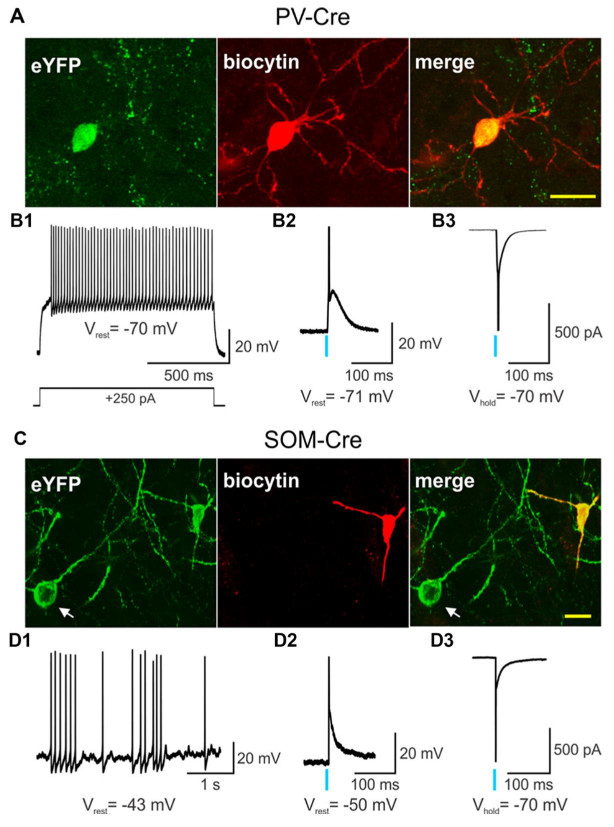

FIGURE 1 | Single action potentials are generated by a brief light pulse in parvalbumin (PV)- and somatostatin (SOM)-expressing interneurons. Confocal images of biocytin-filled PV- **(A)** or SOM-expressing **(C)** interneurons (red) that also express eYFP from 2 months-old wildtype (WT) PV- and SOM-Cre mice. In **(C)** the cell body of a SOM-expressing interneuron that also expresses eYFP but was not recorded from is visible (white arrow). Scale bar = 20 μm. **(B1)** Voltage response to a depolarizing, suprathreshold current injection in a PV-expressing interneuron that also expresses channelrhodopsin-2 (ChR2) and eYFP. Recordings of a PV-expressing interneuron co-expressing ChR2/eYFP in current-clamp **(B2)** and in voltage-clamp **(B3)** modes show that a brief light pulse (0.5 ms, 470 nm, 3 mW) produces an action potential. The action potential in the bottom trace was truncated for the figure. **(D1)** Spontaneous firing of a SOM-expressing interneuron that expresses ChR2/eYFP in current-clamp mode. A brief light pulse (0.5 ms, 470 nm, 3 mW) produces an action potential in a SOM interneuron recorded in current-clamp **(D2)** and in voltage-clamp **(D3)** modes. The action potential in the bottom trace was truncated for the figure. In this and in subsequent figures, a blue vertical line indicates the delivery point of a single blue light stimulation pulse.

striatal PV- or SOM-expressing interneurons in WT and Q175 mice.

Responses of SPNs to Optogenetic Activation of PV- and SOM-Expressing Interneurons

In order to determine the relative contribution of PV- and SOM-expressing interneurons to IPSCs, we recorded SPNs from WT and Q175 mice that expressed ChR2-eYFP in the two interneuron populations (**Figures 2A1,A2**, **3A1,A2**). We examined three groups of mice: 2 months (range 2–3 months), 8 months (range 8–9 months), and 12 months (range 12–15 months; numbers of mice and cells are in figure legends). At 2 months, heterozygous Q175 mice are not behaviorally symptomatic, while at 8 and 12 months, these mice show noticeable weight loss and deficits on motor-related tasks (Heikkinen et al., 2012; Menalled et al., 2012; Smith et al., 2014). It is also at these later ages when increases in inhibitory synaptic events have been observed in striatal SPNs (Indersmitten et al., 2015). A summary of SPN membrane properties at the three different ages is shown in **Table 1**. We observed a significant increase in input resistance at 8 and 12 months. This increase was also shown previously in Q175 SPNs (Indersmitten et al., 2015). Optical activation of PV interneurons in the presence of glutamate receptor antagonists (10 μM NBQX and 50 μM APV) induced IPSCs in 75%–80% of recorded cells (**Figure 2B**). Lack of responses in a small percentage of SPNs could be due to the inability of ChR2 to induce action potentials in some PV-expressing interneurons (Szydlowski et al., 2013). However, we observed that non-responding SPNs were generally located in regions of slices where the number of opsin-expressing PV cells was either very low or nonexistent. This observation is in line with recent studies demonstrating that FSIs target exclusively striatal SPNs within close proximity (Straub et al., 2016). Therefore, we selected recordings only from SPNs that were within ∼150 μm from PV-expressing interneurons. IPSCs were similar in amplitude and area between genotypes at all ages (**Figures 2B,C**). There was a trend for faster IPSC decay times in Q175 SPNs at 8 months compared to WTs while at 12 months, response decay times were significantly faster ($F_{(1,112)} = 7.17$, $p = 0.009$ for genotype; Holm-Sidak *post hoc* analyses: $p = 0.006$ for Q175 vs. WT at 12 months). Interestingly, *post hoc* analyses indicated the peak amplitudes of evoked responses in 12 months WT SPNs were significantly smaller than the amplitude of responses in 2-month WTs ($p = 0.02$), suggestive of reduced connectivity between PV-expressing interneurons and SPNs with increased age (**Figure 2C**).

All SPNs responded to optical stimulation of SOM-expressing interneurons. However, the amplitude and area of responses were significantly smaller than those evoked by activation of PV-expressing interneurons (compare **Figures 3B**, **2B**; Amplitude: 520.6 ± 29.4 pA for all PV-expressing-induced IPSCs, $n = 118$ vs. 116.0 ± 5.4 pA for all SOM-expressing-induced IPSCs, $n = 142$; $t_{(258)} = 14.78$, $p < 0.001$. Area: 32877.6 ± 2244.1 pA × ms for all PV-expressing-induced IPSCs vs. 6816.5 ± 367.1 pA × ms for SOM-expressing-induced IPSCs; $t_{(258)} = 12.50$, $p < 0.001$). This interneuron subtype-dependent difference in evoked response size was similar to that previously observed in symptomatic R6/2 mice (Cepeda et al., 2013), a rapidly progressing transgenic mouse model that better replicates the juvenile form of HD in humans (Mangiarini et al., 1996; Lee et al., 2013). Also similar to observations in R6/2 SPNs, we found no genotype-specific differences in SOM-mediated response amplitudes in Q175 and WT SPNs at any age examined (**Figures 3B,C**). However, the response area was reduced in Q175 mice compared to WTs at 12 months ($F_{(2,136)} = 3.33$, $p = 0.039$ for genotype × age; Holm-Sidak *post hoc* analyses: $p = 0.002$ for Q175 vs. WT at 12 months), due to a significantly

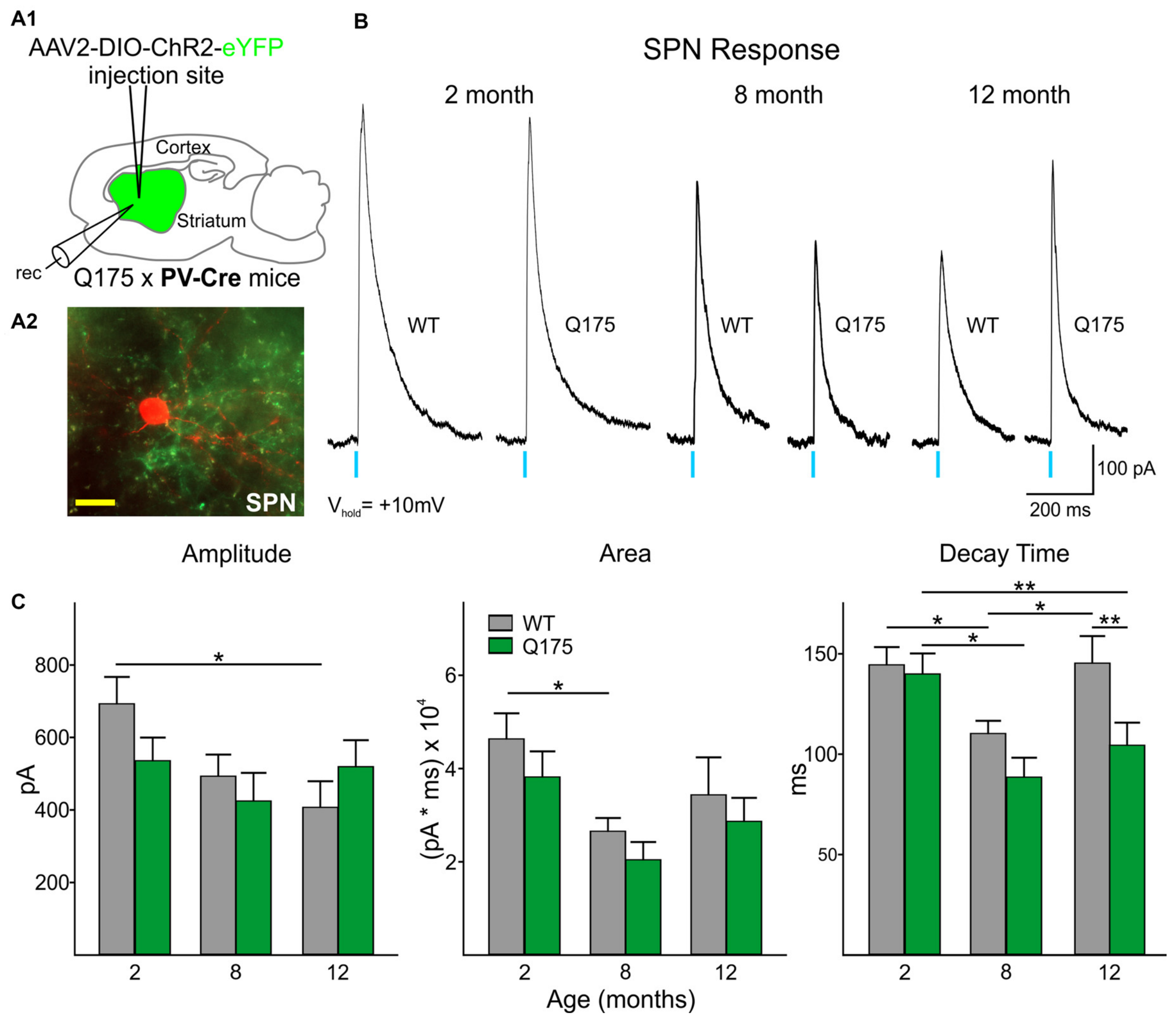

FIGURE 2 | Optical activation of PV-expressing interneurons in Q175 and WT mice at three ages. **(A1)** Schematic of AAV injection site and recording area in Q175xPV-Cre mice. **(A2)** Confocal z-stack image of a biocytin-filled spiny projection neuron (SPN; red) that was recorded from a 15 months-old Q175 mouse. Processes expressing ChR2-eYFP can be seen surrounding the recorded cell. Scale bar = 20 μm. **(B)** Sample traces of evoked GABAergic responses in WT and Q175 SPNs from 2-, 8- and 12 months-old mice following optical activation of PV-expressing interneurons. **(C)** Summary of optically-evoked GABA response properties in WT and Q175 SPNs at 2 (WT *n* = 21, 10 mice; Q175 *n* = 22, 10 mice), 8 (WT *n* = 20, 15 mice; Q175 *n* = 16, 11 mice) and 12 months (WT *n* = 16, eight mice; Q175 *n* = 23, 13 mice). Significant differences were determined using two-way ANOVAs and appropriate *post hoc* analyses, where $^{*}p < 0.05$ and $^{**}p < 0.01$.

faster decay time of the evoked response ($F_{(2,136)} = 7.45$, $p < 0.001$ for genotype × age; Holm-Sidak *post hoc* analyses: $p < 0.001$ for Q175 vs. WT at 12 month). Additionally, there was a trend for faster decay times in Q175 SPNs at 8 months ($p = 0.05$). Faster decay times in responses evoked by activation of SOM-expressing interneurons is similar to the progressive changes in decay time seen in responses evoked by activation of PV-expressing interneurons in SPNs from symptomatic animals (**Figure 2C** and **Supplementary Table S1**).

Effects of SOM-Expressing Interneuron Silencing on SPN Spontaneous IPSCs

The frequency of spontaneous GABA synaptic currents in SPNs gradually increases with progression of the phenotype in several genetic mouse models of HD (Cepeda et al., 2004; Dvorzhak et al., 2013; Indersmitten et al., 2015). As LTS interneurons are one of the few classes of spontaneously active GABAergic interneurons in striatum and the increase in sIPSCs is action potential-dependent (Cepeda et al., 2004; Dvorzhak et al., 2013; Indersmitten et al., 2015), we reasoned that one possible source of increased spontaneous GABA synaptic activity in SPNs in the mouse models could be increased firing of LTS interneurons (Cepeda et al., 2013). Utilizing optogenetics, we selectively silenced this class of interneuron by expressing (eNpHR) in 12-month WT and Q175 SOM-Cre mice (six mice for each genotype; **Figures 4A,B**). Exposure to yellow light (1 mW) completely abolished spontaneous firing of SOM interneurons and produced a hyperpolarization of the cell membrane

TABLE 1 | Cell membrane properties of spiny projection neurons (SPNs) in wildtype (WT), Q175 and R6/2 mice.

	Capacitance (pF)	Input resistance (MΩ)	Time constant (ms)
2 months			
WT (*n* = 47)	147.6 ± 6.3	49.8 ± 2.9	2.1 ± 0.08
Q175 (*n* = 49)	143.6 ± 5.1	55.0 ± 3.0	2.1 ± 0.08
8 months			
WT (*n* = 38)	132.6 ± 4.4	64.4 ± 3.6	2.2 ± 0.08
Q175 (*n* = 33)	125.1 ± 5.7	84.9 ± 6.7**	2.1 ± 0.08
12 months			
WT (*n* = 40)	97.4 ± 6.1	78.1 ± 6.1	1.8 ± 0.10
Q175 (*n* = 47)	88.7 ± 3.8	107.5 ± 6.8**	1.8 ± 0.08
60 days			
WT (*n* = 38)	118.8 ± 6.7	66.0 ± 8.3	1.8 ± 0.1
R6/2 (*n* = 53)	80.0 ± 1.9****	161.9 ± 9.1****	1.5 ± 0.05**

*Group means ± SEMs are reported. Comparisons for each membrane property were made between WT and Q175 or R6/2 cells at each age group. Significant differences were determined using Student's t-tests where **p < 0.01 and ****p < 0.0001.*

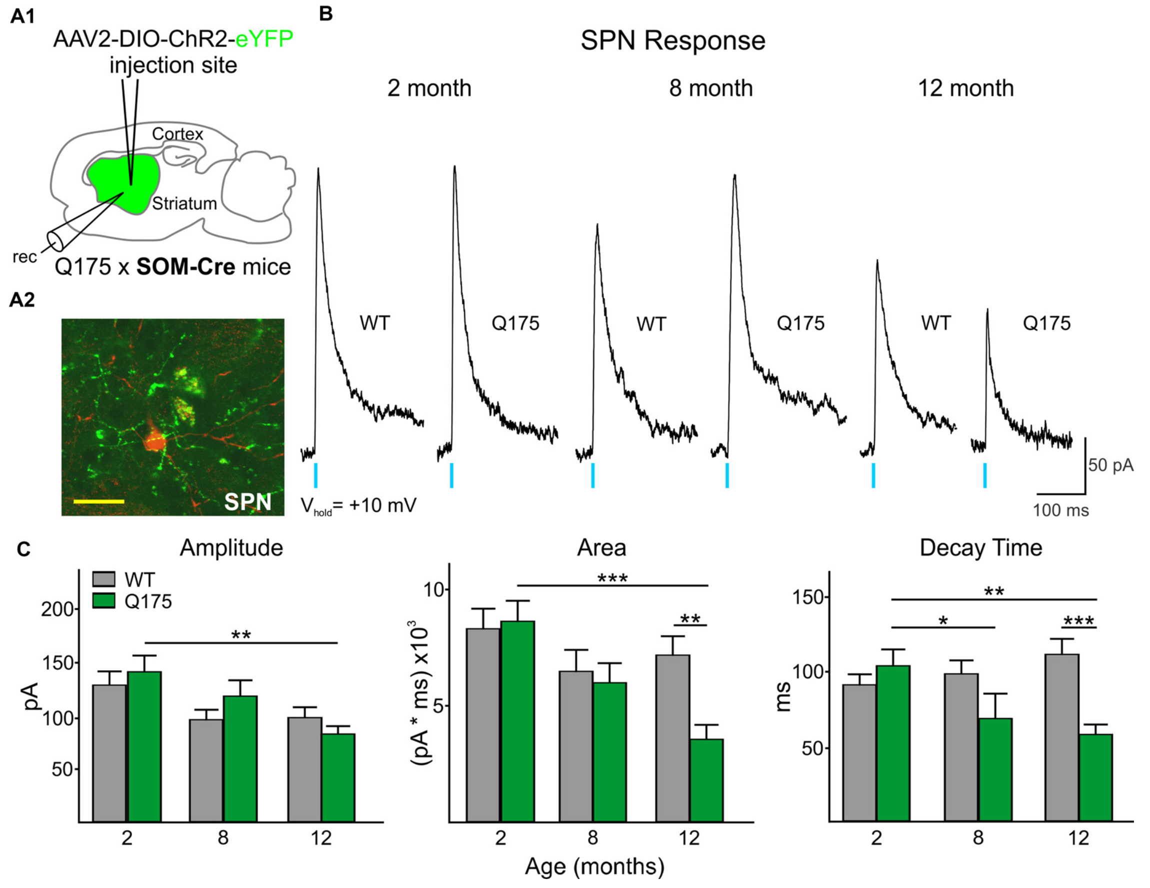

FIGURE 3 | Optical activation of SOM-expressing interneurons in Q175 and WT mice at three ages. **(A1)** Schematic of AAV injection site and recording area in Q175xSOM-Cre mice. **(A2)** Confocal z-stack image of a biocytin-filled SPN (red) that was recorded from a 12 month-old Q175xSom-Cre mouse. SOM-expressing interneuron processes expressing ChR2-eYFP are seen surrounding the recorded cell. Scale bar = 20 μm. **(B)** Sample traces of evoked GABAergic responses in WT and Q175 SPNs following optical activation of SOM-expressing interneurons. **(C)** Summary of optically-evoked γ-aminobutyric acid (GABA) response properties in WT and Q175 SPNs at 2 (WT *n* = 26, 11 mice; Q175 *n* = 27, 10 mice), 8 (WT *n* = 18, seven mice; Q175, *n* = 17, nine mice) and 12 months (WT *n* = 30, 13 mice; Q175, *n* = 34, nine mice). Significant differences were determined using Two-way ANOVAs and appropriate *post hoc* analyses, where $^*p < 0.05$, $^{**}p < 0.01$ and $^{***}p < 0.001$.

(**Figures 4C1,C2**). Notably, in a subset of SPNs, continuous yellow light (1 mW, 60 s) also significantly reduced the frequency of sIPSCs (**Figures 4D1,D2**), such that sIPSC frequencies from Q175 SPNs that were significantly increased compared to WTs (2.21 ± 0.4 Hz for Q175, $n = 13$ vs. 1.22 ± 0.2 Hz for WT, $n = 19$; $t_{(30)} = 2.44$, $p = 0.021$) were no longer significantly

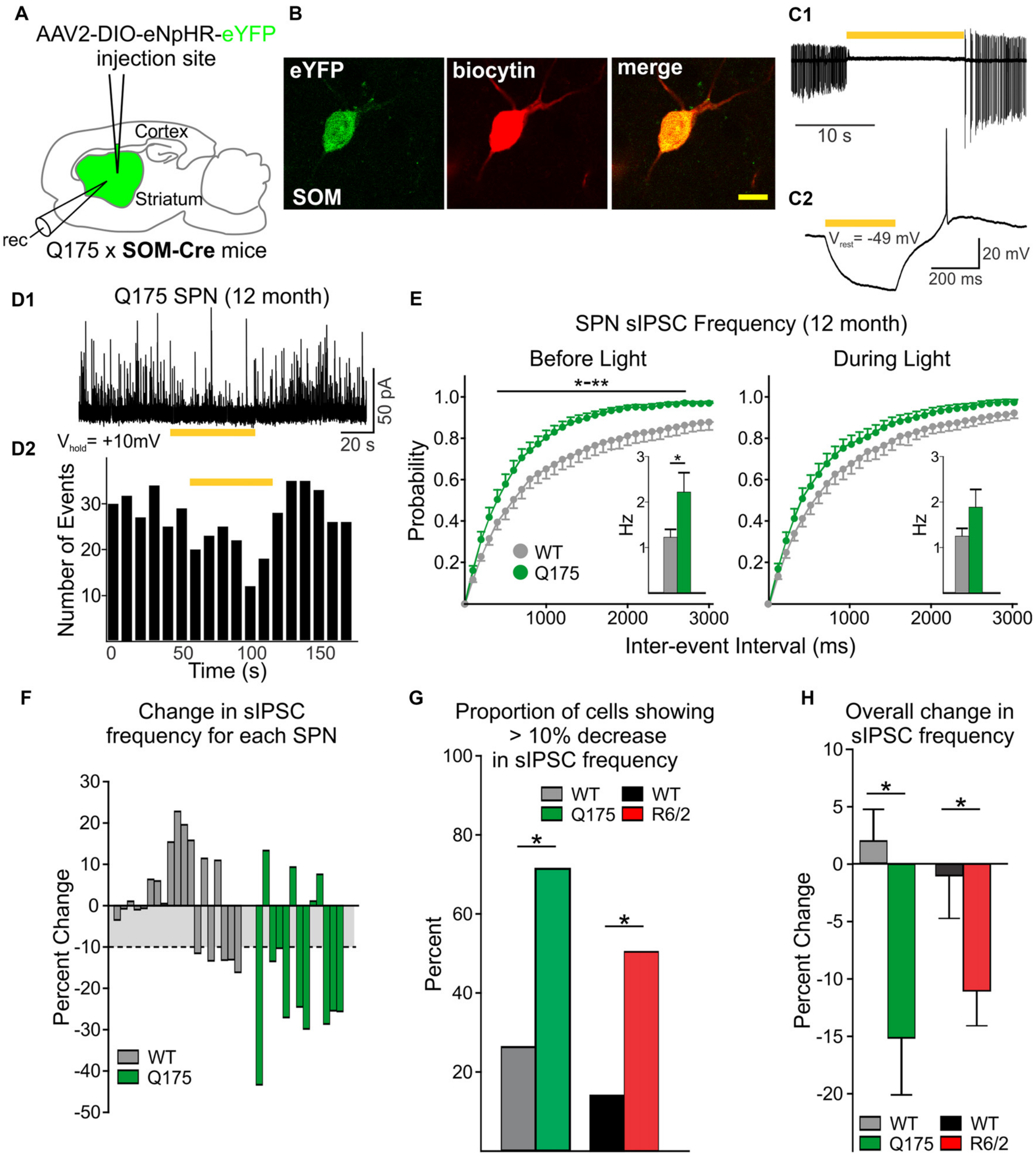

FIGURE 4 | Reduced inhibitory input to SPNs is induced by silencing SOM-expressing interneurons. **(A)** Schematic of AAV injection and recording sites used for silencing experiments. **(B)** Confocal image of a biocytin-filled SOM-expressing interneuron (red) that also expresses eYFP. The cell was recorded from a 12 month old Q175xSOM-Cre mouse. Scale bar = 10 μm. **(C1)** Recording from a Q175 SOM-expressing interneuron in cell-attached mode. Most SOM interneurons are constitutively active at rest with firing frequencies of 1–10 Hz. During yellow light activation of enhanced *Natronomonas pharaonis* halorhodopsin (eNpHR; bar, 585 nm, 1 mW), the cell was silenced. **(C2)** Yellow light illumination (bar, 0.08 mW) hyperpolarizes SOM-expressing interneurons. **(D1)** Sample trace of spontaneous IPSCs (sIPSCs) recorded in an SPN from a 12 month-old Q175 mouse. Activation of eNpHR in SOM-expressing interneurons (bar, 1 mW), decreased sIPSC frequency in a subset of SPNs. **(D2)** Frequency-time histogram of recorded events in the SPN shown in D1 illustrates the decrease in sIPSC frequency during yellow light illumination. **(E)** Cumulative inter-event interval distribution plots of SPN sIPSCs before (left) and during (right) yellow light-induced suppression of SOM-expressing interneurons. Insets show the average sIPSC frequencies for each genotype. **(F)** Plots showing the percent change in sIPSC frequencies for each recorded SPN during yellow light. For WT cells that displayed a reduction in sIPSC frequency during yellow light, the mean percent change was ~10% (gray area). **(G)** Summary of the percent of SPNs that responded with a decrease (>10%) in sIPSC frequency. Proportionately, more SPNs from symptomatic Q175 (12 months) and R6/2 (60 days) mice showed a decrease in frequency compared to WT SPNs (Fisher exact test: $p = 0.029$ and $p = 0.024$, for Q175 and R6/2 vs. WT, respectively). **(H)** The average percent change (decrease) in sIPSC frequencies when SOM interneurons were silenced was greater in Q175 and R6/2 SPNs compared to WT SPNs. Significant differences were determined using Student's t-test or two-way ANOVAs followed by appropriate *post hoc* analyses, where $^{*}p < 0.05$ and $^{**}p < 0.01$.

different and became similar to WTs (1.88 ± 0.4 Hz for Q175 vs. 1.24 ± 0.2 Hz for WT; $t_{(30)} = 1.67$, $p = 0.105$; **Figure 4E**, inset). Cumulative inter-event interval distribution plots also show sIPSC frequencies in SPNs during yellow light-induced silencing of SOM-expressing interneurons became more similar to that of WTs (Before Light: $F_{(40,1200)} = 2.38$, $p < 0.001$ for genotype × interval, Holm-Sidak *post hoc* analyses: $p = 0.004$–0.044 for intervals 400–2,700 ms. During Light: $F_{(40,1200)} = 0.786$, $p = 0.828$ for genotype × interval). The percent change of sIPSC frequencies during yellow light was greater in Q175 SPNs than in WTs (**Figure 4F**). We determined that the proportion of Q175 SPNs that responded to optical silencing of SOM-expressing interneurons with a reduction in sIPSC frequency greater than 10% was higher than the percentage observed in WTs (69% or 9/13 for Q175 SPNs vs. 26% or 5/19 for WTs; Fisher exact test: $p = 0.029$; **Figure 4G**), and for these SPNs, the average percent decrease was larger in Q175s (25.4 ± 3.2% decrease for Q175s vs. 13.4 ± 0.8% decrease for WTs; $t_{(12)} = 2.73$, $p = 0.018$). Thus, the overall change in sIPSC frequency during inhibition of SOM-expressing interneurons for all recorded SPNs was greater in Q175s than in WTs (−15.14 ± 5.0% in Q175 SPNs vs. 1.94 ± 2.7%; $t_{(30)} = 3.24$, $p = 0.003$; **Figure 4H**). We also used the same approach to determine if SOM-expressing interneurons contribute towards increased inhibition in the R6/2 mouse model of HD (seven and nine mice for WT and R6/2 mice, respectively). Here, we observed similar results to those of Q175 SPNs. Silencing SOM-expressing interneurons resulted in a greater proportion of R6/2 SPNs displaying a reduction (>10%) in sIPSC frequency (49% or 16/33 for R6/2 SPNs vs. 17% or 4/23 for WTs, Fisher exact test: $p = 0.024$; **Figure 4G**). Additionally, the overall change in average sIPSC frequency was greater in R6/2 SPNs than in WTs during yellow light (−11.0 ± 2.8% change for R6/2 s vs. −0.9 ± 3.9% change for WTs; $t_{(54)} = 2.11$, $p = 0.04$; **Figure 4H**). These data provide evidence that SOM-expressing interneurons are one of the main sources of increased GABAergic activity in SPNs of HD mouse models.

Increased Frequency of sIPSCs Onto SPNs Is Not a Result of Altered GABA$_B$ Signaling

In order to gain further insight into the mechanism underlying the increased inhibitory input onto SPNs, we investigated whether there were genotype-specific alterations in receptors that are predominantly located at presynaptic sites and that have been shown to modulate neurotransmitter release. First, we examined the effects of activating GABA$_B$ receptor signaling. Activation of GABA$_B$ receptors on presynaptic terminals was previously shown to decrease neurotransmitter release, particularly at glutamatergic corticostriatal terminals (Calabresi et al., 1991; Nisenbaum et al., 1993; Kupferschmidt and Lovinger, 2015). Furthermore, GABA release from nearby SPNs and neurogliaform-NPY interneurons can activate presynaptic GABA$_B$ receptors on excitatory terminals (Logie et al., 2013). Thus, we examined whether activation of GABA$_B$ receptors on PV- and SOM-expressing interneurons affects neurotransmitter release and whether such presynaptic GABA$_B$ receptor signaling is altered in Q175 mice.

We observed a reduction in the amplitude, area and decay time of IPSC responses induced by stimulation of PV-expressing interneurons in both Q175 and WT SPNs following incubation with the GABA$_B$ receptor agonist, baclofen (**Figures 5A–C**). The extent of this reduction was similar in both genotypes at 2 and 8 months (numbers of mice and cells are in the figure legend). We also observed a similar pattern to activation of SOM-expressing interneuron-induced IPSCs in SPNs. Baclofen reduced similarly the amplitude, area and decay time of these responses regardless of the genotype and age (**Figures 5D–F**). Interestingly, the sensitivity of this baclofen-mediated reduction differed between the two interneuron types. The effective concentration of baclofen required to produce significant reductions in PV-expressing interneuron-induced responses was 10 μM. At this concentration, the amplitude decreased 56.1 ± 6.5% and 52.3 ± 3.6% for 8-month-old Q175 and WT SPNs, respectively. At 10 μM the percent reduction of SPN response amplitudes after activating SOM-expressing interneurons was 87.7 ± 1.3% in 8-month-old Q175s and 85.0 ± 2.5% in WTs at the same age. Baclofen at a concentration of 0.5 μM had a negligible effect on PV-expressing interneuron-induced responses in SPNs (data not shown). These data suggest that while the sensitivity of GABA$_B$ receptor-activation differs between responses evoked by activation of the two interneuron types, GABA$_B$ receptor signaling between the genotypes remains unaltered for responses in SPNs evoked by either activation of PV- or SOM-expressing interneurons.

Reduced CB1 Receptor Modulation of GABA Responses Evoked by SOM- but Not by PV-Expressing Interneurons

We next examined the CB1 receptor-mediated modulation of IPSCs evoked in SPNs by optical activation of PV-expressing and SOM-expressing GABAergic interneurons (**Figure 6**). Control responses to activation of PV-expressing interneurons were first recorded in SPNs in the presence of glutamate receptor antagonists (10 μM NBQX and 50 μM APV) alone (**Figure 6B**). After a 20 min exposure to the CB1 receptor agonist, WIN 55,512-2 (3 μM), the peak amplitudes of evoked IPSCs decreased similarly in Q175 and WT SPNs [55.7% of control in SPNs from Q175 mice ($n = 12$, six mice) and to 60.9% in WT mice ($n = 11$, five mice)] at 2 months (**Figure 6C**). We also observed no genotype-specific differences in response areas or decay times. WIN 55,512-2-mediated decreases in evoked IPSC response amplitude and area were greater at 8 and 12 months (8 months: $n = 11$, nine mice for Q175s and $n = 16$, seven mice for WTs; 12 months: $n = 10$, eight mice for Q175 and $n = 11$, three mice for WT) than at 2 months but again, no significant differences between genotypes were observed. Additionally, no differences were observed in the response decay times at 8 and 12 months.

Activation of CB1 receptors with WIN 55,212-2 also reduced current responses in SPNs evoked by activation of SOM-expressing interneurons in both Q175 and WT mice (**Figures 6E–I**). At 2 months, there were no genotypic differences in optically-evoked IPSC responses following a 20 min bath

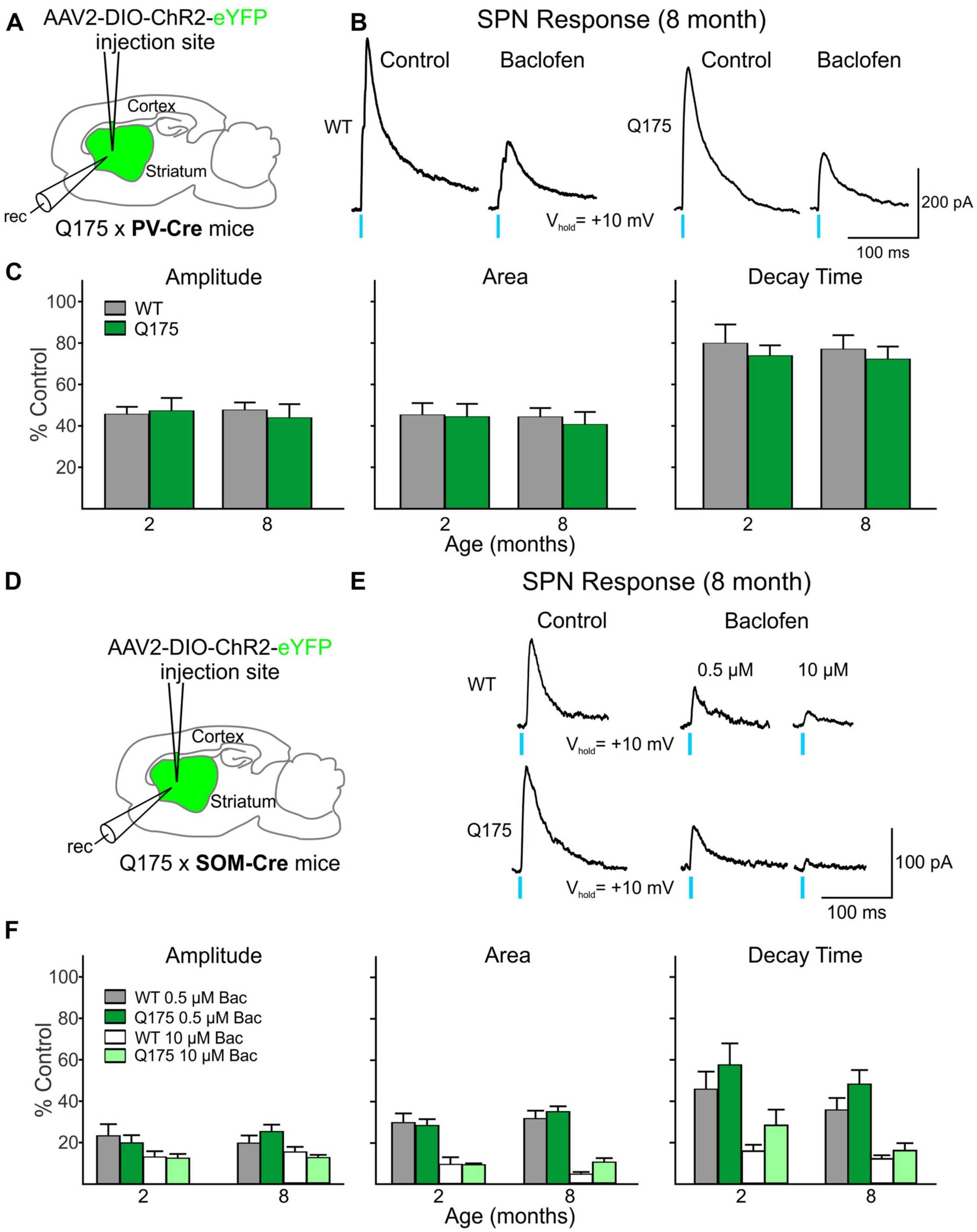

FIGURE 5 | Activation of $GABA_B$ receptors yielded no significant genotype-dependent alterations in PV- or SOM-expressing interneuron-induced IPSCs in Q175 SPNs. **(A)** Schematic of AAV injection/recording site and mouse line used for the data shown in **(B,C)**. **(B)** Sample traces of optically-evoked, GABA responses mediated by activating PV-expressing interneurons in WT and Q175 SPNs before (Control) and after 20 min incubation with Baclofen (Bac, 10 μM). **(C)** Summary of the effects of $GABA_B$ receptor activation in WT, presymptomatic Q175 (2 months; WT *n* = 7 and Q175 *n* = 12; four and five mice, respectively) and symptomatic Q175 (8 months; WT *n* = 7 and Q175 *n* = 8; six and five mice, respectively) SPNs. Average response properties (amplitude, area and decay time) as a percentage of the Control response. **(D)** Schematic of AAV injection/recording site and mouse line used for the data shown in **(E,F)**. **(E)** Sample traces of optically-evoked, GABA responses mediated by activating SOM-expressing interneurons in WT and Q175 SPNs before (Control) and after 20 min incubation with Bac (0.5 μM followed by subsequent incubation with 10 μM). **(F)** Summary of the effects of $GABA_B$ receptor activation by Bac in 2- and 8-month WT and Q175 SPNs (2 months: WT *n* = 11 and Q175 *n* = 9; eight and six mice, respectively; eight month: WT *n* = 11 and Q175 *n* = 12; six mice for each genotype.

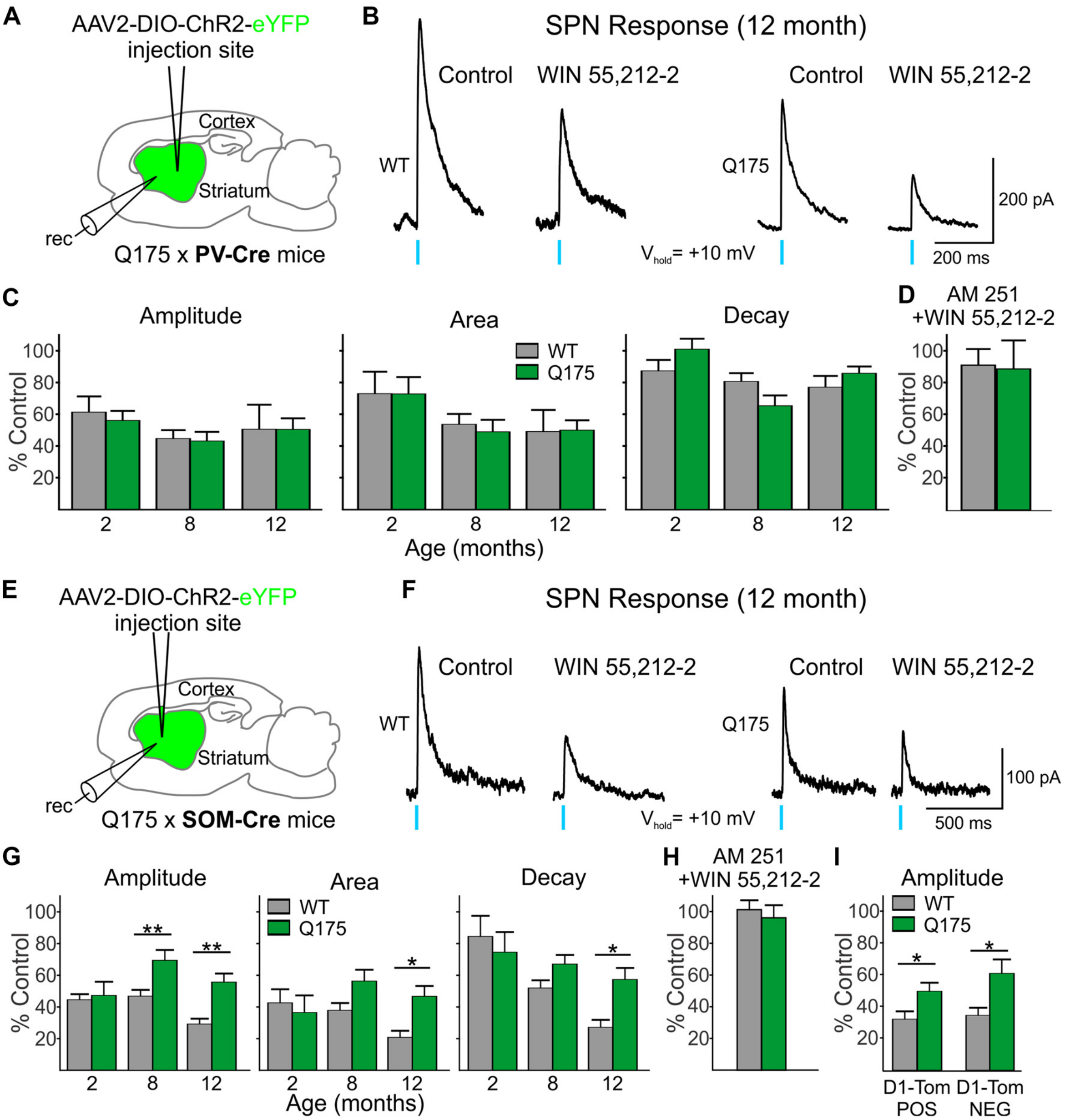

FIGURE 6 | Reduced effect on GABA responses in Q175 SPNs by the cannabinoid type 1 (CB1) receptor agonist WIN 55,212-2 was observed when activating SOM- but not PV-expressing interneurons. **(A)** Schematic of AAV injection/recording site and mouse line used for the data shown in **(B–D)**. **(B)** Sample traces of optically-evoked, PV-expressing interneuron-induced GABA responses in WT and Q175 SPNs before (Control) and at the end of 20 min incubation with WIN 55,212-2 (3 μM). **(C)** Summary of the effects of CB1 activation in WT, presymptomatic Q175 (2 months) and symptomatic Q175 (8 and 12 months) SPNs. Average response properties (amplitude, area and decay time) are reported as a percentage of the Control response. **(D)** The effects of co-application of WIN-55,212-2 and the CB1 antagonist AM 251 (3 μM, 20 min) on GABA responses in WT and Q175 SPNs (2 months) following pre-incubation with AM 251. **(E)** Schematic of AAV injection/recording site and mouse line used for the data shown in **(F–I)**. **(F)** Sample traces of activation of SOM-expressing interneuron-induced GABA responses in WT and Q175 SPNs before (Control) and at the end of a 20 min incubation with WIN 55,212-2 (3 μM). **(G)** Summary of the effects of CB1 receptor activation on WT and Q175 SPNs from 2-, 8- and 12-month-old mice. **(H)** The effects of co-application of WIN-55,212-2 and AM 251 (3 μM) on GABA responses in WT and Q175 SPNs (8 months) following pre-incubation with AM 251. **(I)** The effects of presynaptic CB1 receptor activation by WIN 55,212-2 on GABA response amplitudes in SPNs from 12-month-old WT and symptomatic Q175 D1-Tom POS and D1-Tom NEG SPNs. Significant differences were determined using two-way ANOVAs and appropriate *post hoc* analyses, where $^{*}p < 0.05$ and $^{**}p < 0.01$.

application of WIN 55,212-2 (n = 12 for Q175s and n = 11 for WTs; five mice for each genotype; **Figure 6G**). However, at 8 months, the effect of WIN 55,212-2 on response amplitude was significantly smaller in SPNs from Q175 mice than in those from WTs ($F_{(1,67)}$ = 17.18, $p < 0.001$ for genotype; Holm-Sidak *post hoc* analyses: p = 0.002; n = 12 and seven mice for Q175s and $n = 15$ and eight mice for WTs). This reduced effect of WIN 55,212-2 on response amplitude was maintained in Q175 mice at 12 months ($p = 0.003$; $n = 10$ and four mice for Q175s and $n = 11$ and six mice for WTs). Similarly, average IPSC response areas were reduced but to a lesser extent in 8-month ($p = 0.057$) and 12-month Q175 SPNs ($F_{(1,67)} = 9.15$, $p < 0.004$ for genotype; Holm-Sidak *post hoc* analyses: $p = 0.002$). The difference between mean decay times in 12 month-old SPNs following WIN 55,212-2 treatment also was statistically significant ($F_{(1,67)} = 6.30$, $p = 0.015$ for genotype; Holm-Sidak *post hoc* analyses: $p = 0.003$). If the modulation of evoked IPSCs through activation of CB1 receptors were postsynaptic, one might expect effects to be similar regardless of the type of interneuron releasing GABA. However, WIN 55,212-2 differentially affected SPN responses to activation of PV- and SOM-expressing interneurons, thus indicating that the site of action of WIN 55,212-2 primarily resides at CB1 receptors on presynaptic terminals.

Since expression of CB1 receptors on the terminals of SOM-expressing interneurons in the striatum has not previously been reported in an HD mouse model using electrophysiological techniques, we also investigated the effects of CB1 receptor activation in the R6/2 mouse model. Because Horne et al. (2013) reported reduced CB1 receptors in NPY/nNOS-positive cells in R6/2 mice previously, we chose this model to compare with findings in Q175 mice. In the striatum, there are two types of NPY cells—either those that co-express nNOS or not (Ibáñez-Sandoval et al., 2011). The NPY/nNOS-positive cells are the majority of the two and correspond to the LTS interneurons. We expressed ChR2 in WT and symptomatic (60 days) R6/2 mice and determined the effects of WIN 55,212-2 on responses evoked by activation of SOM-expressing interneurons in SPNs. Similar to the observation in 12-month Q175 SPNs, the effect of CB1 receptor activation was reduced on optically-evoked GABA responses in SPNs from R6/2 mice. There was a genotype-dependent difference with WIN 55,212-2 on the amplitude of responses (50.1 ± 6.3% of control for R6/2s, $n = 14$ and eight mice vs. 32.7 ± 3.7% of control for WTs, $n = 11$ and seven mice; $t_{(23)} = 2.21$, $p = 0.037$), as well as on response areas (46.7 ± 5.1% of control for R6/2s vs. 25.7 ± 3.6% for control in WTs; $t_{(23)} = 3.14$, $p = 0.005$) and decay times (67.5 ± 4.8% of control for R6/2 s vs. 44.8 ± 4.7% of control for WTs; $t_{(23)} = 3.34$, $p = 0.003$; data not illustrated). Thus, CB1 receptor activation on the presynaptic terminals of SOM interneurons modulates GABA responses in SPNs to a lesser degree in both symptomatic Q175 and R6/2 mice compared to WTs.

To test the specificity of the effects of WIN 55,212-2, we pre-incubated slices from WT and symptomatic (8 month) Q175 mice with the CB1 receptor antagonist AM 251 (3 μM). Peak amplitudes of IPSCs evoked in SPNs by optical stimulation of SOM-expressing interneurons were unaltered by treatment with AM 251 (94.4 ± 11.6% of control for Q175 SPNs, $n = 4$ and 99.5 ± 2.2% of control for WT SPNs, $n = 4$). Following incubation with AM 251, a combination of WIN 55,212-2 and AM 251 was applied for 20 min. AM 251 effectively blocked the previously observed effects of WIN 55,212-2 on the response amplitudes in cells of both genotypes (96.1 ± 7.9% of control for Q175 SPNs and 101.2 ± 5.9% of control for WT SPNs; **Figure 6H**). The same selectivity experiment was performed on 2 month-old Q175 and WT PV-Cre mice. No significant changes in the response amplitudes were observed in Q175 and WT SPNs when WIN-55,212-2 was co-applied compared to the amplitudes of control responses in AM 251 alone (96.6 ± 19.5% of control for Q175 SPNs, $n = 3$ and 99.2 ± 11.0% of control for WT SPNs, $n = 4$; **Figure 6D**). These results provide evidence that the reductions seen in SOM- and PV-induced IPSCs after incubation with WIN-55,212-2 were due to selective activation of CB1 receptors.

Previous work in other HD mouse models has shown inhibitory input onto D2 receptor-expressing (D2), indirect pathway SPNs is increased compared to inhibitory input onto D1 receptor-expressing (D1), direct pathway SPNs (Andre et al., 2011; Cepeda et al., 2013). Since evoked responses in SPNs from activation of SOM-expressing interneurons are less affected by WIN 55,212-2 in symptomatic Q175 SPNs compared to WTs, we tested whether or not this effect is differential for the two types of SPNs. We crossed SOM-Cre mice with a Q175 mouse line that expresses tdTomato in D1 receptor-containing SPNs. We expressed ChR2 in SOM-expressing interneurons and recorded evoked IPSCs in D1-tdTomato positive (D1-Tom POS) and negative (D1-Tom NEG) SPNs from both Q175 and WT mice (seven and six mice, respectively) at 8 months of age. Peak amplitudes of optically-evoked responses were statistically similar in D1-Tom POS and D1-Tom NEG cells in both genotypes (Q175: 83.1 ± 12.1 pA in D1-Tom POS and 86.8 ± 11.6 pA in D1-TOM NEG cells, where $n = 10$ and 10 cells, respectively; WT: 111.2 ± 21.6 pA in D1-Tom POS and 100.8 ± 14.7 pA in D1-TOM NEG cells, where $n = 11$ and 10 cells, respectively). After treatment with WIN 55,212-2 for 20 min, both D1-Tom POS and D1-TOM NEG responses were reduced similarly, although the amplitude of evoked IPSCs in Q175 SPNs of both types was less affected than SPNs in WT mice ($F_{(1,37)} = 13.1$, $p < 0.001$ for genotype; Holm-Sidak *post hoc* analyses for genotype effects: $p = 0.045$ and $p = 0.004$ for D1-tom POS and NEG, respectively; **Figure 6I**). Response areas also were less affected in Q175s for both types of SPNs compared to WTs (data not illustrated), although the difference was only statistically significant for D1-Tom POS cells (D1-Tom POS: 46.8 ± 7.3% of control for Q175s vs. 25.2 ± 6.7% of control for WTs; D1-Tom NEG: 47.7 ± 7.0% of control for Q175s vs. 29.9 ± 6.8% of control for WTs; $F_{(1,37)} = 8.30$, $p = 0.007$ for genotype; Holm-Sidak *post hoc* analyses for genotype effects: $p = 0.030$ and $p = 0.076$ for D1-tom POS and NEG, respectively). No significant differences were observed for response decay times for either cell type (D1-Tom POS: 55.7 ± 6.1% of control for Q175s vs. 44.0 ± 5.4% of control for WTs; D1-Tom NEG: 61.0 ± 7.7% of control for Q175s vs. 52.8 ± 7.2% of control for WTs; $F_{(1,37)} = 2.306$, $p = 0.137$; data not illustrated). These data further support our conclusion that CB1 receptors, specifically on the presynaptic terminals of SOM-expressing interneurons, are less effective at reducing the inhibition to SPNs in mouse models of HD.

To investigate whether or not altered CB1 receptors on D1 receptor-expressing SPN terminals contribute to increased inhibitory events in symptomatic Q175 mice, we examined the effects of WIN 55,212-2 on evoked IPSCs in SPNs following activation of D1 receptor-expressing SPN terminals. Here, we selectively expressed ChR2 in 13–15 month-old Q175 and WT mice that were crossed with D1-Cre mice (six and three mice, respectively). Recordings were performed only in SPNs within close proximity to the striatal injection site and that did not express ChR2. We considered these SPNs as D2 receptor-containing since they lacked opsin expression. We found no significant genotype-dependent alterations in optically-evoked IPSC response amplitudes, areas or decay times (Amplitude: 54.2 ± 7.5% of control for Q175s vs. 47.9 ± 3.7% of control for WTs, $p = 0.457$; Area: 42.7 ± 6.8% of control for Q175s vs. 39.1 ± 4.8% of control for WTs, $p = 0.677$; Decay time: 73.4 ± 6.5% of control for Q175s vs. 79.6 ± 8.7% of control for WTs, $p = 0.575$. $n = 9$ cells each). These results suggest CB1 receptor signaling is not differentially affected at Q175 D1 receptor-expressing SPN terminals in WT and Q175 mice and thereby does not contribute to the increase in inhibitory synaptic events observed in D2 receptor-expressing SPNs in HD mouse models.

CB1 Receptor Signaling Is Affected at Corticostriatal Synapses in Symptomatic Q175 Mice

Since it has been shown that activation of CB1 receptors on excitatory cortical afferents can modulate glutamate release in the striatum (Gerdeman and Lovinger, 2001) we also investigated whether CB1 receptor-mediated signaling on corticostriatal terminals is progressively affected in Q175 mice. ChR2 driven by the CaMKII promoter was injected in the right M1 cortical region of 2, 8 and 12 month-old Q175 and WT mice (**Figure 7A1**). Slices were decorticated and optically-evoked EPSCs were recorded in SPNs in the presence of the $GABA_A$ receptor antagonist, bicuculline (BIC, 10 μM; **Figure 7B**). No genotype-specific differences in the amplitude or area of evoked EPSCs were observed until 12 months. At this age, the evoked EPSCs in Q175 SPNs ($n = 22$) were smaller in amplitude (283.8 ± 50.6 pA for Q175 SPNs vs. 533.4 ± 52.4 pA for WTs; $F_{(1,107)} = 4.19$, $p = 0.043$ for genotype; Holm-Sidak *post hoc* analyses: $p = 0.004$) and there was a trend for smaller area (5539.5 ± 1290.6 pA × ms for Q175 SPNs vs. 10388.2 ± 1262.3 pA × ms for WTs, $p = 0.096$ for genotype), but decay times were similar to WTs ($n = 24$, 23.3 ± 2.4 ms for Q175 SPNs and 24.4 ± 1.7 ms for WTs). Similarly, genotype-specific alterations in CB1-mediated modulation of corticostriatal inputs were not apparent until 12 months (**Figure 7C**). Evoked corticostriatal EPSCs in Q175 SPNs ($n = 21$) were less sensitive to CB1 modulation compared to EPSCs in WTs ($n = 22$; amplitude: $F_{(2,95)} = 3.13$, $p = 0.043$ for genotype × age; Holm-Sidak *post hoc* analyses: $p = 0.005$; area: $F_{(2,94)} = 3.37$, $p = 0.039$; Holm-Sidak *post hoc* analyses: $p = 0.025$). The reduced CB1 effect on Q175 SPN IPSCs from SOM-expressing interneurons appears to precede the CB1 receptor-mediated alterations observed in Q175 corticostriatal projections (compare **Figures 6**, **7**).

DISCUSSION

Motor impairment as a result of striatal atrophy and microcircuit dysfunction is a hallmark pathology of HD. While much attention has focused on alterations in glutamatergic signaling due to the excitotoxic nature of glutamate, changes in the corticostriatal pathway may only partially explain the progression of motor abnormalities associated with HD. Alterations in GABAergic synaptic transmission in the striatum are observed in symptomatic HD mice and are also likely to contribute to abnormal movements (Cepeda et al., 2004, 2013; Dvorzhak et al., 2013; Indersmitten et al., 2015; Garret et al., 2018; Reiner and Deng, 2018). We focused on striatal GABAergic interneurons as the main sources of increased inhibitory synaptic transmission since abnormalities in their intrinsic and synaptic properties have been observed in HD mice (Cepeda et al., 2013; Holley et al., 2019). By selectively exciting or inhibiting discrete interneuron subtypes with optogenetic techniques, we examined the synaptic contributions of PV- and SOM-expressing interneurons in the Q175 HD mouse model. Optically silencing striatal SOM-expressing interneurons, which normally fire spontaneously, reduced the activity-dependent enhancement of spontaneous GABA synaptic currents in SPNs from HD mice to levels observed in WT mice. Our results also suggest that a plausible mechanism contributing to the enhancement of GABA synaptic activity in HD mice is the downregulation of CB1 receptors located on presynaptic terminals of SOM- but not PV-expressing interneurons. In addition, we found that although the amplitude of GABA responses induced in SPNs by optical activation of PV- or SOM-expressing interneurons was not different between genotypes, the decay time was significantly faster in SPNs from HD mice. These findings offer insight into the relative impact that each of these two types of interneurons has in altering striatal output by modulating the activity of SPNs in HD.

In agreement with previous studies, we observed the average sIPSC frequency in Q175 SPNs was increased compared to WTs (Dvorzhak et al., 2013; Indersmitten et al., 2015). Since SOM-expressing but not PV-expressing interneurons are spontaneously active at rest and increased sIPSC frequency is activity-dependent, we posited that these interneurons play a pivotal role in this effect. We previously reported in Q175 mice that some LTS interneurons displayed increased action potential firing within oscillating bursts (Holley et al., 2019) thus predicting that while in this more excitable state, they may release more GABA onto SPNs. As such, we demonstrate that optical activation of halorhodopsin in SOM-expressing interneurons induced a decrease in the overall frequency of sIPSCs that was more pronounced and occurred in a greater percentage of SPNs in symptomatic Q175 and R6/2 mice than in WTs. Further, silencing SOM-expressing interneurons reduced sIPSC frequencies in Q175 SPNs to levels observed in WTs. These results support the premise that excessive activity of SOM-expressing interneurons primarily contributes to the

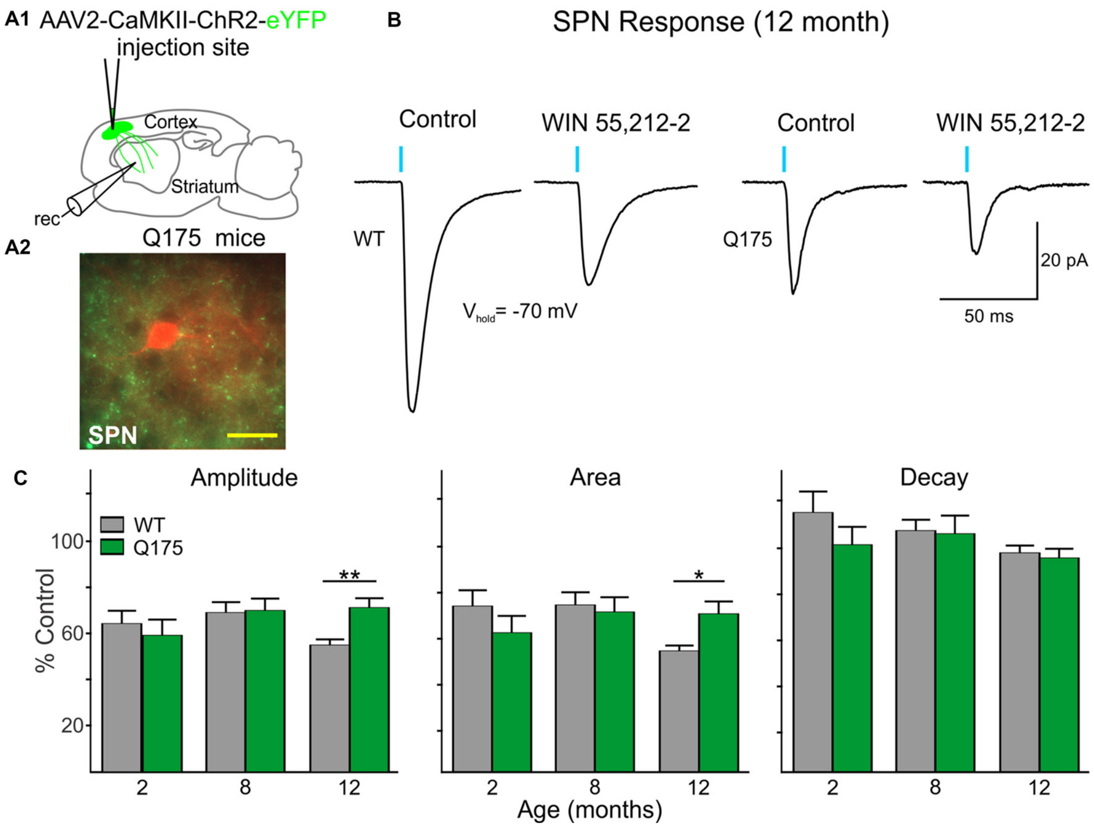

FIGURE 7 | Excitatory postsynaptic currents (EPSCs) from the cortex are reduced in Q175 SPNs recorded in fully symptomatic mice and are less sensitive to modulation by WIN 55,212-2 compared to WT SPNs. **(A1)** Schematic of AAV injection site and recording area in Q175 mice for experiments examining CB1 receptor-mediated modulation of excitatory cortical inputs onto SPNs. **(A2)** Confocal z-stack image of a biocytin-filled SPN (red) that was recorded from an 8 months-old Q175 mouse. Corticostriatal processes expressing ChR2-eYFP are seen surrounding the recorded cell. Scale bar = 20 μm. **(B)** Sample traces of optically-evoked, cortical-induced glutamatergic responses in WT and Q175 SPNs before (Control) and at the end of 20 min incubation with WIN 55,212-2 (3 μM). **(C)** Summary of the effects of WIN 55,212-2 (3 μM) on optically-evoked EPSCs from WT and Q175 SPNs from 2-, 8- and 12-month-old mice. Average response properties (amplitude, area and decay time) are reported as a percentage of the Control response. Significant differences were determined using two-way ANOVAs and appropriate *post hoc* analyses, where $^*p < 0.05$ and $^{**}p < 0.01$.

increased GABA synaptic activity observed in SPNs in HD mouse models. Incidentally, striatal SOM levels are increased in HD patients (Aronin et al., 1983) supporting the hypothesis that increased firing of these interneurons also results in the increased release of neuroprotective factors. Although we can only surmise that the reason for the increase in SOM-expressing interneuron activity is a potential compensatory mechanism to offset the glutamatergic dysregulation observed in HD mice (Cepeda et al., 2007; Bunner and Rebec, 2016), an unintended consequence of SOM upregulation is also an increase in spontaneous, activity-dependent, GABA synaptic activity (Cepeda et al., 2004).

Since we previously observed evoked IPSCs with larger amplitudes in SPNs of R6/2 mice compared to WTs following activation of PV-expressing interneurons (Cepeda et al., 2013), we presumed that PV-expressing interneurons would also be a main contributor to increased GABA synaptic activity in the striatum of symptomatic Q175 mice (Indersmitten et al., 2015). Additionally, FSIs exhibit greater connectivity to SPNs than LTS or other neighboring SPNs (Tepper et al., 2004; Cepeda et al., 2013) and in Q175 mice the resting membrane potentials of these interneurons are more depolarized (Holley et al., 2019), thus making PV-expressing interneurons a likely candidate involved in the increased inhibition onto SPNs. However, unlike what was observed in R6/2 mice (Cepeda et al., 2013), we saw no genotype-dependent differences in evoked IPSC amplitudes after optically-stimulating either PV- or SOM-expressing interneurons in Q175 mice. This is likely due to how responsive intracellular homeostatic mechanisms within PV-expressing interneurons are in the context of a severe vs. a more slowly progressing HD environment. In a recent study from our laboratory, PV-expressing interneurons in the Q175 striatum were found to exhibit signs of degeneration as evidenced by the decreased cell membrane capacitances, smaller somatic areas and reduced neurite arborizations in these interneurons (Holley et al., 2019). Likewise, in HD patients with the adult-onset form of the disease where the progression of the disease phenotype takes decades to fully manifest, the number of PV-expressing interneurons is reduced while the number of SOM-expressing neurons remains constant (Reiner et al., 2013). Thus, PV-expressing interneurons appear to be more vulnerable over long periods of time, implying that they lack the ability to upregulate GABA synaptic activity through possible loss of synaptic connections to SPNs. It would be of interest to determine if PV-interneuron connectivity to other striatal neurons is altered in HD. Interestingly, loss of PV-expressing neurons in addition to morphological signs of degeneration have also been observed in the brains of multiple sclerosis patients and mouse models (Dutta et al., 2006; Clements et al., 2008; Falco et al., 2014).

We provide evidence that a plausible contributing mechanism underlying the overall increase in the frequency of sIPSCs induced by the hyperactivity of SOM-expressing interneurons is a dysregulation of the endocannabinoid system in these interneurons. Selectively activating SOM-expressing interneurons in the presence of WIN 55,212-2 demonstrated that CB1 receptors on the terminals of these interneurons are either reduced or less sensitive in Q175 mice, beginning at 8 months of age. The prevailing function of CB1 receptor activation is to inhibit synaptic activity and likewise, activation of CB1 receptors has been shown to suppress both excitatory and inhibitory neurotransmitter release in multiple brain regions (Szabo et al., 1998; Katona et al., 1999; Hajos et al., 2000; Gerdeman and Lovinger, 2001; Hentges et al., 2005; reviewed in Katona and Freund, 2012). In the striatum of HD patients and in mouse models, CB1 receptor mRNA transcript levels and binding of exogenous cannabimimetics is reduced (Denovan-Wright and Robertson, 2000; Glass et al., 2000; Lastres-Becker et al., 2002; McCaw et al., 2004; Menalled et al., 2012). Additionally, previous studies showed the sensitivity of striatal GABA synapses to cannabinoid receptor stimulation is severely impaired in R6/2 mice (Centonze et al., 2005). We now demonstrate that this effect is selective for SOM-, not PV-expressing interneurons in symptomatic 8-month-old mice at synapses on both direct (D1) and indirect (D2) pathway SPNs. This observation agrees with a previous study in HD showing that CB1 receptors are downregulated specifically in NPY/NOS-expressing interneurons while remaining unchanged in PV-expressing interneurons (Horne et al., 2013). We also observed decreased CB1 sensitivity to cortical inputs, but not until 12 months of age suggesting that HD-related alterations of CB1 receptors on inhibitory SOM-interneuron terminals may precede those on excitatory corticostriatal projections. However, solid evidence would require additional quantitative immunohistochemical analyses in addition to ligand binding studies.

While attempting to elucidate a mechanism behind this increased inhibitory synaptic activity in the HD striatum, we also sought to determine if interneuron-specific $GABA_B$ signaling was affected in Q175 mice. Additionally, excess GABA may affect neurotransmitter release (excitatory and inhibitory) through activation of presynaptic $GABA_B$ receptors. Although we observed that $GABA_B$ signaling at interneuron-SPN synapses is intact in presymptomatic and symptomatic mice, we found the sensitivity of the IPSC depression differed between PV- and SOM-expressing interneuron synapses. Unlike ionotropic $GABA_A$ receptors that rapidly activate upon ligand binding and can alter membrane potentials due to their permeability to Cl^- ions (Olsen and Sieghart, 2009), $GABA_B$ receptors are coupled to intracellular G-protein signaling cascades and are able to modulate neurotransmitter release by inhibiting voltage-dependent Ca^{2+} channels (Wu and Saggau, 1995). Thus, it would seem likely that if terminals of SOM-expressing interneurons contain more $GABA_B$ receptors than the terminals of PV-expressing interneurons, a $GABA_B$ receptor agonist would produce greater inhibition of neurotransmitter release at these synapses. Although the density of $GABA_B$ receptors on striatal interneuron terminals has not been well characterized, this does seem to be the case for SOM interneuron synapses in the rat hippocampus where immunolabeling of the $GABA_B$R-1 subunit is stronger than for all other cells (Sloviter et al., 1999). Additionally, baclofen produced a greater depression of SOM-expressing interneuron-mediated IPSCs compared to those mediated by activation of PV-expressing interneurons in the dorso-medial prefrontal cortex of mice (Liu et al., 2017). Thus, we contend that the increased frequency of sIPSCs in HD mice is not dependent on dysfunctional $GABA_B$ signaling at PV and SOM-expressing interneuron terminals. However, alterations in $GABA_B$ receptor signaling at other interneuron or SPN synapses in HD mice cannot be excluded.

We observed that the amplitude of GABA responses evoked in SPNs by photoactivation of PV- and SOM-expressing interneurons was not affected between genotypes, but the decay time was significantly faster in cells from Q175 mice, beginning at 8 months for responses evoked by SOM-expressing interneuron activation and at 12 months for responses evoked by PV-expressing interneuron activation, although there was a trend for more rapid kinetics at 8 months as well. Non-selectively activating all GABAergic inputs with electrical stimulation also resulted in IPSC responses with similar amplitudes in Q175 and WT SPNs but displayed more rapid decay times (unpublished observation). Faster decay times of spontaneous, electrically- and pharmacologically-evoked GABA responses also were observed in slices and dissociated SPNs from R6/2 mice (Cepeda et al., 2004, 2013). Similar to observations in symptomatic Q175 mice, evoked IPSCs following activation of PV- and SOM-expressing interneurons in R6/2 mice exhibited faster decay times. It is enigmatic to observe more rapid kinetics in responses evoked by stimulating GABAergic interneurons while decay time kinetics appear similar to WTs for evoked excitatory responses in Q175 SPNs and for inhibitory responses induced by stimulation of other SPNs. Given that rapid decay times appear to be associated with mainly interneurons than other cell types in HD mice, possible explanations include alterations in mechanisms of presynaptic neurotransmitter release (Hefft and Jonas, 2005; Keros and Hablitz, 2005), differential expression of GABA transporters (Overstreet and Westbrook, 2003), modulation of postsynaptic GABA receptor subunit composition or subtypes or a combination of any of the above. Nevertheless. more rapid kinetics was shown to be associated with enhanced expression of the α1 subunit, corroborating the idea that this subunit contributes to faster IPSCs (Okada et al., 2000; Barberis et al., 2007). Incidentally, α1 subunit expression also is increased in the striatum of early and fully symptomatic HD mice (Cepeda et al., 2004; Du et al., 2017).

In the present study, we also observed a reduction in the amplitude of PV-expressing interneuron-evoked IPSCs as a function of age in WT but not in Q175 mice. This effect suggests reduced connectivity between FSIs and SPNs with age. In our previous studies looking at the effects of age on corticostriatal neurotransmission, we demonstrated an age-dependent decline of evoked excitatory responses (Cepeda et al., 1996). Here we show this effect can be generalized to PV-expressing interneuron-mediated inhibitory neurotransmission, consistent with neurochemical studies showing reduced levels of GABA transmission in old mice (see for example Duarte et al., 2014).

While the present findings point to SOM interneurons as the primary source of increased GABA synaptic activity in HD mice, other potential sources should be considered. For example, a subset of pallidal neurons project back to the striatum (Mastro et al., 2014; Abdi et al., 2015; Glajch et al., 2016). Although the main target of GPe inhibitory input is the FSIs, it is possible that a small proportion innervates MSNs (Glajch et al., 2016). In addition, long-range, PV- and SOM-mediated inhibitory cortical inputs to striatal SPNs were described recently (Rock et al., 2016; Melzer et al., 2017) and other types of striatal interneurons (e.g., TH- and calretinin-expressing interneurons) could potentially contribute to aberrant GABAergic synaptic activity in HD. The role of these inputs needs to be elucidated in future studies. In addition, although a postsynaptic mechanism is the most likely explanation for faster decay times, further experiments exploring changes in paired-pulse ratios using an opsin with a high temporal resolution, as well as changes in $GABA_A$ receptor subunit composition in the striatum of Q175 mice seem warranted.

Finally, in the present study, we could not determine if differences in frequency of sIPSCs occur in SPNs belonging to the direct or indirect pathway. Our previous studies in the more severe R6/2 transgenic mouse model showed that the increase in GABA activity affects mostly MSNs of the indirect pathway (Cepeda et al., 2013). The changes in IPSC frequency observed in Q175 knock-in mice are more complex as they are age- and gene dose-dependent. In $Q175^{+/-}$ mice the change in frequency is subtle and does not reach statistical significance, whereas, in homozygous mice ($Q175^{+/+}$), increased frequency of sIPSCs is statistically significant (Indersmitten et al., 2015). As the present study was constrained to using heterozygous Q175 mice, this experiment could not be performed.

CONCLUSIONS AND INTERPRETATIONS

The present findings demonstrate that SOM- but not PV-expressing interneurons are the main contributors to increased GABA synaptic activity observed in genetic mouse models of HD. Upregulation of SOM-expressing interneuron function is associated with loss and/or reduced sensitivity of CB1 receptors specifically on this type of interneuron. Furthermore, optogenetic silencing of SOM-expressing interneurons reestablished normal GABA synaptic activity, suggesting novel avenues to restore the excitatory/inhibitory balance lost in HD. However, if indeed SOM has neuroprotective properties, caution must be exerted not to perturb this homeostatic mechanism.

At present, it is still premature to explain why SOM-expressing interneuron activity is upregulated in HD. Although we could speculate that increased activity is a compensatory mechanism to prevent excitotoxic levels of glutamate released from cortical and thalamic terminals, previous studies have demonstrated that neurogliaform, not SOM-expressing, interneurons are able to modulate cortical inputs (Logie et al., 2013). Further, we also have to consider that in HD GABA could be excitatory, at least in the hippocampus of symptomatic mice (Dargaei et al., 2019). Interestingly, a recent study found that both GABA and glutamate can be released simultaneously onto striatal SPNs in response to photoactivation of SOM-expressing interneurons (Cattaneo et al., 2019). While the glutamatergic response is short-lived, the GABA response is persistent. In HD mouse models we demonstrated a progressive reduction in glutamatergic inputs onto SPNs (Cepeda et al., 2003). It is possible that, if indeed SOM-expressing interneuron activation is both excitatory and inhibitory, reduced excitatory input can be supplanted by intrinsic activation from SOM-expressing interneurons. Thus, at present, the most parsimonious explanation for SOM-expressing interneuron upregulation in HD is either to fulfill a neuroprotective role or to compensate for the loss of excitatory inputs.

ETHICS STATEMENT

This study was carried out in accordance with the recommendations of the United States Public Health Service Guide for Care and Use of Laboratory Animals.

AUTHOR CONTRIBUTIONS

SH, LG, ML and CC designed research. SH and LG performed research. SH, LG, TK and AD analyzed data. SH, ML and CC wrote the article.

FUNDING

This work was funded by the CHDI Foundation (contracts A5666, A8462).

ACKNOWLEDGMENTS

We thank Drs Vahri Beaumont and Joshua Barry for providing insightful discussions. We also thank Janelle Asai, Poonam Sachan and Zhongliang Zhao for technical assistance with mouse breeding and genotyping.

SUPPLEMENTARY MATERIAL

The Supplementary Material for this article can be found online at: https://www.frontiersin.org/articles/10.3389/fnsyn.2019.00014/full#supplementary-material

REFERENCES

Abdi, A., Mallet, N., Mohamed, F. Y., Sharott, A., Dodson, P. D., Nakamura, K. C., et al. (2015). Prototypic and arkypallidal neurons in the dopamine-intact external globus pallidus. *J. Neurosci.* 35, 6667–6688. doi: 10.1523/JNEUROSCI.4662-14.2015

Albin, R. L., Reiner, A., Anderson, K. D., Penney, J. B., and Young, A. B. (1990). Striatal and nigral neuron subpopulations in rigid Huntington's disease: implications for the functional anatomy of chorea and rigidity-akinesia. *Ann. Neurol.* 27, 357–365. doi: 10.1002/ana.410270403

Andre, V. M., Fisher, Y. E., and Levine, M. S. (2011). Altered balance of activity in the striatal direct and indirect pathways in mouse models of Huntington's disease. *Front. Syst. Neurosci.* 5:46. doi: 10.3389/fnsys.2011.00046

Aronin, N., Cooper, P. E., Lorenz, L. J., Bird, E. D., Sagar, S. M., Leeman, S. E., et al. (1983). Somatostatin is increased in the basal ganglia in Huntington disease. *Ann. Neurol.* 13, 519–526. doi: 10.1002/ana.410130508

Barberis, A., Mozrzymas, J. W., Ortinski, P. I., and Vicini, S. (2007). Desensitization and binding properties determine distinct $\alpha1\beta2\gamma2$ and $\alpha3\beta2\gamma2$ $GABA_A$ receptor-channel kinetic behavior. *Eur. J. Neurosci.* 25, 2726–2740. doi: 10.1111/j.1460-9568.2007.05530.x

Bates, G. P., Dorsey, R., Gusella, J. F., Hayden, M. R., Kay, C., Leavitt, B. R., et al. (2015). Huntington disease. *Nat. Rev. Dis. Primers* 1:15005. doi: 10.1038/nrdp.2015.5

Bolam, J. P., Hanley, J. J., Booth, P. A., and Bevan, M. D. (2000). Synaptic organisation of the basal ganglia. *J. Anat.* 196, 527–542. doi: 10.1046/j.1469-7580.2000.19640527.x

Bunner, K. D., and Rebec, G. V. (2016). Corticostriatal dysfunction in Huntington's disease: the basics. *Front. Hum. Neurosci.* 10:317. doi: 10.3389/fnhum.2016.00317

Calabresi, P., Mercuri, N. B., De Murtas, M., and Bernardi, G. (1991). Involvement of GABA systems in feedback regulation of glutamate-and GABA-mediated synaptic potentials in rat neostriatum. *J. Physiol.* 440, 581–599. doi: 10.1113/jphysiol.1991.sp018726

Cattaneo, S., Zaghi, M., Maddalena, R., Bedogni, F., Sessa, A., and Taverna, S. (2019). Somatostatin-expressing interneurons co-release GABA and glutamate onto different postsynaptic targets in the striatum. *bioRxiv*. doi: 10.1101/566984 Available online at: https://www.biorxiv.org/content/10.1101/566984v2. Accessed May 1, 2019.

Centonze, D., Rossi, S., Prosperetti, C., Tscherter, A., Bernardi, G., Maccarrone, M., et al. (2005). Abnormal sensitivity to cannabinoid receptor stimulation might contribute to altered γ-aminobutyric acid transmission in the striatum of R6/2 Huntington's disease mice. *Biol. Psychiatry* 57, 1583–1589. doi: 10.1016/j.biopsych.2005.03.008

Cepeda, C., Cummings, D. M., André, V. M., Holley, S. M., and Levine, M. S. (2010). Genetic mouse models of Huntington's disease: focus on electrophysiological mechanisms. *ASN Neuro* 2:e00033. doi: 10.1042/an20090058

Cepeda, C., Galvan, L., Holley, S. M., Rao, S. P., André, V. M., Botelho, E. P., et al. (2013). Multiple sources of striatal inhibition are differentially affected in Huntington's disease mouse models. *J. Neurosci.* 33, 7393–7406. doi: 10.1523/JNEUROSCI.2137-12.2013

Cepeda, C., Hurst, R. S., Calvert, C. R., Hernández-Echeagaray, E., Nguyen, O. K., Jocoy, E., et al. (2003). Transient and progressive electrophysiological alterations in the corticostriatal pathway in a mouse model of Huntington's disease. *J. Neurosci.* 23, 961–969. doi: 10.1523/JNEUROSCI.23-03-00961.2003

Cepeda, C., Li, Z., and Levine, M. S. (1996). Aging reduces neostriatal responsiveness to N-methyl-D-aspartate and dopamine: an *in vitro* electrophysiological study. *Neuroscience* 73, 733–750. doi: 10.1016/0306-4522(96)00056-5

Cepeda, C., Starling, A. J., Wu, N., Nguyen, O. K., Uzgil, B., Soda, T., et al. (2004). Increased GABAergic function in mouse models of Huntington's disease: reversal by BDNF. *J. Neurosci. Res.* 78, 855–867. doi: 10.1002/jnr.20344

Cepeda, C., Wu, N., Andre, V. M., Cummings, D. M., and Levine, M. S. (2007). The corticostriatal pathway in Huntington's disease. *Prog. Neurobiol.* 81, 253–271. doi: 10.1016/j.pneurobio.2006.11.001

Chuhma, N., Tanaka, K. F., Hen, R., and Rayport, S. (2011). Functional connectome of the striatal medium spiny neuron. *J. Neurosci.* 31, 1183–1192. doi: 10.1523/JNEUROSCI.3833-10.2011

Clements, R. J., McDonough, J., and Freeman, E. J. (2008). Distribution of parvalbumin and calretinin immunoreactive interneurons in motor cortex from multiple sclerosis post-mortem tissue. *Exp. Brain Res.* 187, 459–465. doi: 10.1007/s00221-008-1317-9

Dargaei, Z., Liang, X., Serranilla, M., Santos, J., and Woodin, M. A. (2019). Alterations in hippocampal inhibitory synaptic transmission in the R6/2 mouse model of Huntington's disease. *Neuroscience* 404, 130–140. doi: 10.1016/j.neuroscience.2019.02.007

Denovan-Wright, E. M., and Robertson, H. A. (2000). Cannabinoid receptor messenger RNA levels decrease in a subset of neurons of the lateral striatum, cortex and hippocampus of transgenic Huntington's disease mice. *Neuroscience* 98, 705–713. doi: 10.1016/s0306-4522(00)00157-3

Du, Z., Tertrais, M., Courtand, G., Leste-Lasserre, T., Cardoit, L., Masmejean, F., et al. (2017). Differential alteration in expression of striatal GABAAR subunits in mouse models of Huntington's disease. *Front. Mol. Neurosci.* 10:198. doi: 10.3389/fnmol.2017.00198

Duarte, J. M., Do, K. Q., and Gruetter, R. (2014). Longitudinal neurochemical modifications in the aging mouse brain measured *in vivo* by 1H magnetic resonance spectroscopy. *Neurobiol. Aging* 35, 1660–1668. doi: 10.1016/j.neurobiolaging.2014.01.135

Dutta, R., McDonough, J., Yin, X., Peterson, J., Chang, A., Torres, T., et al. (2006). Mitochondrial dysfunction as a cause of axonal degeneration in multiple sclerosis patients. *Ann. Neurol.* 59, 478–489. doi: 10.1002/ana.20736

Dvorzhak, A., Semtner, M., Faber, D. S., and Grantyn, R. (2013). Tonic mGluR5/CB1-dependent suppression of inhibition as a pathophysiological hallmark in the striatum of mice carrying a mutant form of huntingtin. *J. Physiol.* 591, 1145–1166. doi: 10.1113/jphysiol.2012.241018

Falco, A., Pennucci, R., Brambilla, E., and de Curtis, I. (2014). Reduction in parvalbumin-positive interneurons and inhibitory input in the cortex of mice with experimental autoimmune encephalomyelitis. *Exp. Brain Res.* 232, 2439–2449. doi: 10.1007/s00221-014-3944-7

Garret, M., Du, Z., Chazalon, M., Cho, Y. H., and Baufreton, J. (2018). Alteration of GABAergic neurotransmission in Huntington's disease. *CNS Neurosci. Ther.* 24, 292–300. doi: 10.1111/cns.12826

Gerdeman, G., and Lovinger, D. M. (2001). CB1 cannabinoid receptor inhibits synaptic release of glutamate in rat dorsolateral striatum. *J. Neurophysiol.* 85, 468–471. doi: 10.1152/jn.2001.85.1.468

Glajch, K. E., Kelver, D. A., Hegeman, D. J., Cui, Q., Xenias, H. S., Augustine, E. C., et al. (2016). $Npas1^+$ pallidal neurons target striatal projection neurons. *J. Neurosci.* 36, 5472–5488. doi: 10.1523/JNEUROSCI.1720-15.2016

Glass, M., Dragunow, M., and Faull, R. L. (2000). The pattern of neurodegeneration in Huntington's disease: a comparative study of cannabinoid, dopamine, adenosine and $GABA_A$ receptor alterations in the human basal ganglia in Huntington's disease. *Neuroscience* 97, 505–519. doi: 10.1016/s0306-4522(00)00008-7

Hajos, N., Katona, I., Naiem, S. S., MacKie, K., Ledent, C., Mody, I., et al. (2000). Cannabinoids inhibit hippocampal GABAergic transmission and network oscillations. *Eur. J. Neurosci.* 12, 3239–3249. doi: 10.1046/j.1460-9568.2000.00217.x

Hefft, S., and Jonas, P. (2005). Asynchronous GABA release generates long-lasting inhibition at a hippocampal interneuron-principal neuron synapse. *Nat. Neurosci.* 8, 1319–1328. doi: 10.1038/nn1542

Heikkinen, T., Lehtimaki, K., Vartiainen, N., Puoliväali, J., Hendricks, S. J., Glaser, J. R., et al. (2012). Characterization of neurophysiological and behavioral changes, MRI brain volumetry and 1H MRS in zQ175 knock-in mouse model of Huntington's disease. *PLoS One* 7:e50717. doi: 10.1371/journal.pone.0050717

Hentges, S. T., Low, M. J., and Williams, J. T. (2005). Differential regulation of synaptic inputs by constitutively released endocannabinoids and exogenous cannabinoids. *J. Neurosci.* 25, 9746–9751. doi: 10.1523/JNEUROSCI.2769-05.2005

Holley, S. M., Galvan, L., Kamdjou, T., Cepeda, C., and Levine, M. S. (2019). Striatal GABAergic interneuron dysfunction in the Q175 mouse model of Huntington's disease. *Eur. J. Neurosci.* 49, 79–93. doi: 10.1111/ejn.14283

Holley, S. M., Joshi, P. R., Parievsky, A., Galvan, L., Chen, J. Y., Fisher, Y. E., et al. (2015). Enhanced GABAergic inputs contribute to functional alterations of cholinergic interneurons in the R6/2 mouse model of Huntingtin's disease. *eNeuro* 2:e0008. doi: 10.1523/eneuro.0008-14.2015

Horne, E. A., Coy, J., Swinney, K., Fung, S., Cherry, A. E., Marrs, W. R., et al. (2013). Downregulation of cannabinoid receptor 1 from neuropeptide Y interneurons in the basal ganglia of patients with Huntington's disease and mouse models. *Eur. J. Neurosci.* 37, 429–440. doi: 10.1111/ejn.12045

Hsu, Y. T., Chang, Y. G., and Chern, Y. (2018). Insights into GABAAergic system alteration in Huntington's disease. *Open Biol.* 8:180165. doi: 10.1098/rsob.180165

Ibáñez-Sandoval, O., Tecuapetla, F., Unal, B., Shah, F., Koós, T., and Tepper, J. M. (2011). A novel functionally distinct subtype of striatal neuropeptide Y interneuron. *J. Neurosci.* 31, 16757–16769. doi: 10.1523/JNEUROSCI.2628-11.2011

Indersmitten, T., Tran, C. H., Cepeda, C., and Levine, M. S. (2015). Altered excitatory and inhibitory inputs to striatal medium-sized spiny neurons and cortical pyramidal neurons in the Q175 mouse model of Huntington's disease. *J. Neurophysiol.* 113, 2953–2966. doi: 10.1152/jn.01056.2014

Katona, I., and Freund, T. F. (2012). Multiple functions of endocannabinoid signaling in the brain. *Annu. Rev. Neurosci.* 35, 529–558. doi: 10.1146/annurev-neuro-062111-150420

Katona, I., Sperlágh, B., Sík, A., Käfalvi, A., Vizi, E. S., Mackie, K., et al. (1999). Presynaptically located CB1 cannabinoid receptors regulate GABA release from axon terminals of specific hippocampal interneurons. *J. Neurosci.* 19, 4544–4558. doi: 10.1523/JNEUROSCI.19-11-04544.1999

Keros, S., and Hablitz, J. J. (2005). Subtype-specific GABA transporter antagonists synergistically modulate phasic and tonic GABA_A conductances in rat neocortex. *J. Neurophysiol.* 94, 2073–2085. doi: 10.1152/jn.00520.2005

Kumar, U. (2008). Somatostatin in medium-sized aspiny interneurons of striatum is responsible for their preservation in quinolinic acid and N-methyl-D-asparate-induced neurotoxicity. *J. Mol. Neurosci.* 35, 345–354. doi: 10.1007/s12031-008-9093-3

Kupferschmidt, D. A., and Lovinger, D. M. (2015). Inhibition of presynaptic calcium transients in cortical inputs to the dorsolateral striatum by metabotropic GABA_B and mGlu2/3 receptors. *J. Physiol.* 593, 2295–2310. doi: 10.1113/jp270045

Lastres-Becker, I., Berrendero, F., Lucas, J. J., Martín-Aparicio, E., Yamamoto, A., Ramos, J. A., et al. (2002). Loss of mRNA levels, binding and activation of GTP-binding proteins for cannabinoid CB1 receptors in the basal ganglia of a transgenic model of Huntington's disease. *Brain Res.* 929, 236–242. doi: 10.1016/s0006-8993(01)03403-5

Lee, C. Y., Cantle, J. P., and Yang, X. W. (2013). Genetic manipulations of mutant huntingtin in mice: new insights into Huntington's disease pathogenesis. *FEBS J.* 280, 4382–4394. doi: 10.1111/febs.12418

Liu, L., Ito, W., and Morozov, A. (2017). GABAb receptor mediates opposing adaptations of GABA release from two types of prefrontal interneurons after observational fear. *Neuropsychopharmacology* 42, 1272–1283. doi: 10.1038/npp.2016.273

Logie, C., Bagetta, V., and Bracci, E. (2013). Presynaptic control of corticostriatal synapses by endogenous GABA. *J. Neurosci.* 33, 15425–15431. doi: 10.1523/JNEUROSCI.2304-13.2013

MacDonald, M. E., Ambrose, C. M., Duyao, M. P., Myers, R. H., Lin, C., Srinidhi, L., et al. (1993). A novel gene containing a trinucleotide repeat that is expanded and unstable on Huntington's disease chromosomes. *Cell* 72, 971–983. doi: 10.1016/0092-8674(93)90585-e

Mangiarini, L., Sathasivam, K., Seller, M., Cozens, B., Harper, A., Hetherington, C., et al (1996). Exon 1 of the HD gene with an expanded CAG repeat is sufficient to cause a progressive neurological phenotype in transgenic mice. *Cell* 87, 493–506. doi: 10.1016/S0092-8674(00)81369-0

Mastro, K. J., Bouchard, R. S., Holt, H. A., and Gittis, A. H. (2014). Transgenic mouse lines subdivide external segment of the globus pallidus (GPe) neurons and reveal distinct GPe output pathways. *J. Neurosci.* 34, 2087–2099. doi: 10.1523/JNEUROSCI.4646-13.2014

McCaw, E. A., Hu, H., Gomez, G. T., Hebb, A. L., Kelly, M. E., and Denovan-Wright, E. M. (2004). Structure, expression and regulation of the cannabinoid receptor gene (CB1) in Huntington's disease transgenic mice. *Eur. J. Biochem.* 271, 4909–4920. doi: 10.1111/j.1432-1033.2004.04460.x

Melzer, S., Gil, M., Koser, D. E., Michael, M., Huang, K. W., and Monyer, H. (2017). Distinct corticostriatal GABAergic neurons modulate striatal output neurons and motor activity. *Cell Rep.* 19, 1045–1055. doi: 10.1016/j.celrep.2017.04.024

Menalled, L. B., Kudwa, A. E., Miller, S., Fitzpatrick, J., Watson-Johnson, J., Keating, N., et al. (2012). Comprehensive behavioral and molecular characterization of a new knock-in mouse model of Huntington's disease: zQ175. *PLoS One* 7:e49838. doi: 10.1371/journal.pone.0049838

Nisenbaum, E. S., Berger, T. W., and Grace, A. A. (1993). Depression of glutamatergic and GABAergic synaptic responses in striatal spiny neurons by stimulation of presynaptic GABA_B receptors. *Synapse* 14, 221–242. doi: 10.1002/syn.890140306

Okada, M., Onodera, K., Van Renterghem, C., Sieghart, W., and Takahashi, T. (2000). Functional correlation of GABA_A receptor α subunits expression with the properties of IPSCs in the developing thalamus. *J. Neurosci.* 20, 2202–2208. doi: 10.1523/JNEUROSCI.20-06-02202.2000

Olsen, R. W., and Sieghart, W. (2009). GABA_A receptors: subtypes provide diversity of function and pharmacology. *Neuropharmacology* 56, 141–148. doi: 10.1016/j.neuropharm.2008.07.045

Overstreet, L. S., and Westbrook, G. L. (2003). Synapse density regulates independence at unitary inhibitory synapses. *J. Neurosci.* 23, 2618–2626. doi: 10.1523/JNEUROSCI.23-07-02618.2003

Paldino, E., Cardinale, A., D'Angelo, V., Sauve, I., Giampà, C., and Fusco, F. R. (2017). Selective sparing of striatal interneurons after poly (ADP-Ribose) polymerase 1 inhibition in the R6/2 mouse model of Huntington's disease. *Front. Neuroanat.* 11:61. doi: 10.3389/fnana.2017.00061

Parievsky, A., Moore, C., Kamdjou, T., Cepeda, C., Meshul, C. K., and Levine, M. S. (2017). Differential electrophysiological and morphological alterations of thalamostriatal and corticostriatal projections in the R6/2 mouse model of Huntington's disease. *Neurobiol. Dis.* 108, 29–44. doi: 10.1016/j.nbd.2017.07.020

Rajput, P. S., Kharmate, G., Norman, M., Liu, S. H., Sastry, B. R., Brunicardi, C. F., et al. (2011). Somatostatin receptor 1 and 5 double knockout mice mimic neurochemical changes of Huntington's disease transgenic mice. *PLoS One* 6:e24467. doi: 10.1371/journal.pone.0024467

Reiner, A., and Deng, Y. P. (2018). Disrupted striatal neuron inputs and outputs in Huntington's disease. *CNS Neurosci. Ther.* 24, 250–280. doi: 10.1111/cns.12844

Reiner, A., Shelby, E., Wang, H., Demarch, Z., Deng, Y., Guley, N. H., et al. (2013). Striatal parvalbuminergic neurons are lost in Huntington's disease: implications for dystonia. *Mov. Disord.* 28, 1691–1699. doi: 10.1002/mds.25624

Rock, C., Zurita, H., Wilson, C., and Apicella, A. J. (2016). An inhibitory corticostriatal pathway. *Elife* 5:e15890. doi: 10.7554/eLife.15890

Simmons, D. A., Belichenko, N. P., Yang, T., Condon, C., Monbureau, M., Shamloo, M., et al. (2013). A small molecule TrkB ligand reduces motor impairment and neuropathology in R6/2 and BACHD mouse models of Huntington's disease. *J. Neurosci.* 33, 18712–18727. doi: 10.1523/JNEUROSCI.1310-13.2013

Sloviter, R. S., Ali-Akbarian, L., Elliott, R. C., Bowery, B. J., and Bowery, N. G. (1999). Localization of GABA_B (R1) receptors in the rat hippocampus by immunocytochemistry and high resolution autoradiography, with specific reference to its localization in identified hippocampal interneuron subpopulations. *Neuropharmacology* 38, 1707–1721. doi: 10.1016/s0028-3908(99)00132-x

Smith, G. A., Rocha, E. M., McLean, J. R., Hayes, M. A., Izen, S. C., Isacson, O., et al. (2014). Progressive axonal transport and synaptic protein changes correlate with behavioral and neuropathological abnormalities in the heterozygous Q175 KI mouse model of Huntington's disease. *Hum. Mol. Genet.* 23, 4510–4527. doi: 10.1093/hmg/ddu166

Snowden, J. S. (2017). The neuropsychology of Huntington's disease. *Arch. Clin. Neuropsychol.* 32, 876–887. doi: 10.1093/arclin/acx086

Straub, C., Saulnier, J. L., Begue, A., Feng, D. D., Huang, K. W., and Sabatini, B. L. (2016). Principles of synaptic organization of GABAergic interneurons in the striatum. *Neuron* 92, 84–92. doi: 10.1016/j.neuron.2016.09.007

Szabo, B., Dörner, L., Pfreundtner, C., Nörenberg, W., and Starke, K. (1998). Inhibition of GABAergic inhibitory postsynaptic currents by cannabinoids in rat corpus striatum. *Neuroscience* 85, 395–403. doi: 10.1016/s0306-4522(97)00597-6

Szydlowski, S. N., Pollak Dorocic, I., Planert, H., Carlén, M., Meletis, K., and Silberberg, G. (2013). Target selectivity of feedforward inhibition by striatal fast-spiking interneurons. *J. Neurosci.* 33, 1678–1683. doi: 10.1523/JNEUROSCI.3572-12.2013

Tanimura, A., Lim, S. A., Aceves Buendia, J. J., Goldberg, J. A., and Surmeier, D. J. (2016). Cholinergic interneurons amplify corticostriatal synaptic responses in the Q175 model of Huntington's disease. *Front. Syst. Neurosci.* 10:102. doi: 10.3389/fnsys.2016.00102

Tepper, J. M., Koós, T., and Wilson, C. J. (2004). GABAergic microcircuits in the neostriatum. *Trends Neurosci.* 27, 662–669. doi: 10.1016/j.tins.2004.08.007

Tepper, J. M., Koós, T., Ibanez-Sandoval, O., Tecuapetla, F., Faust, T. W., and Assous, M. (2018). Heterogeneity and diversity of striatal GABAergic interneurons: update 2018. *Front. Neuroanat.* 12:91. doi: 10.3389/fnana.2018.00091

Tepper, J. M., Tecuapetla, F., Koos, T., and Ibáñez-Sandoval, O. (2010). Heterogeneity and diversity of striatal GABAergic interneurons. *Front. Neuroanat.* 4:150. doi: 10.3389/fnana.2010.00150

Waldvogel, H. J., Kim, E. H., Tippett, L. J., Vonsattel, J. P., and Faull, R. L. (2015). The neuropathology of Huntington's disease. *Curr. Top. Behav. Neurosci.* 22, 33–80. doi: 10.1007/7854_2014_354

Walker, F. O. (2007). Huntington's disease. *Lancet* 369, 218–228. doi: 10.1016/S0140-6736(07)60111-1

Wu, L. G., and Saggau, P. (1995). $GABA_B$ receptor-mediated presynaptic inhibition in guinea-pig hippocampus is caused by reduction of presynaptic Ca^{2+} influx. *J. Physiol.* 485, 649–657. doi: 10.1113/jphysiol.1995.sp020759

Conflict of Interest Statement: The authors declare that the research was conducted in the absence of any commercial or financial relationships that could be construed as a potential conflict of interest.

frontiers
in Synaptic Neuroscience

ORIGINAL RESEARCH
published: 22 May 2019
doi: 10.3389/fnsyn.2019.00017

Mechanisms of PTPσ-Mediated Presynaptic Differentiation

*Claire Bomkamp[1], Nirmala Padmanabhan[2,3,4], Benyamin Karimi[2,3,4], Yuan Ge[1], Jesse T. Chao[5], Christopher J. R. Loewen[5], Tabrez J. Siddiqui[2,3,4] and Ann Marie Craig[1]**

[1] Djavad Mowafaghian Centre for Brain Health, Department of Psychiatry, University of British Columbia, Vancouver, BC, Canada, [2] Health Sciences Centre, Kleysen Institute for Advanced Medicine, University of Manitoba, Winnipeg, MB, Canada, [3] Department of Physiology and Pathophysiology, Rady Faculty of Health Sciences, University of Manitoba, Winnipeg, MB, Canada, [4] The Children's Hospital Research Institute of Manitoba (CHRIM), Winnipeg, MB, Canada, [5] Department of Cellular and Physiological Sciences, Faculty of Medicine, Life Sciences Institute, University of British Columbia, Vancouver, BC, Canada

Formation of synapses between neurons depends in part on binding between axonal and dendritic cell surface synaptic organizing proteins, which recruit components of the developing presynaptic and postsynaptic specializations. One of these presynaptic organizing molecules is protein tyrosine phosphatase σ (PTPσ). Although the protein domains involved in adhesion between PTPσ and its postsynaptic binding partners are known, the mechanisms by which it signals into the presynaptic neuron to recruit synaptic vesicles and other necessary components for regulated transmitter release are not well understood. One attractive candidate to mediate this function is liprin-α, a scaffolding protein with well-established roles at the synapse. We systematically mutated residues of the PTPσ intracellular region (ICR) and used the yeast dihydrofolate reductase (DHFR) protein complementation assay to screen for disrupted interactions between these mutant forms of PTPσ and its various binding partners. Using a molecular replacement strategy, we show that disrupting the interaction between PTPσ and liprin-α, but not between PTPσ and itself or another binding partner, caskin, abolishes presynaptic differentiation. Furthermore, phosphatase activity of PTPσ and binding to extracellular heparan sulfate (HS) proteoglycans are dispensable for presynaptic induction. Previous reports have suggested that binding between PTPσ and liprin-α is mediated by the PTPσ membrane-distal phosphatase-like domain. However, we provide evidence here that both of the PTPσ phosphatase-like domains mediate binding to liprin-α and are required for PTPσ-mediated presynaptic differentiation. These findings further our understanding of the mechanistic basis by which PTPσ acts as a presynaptic organizer.

Keywords: synapse, synaptogenesis, LAR-RPTP, phosphatase, adhesion proteins, liprin, scaffolding proteins

Edited by:
Carlos B. Duarte,
University of Coimbra, Portugal

Reviewed by:
Shuya Fukai,
The University of Tokyo, Japan
Kurt Gottmann,
Heinrich Heine Universität Düsseldorf, Germany

****Correspondence:***
Ann Marie Craig
acraig@mail.ubc.ca

Received: *12 March 2019*
Accepted: *06 May 2019*
Published: *22 May 2019*

Citation:
Bomkamp C, Padmanabhan N, Karimi B, Ge Y, Chao JT, Loewen CJR, Siddiqui TJ and Craig AM (2019) Mechanisms of PTPσ-Mediated Presynaptic Differentiation. Front. Synaptic Neurosci. 11:17. doi: 10.3389/fnsyn.2019.00017

INTRODUCTION

A key early step in the formation of a new synapse involves binding between synaptic organizing proteins expressed on the axon of one neuron and the dendrite of another, which triggers clustering of intracellular synaptic proteins in both neurons. The presentation of a single synaptic organizing protein expressed on the surface of a non-neuronal cell is sufficient to induce local clustering of presynaptic or postsynaptic machinery. This is exemplified by the first discovered and best known pair of synaptic organizing proteins, the postsynaptic neuroligins (Scheiffele et al., 2000) and the presynaptic neurexins (Graf et al., 2004). In addition to the neuroligins and neurexins, a variety of other organizing proteins with similar synaptogenic activities have been described (Südhof, 2018). These include the presynaptically-expressed LAR, protein tyrosine phosphatase σ (PTPσ), and PTPδ, which together make up the LAR-RPTP family and interact with postsynaptic NGL-3 (Woo et al., 2009), TrkC (Takahashi et al., 2011), Slitrk1-6 (Takahashi et al., 2012; Um et al., 2014), Il1RAPL1 (Yoshida et al., 2011), IL1RAcP (Yoshida et al., 2012), SALM3, and SALM5 (Mah et al., 2010; Li et al., 2015).

The mechanism by which synaptic organizing proteins signal the formation of a nascent synapse must involve more than simply adhesion. In the case of neurexin, recruitment of intracellular proteins can occur at least under some circumstances without the presence of the neurexin intracellular region (ICR; Gokce and Südhof, 2013), presumably through an unidentified co-receptor. The same does not appear to be true for the LAR-RPTPs, since a version of PTPσ lacking its ICR acted as a dominant-negative suppressor of synaptogenesis (Takahashi et al., 2011). However, the mechanism by which these proteins exert their effects, including which intracellular interacting proteins and/or co-receptors are involved, is poorly understood.

LAR-RPTPs are comprised of extracellular Ig and FNIII domains which mediate binding to postsynaptic NGL-3, TrkC, Slitrks, IL1RAPL1, IL1RAcP, and SALM ligands (Takahashi and Craig, 2013). The LAR-RPTP Ig1 domain also binds chondroitin sulfate and heparan sulfate (HS), interactions that regulate axon growth (Aricescu et al., 2002; Shen et al., 2009). In the context of synaptogenesis, HS competes with TrkC for PTPσ binding (Coles et al., 2014) but HS may mediate the formation of additional synaptogenic complexes as suggested for a PTPσ-glypican-4-LRRTM4 complex (Ko et al., 2015). The other major family of presynaptic organizers, neurexins, are HSPGs (Zhang et al., 2018). It is not yet clear whether HS-mediated LAR-RPTP interaction with neurexins or other axonal co-receptors may contribute to synaptogenic function.

Following the single transmembrane domain, the LAR-RPTPs have a small wedge domain followed by two phosphatase-like domains, termed D1 and D2, of which only D1 is catalytically active (Streuli et al., 1990; Takahashi and Craig, 2013). There are several known enzymatic substrates of the LAR-RPTPs including p250GAP (Chagnon et al., 2010), β-catenin (Müller et al., 1999; Dunah et al., 2005), and N-cadherin (Siu et al., 2007), which could potentially mediate their synaptogenic effects. The D2 domain binds to the scaffolding proteins of the liprin-α family (Serra-Pagès et al., 1995), the GEF/kinase trio (Debant et al., 1996), and to the CASK-interacting proteins caskin1 and caskin2 (Weng et al., 2011).

Whereas there is little evidence for roles of trio (Astigarraga et al., 2010) or caskin (Weng et al., 2011) in synapse development, considerable genetic and functional evidence from multiple systems implicate liprin-α in presynaptic differentiation. The liprin-α sterile alpha motif (SAM) domains bind CASK (Olsen et al., 2005; Wei et al., 2011), liprin-β (Serra-Pagès et al., 1998), mSyd-1a (Wentzel et al., 2013), and PTPσ (Serra-Pagès et al., 1995). The liprin-α coiled coil domains bind RIM (Schoch et al., 2002) and ELKS (Ko et al., 2003) as well as liprin-α itself (Serra-Pagès et al., 1998). Thus, liprin-α may function as a "hub" for recruitment of other presynaptic molecules. The *C. elegans* homolog of liprin-α is required for normal synapse morphogenesis and synaptic transmission, and its loss results in the mislocalization of multiple presynaptic components (Zhen and Jin, 1999). Additionally, the homologs of the LAR-RPTPs and liprin-α interact genetically in the context of synapse formation in both *C. elegans* (Ackley et al., 2005) and *Drosophila* (Kaufmann et al., 2002). The role of the mammalian liprin-α family, which contains four members (termed liprin-α1–liprin-α4) encoded by four separate genes, is less well characterized. Liprin-α2 and liprin-α3 are the most abundant liprin-α isoforms in the brain (Zürner and Schoch, 2009), show different but overlapping expression patterns, and colocalize with synaptic markers (Spangler et al., 2011; Zürner et al., 2011). Knockdown of liprin-α2 leads to defects in presynaptic release as well as reduced localization of several presynaptic components including CASK and RIM (Spangler et al., 2013). Hippocampal neurons from mice with a knockout of liprin-α3 show defects in synaptic vesicle docking, tethering, and exocytosis (Wong et al., 2018). Together, these observations point to liprin-α as an attractive candidate for mediating presynaptic differentiation in response to binding between LAR-RPTPs and their postsynaptic partners.

Here, we used a molecular replacement strategy in which one or more intermolecular interactions were disrupted by domain deletion or point mutagenesis in order to provide insight into the mechanism by which PTPσ signals the formation of a nascent synapse. We find that the ability of PTPσ to mediate the induction of new presynaptic sites through its canonical trans-synaptic partners does not depend on its ability to dephosphorylate targets or to bind HSPGs, but it does require the binding site for liprin-α. Our results also suggest that, contrary to previous reports, binding between PTPσ and liprin-α involves both the D1 and D2 domains of PTPσ.

MATERIALS AND METHODS

DNA Constructs and Viral Vectors

The pFB-shPTP vector used to package AAV6-shPTP was generated based on L315-shCtrlx4 (Gokce and Südhof, 2013), pFB-AAV-GFP-4xshRNA (Zhang et al., 2018), and shRNA sequences against PTPσ (5′-GGCATCATGGGTAGTGATT-3′), PTPδ [5′-GTGCCGGCTAGAAACTTGT-3′ (Dunah et al., 2005)], and LAR [5′-GGCCTACATAGCTACACAG-3′ (Mander et al., 2005)]. This plasmid was packaged into AAV6 by Virovek. AAV6-GFP-4xshRNA called here shCtrl was described previously (Zhang et al., 2018).

The following constructs were described previously: HA-CD4, pLL-CFP (shCtrl-resistant; Zhang et al., 2018), HA-TrkC and TrkC-CFP (both the non-catalytic form; Takahashi et al., 2011). HA-NGL-3 was created based on NGL-3-CFP (Siddiqui et al., 2013) by inserting an HA tag (YPYDVPDYA) following the signal peptide and removing the C-terminal CFP, and V5-CD4 was created from YFP-CD4 (Takahashi et al., 2011) by replacing the YFP tag with V5 (GKPIPNPLLGLDST) following the signal peptide.

pLL3.7-hSyn-V5-PTPσ wild-type (WT), ICR deletion (ΔICR, missing amino acids 974–1530, KLSQ…HYAT), C1142S, 4K4A, D1 deletion (ΔD1, missing amino acids 993–1232, SNLE…EAVG), D2 deletion (ΔD2, missing amino acids 1251–1523, AQVE…EYLG), D2D2 (amino acids 993–1232 replaced by amino acids 1251–1523), PPLL, QFG, and EGFID were generated based on C1-YFP-mouse PTPσ with four FNIII domains and lacking both the meA and meB splice inserts (Takahashi et al., 2011). The V5 tag was inserted directly after the signal peptide and YFP was removed, and the WT construct (which was used as the template to construct all mutants) was made shRNA-resistant by mutating the sequence GGCATCATGGGTAGTGATT to GGaATaATGGGaAGcGATT.

C1-myc-trio (Terry-Lorenzo et al., 2016) was a kind gift from Dr Craig Garner (German Center for Neurodegenerative Diseases, Bonn, Germany) and contains the human trio cDNA sequence. Mouse caskin1 cDNA (accession number BC060720) was obtained from Open Biosystems. A small portion of the 5′ end of the cDNA was missing and was restored by PCR.

CMV-HA-liprin-α2 containing the mouse liprin-α2 gene was a kind gift from Dr. Susanne Schoch (Institute of Neuropathology, Bonn, Germany) containing the mouse liprin-α2 gene. We mutated the sequence GGGGCTGATCCACCGGAGTTT to GGaGCcGATCCtCCaG AaTTT in order to make the sequence resistant to an shRNA (not used in this work) without changing the amino acid sequence. From the resulting plasmid, we transferred the open reading frame to the pBA vector, which contains the CAG chicken β-actin promoter and was a kind gift from Dr Gary Banker (Oregon Health and Sciences University, Portland, OR, USA), and replaced the N-terminal HA tag with a myc tag (EQKLISEEDL) to generate pBA-myc-liprin-α2.

Fusions with the dihydrofolate reductase (DHFR) F3 C-terminal fragment were made based on p41-HPH-TEF-SspBYGMF-linker-DHFR-F3 (Tarassov et al., 2008). PTPσ, liprin-α2, caskin1, and trio sequences were subcloned either in full or in truncated form from the plasmids described above so that they were fused at their C-termini *via* a short linker to the F3 fragment. PTPσ ICR consisted of amino acids 974–1530 (KLSQ…HYAT), liprin-α2 SAM consisted of amino acids 877–1192 (KDRR…SDDK), caskin1 SAM consisted of amino acids 344–636 (AIVK…MAIE), and trio IgPSK consisted of amino acids 2237–3062 (NQRN…LPRV). Fusions with the DHFR F1–2 N-terminal fragment were cloned into the p413 vector (Mumberg et al., 1995). A cassette containing the DHFR F1–2 fragment and the Adh1 terminator from pAG25-F1–2 (Tarassov et al., 2008) was fused to the C-terminus of PTPσ full-length (FL) or ICR under the control of the TEF promoter. PTPσ-FL-DHFR both F1–2 and F3 contained an N-terminal V5 tag. NgCAM, which was a kind gift from Dr Peter Sonderegger (University of Zurich, Zurich, Switzerland), and YFP were each separately fused to F1–2 and to F3 as controls. Point mutations were introduced into PTPσ FL or ICR DHFR F1–2 fusions, and also into the PTPσ FL DHFR F3 fusion in the case of the PPLL mutant (Hofmeyer and Treisman, 2009).

Neuron Culture, Transfection, and AAV Transduction

This study was carried out in accordance with the recommendations of the Canadian Council on Animal Care. The protocol was approved by the University of British Columbia Animal Care Committee.

Primary embryonic day 18 (E18) rat hippocampal neurons were cultured essentially according to the method described in Kaech and Banker (2006). For expression of DNA constructs, the AMAXA nucleofector system (Lonza) was used to deliver an appropriate amount of plasmid (2–4 μg per construct) to 1–2 million freshly dissociated cells. Cells were plated on poly-L-lysine-coated coverslips at an initial density of approximately 700,000–900,000 for transfected neurons, or 500,000 for untransfected neurons, per 6-cm dish. Neurons were maintained with a glial feeder layer, and cytosine arabinoside (5 μM) was added at DIV 2 to prevent glial overgrowth. DL-2-amino-5-phosphonovaleric acid (APV, 100 μM) was added starting from DIV 5 in order to limit excitotoxicity and improve neuronal survival.

Delivery of AAVs was accomplished by incubating DIV 6 neurons face-up in 12-well plates, each well containing 700 μL of glial-conditioned media with 5×10^9 viral genomes (vg) of the appropriate viral construct. Conditioned media was harvested from either the neurons' own dishes or from similar dishes and was centrifuged for 5 min at 1,500 × *g* before use. APV was added at a concentration of 100 μM. Neurons were incubated in the virus-containing solution for 4 h and then transferred back to their home dishes.

Real Time Quantitative PCR (RT-qPCR)

RT-qPCR was performed to confirm triple knockdown of PTPσ, PTPδ, and LAR by AAV6-shPTP. Neurons were treated with AAV carrying shCtrl or shPTP as above, harvested on DIV 16 in cold PBS, and then lysed in TRIzol reagent (Invitrogen). RNA extraction from lysates was performed immediately using the PureLink RNA Mini Kit (Thermo Fisher Scientific). Elimination of genomic DNA and retro-transcription to cDNA were performed using SuperScript IV Vilo Master Mix with ezDNase Enzyme (Thermo Fisher Scientific). SYBRGreen qPCR (PowerUp™ SYBR Green Master Mix, Thermo Fisher Scientific) was performed using the resulting cDNA, with glyceraldehyde-3-phosphate dehydrogenase (GAPDH) and β-actin (Actb) as reference genes. Primers used are listed in the table below, and their efficiency was estimated as between 0.87 and 1.05. All quantitation cycle (Cq) values were detected prior to completion of the 38th cycle.

List of primers used in quantitative RT-PCR assays.

Gene (Rat)	Forward Primer 5′–3′	Reverse Primer 3′–5′
PTPσ	CTTGAGTTCAAGAGGCTTGC	GTCTGTAGCCGTCGATGAAG
PTPδ	CCATGCAGAGTCCAAGATGT	GACAGGACCTACGACCCATA
LAR	CTTCAAGCTCTCTGTTCACTGC	ACCCCGCCTAATGTATAAACG
GAPDH	AGACAAGATGGTGAAGGTCG	TCGTTGATGGCAACAATGTC
Actb	GATCAAGATCATTGCTCCTCCTG	AAGGGTGTAAAACGCAGCTC

Knockdown Confirmation by Western Blot

Neurons were treated with AAV carrying shCtrl or shPTP as above and harvested for Western blotting at DIV 17–18 using Complexiolyte-48 (50 μL/coverslip, Logopharm). Protein concentrations were determined, and equal amounts were run on 10% SDS-polyacrylamide gels. Proteins were blotted using Immobilon P membranes (Millipore). Membranes were blocked using 5% skim milk in Tris-buffered saline with 0.001% Tween-20 and incubated in antibody solution. Primary antibodies used were anti-PTPσ (mouse, 17G7.2, MM-0020, Medimabs) and anti-β-actin (rabbit, 1:5,000, ab8227, Abcam). Secondary antibodies were goat anti-mouse or goat anti-rabbit HRP conjugate from Southern Biotech. Detection was performed using Immobilon Western Chemiluminescent substrate (Millipore).

Coculture Assay

COS cells were maintained in Dulbecco's modified Eagle's medium (DMEM) with 10% bovine growth serum (BGS). When neurons reached the age of DIV 12, near-confluent COS cells were harvested using 0.25% trypsin-EDTA and plated in 12-well plates, then transfected the following day at ∼85% confluence using polyethylenimine (Boussif et al., 1995) with 1 μg of plasmid DNA encoding a tagged form of either a postsynaptic organizing protein or CD4 as a non-synaptogenic control. The day after transfection, when neurons were at DIV 13, COS cells were harvested again as before, washed twice with DMEM with 10% BGS, resuspended in glial conditioned media (treated as above for viral infection), and plated at a density of ∼20,000 cells per coverslip on top of the neurons. Cocultures were allowed to incubate for 18–24 h prior to fixation and staining.

HEK Cell Cultures and Clustering Assay

Maintenance, harvesting, and transfection of HEK 293 (HEK) cells were performed in the same manner as for COS cells, except that the concentration of trypsin-EDTA used was 0.05%. Prior to transfection, cells were plated in 12-well plates on coverslips coated in poly-D-lysine (PDL). The clustering assay was performed by transfecting HEK cells with a mixture of 0.2 μg of pBA-myc-liprin-α2, 0.6 μg of pLL-V5-PTPσ WT or mutant, and 0.2 μg of pLL CFP. Control coverslips replaced either the liprin-α2 or the PTPσ plasmid with an equal amount of additional pLL CFP plasmid, such that the total DNA amount was always 1 μg.

Immunocytochemistry and Imaging

Live surface staining for both HEK cells (**Figure 7**) and cocultures (**Figures 2–4**) was performed by incubating coverslips face-up in antibody solution for 30 min on an ice block in a 37°C, 5% CO_2, humidified incubator. Antibody solution was made with fresh Neurobasal media. APV was added at a concentration of 100 μM for experiments involving neurons. Coverslips were washed with Neurobasal media three times prior to fixation.

Cells were fixed in warm phosphate-buffered saline (PBS) with 4% paraformaldehyde and 4% sucrose for 12 min. Surface staining of V5-PTPσ in neurons was performed after fixation but before permeabilization. For experiments involving surface staining of both V5-PTPσ and HA, staining was performed after fixation for both antibodies. Non-permeabilized cells were blocked for 30 min in blocking buffer (3% BSA, 5% normal goat serum in PBS) at 37°C, then incubated in primary antibody solution in blocking buffer at 4°C for two nights prior to permeabilization. Cultures were permeabilized using 0.2% Triton-X100 in PBS for 5 min. Cultures were blocked as above and remaining primary antibodies were applied in blocking buffer overnight at 4°C. Secondary antibodies were applied in blocking buffer for 45 min at 37°C.

Primary antibodies used were mouse IgG1 anti-SynapsinI (Synaptic Systems, cat no. 106011, 1:40,000, used in **Figures 2–4**), rabbit anti-SynapsinI (Millipore, cat no. ab5905, 1:10,000, used for all other synapsin staining), mouse IgG2a anti-TauI (Millipore, cat no. PC1C6, 1:2,000), chicken anti-microtubule-associated protein 2 (anti-MAP2; Abcam, cat no. ab5392, 1:2,000), mouse IgG2b anti-HA (Abcam, cat no. 12CA5, 1:500), mouse IgG1 anti-myc (Santa Cruz, cat no. sc-40, 1:500, used in **Figure 7**) rabbit anti-myc (Sigma, cat no. C3956, 1:2,000, used for all other myc staining), rabbit anti-V5 (Cell Signalling Technology, cat no. 13202, 1:5,000, used in **Figure 7** for total V5 staining), and mouse IgG2a anti-V5 (Thermo Fisher, cat no. R960, 1:5,000, used for all V5 surface staining). Secondary antibody against chicken was AMCA AffiniPure Goat Anti-Chicken IgY (IgG; H + L; Jackson, cat no. 103155, 1:200). All other secondary antibodies were from Thermo Fisher and generated in goat, conjugated to Alexa Fluor 488, 568, or 647. Alexa Fluor-conjugated secondary antibodies were used at a concentration of 1:1,000.

Imaging of HEK cells for the co-clustering assay was performed on a Zeiss LSM700 with a 40×/1.4 NA oil immersion objective at 2× zoom, using single optical sections. Cells were selected based on the channels containing CFP and liprin-α2 only. Cells without expression of both CFP and liprin-α, as well as cells showing diffuse liprin-α signal, were avoided.

For all other experiments, imaging was performed on either the same microscope in epifluorescence mode or on an Axioplan 2, with either a 10×/0.45 NA air (morphology experiments shown in **Figure 1**) or a 40×/1.4 NA oil immersion (all others) objective and a Hamamatsu Orca-Flash4.0 CMOS camera. For experiments imaged using the LSM700, images were acquired as a z-stack containing three slices at 1.46 μm spacing (10×), or 11 slices at 0.23 μm spacing (40×), then combined into a single plane using the Zeiss Extended Depth of Focus module. All imaging was performed blind to experimental condition.

Quantification, Statistical Analysis, and Data Visualization

The order of images was randomized, and measures were performed blind to experimental condition. Images were analyzed in FIJI (NIH) using custom-written Python scripts. Regions of interest (ROIs) were generated by manually choosing a lower brightness threshold for each image and then converting the thresholded image to an ROI using the command "Create Selection." For experiments where measurements were taken from an ROI based on multiple channels, single-channel ROIs were combined using the ROI Manager tool. For coculture

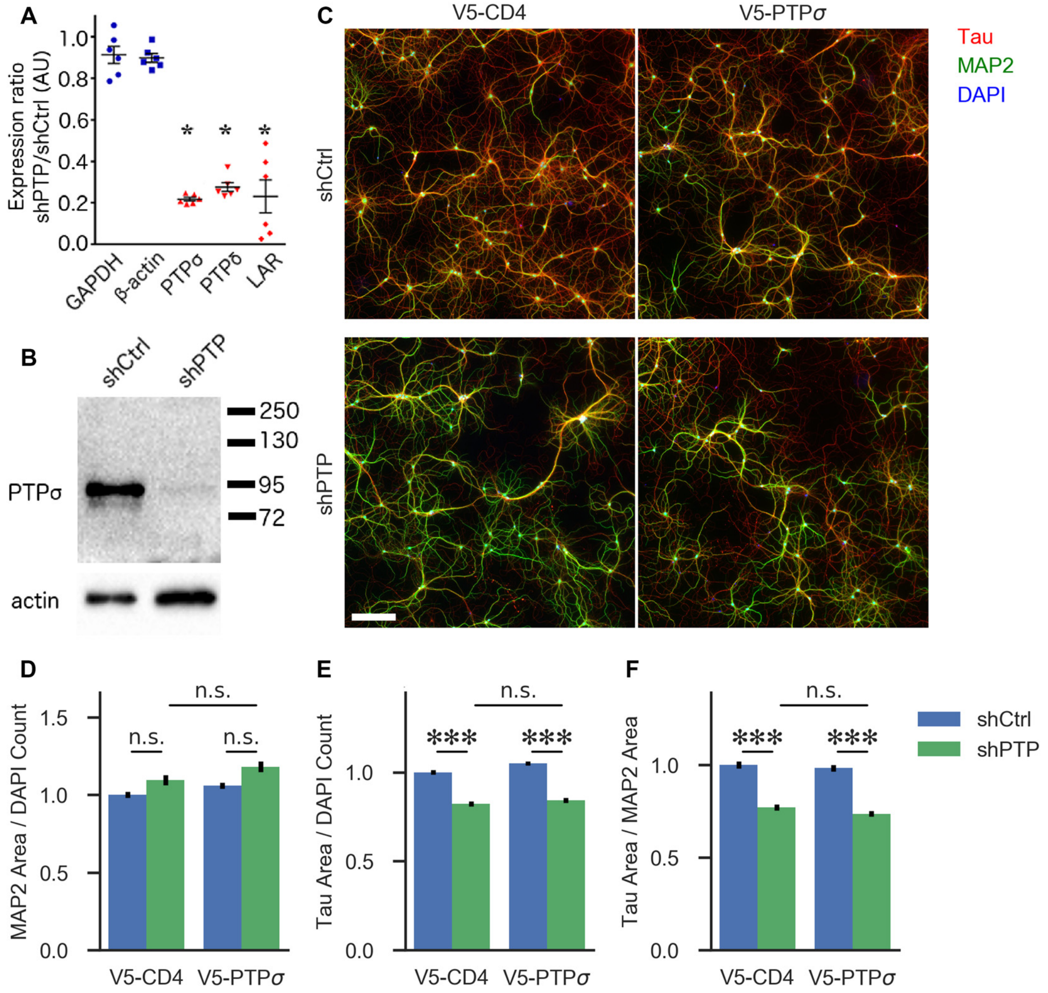

FIGURE 1 | Knockdown confirmation and morphological characterization of neurons with reduced levels of LAR-RPTPs. **(A)** Quantification of mRNA levels for the three LAR-RPTPs, as well as glyceraldehyde-3-phosphate dehydrogenase (GAPDH) and β-actin as control reference genes, measured by RT-qPCR in hippocampal neurons treated with AAV shPTP relative to shCtrl. $*p < 0.0001$ vs. GAPDH, ANOVA with *post hoc* Dunnett's multiple comparison test, $n = 3$ biological and three technical replicates each from two independent cultures (each point represents one biological replicate). AAVs were applied at DIV 6, and neurons were harvested at DIV 16. **(B)** Western blot against protein tyrosine phosphatase σ (PTPσ) in hippocampal neurons treated with either shCtrl or shPTP. AAVs were applied at DIV 6, and neurons were harvested at DIV 16. The full-size blot is shown in **Supplementary Figure S1**. **(C)** Example images of hippocampal neurons electroporated with either V5-CD4 or V5-PTPσ (columns) and treated at DIV 6 with AAVs carrying either shCtrl or shPTP sequences (rows). Neurons were fixed at DIV 14, stained for Tau (axons), MAP2 (dendrites), and DAPI (nuclei), and imaged. Scale bar represents 200 μm. **(D)** Quantification of total MAP2-positive area per field, normalized to the number of DAPI-stained nuclei in the field. Overall p-value for the experiment was 0.00157, Kruskal-Wallis, $n = 160–161$ fields per condition from four independent cultures. n.s., not significant, $p > 0.05$ by Dunn's *post hoc* test. **(E)** Quantification of total Tau-positive area per field, normalized to the number of DAPI-stained nuclei in the same field. Overall p-value for the experiment was 2.021×10^{-36}, Kruskal-Wallis. $***p < 0.001$, Dunn's *post hoc* test, n.s., not significant. **(F)** Quantification of the ratio between Tau and MAP2 total area per field. Overall p-value for the experiment was 1.578×10^{-36}, Kruskal-Wallis. $***p < 0.001$, Dunn's *post hoc* test, n.s., not significant.

experiments, the ROI based on the MAP2 channel was first dilated by five pixels using the command "Enlarge," then inverted using "Make Inverse." The purpose of these two steps was to limit the final ROI to areas of the image which did not contain dendrites and to also exclude the area immediately around the dendrite which could contain spine-associated synapses not directly overlapping the MAP2 signal. In the coculture assay, the threshold for synapsin or myc-liprin-α2 was chosen to include only punctate signal. Thus, the final measure was punctate synapsin or myc-liprin-α2 per COS cell area or per COS cell axon contact area, all lacking dendrite contact. For the HEK cell co-clustering assay, a background subtraction step was first performed on the myc-liprin-α2 channel using the rolling ball method with a radius of 14 pixels. ROIs were generated by thresholding the CFP cell-fill and background-subtracted myc-liprin-α2 channels. Combined ROIs representing CFP-positive, myc-liprin-α2-positive; and CFP-positive, myc-liprin-α2-negative regions were used to measure the surface and total V5-PTPσ channels. The V5-PTPσ channels were not thresholded. The mean intensity within the first ROI divided by that within the second was used as a measure of the strength of co-clustering.

For experiments in which cells were chosen in order to ensure even surface expression of V5 across conditions, cells showing high or low V5 levels were excluded before analyzing downstream measures such as synapsin intensity.

Analysis of image measurement results and DHFR assay growth data, statistical analysis, and data visualization were performed using Jupyter Notebook (Kluyver et al., 2016), Python 3, and the following packages: pandas, numpy, re, scipy.stats, scikit_posthocs, seaborn, and matplotlib. Data were tested for normality using scipy.stats.normaltest, and analyzed using non-parametric tests as indicated in figure legends if found to be non-normal. Visualization of protein crystal structures was performed using the PyMOL Molecular Graphics System, Version 1.8.6.0 Schrödinger, LLC.

Yeast Cultures and DHFR Assay

Yeast (strain BY4741) were transformed with two plasmids, the first containing DHFR-F1–2 fused to the C-terminus of either PTPσ FL or ICR or a control, and the second containing DHFR-F3 fused to the C-terminus of the indicated interacting protein or a control. DHFR-F3 constructs contained the SAM domains of liprin-α2 and caskin1, the immunoglobulin-like and protein serine kinase domains (IgPSK) of trio, or the FL version of PTPσ. PTPσ ICR-DHFR-F1–2 was used to test for interactions with trio IgPSK since preliminary experiments (not shown) revealed that the growth rate of yeast transformed with trio IgPSK and PTPσ FL was very low. All other DHFR-F3 constructs were transformed along with PTPσ FL-DHFR-F1–2. Negative controls replaced either the F1–2 or the F3 fusion with a control protein of a similar size. PTPσ FL was replaced by NgCAM. PTPσ ICR, liprin-α2 SAM, caskin1 SAM, and trio IgPSK were all replaced by YFP. Transformed strains were grown on synthetic defined (SD) media lacking histidine and containing hygromycin (100 μg/mL) to select for doubly transformed cells.

Transformed strains were grown in SD media lacking histidine and adenine (Michnick et al., 2016) and containing hygromycin overnight at 30°C with shaking, then diluted in a 96-well plate with 200 μL/well to an OD of 0.05 in the same media containing 1% DMSO with or without 200 μg/mL methotrexate (MTX). Each plate contained a positive control strain with two WT interacting proteins and two YFP or NgCAM negative controls. Each yeast strain had three replicate wells each with DMSO alone or DMSO + MTX. The plate lid was coated with TritonX-100 (0.05% in 20% ethanol) to minimize condensation, and the cultures were incubated in a BioTek Epoch 2 plate reader at 29–31°C (2° gradient intended to prevent condensation on the plate lid) with OD_{600} readings taken every 10 min at least until the blanked $\log_2(OD_{600})$ of all samples reached a value of −2, which generally took between 20 and 30 h.

Data were inspected visually for any wells showing abrupt drops in OD_{600} readings or other abnormalities, and such wells were excluded from the dataset. Data were $\log_2$ transformed. For each well, the slope of the growth curve in the linear range between $\log_2(OD_{600})$ values of −3 and −2 (or between −3 and −2.2 in the case of one experiment) was calculated. For each MTX-containing well, the ratio between that well's slope value and the mean slope value for DMSO-containing wells from the same experiment containing the same strain was calculated. Interaction scores were calculated according to the formula $(\text{ratio}_x - \text{ratio}_{NC})/(\text{ratio}_{PC} - \text{ratio}_{NC})$, where ratio_x, ratio_{NC}, and ratio_{PC} are the MTX/DMSO ratios of the strain of interest, the negative control containing either NgCAM-DHFR-F3 or YFP-DHFR-F3, and the positive control which was PTPσ WT-F1–2 co-transfected with the appropriate WT interacting protein-F3, respectively.

RESULTS

Role of LAR-RPTPs in Neuronal Morphology and Presynaptic Differentiation

First, we assessed the role of the LAR-RPTP family in regulating neuronal morphology in cultured hippocampal neurons. Although this aspect of LAR-RPTP function has been extensively studied in other contexts (Ledig et al., 1999; McLean et al., 2002; Thompson et al., 2003; Chagnon et al., 2004; Sapieha et al., 2005; Siu et al., 2007; Horn et al., 2012; Stoker, 2015) and was not a primary focus of this work, understanding the effects of LAR-RPTP knockdown on outgrowth in our system was necessary for designing experiments focused on their role in synapse formation. To this end, we employed an AAV carrying shRNAs targeting PTPσ, PTPδ, and LAR (shPTP) or carrying four copies of an shRNA targeting GFP (shCtrl) as a control. Infection of primary hippocampal neurons with shPTP reduced levels of all three LAR-RPTPs by 70%–80% compared to shCtrl as assessed by RT-qPCR (**Figure 1A**), and strongly reduced levels of PTPσ as assessed by Western blot (**Figure 1B**). Neurons were fixed at DIV 14 and stained with antibodies against Tau and MAP2 to mark axons and dendrites, respectively (example images shown in **Figure 1C**). We observed a consistent reduction in the area occupied by Tau-positive axons, either alone or as a ratio with MAP2-positive dendrite area, in response to shPTP (**Figures 1E,F**). In order to test the ability of PTPσ to rescue this defect, we transfected neurons with either shRNA-resistant V5-PTPσ or V5-CD4 as a control prior to infection with shCtrl or shPTP. However, this manipulation was not able to rescue the outgrowth phenotype (**Figures 1E,F**; see "Discussion" section). Thus, LAR-RPTPs were required for normal axon outgrowth.

To assess the role of LAR-RPTPs in presynaptic differentiation, we used a neuron-fibroblast coculture assay. When COS cells are transfected with the appropriate postsynaptic organizing protein and then added to primary neuronal cultures, presynaptic differentiation is induced at contact sites by local aggregation of axonal LAR-RPTPs or neurexins (Scheiffele et al., 2000; Takahashi and Craig, 2013). The coculture assay allowed us to control for differences in axon growth by normalizing recruitment of the presynaptic marker synapsin to the axon contact area. Further, in the coculture

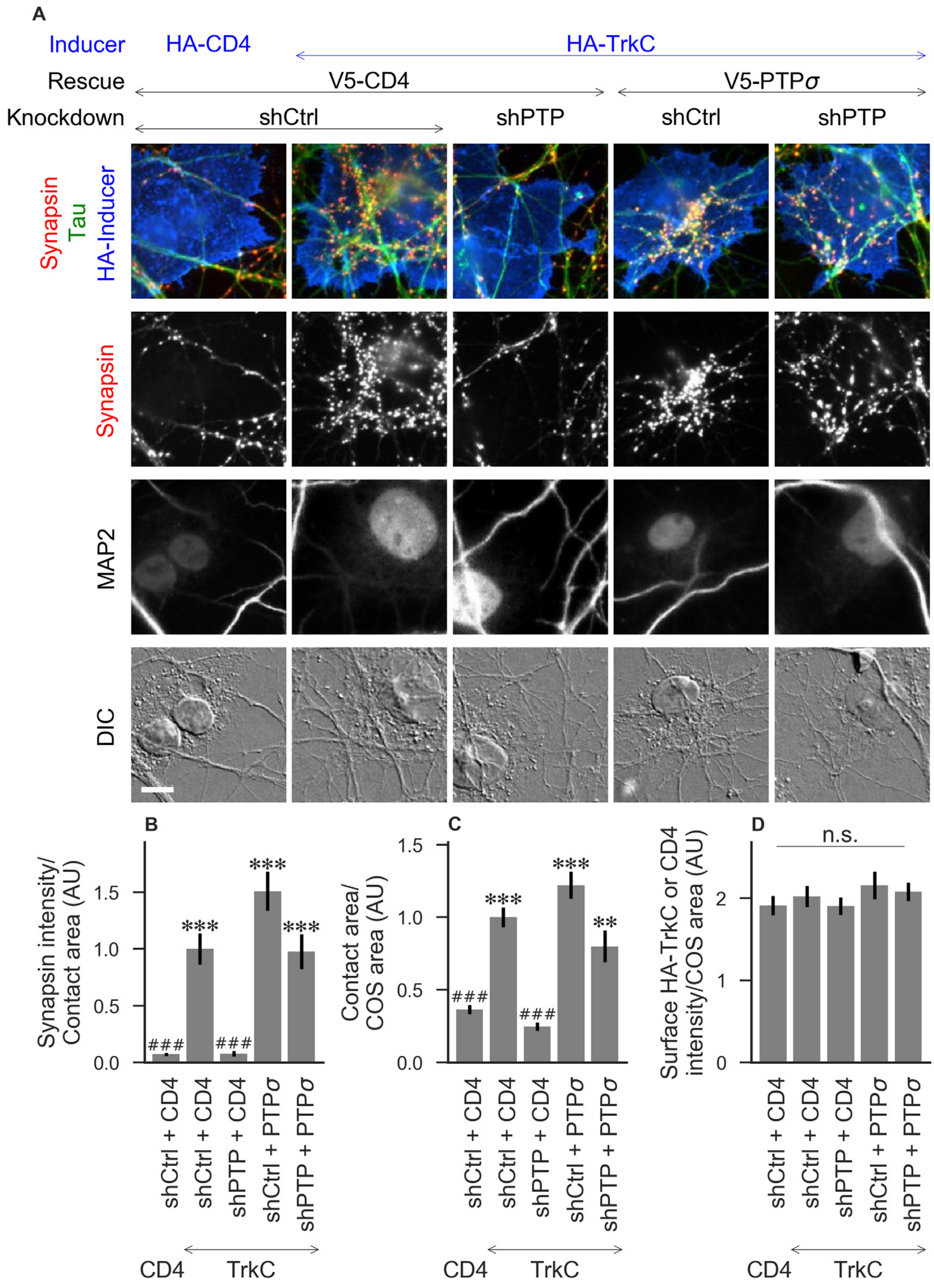

FIGURE 2 | Synaptogenic activity of TrkC is abolished by LAR-RPTP triple knockdown and rescued by PTPσ. **(A)** Representative images of HA-TrkC cocultures in which neurons were treated with either control (shCtrl) or LAR-RPTP triple knockdown (shPTP)-expressing AAVs, and rescued using V5-CD4 as a control or RNAi-resistant V5-PTPσ. Left-most column shows neurons cocultured with COS cells expressing HA-CD4 as a negative control. Rescue constructs were introduced by nucleofection at DIV 0, AAV shRNAs were applied at DIV 6, and coculture assays were performed at DIV 13–14. Synapsin was recruited in tau-positive axons at sites of contact with TrkC-expressing (but not CD4-expressing) COS cells. Microtubule-associated protein 2 (MAP2) labeling of dendrites was used to exclude native synapses from analysis. Scale bar represents 10 μm. **(B–D)** Quantification of synapsin recruitment, contact area between tau-positive axons and transfected COS cells, and intensity of HA-CD4 or HA-TrkC on the COS cell surface, from the experiment shown in **(A)**. "Contact area" is defined as the region where axons contact the inducer-expressing COS cell, excluding the area overlapped by MAP2-positive dendrites. "COS area" also excludes areas of MAP2 overlap. Values are normalized to the mean value in the shCtrl + CD4 with TrkC coculture condition from the same culture. Data are expressed as mean ± SEM. Overall p-values were 5.05×10^{-20} **(B)**, 4.02×10^{-19} **(C)**, and 0.66 **(D)**, Kruskal-Wallis, $n = 28$–32 cells per condition from three independent cultures. $^{***}p < 0.001$, $^{**}p < 0.01$ compared to shCtrl + CD4 with CD4 coculture, $^{###}p < 0.001$ compared to shCtrl + CD4 with TrkC coculture, Dunn's *post hoc* test, n. s., not significant.

assay, we could isolate presynaptic differentiation induced by LAR-RPTP ligands TrkC and NGL-3 from differentiation induced by neurexin ligands such as neuroligin-2 (NL2). We cocultured neurons treated as above with COS cells expressing HA-tagged CD4, TrkC, NGL-3, or NL2 from DIV 13–14 (example images shown in **Figure 2A** for CD4 and TrkC, **Figure 3A** for NGL-3, and **Figure 4A** for NL2). As expected, the non-synaptogenic molecule CD4 did not induce clustering of synapsin. Under control conditions (V5-CD4 and shCtrl), TrkC induced robust recruitment of synapsin reflecting presynaptic differentiation at sites of contact between the axons and COS cells, and this was abolished by treatment with shPTP. Cultures transfected with V5-PTPσ showed synapsin recruitment when treated with either shCtrl or shPTP, indicating that PTPσ was able to rescue the synaptogenic activity of TrkC (**Figure 2B**). These measures of synapsin recruitment were normalized to axon contact area, reflecting local presynaptic differentiation. Measuring the extent to which axons were recruited to transfected COS cells revealed the same broad trend in that axon recruitment to TrkC-expressing COS cells was reduced by shPTP and largely rescued by expression of V5-PTPσ (**Figure 2C**). Differences in recruitment of axons and in synapsin clustering could not be explained by differences in surface levels of TrkC between conditions (**Figure 2D**). NGL-3 showed similar results as TrkC, although the ability of PTPσ to rescue axon recruitment was somewhat weaker in this case (**Figures 3B–D**). Neurons treated with shPTP + V5-PTPσ and cocultured with NGL-3 did not show significant differences in axon recruitment from either the positive (shCtrl + V5-CD4, cocultured with NGL-3) or the negative (shCtrl + V5-CD4, cocultured with CD4) control. This partial rescue is consistent with NGL-3's dependence on other ligands within the LAR-RPTP family (Kwon et al., 2010). Synaptogenic activity of NL2 as measured by recruitment of synapsin was unaffected by shPTP. There was a slight reduction in axon recruitment by NL2 in shPTP-treated neurons, which was significant compared to the positive control (shCtrl + V5-CD4, cocultured with NL2) in the shPTP + V5-PTPσ condition, consistent with an overall reduction in axon outgrowth as a result of knockdown of LAR-RPTPs (**Figures 4B–D**).

Domain Analysis of PTPσ

We next sought to understand which domains, molecular interaction sites, and enzymatic activities of PTPσ were required for its synaptogenic activity. To do this, we used a molecular replacement strategy in which neurons were treated with shPTP-containing AAV to knock down native PTPσ and rescued with V5-tagged WT or mutant PTPσ, or CD4 as a negative control. In this and all other experiments involving transfection in neurons, shRNA-resistant versions of PTPσ (either WT or mutant) were used. Since the synaptogenic activity of TrkC was abolished by LAR-RPTP knockdown and fully rescued by PTPσ, for this and all subsequent assays to dissect mechanisms of PTPσ-mediated presynaptic differentiation, we used TrkC cocultures.

We hypothesized that, because liprin-α, caskin, and trio all bind to the D2 domain, while there are no known binding partners of the D1 domain aside from PTPσ itself, loss of the D2 domain would prevent PTPσ from mediating presynaptic differentiation in the coculture assay. We also thought it possible that phosphatase activity against p250GAP, β-catenin, N-cadherin, or an unknown target could be necessary for PTPσ's synaptogenic activity, meaning that the D1 domain would also be required. Alternatively or in addition, the D1 domain could act as a spacer between the cell membrane and the D2 domain thus allowing D2 to assemble a multi-protein presynaptic complex. Replacing the D1 domain with a second copy of D2 would restore such a steric role for the D1 domain but not a specific catalytic or interaction role. We further asked whether HSPG binding to a co-receptor might be needed for PTPσ's synaptogenic activity. Thus, we tested the following mutants: a deletion of the entire intracellular region (ΔICR), a deletion of the D1 or D2 domain (ΔD1 and ΔD2), a mutant in which the D1 domain was replaced with a second copy of D2 (D2D2), a phosphatase-dead point mutant (C1142S; Streuli et al., 1990), and a mutation of the extracellular region known to disrupt binding to HSPGs (4K4A; Aricescu et al., 2002). A schematic view of these mutants is shown in **Figure 5A**.

Consistent with our hypothesis, we found that deletion of the PTPσ D2 domain completely abolished synaptogenic activity in the coculture assay with TrkC (**Figures 5B,C**). Surprisingly, however, we also found that loss of D1 abolished synaptogenic activity, but loss of phosphatase activity *via* the C1142S mutation had no effect. The D2D2 mutation also abolished synaptogenic activity, ruling out the possibility that the effects of the ΔD1 mutation were due to steric effects related to the position of the D2 domain relative to the cell membrane. Finally, we found no effect of the 4K4A mutation, indicating that the synaptogenic activity of PTPσ does not depend on extracellular HSPG binding. These effects were not due to differences in surface expression or local recruitment of the V5-PTPσ mutants since we stained for the extracellular V5 tag and chose fields for analysis based on equal surface levels (**Supplementary Figure S2A**). The lack of activity of the ΔD1 and D2D2 mutants is surprising given the high degree of 3D structural similarity of the wedge and D1 domains with the D2 domain. Aside from a small linker region between the wedge and D1 domain, the combined wedge and D1 structure overlaps almost perfectly with the D2 domain (**Supplementary Figures S2B–D**). Altogether, these data suggest that specific interactions with both the D1 and D2 domains of PTPσ are required for its function in presynaptic differentiation.

Identification of PTPσ Point Mutants to Disrupt Specific Interactions

To further elucidate the mechanisms by which the PTPσ intracellular domain signals the formation of a new presynaptic compartment, we sought to identify mutations that would specifically disrupt the binding of PTPσ to one or another of its known intracellular interaction partners. We chose to use this approach rather than one based on knockdown of each individual interacting protein because it more directly addresses whether binding between PTPσ and the protein of interest is required, which is a different question from whether the interaction partner itself is required. While this work was in progress, it was shown that knockdown of liprin-α2 and liprin-α3 reduced the

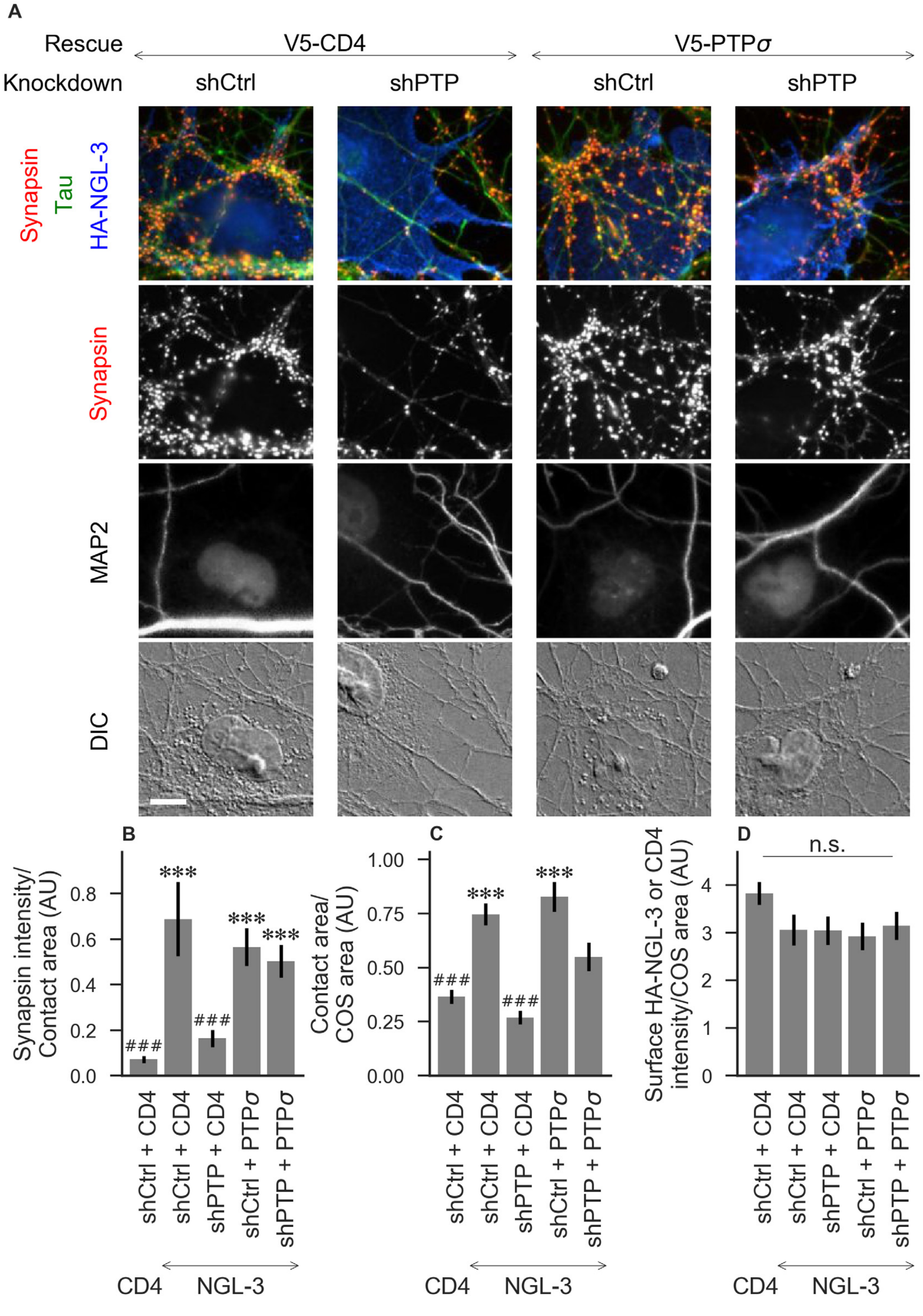

FIGURE 3 | Synaptogenic activity of NGL-3 is abolished by LAR-RPTP triple knockdown and rescued by PTPσ. **(A)** Representative images of HA-NGL-3 cocultures in which neurons were treated with either control (shCtrl) or LAR-RPTP triple knockdown (shPTP)-expressing AAVs, and rescued using V5-CD4 as a control or RNAi-resistant V5-PTPσ. Rescue constructs were introduced by nucleofection at DIV 0, AAV shRNAs were applied at DIV 6, and coculture assays were performed at DIV 13–14. Synapsin was recruited in tau-positive axons at sites of contact with NGL-3-expressing COS cells. MAP2 labeling of dendrites was used to exclude native synapses from analysis. Scale bar represents 10 μm. **(B–D)** Quantification of synapsin recruitment, contact area between tau-positive axons and transfected COS cells, and intensity of HA-CD4 or HA-NGL-3 on the COS cell surface, from the experiment shown in **(A)**. "Contact area" is defined as the region where axons contact the inducer-expressing COS cell, excluding the area overlapped by MAP2-positive dendrites. "COS area" also excludes areas of MAP2 overlap. Values are normalized to the mean value in the shCtrl + CD4 with TrkC coculture condition from the same culture. Data are expressed as mean ± SEM. Overall *p*-values were 6.69×10^{-13} **(B)**, 4.07×10^{-13} **(C)**, and 0.034 (**D**, although none of the individual comparisons were significant based on Dunn's *post hoc* test), Kruskal-Wallis, $n = 27–31$ cells per condition from three independent cultures. $^{***}p < 0.001$ compared to shCtrl + CD4 with CD4 coculture, $^{\#\#\#}p < 0.001$ compared to shCtrl + CD4 with NGL-3 coculture, Dunn's *post hoc* test. CD4 coculture condition is the same as that shown in **Figure 2** (see **Figure 2A** for example image), n. s., not significant.

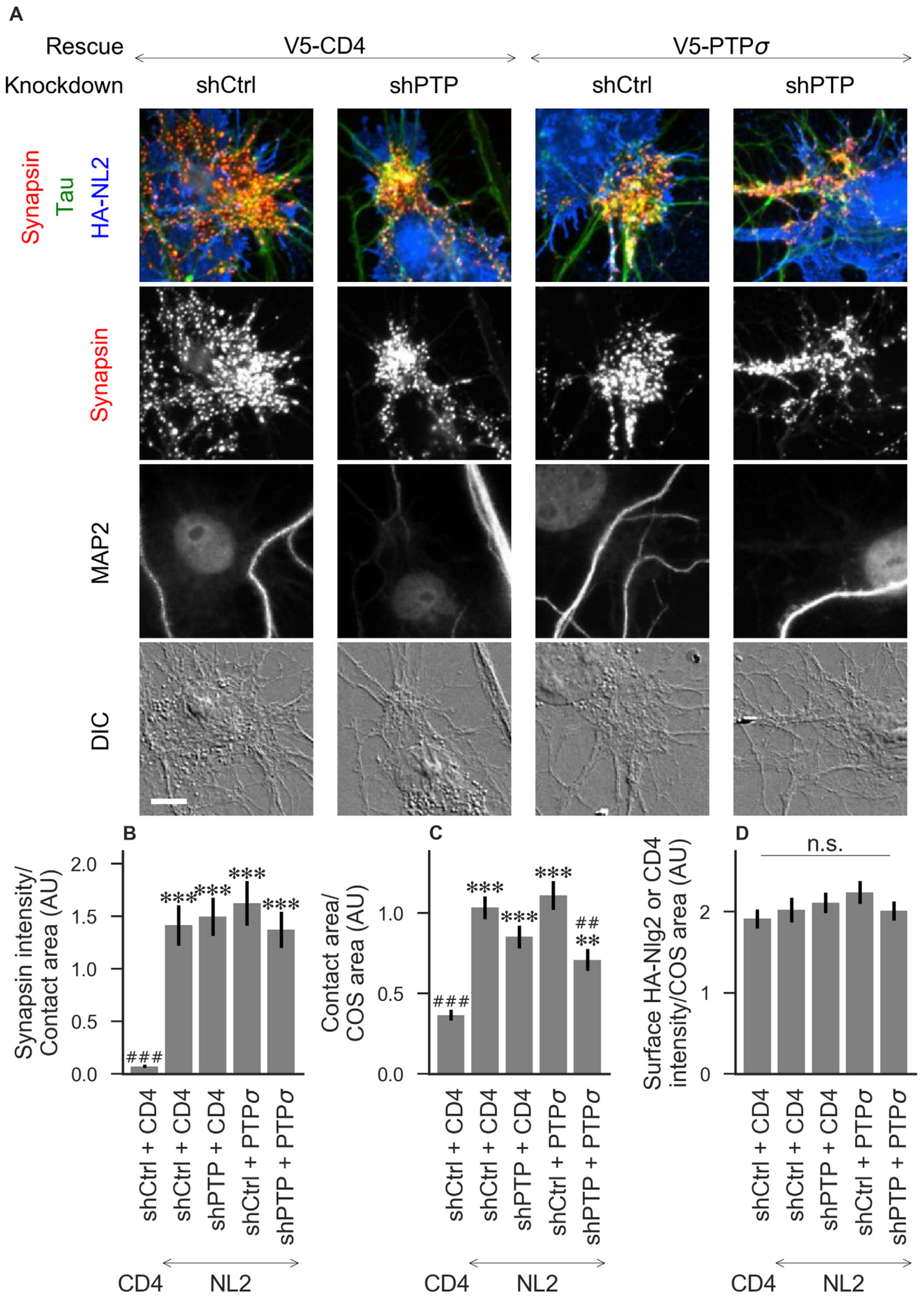

FIGURE 4 | Synaptogenic activity of neuroligin-2 (NL2) is unaffected by LAR-RPTP triple knockdown or expression of PTPσ. **(A)** Representative images of HA-NL2 cocultures in which neurons were treated with either control (shCtrl) or LAR-RPTP triple knockdown (shPTP)-expressing AAVs, and rescued using V5-CD4 as a control or RNAi-resistant V5-PTPσ. Rescue constructs were introduced by nucleofection at DIV 0, AAV shRNAs were applied at DIV 6, and coculture assays were performed at DIV 13–14. Synapsin was recruited in tau-positive axons at sites of contact with NL2-expressing COS cells. MAP2 labeling of dendrites was used to exclude native synapses from analysis. Scale bar represents 10 μm. **(B–D)** Quantification of synapsin recruitment, contact area between tau-positive axons and transfected COS cells, and intensity of HA-CD4 or HA-NL2 on the COS cell surface, from the experiment shown in **(A)**. "Contact area" is defined as the region where axons contact the inducer-expressing COS cell, excluding the area overlapped by MAP2-positive dendrites. "COS area" also excludes areas of MAP2 overlap. Values are normalized to the mean value in the shCtrl + CD4 with TrkC coculture condition from the same culture. Data are expressed as mean ± SEM. Overall *p*-values were 4.70×10^{-15} **(B)**, 2.44×10^{-13} **(C)**, and 0.40 **(D)**, Kruskal-Wallis, $n = 26–32$ cells per condition from three independent cultures. $^{***}p < 0.001$, $^{**}p < 0.01$ compared to shCtrl + CD4 with CD4 coculture, $^{###}p < 0.001$, $^{##}p < 0.01$ compared to shCtrl + CD4 with NL2 coculture, Dunn's *post hoc* test. CD4 coculture condition is the same as that shown in **Figure 2** (see **Figure 2A** for example image), n. s., not significant.

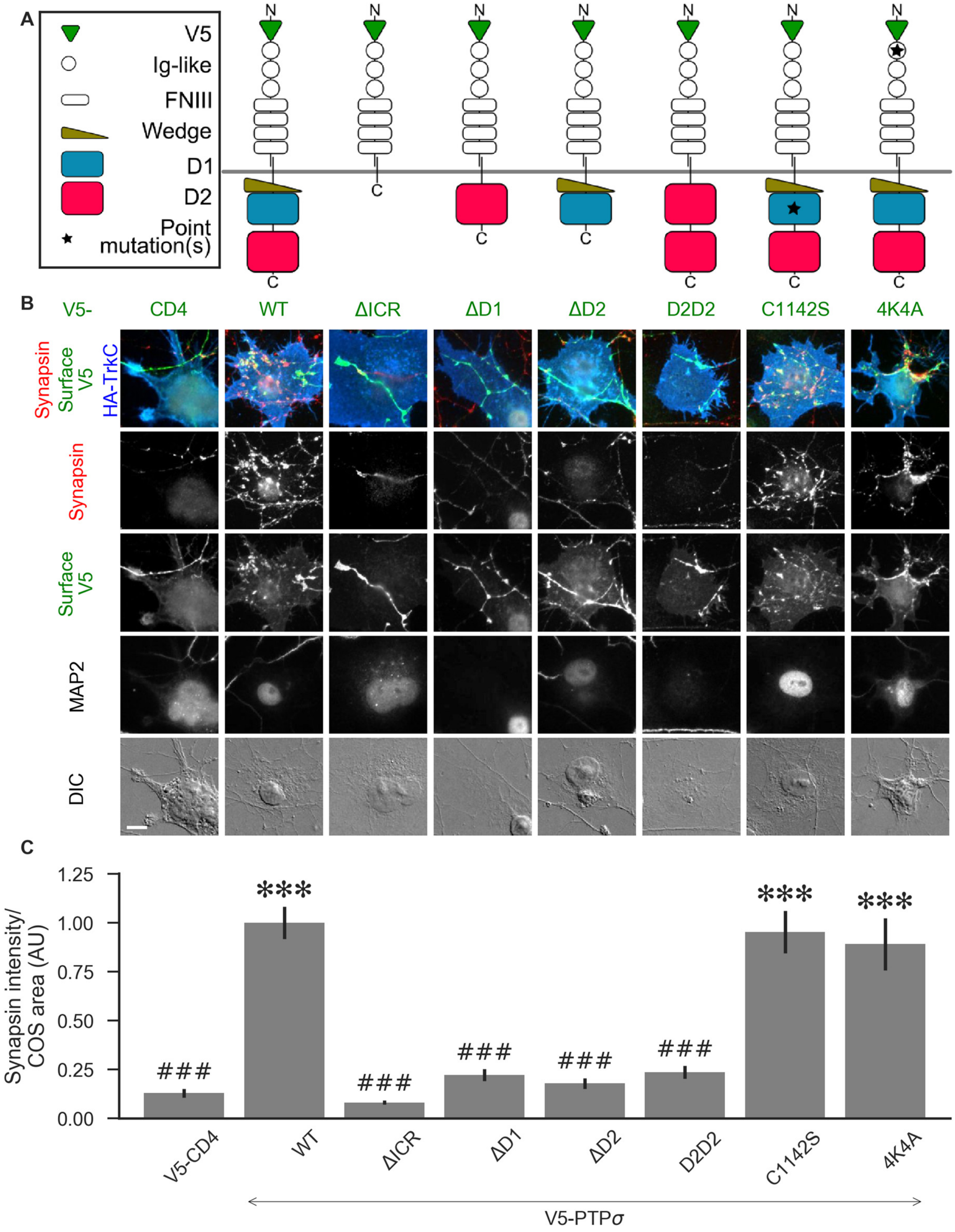

FIGURE 5 | PTPσ requires its D1 and D2 domains, but not its phosphatase activity or heparan sulfate (HS)-binding, to mediate TrkC synaptogenic activity. **(A)** Schematic view of PTPσ mutants used in this experiment. Each schematic corresponds to the label and column of images directly below it in **(B)**. **(B)** Representative images of HA-TrkC cocultures where neurons were treated with shPTP-expressing AAVs, and rescued using V5-CD4 as a control or RNAi-resistant V5-PTPσ carrying the indicated mutations. Rescue constructs were introduced by nucleofection at DIV 0, AAV shRNAs were applied at DIV 6, and coculture assays were performed at DIV 13–14. MAP2 labeling of dendrites was used to exclude native synapses from analysis. Scale bar represents 10 μm. **(C)** Quantification of synapsin recruitment shown in **(B)**. "COS area" indicates only the portion of the TrkC-expressing COS cell not overlapping with MAP2 signal. All values are normalized to the mean of the wild-type (WT) condition from the same culture. Data are expressed as mean ± SEM. Overall *p*-value for this experiment was 1.32×10^{-44}, Kruskal-Wallis, $n = 33$–100 cells per condition from 2–3 cultures. $^{***}p < 0.001$ compared to CD4, $^{\#\#\#}p < 0.001$ compared to WT, Dunn's *post hoc* test. There were no differences in surface levels of the V5-PTPσ mutants (**Supplementary Figure S2A**).

ability of both TrkC and NL2 to induce synapses in the coculture assay (Han et al., 2018). This result is consistent with the hypothesis that direct binding of PTPσ to liprin-α (Serra-Pagès et al., 1995), and indirect binding of neurexin to liprin-α through a mutual binding partner such as CASK (Hata et al., 1996; Olsen et al., 2005) might be a necessary step in the synaptogenic process. However, it is also consistent with alternative models in which liprin-α is either recruited to the synapse *via* other proteins with which it interacts or is required within the neuron but does not need to be recruited to nascent synapses.

We tested 22 candidate mutations consisting of between two and seven amino acids each which were well-conserved at least within mammalian LAR-RPTP family members and in many cases in *C. elegans* and *Drosophila* homologs as well. These candidate mutations were surface-accessible and located close to one another on the protein surface (**Supplementary Figure S3**). We also assayed the PPLL mutation which was previously shown to disrupt PTPσ homodimerization (Hofmeyer and Treisman, 2009). We screened these mutants for their ability to bind to liprin-α2, caskin1, trio, or to a second molecule of PTPσ. To do this, we used the DHFR protein complementation assay, in which the ability of yeast to grow in the presence of the drug methotrexate (MTX) is dependent on the amount of binding between two putative interacting proteins, each of which is fused to one of two fragments of an MTX-insensitive mutant of the DHFR enzyme (Tarassov et al., 2008; Rochette et al., 2015). We assessed the association of PTPσ or its intracellular domain fused to the DHFR N-terminal fragment with the interacting regions of liprin-α2, caskin1, and trio, as well as with PTPσ itself, fused to the DHFR C-terminal fragment. Negative control strains were constructed in which one of the two interacting proteins was replaced with either YFP or NgCAM. This maintained a constant size of the DHFR fusion proteins which, consistent with previous reports (Rochette et al., 2015), we found to be important for consistency of the assay. Growth of the resulting strains was measured in media containing either MTX (200 μg/mL, 1% DMSO) or DMSO alone. For each strain, an interaction score was calculated (see "Materials and Methods" section) such that a score of 0 indicates growth equivalent to that of the negative control strain, and 1 indicates WT growth.

Several mutations (MELEFK, WENNS, KLREMG, and HQYWP) moderately to severely disrupted all interactions tested and thus were considered nonspecific (interaction score <0.3 for at least three out of four ligands, shown in gray in **Figure 6A**). These mutations may disrupt activity in the DHFR assay by affecting protein folding, trafficking, or stability. Once these nonspecific mutations are ignored, mutations affecting binding to liprin-α2 and caskin1 each form a cluster on the surface of the protein (**Figure 6A**, top row). Binding of PTPσ to liprin-α2 is partially disrupted (with interaction scores between 0.21 and 0.37) by the closely spaced AEY, DWPE, QVHK, QFG, and MRYE mutations (blue). The caskin1 interaction is abolished completely by the MRYE and EGFID mutations (purple). Mutations on the opposite side of the protein, aside from those which were nonspecific, had minimal effect on binding of either protein to PTPσ (**Figure 6A**, bottom row). These results represent the gross mapping of binding sites on the PTPσ D2 domain for liprin-α2 and caskin1. The apparent liprin-α2 binding site on PTPσ constitutes a larger interaction surface than that for caskin1. It is noteworthy that these putative binding sites overlap, suggesting that simultaneous binding of PTPσ to liprin-α2 and caskin1 may not be possible. Supporting a competitive binding model, LAR is unable to act as a bridge between caskin and liprin-α in yeast two-hybrid assays (Weng et al., 2011). Based on the mutations we tested, clear binding sites were not seen in the D2 domain for PTPσ homodimerization or for trio. For homodimerization, this is not surprising given that binding is thought to be mediated by the wedge domain and the D1 domain (Hofmeyer and Treisman, 2009).

There were several mutations that primarily disrupted binding to liprin-α2, and of these QFG appeared to be the most specific, with an interaction score of 0.37, compared to between 0.77 and 0.88 for its interaction with caskin1, trio, and PTPσ WT (**Figures 6B,C**). The EGFID mutation is highly effective as well as specific in its disruption of caskin1 binding, with an interaction score of −0.11 for caskin1, and between 0.73 and 1.02 for the other interactions. These two mutations were chosen for further study to determine whether the binding sites on PTPσ for liprin-α, caskin, or both were required for its role in synaptogenesis. The PPLL mutation, which was previously reported to disrupt PTPσ homodimerization only when present on both copies of the protein (Hofmeyer and Treisman, 2009), did indeed disrupt activity in the DHFR assay. In contrast to the previous report, in the DHFR assay, we observed impaired binding between PTPσ WT and PPLL (interaction score of 0.46) as well as between PTPσ PPLL and PPLL (interaction score of 0.35). We also found that this mutation partially disrupts binding to caskin1 (interaction score of 0.51), although not as strongly as EGFID, and does not disrupt binding to liprin-α2.

Co-clustering of PTPσ Mutants With Liprin-α2 in HEK Cells

Liprin-α has been previously shown to form clusters when transfected in cell lines and to recruit LAR-RPTPs to these clusters (Serra-Pagès et al., 1998). As a second measure of the interaction strength between the PTPσ mutants and liprin-α2, we co-transfected myc-liprin-α2 with V5-PTPσ WT or mutant as well as CFP as a cell fill into HEK 293 cells. In the absence of liprin-α2, PTPσ was mostly diffuse (**Figure 7A**, left-most column). Consistent with previous reports, liprin-α2 formed small puncta in some cells when transfected alone (**Figure 7A**, second column from left). When co-transfected with PTPσ, the distribution of liprin-α2 became more distinctly clustered. Notably, PTPσ was recruited to sites of liprin-α2 clustering (**Figure 7A**, third column from left). To quantitate these interactions, we calculated a ratio between the intensity of PTPσ fluorescence within the liprin-α2 patches and that in the remainder of the cell. Analogous experiments were not possible for caskin1, trio, or PTPσ homodimerization because they did not exhibit the same co-clustering phenomenon.

When we transfected HEK cells with liprin-α2 together with mutant versions of PTPσ, we found that the ΔICR, ΔD2, and QFG mutants disrupted the co-clustering of the two proteins, such that the distribution of both resembled that seen in

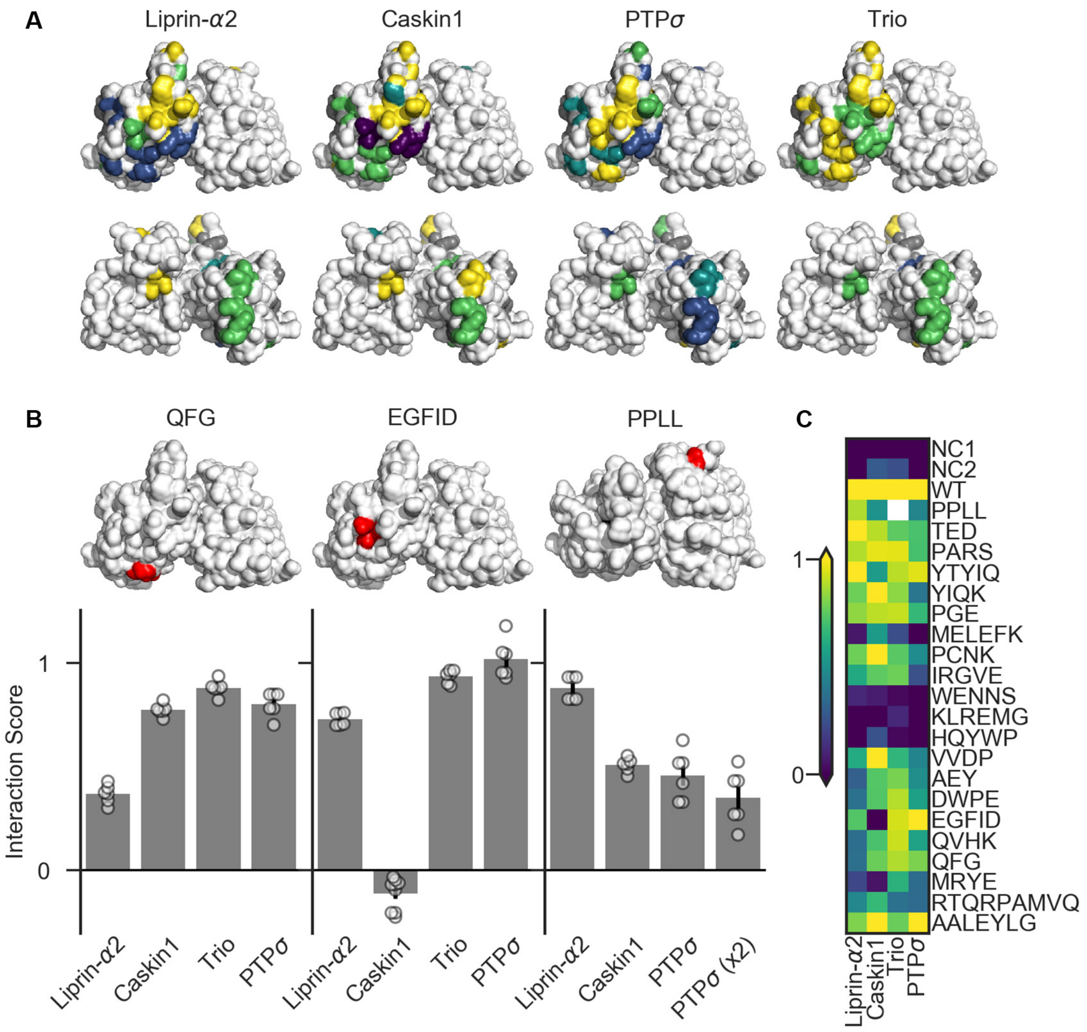

FIGURE 6 | Identification of PTPσ mutations to disrupt specific interactions. **(A)** Interaction scores for each ligand in the dihydrofolate reductase (DHFR) protein complementation assay mapped onto the PTPσ crystal structure (Hou et al., 2011). Interaction scores are divided into five bins and colored accordingly: <0.2 purple; 0.2–0.4 blue; 0.4–0.6 teal; 0.6–0.8 green; >0.8 yellow. Mutants which showed an interaction score <0.3 for at least three ligands are shown in gray. Top row shows the D1 domain on the right and D2 on the left. Second row shows the same structures, flipped horizontally. **(B)** Quantification of mutants that were used in subsequent experiments. Models above each plot are the same crystal structures as shown in the top row in **(A)**, with the indicated mutation shown in red. The model for PPLL is rotated forward slightly relative to the others in order to make these residues visible. Note that horizontal axis is different for PPLL since this mutation was not tested for interaction with trio, and since in the case of PTPσ homodimerization we also tested the condition where both copies of PTPσ carried the mutation [PTPσ (x2)]. Data are mean ± SEM. **(C)** Heatmap showing interaction scores for 22 different PTPσ multi-point mutations. NC1 indicates the negative control where the DHFR C-terminal fragment was fused to YFP or NgCAM instead of the indicated ligand; NC2 indicates the negative control where the DHFR N-terminal fragment was fused to NgCAM or YFP instead of to PTPσ. Interaction scores represent the growth rate of the indicated strain in MTX-containing media relative to MTX-free media and relative to controls, with 0 indicating the same relative growth rate as NC1 and one indicating the same relative growth rate as WT PTPσ. Values higher than 1 or lower than 0 are clipped to 1 and 0. White indicates no data (residues affected by the PPLL mutation are not present in the fragment of PTPσ used to test interaction with trio). Data are based on two experiments per condition and three replicates per experiment.

singly-transfected cells. The PPLL and EGFID mutants were essentially unaffected, and the ΔD1 and D2D2 mutants showed a partial disruption of the co-clustering phenomenon. Visually, the liprin-α2 clusters in cells co-transfected with ΔD1 or D2D2 appeared intermediate between the WT and ΔICR forms, and the mutant PTPσ was recruited to these patches, though to a lesser extent than with the WT protein. Quantification also revealed an intermediate phenotype. When recruitment was measured based on total PTPσ staining both ΔD1 and D2D2 were statistically different from WT but not ΔICR, whereas when surface PTPσ was measured, the ΔD1 mutant was significantly different from ΔICR but not WT (**Figures 7B,C**). These results are consistent with a model in which binding between liprin-α and PTPσ is mainly mediated by the PTPσ D2 domain as previously reported (Serra-Pagès et al., 1995) and involve the QFG residues, but also involves some contribution

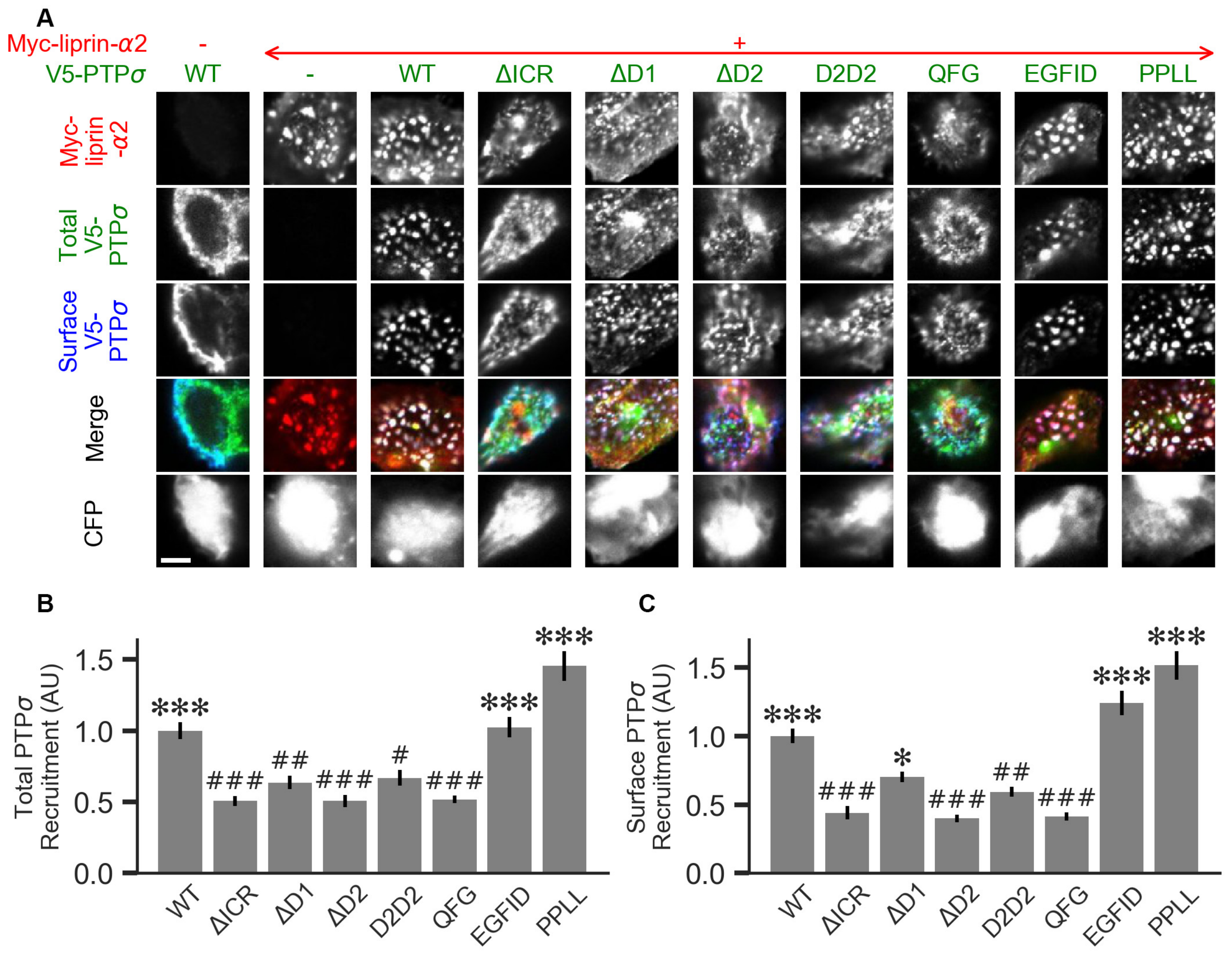

FIGURE 7 | Measurement of PTPσ/liprin-α2 interaction based on co-clustering in HEK cells. **(A)** Representative images of HEK cells transfected with myc-liprin-α2, V5-PTPσ WT or mutant, and CFP. Scale bar represents 5 μm. **(B)** Quantification of the extent to which PTPσ was recruited to sites of liprin-α clustering. "Total PTPσ Recruitment" refers to the ratio between the intensity of V5-PTPσ colocalized with myc-liprin-α2 puncta vs. the remaining area of the cell, normalized to the mean value for cells in the WT condition from the same culture. Overall *p*-value was 7.5×10^{-23}, Kruskal-Wallis. $^{*}p < 0.05$, $^{***}p < 0.001$ compared to WT, $^{\#}p < 0.05$, $^{\#\#}p < 0.01$, $^{\#\#\#}p < 0.001$ compared to intracellular region (ΔICR), Dunn's *post hoc* test. **(C)** Same as **(B)**, but using surface stained V5-PTPσ rather than total. Overall *p*-value was 2.3×10^{-31}, Kruskal-Wallis. $^{*}p < 0.05$, $^{***}p < 0.001$ compared to WT, $^{\#}p < 0.05$, $^{\#\#}p < 0.01$, $^{\#\#\#}p < 0.001$ intracellular region (ΔICR), Dunn's *post hoc* test.

from the D1 domain. Thus, D1 and D2 together mediate full-strength binding of PTPσ to liprin-α.

Recruitment of Liprin-α2 to Nascent Synapses in the Presence of PTPσ Mutants

We predicted that the same PTPσ mutants which disrupted binding to liprin-α in yeast or in HEK cells would also impair recruitment of liprin-α to sites of presynaptic differentiation. To visualize recruitment of liprin-α to presynaptic sites, we transfected neurons with myc-liprin-α2, along with V5-PTPσ, at the time of plating. When we performed cocultures with neurons treated in this manner, we observed significant recruitment of myc-liprin-α2 to COS cells expressing TrkC, compared to those expressing the control protein CD4 (**Figures 8A,B**).

To visualize liprin-α recruitment by PTPσ mutants, we performed additional cocultures in the same manner, except that neurons were treated with shPTP to remove native LAR-RPTPs. In addition to WT PTPσ, we tested the ΔD1, ΔD2, D2D2, QFG, EGFID, and PPLL mutants. As in **Figure 5**, we selected cells such that the surface levels of V5-PTPσ were equal across conditions (**Supplementary Figure S2E**). We found that ΔD1, ΔD2, D2D2, and QFG all reduced the extent of liprin-α2 recruitment substantially. Although ΔD1 mediated very weak recruitment, it was significantly higher than that of ΔD2 (**Figures 8C,D**). The level of recruitment by PPLL was similar to WT. Recruitment by EGFID was significantly different from both WT and ΔD2, although it was much closer to WT. These results suggest that direct binding between PTPσ and liprin-α is required

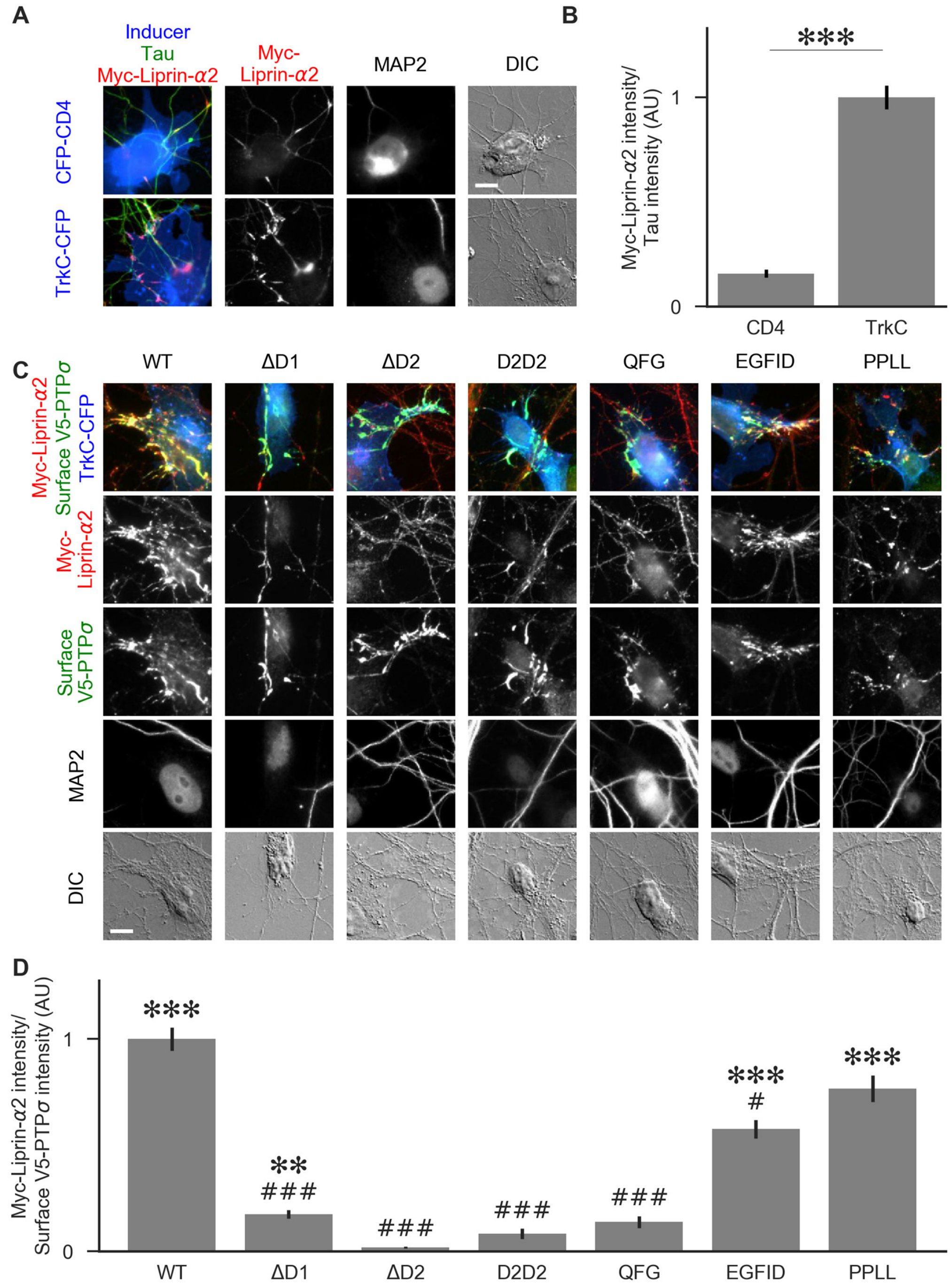

FIGURE 8 | Recruitment of liprin-α2 by TrkC coculture in the presence of PTPσ mutants. **(A)** Representative images of cocultures with either CFP-CD4 or TrkC-CFP in which neurons were transfected with and stained for myc-liprin-α2. Transfections were performed at DIV 0 and coculture assays were performed at DIV 13–14. The transfected protein was recruited by COS cells expressing TrkC but not by those expressing CD4. MAP2 labeling of dendrites was used to exclude native synapses from analysis. Scale bar represents 10 μm. **(B)** Quantification of recruitment shown in **(A)**. Measurement was performed on the contact area only, defined as the region where axons contact the inducer-expressing COS cell, excluding the area overlapped by MAP2-positive dendrites. Values are normalized to the mean value of recruitment by TrkC from the same culture. Data are mean ± SEM. $^{***}p < 0.001$, Mann-Whitney, $n = 96$ cells per condition from three independent cultures. **(C)** Representative images of neurons co-transfected with myc-liprin-α2 and V5-PTPσ WT or mutant, treated with shPTP-expressing AAVs at DIV 6, and cocultured with COS cells expressing TrkC. Scale bar represents 10 μm. **(D)** Quantification of the extent of myc-liprin-α2 recruitment relative to V5-PTPσ recruitment as shown in **(C)**. There were no differences in surface levels of the V5-PTPσ mutants in the areas assayed (**Supplementary Figure S2E**). Measurements were limited to the area of the COS cell which lacked MAP2 signal. All values are normalized to the mean of the WT condition from the same culture. Data are expressed as mean ± SEM. Overall *p*-value for this experiment was 3.43×10^{-39}, Kruskal-Wallis, $n = 20–50$ cells per condition from two cultures. $^{***}p < 0.001$, $^{***}p < 0.01$ compared to ΔD2; $^{\#\#\#}p < 0.001$, $^{\#}p < 0.05$ compared to WT, Dunn's *post hoc* test.

for liprin-α to be recruited to a nascent synapse and that indirect interactions through mutual binding partners are not sufficient.

Synaptogenic Activity of PTPσ Point Mutants

To determine the relative contributions to PTPσ's synaptogenic activity of the binding interactions between PTPσ and liprin-α, caskin, and itself, we used the QFG, EGFID, and PPLL mutants to rescue activity in the coculture assay. Transfection of shRNA-resistant V5-PTPσ, infection by shPTP, and coculture with HA-TrkC were performed as in **Figure 5**. Fields were selected in order to ensure equal levels of axonal surface V5-PTPσ in contact with the TrkC-expressing COS cells (**Supplementary Figure S2F**), and recruitment of synapsin was measured. We found that the QFG mutation reduced synapsin clustering to levels similar to the ΔICR mutant (**Figure 9**). In contrast, synapsin clustering by the PPLL and EGFID mutants was not significantly different from WT. Taken together, our results revealed a parallel in the extent of interaction with liprin-α2 in the yeast and HEK cell assays (**Figures 6**, **7**), recruitment of myc-liprin-α2 in neurons (**Figure 8**), and presynaptic differentiation (**Figures 5**, **9**). Thus, binding of PTPσ to liprin-α is likely essential for synaptogenesis induced by the TrkC/PTPσ trans-synaptic complex. In contrast, mutations which disrupt PTPσ homodimerization and binding to caskin had minimal effect on PTPσ-mediated presynaptic differentiation.

DISCUSSION

The results presented here provide insight into the roles of the LAR-RPTP family in presynaptic differentiation. The ability of the TrkC/PTPσ complex to induce new presynaptic sites was not impaired by mutations which disrupted PTPσ homodimerization, phosphatase activity, or binding to HSPGs or to caskin. In contrast, we found that PTPσ-mediated presynaptic differentiation requires liprin-α-binding regions in the PTPσ D2 and D1 domains. While this article was in preparation, Han et al. (2018) reported an overlapping study, but with some important differences. Their findings are consistent with ours regarding the importance of liprin-α but diverge regarding the role of PTPσ's phosphatase activity.

The LAR-RPTP Family Functions in Axon Growth

We observed a reduction in axon outgrowth by neurons treated with shPTP compared to those treated with shCtrl, with no difference in dendritic outgrowth. The inability of V5-PTPσ to rescue this phenotype could result both from technical factors, such as the electroporation method used, which only targets a portion (∼50%) of the cells, or from off-target effects of the shRNA on neuronal process growth. Alternatively, the lack of rescue could result from the fact that we used only a single LAR-RPTP family member. In other words, the reduction in growth might be caused primarily by the loss of LAR and/or PTPδ, rather than by loss of PTPσ. Whereas TrkC-mediated presynaptic differentiation assessed in the other experiments involves only PTPσ (Takahashi et al., 2011), much evidence indicates a role of all three LAR-RPTPs in axon outgrowth, targeting, and regeneration (Chagnon et al., 2004; Stoker, 2015). Furthermore, the roles of LAR-RPTPs in regulating axon growth may be context dependent. PTPσ knockout mice have shown accelerated axon outgrowth following nerve injury and in cultures of cortical or dorsal root ganglion neurons (McLean et al., 2002; Thompson et al., 2003; Sapieha et al., 2005; Siu et al., 2007) and increased hippocampal mossy fiber sprouting with aging or seizures (Horn et al., 2012). In contrast, disrupting the function of CRYPα, the chicken homolog of PTPσ, inhibited retinal axon outgrowth (Ledig et al., 1999). Uninjured PTPσ knockout mice show a thinner corpus callosum compared to WT controls, which could indicate defects in either outgrowth or targeting (Meathrel et al., 2002). The extracellular region of PTPσ can bind to both HSPGs and chondroitin sulfate proteoglycans (CSPGs), and its status as an activator or inhibitor of axon outgrowth appears to depend on the local balance of HSPGs and CSPGs (Coles et al., 2011). Interestingly, the extracellular ligand needed for CRYPα-dependent promotion of axon outgrowth, although it was not identified specifically, was determined to come from glial endfeet (Ledig et al., 1999). It is possible that the culture system used in our experiments, in which neurons contact substrates coated with glial-derived factors, results in an environment in which the ligands that PTPσ (and possibly PTPδ and LAR) are exposed to are, on the whole, growth-promoting rather than growth-inhibiting.

Whatever the reason for the reduction in axon outgrowth with shPTP, this change in neuronal morphology would complicate the interpretation of many assays for native synapses. Any potential reductions in synapse density could result from either a reduction in axon/dendrite contacts as a result of reduced axon length overall, or from specific roles of the LAR-RPTPs in local differentiation of contacts into functional synapses. Thus, the reductions in synapse density and in the frequency of miniature synaptic currents reported with knock-down of LAR-RPTPs in hippocampal cultures (Han et al., 2018) could reflect deficits in axon outgrowth and/or in synapse development.

Effects of the shPTP treatment on axon outgrowth were also apparent in the diminished level of axon recruitment in the coculture experiments. Expression of shRNA-resistant V5-PTPσ partially rescued axon recruitment, to a greater extent for cells expressing TrkC than NGL-3 or NL2. In the statistical analyses, axon recruitment was significantly diminished in the shPTP knockdown and PTPσ rescue group compared with the shCtrl group only for NL2 and not for TrkC or NGL-3. Considering that NL2 is not a LAR-RPTP ligand, these effects on axon recruitment in coculture are likely due to the effects of shPTP treatment on axon growth in general. Thus to specifically assay synaptogenic activity, we controlled for differences in axon recruitment in the coculture assays.

Role of LAR-RPTPs in Synaptogenesis

We found that LAR-RPTP knockdown abolished the synaptogenic coculture activity of both TrkC and NGL-3 almost entirely, whereas there was no effect on the activity of the neurexin ligand NL2. Our findings contrast with those of another recent study, which found no effect on coculture with NGL-3 in

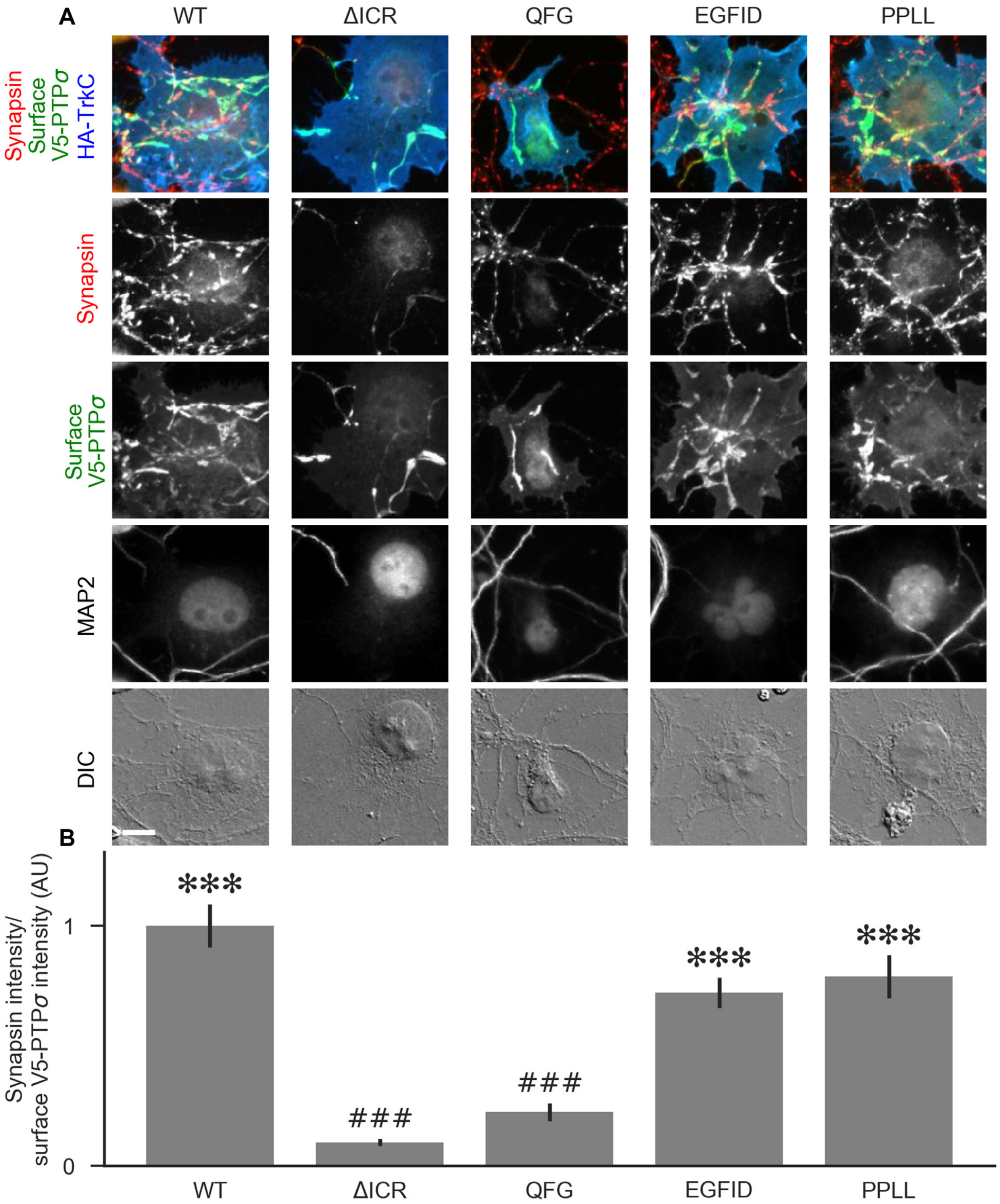

FIGURE 9 | The liprin-α2 binding site, but not the caskin1 binding site or homodimerization site, of PTPσ is required for TrkC synaptogenic activity. **(A)** Representative images of HA-TrkC cocultures where neurons were treated with shPTP-expressing AAVs, and rescued using RNAi-resistant V5-PTPσ carrying the indicated mutations. Rescue constructs were introduced by nucleofection at DIV 0, AAV shRNAs were applied at DIV 6, and coculture assays were performed at DIV 13–14. The V5-PTPσ constructs were recruited by TrkC-expressing COS cells, in some cases inducing local clustering of synapsin. MAP2 labeling of dendrites was used to exclude native synapses from analysis. The QFG, EGFID, and PPLL mutations were shown to primarily disrupt binding of PTPσ to liprin-α2, caskin1 and to itself, respectively (see **Figures 6**, **7**). Scale bar represents 10 μm. **(B)** Quantification of induced synapsin clustering in **(A)**. There were no differences in surface levels of the V5-PTPσ mutants (**Supplementary Figure S2F**). Measurements were limited to the area of the COS cell which lacked MAP2 signal. All values are normalized to the mean of the WT condition from the same culture. Data are expressed as mean ± SEM. Overall p-value for this experiment was 9.86×10^{-31}, Kruskal-Wallis, $n = 34$–71 cells per condition from three cultures. $^{***}p < 0.001$ compared to ΔICR, $^{\#\#\#}p < 0.001$ compared to WT, Dunn's *post hoc* test.

response to knockdown of any or all of the LAR-RPTPs (Han et al., 2018). It could be that NGL-3's activity requires a fairly low threshold amount of LAR-RPTPs and that the extent of knockdown differed between the two studies. The finding that loss of the LAR-RPTPs is sufficient to abolish NGL-3 activity is consistent with the observation that NGL-3 binds to all three LAR-RPTP family members (Kwon et al., 2010) and has no other known extracellular binding partners. In the case of TrkC, we observed an increase in clustering of synapsin in response to transfection with V5-PTPσ relative to control V5-CD4, although this difference was not significant. This could indicate that the total level of LAR-RPTPs in untreated neurons is not saturating with respect to presynaptic differentiation induced by TrkC.

Despite compelling evidence for a central role of LAR-RPTPs in synaptogenesis in invertebrate systems (Kaufmann et al., 2002; Ackley et al., 2005), assessing their roles in native synaptogenesis in mammals has been more difficult, confounded in part by their roles in axon growth. Mice lacking PTPσ show increased hippocampal synapse density which may be related to increased axon growth (Horn et al., 2012). Importantly, these PTPσ deficient mice also show differences in synapse properties, including elevated paired-pulse facilitation suggesting a reduced probability of release, and reduced long term potentiation (Horn et al., 2012). TrkC-PTPσ and NGL-3-LAR-RPTP complexes may contribute to these synapse properties, and potentially to synapse density as indicated by deficits upon knockdown of TrkC or NGL-3 (Woo et al., 2009; Takahashi et al., 2011).

Domain Requirements for Liprin-α Binding to PTPσ

Since no binding partners of the D1 domain besides PTPσ itself are known, our initial hypothesis was that the D1 domain would either be dispensable for synaptogenic activity or would be required for its phosphatase activity or for homodimerization. The finding that the ΔD1 mutation abolished coculture activity, but the C1142S phosphatase-dead and PPLL non-homodimerizing mutations had no effect, was surprising. Another hypothesis which we considered was that the D1 domain was not required for any catalytic or binding function, but instead acted as a spacer which positioned the D2 domain some distance from the plasma membrane, allowing for the formation of multi-protein complexes required for synapse formation. This hypothesis also turned out to be incorrect, as the D2D2 mutation in which the D1 domain was replaced by a second copy of the similarly-sized D2 domain also abolished activity. Thus, it appeared that the D1 domain must be performing some function which was previously unknown. One clue to this puzzle came from the fact that the ΔD1 mutant surprisingly showed a phenotype intermediate between WT and ΔICR when we tested its ability to co-cluster with liprin-α2 in HEK cells. Similarly, replacement of the D1 domain by a second D2 domain (D2D2) disrupted the ability of PTPσ to co-cluster with liprin-α2 in HEK cells. Furthermore, the ΔD1 and D2D2 mutants were deficient at recruiting liprin-α2 to TrkC-induced presynaptic sites in neurons. Our data are consistent with a model in which binding to liprin-α2 is primarily mediated by the D2 domain of PTPσ, but the D1 domain is required for full-strength binding. Binding between LAR and liprin-α was previously reported to be mediated by the D2 domain, based on the observation that the isolated D2 domain but not the isolated D1 domain showed interaction with liprin-α in a yeast two-hybrid assay (Serra-Pagès et al., 1995). However, this does not rule out the possibility that D1 contributes to the strength of the interaction.

PTPσ-Liprin-α Interaction in Presynaptic Differentiation

A major aim of this study was to examine the downstream pathways and mechanisms which might mediate the synaptogenic effects of PTPσ's interactions with its postsynaptic ligands. To test the functional relevance of PTPσ's ability to bind liprin-α, caskin, and itself, we employed a series of point mutants identified using a protein complementation assay. Unfortunately, we were not able to test the importance of a third D2-interacting protein, trio, using this strategy because we did not find any appropriate point mutants. This experiment pointed to liprin-α as the likely most important downstream interacting partner of PTPσ. The QFG mutant, which was able to bind caskin and to homodimerize with PTPσ WT, but not bind liprin-α, almost completely abolished coculture activity. The EGFID and PPLL mutants, which disrupted caskin binding and homodimerization respectively, had mild if any effects.

Our results agree with those of Han et al. (2018) in identifying liprin-α as a likely mediator of PTPσ's synaptogenic effects. If binding between PTPσ and liprin-α is required, one would expect that both proteins themselves would be necessary for PTPσ-mediated synaptogenesis. Han et al. (2018) found that knockdown of either PTPσ or of liprin-α2 and -α3 impaired the ability of PTPσ ligands to induce synaptogenesis in the coculture assay. Our work corroborates and extends upon this finding by providing evidence that not only are LAR-RPTPs and liprin-α required for synaptogenesis but that these two proteins must be able to bind one another.

We did not find any effect of the extracellular 4K4A mutation on coculture activity, indicating that PTPσ's ability to bind HSPGs is not required for its synaptogenic effects, at least when triggered by binding to TrkC. Homodimerization *via* the ICR of PTPσ also appeared to be dispensable, based on the ability of the non-homodimerizing PPLL mutant to induce clustering of both liprin-α2 and synapsin. However, this does not preclude the possibility that indirect multimerization of PTPσ might be necessary. The PTPδ postsynaptic ligand SALM5 has been shown to induce formation of tetramers containing two molecules each of PTPδ and SALM5, independently of any direct interactions between PTPδ molecules (Goto-Ito et al., 2018; Lin et al., 2018).

We also found no effect of the phosphatase-dead C1142S mutant on coculture activity of TrkC, indicating that dephosphorylation of targets is not necessary for PTPσ to mediate presynaptic differentiation. In contrast to this finding, Han et al. (2018) reported that the same mutation (C1157S in their PTPσ construct) impairs or abolishes coculture activity of Slitrk1 and TrkC. Two potentially important methodological differences between our study and Han et al. (2018) may contribute to these differences in findings. First, we assessed coculture regions with equal surface expression of the various

PTPσ constructs, as differences in surface trafficking could confound measures of presynaptic differentiation. Second, we excluded native synapses (synapsin puncta associated with MAP2-positive dendrites) from our measures and quantified only presynaptic sites induced by contact with TrkC-expressing cells. This issue may be particularly significant given the finding that PTPσ phosphatase activity regulates native synapse density in hippocampal cultures through a postsynaptic mechanism (Dunah et al., 2005).

In summary, our results indicate that liprin-α binding is likely required for PTPσ-mediated presynaptic differentiation, and that caskin binding, homodimerization, phosphatase activity, and HSPG binding are all dispensable. We cannot be certain that the PTPσ mutations used in our molecular replacement experiments did not disrupt multiple interactions, including potentially those with as yet unidentified binding partners of PTPσ. However, the correspondence between those mutations which disrupted binding to liprin-α in yeast and/or HEK cells and those which abolished recruitment of both liprin-α2 itself and synapsin in the coculture assay is consistent with the hypothesis that binding to liprin-α is necessary for PTPσ to induce presynaptic differentiation.

DATA AVAILABILITY

The raw data supporting the conclusions of this manuscript will be made available by the authors, without undue reservation, to any qualified researcher. The datasets generated for this study are available on request to the corresponding author.

ETHICS STATEMENT

This study was carried out in accordance with the recommendations of the Canadian Council on Animal Care. The protocol was approved by the University of British Columbia Animal Care Committee.

AUTHOR CONTRIBUTIONS

CB and AC conceived the project and wrote the article with assistance from all authors. NP, BK, and TS performed confirmation of viral-mediated knockdowns and YG did some preliminary characterization. CB generated and analyzed all other data. CL and JC provided expertise and training for the yeast DHFR assay.

FUNDING

This work was supported by Canadian Institutes of Health Research FDN 143206 and Canada Research Chair Awards (to AC), a Natural Sciences and Engineering Research Council of Canada Discovery Grant RGPIN-2015-05994 and Canadian Institutes of Health Research Grant MOP-142209 (to TS), and Faculty of Graduate Studies, University of British Columbia Four-Year Fellowship (to CB).

ACKNOWLEDGMENTS

We thank Xiling Zhou for excellent technical assistance. A version of this work appears in CB's thesis in the University of British Columbia repository, available at http://hdl.handle.net/2429/69744.

SUPPLEMENTARY MATERIAL

The Supplementary Material for this article can be found online at: https://www.frontiersin.org/articles/10.3389/fnsyn.2019.00017/full#supplementary-material

REFERENCES

Ackley, B. D., Harrington, R. J., Hudson, M. L., Williams, L., Kenyon, C. J., Chisholm, A. D., et al. (2005). The two isoforms of the *Caenorhabditis elegans* leukocyte-common antigen related receptor tyrosine phosphatase PTP-3 function independently in axon guidance and synapse formation. *J. Neurosci.* 25, 7517–7528. doi: 10.1523/JNEUROSCI.2010-05.2005

Aricescu, A. R., McKinnell, I. W., Halfter, W., and Stoker, A. W. (2002). Heparan sulfate proteoglycans are ligands for receptor protein tyrosine phosphatase σ. *Mol. Cell. Biol.* 22, 1881–1892. doi: 10.1128/mcb.22.6.1881-1892.2002

Astigarraga, S., Hofmeyer, K., Farajian, R., and Treisman, J. E. (2010). Three Drosophila liprins interact to control synapse formation. *J. Neurosci.* 30, 15358–15368. doi: 10.1523/JNEUROSCI.1862-10.2010

Boussif, O., Lezoualc'h, F., Zanta, M. A., Mergny, M. D., Scherman, D., Demeneix, B., et al. (1995). A versatile vector for gene and oligonucleotide transfer into cells in culture and *in vivo*: polyethylenimine. *Proc. Natl. Acad. Sci. U S A* 92, 7297–7301. doi: 10.1073/pnas.92.16.7297

Chagnon, M. J., Uetani, N., and Tremblay, M. L. (2004). Functional significance of the LAR receptor protein tyrosine phosphatase family in development and diseases. *Biochem. Cell Biol.* 82, 664–675. doi: 10.1139/o04-120

Chagnon, M. J., Wu, C., Nakazawa, T., Yamamoto, T., Noda, M., Blanchetot, C., et al. (2010). Receptor tyrosine phosphatase sigma (RPTPσ) regulates p250GAP, a novel substrate that attenuates Rac signaling. *Cell. Signal.* 22, 1626–1633. doi: 10.1016/j.cellsig.2010.06.001

Coles, C. H., Mitakidis, N., Zhang, P., Elegheert, J., Lu, W., Stoker, A. W., et al. (2014). Structural basis for extracellular cis and trans RPTPσ signal competition in synaptogenesis. *Nat. Commun.* 5:5209. doi: 10.1038/ncomms6209

Coles, C. H., Shen, Y., Tenney, A. P., Siebold, C., Sutton, G. C., Lu, W., et al. (2011). Proteoglycan-specific molecular switch for RPTPσ clustering and neuronal extension. *Science* 332, 484–488. doi: 10.1126/science.1200840

Debant, A., Serra-Pagès, C., Seipel, K., O'Brien, S., Tang, M., Park, S. H., et al. (1996). The multidomain protein Trio binds the LAR transmembrane tyrosine phosphatase, contains a protein kinase domain and has separate rac-specific and rho-specific guanine nucleotide exchange factor domains. *Proc. Natl. Acad. Sci. U S A* 93, 5466–5471. doi: 10.1073/pnas.93.11.5466

Dunah, A. W., Hueske, E., Wyszynski, M., Hoogenraad, C. C., Jaworski, J., Pak, D. T., et al. (2005). LAR receptor protein tyrosine phosphatases in the development and maintenance of excitatory synapses. *Nat. Neurosci.* 8, 458–467. doi: 10.1038/nn1416

Gokce, O., and Südhof, T. C. (2013). Membrane-tethered monomeric neurexin LNS-domain triggers synapse formation. *J. Neurosci.* 33, 14617–14628. doi: 10.1523/JNEUROSCI.1232-13.2013

Goto-Ito, S., Yamagata, A., Sato, Y., Uemura, T., Shiroshima, T., Maeda, A., et al. (2018). Structural basis of trans-synaptic interactions between PTPδ and SALMs for inducing synapse formation. *Nat. Commun.* 9:269. doi: 10.1038/s41467-017-02417-z

Graf, E. R., Zhang, X., Jin, S. X., Linhoff, M. W., and Craig, A. M. (2004). Neurexins induce differentiation of GABA and glutamate postsynaptic specializations *via* neuroligins. *Cell* 119, 1013–1026. doi: 10.1016/j.cell.2004.11.035

Han, K. A., Ko, J. S., Pramanik, G., Kim, J. Y., Tabuchi, K., Um, J. W., et al. (2018). PTPσ drives excitatory presynaptic assembly *via* various extracellular and intracellular mechanisms. *J. Neurosci.* 38, 6700–6721. doi: 10.1523/JNEUROSCI.0672-18.2018

Hata, Y., Butz, S., and Südhof, T. C. (1996). CASK: a novel dlg/PSD95 homolog with an N-terminal calmodulin-dependent protein kinase domain identified by interaction with neurexins. *J. Neurosci.* 16, 2488–2494. doi: 10.1523/JNEUROSCI.16-08-02488.1996

Hofmeyer, K., and Treisman, J. E. (2009). The receptor protein tyrosine phosphatase LAR promotes R7 photoreceptor axon targeting by a phosphatase-independent signaling mechanism. *Proc. Natl. Acad. Sci. U S A* 106, 19399–19404. doi: 10.1073/pnas.0903961106

Horn, K. E., Xu, B., Gobert, D., Hamam, B. N., Thompson, K. M., Wu, C., et al. (2012). Receptor protein tyrosine phosphatase sigma regulates synapse structure, function and plasticity. *J. Neurochem.* 122, 147–161. doi: 10.1111/j.1471-4159.2012.07762.x

Hou, L., Wang, J., Zhou, Y., and Li, J., Zang, Y., Li, J. (2011). Structural insights into the homology and differences between mouse protein tyrosine phosphatase-sigma and human protein tyrosine phosphatase-sigma. *Acta Biochim. Biophys. Sin.* 43, 977–988. doi: 10.1093/abbs/gmr095

Kaech, S., and Banker, G. (2006). Culturing hippocampal neurons. *Nat. Protoc.* 1, 2406–2415. doi: 10.1038/nprot.2006.356

Kaufmann, N., DeProto, J., Ranjan, R., Wan, H., and Van Vactor, D. (2002). *Drosophila* liprin-α and the receptor phosphatase Dlar control synapse morphogenesis. *Neuron* 34, 27–38. doi: 10.1016/s0896-6273(02)00643-8

Kluyver, T., Ragan-Kelley, B., Pérez, F., Granger, B., Bussonnier, M., Frederic, J., et al. (2016). "Jupyter notebooks—a publishing format for reproducible computational workflows," in *Proceedings of the 20th International Conference on Electronic Publishing* (Gottingen), 87–90. doi: 10.3233/978-1-61499-649-1-87

Ko, J., Na, M., Kim, S., Lee, J., and Kim, E. (2003). Interaction of the ERC family of RIM-binding proteins with the liprin-α family of multidomain proteins. *J. Biol. Chem.* 278, 42377–42385. doi: 10.1074/jbc.m307561200

Ko, J. S., Pramanik, G., Um, J. W., Shim, J. S., Lee, D., Kim, K. H., et al. (2015). PTPσ functions as a presynaptic receptor for the glypican-4/LRRTM4 complex and is essential for excitatory synaptic transmission. *Proc. Natl. Acad. Sci. U S A* 112, 1874–1879. doi: 10.1073/pnas.1410138112

Kwon, S.-K., Woo, J., Kim, S. Y., Kim, H., and Kim, E. (2010). Trans-synaptic adhesions between netrin-G ligand-3 (NGL-3) and receptor tyrosine phosphatases LAR, protein-tyrosine phosphatase δ (PTPδ), and PTPσ *via* specific domains regulate excitatory synapse formation. *J. Biol. Chem.* 285, 13966–13978. doi: 10.1074/jbc.M109.061127

Ledig, M. M., Haj, F., Bixby, J. L., Stoker, A. W., and Mueller, B. K. (1999). The receptor tyrosine phosphatase CRYPα promotes intraretinal axon growth. *J. Cell Biol.* 147, 375–388. doi: 10.1083/jcb.147.2.375

Li, Y., Zhang, P., Choi, T.-Y., Park, S. K., Park, H., Lee, E.-J., et al. (2015). Splicing-dependent trans-synaptic SALM3-LAR-RPTP interactions regulate excitatory synapse development and locomotion. *Cell Rep.* 12, 1618–1630. doi: 10.1016/j.celrep.2015.08.002

Lin, Z., Liu, J., Ding, H., Xu, F., and Liu, H. (2018). Structural basis of SALM5-induced PTPδ dimerization for synaptic differentiation. *Nat. Commun.* 9:268. doi: 10.1038/s41467-017-02414-2

Mah, W., Ko, J., Nam, J., Han, K., Chung, W. S., and Kim, E. (2010). Selected SALM (synaptic adhesion-like molecule) family proteins regulate synapse formation. *J. Neurosci.* 30, 5559–5568. doi: 10.1523/JNEUROSCI.4839-09.2010

Mander, A., Hodgkinson, C. P., and Sale, G. J. (2005). Knock-down of LAR protein tyrosine phosphatase induces insulin resistance. *FEBS Lett.* 579, 3024–3028. doi: 10.1016/j.febslet.2005.04.057

McLean, J., Batt, J., Doering, L. C., Rotin, D., and Bain, J. R. (2002). Enhanced rate of nerve regeneration and directional errors after sciatic nerve injury in receptor protein tyrosine phosphatase σ knock-out mice. *J. Neurosci.* 22, 5481–5491. doi: 10.1523/JNEUROSCI.22-13-05481.2002

Meathrel, K., Adamek, T., Batt, J., Rotin, D., and Doering, L. C. (2002). Protein tyrosine phosphatase σ-deficient mice show aberrant cytoarchitecture and structural abnormalities in the central nervous system. *J. Neurosci. Res.* 70, 24–35. doi: 10.1002/jnr.10382

Michnick, S. W., Levy, E. D., Landry, C. R., Kowarzyk, J., and Messier, V. (2016). The dihydrofolate reductase protein-fragment complementation assay: a survival-selection assay for large-scale analysis of protein-protein interactions. *Cold Spring Harb. Protoc.* 2016. doi: 10.1101/pdb.prot090027

Müller, T., Choidas, A., Reichmann, E., and Ullrich, A. (1999). Phosphorylation and free pool of β-catenin are regulated by tyrosine kinases and tyrosine phosphatases during epithelial cell migration. *J. Biol. Chem.* 274, 10173–10183. doi: 10.1074/jbc.274.15.10173

Mumberg, D., Müller, R., and Funk, M. (1995). Yeast vectors for the controlled expression of heterologous proteins in different genetic backgrounds. *Gene* 156, 119–122. doi: 10.1016/0378-1119(95)00037-7

Olsen, O., Moore, K. A., Fukata, M., Kazuta, T., Trinidad, J. C., Kauer, F. W., et al. (2005). Neurotransmitter release regulated by a MALS-liprin-α presynaptic complex. *J. Cell Biol.* 170, 1127–1134. doi: 10.1083/jcb.200503011

Rochette, S., Diss, G., Filteau, M., Leducq, J.-B., Dubé, A. K., and Landry, C. R. (2015). Genome-wide protein-protein interaction screening by protein-fragment complementation assay (PCA) in living cells. *J. Vis. Exp.* 97:e52255. doi: 10.3791/52255

Sapieha, P. S., Duplan, L., Uetani, N., Joly, S., Tremblay, M. L., Kennedy, T. E., et al. (2005). Receptor protein tyrosine phosphatase sigma inhibits axon regrowth in the adult injured CNS. *Mol. Cell. Neurosci.* 28, 625–635. doi: 10.1016/j.mcn.2004.10.011

Scheiffele, P., Fan, J., Choih, J., Fetter, R., and Serafini, T. (2000). Neuroligin expressed in nonneuronal cells triggers presynaptic development in contacting axons. *Cell* 101, 657–669. doi: 10.1016/s0092-8674(00)80877-6

Schoch, S., Castillo, P. E., Jo, T., Mukherjee, K., Geppert, M., Wang, Y., et al. (2002). RIM1α forms a protein scaffold for regulating neurotransmitter release at the active zone. *Nature* 415, 321–326. doi: 10.1038/415321a

Serra-Pagès, C., Kedersha, N. L., Fazikas, L., Medley, Q., Debant, A., and Streuli, M. (1995). The LAR transmembrane protein tyrosine phosphatase and a coiled-coil LAR-interacting protein co-localize at focal adhesions. *EMBO J.* 14, 2827–2838. doi: 10.1002/j.1460-2075.1995.tb07282.x

Serra-Pagès, C., Medley, Q. G., Tang, M., Hart, A., and Streuli, M. (1998). Liprins, a family of LAR transmembrane protein-tyrosine phosphatase-interacting proteins. *J. Biol. Chem.* 273, 15611–15620. doi: 10.1074/jbc.273.25.15611

Shen, Y., Tenney, A. P., Busch, S. A., Horn, K. P., Cuascut, F. X., Liu, K., et al. (2009). PTPσ is a receptor for chondroitin sulfate proteoglycan, an inhibitor of neural regeneration. *Science* 326, 592–596. doi: 10.1126/science.1178310

Siddiqui, T. J., Tari, P. K., Connor, S. A., Zhang, P., Dobie, F. A., She, K., et al. (2013). An LRRTM4-HSPG complex mediates excitatory synapse development on dentate gyrus granule cells. *Neuron* 79, 680–695. doi: 10.1016/j.neuron.2013.06.029

Siu, R., Fladd, C., and Rotin, D. (2007). N-cadherin is an *in vivo* substrate for protein tyrosine phosphatase sigma (PTPσ) and participates in PTPσ-mediated inhibition of axon growth. *Mol. Cell. Biol.* 27, 208–219. doi: 10.1128/mcb.00707-06

Spangler, S. A., Jaarsma, D., de Graaff, E., Wulf, P. S., Akhmanova, A., and Hoogenraad, C. C. (2011). Differential expression of liprin-α family proteins in the brain suggests functional diversification. *J. Comp. Neurol.* 519, 3040–3060. doi: 10.1002/cne.22665

Spangler, S. A., Schmitz, S. K., Kevenaar, J. T., de Graaff, E., de Wit, H., Demmers, J., et al. (2013). Liprin-α2 promotes the presynaptic recruitment and turnover of RIM1/CASK to facilitate synaptic transmission. *J. Cell Biol.* 201, 915–928. doi: 10.1083/jcb.201301011

Stoker, A. W. (2015). RPTPs in axons, synapses and neurology. *Semin. Cell Dev. Biol.* 37, 90–97. doi: 10.1016/j.semcdb.2014.09.006

Streuli, M., Krueger, N. X., Thai, T., Tang, M., and Saito, H. (1990). Distinct functional roles of the two intracellular phosphatase like domains of the receptor-linked protein tyrosine phosphatases LCA and LAR. *EMBO J.* 9, 2399–2407. doi: 10.1002/j.1460-2075.1990.tb07415.x

Südhof, T. C. (2018). Towards an understanding of synapse formation. *Neuron* 100, 276–293. doi: 10.1016/j.neuron.2018.09.040

Takahashi, H., Arstikaitis, P., Prasad, T., Bartlett, T. E., Wang, Y. T., Murphy, T. H., et al. (2011). Postsynaptic TrkC and presynaptic PTPσ function as a bidirectional excitatory synaptic organizing complex. *Neuron* 69, 287–303. doi: 10.1016/j.neuron.2010.12.024

Takahashi, H., and Craig, A. M. (2013). Protein tyrosine phosphatases PTPδ, PTPσ, and LAR: presynaptic hubs for synapse organization. *Trends Neurosci.* 36, 522–534. doi: 10.1016/j.tins.2013.06.002

Takahashi, H., Katayama, K., Sohya, K., Miyamoto, H., Prasad, T., Matsumoto, Y., et al. (2012). Selective control of inhibitory synapse development by Slitrk3-PTPδ trans-synaptic interaction. *Nat. Neurosci.* 15, 389–398. doi: 10.1038/nn.3040

Tarassov, K., Messier, V., Landry, C. R., Radinovic, S., Serna Molina, M. M., Shames, I., et al. (2008). An *in vivo* map of the yeast protein interactome. *Science* 320, 1465–1470. doi: 10.1126/science.1153878

Terry-Lorenzo, R. T., Torres, V. I., Wagh, D., Galaz, J., Swanson, S. K., Florens, L., et al. (2016). Trio, a rho family GEF, interacts with the presynaptic active zone proteins piccolo and bassoon. *PLoS One* 11:e0167535. doi: 10.1371/journal.pone.0167535

Thompson, K. M., Uetani, N., Manitt, C., Elchebly, M., Tremblay, M. L., and Kennedy, T. E. (2003). Receptor protein tyrosine phosphatase sigma inhibits axonal regeneration and the rate of axon extension. *Mol. Cell. Neurosci.* 23, 681–692. doi: 10.1016/s1044-7431(03)00120-9

Um, J. W., Kim, K. H., Park, B. S., Choi, Y., Kim, D., Kim, C. Y., et al. (2014). Structural basis for LAR-RPTP/Slitrk complex-mediated synaptic adhesion. *Nat. Commun.* 5:5423. doi: 10.1038/ncomms6423

Wei, Z., Zheng, S., Spangler, S. A., Yu, C., Hoogenraad, C. C., and Zhang, M. (2011). Liprin-mediated large signaling complex organization revealed by the liprin-α/CASK and liprin-α/liprin-β complex structures. *Mol. Cell* 43, 586–598. doi: 10.1016/j.molcel.2011.07.021

Weng, Y.-L., Liu, N., DiAntonio, A., and Broihier, H. T. (2011). The cytoplasmic adaptor protein Caskin mediates Lar signal transduction during *Drosophila* motor axon guidance. *J. Neurosci.* 31, 4421–4433. doi: 10.1523/JNEUROSCI.5230-10.2011

Wentzel, C., Sommer, J. E., Nair, R., Stiefvater, A., Sibarita, J. B., and Scheiffele, P. (2013). mSYD1A, a mammalian synapse-defective-1 protein, regulates synaptogenic signaling and vesicle docking. *Neuron* 78, 1012–1023. doi: 10.1016/j.neuron.2013.05.010

Wong, M. Y., Liu, C., Wang, S. S. H., Roquas, A. C. F., Fowler, S. C., and Kaeser, P. S. (2018). Liprin-α3 controls vesicle docking and exocytosis at the active zone of hippocampal synapses. *Proc. Natl. Acad. Sci. U S A* 115, 2234–2239. doi: 10.1073/pnas.1719012115

Woo, J., Kwon, S.-K., Choi, S., Kim, S., Lee, J.-R., Dunah, A. W., et al. (2009). Trans-synaptic adhesion between NGL-3 and LAR regulates the formation of excitatory synapses. *Nat. Neurosci.* 12, 428–437. doi: 10.1038/nn.2279

Yoshida, T., Shiroshima, T., Lee, S.-J., Yasumura, M., Uemura, T., Chen, X., et al. (2012). Interleukin-1 receptor accessory protein organizes neuronal synaptogenesis as a cell adhesion molecule. *J. Neurosci.* 32, 2588–2600. doi: 10.1523/JNEUROSCI.4637-11.2012

Yoshida, T., Yasumura, M., Uemura, T., Lee, S.-J., Ra, M., Taguchi, R., et al. (2011). IL-1 receptor accessory protein-like 1 associated with mental retardation and autism mediates synapse formation by trans-synaptic interaction with protein tyrosine phosphatase δ. *J. Neurosci.* 31, 13485–13499. doi: 10.1523/JNEUROSCI.2136-11.2011

Zhang, P., Lu, H., Peixoto, R. T., Pines, M. K., Ge, Y., Oku, S., et al. (2018). Heparan sulfate organizes neuronal synapses through neurexin partnerships. *Cell* 174, 1450.e23–1464.e23. doi: 10.1016/j.cell.2018.07.002

Zhen, M., and Jin, Y. (1999). The liprin protein SYD-2 regulates the differentiation of presynaptic termini in *C. elegans*. *Nature* 401, 371–375. doi: 10.1038/43886

Zürner, M., Mittelstaedt, T., tom Dieck, S., Becker, A., and Schoch, S. (2011). Analyses of the spatiotemporal expression and subcellular localization of liprin-α proteins. *J. Comp. Neurol.* 519, 3019–3039. doi: 10.1002/cne.22664

Zürner, M., and Schoch, S. (2009). The mouse and human Liprin-α family of scaffolding proteins: genomic organization, expression profiling and regulation by alternative splicing. *Genomics* 93, 243–253. doi: 10.1016/j.ygeno.2008.10.007

Conflict of Interest Statement: The authors declare that the research was conducted in the absence of any commercial or financial relationships that could be construed as a potential conflict of interest.

frontiers
in Synaptic Neuroscience

ORIGINAL RESEARCH
published: 03 September 2019
doi: 10.3389/fnsyn.2019.00024

LSO:Ce Inorganic Scintillators Are Biocompatible With Neuronal and Circuit Function

Aundrea F. Bartley[1,2,3,4†], Kavitha Abiraman[4,5†], Luke T. Stewart[4,5], Mohammed Iqbal Hossain[6], David M. Gahan[1], Abhishek V. Kamath[1], Mary K. Burdette[7], Shaida Andrabe[6], Stephen H. Foulger[7,8,9], Lori L. McMahon[2,3,4,5] and Lynn E. Dobrunz[1,2,3,4]**

[1]Department of Neurobiology, University of Alabama at Birmingham, Birmingham, AL, United States, [2]Civitan International Research Center, University of Alabama at Birmingham, Birmingham, AL, United States, [3]Evelyn F. McKnight Brain Institute, University of Alabama at Birmingham, Birmingham, AL, United States, [4]Comprehensive Neuroscience Center, University of Alabama at Birmingham, Birmingham, AL, United States, [5]Department of Cell, Developmental, and Integrative Biology, University of Alabama at Birmingham, Birmingham, AL, United States, [6]Department of Pharmacology, University of Alabama at Birmingham, Birmingham, AL, United States, [7]Department of Materials Science and Engineering, Clemson University, Anderson, SC, United States, [8]Center for Optical Materials Science and Engineering Technologies, Clemson University, Anderson, SC, United States, [9]Department of Bioengineering, Clemson University, Clemson, SC, United States

Edited by:
Carl R. Lupica,
National Institute on Drug Abuse (NIDA), United States

Reviewed by:
Carlos Fernando Valenzuela,
University of New Mexico, United States
Laura Schrader,
Tulane University, United States

***Correspondence:**
Lori L. McMahon
mcmahon@uab.edu
Lynn E. Dobrunz
dobrunz@uab.edu

†These authors have contributed equally to this work

Received: *22 March 2019*
Accepted: *06 August 2019*
Published: *03 September 2019*

Citation:
Bartley AF, Abiraman K, Stewart LT, Hossain MI, Gahan DM, Kamath AV, Burdette MK, Andrabe S, Foulger SH, McMahon LL and Dobrunz LE (2019) LSO:Ce Inorganic Scintillators Are Biocompatible With Neuronal and Circuit Function. Front. Synaptic Neurosci. 11:24. doi: 10.3389/fnsyn.2019.00024

Optogenetics is widely used in neuroscience to control neural circuits. However, non-invasive methods for light delivery in brain are needed to avoid physical damage caused by current methods. One potential strategy could employ x-ray activation of radioluminescent particles (RPLs), enabling localized light generation within the brain. RPLs composed of inorganic scintillators can emit light at various wavelengths depending upon composition. Cerium doped lutetium oxyorthosilicate (LSO:Ce), an inorganic scintillator that emits blue light in response to x-ray or ultraviolet (UV) stimulation, could potentially be used to control neural circuits through activation of channelrhodopsin-2 (ChR2), a light-gated cation channel. Whether inorganic scintillators themselves negatively impact neuronal processes and synaptic function is unknown, and was investigated here using cellular, molecular, and electrophysiological approaches. As proof of principle, we applied UV stimulation to 4 μm LSO:Ce particles during whole-cell recording of CA1 pyramidal cells in acute hippocampal slices from mice that expressed ChR2 in glutamatergic neurons. We observed an increase in frequency and amplitude of spontaneous excitatory postsynaptic currents (sEPSCs), indicating activation of ChR2 and excitation of neurons. Importantly, LSO:Ce particles did not affect survival of primary mouse cortical neurons, even after 24 h of exposure. In extracellular dendritic field potential recordings, no change in the strength of basal glutamatergic transmission was observed during exposure to LSO:Ce microparticles. However, the amplitude of the fiber volley was slightly reduced with high stimulation. Additionally, there was a slight decrease in the frequency of sEPSCs in whole-cell voltage-clamp recordings from CA1 pyramidal cells, with no change in current amplitudes. The amplitude and frequency of spontaneous inhibitory postsynaptic currents were unchanged. Finally,

---

Abbreviations: aCSF, artificial cerebral spinal fluid; ChR2, channelrhodopsin-2; fEPSP, field excitatory postsynaptic potentials; GFAP, glial fibrillary acidic protein; LED, light emitting diodes; LSO:Ce, Cerium doped lutetium oxyorthosilicate; LTP, long term potentiation; PBS, phosphate buffered saline; RLP, radioluminescent particle; sEPSCs, spontaneous excitatory postsynaptic currents; sIPSCs, spontaneous inhibitory postsynaptic currents; UV, ultraviolet.

long term potentiation (LTP), a synaptic modification believed to underlie learning and memory and a robust measure of synaptic integrity, was successfully induced, although the magnitude was slightly reduced. Together, these results show LSO:Ce particles are biocompatible even though there are modest effects on baseline synaptic function and long-term synaptic plasticity. Importantly, we show that light emitted from LSO:Ce particles is able to activate ChR2 and modify synaptic function. Therefore, LSO:Ce inorganic scintillators are potentially viable for use as a new light delivery system for optogenetics.

Keywords: radioluminescent, scintillator, optogenetics, biocompatible, LTP, LSO:Ce

INTRODUCTION

Over the past decade, the field of optogenetics has expanded our knowledge about the role of individual neuronal cells and specific brain circuits in behavior and disease states (Gradinaru et al., 2009; Yizhar et al., 2011; Lim et al., 2013; Gunaydin et al., 2014; Emiliani et al., 2015; Fenno et al., 2015; Rost et al., 2017; Selimbeyoglu et al., 2017; Barnett et al., 2018). Optogenetics relies on the expression of exogenous light-activated ion channels, including the blue light-activated channelrhodopsin-2 (ChR2), that causes depolarization, or the orange-light activated halorhodopsin, which causes hyperpolarization, of the membrane potential of brain cells of interest. Despite these great advances, improvements to the method are constantly being developed (Rein and Deussing, 2012; Lim et al., 2013; Lin et al., 2017; Chen et al., 2018). The use of optogenetics *in vivo* requires delivery of light into the brain, which is most commonly done through implantation of fiber optic waveguides (fibers) or light emitting diodes (LEDs). These can be as large as several 100 microns, which causes damage to delicate brain tissues, especially when implanted deep within brain structures (Aravanis et al., 2007; Ozden et al., 2013; Canales et al., 2018). In addition, attenuation of light occurs through absorption and scattering in brain tissue, resulting in the need for higher intensities of light at the source. This illumination often results in enhanced local temperatures, a consequence that is greater with stronger and more frequent irradiance (Senova et al., 2017), and can lead to as much as a 30% increase in local neuron firing rates (Stujenske et al., 2015). Lastly, glial scarring can occur at the light source (Podgorski and Ranganathan, 2016), decreasing effective light intensities and leading to variability in neuronal control. Currently, there are very few options for noninvasive methods of light delivery into the brain for optogenetics.

Efforts are ongoing to develop and refine minimally invasive strategies for the generation of light within the brain to combat the challenges mentioned above (Chen et al., 2018). One potential strategy could employ the use of x-rays to activate radioluminescent materials (Berry et al., 2015; French et al., 2018; Shuba, 2019). Radioluminescence is the production of visible light by a material exposed to ionizing radiation. Radioluminescent particles (RLPs) can be generated from inorganic scintillator material, which would emit light at different wavelengths depending upon its composition. RLP technology could be superior to current invasive methods because it obviates the need for implanting devices into brain tissue that can cause damage and lose effectiveness over time. In addition, the light will be generated locally and have less attenuation due to tissue scattering. This should allow for much lower power densities needed to achieve opsin activation, thereby reducing nonspecific heat-related effects to the tissue. Finally, the uniformity of light delivery will reduce non-specific effects of a graded response due to light absorption and scatter from a single point source. However, it is unknown whether these inorganic RLPs themselves will impact neuronal processes and synaptic function.

One of the most common inorganic scintillators used in medical imaging is Cerium-doped lutetium oxyorthosilicate (LSO:Ce). LSO:Ce crystals are used as detectors in medical imaging devices because they absorb x-rays and γ-rays extremely well (high density of 7.41 g/cm^3), have a high light output ($\sim$30,000 photons/MeV) and extremely fast decay kinetics ($\sim$40 ns; Melcher and Schweitzer, 1992; Roy et al., 2013). The polycrystalline powder form of LSO:Ce has similar properties to the single crystal (Lempicki et al., 2008), and would be within the appropriate size range to be used as a RLP in less invasive optogenetic control of brain circuits. Importantly for optogenetics, activation of LSO:Ce by x-rays emits light in the appropriate range to activate ChR2 (Melcher and Schweitzer, 1992). Since it is a rare-earth metal, it is considered to have a low degree of toxicity. However, little is known about the effect of LSO:Ce particles on neurons, which are extremely sensitive to their environment.

Here, we demonstrate that LSO:Ce particles, applied for 24 h, had no effect on neuronal survival in primary cortical cultures. Using hippocampal brain slices, LSO:Ce particles did not alter basal synaptic excitatory field potentials (fEPSPs) at CA3-CA1 synapses, however, there was a slight decrease in the fiber volley. The frequency of spontaneous excitatory post-synaptic currents (sEPSCs) in CA1 pyramidal cells was slightly reduced. LSO:Ce microparticles did not impair the induction of long term potentiation (LTP), although there was a slight decrease in LTP amplitude. Importantly, we also demonstrate that light emitted from LSO:Ce microparticles following irradiation is able to activate ChR2 and modulate synaptic function. Together, these results show that LSO:Ce particles are not overtly toxic to neurons or brain slices, although there are modest effects on baseline synaptic function and plasticity. Therefore, the LSO:Ce particles are a potentially viable tool for a less invasive form of *in vivo* optogenetics.

MATERIALS AND METHODS

Animals

Approval was obtained for all experimental protocols from the University of Alabama at Birmingham Institutional Animal Care and Use Committee. All experiments were conducted in accordance with the Guide for the Care and Use of Laboratory Animals adopted by the National Institutes of Health. Young adult male Sprague–Dawley rats were housed in a 22 ± 2°C room with food and water *ad libitum*. For a subset of experiments, young adult C57Bl/6 mice and adult Emx:ChR2 mice were used. The expression of ChR2 in excitatory neurons was accomplished by crossing Emx-cre mice (B6.129S2-Emx1$^{tm1(cre)Krj}$/J, JAX #005628; Gorski et al., 2002) with floxed ChR2/EYFP mice Ai32 [RCL-ChR2 (H134R)/EYFP, JAX #012569; Madisen et al., 2012]. C57Bl/6 and Emx:ChR2 mice were housed in a 26 ± 2°C room with food and water *ad libitum*. Mice were housed with the whole litter until weaned (P25-P28). Weaned mice were housed with no more than seven mice in a cage. Mouse genotypes were determined from tail biopsies using real-time PCR with specific probes designed for cre and EYFP (Transnetyx, Cordova, TN, USA). Pregnant mice (CD-1) were group-housed (four mice to a cage) in a 22 ± 2°C room with food and water *ad libitum* and were monitored daily prior to use for neuronal cultures. The animal rooms maintained a standard 12-h light/dark cycle.

Incubation of LSO:Ce Microparticles With Acute Hippocampal Slices

Acute hippocampal slices were allowed to recover for an hour before application of either vehicle (artificial cerebral spinal fluid, aCSF) or 0.2–0.5 mg/mL of LSO:Ce radioluminescent microparticles. The slices were incubated with and without LSO:Ce microparticles for at least an hour, and up to 6 h. Incubation of microparticles with hippocampal slices were performed using two types of chambers. Experiments measuring spontaneous postsynaptic currents and baseline synaptic transmission properties used a small incubation chamber that contained 5 mLs of aCSF and was bubbled with 95% O_2, pH 7.35–7.45 for the incubation period. For immunohistochemistry and LTP experiments, slices were placed in 2 mLs of aCSF on top of a piece of filter paper within a humidified oxygenated interface recovery chamber, both for recovery and microparticle incubation.

Electrophysiology Using Rats

Rat Hippocampal Slice Preparation

Young adult male Sprague–Dawley rats (age 6–10 weeks; Charles River Laboratories) were anesthetized with isoflurane, decapitated, and brains removed; 400 μm coronal slices from dorsal hippocampus were made on a VT1000P vibratome (Leica Biosystems) in oxygenated (95% O_2/5% CO_2) ice-cold high sucrose cutting solution (in mm as follows: 85.0 NaCl, 2.5 KCl, 4.0 $MgSO_4$, 0.5 $CaCl_2$, 1.25 NaH_2PO_4, 25.0 glucose, 75.0 sucrose). After cutting, slices were held at room temperature from 1 to 5 h with continuously oxygenated standard aCSF (in mm as follows: 119.0 NaCl, 2.5 KCl, 1.3 $MgSO_4$, 2.5 $CaCl_2$, 1.0 NaH_2PO_4, 26.0 $NaHCO_3$, 11.0 glucose).

Electrophysiology—Field Recordings

Vehicle and LSO:Ce incubated slices were interleaved to account for slice health. Extracellular field excitatory postsynaptic potentials (fEPSPs) recorded from the dendritic region in hippocampal area CA1 were performed in a submersion chamber perfused with standard aCSF at room temperature. All data were obtained using the electrophysiology data acquisition software pClamp10 (Molecular Devices, LLC, Sunnyvale, CA, USA) and analyzed using Clampfit within the pClamp10 suite, and Graphpad Prism 7 (GraphPad Software, Inc.). For CA3-CA1 synapses, Schaffer collateral axons were stimulated using a twisted insulated nichrome wire electrode placed in CA1 stratum radiatum within 200–300 μm of an aCSF-filled glass recording electrode, and paired-pulse facilitation (PPF) characteristic of this synapse (Wu and Saggau, 1994) was recorded. Baseline fEPSPs were obtained by delivering 0.1 Hz stimulation for 200 μs to generate fEPSPs of 0.2–0.3 mV in amplitude. Only experiments with ≤10% baseline variance were included in the final data sets.

Input-Output Curves

After a stable 10 min baseline, input-output (I/O) curves were generated by increasing the stimulus intensity (20 μA increments) until a maximal fEPSP slope was obtained, usually at 200 μA. Initial slope of the five fEPSPs generated at each stimulus intensity was averaged and plotted as a single value. Statistical significance was determined by two-way ANOVA with Sidak's multiple comparison test.

Paired Pulse Ratio

After a 10 min stable baseline, pairs of stimulation were delivered at a 50 millisecond (ms) inter-stimulus interval (ISIs). The paired pulse ratio (PPR) was calculated by dividing the initial slope of the second fEPSP by the initial slope of the first fEPSP.

Long Term Potentiation

At CA3-CA1 synapses, following a 10 min stable baseline (0.1 Hz, 200 μs with stimulation intensity set to elicit initial fEPSP amplitude of 0.3–0.4 mV), NMDA receptor (NMDAR)-dependent LTP was induced using high-frequency stimulation (HFS, 100 Hz, 1 s duration × 5, 60 s interval). Statistical significance was determined using unpaired Student's *t*-test by comparing the average of the fEPSP slope from the last 5 min of the recording (35–40 min) to baseline for each genotype ($^*p < 0.05$).

Electrophysiology—Whole Cell

All recordings were performed in a submersion chamber with continuous perfusion of oxygenated standard aCSF. Whole-cell voltage clamp recordings were carried out in blind patched CA1 pyramidal neurons. Inhibitory postsynaptic currents (IPSCs) were pharmacologically isolated with bath perfusion of DNQX (10 μM; Sigma) and DL-AP5 (50 μM; Tocris). Spontaneous IPSCs (sIPSCs) were recorded using CsCl internal solution (in mM: 140.0 CsCl, 10.0 EGTA, 5.0 $MgCl_2$, 2.0 Na-ATP, 0.3 Na-GTP, 10.0 HEPES; E_{Cl} = 0 mV). All cells were dialized for 3–7 min prior to the beginning of experimental recordings. Stability of series resistance during the recording was verified posthoc through comparing the average rise and decay time of sIPSCs. Recordings were discarded if the rise or decay time changed by >20%.

Electrophysiology in Mice

Mouse Hippocampal Slice Preparation

Male and female mice, 4–7 months of age, were anesthetized with isoflurane and sacrificed by decapitation using a rodent guillotine. Due to the age of the mice, a more neuroprotective dissection solution was used during acute hippocampal slice preparation (Tanaka et al., 2008). The brains were rapidly removed and placed in ice-cold dissection solution containing the following (in mM): 135 N-Methyl-D-glucamine, 1.5 KCl, 1.5 KH_2PO_4, 0.5 $CaCl_2$, 3.5 $MgCl_2$, 23 $NaHCO_3$, 0.4 L-Ascorbic acid, and 10 glucose, bubbled with 95% O_2/5% CO_2, pH 7.35–7.45, and osmolarity 295–305 (Albertson et al., 2017). A vibratome (Campden 7000smz-2, Lafayette Instrument) was used to cut 300 μM thick hippocampal brain slices. The slices were maintained for 45–60 min at 37°C in oxygenated recovery solution containing (in mM) 120 NaCl, 3.5 KCl, 0.7 $CaCl_2$, 4.0 $MgCl_2$, 1.25 NaH_2PO_4, 26 $NaHCO_3$, and 10 glucose and then kept at room temperature. Slices were stored at room temperature in a holding chamber containing the recovery solution and bubbled with 95% O_2/5% CO_2 for >30 min before recording.

Whole Cell Electrophysiology Recording

Photostimulation of the microparticles occurred by using pulses of ultraviolet (UV) light (315 nm or 365 nm, 500 ms pulse duration). The 365 nm UV light was generated by a Colibri.2 LED Light Source (Zeiss) applied to acute hippocampal slices through a 10× objective, resulting in an illumination area of 5.29 mm^2. The 365 nm light intensity was measured as being approximately 0.003 mW/mm^2 by ThorLabs PM100D Optical Power Meter. The 315 nm UV light was generated by custom building the unit using components obtained from ThorLabs (**Figure 1**). The 315 nm UV light is applied to the acute hippocampal slice through a 2.5 mm stainless steel ferrule, therefore allowing a similar illumination area to that of the 10× objective. Both the Colibri.2 and the custom-built 315 nm portable unit were triggered by a Master-9 digital stimulator (A.M.P.I).

For the recordings, slices were placed in a submersion recording chamber and perfused (3–4 ml/min) with aCSF. Experiments were performed at 28–32°C. For spontaneous EPSC (sEPSC) recordings, CA1 pyramidal cells were blindly patched on a Zeiss Examiner A1 upright microscope. Neurons were patched in the voltage-clamp configuration and recorded at a holding potential of −60 mV using an Axopatch 200B amplifier (Molecular Devices). Patch electrodes (4–6 MΩ) were filled with a potassium gluconate based internal solution composed of the following (in mM): 130 K-gluconate, 0.1 EGTA, 20 KCl, 2 $MgSO_4 \cdot 7\ H_2O$, 10 HEPES, 5 phosphocreatine-tris, 10 ATP, and 0.3 GTP. The pH was adjusted to 7.2 with KOH and osmolarity was 290–295. The access resistance and holding current (<200 pA) were monitored continuously. Recordings were rejected if either access resistance or holding current increased ≥25% during the experiment. The access resistance for experiments performed without the particles was 29.6 ± 2.4 MΩ and the slices with LSO:Ce microparticles was 26.2 ± 1.9 MΩ (n = 16, 12 cells respectively, unpaired t-test, $p > 0.3$).

Analysis of sEPSC frequency and amplitude were performed using custom software written in Visual Basic, which measured amplitude and interevent interval. Events were fit to a template response and all events that fit the template and passed visual inspection were included in the analysis. The rise time and the decay time constant were measured from averaged sEPSC events for each individual experiment. The rise time is defined as the time required to travel from 20% to 80% of the amplitude. The decay time constant was determined by fitting with a single exponential function equation.

Immunohistochemistry

Acute 300 μm hippocampal slices were obtained from P50 to P70 C57Bl/6 mice. Slices were incubated with and without 0.25–0.5 mg/mL of LSO:Ce RPLs for 0, 1, 3, and 6 h. Slices were fixed overnight at 4°C in 4% paraformaldehyde in 0.1 M phosphate buffered saline (PBS) and immunohistochemistry was performed based on a modified protocol (Dissing-Olesen and MacVicar, 2015; Miller et al., 2017; Yang et al., 2018). Briefly, the free-floating fixed slices were washed five times for 10 min in PBS. The slices were permeabilized for 1 h at room temperature in 0.1 M PBS (pH 7.4) with 0.3% Triton X-100 and 20% DMSO (PBSTD). Slices were blocked with 10% donkey serum (cat# 017-000-121, Jackson ImmunoResearch Inc.) in PBSTD for 3 h at room temperature. Following blocking, the sections were immunostained with a monoclonal mouse antibody against glial fibrillary acidic protein (GFAP; 1:1,000, cat# 3670, Cell Signaling Technology) for 48–96 h at 4°C in blocking solution. After washing, the slices underwent another blocking step. Then the slices were incubated with Alexa Fluor 488 conjugated polyclonal donkey anti-mouse antibody secondary (cat# 715-545-150, Jackson ImmunoResearch Inc.) diluted 1:400 in blocking solution for 16–40 h at 4°C. Staining specificity was confirmed by the omission of primary antibody. Sections were mounted with the nuclear dye 4′,6-diamindino-2-phenylindole dihydrochloride (DAPI) in the VECTASHIELD HardSet mounting medium (cat# H-1500, Vector Laboratories). Immunostained slices were imaged using an epifluorescent Nikon eclipse ni microscope and NIS Elements v. 4.20.02 software. To individually count CA1 pyramidal cells, images were taken using the 40× objective of the DAPI stain. Images for GFAP analysis were taken using a 10× objective. Analysis of images was performed using ImageJ (Fiji).

Primary Cortical Neuronal Culture

Mouse primary cortical neuronal culture from pregnant CD-1 mice was made as previously described (Andrabi et al., 2014). Embryos obtained from mice at Day 15–16 of gestation were used to prepare primary cortical neuron cultures. Briefly, the cortical regions of the embryonic brains were aseptically dissected, freed of meninges and dissociated in dissecting medium (DMEM + 20% fetal bovine serum) and subjected to trypsin digestion at 37°C for 5 min. Tryptic digestion was stopped by the addition of dissecting medium and the cell suspension was centrifuged at 1,000 *g* for 5 min. Next, the pelleted cells were subjected to mechanical trituration in complete Neurobasal medium (10 mM glucose, 1 mM GlutaMAX-I, 1 mM Na-Pyruvate and 2% B-27) and passed through a 40 μm filter. The cells were plated to a density of 5×10^5 cells/ml. On day *in vitro* (DIV) 1, the cultures were treated with 5-fluoro 2-deoxyuridine (40 μM) to inhibit glial cell growth and proliferation. Experiments were performed between DIV 10 and 11. Under these conditions, mature neurons represent 90% of the cells in the culture.

Cell Death Assay

Neurons at DIV 10 were incubated with either microparticles (LSO:Ce, dispersed in PBS), at concentrations ranging from 0.05 to 0.2 mg/ml, or PBS for 24 h. Cell viability after addition of nanoparticles was determined by using Alamar blue reagent, a water-soluble resazurin dye (blue colored) which is reduced to red fluorescent resorufin dye by metabolically active cells. Alamar blue reagent [10% (v/v)] was then added to each well containing Neurobasal medium and incubated for 3 h at 37°C. Blank control well containing microparticles only were used to exclude possible interactions with the assay. Neurobasal medium containing Alamar blue reagent was added to these wells. Following 3 h of incubation, 100 μL of the medium was collected from each well and transferred to a 96-well microplate. The fluorescence was measured at the excitation and emission wavelength of 540 and 595 nm, respectively using a microplate reader. The fluorescence values were normalized by the control (PBS) and expressed as percent viability.

Materials

Commercial lutetium oxyorthosilicate particles (median particle size: 4 μm) were purchased from Phosphor Technologies and were doped with cerium at a 1–10 atomic % cerium (LSO:Ce). Prior to their use, the particles were washed with deionized water and vacuum air-dried.

RESULTS

Light Emitted From LSO:Ce Particles Can Weakly Activate Channelrhodopsin-2

LSO:Ce particles emit within the activation spectrum for ChR2. Interestingly, these particles can be activated with UV light. As a proof of principle, we took advantage of this property to test whether light emitted from LSO:Ce microparticles could enhance synaptic activity. However, it was necessary to first test whether ChR2 is activated by UV light. We used Emx:ChR2 mice to determine the extent to which ChR2 is activated by various wavelengths of UV light. Using UV light at 365 nm, we observed a photocurrent (−22.4 ± −2.3 pA, n = 10 cells) in recordings from CA1 pyramidal cells in acute slices, even with a relatively low light intensity (0.003 mW/mm^2). We were concerned that the activation of ChR2 with 365 nm light would hamper our ability to see the activation of ChR2 from light generated by the LSO:Ce particles. Therefore, we built a portable UV system that would emit light around 315 nm (**Figure 1**). Application of 315 nm light onto CA1 pyramidal cells that express ChR2 generated an extremely small, but detectable, photocurrent (−5.5 ± −2.0 pA, n = 5 cells, **Figure 2B**).

As the light emitted from the LSO:Ce particles might not be uniform enough to generate a synchronized synaptic event, we analyzed the impact on the amplitude and frequency of

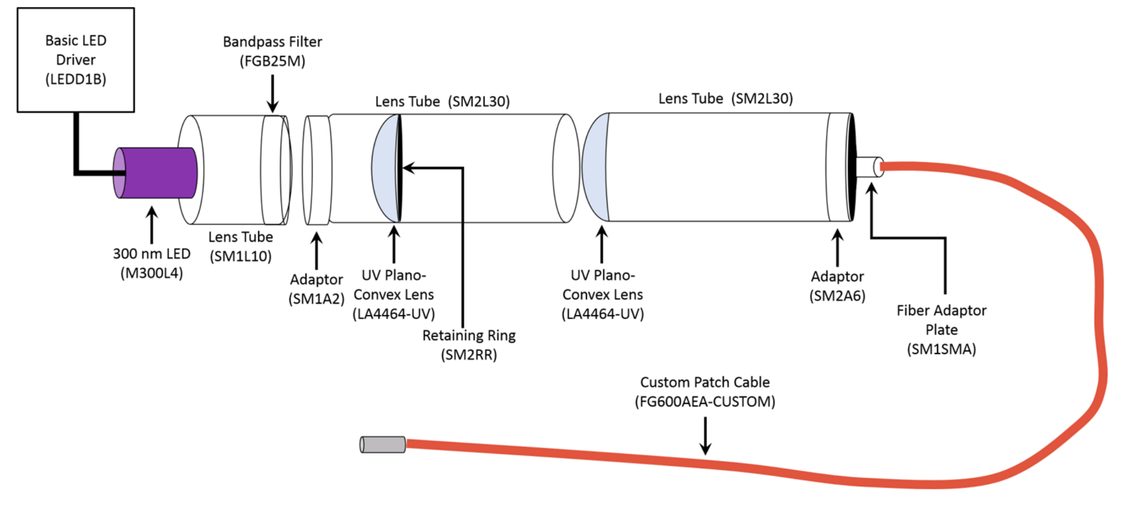

FIGURE 1 | Schematic of Portable 315 nm ultraviolet (UV) light emitting diode (LED). All the components were obtained from ThorLabs. The general name of each component is labeled, and the part number is in the parentheses. The LED Driver is the power source for the unit. The emission spectrum for the 300 nm LED ranges from approximately 285 nm to 325 nm, with it peaking at 300 nm. The bandpass filter allows transmission between 315 nm to 445 nm, thereby narrowing the range of emitted light to 315–320 nm. The custom 1 m long patch cable had the following parameters: Fiber-FG600AEA, Tubing-FT038, End 1-SMA, and End 2–2.5 mm (FC) stainless steel ferrule.

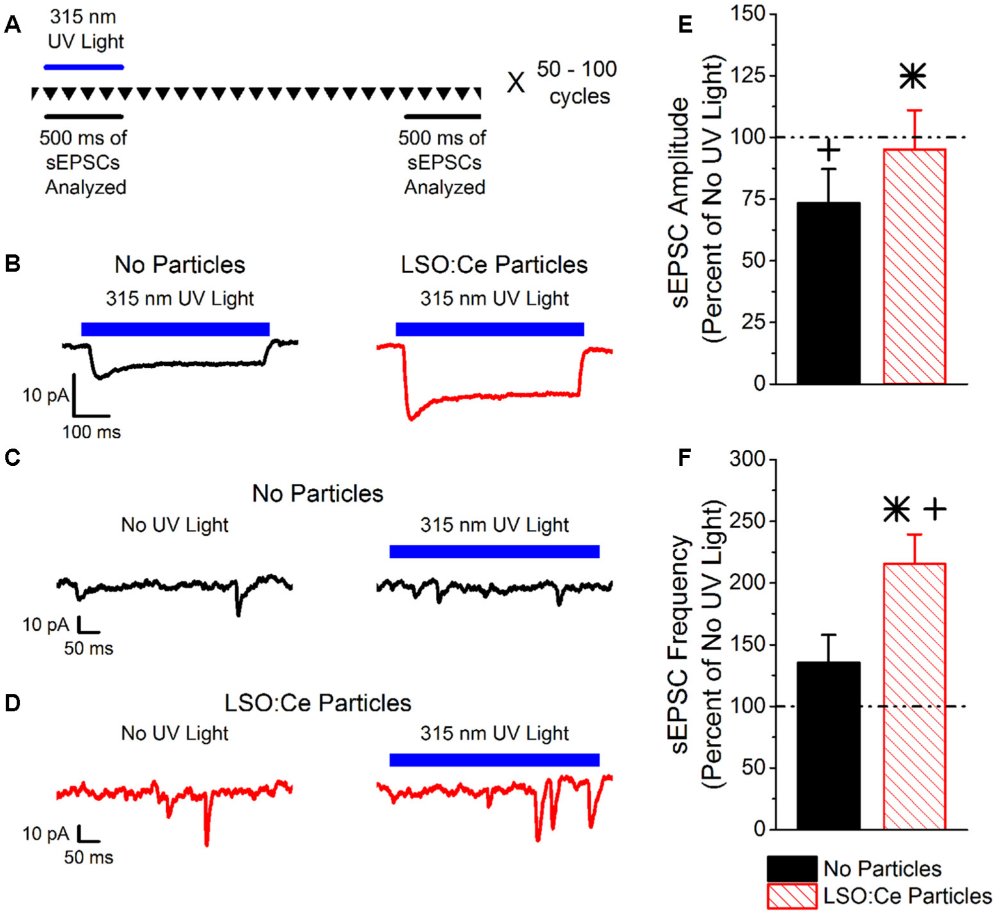

FIGURE 2 | Light emitted from Cerium doped lutetium oxyorthosilicate (LSO:Ce) microparticles enhances synaptic transmission from channelrhodopsin-2 (ChR2) expressing CA1 pyramidal cells. **(A)** Experimental schematic that shows the interleave nature of the application of the 315 nm UV light and the analysis. Every 10 s, traces that lasted for 3 s were recorded (depicted by the inverted triangles), and each trace was repeated 50–100 times. The spontaneous excitatory postsynaptic currents (sEPSC) events for each individual trace was analyzed during the 500 ms when the UV light was on or at the end of the trace when there was no UV light. **(B)** Example averaged trace (at least 25 traces) of 315 nm induced photocurrents in acute hippocampal Emx:ChR2 mouse slices with (red trace) or without (black trace) LSO:Ce particles. **(C)** Example of an individual trace of sEPSCs recorded from a CA1 pyramidal cell in an acute hippocampal slice from an Emx:ChR2 mouse that was not incubated with LSO:Ce particles in the absence (left) or presence (right) of the 315 nm UV light. **(D)** Example of an individual trace of sEPSCs onto CA1 pyramidal cells from an acute hippocampal Emx:ChR2 mouse slice that was incubated with LSO:Ce particles for at least 1 h in the absence (left) or presence (right) of the 315 nm UV light. **(E,F)** For each experiment, the sEPSC amplitude and frequency measured in the presence of the 315 nm UV light was normalized to a section of the same trace that was not exposed to UV light to account for cell to cell variability and recording stability. **(E)** Application of UV light alone decreased the amplitude of sEPSCs compared to baseline ($n = 5$ cells/4 animals, Student's t-test, $p = 0.01$). Nevertheless, the presence of the LSO:Ce particles enhanced the sEPSC amplitude as compared to UV alone ($n = 5$ cells/4 animals no particles, 7 cells/5 animals LSO:Ce particles, Student's t-test, $p = 0.03$). **(F)** There was a trend for exposure to UV light alone to enhance the frequency of sEPSCs ($n = 5$ cells/4 animals, Student's t-test, $p = 0.19$). The light emitted from LSO:Ce particles by UV activation almost doubles the number of sEPSCs compared to baseline ($n = 5$ cells/4 animals no particles, 7 cells/5 animals LSO:Ce particles, Student's t-test, $p = 0.04$). *Indicates significant difference ($p < 0.05$) with and without LSO:Ce particles; $^+$Indicates significant difference ($p < 0.05$) compared to no UV light.

sEPSCs. As there is cell to cell variability with sEPSCs, we used a within cell control (no UV light) to normalize the amplitude and frequency of sEPSCs. **Figure 2A** depicts the experimental paradigm showing that the periods of UV light stimulation and no stimulation were interleaved throughout the experiment. Even though only a small photocurrent was generated with the application of 315 nm light, there was a trend for an increase in the frequency of sEPSCs during UV light exposure (**Figures 2C,F**). Importantly, the enhancement is much larger when the LSO:Ce particles are present (**Figures 2D,F**). A similar enhancement of the frequency of sEPSCs was seen when 365 nm UV light was applied (UV only 149.4 ± 20.9% vs. UV + LSO:Ce 225.2 ± 24.4%, $n = 8$ cells, 7 cells, Student's t-test, $p = 0.04$). Interestingly, the amplitude of the sEPSCs is decreased with the application of 315 nm light (**Figure 2E**). However, the addition of the LSO:Ce particles enhances the amplitude of the sEPSCs compared to UV alone (**Figure 2E**). Additionally, the overall size of the photocurrent induced by the 315 nm UV light was enhanced in the presence of the particles as compared to UV light application alone (Vehicle slices -5.5 ± -2.0 pA, vs. LSO:Ce slices −12.3 ± 1.8 pA, $n = 5$ cells/4 animals, 7 cells/5 animals, Student's t-test, $p = 0.03$, **Figure 2B**). These data indicate that the light emitted from LSO:Ce particles is able to activate ChR2 and increase the frequency of sEPSCs.

Prolonged Exposure to LSO:Ce Microparticles Does Not Alter Neuronal Survival or Properties

We next tested the biocompatibility of LSO:Ce microparticles. Neurons are extremely sensitive to changes in their environment and any perturbations could lead to neuronal cell death, in as little as 4 h (Hoque et al., 2019). We determined if prolonged exposure to LSO:Ce particles had any effect on neuronal survival using the Alamar Blue assay and primary cortical cultures. The result demonstrates no significant sign of toxicity exerted by the microparticles at any of the doses tested, even with 24 h of exposure to the LSO:Ce microparticles (**Figure 3**).

Primary cortical cultures are more sensitive to extracellular perturbations than acute slices. However, we confirmed the results that neuronal survival was not affected by acute application of the LSO:Ce microparticles using acute hippocampal slices. We incubated slices with 0.25–0.5 mg/mL of LSO:Ce microparticles for 0–6 h, and manually counted the number of DAPI positive neurons in the pyramidal layer. We saw no difference in the density of CA1 pyramidal cells between unexposed and exposed slices even after 6 h of treatment (No particle slices 109.0 ± 8.9 cells/mm^2 vs. LSO:Ce slices 105.9 ± 16.3 cells/mm^2, $n = 11$ images/4 animals, 9 images/4 animals, Student's t-test, $p = 0.86$). Additionally, acute incubation of LSO:Ce particles did not change the resting membrane potential of CA1 pyramidal cells (No particle slices −63.9 ± 2.7 mV vs. LSO:Ce particle slices −66.1 ± 2.1 mV, $n = 16$ cells/11 animals, 13 cells/7 animals, Student's t-test, $p = 0.55$). However, the input resistance of the cells was slightly reduced (No particle slices 99.1 ± 6.6 MΩ vs. LSO:Ce particle slices 80.4 ± 5.1 MΩ, $n = 16$ cells/11 animals, 13 cells/7 animals, Student's t-test, $p = 0.04$). Overall, exposure to LSO:Ce microparticles did not affect neuronal health.

Implanted probes have been shown to increase glial scarring (Canales et al., 2018), which takes several days to develop (Wanner et al., 2013). One of the early steps in glial scar development is the activation of astrocytes. GFAP can be used as a way to measure astrocyte activation and has been shown to be increased within 2–4 h after damage (Schmidt-Kastner et al., 1993). Therefore, to determine if astrocytes became reactive in the presence of these particles, we used immunohistochemistry to analyze GFAP in LSO:Ce preincubated slices compared to control slices (no particles). As the LSO:Ce particles could potentially influence the visualization of GFAP staining, we performed control experiments in which we immediately processed slices after application of vehicle (aCSF) or the particles (**Figure 4**) to test for differences in GFAP fluorescent intensity caused by light being emitted or absorbed by the particles. However, the overall fluorescent intensity of GFAP staining was not different between vehicle-treated slices and LSO:Ce-treated slices at the 0 h time point, indicating that measurement of GFAP fluorescence was not altered due to the emission and absorbance capabilities of the LSO:Ce particles (No particles slices $1.03 \times 10^6 \pm 1.14 \times 10^5$ vs. LSO:Ce particles slices $1.02 \times 10^6 \pm 6.02 \times 10^4$, $n = 8$ slices/4 animals, 8 slices/4 animals, Student's t-test, $p = 0.98$). Since the LSO:Ce particles fluorescent properties do not alter our ability to visualize GFAP staining, we can determine if their presence over time causes changes in the GFAP intensity. Slices were incubated for up to 6 h with either vehicle or the LSO:Ce microparticles. The results show that there was no increase in the level of GFAP staining due to prolonged incubation with the LSO:Ce particles (**Figure 4**). Our data suggest that there is no gross changes in astrocyte activation with the application of LSO:Ce particles.

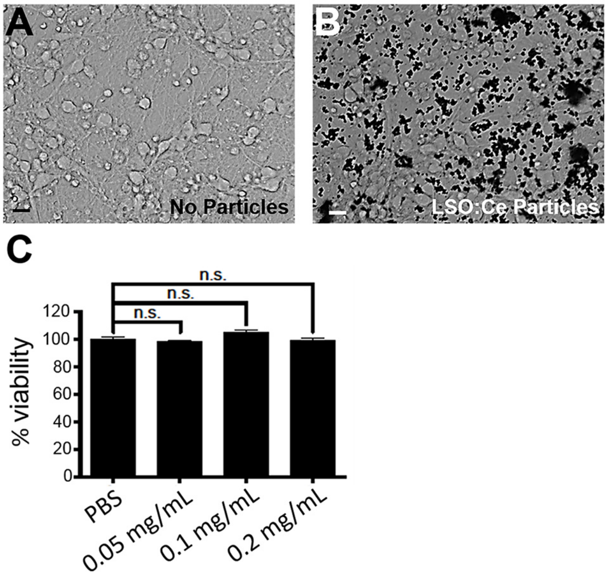

FIGURE 3 | Prolonged exposure of LSO:Ce microparticles is not toxic to neurons. **(A)** Representative image of primary cortical neurons at 11 days *in vitro* (DIV). **(B)** Representative image of 11 DIV primary cortical culture that were incubated with LSO:Ce particles (black dots) for 24 h. **(C)** Group data for indicated LSO:Ce particles concentrations that were added to the neurons at 10 DIV and the cell death assay was performed on DIV 11 using Alamar Blue reagent. Results are expressed as percent of control. Data represent as mean ± SEM, $n = 6$ wells per condition, one-way ANOVA with Tukey's *post hoc* test. n.s, not significant. Scale bars: 25 μm.

LSO:Ce Microparticles Modestly Alter Synaptic Transmission

Even though overall cell health was unaltered by exposure to LSO:Ce particles, the synaptic transmission could still be affected. We further analyzed this by incubating hippocampal slices with LSO:Ce particles for 1–3 h, followed by recording extracellular dendritic fields potentials (fEPSPS) from CA1 pyramidal cells in stratum radiatum in response to increasing the number of CA3 Schaffer collateral axons stimulated (**Figures 5A–C**). The initial slope of the fEPSP represents the postsynaptic response, and we found no difference in the maximal response generated between the control and LSO:Ce-treated slices (**Figure 5B**).

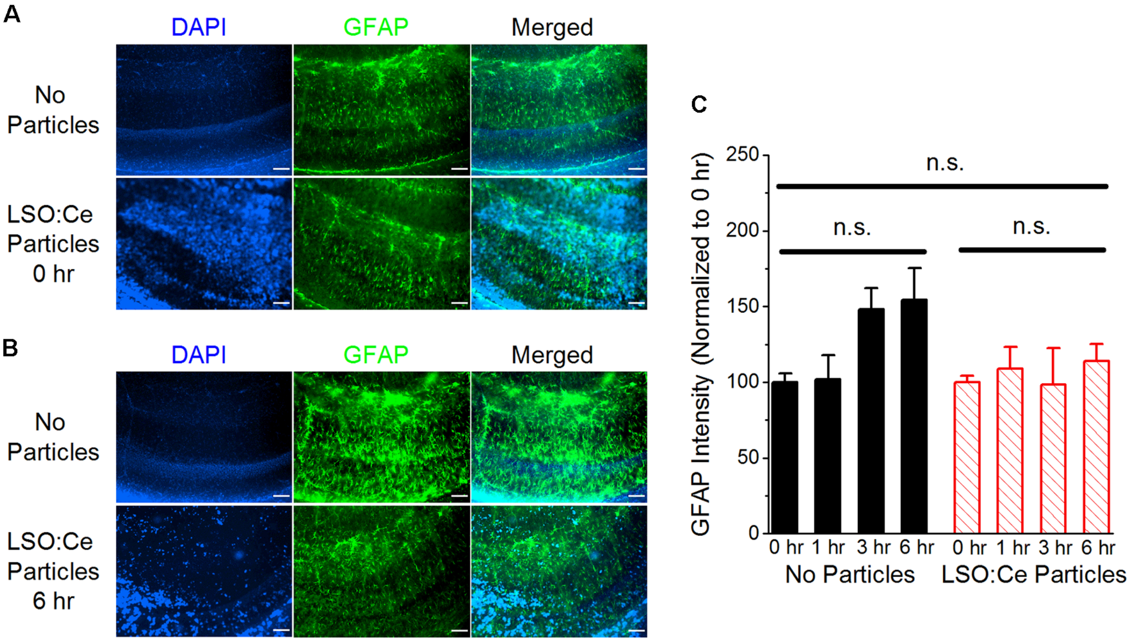

FIGURE 4 | Exposure of LSO:Ce microparticles to acute hippocampal slices does not elevate glial fibrillary acidic protein (GFAP). **(A)** Example images of GFAP staining in acute hippocampal slices immediately after application of vehicle (no particles) or LSO:Ce particles. Merged images include 4′,6-diamindino-2-phenylindole dihydrochloride (DAPI; blue) and GFAP (green) staining. Scale bars: 100 μm. **(B)** Example images of GFAP staining in acute hippocampal slices 6 h after application of vehicle or LSO:Ce particles. Merged images include DAPI (blue) and GFAP (green) staining. Scale bars: 100 μm. **(C)** Group data shows that the intensity of GFAP staining is not altered with the addition of the LSO:Ce particles (n = 8 slices/4 animals per condition, two-way ANOVA, $F_{(3,63)} = 1.76$, $p = 0.17$). n.s, not significant.

However, a small decrease in the amplitude of the fiber volley, a measurement of the number of axons activated, was seen with high stimulation (**Figure 5C**). In addition, we saw a small, but significant, increase in the PPR, suggesting that the LSO:Ce particles may alter presynaptic function (**Figure 5D**).

To further investigate whether incubation with LSO:Ce particles affects synaptic transmission, we preincubated acute hippocampal slices with LSO:Ce particles for 1–3 h. We then performed whole-cell recordings from CA1 pyramidal cells and recorded spontaneous excitatory (sEPSCs; **Figure 6**) and inhibitory postsynaptic currents (sIPSCs; **Figure 7**). There was no change in the amplitude of sEPSCs (**Figures 6A,B**), however, the frequency of the events was slightly but significantly reduced with exposure to LSO:Ce particles (**Figures 6A,C**). On the other hand, sIPSCs frequency and amplitude were unaltered in the presence of the particles (**Figure 7**). Additionally, the kinetics of the sEPSCs (**Figures 6D,E**) and sIPSCs (**Figure 7C**) were unaltered in the presence of the LSO:Ce microparticles. This suggests either that the particles are reducing the number of excitatory synapses, modifying presynaptic function, or altering axonal excitability.

LSO:Ce Microparticles Modestly Alter Long Term Potentiation

Next, we asked if long-term plasticity, a more robust measure of synaptic health and integrity, is compromised by pre-incubation with LSO:Ce particles. LTP, an increase in synaptic strength that lasts for at least 40 min *in vitro* and hours to days *in vivo* and is thought to underlie learning and memory, has been extensively characterized at CA3-CA1 synapses, and involves the insertion of excitatory AMPA receptors (AMPARs) on post-synaptic CA1 pyramidal cells. We again incubated acute hippocampal slices for 1–3 h with LSO:Ce particles, and then recorded extracellular fEPSPs in response to Schaffer collateral stimulation in an interleaved fashion where control and LSO:Ce microparticles treated slices were alternated. Following the establishment of a 10-min baseline, we electrically induced LTP at CA3-CA1 synapses by stimulating Schaffer collateral axons at 100 Hz for 0.5 s, five times, separated by intervals of 20 s. While this protocol produced identical post-tetanic potentiation and LTP up to 20 min post-tetanus in control and LSO:Ce treated slices, there was a very small but significant decrease in LTP expression at 40 min post-tetanus in the LSO:Ce treated vs. control slices, which may suggest that the particles have a slightly negative impact on long-term expression of LTP (**Figure 8**).

DISCUSSION

Our results provide proof of principle that light from LSO:Ce microparticles can activate ChR2 and modulate synaptic function. In addition, we demonstrate that LSO:Ce particles are not overtly toxic to neurons, as there was no effect of the particles on neuronal survival in culture even with incubations as long as 24 h. Synaptic function and plasticity also appear to be intact, as

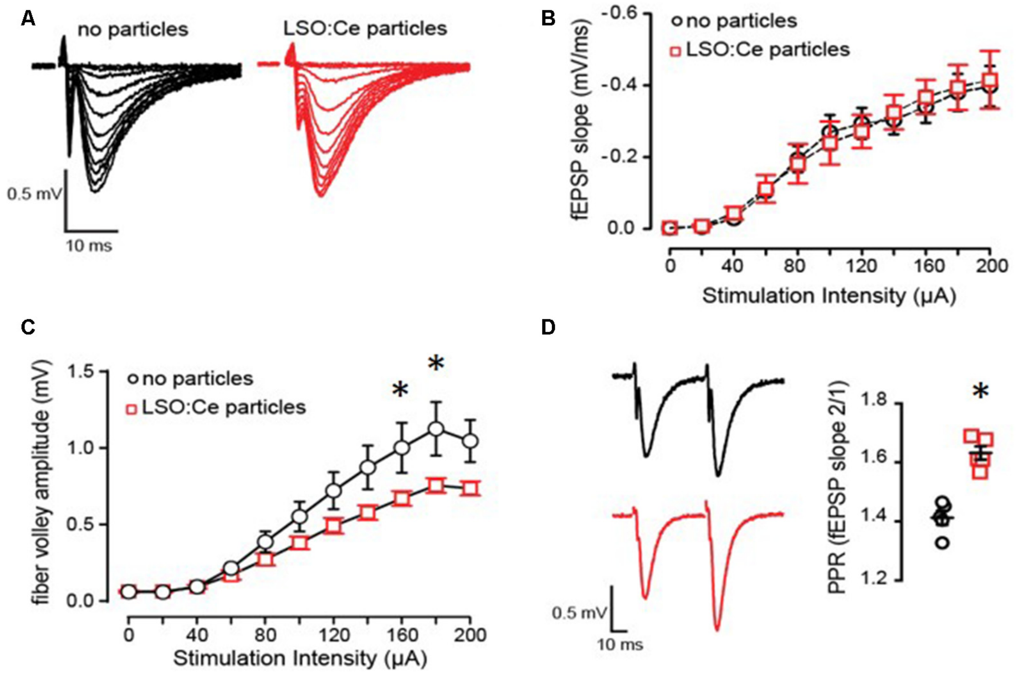

FIGURE 5 | Acute application of LSO:Ce microparticles has no effect on the strength of basal synaptic transmission but reduces axonal excitability at CA3-CA1 synapses. **(A)** Representative traces of field excitatory postsynaptic potentials (fEPSPs) at CA3-CA1 synapses in response to increasing stimulus intensity from acute hippocampal slices incubated without and with LSO:Ce particles (black traces: no particles and red traces: particles). **(B)** No change in the input/output (I/O) curve in in the presence of LSO:Ce particles (n = 6 slices/6 animals no particles, n = 6 slices/6 animals LSO:Ce; $^*p > 0.05$). Data represent mean ± SEM. Significance determined by two-way ANOVA with Sidak's multiple comparison test. **(C)** Group data showing a reduction in fiber volley amplitude with increasing stimulus intensity in the presence of LSO:Ce particles (n = 6 slices/6 animals no particles, n = 6 slices/6 animals LSO:Ce; two-way ANOVA, $F_{(1,110)} = 24.48$, $p < 0.001$, $^*p < 0.05$ with Sidak's multiple comparisons test. (**D**; left) Representative traces of paired fEPSPs (black traces: no particles and red traces: particles). (right) Paired-pulse ratio (PPR) was significantly increased following incubation with particles (n = 6 slices/6 animals control, n = 6 slices/6 animals LSO:Ce; $^*p < 0.05$).

there was no change in the input/output relationship in CA1, and LTP was able to be induced. However, there were indications that LSO:Ce particles themselves have effects on synaptic function and plasticity, although the effects were small. Together, these results suggest that LSO:Ce particles could potentially be suitable for *in vivo* optogenetics.

LSO:Ce was introduced as a scintillator in the early 90s (Melcher and Schweitzer, 1992) and has been extensively characterized since. Cerium forms the luminescence centers in LSO, and the Ce doped LSO displays a high emission intensity under X-ray illumination, with an emission maximum at 420 nm. This emission peak makes LSO:Ce well suited for optogenetics applications using ChR2, which has maximal activation using 450 nm light (Berndt et al., 2011; Lin, 2011). The use of X-rays has the distinct advantage over implanted LEDs to activate ChR2, as X-rays are able to penetrate the skull, removing the need for an invasive delivery method. However, before this study, it was not known if LSO:Ce particles themselves could emit enough light to activate ChR2.

Implantation of LEDs or a fiber requires the light output to be proportionally higher than necessary to activate ChR2 because of light scattering properties in brain tissue. One study using a fiber to deliver light reported that local tissue temperature increased by 0.8°C (Senova et al., 2017). Interestingly in that study, no effect was seen on neuronal cell death with acute light applications at the highest illumination used (Senova et al., 2017), however, the question still remains how the tissue can handle local heating with longer duration or repeated applications. If the conditions are right, tissue heating under illumination can cause damage and contribute to observed behavioral or physiological effects (Long and Fee, 2008). The use of nanoparticles made from inorganic scintillators will allow for the light source to be extremely close to ChR2 and therefore less light would be needed to activate ChR2, reducing the risk of damage caused by heat.

Here, we observed that light emitted from LSO:Ce microparticles in response to UV stimulation caused an increase in the frequency of sEPSCs onto CA1 pyramidal cells, indicating activation of ChR2. However, we did not detect firing of action potentials or large light-evoked EPSCs, suggesting that the activation of ChR2 is modest. UV light alone is also able to provide weak activation of ChR2, as seen by small photocurrents and an increase in sEPSC frequency. The photocurrents were modest with stimulation at 365 nm, and even smaller at 315 nm. Even though UV light activates ChR2, using the 315 nm wavelength improved our ability to detect events caused by light emission from the microparticles. One limitation of the current experiment is that the particles were applied to the surface of the slice, and therefore are likely to be 100 microns or more from

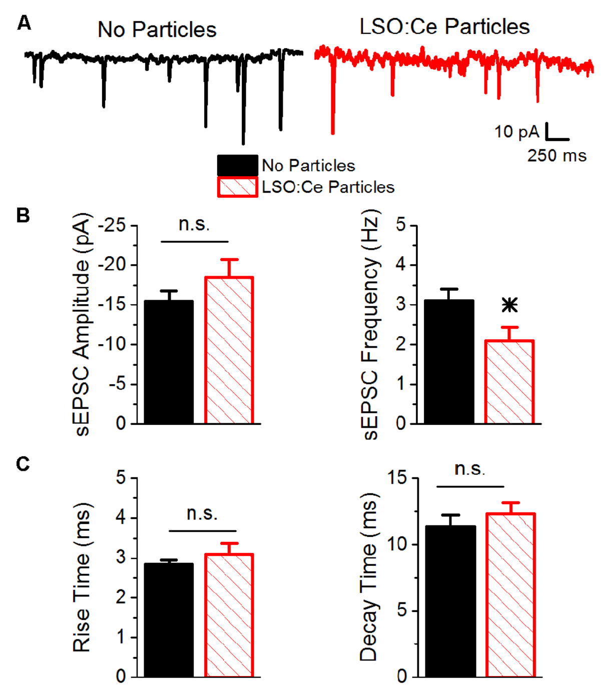

FIGURE 6 | Acute application of LSO:Ce microparticles reduces the frequency, but not amplitude, of sEPSCs recorded from CA1 pyramidal cells. **(A)** Example traces of spontaneous EPSCs onto CA1 pyramidal cells from acute hippocampal slices incubated with (red trace) and without (black trace) the particles for at least 1 h. (**B**; left) Group data showing that the amplitude of sEPSCs was unaltered in the presence of LSO:Ce particles ($n = 15$ cells/11 animals no particles, 11 cells/7 animals LSO:Ce particles, Student's *t*-test, $p = 0.24$). (right) Group data showing the frequency of sEPSCs was significantly reduced in the presence of LSO:Ce particles ($n = 15$ cells/11 animals no particles, 11 cells/7 animals LSO:Ce particles, Student's *t*-test, $p = 0.03$). (**C**; left) No change in the 20% to 80% rise time of the sEPSC when incubated with the LSO:Ce particles ($n = 15$ cells/11 animals no particles, 11 cells/7 animals LSO:Ce particles, Student's *t*-test, $p = 0.35$). (right) The decay time constant of the sEPSC is unaltered in the presence of the LSO:Ce particles ($n = 15$ cells/11 animals no particles, 11 cells/7 animals LSO:Ce particles, Student's *t*-test, $p = 0.46$). *Indicates significant difference ($p < 0.05$) with and without LSO:Ce particles; n.s, not significant.

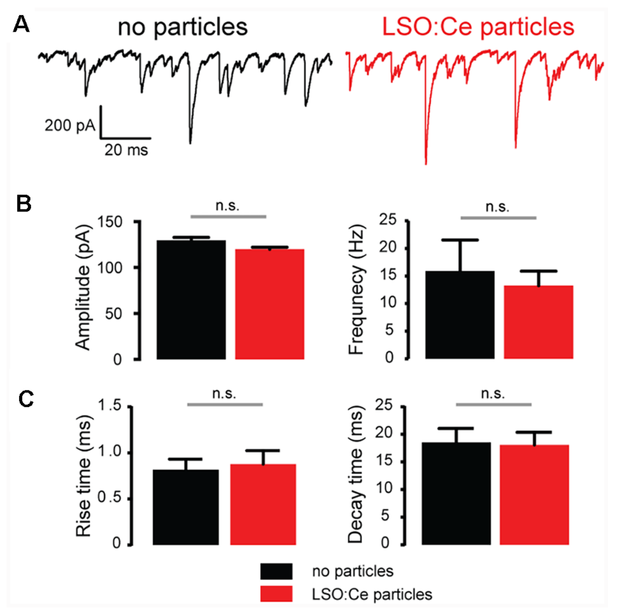

FIGURE 7 | Acute application of LSO:Ce microparticles had no effect on spontaneous inhibitory postsynaptic currents (sIPSCs) recorded from CA1 pyramidal cells. **(A)** Example traces of sIPSCs onto CA1 pyramidal cells from acute hippocampal slices incubated with (red trace) and without (black trace) the particles for 1 h. (**B**; left) Group data showing the amplitude of sIPSCs ($n = 5$ cells/2 animals no particles, 9 cells/2 animals LSO:Ce particles, Mann-Whitney test, $p = 0.18$) and (right) frequency of the sIPSCs ($n = 5$ cells/2 animals no particles, 9 cells/2 animals LSO:Ce particles, Mann-Whitney test, $p = 0.79$) was unaltered in the presence of LSO:Ce particles. (**C**; left) Group data showing that the rise time ($n = 5$ cells/2 animals no particles, 9 cells/2 animals LSO:Ce particles, unpaired *t*-test, $p = 0.78$) and (right) decay of sIPSCs ($n = 5$ cells/2 animals no particles, 9 cells/2 animals LSO:Ce particles, unpaired *t*-test, $p = 0.89$) was unaltered in the presence of LSO:Ce particles. n.s, not significant.

the cell expressing ChR2, which would partially account for the modest ChR2 activation observed. However, the proposed use of RLPs for *in vivo* optogenetics would use smaller particles that will be located much closer to ChR2, thus reducing light attenuation from scattering. As a result, the light needed for ChR2 activation *in vivo* should be even less.

We observed no toxicity in primary neuronal cultures following 24 h of LSO:Ce microparticle exposure, consistent with another study using coated LSO:Ce nanoparticles (Burdette et al., 2019). In acute hippocampal slices, there was no reactivity of the astrocytes as assessed by GFAP staining or decrease in the maximal strength of basal transmission assessed by I/O curves at CA3-CA1 synapses. However, there were still some minor effects on synaptic function. While there was no effect on sIPSCs, there was a small reduction in the frequency but not amplitude of sEPSCs together with an increase in PPR of evoked excitatory transmission, indicating an effect of the particles on presynaptic function (Dobrunz and Stevens, 1997). There was also a small reduction in the input resistance of CA1 pyramidal cells, which could contribute to reduced cell excitability. Alterations in neuronal excitability have been shown to modulate presynaptic release probability (Crabtree et al., 2017). The axonal excitability was slightly diminished in the presence of the microparticles. Therefore, an alteration in presynaptic function that diminishes vesicular release probability could be the underlying mechanism for the minor effects on synaptic function with LSO:Ce microparticles exposure.

We also observed a slight but significant decrease in the magnitude of LTP, the long-term enhancement of synaptic strength and a cellular correlate of learning and memory (Malenka and Bear, 2004). Because LTP induction and expression is highly susceptible to cellular and behavioral stress, it is a sensitive measure of neuronal and synaptic health. LTP was induced using high-frequency stimulation and was monitored for 40 min post-tetanus. While the LSO:Ce particles did not affect the magnitude of the post-tetanic potentiation or the magnitude of LTP up to 20 min post-tetanus, there was a slight but significant decrease in the LTP magnitude at 40 min post-tetanus in the LSO:Ce treated slices. This suggests the possibility of a small

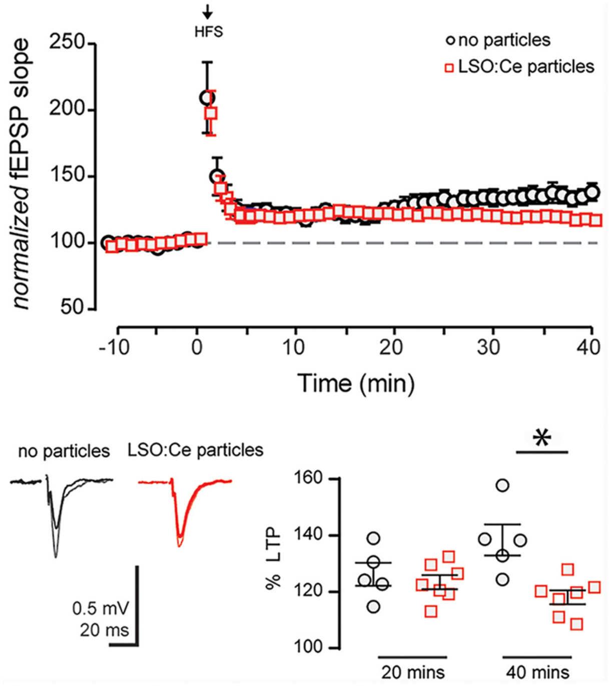

FIGURE 8 | Acute application of LSO:Ce microparticles decreases long term potentiation (LTP) at CA3-CA1 synapses. **(A)** The magnitude of High Frequency Stimulation (HFS, 5× 1 s at 100 Hz) induced LTP at CA3-CA1 synapses was significantly decreased in slices incubated with particles. **(B)** Averaged representative responses at −5 and +35 min to HFS stimulation (black and gray traces: no particles and red and light red traces: particles). The deficit in the LTP magnitude did not occur until 30 min post HFS in slices incubated with particles for at least an hour (40 min LTP: 138 ± 5% and 118 ± 2%, n = 5 slices/5 animals no particles, n = 7 slices/7 animals LSO:Ce particles, respectively; p = 0.0038; 20 min LTP: 124 ± 4% and 121 ± 2%, n = 5 slices/5 animals no particles, n = 7 slices/7 animals LSO:Ce particles, respectively; $^*p < 0.05$). Data represent mean ± SEM. Significance determined by unpaired Student's t-test.

effect on the long-term expression of LTP, however, whether this change is biologically relevant to learning and memory is unknown.

Overall, the effects on synaptic and intrinsic neuronal properties were modest, indicating that the LSO:Ce particles do not majorly disrupt synaptic transmission and circuit function. Whether these minor effects on synaptic transmission are a result of physical interaction and the weight of the particles on the delicate neuronal structures is not clear. This study used particles that are larger (4 μM) than would be used *in vivo* (<100–200 nm). It is possible that the effects of the smaller particles on synaptic transmission may be different, although they are unlikely to be greater. However, if toxic chemicals were leaching out of the particles to negatively impact cell health or if the weight of the particles was causing major cellular damage, we would likely have observed cell death in the primary neuronal cultures after 24 h of exposure. The GFAP staining is only able to detect gross changes in astrocyte morphology, therefore we cannot rule out small alterations in astrocytic processes in the presence of the microparticles. Additional effects on neuronal or astrocyte function or morphology might be observed with longer exposure times to the particles. Future studies are needed to determine if there are detrimental effects of LSO:Ce particles with UV or X-ray exposure potentially through the release of free radicals, as observed with cadmium-based quantum dots (Jamieson et al., 2007). However, any potential toxic effects might be overcome by PEGylation of the particles for *in vivo* use (Cheng et al., 2011).

Together, our results support the possibility of using LSO-Ce particles combined with ChR2 expression to non-invasively regulate synaptic circuit function *in vivo*.

DATA AVAILABILITY

The datasets generated for this study are available on request to the corresponding author.

ETHICS STATEMENT

Approval was obtained for all experimental protocols from the University of Alabama at Birmingham Institutional Animal Care and Use Committee. All experiments were conducted in accordance with the Guide for the Care and Use of Laboratory Animals adopted by the National Institutes of Health.

AUTHOR CONTRIBUTIONS

LD, LM, AB, KA, LS, and SA designed the experiments. AB, KA, LS, DG, AK, and MH performed the experiments and analyzed the data. LD, LM, AB, KA, SF, MB, MH, and SA wrote the initial draft, and LD, AB, and LM edited the manuscript.

FUNDING

This work was funded by NSF Track 2 FEC OIA-1632881 to LM and SF, and an Alabama State Funded EPSCoR Graduate Research Scholars Fellowship to KA.

ACKNOWLEDGMENTS

This manuscript has been released as a preprint at *bioRXiv* (Bartley et al., 2019; https://doi.org/10.1101/579722).

REFERENCES

Albertson, A. J., Bohannon, A. S., and Hablitz, J. J. (2017). HCN channel modulation of synaptic integration in gabaergic interneurons in malformed rat neocortex. *Front. Cell. Neurosci.* 11:109. doi: 10.3389/fncel.2017.00109

Andrabi, S. A., Umanah, G. K. E., Chang, C., Stevens, D. A., Karuppagounder, S. S., Gagné, J.-P., et al. (2014). Poly(ADP-ribose) polymerase-dependent energy depletion occurs through inhibition of glycolysis. *Proc. Natl. Acad. Sci. U S A* 111, 10209–10214. doi: 10.1073/pnas.1405158111

Aravanis, A. M., Wang, L.-P., Zhang, F., Meltzer, L. A., Mogri, M. Z., Schneider, M. B., et al. (2007). An optical neural interface: *in vivo* control of rodent motor cortex with integrated fiberoptic and optogenetic technology. *J. Neural Eng.* 4, S143–S156. doi: 10.1088/1741-2560/4/3/s02

Barnett, S. C., Perry, B. A. L., Dalrymple-Alford, J. C., and Parr-Brownlie, L. C. (2018). Optogenetic stimulation: understanding memory and treating deficits. *Hippocampus* 28, 457–470. doi: 10.1002/hipo.22960

Bartley, A. F., Abiraman, K., Stewart, L. T., Hossain, M. I., Gahan, D. M., Kamath, A. V., et al. (2019). LSO:Ce inorganic scintillators are biocompatible with neuronal and circuit function. *BioRxiv* [Preprint]. doi: 10.1101/579722

Berndt, A., Schoenenberger, P., Mattis, J., Tye, K. M., Deisseroth, K., Hegemann, P., et al. (2011). High-efficiency channelrhodopsins for fast neuronal stimulation at low light levels. *Proc. Natl. Acad. Sci. U S A* 108, 7595–7600. doi: 10.1073/pnas.1017210108

Berry, R., Getzin, M., Gjesteby, L., and Wang, G. (2015). X-Optogenetics and U-Optogenetics: Feasibility and Possibilities. *Photonics* 2, 23–39. doi: 10.3390/photonics2010023

Burdette, M. K., Bandera, Y. P., Zhang, E., Trofimov, A., Dickey, A., Foulger, I., et al. (2019). Organic fluorophore coated polycrystalline ceramic LSO:Ce scintillators for X-ray bioimaging. *Langmuir* 35, 171–182. doi: 10.1021/acs.langmuir.8b03129

Canales, A., Park, S., Kilias, A., and Anikeeva, P. (2018). Multifunctional fibers as tools for neuroscience and neuroengineering. *Acc. Chem. Res.* 51, 829–838. doi: 10.1021/acs.accounts.7b00558

Chen, S., Weitemier, A. Z., Zeng, X., He, L., Wang, X., Tao, Y., et al. (2018). Near-infrared deep brain stimulation *via* upconversion nanoparticle-mediated optogenetics. *Science* 359, 679–684. doi: 10.1126/science.aaq1144

Cheng, Y., Zhao, L., Li, Y., and Xu, T. (2011). Design of biocompatible dendrimers for cancer diagnosis and therapy: current status and future perspectives. *Chem. Soc. Rev.* 40, 2673–2703. doi: 10.1039/c0cs00097c

Crabtree, G. W., Sun, Z., Kvajo, M., Broek, J. A. C., Fénelon, K., McKellar, H., et al. (2017). Alteration of neuronal excitability and short-term synaptic plasticity in the prefrontal cortex of a mouse model of mental illness. *J. Neurosci.* 37, 4158–4180. doi: 10.1523/jneurosci.4345-15.2017

Dissing-Olesen, L., and MacVicar, B. A. (2015). Fixation and immunolabeling of brain slices: SNAPSHOT method. *Curr. Protoc. Neurosci.* 71, 1.23.1–1.23.12. doi: 10.1002/0471142301.ns0123s71

Dobrunz, L. E., and Stevens, C. F. (1997). Heterogeneity of release probability, facilitation, and depletion at central synapses. *Neuron* 18, 995–1008. doi: 10.1016/s0896-6273(00)80338-4

Emiliani, V., Cohen, A. E., Deisseroth, K., and Häusser, M. (2015). All-optical interrogation of neural circuits. *J. Neurosci.* 35, 13917–13926. doi: 10.1523/JNEUROSCI.2916-15.2015

Fenno, L. E., Gunaydin, L. A., and Deisseroth, K. (2015). Mapping anatomy to behavior in Thy1:18 ChR2-YFP transgenic mice using optogenetics. *Cold Spring Harb. Protoc.* 2015, 537–548. doi: 10.1101/pdb.prot075598

French, D. N., Cannon, K., Bartley, A., McMahon, L., and Gray, G. (2018). "Novel X-ray fluorescent organic monomer and polymer materials for optogenetic applications," in *Biophotonics Congress: Biomedical Optics Congress 2018 (Microscopy/Translational/Brain/OTS)*, Washington, DC: USA, JTu3A.55.

Gorski, J. A., Talley, T., Qiu, M., Puelles, L., Rubenstein, J. L. R., and Jones, K. R. (2002). Cortical excitatory neurons and glia, but not GABAergic neurons, are produced in the Emx1-expressing lineage. *J. Neurosci.* 22, 6309–6314. doi: 10.1523/jneurosci.22-15-06309.2002

Gradinaru, V., Mogri, M., Thompson, K. R., Henderson, J. M., and Deisseroth, K. (2009). Optical deconstruction of parkinsonian neural circuitry. *Science* 324, 354–359. doi: 10.1126/science.1167093

Gunaydin, L. A., Grosenick, L., Finkelstein, J. C., Kauvar, I. V., Fenno, L. E., Adhikari, A., et al. (2014). Natural neural projection dynamics underlying social behavior. *Cell* 157, 1535–1551. doi: 10.1016/j.cell.2014.05.017

Hoque, A., Williamson, N. A., Ameen, S. S., Ciccotosto, G. D., Hossain, M. I., Oakhill, J. S., et al. (2019). Quantitative proteomic analyses of dynamic signalling events in cortical neurons undergoing excitotoxic cell death. *Cell Death Dis.* 10:213. doi: 10.1038/s41419-019-1445-0

Jamieson, T., Bakhshi, R., Petrova, D., Pocock, R., Imani, M., and Seifalian, A. M. (2007). Biological applications of quantum dots. *Biomaterials* 28, 4717–4732. doi: 10.1016/j.biomaterials.2007.07.014

Lempicki, A., Brecher, C., Lingertat, H., Miller, S. R., Glodo, J., and Sarin, V. K. (2008). A ceramic version of the LSO scintillator. *IEEE Trans. Nucl. Sci.* 55, 1148–1151. doi: 10.1109/tns.2007.914368

Lim, D. H., Ledue, J., Mohajerani, M. H., Vanni, M. P., and Murphy, T. H. (2013). Optogenetic approaches for functional mouse brain mapping. *Front. Neurosci.* 7:54. doi: 10.3389/fnins.2013.00054

Lin, J. Y. (2011). A user's guide to channelrhodopsin variants: features, limitations and future developments. *Exp. Physiol.* 96, 19–25. doi: 10.1113/expphysiol.2009.051961

Lin, X., Wang, Y., Chen, X., Yang, R., Wang, Z., Feng, J., et al. (2017). Multiplexed optogenetic stimulation of neurons with spectrum-selective upconversion nanoparticles. *Adv. Healthc. Mater.* 6:17. doi: 10.1002/adhm.201770090

Long, M. A., and Fee, M. S. (2008). Using temperature to analyse temporal dynamics in the songbird motor pathway. *Nature* 456, 189–194. doi: 10.1038/nature07448

Madisen, L., Mao, T., Koch, H., Zhuo, J. M., Berenyi, A., Fujisawa, S., et al. (2012). A toolbox of Cre-dependent optogenetic transgenic mice for light-induced activation and silencing. *Nat. Neurosci.* 15, 793–802. doi: 10.1038/nn.3078

Malenka, R. C., and Bear, M. F. (2004). LTP and LTD: an embarrassment of riches. *Neuron* 44, 5–21. doi: 10.1016/j.neuron.2004.09.012

Melcher, C. L., and Schweitzer, J. S. (1992). Cerium-doped lutetium oxyorthosilicate: a fast, efficient new scintillator. *IEEE Trans. Nucl. Sci.* 39, 502–505. doi: 10.1109/23.159655

Miller, A. P., Shah, A. S., Aperi, B. V., Kurpad, S. N., Stemper, B. D., and Glavaski-Joksimovic, A. (2017). Acute death of astrocytes in blast-exposed rat organotypic hippocampal slice cultures. *PLoS One* 12:e0173167. doi: 10.1371/journal.pone.0173167

Ozden, I., Wang, J., Lu, Y., May, T., Lee, J., Goo, W., et al. (2013). A coaxial optrode as multifunction write-read probe for optogenetic studies in non-human primates. *J. Neurosci. Methods* 219, 142–154. doi: 10.1016/j.jneumeth.2013.06.011

Podgorski, K., and Ranganathan, G. (2016). Brain heating induced by near-infrared lasers during multiphoton microscopy. *J. Neurophysiol.* 116, 1012–1023. doi: 10.1152/jn.00275.2016

Rein, M. L., and Deussing, J. M. (2012). The optogenetic (r)evolution. *Mol. Genet. Genomics* 287, 95–109. doi: 10.1007/s00438-011-0663-7

Rost, B. R., Schneider-Warme, F., Schmitz, D., and Hegemann, P. (2017). Optogenetic tools for subcellular applications in neuroscience. *Neuron* 96, 572–603. doi: 10.1016/j.neuron.2017.09.047

Roy, S., Lingertat, H., Brecher, C., and Sarin, V. (2013). Optical properties of anisotropic polycrystalline Ce^{+3} activated LSO. *Opt. Mater.* 35, 827–832. doi: 10.1016/j.optmat.2012.09.039

Schmidt-Kastner, R., Wietasch, K., Weigel, H., and Eysel, U. T. (1993). Immunohistochemical staining for glial fibrillary acidic protein (GFAP) after deafferentation or ischemic infarction in rat visual system: features of reactive and damaged astrocytes. *Int. J. Dev. Neurosci.* 11, 157–174. doi: 10.1016/0736-5748(93)90076-p

Selimbeyoglu, A., Kim, C. K., Inoue, M., Lee, S. Y., Hong, A. S. O., Kauvar, I., et al. (2017). Modulation of prefrontal cortex excitation/inhibition balance rescues social behavior in CNTNAP2-deficient mice. *Sci. Transl. Med.* 9:eaah6733. doi: 10.1126/scitranslmed.aah6733

Senova, S., Scisniak, I., Chiang, C.-C., Doignon, I., Palfi, S., Chaillet, A., et al. (2017). Experimental assessment of the safety and potential efficacy of high irradiance photostimulation of brain tissues. *Sci. Rep.* 7:43997. doi: 10.1038/srep43997

Shuba, Y. M. (2019). *Use of scintillator-base nanoparticles for in vivo control of light-sensitive bioactive molecules. US Patent No 10,183,081.* Washington, DC: U.S. Patent and Trademark Office. Filed February 7, 2013 and Issued January 22, 2019.

Stujenske, J. M., Spellman, T., and Gordon, J. A. (2015). Modeling the spatiotemporal dynamics of light and heat propagation for *in vivo* optogenetics. *Cell Rep.* 12, 525–534. doi: 10.1016/j.celrep.2015.06.036

Tanaka, Y., Tanaka, Y., Furuta, T., Yanagawa, Y., and Kaneko, T. (2008). The effects of cutting solutions on the viability of GABAergic interneurons in cerebral cortical slices of adult mice. *J. Neurosci. Methods* 171, 118–125. doi: 10.1016/j.jneumeth.2008.02.021

Wanner, I. B., Anderson, M. A., Song, B., Levine, J., Fernandez, A., Gray-Thompson, Z., et al. (2013). Glial scar borders are formed by newly proliferated, elongated astrocytes that interact to corral inflammatory and fibrotic cells *via* STAT3-dependent mechanisms after spinal cord injury. *J. Neurosci.* 33, 12870–12886. doi: 10.1523/JNEUROSCI.2121-13.2013

Wu, L. G., and Saggau, P. (1994). Presynaptic calcium is increased during normal synaptic transmission and paired-pulse facilitation, but not in long-term potentiation in area CA1 of hippocampus. *J. Neurosci.* 14, 645–654.

Yang, H., Yan, H., Li, X., Liu, J., Cao, S., Huang, B., et al. (2018). Inhibition of connexin 43 and phosphorylated NR2B in spinal astrocytes attenuates bone cancer pain in mice. *Front. Cell. Neurosci.* 12:129. doi: 10.3389/fncel.2018.00129

Yizhar, O., Fenno, L. E., Prigge, M., Schneider, F., Davidson, T. J., O'Shea, D. J., et al. (2011). Neocortical excitation/inhibition balance in information processing and social dysfunction. *Nature* 477, 171–178. doi: 10.1038/nature10360

Conflict of Interest Statement: The authors declare that the research was conducted in the absence of any commercial or financial relationships that could be construed as a potential conflict of interest.

frontiers
in Synaptic Neuroscience

ORIGINAL RESEARCH
published: 09 October 2019
doi: 10.3389/fnsyn.2019.00027

Alpha1-Adrenergic Receptor Mediated Long-Term Depression at CA3-CA1 Synapses Can Be Induced *via* Accumulation of Endogenous Norepinephrine and Is Preserved Following Noradrenergic Denervation

Katie Dyer-Reaves[1], Anthoni M. Goodman[1,2], Amy R. Nelson[1] and Lori L. McMahon[1]*

[1]Department of Cell, Developmental, and Integrative Biology (CDIB), School of Medicine, University of Alabama at Birmingham, Birmingham, AL, United States, [2]Department of Psychology, University of Alabama at Birmingham, Birmingham, AL, United States

Locus coeruleus (LC) provides the sole source of noradrenergic (NA) innervation to hippocampus, and it undergoes significant degeneration early in Alzheimer's disease (AD). Norepinephrine (NE) modulates synaptic transmission and plasticity at hippocampal synapses which likely contributes to hippocampus-dependent learning and memory. We previously reported that pharmacological activation of α_1 adrenergic receptors (α_1ARs) induces long-term depression (LTD) at CA3-CA1 synapses. Here, we investigated whether accumulation of endogenous NE *via* pharmacological blockade of norepinephrine transporters (NETs) and the NE degradative enzyme, monoamine oxidase (MAO), can induce α_1AR LTD, as these inhibitors are used clinically. Further, we sought to determine how degeneration of hippocampal NA innervation, as occurs in AD, impacts α_1AR function and α_1AR LTD. Bath application of NET and MAO inhibitors in slices from control rats reliably induced α_1AR LTD when β adrenergic receptors were inhibited. To induce degeneration of LC-NA innervation, rats were treated with the specific NA neurotoxin DSP-4 and recordings performed 1–3 weeks later when NA axon degeneration had stabilized. Even with 85% loss of hippocampal NA innervation, α_1AR LTD was successfully induced using either the α_1AR agonist phenylephrine or the combined NET and MAO inhibitors, and importantly, the LTD magnitude was not different from saline-treated control. These data suggest that despite significant decreases in NA input to hippocampus, the mechanisms necessary for the induction of α_1AR LTD remain functional. Furthermore, we posit that α_1AR activation could be a viable therapeutic target for pharmacological intervention in AD and other diseases involving malfunctions of NA neurotransmission.

Keywords: hippocampus, norepinephrine, LTD, α_1-AR, locus coeruleus

Edited by:
Fereshteh S. Nugent,
Uniformed Services University of the Health Sciences, United States

Reviewed by:
Ludovic David Langlois,
Uniformed Services University of the Health Sciences, United States
Nicholas Michael Graziane,
Pennsylvania State University, United States

***Correspondence:**
Lori L. McMahon
mcmahon@uab.edu

Received: *09 June 2019*
Accepted: *20 September 2019*
Published: *09 October 2019*

Citation:
Dyer-Reaves K, Goodman AM, Nelson AR and McMahon LL (2019) Alpha1-Adrenergic Receptor Mediated Long-Term Depression at CA3-CA1 Synapses Can Be Induced via Accumulation of Endogenous Norepinephrine and Is Preserved Following Noradrenergic Denervation. Front. Synaptic Neurosci. 11:27. doi: 10.3389/fnsyn.2019.00027

Abbreviations: AD, Alzheimer's disease; AR, adrenergic receptor; Atmx, atomoxetine; Clor, clorgiline; DβH, dopamine β-hydroxylase; DSP-4, N-(2-chloroethyl)-N-ethyl-2-bromobenzylamine; fEPSP, field excitatory postsynaptic potential; LTD, long-term depression; MAO, monoamine oxidase; NA, noradrenergic; NE, norepinephrine; NET, norepinephrine transporter; Phe, phenylephrine; PD, Parkinson's disease; s. radiatum, stratum radiatum; TH, tyrosine hydroxylase.

INTRODUCTION

Noradrenergic (NA) input from the locus coeruleus (LC) to hippocampus is critical for hippocampus-dependent learning and memory (Koob et al., 1978; Harro et al., 1999; Lemon et al., 2009; Gibbs et al., 2010), and its degeneration in Alzheimer's disease (AD) has been well documented (Forno, 1966; Yamada and Mehraein, 1977; Zarow et al., 2003). Specifically, loss of LC cell bodies positively correlates with the severity of dementia and duration of the disease in AD patients. In fact, the LC is the first target of pretangle tau pathology, with measurable cell loss occurring in the prodromal phase of AD (Grudzien et al., 2007; Braak et al., 2011; Jucker and Walker, 2011; Arendt et al., 2015; Chalermpalanupap et al., 2017) that may mediate the emergence of cognitive changes (Braak et al., 2011; Arendt et al., 2015; Chalermpalanupap et al., 2017; Kelly et al., 2017; Theofilas et al., 2017). Despite this body of evidence, the effect of early LC degeneration on hippocampal synaptic function is poorly understood.

The LC is the sole provider of NA innervation in hippocampus (Aston-Jones, 2004), and norepinephrine (NE) modulates synaptic efficiency critical for learning and memory (Harley, 1991, 2007; Scheiderer et al., 2004; Kemp and Manahan-Vaughan, 2008; Hagena et al., 2016). Selective electrolytic lesioning using the neurotoxin N-(2-chloroethyl)-N-ethyl-2-bromobenzylamine (DSP-4) or silencing of LC neurons using optogenetics in murine models leads to deficits in learning, memory, and cognitive flexibility (Koob et al., 1978; Harro et al., 1999; Janitzky et al., 2015). NE, *via* activation of adrenergic receptors (ARs), modifies the strength of synaptic transmission at glutamatergic synapses and the ability of these synapses to undergo long-term plasticity (Hopkins and Johnston, 1984; Harley, 1991; Bröcher et al., 1992; Harley and Sara, 1992; Bramham et al., 1997; Erickson et al., 1997; Katsuki et al., 1997; Thomas and Palmiter, 1997a,b,c; Izumi and Zorumski, 1999). Accordingly, blockade of β adrenergic receptors (ARs) reduces NMDAR-dependent LTP in hippocampal slices (Harley, 1991), while NE application facilitates the induction of LTP in dentate and spatial memory formation through activation of β-ARs (Hopkins and Johnston, 1984; Bröcher et al., 1992; Katsuki et al., 1997; Izumi and Zorumski, 1999; Kemp and Manahan-Vaughan, 2008; André et al., 2015). Along with β-ARs, α-ARs are necessary for spatial memory learning tasks, as α_1AR agonists enhance and antagonists block the formation of memory (Pussinen et al., 1997; Puumala et al., 1998). Activation of α_1- and β-ARs by NE can also facilitate tetanus-induced LTP at mossy-fibers synapses in area CA3 (Hopkins and Johnston, 1984; Huang et al., 1996). Transgenic mice harboring constitutively active α_1 adrenergic receptors (α_1ARs) have enhanced learning and memory, while α_1AR knock-out mice showed deficits compared to WT (Doze et al., 2011; Collette et al., 2014). We previously reported that NE, or the selective α_1AR agonist methoxamine, induces a form of long-term depression (LTD) at CA3-CA1 synapses that is activity and NMDA receptor-dependent, and also requires activation of Src kinase and an increase in extracellular signal-regulated protein kinase (ERK) activation (Scheiderer et al., 2004, 2008). During expression of α_1AR LTD, there is no change in the paired-pulse ratio compared to baseline, consistent with a post-synaptic locus of expression (Scheiderer et al., 2004). Furthermore, α_1AR LTD shares the same mechanism as a form of LTD induced by activation of M1 muscarinic receptors (mAChRs), which are also coupled to Gq signaling. When weak activation of α_1ARs is paired with weak activation of M1 mAChRs, LTD can be successfully induced, demonstrating the shared signaling pathways (Scheiderer et al., 2008).

Given that activation of α_1ARs using exogenous agonists induces LTD at hippocampal CA3-CA1 synapses (Scheiderer et al., 2004, 2008), we wanted to determine if increasing endogenous extracellular NE accumulation *via* pharmacological inhibition of the norepinephrine transporter (NET) and the degradative enzyme monoamine oxidase (MAO) similarly induces α_1AR LTD. This is important since these inhibitors are widely used as therapeutic treatments in disorders such as ADHD and depression, where imbalances in catecholamine neurotransmission, specifically NE, are known to occur (Zametkin and Rapoport, 1987; Castellanos et al., 1996; Vanicek et al., 2014; Israel, 2015). Furthermore, because LC degeneration, and loss of hippocampal NA innervation, is clinically relevant to normal aging, AD, and Parkinson's disease (PD; Mann, 1983; Mann et al., 1983; Marien et al., 2004; Szot, 2012), we set out to investigate the impact of NA degeneration on the ability of pharmacological activation of α_1ARs to induce LTD at hippocampal CA3-CA1 synapses.

MATERIALS AND METHODS

Animal Care

All experiments were conducted with an approved protocol from the University of Alabama at Birmingham Institutional Animal Care and Use Committee in compliance with the National Institutes of Health guidelines. All efforts were made to minimize animal suffering and to reduce the number of animals used. Six-week-old male Sprague–Dawley rats (Charles River) were used in all experiments. Animals were housed two per cage and were kept on a 12-h light/dark cycle with *ad libitum* food and water.

LC Lesion

Hippocampal NA denervation was performed using the NA axon specific neurotoxin DSP-4 (Tocris, Ellisville, MO, USA), known to cause terminal retrograde degeneration by targeting the NE uptake system (Jaim-Etcheverry and Zieher, 1980; Ross and Stenfors, 2015). DSP-4, delivered intraperitoneally (IP), readily crosses the blood-brain-barrier and targets NA axons of the central nervous system while peripheral NA systems are unaffected (Jaim-Etcheverry and Zieher, 1980; Fritschy and Grzanna, 1989; Ross and Stenfors, 2015). NE uptake in these axons is rapidly blocked with maximum effect achieved by 4–6 h and within 4–5 days DβH immunoreactivity declines (Ross, 1976; Fritschy et al., 1990). NA sprouting occurs in a region-specific manner over approximately 5 weeks (Booze et al., 1988) along with an observed 57% decline in LC cell bodies 1 year after DSP-4 treatment (Fritschy and Grzanna, 1992). Rats were lightly anesthetized with isofluorane and injected IP with DSP-4

(50 mg/kg) in saline or saline alone at 48-h intervals for a total of three injections.

Drugs and Solutions

All drugs (Sigma, St. Louis, MO, USA) were prepared as stock solutions and diluted to the appropriate working concentration at the time of electrophysiology. Phenylephrine (Phe, α_1AR agonist; in deionized water), propranolol (β-AR antagonist; in DMSO) and prazosin (α_1AR antagonist; in DMSO) were prepared fresh daily and atomoxetine (Atmx, NET inhibitor; in deionized water) and clorgiline (Clor, MAO inhibitor; in deionized water) were frozen in 300 μL aliquots until used for recordings.

Slice Preparation and Electrophysiological Recordings

α_1AR LTD was induced using the α_1AR agonist phenylephrine (Phe, 100 μM) that was bath applied for 10 or 15 min following a 20 min stable baseline of recorded field excitatory post-synaptic potentials (fEPSPs) as done previously (Scheiderer et al., 2004, 2008). Experiments to test whether extracellular accumulation of endogenous NE could induce LTD, as well as to test the functionality of the NA fibers remaining following DSP-4-mediated lesion, slices prepared from rats 7–8 days post-DSP-4 treatment were exposed to bath application of the NET inhibitor Atmx (500 nM) plus the MAO inhibitor Clor (10 μM) for 10 or 20 min following stable baseline transmission. Previous reports have documented the ability of NET inhibition to block reuptake of NE and induce increases in extracellular NE (Youdim and Riederer, 1993). Additionally, selective inhibition of MAO, the enzyme responsible for NE degradation, has also been shown to cause accumulation of NE extrasynaptically (Youdim and Riederer, 1993). Because NE has similar affinity for α- and β-ARs, it was necessary to pharmacologically inhibit β-AR activation with propranolol (10 μm) to reveal LTD following accumulation of extracellular NE. To ensure the α_1AR specificity of the LTD induced by endogenous NE in these recordings, interleaved experiments were conducted in the presence of 10 μM prazosin (in addition to the cocktail of Clor, Atmx and propranolol, which is referred to as CAP).

Immunohistochemistry

Following electrophysiological recordings, 400 μm-thick hippocampal slices were stored in 4% paraformaldehyde at 4°C until the time of staining. Twenty-four hours prior to staining, slices were rinsed in phosphate buffered saline (PBS) and then transferred to a 30% sucrose/PBS solution. Tissue was resectioned to 50 μm using a freezing microtome. Sections were washed 3 × 10 min in PBS at room temperature and incubated in blocking buffer [10% normal donkey serum (NDS) in 0.3% PBS Triton/PBS] for 90 min. Primary antibodies [rabbit anti-tyrosine hydroxylase (TH, 1:200) and mouse anti-dopamine β-hydroxylase (DβH, 1:300); Chemicon, Temecula, CA, USA] were diluted in blocking buffer, and applied to free-floating sections and incubated overnight at 4°C. Slices were washed 3 × 10 min with PBS and were labeled with fluorescence-activated secondary antibodies [donkey anti-rabbit Alexa 594 (1:200) and donkey anti-mouse Alexa 488 (1:200); Invitrogen, Eugene, OR, USA] diluted in blocking buffer and incubated for 1–2 h at room temperature. Slices were washed 3 × 30 min and incubated with Hoescht nuclear stain (1 μl stock/10 ml PBS) for 15 min at room temperature. Slices were mounted on slides using Permafluor (Immunon, Waltman, MA, USA) and viewed on a Leica (Exton, PA, USA) DM IRBE laser scanning confocal microscope. The CA1 s. radiatum within the field of view from one slice per animal was analyzed using ImageJ software. Sequential scans of blue, green, and red channels were obtained and ∼20 μm stacks of images were collected in a z-axis of 1.0–1.5 μm step size, averaging two scans per image. Maximum projections were generated and used for NE fiber quantification. DβH-positive fibers were measured and counted, following the criterion that only fibers with four or more consecutive boutons be considered as a fragment of axon.

Data Analysis

Electrophysiology data were analyzed using custom-written Labview data acquisition and analysis software (Scheiderer et al., 2004, 2008) after being filtered at 3 kHz and digitized at 10 kHz. The fEPSP slope was measured and evaluated as a series of five averaged raw data points plotted vs. time. The LTD magnitude was calculated by comparing the average fEPSP slope recorded during the last 10 min of baseline transmission to the slope at 20 min post-drug washout. When more than one slice was recorded per animal for a given experiment (e.g., Phe or Amtx ± Clor), the data were averaged together to represent the finding for that animal. Therefore, the reported *n* refers to animal number. Paired student's *t*-tests were used for statistical analysis within groups. Unpaired student's *t*-tests or one-way analysis of variances (ANOVAs) were used to evaluate statistical significance between groups. The significance level was set at $p < 0.05$ and the data are presented as the mean ± SEM.

RESULTS

α_1AR Activation Induces LTD at CA3-CA1 Synapses in Rat Hippocampus

Our laboratory previously reported that bath application of NE or the selective α_1AR agonist methoxamine is sufficient to induce a NMDAR-dependent LTD of extracellular fEPSPs at CA3-CA1 glutamatergic synapses in hippocampal slices (Scheiderer et al., 2004, 2008). Here, we show that application of another α_1AR agonist, Phe (100 μM; phenylephrine) also reliably induces α_1AR LTD [**Figure 1A**, 84 ± 4% of baseline fEPSP slope ($n = 6$); $p < 0.01$] similar to our previous report (Scheiderer et al., 2004, 2008). To test whether α_1AR LTD can also be induced *via* extracellular accumulation of endogenous NE in hippocampus, the selective NET inhibitor Atmx (500 nM) was applied together with an inhibitor of NE degradative enzyme MAO, Clor (10 μM). Bath application of Atmx and Clor did not elicit a significant change in synaptic strength compared to baseline (**Figure 1B1**, 94 ± 5% of baselined fEPSP slope, $n = 6$, $p = 0.14$).

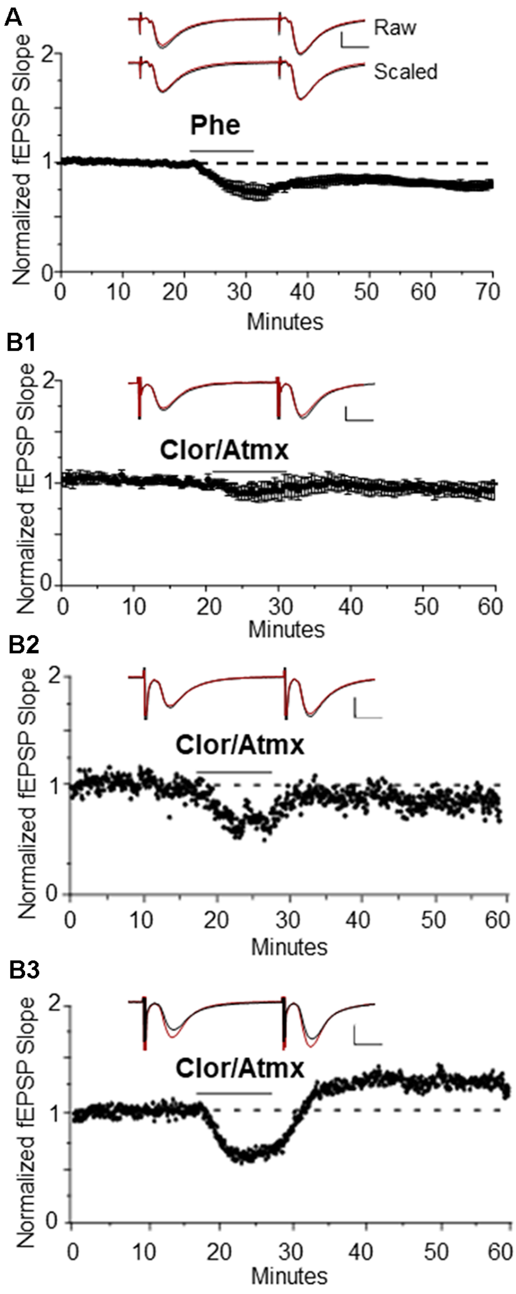

FIGURE 1 | Long-term depression (LTD) is induced by the α_1AR agonist, phenylephrine, or endogenous NE when β-ARs are pharmacologically blocked. **(A)** α_1AR LTD is induced by the selective α_1AR agonist Phe. One-hundred micro molar is able to induce α_1AR LTD in control animals [84 ± 4% of baselined field excitatory postsynaptic potential (fEPSP) slope, $n = 6$]. Top traces are averaged raw fEPSPs before (black) and after (red) application of phenylephrine. Bottom traces are averaged, scaled fEPSPs (red) during LTD expression overlaid onto baseline traces (black) showing no change in the pair-pulse facilitation ratio (scale bar: 0.5 mV, 10 ms). **(B1)** Averaged experiments in Clor/Atmx results in no significant change in baseline transmission (94 ± 5% of baseline fEPSP slope, $n = 6$). **(B2)** Representative example of LTD induced *via* norepinephrine transporter (NET) and monoamine oxidase (MAO) inhibition by Atmx (500 nM) and Clor (10 μM, respectively). **(B3)** Single example of LTP induced *via* endogenous NE accumulation in the presence of Clor/Atmx.

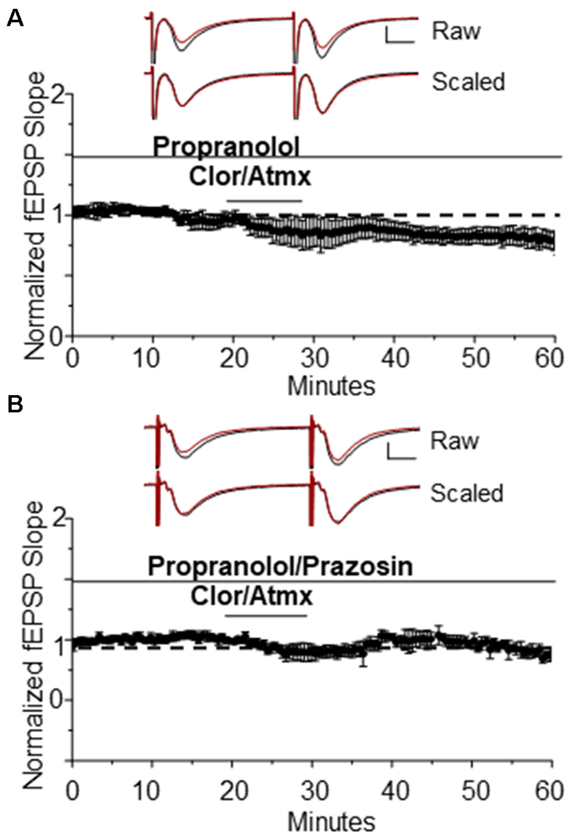

FIGURE 2 | The β AR antagonist propranolol is able to unmask α_1AR LTD when used in addition to Clor and Atmx. **(A)** In the presence of the β AR antagonist propranolol (1 μM) accumulation of endogenous NE induces α_1AR LTD (83 ± 6%of baselined fEPSP slope, $n = 4$). Top traces are averaged raw fEPSPs before (black) and after (red) application of phenylephrine. Bottom traces are averaged, scaled fEPSPs (red) during LTD expression overlaid onto baseline traces (black) showing no change in the pair-pulse facilitation ratio (scale bar: 0.5 mV, 10 ms). **(B)** α_1AR LTD is prevented by application of the α_1AR antagonist prazosin (10 μM) in the presence of propranolol, Clor, and Atmx ($p > 0.05$).

However, when we evaluated individual experiments there were clear cases of Atmx and Clor induced depression (**Figure 1B2**) and potentiation (**Figure 1B3**) of the extracellular fEPSP that were masked when all of the experiments were averaged. This variable response can be attributed to coincident global activation of α_1, α_2, and β-ARs, as all of these receptors are located at pre- or post-synaptic locations at CA3-CA1 synapses.

Because activation of β-ARs causes potentiation at CA3-CA1 synapses (Hopkins and Johnston, 1984; Bröcher et al., 1992; Katsuki et al., 1997; Izumi and Zorumski, 1999), their activation by endogenous accumulation of NE could be masking possible α_1AR LTD expression induced by Atmx and Clor application. To determine whether blockade of β-AR activation would unmask LTD, propranolol (10 μM) was applied for the duration of the recording period during the Atmx and Clor experiments (collectively named CAP), and this resulted in reliable, and significant LTD expression (**Figure 2A**, 83% ± 6% of baseline fEPSP slope, $n = 4$, $p = 0.02$). The LTD magnitude induced by

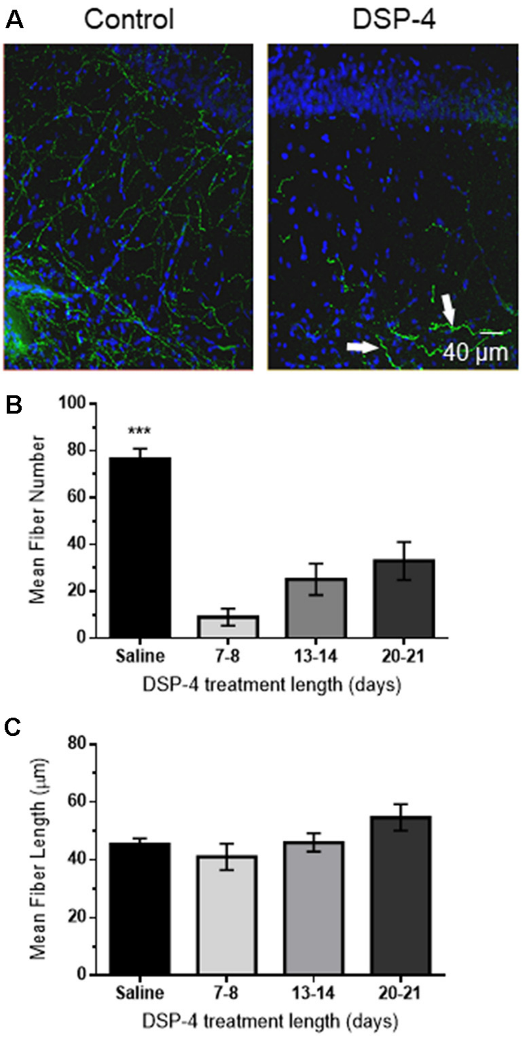

FIGURE 3 | DSP-4 treatment causes significant NE degeneration in CA1 of hippocampus. **(A)** Anti-DβH (green) and DAPI (blue) hippocampal staining of NE fibers in area CA1 s. radiatum from a saline-treated (control) animal or following DSP-4 treatment (scale bar: 40 μm). Arrows denote thicker, knobby appearance of some remaining NE fibers. **(B)** Mean fiber number in DSP-4 treated animals in CA1 s. radiatum is significantly decreased compared to saline-treated measured 7–21 days post-treatment. **(C)** Mean NE fiber length is unchanged following DSP-4 treatment. **(C)** Total NE fiber number is significantly decreased by DSP-4 treatment by ~85% (saline, $n = 7$; DSP-4, $n = 19$).

the selective α_1AR agonist Phe (**Figure 1A**) is not significantly different from that induced by the combination of NET, MAO, and β-AR inhibition (**Figure 2A**; $p = 0.8$). Importantly, when the raw traces during expression of LTD are scaled and overlaid with traces during baseline control conditions, it is clear that there is no difference in the paired-pulse facilitation ratio during LTD expressed induced either with phenylephrine or by CAP, similar to our previous reports (Scheiderer et al., 2004, 2008), suggesting a postsynaptic mechanism. To confirm that the LTD following accumulation of endogenous NE is also mediated by α_1AR activation, interleaved experiments were performed with the α_1AR antagonist prazosin (10 μM) resulting in a complete block of LTD (**Figure 2B**, CAP plus prazosin, 96.5 ± 4% of baseline fEPSP slope, $n = 3$, $p = 0.4$).

DSP-4 Causes a Significant Decrease in NA Innervation in CA1 of Hippocampus

To determine whether loss of NA input to hippocampus is sufficient to cause deficits in α_1AR LTD, the NE specific neurotoxin DSP-4 (50 mg/kg, in saline), was administered intraperitoneally at 48-h intervals for a total of three injections (control animals received injections of saline only). DSP-4 targets the NE uptake system and induces alkylation of vital neuronal structures (Ross, 1976) causing degeneration of hippocampal NA innervation (Jonsson et al., 1981; Fritschy and Grzanna, 1989; Fritschy et al., 1990). This robust treatment protocol was used because a previous study reported that mice treated with one dose of DSP-4 had an increased probability of hippocampal NA axon sprouting compared to mice treated three times with the toxin (Puoliväli et al., 2000). NA innervation in s. radiatum of area CA1 following DSP-4 treatment was evaluated using anti-DβH immunohistochemical staining of NA fibers, which were then imaged *via* confocal microscopy. DSP-4 induced a significant decrease in NA fiber number (**Figure 3B**; $F_{(3,19)} = 23.28$, $p < 0.001$) but no change in individual fiber length in CA1 s. radiatum in animals sacrificed 7–21 days following the first injection (**Figure 3C**; $F_{(3,658)} = 2.03$, $p = 0.108$). This protocol led to a reduction of ~85% of DβH-positive immunostaining. Interestingly, the morphology of some of the remaining DβH-positive fibers in the DSP-4-treated animals have a thicker, knobby appearance compared to the thin, more delicate fibers found in the control group (**Figure 3A**, arrows).

α_1AR LTD Remains Intact Following NA-Fiber Degeneration

We next tested whether systemic treatment with DSP-4 and subsequent ~85% reduction of NA innervation would negatively impact the ability of direct activation of α_1ARs by the selective α_1AR agonist Phe to induce LTD. Surprisingly, we found that the magnitude of α_1AR LTD was not significantly different between saline-treated and DSP-4 treated animals (**Figure 4A**, DSP-4: 85 ± 3%, $n = 7$, $p < 0.001$ vs. **Figure 4B**, saline vs. DSP-4, $p = 0.85$). Thus, despite an ~85% decrease in NA innervation in s. radiatum of area CA1, α_1ARs remain coupled to downstream signaling cascades (Src kinase and pERK; Scheiderer et al., 2008) necessary for the induction of LTD. However, it is unclear whether α_1AR LTD can be induced by endogenously released NE from the remaining 15% of NE fibers following DSP-4 treatment.

To determine whether the NA fibers surviving neurotoxic damage are able to functionally release NE and activate α_1ARs effectively to induce LTD, NET, MAO, and β-ARs antagonists were bath applied. Again surprisingly, α_1AR LTD was observed (**Figure 4B**, DSP-4: 83 ± 3%, $n = 11$, $p < 0.001$) and the magnitude was not different from saline-treated animals; (**Figure 4B**, saline vs. DSP-4, $p = 0.97$). Furthermore, the magnitude of LTD induced *via* activation of α_1ARs by

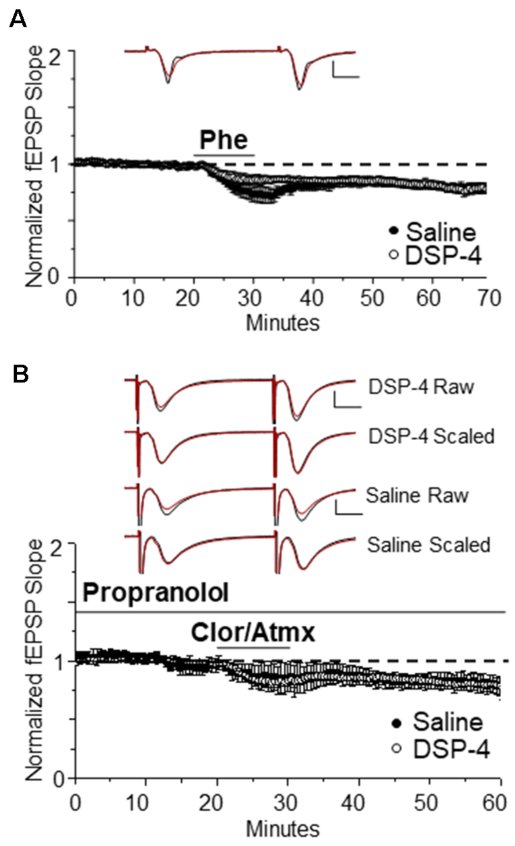

FIGURE 4 | α_1AR LTD remains intact following NE degeneration and is able to be induced by endogenous NE. **(A)** DSP-4 treatment does not prevent α_1AR LTD (85% ± 3% of baselined fEPSP slope, $n = 7$). The magnitude of α_1AR LTD induced by Phe is not significantly different between saline and DSP-4 treatment groups ($p > 0.05$; control data replotted from **Figure 1A**). Top traces are averaged raw fEPSPs before (black) and after (red) application of phenylephrine. Bottom traces are averaged, scaled fEPSPs (red) during LTD expression overlaid onto baseline traces (black) showing no change in the paired-pulse facilitation ratio (scale bar: 0.5 mV, 10 ms). **(B)** α_1AR LTD is induced by endogenous NE accumulation in slices from DSP-4-treated rats (83 ± 3% of baseline fEPSP slope, $n = 11$). The magnitude of α_1AR LTD induced by accumulation of endogenous NE is not significantly different between saline and DSP-4 treatment groups ($p > 0.05$; control data replotted from **Figure 2A**).

endogenously released NE was not significantly different from that *via* direct α_1AR activation by Phe (**Figures 4A,B**, DSP-4, CAP vs. Phe $p = 0.58$).

To determine if α_1AR LTD induced by endogenous NE release elicits maximal depression and occludes further depression induced by subsequent application of Phe, the drug mixture CAP was bath applied for 10 min to induce LTD. In interleaved slices, Phe (100 μM) was coapplied with CAP for 15 min beginning 20 min after CAP application to determine if additional LTD could be elicited (**Figure 5**). We found that no additional LTD could be induced by Phe in the presence of CAP, such that α_1AR LTD induced by CAP that was not significantly different when Phe was added to the CAP mixture (denoted CAPP; **Figure 5**, CAP: $n = 6$; CAPP: $n = 10$, $t_{(6)} = 2.08$ $p = 0.0827$).

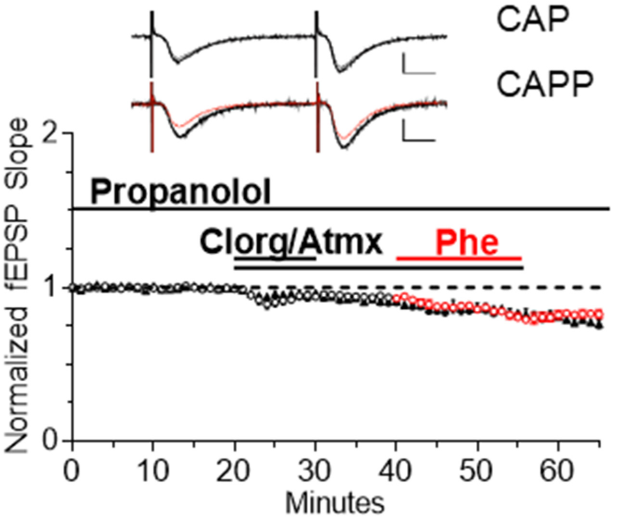

FIGURE 5 | Endogenous NE accumulation is sufficient to cause maximal α_1AR LTD. α_1AR LTD is induced by endogenous NE accumulation in slices and subsequent application of Phe is unable to induce further LTD (CAP: $n = 6$; CAPP: $n = 10$, $t_{(6)} = 2.08$, $p = 0.0827$). Red data points denote the interleaved experiments in which the addition of Phe was included in the CAP mixture following 20 min of CAP application CAPP is CAP plus Phe.

DISCUSSION

α_1AR LTD

Here, we have established that increasing extracellular accumulation of endogenously released NE can activate α_1ARs and induce α_1AR LTD at CA3-CA1 synapses in hippocampus. Furthermore, lesion of NA input to hippocampus from the LC did not prevent induction or expression of α_1AR LTD, despite the loss of ~85% of hippocampal NA innervation. Surprisingly, the NA fibers that remained following DSP-4 induced lesion release enough NE that can accumulate following NET and MAO inhibition to activate postsynaptic α_1ARs at CA3-CA1 synapses to induce LTD. NET and MAO inhibitors increase the accumulation of DA and 5-HT, especially in the hippocampus where NET serves as the primary reuptake mechanism for DA (Borgkvist et al., 2012). Although accumulation of DA and 5-HT are likely present, the LTD induced by NET and MAO inhibition was completely prevented by the α_1AR antagonist prazosin, indicating that this LTD is dependent on activation of α_1ARs. The blockade by prazosin also suggests that DA and 5HT must not be accumulating enough to induce LTD through D4 receptors (Navakkode et al., 2017) or 5HT4 receptors (Wawra et al., 2014). Therefore, these data suggest that in light of severe NE degeneration, α_1ARs remain coupled to their signaling cascade and are able to be activated by specific α_1AR agonists or *via* endogenously released NE from surviving NA fibers to induce LTD at CA3-CA1 synapses.

Previously, our lab has shown that M1 mAChRs LTD (mLTD) is lost following degeneration of hippocampal cholinergic innervation from the medial septum, but is rescued when hippocampal NA sympathetic sprouting occurs with an accompanying cholinergic reinnervation of hippocampus at 15% of control levels (Scheiderer et al., 2006). Because M1 mAChRs and α_1ARs couple to the same G protein signaling pathway (Porter et al., 2002), and we have shown that their simultaneous weak pharmacological activation induces LTD (Scheiderer et al., 2008), we expected that loss of NA innervation to hippocampus would cause the same deficit in α_1AR LTD as we have observed for M1 mAChR LTD following cholinergic degeneration in the absence of sprouting (Scheiderer et al., 2006). However, the successful expression of α_1AR LTD at synapses in slices with 15% NA fibers remaining is consistent with the "rescued" mLTD by the approximate 15% cholinergic reinnervation stimulated by NA sympathetic sprouting after medial septal lesion. Thus, 15% of control cholinergic or NA innervation in hippocampus is enough to maintain the function of M1 mAChRs or α_1ARs, respectively. Based on these findings, we speculate that α_1ARs remain functional in AD and PD patients even with 67.9% and 83.2% cell loss (Marien et al., 2004). In fact, α_1AR expression is increased in AD patients, but unfortunately, this has been associated with increased aggression in these patients (Szot et al., 2006; Sharp et al., 2007). Due to this, prazosin, an α_1AR antagonist, has been used clinically in AD patients and has been shown to improve aggravation and aggression symptoms (Wang et al., 2010).

DSP-4 Induced Lesion of Hippocampal NA Innervation

In humans, the severity of LC degeneration is positively correlated with intensity of AD symptoms and is detectable in the prodromal phase, prior to the onset of cognitive deficits (Grudzien et al., 2007; Braak et al., 2011; Arendt et al., 2015). While the onset of this degeneration is driven by tauopathy in humans (Hertz, 1989; Parvizi et al., 2001; Geula et al., 2008; Grinberg et al., 2009; Simic et al., 2009), we were able to recapitulate the effects of AD-driven LC degeneration with the neurotoxin, DSP-4 in healthy rats.

The DSP-4 treatment protocol employed reduced NA innervation by ~85%; additional injections or increases in DSP-4 concentration were not used due to observed increases in animal mortality (unpublished observations). It is important to note that the DSP-4 induced NA lesion is a variable model, as DSP-4 only provides a temporary decrease in NA innervation, whereas neurodegeneration is permanent. In fact, several studies have shown that DSP-4 induced NA degeneration is reversed several months following treatment (Fritschy and Grzanna, 1989, 1992; Fritschy et al., 1990). The LC-NA system is known to be capable of initiating these compensatory mechanisms in response to damage, which includes an increase in NE turnover (Jonsson et al., 1981) and release (Abercrombie and Zigmond, 1989) in surviving cell axons, as well as inducing α and β receptor supersensitivity (Dooley et al., 1983; Berridge and Dunn, 1990; Starke, 2001). Interestingly, AD patients have elevated NE levels even though there is LC cell loss (Szot et al., 2006), and α_2-AR positive axonal sprouting has been identified in AD post-mortem human hippocampus (Szot et al., 2006). Thus, it can be postulated that excessive release, in addition to depletion, of NE could also lead to deficits in hippocampal-dependent learning and memory, and therefore, synaptic plasticity. Furthermore, the lesion protocol used here may cause increased activation of the NA compensatory mechanisms thought to be responsible for lesion reversal (Fritschy and Grzanna, 1992). In support of this idea, the DβH positive fiber morphology appears thicker and has a knobby appearance in the DSP-4 treated group compared to saline-treated control (**Figure 3A**, arrows). This morphology change could be an early indication of compensatory LC sprouting because as mentioned above, it has been shown that DSP-4 induced lesions are not permanent, and after a variable period of time hyperinnervation of NA fibers can occur (Booze et al., 1988; Fritschy and Grzanna, 1992; Kalinin et al., 2006). Altogether, we were unable to induce a complete loss of all NA hippocampal innervation using DSP-4 and were therefore unable to observe α_1AR uncoupling and α_1AR LTD loss that we predict would happen in the complete absence of endogenous NE, similar to our previous studies of M1 mAChR LTD following complete medial septal lesion (Scheiderer et al., 2006). It is interesting to note that uncoupling of α_1AR function and loss of α_1AR LTD occurs at glutamatergic synapses in mPFC in adult rats as a consequence of neonatal lesion of the ventral hippocampus (Bhardwaj et al., 2014).

The maintenance of α_1AR function we observe following DSP-4 induced lesion could explain the inconsistent findings in learning and memory assays following DSP-4 treatment, with some studies reporting minimal effects (Prado de Carvalho and Zornetzer, 1981; Decker and McGaugh, 1991; Ohno et al., 1993, 1997), whereas others find deficits (Prado de Carvalho and Zornetzer, 1981; Decker and McGaugh, 1991). The reversibility of DSP-4 treatment, as well as variable treatment paradigms could lead to the confounding behavioral results following NA degeneration.

CONCLUSION

Here, we show that pharmacological inhibition of NET and MAO leads to extracellular accumulation of NE which is capable of activating ARs that modulate synaptic efficacy at CA3-CA1 synapses. This finding is important, as NET and MAO inhibitors are used clinically in the treatment of several neurological and neuropsychiatric illness (Zametkin and Rapoport, 1987; Castellanos et al., 1996). Furthermore, the DSP-4-driven loss of ~85% of NA fibers in hippocampus recapitulates the loss of cortical projecting LC-cells in human AD (German et al., 1992; Grudzien et al., 2007; Braak et al., 2011; Arendt et al., 2015). The present findings suggest that α_1ARs are preserved in CA3-CA1 glutamatergic synapses following extensive NA fiber denervation. This preservation of α_1AR function may be due to compensatory NE levels released from remaining fibers or may suggest that these receptors are resilient to change even under conditions of chronically low stimulation. Thus, possible use of NET and MAO inhibitors in the treatment of AD will need much more investigation, as chronic elevation of NE may lead to receptor desensitization, and the role of each α and β AR subtype in modulating hippocampal function and learning and memory is complex.

DATA AVAILABILITY STATEMENT

The raw data supporting the conclusions of this manuscript will be made available by the authors, without undue reservation, to any qualified researcher.

ETHICS STATEMENT

The animal study was reviewed and approved by University of Alabama at Birmingham Institutional Care and Use Committee.

AUTHOR CONTRIBUTIONS

KD-R and LM conceived and designed the study. KD-R and AG contributed to the execution of the experiments and performed the statistical analyses. KD-R wrote the first draft of the manuscript. AN, AG and LM wrote sections of the manuscript. All authors contributed to the manuscript revision, read and approved the submitted version.

FUNDING

This work was funded by NIA R01 AG021612 to LM. NINDS T32NS061788 supported AG, and Alzheimer's of Central Alabama supported AN.

ACKNOWLEDGMENTS

Much of this work was done as partial fulfillment to the requirements for a master's thesis and is available online (Dyer, 2009). We would like to thank the UAB-High Resolution Imaging Facility for use of their confocal microscope. This work has also appeared on bioRxiv (Dyer-Reaves et al., 2019).

REFERENCES

Abercrombie, E. D., and Zigmond, M. J. (1989). Partial injury to central noradrenergic neurons: reduction of tissue norepinephrine content is greater than reduction of extracellular norepinephrine measured by microdialysis. *J. Neurosci.* 9, 4062–4067. doi: 10.1523/jneurosci.09-11-04062.1989

André, M. A. E., Wolf, O. T., and Manahan-Vaughan, D. (2015). β-adrenergic receptors support attention to extinction learning that occurs in the absence, but not the presence, of a context change. *Front. Behav. Neurosci.* 9:125. doi: 10.3389/fnbeh.2015.00125

Arendt, T., Brückner, M. K., Morawski, M., Jäger, C., and Gertz, H.-J. (2015). Early neurone loss in Alzheimer's disease: cortical or subcortical? *J. Neurosci. Methods* 3:10. doi: 10.1186/s40478-015-0187-1

Aston-Jones, G. (2004). "Locus coeruleus, A5 and A7 noradrenergic cell groups," in *The Rat Nervous System*, ed. G. Paxinos (San Diego, CA: Elsevier), 259–294.

Berridge, C. W., and Dunn, A. J. (1990). DSP-4-induced depletion of brain norepinephrine produces opposite effects on exploratory behavior 3 and 14 days after treatment. *Psychopharmacology* 100, 504–508. doi: 10.1007/bf02244003

Bhardwaj, S. K., Tse, Y. C., Ryan, R., Wong, T. P., and Srivastava, L. K. (2014). Impaired adrenergic-mediated plasticity of prefrontal cortical glutamate synapses in rats with developmental disruption of the ventral hippocampus. *Neuropsychopharmacology* 39, 2963–2973. doi: 10.1038/npp.2014.142

Booze, R. M., Hall, J. A., Cress, N. M., Miller, G. D., and Davis, J. N. (1988). DSP-4 treatment produces abnormal tyrosine hydroxylase immunoreactive fibers in rat hippocampus. *Exp. Neurol.* 101, 75–86. doi: 10.1016/0014-4886(88)90066-0

Borgkvist, A., Malmlöf, T., Feltmann, K., Lindskog, M., and Schilström, B. (2012). Dopamine in the hippocampus is cleared by the norepinephrine transporter. *Int. J. Neuropsychopharmacol.* 15, 531–540. doi: 10.1017/S1461145711000812

Braak, H., Thal, D. R., Ghebremedhin, E., and Del Tredici, K. (2011). Stages of the pathologic process in Alzheimer disease: age categories from 1 to 100 years. *J. Neuropathol. Exp. Neurol.* 70, 960–969. doi: 10.1097/nen.0b013e318232a379

Bramham, C. R., Bacher-Svendsen, K., and Sarvey, J. M. (1997). LTP in the lateral perforant path is β-adrenergic receptor-dependent. *Neuroreport* 8, 719–724. doi: 10.1097/00001756-199702100-00028

Bröcher, S., Artola, A., and Singer, W. (1992). Agonists of cholinergic and noradrenergic receptors facilitate synergistically the induction of long-term potentiation in slices of rat visual cortex. *Brain Res.* 573, 27–36. doi: 10.1016/0006-8993(92)90110-u

Castellanos, F. X., Giedd, J. N., Marsh, W. L., Hamburger, S. D., Vaituzis, A. C., Dickstein, D. P., et al. (1996). Quantitative brain magnetic resonance imaging in attention-deficit hyperactivity disorder. *Arch. Gen. Psychiatry* 53, 607–616. doi: 10.1001/archpsyc.1996.01830070053009

Chalermpalanupap, T., Weinshenker, D., and Rorabaugh, J. M. (2017). Down but not out: the consequences of pretangle tau in the locus coeruleus. *Neural Plast.* 2017:7829507. doi: 10.1155/2017/7829507

Collette, K. M., Zhou, X. D., Amoth, H. M., Lyons, M. J., Papay, R. S., Sens, D. A., et al. (2014). Long-term α1B-adrenergic receptor activation shortens lifespan, while α1A-adrenergic receptor stimulation prolongs lifespan in association with decreased cancer incidence. *Age* 36:9675. doi: 10.1007/s11357-014-9675-7

Decker, M. W., and McGaugh, J. L. (1991). The role of interactions between the cholinergic system and other neuromodulatory systems in learning and memory. *Synapse* 7, 151–168. doi: 10.1002/syn.890070209

Dooley, D. J., Mogilnicka, E., Delini-Stula, A., Waechter, F., Truog, A., and Wood, J. (1983). Functional supersensitivity to adrenergic agonists in the rat after DSP-4, a selective noradrenergic neurotoxin. *Psychopharmacology* 81, 1–5. doi: 10.1007/bf00439263

Doze, V. A., Papay, R. S., Goldenstein, B. L., Gupta, M. K., Collette, K. M., Nelson, B. W., et al. (2011). Long-term α1A-adrenergic receptor stimulation improves synaptic plasticity, cognitive function, mood, and longevity. *Mol. Pharmacol.* 80, 747–758. doi: 10.1124/mol.111.073734

Dyer, K. (2009). *Effects of Locus Coeruleus Lesion on α1-Adrenoceptor Mediatedlong-Term Depression at CA3-CA1 Synapses in Rat Hippocampus.* Birmingham, AL: Univeristy of Alabama at Birmingham.

Dyer-Reaves, K., Goodman, A. M., Nelson, A. R., and McMahon, L. L. (2019). α1-adrenergic receptor mediated long-term depression at ca3-ca1 synapses can be induced *via* accumulation of endogenous norepinephrine and is preserved following noradrenergic denervation. *BioRxiv* [Preprint]. doi: 10.1101/648873

Erickson, J. C., Hollopeter, G., Thomas, S. A., Froelick, G. J., and Palmiter, R. D. (1997). Disruption of the metallothionein-III gene in mice: analysis of brain zinc, behavior, and neuron vulnerability to metals, aging, and seizures. *J. Neurosci.* 17, 1271–1281. doi: 10.1523/jneurosci.17-04-01271.1997

Forno, L. S. (1966). Pathology of parkinsonism-A preliminary report of 24 cases. *J. Neurosurg.* 24, 266–271.

Fritschy, J. M., Geffard, M., and Grzanna, R. (1990). The response of noradrenergic axons to systemically administered DSP-4 in the rat: an immunohistochemical study using antibodies to noradrenaline and dopamine-β-hydroxylase. *J. Chem. Neuroanat.* 3, 309–321.

Fritschy, J. M., and Grzanna, R. (1989). Immunohistochemical analysis of the neurotoxic effects of DSP-4 identifies two populations of noradrenergic axon terminals. *Neuroscience* 30, 181–197. doi: 10.1016/0306-4522(89)90364-3

Fritschy, J. M., and Grzanna, R. (1992). Restoration of ascending noradrenergic projections by residual locus coeruleus neurons: compensatory response to neurotoxin-induced cell death in the adult rat brain. *J. Comp. Neurol.* 321, 421–441. doi: 10.1002/cne.903210309

German, D. C., Manaye, K. F., White, C. L., Woodward, D. J., McIntire, D. D., Smith, W. K., et al. (1992). Disease-specific patterns of locus coeruleus cell loss. *Ann. Neurol.* 32, 667–676. doi: 10.1002/ana.410320510

Geula, C., Nagykery, N., Nicholas, A., and Wu, C.-K. (2008). Cholinergic neuronal and axonal abnormalities are present early in aging and in Alzheimer disease. *J. Neuropathol. Exp. Neurol.* 67, 309–318. doi: 10.1097/nen.0b013e31816a1df3

Gibbs, M. E., Hutchinson, D. S., and Summers, R. J. (2010). Noradrenaline release in the locus coeruleus modulates memory formation and consolidation; roles for α- and β-adrenergic receptors. *Neuroscience* 170, 1209–1222. doi: 10.1016/j.neuroscience.2010.07.052

Grinberg, L. T., Rüb, U., Ferretti, R. E. L., Nitrini, R., Farfel, J. M., Polichiso, L., et al. (2009). The dorsal raphe nucleus shows phospho-tau neurofibrillary changes before the transentorhinal region in Alzheimer's disease. A precocious onset? *Neuropathol. Appl. Neurobiol.* 35, 406–416. doi: 10.1111/j.1365-2990.2009.00997.x

Grudzien, A., Shaw, P., Weintraub, S., Bigio, E., Mash, D. C., and Mesulam, M. M. (2007). Locus coeruleus neurofibrillary degeneration in aging, mild cognitive impairment and early Alzheimer's disease. *Neurobiol. Aging* 28, 327–335. doi: 10.1016/j.neurobiolaging.2006.02.007

Hagena, H., Hansen, N., and Manahan-Vaughan, D. (2016). β-adrenergic control of hippocampal function: subserving the choreography of synaptic information storage and memory. *Cereb. Cortex* 26, 1349–1364. doi: 10.1093/cercor/bhv330

Harley, C. (1991). Noradrenergic and locus coeruleus modulation of the perforant path-evoked potential in rat dentate gyrus supports a role for the locus coeruleus in attentional and memorial processes. *Prog. Brain Res.* 88, 307–321. doi: 10.1016/s0079-6123(08)63818-2

Harley, C. W. (2007). Norepinephrine and the dentate gyrus. *Prog. Brain Res.* 163, 299–318. doi: 10.1016/S0079-6123(07)63018-0

Harley, C. W., and Sara, S. J. (1992). Locus coeruleus bursts induced by glutamate trigger delayed perforant path spike amplitude potentiation in the dentate gyrus. *Exp. Brain Res.* 89, 581–587. doi: 10.1007/bf00229883

Harro, J., Pähkla, R., Modiri, A.-R., Harro, M., Kask, A., and Oreland, L. (1999). Dose-dependent effects of noradrenergic denervation by DSP-4 treatment on forced swimming and β-adrenoceptor binding in the rat. *J. Neural Transm.* 106, 619–629. doi: 10.1007/s007020050184

Hertz, L. (1989). Is Alzheimer's disease an anterograde degeneration, originating in the brainstem, and disrupting metabolic and functional interactions between neurons and glial cells? *Brain Res. Rev.* 14, 335–353. doi: 10.1016/0165-0173(89)90017-9

Hopkins, W. F., and Johnston, D. (1984). Frequency-dependent noradrenergic modulation of long-term potentiation in the hippocampus. *Science* 226, 350–352. doi: 10.1126/science.6091272

Huang, Y. Y., Nguyen, P. V., Abel, T., and Kandel, E. R. (1996). Long-lasting forms of synaptic potentiation in the mammalian hippocampus. *Learn. Mem.* 3, 74–85. doi: 10.1101/lm.3.2-3.74

Israel, J. A. (2015). Combining stimulants and monoamine oxidase inhibitors: a reexamination of the literature and a report of a new treatment combination. *Prim. Care Companion CNS Disord.* 17:6. doi: 10.4088/pcc.15br01836

Izumi, Y., and Zorumski, C. F. (1999). Norepinephrine promotes long-term potentiation in the adult rat hippocampus *in vitro*. *Synapse* 31, 196–202. doi: 10.1002/(SICI)1098-2396(19990301)31:3<196::AID-SYN4>3.0.CO;2-K

Jaim-Etcheverry, G., and Zieher, L. M. (1980). DSP-4: a novel compound with neurotoxic effects on noradrenergic neurons of adult and developing rats. *Brain Res.* 188, 513–523. doi: 10.1016/0006-8993(80)90049-9

Janitzky, K., Lippert, M. T., Engelhorn, A., Tegtmeier, J., Goldschmidt, J., Heinze, H.-J., et al. (2015). Optogenetic silencing of locus coeruleus activity in mice impairs cognitive flexibility in an attentional set-shifting task. *Front. Behav. Neurosci.* 9:286. doi: 10.3389/fnbeh.2015.00286

Jonsson, G., Hallman, H., Ponzio, F., and Ross, S. (1981). DSP4 (N-(2-chloroethyl)-N-ethyl-2-bromobenzylamine)—a useful denervation tool for central and peripheral noradrenaline neurons. *Eur. J. Pharmacol.* 72, 173–188. doi: 10.1016/0014-2999(81)90272-7

Jucker, M., and Walker, L. C. (2011). Pathogenic protein seeding in Alzheimer disease and other neurodegenerative disorders. *Ann. Neurol.* 70, 532–540. doi: 10.1002/ana.22615

Kalinin, S., Feinstein, D. L., Xu, H.-L., Huesa, G., Pelligrino, D. A., and Galea, E. (2006). Degeneration of noradrenergic fibres from the locus coeruleus causes tight-junction disorganisation in the rat brain. *Eur. J. Neurosci.* 24, 3393–3400. doi: 10.1111/j.1460-9568.2006.05223.x

Katsuki, H., Izumi, Y., and Zorumski, C. F. (1997). Noradrenergic regulation of synaptic plasticity in the hippocampal CA1 region. *J. Neurophysiol.* 77, 3013–3020. doi: 10.1152/jn.1997.77.6.3013

Kelly, S. C., He, B., Perez, S. E., Ginsberg, S. D., Mufson, E. J., and Counts, S. E. (2017). Locus coeruleus cellular and molecular pathology during the progression of Alzheimer's disease. *Acta Neuropathol. Commun.* 5:8. doi: 10.1186/s40478-017-0411-2

Kemp, A., and Manahan-Vaughan, D. (2008). β-adrenoreceptors comprise a critical element in learning-facilitated long-term plasticity. *Cereb. Cortex* 18, 1326–1334. doi: 10.1093/cercor/bhm164

Koob, G. F., Kelley, A. E., and Mason, S. T. (1978). Locus coeruleus lesions: learning and extinction. *Physiol. Behav.* 20, 709–716. doi: 10.1016/0031-9384(78)90296-2

Lemon, N., Aydin-Abidin, S., Funke, K., and Manahan-Vaughan, D. (2009). Locus coeruleus activation facilitates memory encoding and induces hippocampal LTD that depends on β-adrenergic receptor activation. *Cereb. Cortex* 19, 2827–2837. doi: 10.1093/cercor/bhp065

Mann, D. M. (1983). The locus coeruleus and its possible role in ageing and degenerative disease of the human central nervous system. *Mech. Ageing Dev.* 23, 73–94. doi: 10.1016/0047-6374(83)90100-8

Mann, D. M., Yates, P. O., and Hawkes, J. (1983). The pathology of the human locus ceruleus. *Clin. Neuropathol.* 2, 1–7.

Marien, M. R., Colpaert, F. C., and Rosenquist, A. C. (2004). Noradrenergic mechanisms in neurodegenerative diseases: a theory. *Brain Res. Rev.* 45, 38–78. doi: 10.1016/j.brainresrev.2004.02.002

Navakkode, S., Chew, K. C. M., Tay, S. J. N., Lin, Q., Behnisch, T., and Soong, T. W. (2017). Bidirectional modulation of hippocampal synaptic plasticity by Dopaminergic D4-receptors in the CA1 area of hippocampus. *Sci. Rep.* 7:15571. doi: 10.1038/s41598-017-15917-1

Ohno, M., Yamamoto, T., Kobayashi, M., and Watanabe, S. (1993). Impairment of working memory induced by scopolamine in rats with noradrenergic DSP-4 lesions. *Eur. J. Pharmacol.* 238, 117–120. doi: 10.1016/0014-2999(93)90514-i

Ohno, M., Yoshimatsu, A., Kobayashi, M., and Watanabe, S. (1997). Noradrenergic DSP-4 lesions aggravate impairment of working memory produced by hippocampal muscarinic blockade in rats. *Pharmacol. Biochem. Behav.* 57, 257–261. doi: 10.1016/s0091-3057(96)00353-x

Parvizi, J., Van Hoesen, G. W., and Damasio, A. (2001). The selective vulnerability of brainstem nuclei to Alzheimer's disease. *Ann. Neurol.* 49, 53–66. doi: 10.1002/1531-8249(200101)49:1<53::aid-ana30>3.0.co;2-q

Porter, A. C., Bymaster, F. P., DeLapp, N. W., Yamada, M., Wess, J., Hamilton, S. E., et al. (2002). M1 muscarinic receptor signaling in mouse hippocampus and cortex. *Brain Res.* 944, 82–89. doi: 10.1016/s0006-8993(02)02721-x

Prado de Carvalho, L., and Zornetzer, S. F. (1981). The involvement of the locus coeruleus in memory. *Behav. Neural Biol.* 31, 173–186. doi: 10.1016/s0163-1047(81)91204-8

Puoliväli, J., Pradier, L., and Riekkinen, P. (2000). Impaired recovery of noradrenaline levels in apolipoprotein E-deficient mice after N-(2-chloroethyl)-N-ethyl-2-bromobenzylamine lesion. *Neuroscience* 95, 353–358. doi: 10.1016/s0306-4522(99)00448-0

Pussinen, R., Nieminen, S., Koivisto, E., Haapalinna, A., Riekkinen, P., and Sirvio, J. (1997). Enhancement of intermediate-term memory by an α-1 agonist or a partial agonist at the glycine site of the NMDA receptor. *Neurobiol. Learn. Mem.* 67, 69–74. doi: 10.1006/nlme.1996.3738

Puumala, T., Greijus, S., Narinen, K., Haapalinna, A., Riekkinen, P., and Sirviö, J. (1998). Stimulation of α-1 adrenergic receptors facilitates spatial learning in rats. *Eur. Neuropsychopharmacol.* 8, 17–26. doi: 10.1016/s0924-977x(97)00040-0

Ross, S. B. (1976). Long-term effects of N-2-chlorethyl-N-ethyl-2-bromobenzylamine hydrochloride on noradrenergic neurones in the rat brain and heart. *Br. J. Pharmacol.* 58, 521–527. doi: 10.1111/j.1476-5381.1976.tb08619.x

Ross, S. B., and Stenfors, C. (2015). DSP4, a selective neurotoxin for the locus coeruleus noradrenergic system. A review of its mode of action. *Neurotox. Res.* 27, 15–30. doi: 10.1007/s12640-014-9482-z

Scheiderer, C. L., Dobrunz, L. E., and McMahon, L. L. (2004). Novel form of long-term synaptic depression in rat hippocampus induced by activation of α 1 adrenergic receptors. *J. Neurophysiol.* 91, 1071–1077. doi: 10.1152/jn.00420.2003

Scheiderer, C. L., McCutchen, E., Thacker, E. E., Kolasa, K., Ward, M. K., Parsons, D., et al. (2006). Sympathetic sprouting drives hippocampal cholinergic reinnervation that prevents loss of a muscarinic receptor-dependent long-term depression at CA3-CA1 synapses. *J. Neurosci.* 26, 3745–3756. doi: 10.1523/JNEUROSCI.5507-05.2006

Scheiderer, C. L., Smith, C. C., McCutchen, E., McCoy, P. A., Thacker, E. E., Kolasa, K., et al. (2008). Coactivation of M_1 muscarinic and α1 adrenergic receptors stimulates extracellular signal-regulated protein kinase and induces long-term depression at CA3-CA1 synapses in rat hippocampus. *J. Neurosci.* 28, 5350–5358. doi: 10.1523/JNEUROSCI.5058-06.2008

Sharp, S. I., Ballard, C. G., Chen, C. P. L.-H., and Francis, P. T. (2007). Aggressive behavior and neuroleptic medication are associated with increased number of α1-adrenoceptors in patients with Alzheimer disease. *Am. J. Geriatr. Psychiatry* 15, 435–437. doi: 10.1097/01.jgp.0000237065.78966.1b

Simic, G., Stanic, G., Mladinov, M., Jovanov-Milosevic, N., Kostovic, I., and Hof, P. R. (2009). Does Alzheimer's disease begin in the brainstem? *Neuropathol. Appl. Neurobiol.* 35, 532–554. doi: 10.1111/j.1365-2990.2009.01038.x

Starke, K. (2001). Presynaptic autoreceptors in the third decade: focus on α2-adrenoceptors. *J. Neurochem.* 78, 685–693. doi: 10.1046/j.1471-4159.2001.00484.x

Szot, P. (2012). Common factors among Alzheimer's disease, Parkinson's disease, and epilepsy: possible role of the noradrenergic nervous system. *Epilepsia* 53, 61–66. doi: 10.1111/j.1528-1167.2012.03476.x

Szot, P., White, S. S., Greenup, J. L., Leverenz, J. B., Peskind, E. R., and Raskind, M. A. (2006). Compensatory changes in the noradrenergic nervous system in the locus ceruleus and hippocampus of postmortem subjects with Alzheimer's disease and dementia with Lewy bodies. *J. Neurosci.* 26, 467–478. doi: 10.1523/JNEUROSCI.4265-05.2006

Theofilas, P., Ehrenberg, A. J., Dunlop, S., Di Lorenzo Alho, A. T., Nguy, A., Leite, R. E. P., et al. (2017). Locus coeruleus volume and cell population changes during Alzheimer's disease progression: a stereological study in human postmortem brains with potential implication for early-stage biomarker discovery. *Alzheimers Dement.* 13, 236–246. doi: 10.1016/j.jalz.2016.06.2362

Thomas, S. A., and Palmiter, R. D. (1997a). Disruption of the dopamine B-hydroxylase gene in mice suggests roles for norepinephrine in motor function, learning, and memory. *Behav. Neurosci.* 111, 579–589. doi: 10.1037/0735-7044.111.3.579

Thomas, S. A., and Palmiter, R. D. (1997b). Impaired maternal behavior in mice lacking norepinephrine and epinephrine. *Cell* 91, 583–592. doi: 10.1016/s0092-8674(00)80446-8

Thomas, S. A., and Palmiter, R. D. (1997c). Thermoregulatory and metabolic phenotypes of mice lacking noradrenaline and adrenaline. *Nature* 387, 94–97. doi: 10.1038/387094a0

Vanicek, T., Spies, M., Rami-Mark, C., Savli, M., Höflich, A., Kranz, G. S., et al. (2014). The norepinephrine transporter in attention-deficit/hyperactivity disorder investigated with positron emission tomography. *JAMA Psychiatry* 71, 1340–1349. doi: 10.1001/jamapsychiatry.2014.1226

Wang, L. Y., Shofer, J. B., Rohde, K., Hart, K. L., Hoff, D. J., McFall, Y. H., et al. (2010). Prazosin for the treatment of behavioral symptoms in Alzheimer's disease patients with agitation and aggression. *Am. J. Geriatr. Psychiatry* 17, 744–751. doi: 10.1097/JGP.0b013e3181ab8c61

Wawra, M., Fidzinski, P., Heinemann, U., Mody, I., and Behr, J. (2014). 5-HT4-receptors modulate induction of long-term depression but not potentiation at hippocampal output synapses in acute rat brain slices. *PLoS One* 9:e88085. doi: 10.1371/journal.pone.0088085

Yamada, M., and Mehraein, P. (1977). Verteilungsmuster der senilen Veränderungen in den Hirnstammkernen. *Psychiatry Clin. Neurosci.* 31, 219–224. doi: 10.1111/j.1440-1819.1977.tb02722.x

Youdim, M. B., and Riederer, P. (1993). Dopamine metabolism and neurotransmission in primate brain in relationship to monoamine oxidase A and B inhibition. *J. Neural Transm. Gen. Sect.* 91, 181–195. doi: 10.1007/bf01245231

Zametkin, A. J., and Rapoport, J. L. (1987). Neurobiology of attention deficit disorder with hyperactivity: where have we come in 50 years? *J. Am. Acad. Child Adolesc. Psychiatry* 26, 676–686. doi: 10.1097/00004583-198709000-00011

Zarow, C., Lyness, S. A., Mortimer, J. A., and Chui, H. C. (2003). Neuronal loss is greater in the locus coeruleus than nucleus basalis and substantia nigra in Alzheimer and Parkinson diseases. *Arch. Neurol.* 60, 337–341. doi: 10.1001/archneur.60.3.337

Conflict of Interest: The authors declare that the research was conducted in the absence of any commercial or financial relationships that could be construed as a potential conflict of interest.

frontiers
in Synaptic Neuroscience

ORIGINAL RESEARCH
published: 15 October 2019
doi: 10.3389/fnsyn.2019.00028

Gradient of Expression of Dopamine D2 Receptors Along the Dorso-Ventral Axis of the Hippocampus

*Valentyna Dubovyk[1,2] and Denise Manahan-Vaughan[1]**

[1]Medical Faculty, Department of Neurophysiology, Ruhr University Bochum, Bochum, Germany, [2]International Graduate School of Neuroscience, Ruhr University Bochum, Bochum, Germany

Dopamine D2-like receptors (D2R) play an important role in the regulation of hippocampal neuronal excitability and contribute to the regulation of synaptic plasticity, the encoding of hippocampus-dependent memories and the regulation of affective state. In line with this, D2R are targeted in the treatment of psychosis and affective disorders. It has been proposed that the dorso-ventral axis of the hippocampus can be functionally delineated into the dorsal pole that predominantly processes spatial information and the ventral pole that mainly addresses hippocampal processing of emotional and affective state. Although dopaminergic control of hippocampal information processing has been the focus of a multitude of studies, very little is known about the precise distribution of D2R both within anatomically defined sublayers of the hippocampus and along its dorsoventral axis, that could in turn yield insights as to the functional significance of this receptor in supporting hippocampal processing of spatial and affective information. Here, we used an immunohistochemical approach to precisely scrutinize the protein expression of D2R both within the cellular and dendritic layers of the hippocampal subfields, and along the dorso-ventral hippocampal axis. In general, we detected significantly higher levels of protein expression of D2R in the ventral, compared to the dorsal poles with regard to the CA1, CA2, CA3 and dentate gyrus (DG) regions. Effects were very consistent: the molecular layer, granule cell layer and polymorphic layer of the DG exhibited higher D2R levels in the ventral compared to dorsal hippocampus. D2R levels were also significantly higher in the ventral Stratum oriens, Stratum radiatum, and Stratum lacunosum-moleculare layers of the CA1 and CA3 regions. The apical dendrites of the ventral CA2 region also exhibited higher D2R expression compared to the dorsal pole. Taken together, our study suggests that the higher D2R expression levels of the ventral hippocampus may contribute to reported gradients in the degree of expression of synaptic plasticity along the dorso-ventral hippocampal axis, and may support behavioral information processing by the ventral hippocampus.

Keywords: dopamine receptor, hippocampus, immunohistochemistry, rodent, dorso-ventral axis

Edited by:
Lisa Topolnik,
Laval University, Canada

Reviewed by:
Costas E. Papatheodoropoulos,
University of Patras, Greece
Emmanuel Valjent,
Centre National de la Recherche Scientifique (CNRS), France

***Correspondence:**
Denise Manahan-Vaughan
denise.manahan-vaughan@rub.de

***Received:** 15 August 2019*
***Accepted:** 24 September 2019*
***Published:** 15 October 2019*

Citation:
Dubovyk V and Manahan-Vaughan D (2019) Gradient of Expression of Dopamine D2 Receptors Along the Dorso-Ventral Axis of the Hippocampus.
Front. Synaptic Neurosci. 11:28.
doi: 10.3389/fnsyn.2019.00028

INTRODUCTION

Synaptic plasticity and memory formation in the hippocampus, in their essence, are dependent on excitatory glutamatergic transmission (Citri and Malenka, 2008; Lisman, 2017). However, various neurotransmitter systems exert a modulatory role, thereby influencing the direction of change (Kemp and Manahan-Vaughan, 2005), effectiveness (Hansen and Manahan-Vaughan, 2015), duration (Twarkowski and Manahan-Vaughan, 2016) or robustness (Manahan-Vaughan and Kulla, 2003) of synaptic strength, and learning and memory. The dopaminergic system is one such modulatory influence on neuronal and synaptic activity (Kulla and Manahan-Vaughan, 2000; Lemon and Manahan-Vaughan, 2012; Hansen and Manahan-Vaughan, 2014; Madadi Asl et al., 2019).

Dopamine exerts its action by means of slow modulation of fast neurotransmission through its G-protein-coupled receptors. Five types of dopaminergic receptors have been identified that are subdivided into D1 (D1 and D5) and D2 (D2, D3 and D4) classes of receptors based on their ability to modulate cAMP production and their structural, biochemical and pharmacological properties (Sibley and Monsma, 1992; Vallone et al., 2000; Beaulieu and Gainetdinov, 2011). While the D1-class receptors stimulate adenylyl cyclase (AC) activity and therefore cAMP production, the D2-class receptors inhibit AC activity, thus hindering cAMP production. D2 receptors also modulate the beta-arrestin/GSK3 pathway and can alter the excitability of hippocampal mossy cells through this mechanism (Etter and Krezel, 2014). Both classes of dopamine receptors are postsynaptically expressed on dopamine-receptive cells (Rankin et al., 2009). Interestingly, only the D2-class receptors exist in different isoforms (Gingrich and Caron, 1993). The D2 dopamine receptor (D2R) exists in D2S (short) and D2L (long) variants. Whereas D2S is predominantly expressed presynaptically, D2L is mostly postsynaptically expressed (Usiello et al., 2000; De Mei et al., 2009). Thus, the D2R enables a more complex modulation of neuronal circuitry than that exerted by other dopamine receptor types. Moreover, the D2R is the only dopamine receptor that has been directly implicated in several brain conditions, such as drug addiction, Parkinson's disease and schizophrenia (Wong et al., 1986; Volkow et al., 2007; Chaudhuri and Schapira, 2009). Therefore, in-depth knowledge about the spatial expression pattern of D2R would be beneficial for understanding not only the physiological role, but also, the pathological role of this receptor.

Surprisingly, despite the wealth of studies on the dopaminergic system, very little is known about D2R expression in the hippocampus proper (Gasbarri et al., 1997; Beaulieu and Gainetdinov, 2011); most studies to date, focused on the basal ganglia and occasionally on the frontal cortex (Levey et al., 1993; Yung et al., 1995; Santana et al., 2009; Lavian et al., 2018). The most extensive examination of D2R expression in rat hippocampus up to now was performed by Yu et al. (2019). In their work they showed that D2R is mainly expressed in cells of the Stratum pyramidale (sp) and Stratum radiatum (sr) layers of the CA1–3 regions, in the dentate gyrus (DG), and in axon terminals innervating the Stratum lacunosum-moleculare (slm) of the CA1 of the dorsal hippocampus. Despite their extensive investigation, the authors omitted scrutiny of the overall expression level of D2R across the layers of the trisynaptic circuit of the hippocampus, as well as across its dorso-ventral axis.

The hippocampal dorso-ventral axis is functionally segregated into the dorsal part that is essential for visuo-spatial information processing, the ventral part that is involved in emotional, motivational and affective responses, and the intermediate part that integrates information from both poles (Bast et al., 2009; Fanselow and Dong, 2010; Strange et al., 2014). Hippocampal dopamine originates from neurons of the ventral tegmental area (VTA) and locus coeruleus (LC; Lisman and Otmakhova, 2001; Lemon et al., 2009; Smith and Greene, 2012) . Projections from the LC predominantly terminate in the dorsal hippocampus (Kempadoo et al., 2016), whereas projections from the VTA are the strongest in the ventro-intermediate hippocampal two-thirds (Gasbarri et al., 1994). This segregation in innervation by dopamine-containing terminals (Duszkiewicz et al., 2019) further suggests that dopaminergic transmission may exert a non-uniform influence across the hippocampal longitudinal axis. This may be mediated by the degree of dopamine release, but also by differences in receptor expression. Here, the D2R is of particular interest: it is intrinsically involved in the regulation of hippocampal basal synaptic transmission and of the robustness of synaptic plasticity (Manahan-Vaughan and Kulla, 2003).

In this work, we used an immunohistochemical approach to conduct a detailed study of the expression and distribution pattern of D2R across the layers of the DG and cornu ammonis (CA) regions of the dorsal, intermediate and ventral hippocampus of the rat. We observed differences in the expression gradient of this receptor along the dorso-ventral hippocampal axis, and within the microcircuitry of the hippocampus. Our data provide new insights into hippocampal D2R expression that may help in understanding the cellular mechanisms behind D2R modulation of neuronal excitability and synaptic plasticity in the hippocampus.

MATERIALS AND METHODS

Animals

All experiments were conducted using 8–12-week-old male Wistar rats (Charles River Laboratories, Sulzfeld, Germany). Animals were housed in custom-made climatized and ventilated holding cupboards in an animal-housing room with a controlled 12-h light/dark cycle. No female rats were housed in the room. Water and food were available *ad libitum*. The study was carried out in accordance with the European Communities Council Directive of September 22nd, 2010 (2010/63/EU) for care of laboratory animals and all experiments were conducted according to the guidelines of the German Animal Protection Law. They were approved in advance by the North Rhine-Westphalia (NRW) State Authority (Landesamt für Arbeitsschutz, Naturschutz, Umweltschutz und Verbraucherschutz, NRW). All efforts were made to reduce the number of animals used.

Slice Preparation

Wistar rats were deeply anesthetized with sodium pentobarbital and transcardially perfused with cold Ringer's solution + heparin (0.2%) followed by 4% paraformaldehyde (PFA) in phosphate buffered saline (PBS, 0.025 M). Brains were removed, fixed in 4% PFA for 24 h, and cryoprotected in 30% sucrose in 0.1 M PBS for at least 3 days. Serial 30-µm thick horizontal sections were collected with a freezing microtome. For each animal ($N = 10$), three horizontal sections from the most dorsal (between 3.6 and 4.1 mm posterior to Bregma), middle intermediate (around 5.6 mm posterior to Bregma) and most ventral hippocampal parts (between 7.1 and 7.6 mm posterior to Bregma) were simultaneously used for immunohistochemical staining (**Figure 2**).

Verification of Antibody Specificity

The specificity of the D2R antibody was conducted using western blotting (**Figure 1**). Following brain removal, the hippocampus was rapidly isolated and then homogenized in 20 mM Tris–HCl buffer (pH 7.4) containing 10% sucrose, followed by centrifugation at 14,000 rpm for 30 min at 4°C in 20 mM Tris–HCl buffer supplemented with protease inhibitor. The supernatant was removed and the pellet was resuspended in 20 mM Tris–HCl buffer supplemented with protease inhibitor. The protein concentration of the samples was determined with a Bradford assay. Protein samples were separated in 8% SDS polyacrylamide gels that were prepared 1 day before use. Prior to gel electrophoresis, the required amount of sample (minimum 10 µg of protein per sample) was mixed with the same amount of twice-concentrated (2×) Laemmli buffer. Samples were then heated for 5 min at 100°C, briefly centrifuged and loaded on to gels. The first line on the gel was always filled with protein marker in the amount of 5 µg, which was then separated into fragments of distinct molecular weights. Gel-electrophoresis was performed for ∼1.5 h at 400 V and 15 mA settings per gel. Afterward, gels were removed from the running chamber and left in the cold transfer buffer, while the polyvinyl difluoride membranes (PVDF) were incubated with methanol for approx. 5 min. Membranes were then briefly washed with distilled water and covered with transfer buffer. After the transfer "sandwiches" were assembled, they were placed into the transfer chamber, covered with cold transfer buffer and the wet-transfer of proteins from gel onto membranes began (400 V, 300 mA, 1.5 h).

Membranes were then blocked for 1 h [5% non-fat dry milk, 0.1% Tween 20 in tris-buffered saline (TBS)] at room temperature. Blots were then incubated overnight at 4°C with the primary D2R antibody that was used for immunohistochemistry: rabbit polyclonal anti-D2R (ab-1558, Millipore) at 1:1,000 dilution. The primary antibody was dissolved in boost signal solution (Calbiochem). Membranes were then washed 3 times in 0.1% Tween 20 in TBS and incubated with secondary antibody dissolved in boost signal solution (Calbiochem). Protein bands were visualized using an enhanced chemiluminescence reagent. A distinct band was found at ca. 55 kDa (**Figure 1**) consistent with specific labeliing of the D2L receptor that is postsynaptically localized, by the antibody used here (Gemechu et al., 2018).

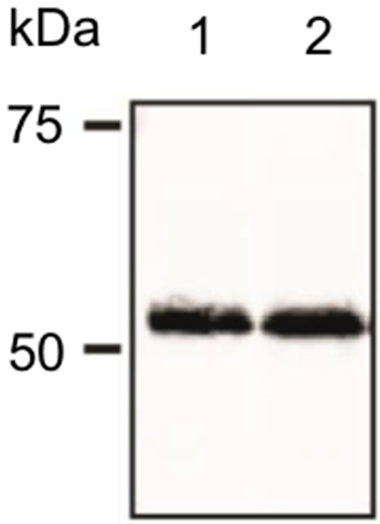

FIGURE 1 | Verification of antibody specificity. Example of a western blot showing binding specificity of the dopamine D2-like receptor (D2R) antibody used in the immunohistochemistry experiments. The antibody labeled a band of ca. 55 kDa, corresponding to the reported kDa weight of the target receptor as reported by others (Gemechu et al., 2018).

Immunohistochemistry

Endogenous peroxidase was blocked by pretreating the free-floating brain sections in 0.3% H_2O_2 for 20 min. They were then rinsed in PBS and incubated with blocking solution containing 10% normal serum and 20% avidin in PBS with 0.2% Triton X-100 (PBS-Tx) for 90 min at room temperature. Sections were incubated overnight at room temperature with primary D2R antibodies (rabbit polyclonal, 1:250; ab-1558, Millipore) in medium containing 1% normal serum in 0.2% PBS-Tx + 20% biotin. Sections were then rinsed in PBS and incubated with biotinylated goat anti-rabbit (1:500; BA-1,000, Vector) antibodies in 1% normal serum in 0.1% PBS-Tx for 90 min at RT. Afterward, sections were washed in PBS and incubated for 90 min at RT with ABC kit (PK-6,100, Vector) in 1% normal serum in 0.1% PBS-Tx. Finally, sections were washed in PBS and treated with diaminobenzidine (DAB) and 0.01% H_2O_2 for approx. 10 min.

Quantitative Analysis

Regions of interest were defined using the rat brain atlas of Paxinos and Watson (1982) and Nissl staining where every 12th section throughout the whole hippocampus was stained with 0.1% Cresylviolet (c5042, Sigma) as a reference. Fifteen areas of interest included: the molecular layer (ml) of the DG; the granule cell layer (gcl) of the DG; the polymorphic layer (pl) of the DG; the Stratum oriens (so) of CA3/CA2/CA1; the pyramidal cell layer (pcl) of CA3/CA2/CA1; the Stratum radiatum (sr) of CA3/CA2/CA1; and the Stratum lacunosum-moleculare (slm) of CA3/CA2/CA1 on sections taken from the dorsal, intermediate and ventral hippocampal subdivisions (**Figure 2**). Both, right and left hippocampi were used for the analysis and considered as replicates. For background

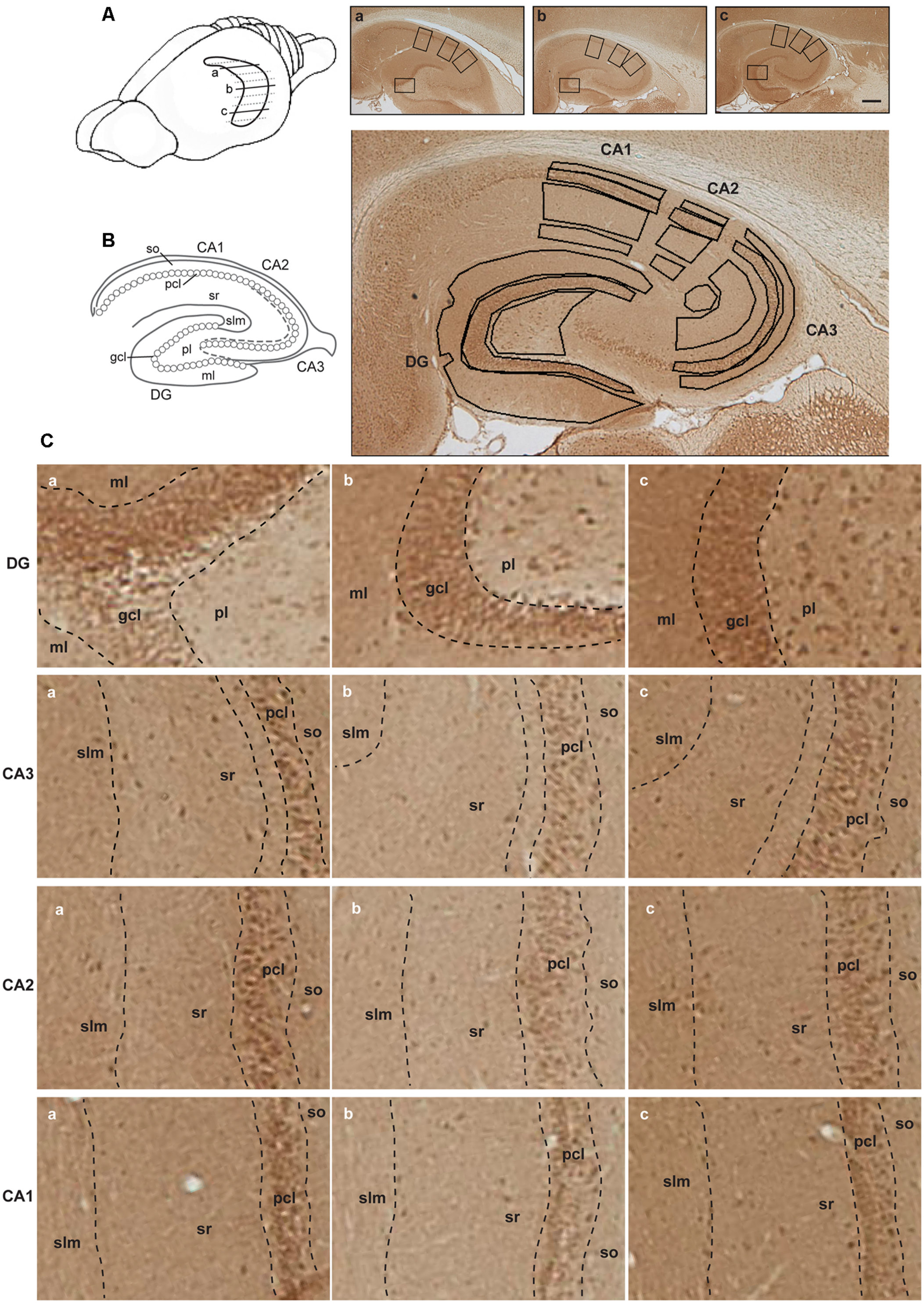

FIGURE 2 | Illustration of hippocampal separation into longitudinal and transverse axes. **(A)** A drawing of the rat brain with horizontally sectioned hippocampus is presented. Representative images of immunohistochemically stained sections against D2R of the dorsal (a), intermediate (b) and ventral hippocampus (c) from the same animal are shown. Scale bar is 500 μm. Squares on each image correspond to zoom-in fragments on the panel **(C)**. **(B)** Schematic representation of the hippocampal transverse axis and laminar separation (left). Immunohistochemically stained section with marked regions taken for the analysis is depicted (right). Abbreviations correspond to: ml, molecular layer of the DG; gcl, granule cell layer of the DG; pl, polymorphic layer of the DG; so, Stratum oriens of CA3/CA2/CA1; pcl, pyramidal cell layer of CA3/CA2/CA1; sr, Stratum radiatum of CA3/CA2/CA1; and slm, Stratum lacunosum-moleculare of CA3/CA2/CA1. **(C)** A closer view of subsections of the dentate gyrus (DG) and CA regions from the dorsal (a), intermediate (b) and ventral (c) hippocampal sections, including the laminar delineation, is shown.

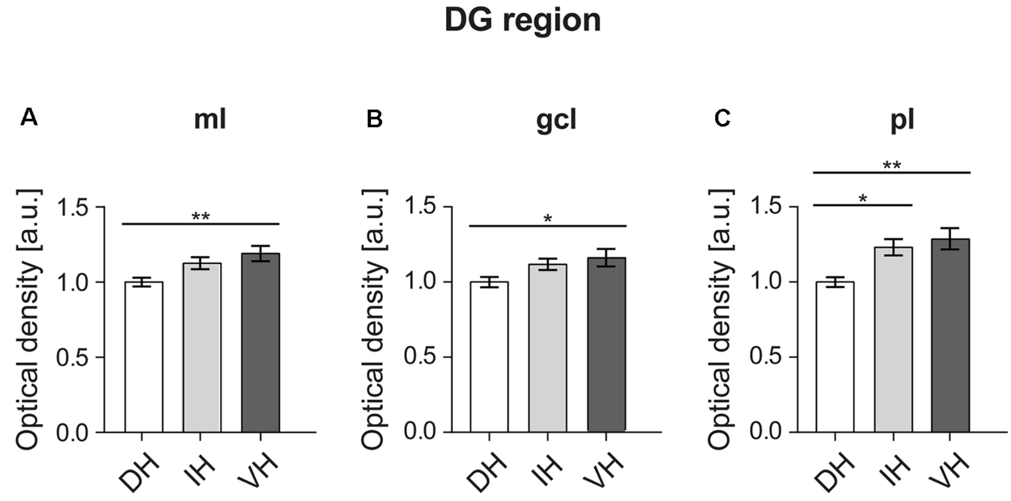

FIGURE 3 | In the DG, the dorsal component exhibits the lowest D2R expression. The molecular layer (ml) **(A)** and granule cell layer (gcl) of the ventral DG **(B)** exhibit higher D2R levels compared to the dorsal DG. The polymorphic layer (pl) **(C)** of the dorsal DG shows the lowest receptor expression as opposed to the ventro-intermediate DG. Values expressed in arbitrary units (a.u.). Error bars indicate standard error of the mean (SEM). $^*p < 0.05$ or $^{**}p < 0.01$. ml, molecular layer; gcl, granule cell layer; pl, polymorphic layer.

subtraction, we used receptor-devoid tissue. In the dorsal sections this comprised the fimbria. In the intermediate sections, this comprised the superior thalamic radiation, and in the ventral sections, this was the internal capsule. Pictures of stained sections were acquired with a light microscope (Leica DMR, Germany), equipped with a digital camera (MBF Bioscience) and stored in TIFF format. The regions of interest were analyzed at 2.5× lens magnification. The digitized high-resolution pictures were obtained using Neurolucida software (MBF Bioscience) and quantified using open-source ImageJ software (National Institute of Health). Given that images were acquired with a RGB camera the "Color Deconvolution" plugin in ImageJ was used to deconvolve the color information as well as to convert images to 8-bit format, thus increasing the dynamic range of the signal. R software was used to scale data from several independent stainings/plates using generalized residual sum of squares algorithm to account for batch variability in staining intensities (Kreutz et al., 2007; von der Heyde et al., 2014).

Statistical Analysis

Receptor expression differences between hippocampal subfields for each layer of the trisynaptic circuit were statistically analyzed using a one-way analysis of variance (ANOVA) followed by Tukey HSD *post hoc* test. Here, statistical comparisons were made for a hippocampal layer of interest between the dorsal, intermediate and ventral subdivisions of 10 animals. In the subsequent text descriptions, "M" corresponds to the mean, while "SD" refers to the standard deviation. All significant differences were defined as $p < 0.05$, $p < 0.01$ or $p < 0.001$. Values are expressed as mean values ± the standard error of the mean (SEM).

RESULTS

In the Dentate Gyrus the Dorsal Component Exhibits the Lowest D2R Expression

In order to better understand the functional differences across the hippocampal longitudinal axis, we examined the protein levels of D2R in the DG, CA3, CA2 and CA1 regions of the rat dorsal, intermediate and ventral hippocampus by immunohistochemical staining. Of all regions examined, the dorsal DG exhibited the lowest levels of D2R compared to expression levels in the ventral hippocampus. Effects were significant for the molecular layer, granule cell layer and the polymorphic layer (**Figure 3**).

A one-way ANOVA analysis revealed a significant effect for the three hippocampal parts in the molecular layer of the DG (**Figure 3A**; $F_{(2,57)} = 5.665$, $p < 0.01$). *Post hoc* Tukey HSD test revealed that the mean score for the dorsal part ($M = 1$, $SD = 0.12$) was significantly lower from the ventral part ($M = 1.19$, $SD = 0.22$). The intermediate part ($M = 1.12$, $SD = 0.17$) did not differ from the other two hippocampal poles (**Figure 3A**).

Similarly, there was a significant effect in the granule cell layer of the DG (**Figure 3B**; $F_{(2,57)} = 3.52$, $p < 0.05$) analysis. Again, the *post hoc* test showed a difference in the mean score between the dorsal part ($M = 1$, $SD = 0.14$) and the ventral one ($M = 1.16$, $SD = 0.26$), while the intermediate part ($M = 1.11$, $SD = 0.16$) was not different compared to the other two (**Figure 3B**).

In case of the polymorphic layer of the DG (**Figure 3C**), the dorsal part ($M = 1$, $SD = 0.14$) displayed significantly lower D2R levels ($F_{(2,57)} = 7.691$, $p < 0.01$) compared to both, the intermediate ($M = 1.23$, $SD = 0.24$) and the ventral hippocampi (M = 1.28, SD = 0.32). Receptor expression did not differ between the intermediate and ventral parts (**Figure 3C**).

In the CA3 Region, the Ventral Component Shows the Highest D2R Expression

Analysis of the D2R expression between the dorsal, intermediate and ventral hippocampal parts for the four layers of the CA3 region (**Figure 4**) revealed uniformly higher D2R levels in the ventral third, compared to the dorso-intermediate two-thirds.

Specifically, in the Stratum oriens of the CA3 statistically significant higher D2R expression was found in the ventral CA3 ($F_{(2,57)} = 8.973$, $p < 0.001$). This was apparent between the ventral (M = 1.3, SD = 0.28) vs. the dorsal part (M = 1, SD = 0.19), and the ventral vs. the intermediate part (M = 1.1, SD = 0.21; **Figure 4A**). In the pyramidal cell layer of the CA3, the ventral part (M = 1.21, SD = 0.2) also showed significantly higher D2R expression ($F_{(2,57)} = 9.386$, $p < 0.001$) compared to the dorsal layer (M = 1, SD = 0.12), as well as compared to the intermediate layer (M = 1.08, SD = 1.44; **Figure 4B**).

Furthermore, D2R expression was higher in the Stratum radiatum of the ventral CA3 region: the dorsal (M = 1, SD = 0.21) and intermediate (M = 1.14, SD = 0.19) parts express significantly less D2R ($F_{(2,57)} = 14.05$, $p < 0.001$) compared to the ventral hippocampus (M = 1.39, SD = 0.29; **Figure 4C**). In addition, the Stratum lacunosum-moleculare of the CA3 region followed the same pattern with D2R expression being higher in the ventral component ($F_{(2,57)} = 8.499$, $p < 0.001$; ventral portion: M = 1.28, SD = 0.26; dorsal: M = 1, SD = 0.18; and intermediate: M = 1.09, SD = 0.2; **Figure 4D**).

In the CA2 Region, D2R Expression Is Highest in the Ventral Apical Dendrites

Statistical analysis did not reveal any differences between the dorsal (M = 1, SD = 0.14), intermediate (M = 1, SD = 0.19) and ventral parts (M = 1.12, SD = 0.19) of the Stratum oriens of the CA2 region ($F_{(2,57)} = 3.324$, $p < 0.05$; **Figure 5A**). Likewise, no differences were found ($F_{(2,57)} = 0.332$, $p = 0.718$) for the pyramidal cell layer of the CA2 region (dorsal: M = 1, SD = 0.12; intermediate: M = 0.97, SD = 0.16; ventral: M = 1.01, SD = 0.13; **Figure 5B**). However, the ventral Stratum radiatum (M = 1.21, SD = 0.2) exhibited significantly higher D2R levels ($F_{(2,57)} = 7.259$, $p < 0.01$) as opposed to the dorsal (M = 1, SD = 0.15) and intermediate parts (M = 1.04, SD = 0.19; **Figure 5C**). In case of the Stratum lacunosum-moleculare of the CA2 region, the ventral portion of the hippocampus (M = 1.22, SD = 0.19) has also exhibited significantly higher expression of D2R ($F_{(2,57)} = 8.427$, $p < 0.001$) compared to the dorsal (M = 1, SD = 0.14) and intermediate parts (M = 1.05, SD = 0.2; **Figure 5D**).

D2R Expression Is Higher in the Ventral CA1 Region

D2R expression levels were uniformly higher across the non-somatic sublayers of the ventral CA1 region compared to the dorsal CA1 (**Figure 6**). Thus, expression was found to be the highest in the ventral Stratum oriens (M = 1.14, SD = 0.19) of the CA1 region ($F_{(2,57)} = 3.492$, $p < 0.05$) as opposed to the dorsal part (M = 1, SD = 0.14), while no differences were observed with the intermediate part (M = 1.02, SD = 0.2; **Figure 6A**). In case of the Stratum radiatum, the ventral hippocampus (M = 1.17, SD = 0.19) showed significantly higher D2R levels ($F_{(2,57)} = 4.561$, $p < 0.05$) compared to the dorsal part (M = 1, SD = 0.17). The intermediate sr (M = 1.04, SD = 0.21) was not significantly different from its counterparts (**Figure 6C**). The Stratum lacunosum-moleculare followed a similar pattern ($F_{(2,57)} = 9.07$, $p < 0.001$) and exhibited higher receptor levels in the ventral portion (M = 1.28, SD = 0.2) as opposed to the dorsal (M = 1, SD = 0.19) and intermediate ones (M = 1.1, SD = 0.23; **Figure 6D**).

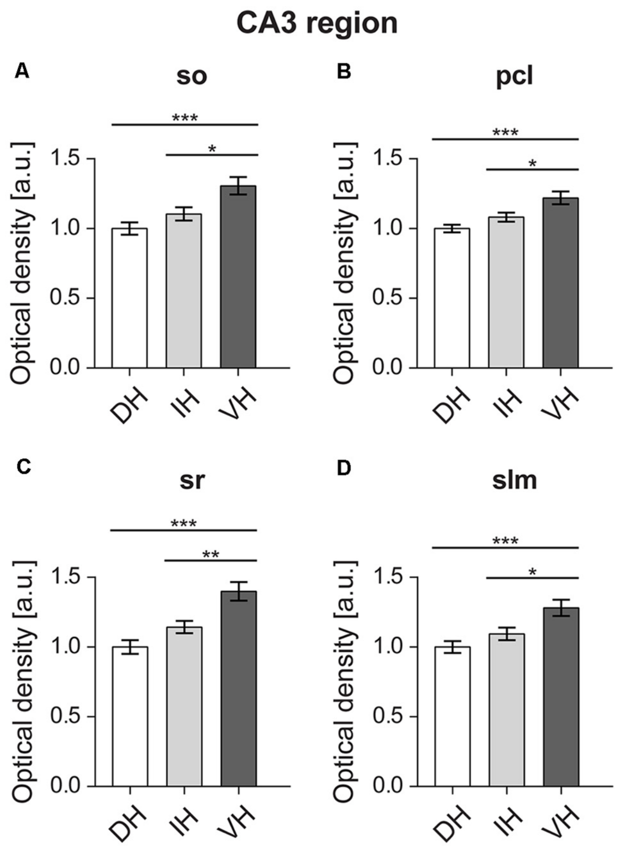

FIGURE 4 | In the CA3 region, the ventral component shows the highest D2R expression. All layers of the ventral CA3 region, namely the Stratum oriens (so) **(A)**, pyramidal cell layer (pcl) **(B)**, Stratum radiatum (sr) **(C)**, and Stratum lacunosum-moleculare (slm) **(D)** display high D2R levels compared to the dorso-intermediate CA3. Values expressed in arbitrary units (a.u.). Error bars indicate SEM. *$p < 0.05$, **$p < 0.01$, ***$p < 0.001$. so, Stratum oriens; pcl, pyramidal cell layer; sr, Stratum radiatum; and slm, Stratum lacunosum-moleculare.

Receptor expression was of similar level ($F_{(2,57)} = 2.018$, $p = 0.142$) in the dorsal (M = 1, SD = 0.16), intermediate (M = 1.02, SD = 0.17) and ventral pyramidal cell layers of the CA1 region (M = 1.1, SD = 0.19; **Figure 6B**).

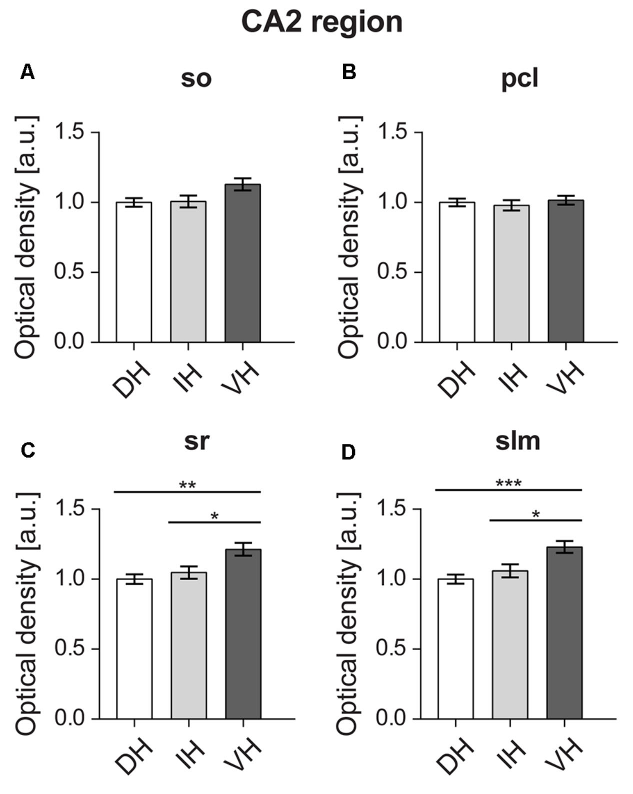

FIGURE 5 | In the CA2 region, D2R expression is highest in the ventral apical dendrites. The D2R is equally expressed in the Stratum oriens (so) **(A)** and pyramidal cell layer (pcl) **(B)** across the longitudinal axis of the CA2 region. Receptor protein expression is highest in the ventral Stratum radiatum (sr) **(C)** and Stratum lacunosum-moleculare (slm) **(D)** as opposed to dorso-intermediate CA2. Values expressed in arbitrary units (a.u.). Error bars indicate SEM. *$p < 0.05$, **$p < 0.01$, ***$p < 0.001$. so, Stratum oriens; pcl, pyramidal cell layer; sr, Stratum radiatum; and slm, Stratum lacunosum-moleculare.

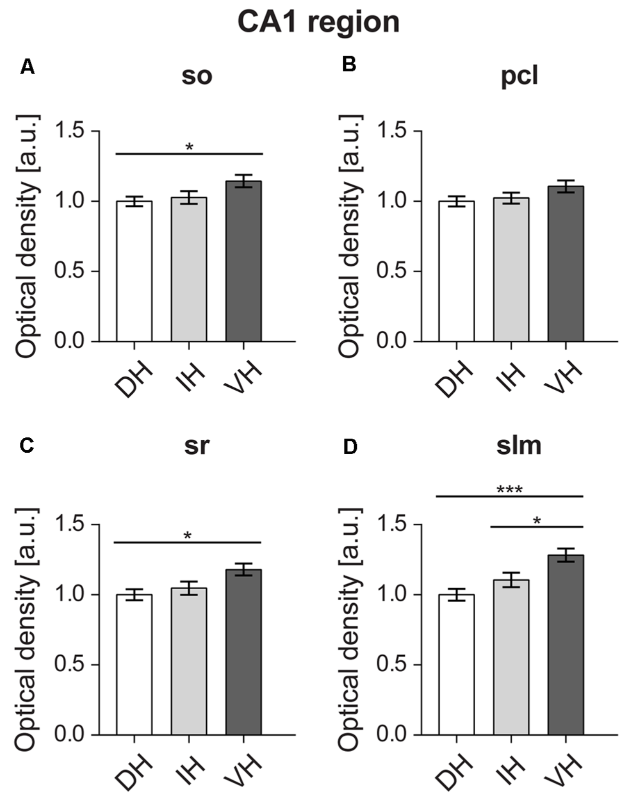

FIGURE 6 | D2R expression is higher in the ventral CA1 region. Proximal dendrites **(A,C)** of the ventral relative to the dorsal CA1 display high D2R protein levels. D2R show similar expression levels throughout the pyramidal cell layer (pcl) layer of the CA1 region **(B)**. Distal dendrites of the ventral CA1 express higher D2R levels compared to the dorso-intermediate parts. **(D)** A gradient of expression of D2R occurs in the Stratum lacunosum moleculare. Expression is highest in the ventral, and lowest in the dorsal SLM. Values expressed in arbitrary units (a.u.). Error bars indicate SEM. *$p < 0.05$ or ***$p < 0.001$. so, Stratum oriens; pcl, pyramidal cell layer; sr, Stratum radiatum; and slm, Stratum lacunosum-moleculare.

DISCUSSION

In this study, we report that the D2R expression differs across the dorsal, intermediate and ventral hippocampus of rat. Specifically, we demonstrate that the total D2R levels are the highest in all layers of the ventral DG and CA3 regions, as well as in the dendritic layers of the ventral CA2 and CA1 regions. The dorsal hippocampus shows the overall lowest D2R content, while the intermediate part shows levels that are either in-between the differing levels of the dorsal and ventral poles, or alternatively are equivalent to levels detected in one of the poles. Testing of antibody specificity revealed protein labeling at 55 kDa. This corresponds to the D2L dopamine receptor that is postsynaptic (Lindgren et al., 2003; Gemechu et al., 2018).

Importantly, our study is the first to provide a more complete picture of D2R expression across the hippocampal dorso-ventral axis, as the majority of already published studies focused on brain regions other than the hippocampus (Vincent et al., 1993; Sesack et al., 1994; Yung et al., 1995; Lazarov and Pilgrim, 1997; Jung and Bolam, 2000) or on animal species other than the rat (Khan et al., 1998; Gangarossa et al., 2012; Puighermanal et al., 2015; Wei et al., 2017). Only very few studies report on aspects of the D2R expression in the rat hippocampus. Among them, an immunocytochemical study by Levey et al. (1993) described relatively low D2R immunoreactivity in the hippocampus on sagittal sections from albino rat brains. An earlier autoradiographic study reported the presence of D2R high-density binding sites in the Stratum lacunosum-moleculare of the dorsal CA1 and lower densities in the rest of the rat hippocampus (Charuchinda et al., 1987). The most recent work by Yu et al. (2019) demonstrated cellular expression patterns of D2R in transgenic rat forebrain. They studied D2R positive cells across the transverse axis of only the dorsal hippocampus and reported on D2R expression in the pyramidal cell layer and Stratum radiatum of the CA1–3 regions and the DG, as well as in axon terminals innervating the Stratum lacunosum-moleculare of the CA1 region. With regard to the dorso-ventral distribution of the D2R only one study has addressed this to date. Using a radioligand binding assay, Bruinink and Bischoff, 1993, demonstrated a bimodal distribution from the dorsal to the ventral hippocampus that comprised a high D2R density in one portion of the dorsal part and in the entire ventral part. The results of our current study are in line with this report. We show here that the ventral hippocampus has the highest expression density of D2R. The discrepancy between a bimodal distribution in the aforementioned study and a lack thereof in our case, is probably because in our examination of the D2R expression we used sections from the dorsal part that are very close to the tip of the hippocampus, while in the Bruinink and Bischoff study the dorsal hippocampus was separated into three subdivisions, whereupon the one closest to the intermediate hippocampus showed the high receptor density. Moreover, this study showed that the proportion of the D2R in the high affinity state is higher in the dorsal hippocampus as opposed to the ventral one (Bruinink and Bischoff, 1993). This may have masked differences in receptor distribution, especially considering that the amount of dopaminergic projections reaching the hippocampus is more dense in the ventral portion (Verney et al., 1985). Interestingly, dopamine D1 receptors show a similar pattern of expression along the dorsoventral axis (Dubovyk and Manahan-Vaughan, 2018), with higher levels being apparent in the ventral and intermediate CA1 region compared to the dorsal part. Here, in particular, expression is higher in the ventral and intermediate Stratum lacunosum-moleculare and Stratum radiatum of the CA1 region (Dubovyk and Manahan-Vaughan, 2018).

Studies that scrutinized the binding affinity of D1-like and D2-like receptors (Edelmann and Lessmann, 2018) showed that, at low concentrations, dopamine activates presynaptic D2R leading to a reduction of excitatory responses in the hippocampal CA1 neurons. These findings suggest that during the tonic firing of dopaminergic neurons projecting to the hippocampus, the D2R become activated first, adding to a generalized inhibition of neuronal excitatory postsynaptic currents. This interpretation is consistent with findings, in behaving rats, that intracerebral application of a D2R agonist reduces basal synaptic transmission in the hippocampus (Manahan-Vaughan and Kulla, 2003). These low concentrations of D2R agonist also inhibit vulnerable forms of LTP (Manahan-Vaughan and Kulla, 2003). This process may serve to enhance signal-to-noise ratios and prevent the long-term storage of less salient information.

At higher concentrations, dopamine begins to activate other D2-like receptors followed by D1-like receptors (Gribkoff and Ashe, 1984; Hsu, 1996; van Wieringen et al., 2013). In line with this, high D2R agonist concentrations increase the spontaneous firing rate of dorsal CA1 pyramidal neurons in rat slices (Smiaowski and Bijak, 1987), as well as in the dorsal DG granule cells of freely moving rats (Yanagihashi et al., 1991). Given our finding of an overall dorso-ventral gradient in the D2R expression, it is tempting to assume that the ventral hippocampus may be under a stronger inhibitory control upon tonic dopamine release, but may have an increased neuronal excitability when phasic elevations of dopamine levels occur. This may explain why neuroleptics that antagonize dopamine D2R ameliorate the symptoms of acute, or positive, symptoms of psychosis (Giannini et al., 2000; Dold et al., 2015): by antagonizing the receptor, the balance of activity is restored to one that mediates neuronal inhibition, as opposed to excitation. Our study suggests that these effects may be mediated predominantly by the ventral hippocampus, an interpretation that is supported by studies that suggest that the ventral (and not the dorsal) hippocampus engages predominantly in information processing related to affective state (Fanselow and Dong, 2010).

The involvement of D2R signaling in the modulation of hippocampal synaptic plasticity has been described by several studies. For example, pharmacological blockade of D2R, using a ligand concentration that does not affect basal synaptic transmission, prevents a weak form of long-term potentiation (LTP) in the dorsal DG *in vivo* (Manahan-Vaughan and Kulla, 2003). This study also reported an involvement of the D2R in the regulation of depotentiation, which involves a reversal of recently induced LTP (Manahan-Vaughan and Kulla, 2003). With regard to the CA1 region of hippocampal slices, antagonism of D2R inhibits LTP maintenance but has no effect on the initiation phase (Frey et al., 1989, 1990). Activation of D2-like receptors results in inhibition of long-term depression (LTD) in the CA1 region *in vitro* (Chen et al., 1996). While all of the reported studies on synaptic plasticity have been performed on the dorsal part of the rat hippocampus, only one such study was performed on the ventral part, in this case, of the mouse hippocampus (Rocchetti et al., 2015). Here, the authors reported that both LTP and LTD were severely impaired in the ventral CA1 of hippocampal slices from D2R knockout mice, as well as following the pharmacological blockade of the D2R in naive mice. Moreover, they showed that specific deletion of presynaptic D2R leads to deficits in LTD, but not in LTP. All of these studies show that D2R plays a significant role in the expression of hippocampal synaptic plasticity at both, dorsal and ventral hippocampal parts and, at least, in the DG and CA1 regions.

Mechanistically, the D2R-dependent modulation of synaptic plasticity may occur through GABAergic interneurons, as receptor activation was shown to reduce GABA synthesis in the hippocampus (Steulet et al., 1990), thus allowing for LTP to occur (Wigström and Gustafsson, 1983). However, higher D2R expression in the ventral hippocampus does not seem to be able to fully compensate for differences in LTP between the dorsal and ventral hippocampal parts, as LTP is known to be of lower magnitude in the ventral CA1 compared to its dorsal counterpart (Dubovyk and Manahan-Vaughan, 2018). This difference relates to expression levels of subunits of the NMDA receptor (Dubovyk and Manahan-Vaughan, 2018), but may also relate to differences in D2R expression and/or to the expression of other neurotransmitter receptors. Further studies are required to access the precise contribution of D2R to synaptic plasticity in other CA regions as well as in the intermediate hippocampus.

Functionally, the D2R has been implicated in hippocampus-dependent learning and memory: systemic application of receptor blockers triggers an array of learning and memory deficits (Gasbarri et al., 1993; Sigala et al., 1997; Stuchlik et al., 2007; Rocchetti et al., 2015). Similarly, D2R knockout mice have impaired both, short-term and long-term spatial memory as well as recognition memory (Rocchetti et al., 2015). Interestingly, a direct infusion of a D2R antagonist into the ventral hippocampus of wildtype mice reproduced learning deficits observed in the D2R knockout mice (Rocchetti et al., 2015). The same was found for the rat upon D2R blockade in the ventral hippocampus (Wilkerson and Levin, 1999; Umegaki et al., 2001), suggesting that the systemic effect on spatial learning and memory may, in fact, be mediated by the ventrally expressed D2R. Interestingly, systemic injection of D2R agonist (Imperato et al., 1993, 1994), as well as focal injection into the ventral hippocampus, dose-dependently stimulates acetylcholine release (Umegaki et al., 2001). However, injection of the D2R agonist into the dorsal hippocampus had no such effect on hippocampal acetylcholine release (Day and Fibiger, 1994). Therefore, the involvement of the D2R in memory performance in the ventral hippocampus may happen through the regulation of acetylcholine release.

Accurate spatial navigation is thought to be mediated by place-cell representation of spatial context (Eichenbaum et al., 1999) that is known to differ in the dorsal and ventral hippocampus (Strange et al., 2014). Here, the density of place cells, size of the place fields and their precision are known to gradually change from pole to pole (Jung et al., 1994). Importantly, in D2R knockout mice, the number of place cells is significantly decreased and is accompanied by changes in basic firing properties (intra-field firing rate, spatial tuning and spatial coherence) and reduced stability of place fields (Nguyen et al., 2014). Therefore, the difference in D2R expression between the dorsal and ventral hippocampus that was found in the current work may also account, in part, for dorso-ventral differences in place cells and place fields properties, whereupon the dorsal part encodes high-resolution spatial information for a small environment, while the ventral part processes low-resolution information for a larger environment.

It has been proposed that the hippocampal dorso-ventral axis is functionally segregated on a cognitive level. Whereas the dorsal part is predominantly engaged in visuo-spatial information processing, the ventral part is involved in emotional, motivational and affective responses (Fanselow and Dong, 2010; Strange et al., 2014). The intermediate part may integrate information from both poles (Bast et al., 2009; Fanselow and Dong, 2010; Strange et al., 2014). Interestingly, the ventro-intermediate hippocampal subfields receive a more intense afferent projection form the VTA than does the dorsal subfield (Gasbarri et al., 1994). The higher expression levels of D2R receptors as reported in the present study, along with higher levels of D1DR as reported previously (Dubovyk and Manahan-Vaughan, 2018), suggest that the ventral hippocampus is subjected to quite potent control by the VTA. This indicates in turn, that the ventral part of the hippocampus should be subjected to much closer scrutiny in terms of obtaining an understanding of how the dopaminergic system engages with the hippocampus, and enables hippocampal information encoding and hippocampus-dependent non-spatial behavior.

CONCLUSION

Taken together, our study demonstrates that the overall expression of dopaminergic D2R is strikingly different between the ventral pole of the hippocampus and its dorso-intermediate two-thirds of the dorso-ventral axis. In all hippocampal sublayers studied, expression levels were always highest in the ventral compared to the dorsal pole. This difference is likely to contribute to known dorso-ventral differences in synaptic plasticity (Dubovyk and Manahan-Vaughan, 2018) as well as to state-dependent learning and memory.

DATA AVAILABILITY STATEMENT

The data that support the findings of this study are available from the corresponding author upon reasonable request.

ETHICS STATEMENT

The animal study was reviewed and approved by Landesamt für Arbeitsschutz, Naturschutz, Umweltschutz und Verbraucherschutz, NRW, Germany.

AUTHOR CONTRIBUTIONS

The study was designed by DM-V and VD. Experiments were conducted by VD and analyzed by both authors. VD and DM-V wrote the article.

FUNDING

This work was supported by a German Research Foundation (Deutsche Forschungsgemeinschaft, DFG) grant to DM-V (SFB 1280/A04, project number: 316803389).

ACKNOWLEDGMENTS

We gratefully thank Ute Neubacher and Beate Krenzek for technical assistance and Nadine Kollosch for animal care.

REFERENCES

Bast, T., Wilson, I. A., Witter, M. P., and Morris, R. G. M. (2009). From rapid place learning to behavioral performance: a key role for the intermediate hippocampus. *PLoS Biol.* 7:e1000089. doi: 10.1371/journal.pbio.1000089

Beaulieu, J. M., and Gainetdinov, R. R. (2011). The physiology, signaling, and pharmacology of dopamine receptors. *Pharmacol. Rev.* 63, 182–217. doi: 10.1124/pr.110.002642

Bruinink, A., and Bischoff, S. (1993). Dopamine D_2 receptors are unevenly distributed in the rat hippocampus and are modulated differently than in striatum. *Eur. J. Pharmacol.* 245, 157–164. doi: 10.1016/0922-4106(93)90123-q

Charuchinda, C., Supavilai, P., Karobath, M., and Palacios, J. M. (1987). Dopamine D2 receptors in the rat brain: autoradiographic visualization using a high-affinity selective agonist ligand. *J. Neurosci.* 7, 1352–1360. doi: 10.1523/JNEUROSCI.07-05-01352.1987

Chaudhuri, K. R., and Schapira, A. H. (2009). Non-motor symptoms of Parkinson's disease: dopaminergic pathophysiology and treatment. *Lancet Neurol.* 8, 464–474. doi: 10.1016/S1474-4422(09)70068-7

Chen, Z., Ito, K., Fujii, S., Miura, M., Furuse, H., Sasaki, H., et al. (1996). Roles of dopamine receptors in long-term depression: enhancement *via* D1 receptors and inhibition *via* D2 receptors. *Receptors Channels* 4, 1–8.

Citri, A., and Malenka, R. C. (2008). Synaptic plasticity: multiple forms, functions, and mechanisms. *Neuropsychopharmacology* 33, 18–41. doi: 10.1038/sj.npp.1301559

Day, J. C., and Fibiger, H. C. (1994). Dopaminergic regulation of septohippocampal cholinergic neurons. *J. Neurochem.* 63, 2086–2092. doi: 10.1046/j.1471-4159.1994.63062086.x

De Mei, C., Ramos, M., Iitaka, C., and Borrelli, E. (2009). Getting specialized: presynaptic and postsynaptic dopamine D2 receptors. *Curr. Opin. Pharmacol.* 9, 53–58. doi: 10.1016/j.coph.2008.12.002

Dold, M., Samara, M. T., Li, C., Tardy, M., and Leucht, S. (2015). Haloperidol versus first-generation antipsychotics for the treatment of schizophrenia and other psychotic disorders. *Cochrane Database Syst. Rev.* 1:CD009831. doi: 10.1002/14651858.cd009831.pub2

Dubovyk, V., and Manahan-Vaughan, D. (2018). Less means more: the magnitude of synaptic plasticity along the hippocampal dorso-ventral axis is inversely related to the expression levels of plasticity-related neurotransmitter receptors. *Hippocampus* 28, 136–150. doi: 10.1002/hipo.22816

Duszkiewicz, A. J., McNamara, C. G., Takeuchi, T., and Genzel, L. (2019). Novelty and dopaminergic modulation of memory persistence: a tale of two systems. *Trends Neurosci.* 42, 102–114. doi: 10.1016/j.tins.2018.10.002

Edelmann, E., and Lessmann, V. (2018). Dopaminergic innervation and modulation of hippocampal networks. *Cell Tissue Res.* 373, 711–727. doi: 10.1007/s00441-018-2800-7

Eichenbaum, H., Dudchenko, P., Wood, E., Shapiro, M., and Tanila, H. (1999). The hippocampus, memory, and place cells: it is spatial memory or a memory space? *Neuron* 23, 209–226. doi: 10.1016/s0896-6273(00)80773-4

Etter, G., and Krezel, W. (2014). Dopamine D2 receptor controls hilar mossy cells excitability. *Hippocampus* 24, 725–732. doi: 10.1002/hipo.22280

Fanselow, M. S., and Dong, H. W. (2010). Are the dorsal and ventral hippocampus functionally distinct structures? *Neuron* 65, 7–19. doi: 10.1016/j.neuron.2009.11.031

Frey, U., Hartmann, S., and Matthies, H. (1989). Domperidone, an inhibitor of the D2-receptor, blocks a late phase of an electrically induced long-term potentiation in the CA1-region in rats. *Biomed. Biochim. Acta* 48, 473–476.

Frey, U., Schroeder, H., and Matthies, H. (1990). Dopaminergic antagonists prevent long-term maintenance of posttetanic LTP in the CA1 region of rat hippocampal slices. *Brain Res.* 522, 69–75. doi: 10.1016/0006-8993(90)91578-5

Gangarossa, G., Longueville, S., De Bundel, D., Perroy, J., Hervé, D., Girault, J. A., et al. (2012). Characterization of dopamine D1 and D2 receptor-expressing neurons in the mouse hippocampus. *Hippocampus* 22, 2199–2207. doi: 10.1002/hipo.22044

Gasbarri, A., Introini-Collison, I. B., Packard, M. G., Pacitti, C., and McGaugh, J. L. (1993). Interaction of cholinergic-dopaminergic systems in the regulation of memory storage in aversively motivated learning tasks. *Brain Res.* 627, 72–78. doi: 10.1016/0006-8993(93)90750-h

Gasbarri, A., Sulli, A., and Packard, M. G. (1997). The dopaminergic mesencephalic projections to the hippocampal formation in the rat. *Prog. Neuropsychopharmacol. Biol. Psychiatry* 21, 1–22. doi: 10.1016/s0278-5846(96)00157-1

Gasbarri, A., Packard, M. G., Campana, E., and Pacitti, C. (1994). Anterograde and retrograde tracing of projections from the ventral tegmental area to the hippocampal formation in the rat. *Brain Res. Bull.* 33, 445–452.

Gemechu, J. M., Sharma, A., Yu, D., Xie, Y., Merkel, O. M., and Moszczynska, A. (2018). Characterization of dopaminergic system in the striatum of young adult Park2$^{-/-}$ knockout rats. *Sci Rep.* 8:1517. doi: 10.1038/s41598-017-18526-0

Giannini, A. J., Underwood, N. A., and Condon, M. (2000). Acute ketamine intoxication treated by haloperidol. *Am. J. Ther.* 7, 389–391. doi: 10.1097/00045391-200007060-00008

Gingrich, J. A., and Caron, M. G. (1993). Recent advances in the molecular biology of dopamine receptors. *Annu. Rev. Neurosci.* 16, 299–321. doi: 10.1146/annurev.ne.16.030193.001503

Gribkoff, V., and Ashe, J. (1984). Modulation by dopamine of population responses and cell membrane properties of hippocampal CA1 neurons *in vitro*. *Brain Res.* 292, 327–338. doi: 10.1016/0006-8993(84)90768-6

Hansen, N., and Manahan-Vaughan, D. (2014). Dopamine D1/D5 receptors mediate informational saliency that promotes persistent hippocampal long-term plasticity. *Cereb. Cortex* 24, 845–858. doi: 10.1093/cercor/bhs362

Hansen, N., and Manahan-Vaughan, D. (2015). Hippocampal long-term potentiation that is elicited by perforant path stimulation or that occurs in conjunction with spatial learning is tightly controlled by β-adrenoreceptors and the locus coeruleus. *Hippocampus* 25, 1285–1298. doi: 10.1002/hipo.22436

Hsu, K. S. (1996). Characterization of dopamine receptors mediating inhibition of excitatory synaptic transmission in the rat hippocampal slice. *J. Neurophysiol.* 76, 1887–1895. doi: 10.1152/jn.1996.76.3.1887

Imperato, A., Obinu, M. C., Dazzi, L., Carta, G., Mascia, M. S., Casu, M. A., et al. (1994). Co-dergocrine (Hydergine) regulates striatal and hippocampal acetylcholine release through D2 receptors. *Neuroreport* 5, 674–676. doi: 10.1097/00001756-199402000-00003

Imperato, A., Obinu, M. C., and Gessa, G. L. (1993). Stimulation of both D_1 and D_2 receptors facilitates *in vivo* acetylcholine release in the hippocampus. *Brain Res.* 618, 341–345. doi: 10.1016/0006-8993(93)91288-4

Jung, K. K., and Bolam, J. P. (2000). Localization of dopamine D1 and D2 receptors in the rat neostriatum: synaptic interaction with glutamate- and GABA-containing axonal terminals. *Synapse* 38, 413–420. doi: 10.1002/1098-2396(20001215)38:4<413::aid-syn6>3.3.co;2-m

Jung, M. W., Wiener, S. I., and McNaughton, B. L. (1994). Comparison of spatial firing characteristics of units in dorsal and ventral hippocampus of the rat. *J. Neurosci.* 14, 7347–7356. doi: 10.1523/JNEUROSCI.14-12-07347.1994

Kemp, A., and Manahan-Vaughan, D. (2005). The 5-hydroxytryptamine4 receptor exhibits frequency-dependent properties in synaptic plasticity and behavioural metaplasticity in the hippocampal CA1 region *in vivo*. *Cereb. Cortex* 15, 1037–1043. doi: 10.1093/cercor/bhh204

Kempadoo, K. A., Mosharov, E. V., Choi, S. J., Sulzer, D., and Kandel, E. R. (2016). Dopamine release from the locus coeruleus to the dorsal hippocampus promotes spatial learning and memory. *Proc. Natl. Acad. Sci. U S A* 113, 14835–14840. doi: 10.1073/pnas.1616515114

Khan, Z. U., Mrzljak, L., Gutierrez, A., de la Calle, A., and Goldman-Rakic, P. S. (1998). Prominence of the dopamine D2 short isoform in dopaminergic pathways. *Proc. Natl. Acad. Sci. U S A* 95, 7731–7736. doi: 10.1073/pnas.95.13.7731

Kreutz, C., Bartolome Rodriguez, M. M., Maiwald, T., Seidl, M., Blum, H. E., Mohr, L., et al. (2007). An error model for protein quantification. *Bioinformatics* 20, 2747–2753. doi: 10.1093/bioinformatics/btm397

Kulla, A., and Manahan-Vaughan, D. (2000). Dopamine D1 receptors modulate depotentiation in the dentate gyrus of freely moving rats. *Cereb. Cortex* 10, 614–620. doi: 10.1093/cercor/10.6.614

Lavian, H., Loewenstern, Y., Madar, R., Almog, M., Bar-Gad, I., Okun, E., et al. (2018). Dopamine receptors in the rat entopeduncu-lar nucleus. *Brain Struct. Funct.* 223, 2673–2684. doi: 10.1007/s00429-018-1657-6

Lazarov, N., and Pilgrim, C. (1997). Localization of D_1 and D_2 dopamine receptors in the rat mesencephalic trigeminal nucleus by immunocytochemistry and in situ hybridization. *Neurosci. Lett.* 236, 83–86. doi: 10.1016/s0304-3940(97)00761-1

Lemon, N., and Manahan-Vaughan, D. (2012). Dopamine D1/D5 receptors contribute to de novo hippocampal LTD mediated by novel spatial exploration or locus coeruleus activity. *Cereb. Cortex* 22, 2131–2138. doi: 10.1093/cercor/bhr297

Lemon, N., Aydin-Abidin, S., Funke, K., and Manahan-Vaughan, D. (2009). Locus coeruleus activation facilitates memory encoding and induces hippocampal LTD that depends on beta-adrenergic receptor activation. *Cereb. Cortex* 19, 2827–2837. doi: 10.1093/cercor/bhp065

Levey, A. I., Hersch, S. M., Rye, D. B., Sunahara, R. K., Niznik, H. B., Kitt, C. A., et al. (1993). Localization of D1 and D2 dopamine receptors in brain with subtype-specific antibodies. *Proc. Natl. Acad. Sci. U S A* 90, 8861–8865. doi: 10.1073/pnas.90.19.8861

Lindgren, N., Usiello, A., Goiny, M., Haycock, J., Erbs, E., Greengard, P., et al. (2003). Distinct roles of dopamine D2L and D2S receptor isoforms in the regulation of protein phosphorylation at presynaptic and postsynaptic sites. *Proc. Natl. Acad. Sci. U S A* 100, 4305–4309. doi: 10.1073/pnas.0730708100

Lisman, J. (2017). Glutamatergic synapses are structurally and biochemically complex because of multiple plasticity processes: long-term potentiation, long-term depression, short-term potentiation and scaling. *Philos. Trans. R. Soc. Lond. B Biol. Sci.* 372:20160260. doi: 10.1098/rstb.2016.0260

Lisman, J. E., and Otmakhova, N. A. (2001). Storage, recall, and novelty detection of sequences by the hippocampus: elaborating on the SOCRATIC model to account for normal and aberrant effects of dopamine. *Hippocampus* 11, 551–568. doi: 10.1002/hipo.1071

Madadi Asl, M., Vahabie, A. H., and Valizadeh, A. (2019). Dopaminergic modulation of synaptic plasticity, its role in neuropsychiatric disorders, and its computation modeling. *Basic Clin. Neurosci.* 10, 1–12. doi: 10.32598/bcn.9.10.125

Manahan-Vaughan, D., and Kulla, A. (2003). Regulation of depotentiation and long-term potentiation in the dentate gyrus of freely moving rats by dopamine D2-like receptors. *Cereb. Cortex* 13, 123–135. doi: 10.1093/cercor/13.2.123

Nguyen, C. L., Tran, A. H., Matsumoto, J., Hori, E., Uwano, T., Ono, T., et al. (2014). Hippocampal place cell responses to distal and proximal cue manipulations in dopamine D2 receptor-knockout mice. *Brain Res.* 1567, 13–27. doi: 10.1016/j.brainres.2014.04.023

Paxinos, G., and Watson, C. (1982). *The Rat Brain in Stereotactic Coordinates.* San Diego: Academic Press.

Puighermanal, E., Biever, A., Espallergues, J., Gangarossa, G., De Bundel, D., and Valjent, E. (2015). drd2-cre:ribotag mouse line unravels the pos-sible diversity of dopamine d2 receptor-expressing cells of the dorsal mouse hippocampus. *Hippocampus* 25, 858–875. doi: 10.1002/hipo.22408

Rankin, M. L., Hazelwood, L. A., Free, R. B., Namkung, Y., Rex, E. B., Roof, R. A., et al. (2009). "Molecular pharmacology of the dopamine receptors," in *Dopamine Handbook*, eds L. L. Iversen, S. D. Iversen, S. B. Dunnet, and A. Bjorklund (New York, NY: Oxford University Press), 63–87.

Rocchetti, J., Isingrini, E., Dal Bo, G., Sagheby, S., Menegaux, A., Tronche, F., et al. (2015). Presynaptic D2 dopamine receptors control long-term depression expression and memory processes in the temporal hippocampus. *Biol. Psychiatry* 77, 513–525. doi: 10.1016/j.biopsych.2014.03.013

Santana, N., Mengod, G., and Artigas, F. (2009). Quantitative analysis of the expression of dopamine D1 and D2 receptors in pyramidal and GABAergic neurons of the rat prefrontal cortex. *Cereb. Cortex* 19, 849–860. doi: 10.1093/cercor/bhn134

Sesack, S. R., Aoki, C., and Pickel, V. M. (1994). Ultrastructural localization of D2 receptor-like immunoreactivity in midbrain dopamine neurons and their striatal targets. *J. Neurosci.* 14, 88–106. doi: 10.1523/jneurosci.14-01-00088.1994

Sibley, D. R., and Monsma, F. J. Jr. (1992). Molecular biology of dopamine receptors. *Trends Pharmacol. Sci.* 13, 61–69. doi: 10.1016/0165-6147(92)90025-2

Sigala, S., Missale, C., and Spano, P. (1997). Opposite effects of dopamine D2 and D3 receptors on learning and memory in the rat. *Eur. J. Pharmacol.* 336, 107–112. doi: 10.1016/s0014-2999(97)01235-1

Smiaowski, A., and Bijak, M. (1987). Excitatory and inhibitory action of dopamine on hippocampal neurons *in vitro*. *Neuroscience* 23, 95–101. doi: 10.1016/0306-4522(87)90274-0

Smith, C. C., and Greene, R. W. (2012). CNS dopamine transmission mediated by noradrenergic innervation. *J Neurosci.* 32, 6072–6080. doi: 10.1523/JNEUROSCI.6486-11.2012

Steulet, A. F., Bernasconi, R., Leonhardt, T., Martin, P., Grünenwald, C., Bischoff, S., et al. (1990). Effects of selective dopamine D1 and D2 receptor agonists on the rate of GABA synthesis in mouse brain. *Eur. J. Pharmacol.* 191, 19–27. doi: 10.1016/0014-2999(90)94092-c

Strange, B. A., Witter, M. P., Lein, E. S., and Moser, E. I. (2014). Functional organization of the hippocampal longitudinal axis. *Nat. Rev. Neurosci.* 15, 655–669. doi: 10.1038/nrn3785

Stuchlik, A., Rehakova, L., Telensky, P., and Vales, K. (2007). Morris water maze learning in Long-Evans rats is differentially affected by blockade of D1-like and D2-like dopamine receptors. *Neurosci. Lett.* 422, 169–174. doi: 10.1016/j.neulet.2007.06.012

Twarkowski, H., and Manahan-Vaughan, D. (2016). Loss of catecholaminergic neuromodulation of persistent forms of hippocampal synaptic plasticity with increasing age. *Front. Synaptic Neurosci.* 8:30. doi: 10.3389/fnsyn.2016.00030

Umegaki, H., Munoz, J., Meyer, R. C., Spanger, E. L., Yoshimura, J., Ikari, H., et al. (2001). Involvement of dopamine D2 receptors in complex maze learning and acetylcholine release in ventral hippocampus of rats. *Neuroscience* 103, 27–33. doi: 10.1016/s0306-4522(00)00542-x

Usiello, A., Baik, J. H., Rougé-Pont, F., Picetti, R., Dierich, A., LeMeur, M., et al. (2000). Distinct functions of the two isoforms of dopamine D2 receptors. *Nature* 408, 199–203. doi: 10.1038/35041572

Vallone, D., Picetti, R., and Borrelli, E. (2000). Structure and function of dopamine receptors. *Neurosci. Biobehav. Rev.* 24, 125–132. doi: 10.1016/S0149-7634(99)00063-9

van Wieringen, J. P., Booij, J., Shalgunov, V., Elsinga, P., and Michel, M. C. (2013). Agonist high- and low-affinity states of dopamine D_2 receptors: methods of detection and clinical implications. *Naunyn Schmiedebergs Arch. Pharmacol.* 386, 135–154. doi: 10.1007/s00210-012-0817-0

Verney, C., Baulac, M., Berger, B., Alvarez, C., Vigny, A., and Helle, K. B. (1985). Morphological evidence for a dopaminergic terminal field in the hippocampal formation of young and adult rat. *Neuroscience* 14, 1039–1052. doi: 10.1016/0306-4522(85)90275-1

Vincent, S. L., Khan, Y., and Benes, F. M. (1993). Cellular distribution of dopamine D1 and D2 receptors in rat medial prefrontal cortex. *J. Neurosci.* 13, 2551–2564. doi: 10.1523/jneurosci.13-06-02551.1993

Volkow, N. D., Fowler, J. S., Wang, G. J., Swanson, J. M., and Telang, F. (2007). Dopamine in drug abuse and addiction: results of imaging studies and treatment implications. *Arch. Neurol.* 64, 1575–1579. doi: 10.1001/archneur.64.11.1575

von der Heyde, S., Sonntag, J., Kaschek, D., Bender, C., Bues, J., and Watcher, A. (2014). RPPanalyzer toolbox: an improved R package for analysis of reverse phase protein array data. *Biotechniques* 57, 125–135. doi: 10.2144/000114205

Wei, X., Ma, T., Cheng, Y., Huang, C. C. Y., Wang, X., Lu, J., et al. (2017). Dopamine D1 or D2 receptor-expressing neurons in the central nervous system. *Addict. Biol.* 23, 569–584. doi: 10.1111/adb.12512

Wigström, H., and Gustafsson, B. (1983). Facilitated induction of hippocampal long-lasting potentiation during blockade of inhibition. *Nature* 301, 603–604. doi: 10.1038/301603a0

Wilkerson, A., and Levin, E. D. (1999). Ventral hippocampal dopamine D1 and D2 systems and spatial working memory in rats. *Neuroscience* 89, 743–749. doi: 10.1016/s0306-4522(98)00346-7

Wong, D. F., Wagner, H. N., Tune, L. E., Dannals, R. F., Pearlson, G. D., Links, J. M., et al. (1986). Positron emission tomography reveals elevated D2 dopamine-receptors in drug-naive schizophrenics. *Science* 234, 1558–1563. doi: 10.1126/science.2878495

Yanagihashi, R., Yamanouchi, K., and Ishikawa, T. (1991). The effects of apomorphine on the hippocampal field potential in freely moving rats: pharmacological evidence of the involvement of D2 receptors. *Neuropharmacology* 30, 177–182. doi: 10.1016/0028-3908(91)90201-l

Yu, Q., Liu, Y. Z., Zhu, Y. B., Wang, Y. Y., Li, Q., and Yin, D. M. (2019). Genetic labeling reveals temporal and spatial expression pattern of D2 dopamine receptor in rat forebrain. *Brain Struct. Funct.* 224, 1035–1049. doi: 10.1007/s00429-018-01824-2

Yung, K. K., Bolam, J. P., Smith, A. D., Hersch, S. M., Ciliax, B. J., and Levey, A. I. (1995). Immunocytochemical localization of D1 and D2 dopamine receptors in the basal ganglia of the rat: light and electron microscopy. *Neuroscience* 65, 709–730. doi: 10.1016/0306-4522(94)00536-e

Conflict of Interest: The authors declare that the research was conducted in the absence of any commercial or financial relationships that could be construed as a potential conflict of interest.

frontiers
in Synaptic Neuroscience

ORIGINAL RESEARCH
published: 15 November 2019
doi: 10.3389/fnsyn.2019.00030

Differential Effect on Hippocampal Synaptic Facilitation by the Presynaptic Protein Mover

Julio S. Viotti and Thomas Dresbach*

Institute of Anatomy and Embryology, University Medical Center Göttingen, Georg-August University of Göttingen, Göttingen, Germany

Neurotransmitter release relies on an evolutionarily conserved presynaptic machinery. Nonetheless, some proteins occur in certain species and synapses, and are absent in others, indicating that they may have modulatory roles. How such proteins expand the power or versatility of the core release machinery is unclear. The presynaptic protein Mover/TPRGL/SVAP30 is heterogeneously expressed among synapses of the rodent brain, suggesting that it may add special functions to subtypes of presynaptic terminals. Mover is a synaptic vesicle-attached phosphoprotein that binds to Calmodulin and the active zone scaffolding protein Bassoon. Here we use a Mover knockout mouse line to investigate the role of Mover in the hippocampal mossy fiber (MF) to CA3 pyramidal cell synapse and Schaffer collateral to CA1. While Schaffer collateral synapses were unchanged by the knockout, the MFs showed strongly increased facilitation. The effect of Mover knockout in facilitation was both calcium- and age-dependent, having a stronger effect at higher calcium concentrations and in younger animals. Increasing cyclic adenosine monophosphate (cAMP) levels by forskolin equally potentiated both wildtype and knockout MF synapses, but occluded the increased facilitation observed in the knockout. These discoveries suggest that Mover has distinct roles at different synapses. At MF terminals, it acts to constrain the extent of presynaptic facilitation.

Keywords: synaptic transmission, short-term plasticity, hippocampus, CA3, mossy fiber, presynapse

Edited by:
Jean-Claude Lacaille,
Université de Montréal, Canada

Reviewed by:
Kurt Gottmann,
Heinrich Heine University Düsseldorf,
Germany
Wayne S. Sossin,
McGill University, Canada

****Correspondence:***
Thomas Dresbach
thomas.dresbach@
med.uni-goettingen.de

Received: *22 July 2019*
Accepted: *31 October 2019*
Published: *15 November 2019*

Citation:
Viotti JS and Dresbach T (2019)
Differential Effect on Hippocampal
Synaptic Facilitation by
the Presynaptic Protein Mover.
Front. Synaptic Neurosci. 11:30.
doi: 10.3389/fnsyn.2019.00030

INTRODUCTION

The molecular machinery mediating neurotransmitter release is strongly conserved throughout evolution: Ca^{2+} triggers exocytosis of neurotransmitter from synaptic vesicles (SVs) in less than a millisecond by binding to Synaptotagmin, which together with Complexins activates a core fusion machinery composed of SNAREs and SV proteins (Südhof, 2013). These events are confined to specialized sites of the presynaptic plasma membrane, called active zones, by a network of proteins including RIMs, RIM binding proteins, Munc13s, α-liprins and CAST/ERC proteins. One of the ways by which these scaffolding molecules act is that RIMs recruit both calcium channels and Munc13s, which make SVs tethered at the active zone fusion competent (Südhof, 2012; Imig et al., 2014; Acuna et al., 2016). The physical and functional interactions of all these proteins represent an evolutionarily conserved machinery mediating regulated neurotransmitter release at active zones. The evolutionarily conserved Ca^{2+} binding proteins Calmodulin and Synaptotagmin-7 further refine the machinery by regulating presynaptic plasticity such as short-term depression and short-term enhancement to transmitter release (Junge et al., 2004; Jackman et al., 2016).

Piccolo/Aczonin and Bassoon are particularly large active zone scaffolding molecules, consisting of approximately 5000 and 4000 amino acids, respectively (Cases-Langhoff et al., 1996; tom Dieck et al., 1998; Wang et al., 1999). Piccolo is evolutionarily related to RIM (Bruckner et al., 2012) and shares 10 Piccolo-Bassoon homology regions with Bassoon (tom Dieck et al., 1998; Gundelfinger et al., 2016). Piccolo and Bassoon do not seem to be essential for the process of transmitter release (Hallermann et al., 2010; Mukherjee et al., 2010; Mendoza Schulz et al., 2014; Butola et al., 2017; Parthier et al., 2018), but maintain synaptic integrity by reducing the degradation of presynaptic molecules by proteasomes and autophagy (Waites et al., 2013; Okerlund et al., 2017). As scaffolding proteins that appear very early at nascent active zones and bind a large number of proteins they may also act to recruit regulatory molecules to active zones (Fejtova and Gundelfinger, 2006; Schoch and Gundelfinger, 2006; Gundelfinger et al., 2016).

In a yeast-2-hybrid assay we identified the SV phosphoprotein Mover – also called SVAP-30 and TPRGL (Burré et al., 2006; Antonini et al., 2008) – as a binding partner for Bassoon (Kremer et al., 2007; Ahmed et al., 2013). Mover is a small, 266 amino acid, protein that does not appear to have orthologs in the nematode *Caenorhabditis elegans* and the fruit fly Drosophila, suggesting that it is not required for the basic functions of the transmitter release machinery. In the rodent brain, its distribution is remarkably heterogeneous. For example, inhibitory synapses in the hippocampal CA3 region lack Mover, while excitatory synapses in the same region contain Mover (Kremer et al., 2007). Quantitative analysis revealed that the levels of Mover relative to the number of SVs vary among synapses throughout the brain (Wallrafen and Dresbach, 2018). These observations suggest that Mover may perform regulatory functions at certain synapses. To test how the absence of Mover affects synaptic transmission, we investigated two different hippocampal synapses. We assumed that synapse function would not be abolished, but a modulatory role would emerge. We found that the absence of Mover affects short-term plasticity in the hippocampal CA3 but not in CA1. We show that this effect is age- and Ca^{2+}-dependent, and interacts with the cyclic adenosine monophosphate (cAMP) pathway in the mossy fiber (MF) synapses.

MATERIALS AND METHODS

KO Generation, Genotyping, and Confirmation

All animal experiments were performed in accordance with the guidelines for the welfare of experimental animals issued by the State Government of Lower Saxony, Germany. All mice (*Mus musculus*) were bred and maintained at the central animal facility of the University Medical Center, Göttingen. Embryonic stem cells (129/Ola) harboring the recombined Mover locus were generated by PolyGene (Switzerland), and injected into blastocysts. Mice with the targeted locus were crossed with a Flp deleter line to remove the Neo cassette. The resulting conditional knockout mice were crossed with mice expressing Cre recombinase under the E2A promoter to generate a global Mover knockout (Akula et al., 2019). Knockout (KO) animals were compared to their wildtype (WT) littermates.

Mice were routinely genotyped by PCR using genomic DNA extracted from tail biopsies using a DNA extraction kit from NextTec (Germany). For amplification the following oligonucleotide primers were used: forward primer P1 (5′-CCAATCACAAGGCGAACGAG-3′); forward primer P2 (5′-CATTCAGTGGGACAAGCAGA-3′); reverse primer P3 (5′-CTTGGATCAGGAGAGCCTTG-3′). The PCR reaction was carried out for 40 cycles with denaturation at 95°C for 30 s, annealing at 56°C for 1 min, and extension at 72°C for 1 min. WT and KO animals were identified by the presence of a specific 867 bp and a 697 bp band, respectively. Initially, the KO was verified by purifying and sequencing the 697 bp band.

For immunohistochemical confirmation of the knockout of Mover, mice were perfused with 4% paraformaldehyde and had their hippocampi sectioned with 50 μm thickness. Commercially available anti-Mover and anti-Synaptophysin antibodies (Synaptic Systems, Germany) were used in combination with Cy2 and Cy5 secondary antibodies (Dianova, Germany). Stainings were visualized by epifluorescence through an Observer Z1 inverted microscope (Zeiss, Germany).

Slice Preparation and Electrophysiology

Acute transverse hippocampal slices 400 μm thick were prepared from male and female 18–22 days old mice unless otherwise noted. Hippocampi were isolated and cut in a Thermo Scientific HM650V vibratome in a cutting solution containing (in mM): 215 sucrose, 2.5 KCl, 20 glucose, 26 $NaHCO_3$, 1.6 NaH_2PO_4, 1 $CaCl_2$, 4 $MgCl_2$, and 4 $MgSO_4$. After sectioning, the slices were incubated for 30 min in a solution comprised of 50% cutting solution and 50% recording solution, which contained (in mM): 124 NaCl, 2.5 KCl, 26 $NaHCO_3$, 1 NaH_2PO_4, 2.5 $CaCl_2$, 1.3 $MgSO_4$, and 10 glucose; 300 mOsm/kg. Recording solution for whole-cell patch clamp recordings, was comprised of (in mM): 119 NaCl, 2.5 KCl, 26 $NaHCO_3$, 1 NaH_2PO_4, 4 $CaCl_2$, 4 $MgSO_4$, and 10 glucose; 300 mOsm/kg. After the aforementioned 30 min incubation, the mixed solution was changed to 100% recording solution. After changing of solution, slices were incubated for at least 60 min at room temperature. All solutions were continuously gassed with carbogen (95% O_2, 5% CO_2) and were recorded at 27 ± 0.2^oC.

Excitatory post synaptic potentials (EPSPs) and receptor excitatory postsynaptic currents (EPSCs) were recorded using a HEKA EPC-10 amplifier connected to a chlorided silver wire in a borosilicate glass pipette. Recording pipettes had 0.5–1.5 MΩ pipette resistance and were filled with 1 M NaCl for extracellular recordings, and 2.0–4.0 MΩ for whole-cell recordings with a solution containing (in mM): 123 Cs-gluconate, 8 NaCl, 10 HEPES, 10 Glucose, 10 BAPTA, 5 ATP-Mg, 0.4 GTP-Na; 300 mOsm/kg, pH 7.2. Stimulation of axons was delivered through a patch-type pipette connected to either a Model A395 linear stimulus isolator (World Precision Instruments) or a Model DS3 isolated current stimulator (Digitimer).

Schaffer collateral responses were recorded at the stratum radiatum of the CA1, with the stimulation electrode placed rostral to the recording electrode. Mossy fiber field EPSPs (fEPSPs) were recorded in the stratum lucidum of the hippocampus, whereas whole-cell recordings were performed by patching CA3 pyramidal cells. In both cases the MFs were stimulated at the border between the dentate gyrus and the hilus. At the end of each MF experiment, the group II metabotropic glutamate receptor agonist DCG-IV (2S,20R,30R-2-[20,30-dicarboxycyclo-propyl] glycine) was applied to the bath (1 μM) to selectively block MF responses (Kamiya et al., 1996). Recordings in which responses did not reduce by at least 80% were excluded from the analysis. For whole-cell recordings 100 μM picrotoxin was added to the solution to avoid inhibitory transmission. For each sample, every recording was repeated at least three times and traces were averaged. Data was sampled at 20 or 50 kHz and low-pass filtered at 2.9 kHz.

Experimental Design and Statistical Analysis

Electrophysiological data were analyzed using custom-written procedures in Igor Pro 6.3 (Wavemetrics). Statistical significance was tested using GraphPad Prism 7.04 (GraphPad Software). Two-way ANOVA tests were used to analyze high-frequency trains of stimulation. Extra sum-of-squares *F* test was used to test differences between curve fits. This statistical method was chosen due to its robustness in comparing two nested models and returning a *p*-value in response to whether one curve adequately fits both data sets or whether two different curves better describe the data (Motulsky and Christopoulos, 2003). For all other tests two-tailed Student's unpaired *T* test was used. For every experiment 3 or more animals were used. Results are reported as mean ± SEM whereas "n" refers to the number of slices recorded. Stimulation artifacts were digitally removed from electrophysiological traces for clarity.

RESULTS

To obtain a global knockout of Mover we bred Mover conditional knockout mice generated in the lab (Akula et al., 2019) with E2A-Cre mice. The E2A promoter drives Cre expression in the early mouse embryo, thus excising Mover in all cells from early embryonic stages on. The entire Mover gene consists of less than 4000 base pairs, including four exons and three introns (**Figure 1A**). We verified the expected excision of Mover exons 1, 2, and 3 by PCR (**Figure 1B**), and by sequencing the PCR product (**Figure 1C**). Western blotting revealed that Mover was not detected in hippocampal lysates from Mover knockout mice (**Figure 1D**). Likewise, there was no Mover immunofluorescence in sections of the hippocampus from Mover knockout mice (**Figure 1E**).

Mover Knockout Affects Mossy Fiber but Not Schaffer Collateral Synaptic Transmission

The absence of Mover in inhibitory synapses of the hippocampus (Wallrafen and Dresbach, 2018), together with its layered structure, makes it an ideal target to study the effect of Mover knockout in glutamatergic transmission. Recording of fEPSPs in the hippocampal CA1 with stimulation of the Schaffer collaterals (SC, **Figure 2A**) with increasing stimulation strength allows for an assessment of synaptic strength based on input–output curves. Input–output curves showed no difference in synaptic strength between WT and KO mice (**Figure 2B**).

To further probe changes in presynaptic transmission we evaluated short-term plasticity with three different protocols: paired-pulse facilitation with two pulses given at different inter-stimulus intervals (ISIs; **Figure 2C**), burst-induced facilitation with a 25 Hz train consisting of five stimuli (**Figure 2D**). In all protocols no differences between WT and KO were detected.

With no apparent differences in SC, we moved to investigate the CA3, more specifically the CA3 pyramidal cell inputs from MFs (**Figure 3A**). Mover was first observed to have high expression in the stratum lucidum, where MF form boutons with CA3 pyramidal cells (Kremer et al., 2007). However, we have recently shown that Mover is also strongly present in the stratum radiatum, where SC synapses are present (Wallrafen and Dresbach, 2018). MF boutons have very low release probability with particularly strong short-term plasticity effects (Nicoll and Schmitz, 2005) and would more easily reveal any possible changes in synaptic function in the absence of Mover.

Similarly to SC, input–output curves were unchanged by the absence of Mover (**Figure 3B**). However, a first assessment of the short-term plasticity parameters of MF KO already indicated a change in the absence of Mover: paired-pulse facilitation was slightly increased in KO synapses (**Figure 3C**), most pronouncedly at 40 ms ISI (p = 0.039, Extra-sum-of-squares *F* test).

These results were surprising considering that a previous report using whole-cell recordings found a reduced paired-pulse ratio in a knockdown of Mover at the calyx of Held (Körber et al., 2015). Therefore, to verify our finding we employed whole-cell patch clamp recordings from CA3 pyramidal cells. We initially characterized spontaneous activity onto the pyramidal cells in the presence of 1 μM tetrodotoxin (TTX) and 100 μM of the GABA receptor blocker picrotoxin, so that recordings comprised of only miniature EPSCs. Amplitude and frequency of miniature EPSCs were unchanged in the KO (**Figures 4A–D**). The kinetics of transmission, namely rise time and decay, were also comparable between WT and KO (**Figures 4E,F**).

With absence of changes in spontaneous synaptic activity in the CA3 pyramidal cells we set out to verify the change in facilitation observed in extracellular recordings using intracellular recordings. These recordings were also done in the presence of 100 μM picrotoxin to abolish possible biases introduced by inhibitory transmission. Because the CA3 is a highly auto-associative area (Hablitz, 1984; Traub et al., 1993) we took extra precautions to prevent polysynaptic inputs

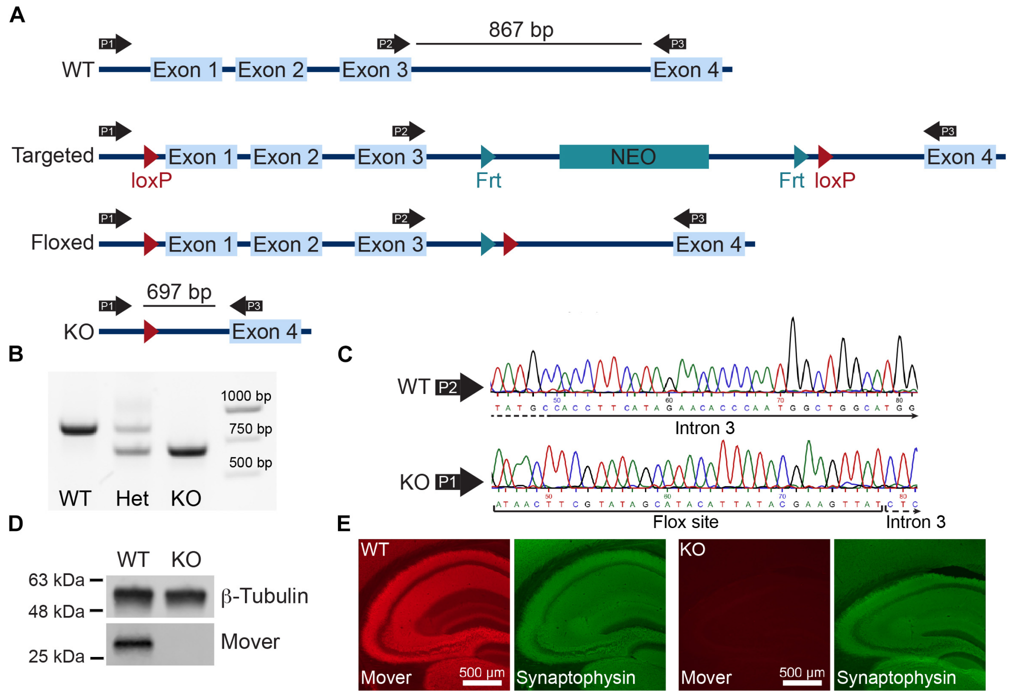

FIGURE 1 | Global knockout of Mover. **(A)** Gene targeting strategy for Mover KO mice. **(B)** Results of the PCR used for genotyping. Primers P1, P2, and P3 shown in panel **(A)** were always used in the same reaction. When a WT and a KO allele were present, P1 and P3 produce a 697 bp band, P2 and P3 produce a 867 bp band (lane "Het"). When only WT alleles are present the primers produce only the 867 bp band (lane "WT"), when only KO alleles are present the primers produce only the 697 (lane "KO"). **(C)** Example of sequencing results for WT (top) and KO (bottom). Examples shown start from nucleotide 45 from sequencing result and show a part of intron 3 using the primer P2 for WT and the flox site followed by intron 3 in KO, showing the absence of exons 1–3. **(D)** Western blot of lysates from dissected hippocampi from WT (left) and KO mice (right) probed for β-Tubulin and Mover. **(E)** Immunofluorescence of WT (left) and KO (right) mouse brain sections stained for Mover and Synaptophysin.

by blocking α-amino-3-5-methyl-4-isoxazolepropionic acid (AMPA) receptors with 10 μM of 2,3-dihydroxy-6-nitro-7-sulfamoylbenzo[f]quinoxaline-2,3-dione (NBQX). Therefore, the responses comprised of *N*-methyl-D-aspartate receptor EPSCs (NMDA-EPSCs).

The amplitude of single evoked NMDA-EPSCs did not vary between WT and KO (**Figure 5A**). Confirming the previous observation in extracellular recordings and adding to it, paired-pulse facilitation was increased across all ISIs tested (**Figure 5B**, $p = 0.016$, Extra-sum-of-squares *F* test). This confirmed the change in short-term plasticity observed with extracellular recordings.

Mover Strongly Affects Release Upon Repetitive Stimulation

One of the hallmarks of MF is the ability to strongly facilitate, not only during a paired-pulse protocol, but also during repetitive stimulation under a vast range of frequencies (Nicoll and Schmitz, 2005). We therefore proceeded to analyze the effect of Mover deletion on responses upon repetitive stimulation, which could make the effects of the deletion even more prominent.

Trains of five stimuli at 25 Hz with extracellular recordings elicited a strong facilitation in both WT and KO MF. However, KO MF had even stronger facilitation than WT ($p = 0.0004$, two-way ANOVA), reaching more than a 10-fold increase in fEPSP amplitude (**Figure 6A**).

An increase in synaptic transmission in response to increasing stimulation frequencies, even at low frequencies, is a hallmark of MF facilitation, often referred as frequency facilitation (Nicoll and Schmitz, 2005). Using low-frequency stimulation led to similar enhanced facilitation of KO responses: change from frequency of stimulation from 0.05 to 0.2 Hz led to KO responses 30% stronger than WT (**Figure 6B**, $p = 0.0007$). Further increasing the frequency of stimulation to 0.5 Hz led to KO responses to facilitate 40% more than WT ($p < 0.0001$).

Furthermore, we probed the paired-pulse facilitation elicited by stimulation of an ISI of 40 ms, repeated with a waiting time of either 20 s (0.05 Hz), 5 s (0.2 Hz), or 2 s (0.5 Hz), i.e., the frequencies described in the previous experiment. Because both frequency facilitation and paired-pulse ratio depend on the residual calcium inside the presynaptic terminal we expected that the two would interact negatively, i.e., as frequency facilitation rises, paired-pulse ratio would decrease; and Mover should still affect paired-pulse ratio. Indeed, as expected, paired-pulse ratios were smaller at higher frequencies and the absence of Mover increase paired-pulse ratio on frequencies 0.05 (**Figure 6C**, $p = 0.042$) and 0.2 Hz ($p = 0.046$).

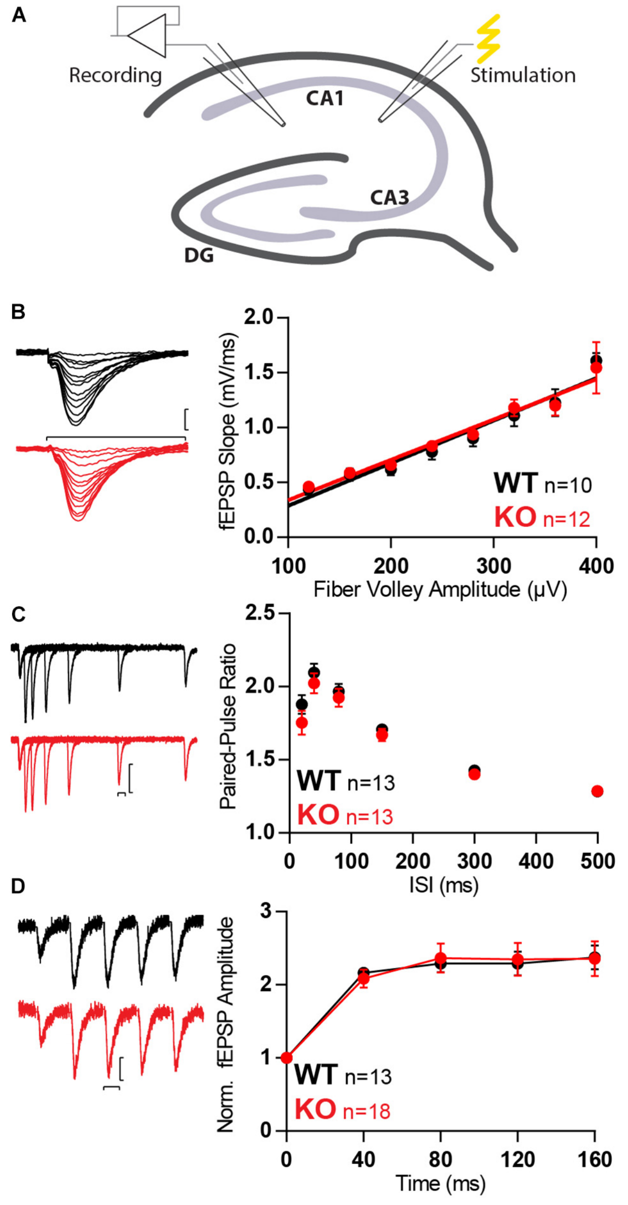

FIGURE 2 | Synaptic transmission is unchanged in SC in absence of Mover. **(A)** Diagram representing stimulation of Schaffer collaterals and extracellular recording at stratum radiatum of the CA1. **(B)** Example traces (left) and quantification (right) of fEPSP slopes versus fiber volley amplitude recorded at increasing stimulation strengths depicts an input–output relationship unchanged by the absence of Mover. **(C)** Paired-pulse ratios recorded from fEPSP amplitudes across varying inter-stimulus intervals show no difference between WT and KO. **(D)** Normalized responses to a 25 Hz train of stimulation showed unchanged facilitation in KO MF when compared to WT. Scale bars: vertical = 250 μV, horizontal = 20 ms. Error bars indicate SEM. WT n = 10–13; KO n = 12–18.

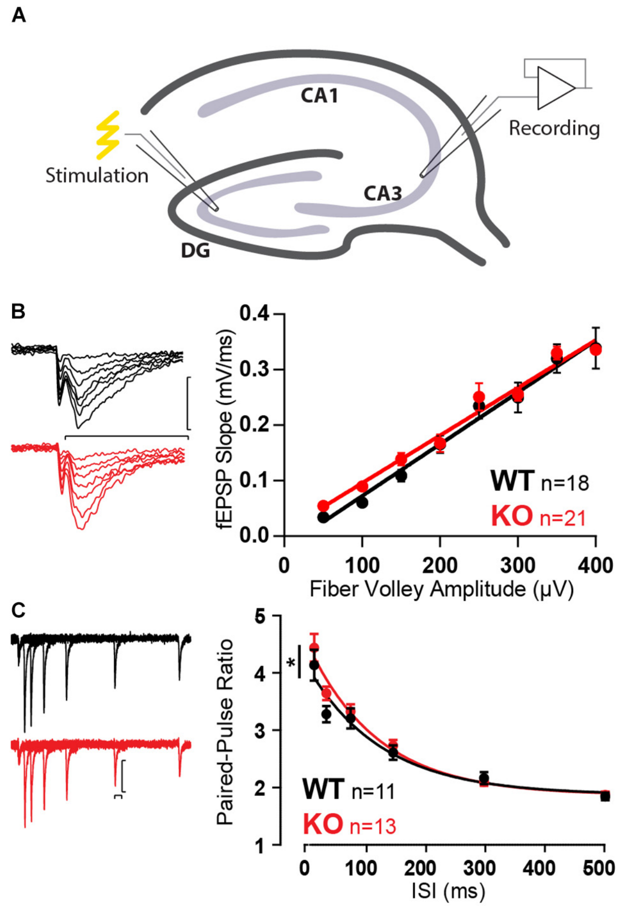

FIGURE 3 | Increased paired-pulse ratio in MF in absence of Mover. **(A)** Diagram representing stimulation of mossy fibers and extracellular recording in the stratum lucidum of the CA3. **(B)** Example traces (left) and quantification (right) of fEPSP slopes versus fiber volley amplitude recorded at increasing stimulation strengths depicts an input–output relationship unchanged by the absence of Mover. **(C)** Paired-pulse ratios recorded from fEPSP amplitudes across varying inter-stimulus intervals reveal increased facilitation in KO when compared to WT. Scale bars: vertical = 250 μV, horizontal = 20 ms. Error bars indicate SEM. MF WT n = 11–18; KO n = 13–22. $^*p < 0.05$.

Because of this recent evidence of its influence on MF short-term facilitation and previous evidence of its influence in calcium-sensitivity of release (Körber et al., 2015), we decided to investigate whether there is a calcium-dependency of Mover effects on synaptic release. And since residual calcium is changed in MF with age (Mori-Kawakami et al., 2003) we decided to investigate the effect of the KO in older animals.

Mover Affects MF Facilitation Under High Calcium Conditions

The extent of facilitation in MF is known to reduce with age (Mori-Kawakami et al., 2003). Hence, to further explore the effect of the absence of Mover we analyzed the effect of MF stimulation in older mice (8-week old) with different extracellular calcium concentrations. The change in calcium concentration was compensated with magnesium, to keep the concentration of divalent ions constant.

Firstly, increasing the concentration of calcium from 1.25 to 2.5 mM and further to 3.5 mM led to an increase in fEPSP amplitude. This increase was similar when comparing WT and KO responses (**Figure 7A**).

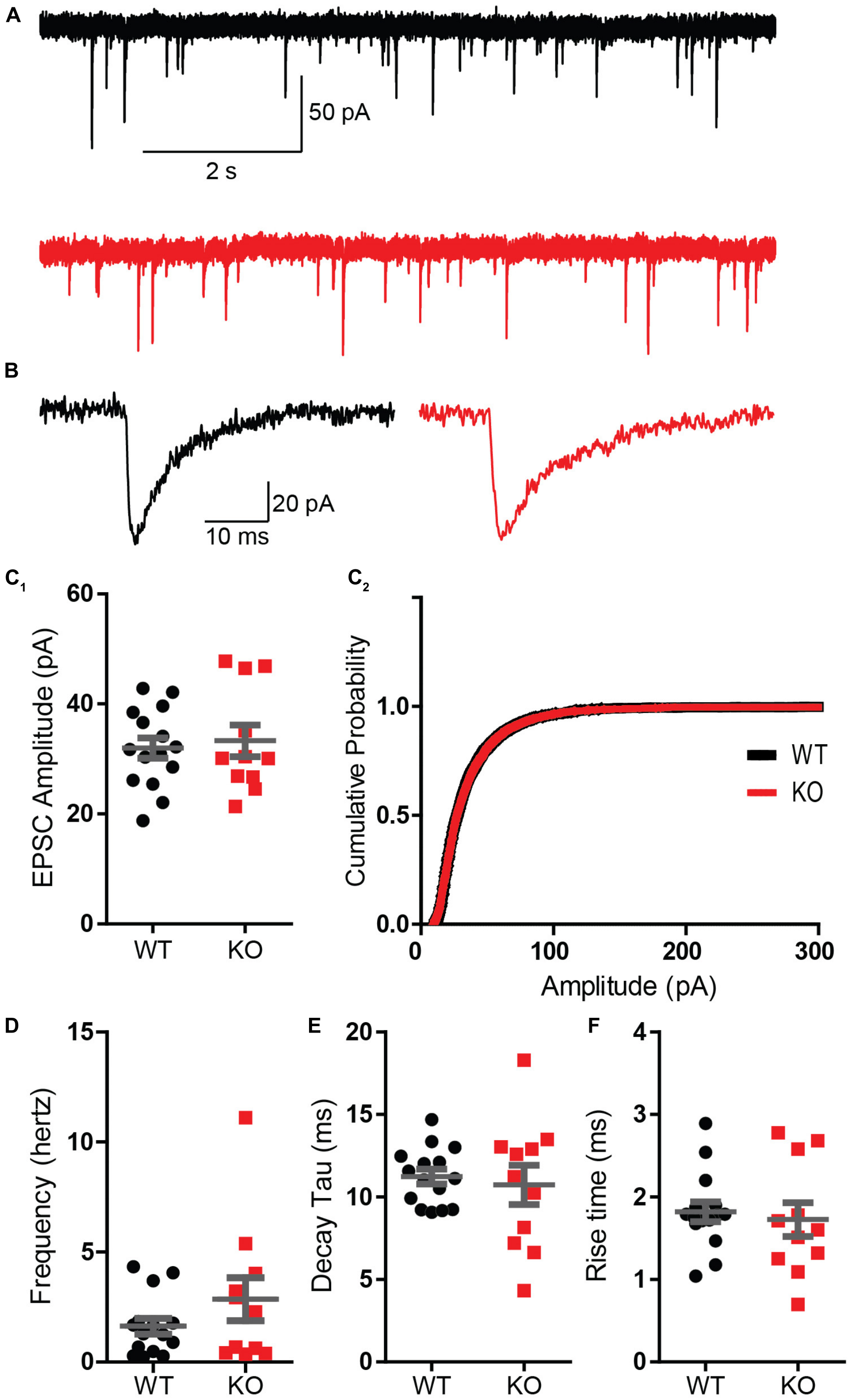

FIGURE 4 | Absence of Mover does not interfere with miniature EPSC parameters in CA3 pyramidal cells. **(A)** Representative traces from WT (gray) and KO (red) CA3 pyramidal cells under presence of 1 μM TTX. **(B)** Representative miniature EPSC waveform from traces in A. **(C)** Amplitudes of miniature EPSC events were unchanged in their average amplitude **(C_1)** and in their cumulative probability **(C_2)**. **(D)** Frequency of events was not changed by the absence of Mover. Miniature EPSC kinetics, namely the time constant of decay **(E)** and the 10–90 rise time **(F)**, showed no difference between WT and KO. Error bars indicate SEM. WT *n* = 15; KO *n* = 11.

When testing the previously used short-term plasticity protocols, at 1.25 mM Ca^{2+} the extent of facilitation did not differ between WT and KO anymore (**Figure 7B**). Surprisingly, after increasing Ca^{2+} to 2.5 mM, WT and KO continued to facilitate to the same extent (**Figure 7C**), whereas the same calcium concentration in 3 week-old animals promoted a stronger

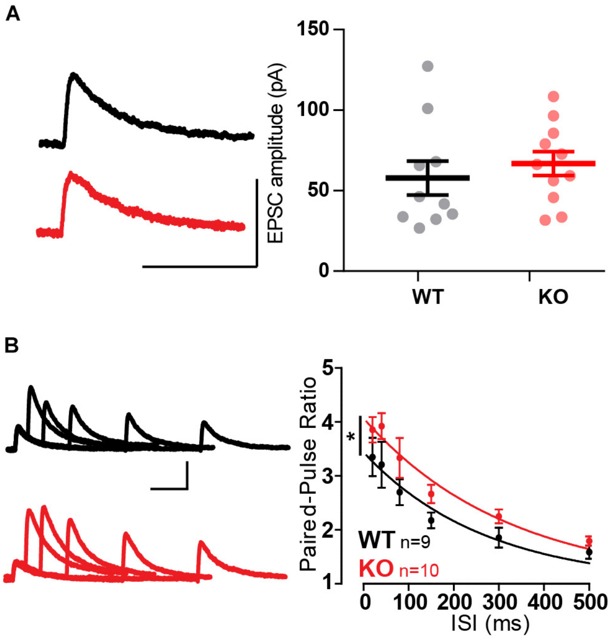

FIGURE 5 | Whole-cell recordings confirm increased paired-pulse ratio in MF-CA3 pyramidal cells in Mover KO. **(A)** Example traces and quantification of single evoked NMDA EPSCs had similar amplitude between WT and KO. **(B)** Paired-pulse ratios recorded from NMDA EPSC amplitudes across varying inter-stimulus intervals show increased ratios in KO pyramidal cells. Scale bars: vertical = 100 pA, horizontal = 100 ms. Error bars indicate SEM. WT *n* = 9; KO *n* = 10. $^{*}p < 0.05$.

facilitation in MF KOs (**Figures 6A,B**). This reveals an age-dependency of the effect that Mover has on facilitation.

When further increasing Ca^{2+} concentration to 3.5 mM, the difference in the extent of facilitation between KO and WT becomes obvious again for both high-frequency (**Figure 7D$_2$**; $p = 0.04$) and low-frequency facilitation (**Figure 7D$_1$**; 0.05 Hz vs. 0.2 Hz: $p = 0.04$; 0.05 Hz vs. 0.5 Hz: $p = 0.03$). The KO responses facilitate more than WT, corroborating what was observed in younger animals and the idea that Mover acts in a calcium-dependent manner.

Forskolin Occludes the Boost in Facilitation Observed in KO

Synaptic plasticity in MF is known to be strongly tied to intracellular levels of cAMP and is, therefore, subject to regulation by forskolin (Weisskopf et al., 1994). Hence, since both forskolin and Mover strongly affect plasticity in MF we decided to investigate if Mover acts in the cAMP pathway.

We anticipated that, if Mover participates in this pathway and is involved in the potentiation caused by forskolin, we would observe changes in the degree of potentiation between WT and KO. However, application of forskolin led to a similar potentiation of WT and KO fEPSPs, suggesting that Mover is not necessary forskolin-driven potentiation. On the other hand, after forskolin potentiation we observed a lack of difference between WT and KO low- and high-frequency facilitation (**Figures 8A,B**).

This lack of a KO effect in facilitation after forskolin potentiation contrasts with the increased facilitation we observed in the absence of forskolin (**Figures 6A,B**, also in **Figure 8B** for comparison). Therefore, potentiation by forskolin occluded the increase in facilitation observed in the KO. These results suggest that Mover interacts with the cAMP pathway in MF, dampening facilitation in situations of high activity.

DISCUSSION

Mover is a synaptic vesicle protein with a remarkably heterogenous expression pattern in the rodent brain (Wallrafen and Dresbach, 2018). In addition, *C. elegans* and Drosophila lack Mover related genes. Thus, Mover is not essential for synaptic transmission. Instead, it may modulate neurotransmitter release at certain synapses, contributing to synaptic heterogeneity. To test whether Mover has a role in transmitter release we analyzed a mouse-line lacking Mover. We found that the knockout of Mover affects short-term synaptic plasticity in the hippocampal MFs but not in the downstream synapses, i.e., SC. Paired-pulse ratio and responses to train of stimulation led to stronger facilitation in MF terminals in the absence of Mover. In particular, frequency facilitation, a hallmark of presynaptic plasticity at MF terminals (Nicoll and Schmitz, 2005), was strongly increased in Mover knockout mice. This increased facilitation was stronger in younger animals and in situations of high calcium concentration, and was occluded by increasing cAMP levels.

Mover Has Synapse-Specific Effects on Neurotransmitter Release

The increase in paired-pulse facilitation in KO MF can be explained by a reduction in synaptic vesicle release probability, because of the inverse relationship between the two (Zucker and Regehr, 2002). The change in MF contrasts with the absence of changes in release in KO SC. Curiously, despite the lack of the effect of the KO in SC, Mover concentration in WT mice is known to be higher in the area of SC synapses than that of MF synapses (Wallrafen and Dresbach, 2018), so the effect of Mover on synaptic release does not seem to scale with its concentration. To add to the heterogeneity of Mover function, a study in the calyx of Held described an increase in release probability in a knockdown of Mover in the calyx of Held (Körber et al., 2015). The contrasting results between the calyx of Held and MF could arise from the different approach (knockdown vs. knockout) or from the different species (rat vs. mouse). However, when seen in combination with the lack of changes in SC, a hypothesis arises: Mover has synapse-specific effects. The synapse-specific way in which Mover seems to regulate transmission could add heterogeneity to the ubiquitous functions of the transmitter release machinery. In addition, we speculate that at certain synapses, i.e., at MF and the calyx of Held, the differential action of Mover could have a common effect in constraining synaptic strength. MF transmission relies heavily on facilitation for efficient information transfer and is, therefore, considered a "conditional detonator" (Vyleta et al., 2016). We have shown that Mover constrains facilitation in this synapse,

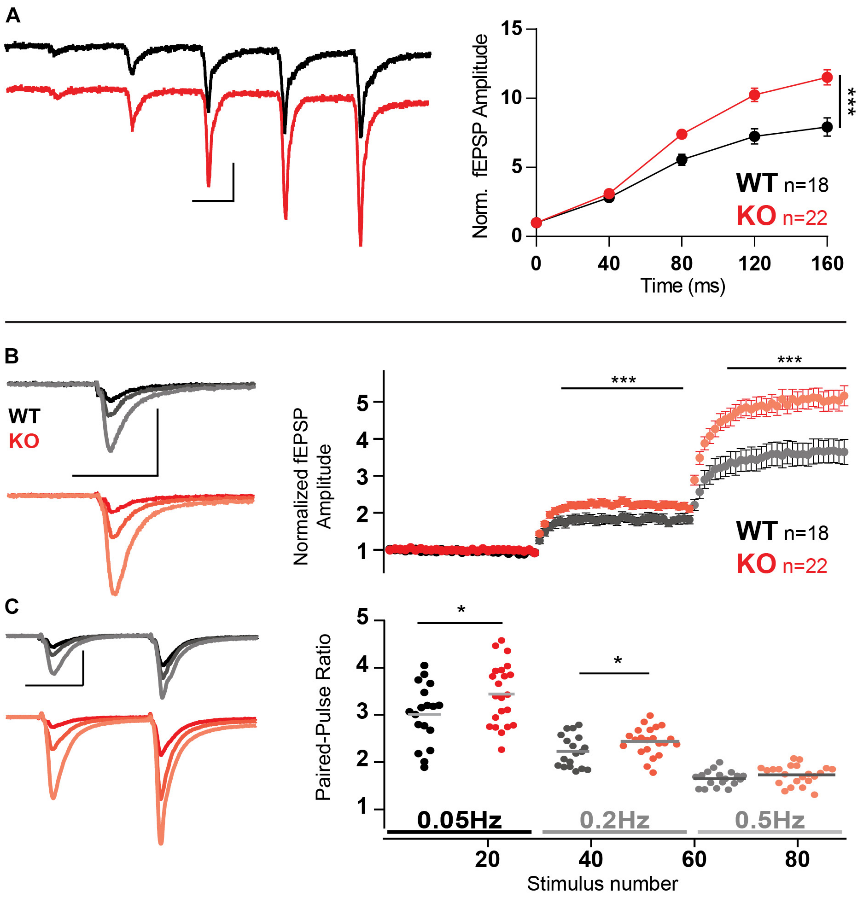

FIGURE 6 | Increased facilitation in MF in the absence of Mover. **(A)** Example traces and normalized responses to 25 Hz trains of stimulation showed increased facilitation in KO MF when compared to WT. **(B)** Normalized responses to stimuli delivered at 0.05, 0.2, and 0.5 Hz reveal increased facilitation in KO MF. Responses were normalized to the amplitude of the first fEPSP. **(C)** Paired-pulse ratio with an inter-stimulus interval of 40 ms using the same stimulation frequencies as above (0.05, 0.2, and 0.5 Hz, see text). Scale bars: vertical = 500 μV, horizontal = 20 ms. Error bars indicate SEM. SC WT n = 10–13; SC KO n = 12–18; MF WT n = 18; KO n = 22. $^{*}p < 0.05$; $^{***}p < 0.001$.

possibly keeping detonation within physiological range. On the other hand, Mover reduces the amplitude of the first response to a train of stimuli and subsequent depression in a synapse where this initial response is vital for transmission of fast and reliable auditory information, the calyx of Held (Englitz et al., 2009; Körber et al., 2015). Thus, in general, Mover could have the potential to act as a buffer for synaptic strength. Further experiments to test this in different synapses and to elucidate the mechanism of action of Mover could help prove or disprove such a hypothesis.

Such a differential effect on synaptic release in different synapses is not exclusive to Mover. For example, a similar synapse-specific effect on hippocampal synaptic transmission and plasticity was previously observed with the priming protein Munc13-2, where deletion of this protein led to increased facilitation and lower release probability in MF but not in SC (Breustedt et al., 2010). In the case of Munc13-2, the mechanism through which it affects neurotransmitter release is more straightforward since the Munc13 proteins are known to be vesicle priming factors (Augustin et al., 1999; Varoqueaux et al., 2002). Alternatively, Mover may affect facilitation directly – with or without affecting release probability – in a similar way like the calcium sensor protein Synaptotagmin 7 (Jackman et al., 2016). In this case, however, Mover would be acting as an inhibitor of facilitation, i.e., in the opposite direction compared to Synaptotagmin 7, which increases facilitation. In any case, Mover seems to be under the influence of Ca^{2+}, as discussed below (see section "Ca^{2+} Dependency of Mover Action").

Calcium Dependency of MF Plasticity: Technical Considerations

Synaptic facilitation is largely dependent on free or bound residual Ca^{2+} in the presynaptic terminal (Zucker and Regehr, 2002; Jackman and Regehr, 2017). One exception to this is the activity-dependent release of polyamine blocks in AMPA receptors (Rozov and Burnashev, 1999), but it is not present in MF to CA3 pyramidal synapses (Toth et al., 2000). Facilitation at MF-CA3 synapse is closely correlated with the concentration of Ca^{2+} in the presynaptic terminal (Regehr et al., 1994) and

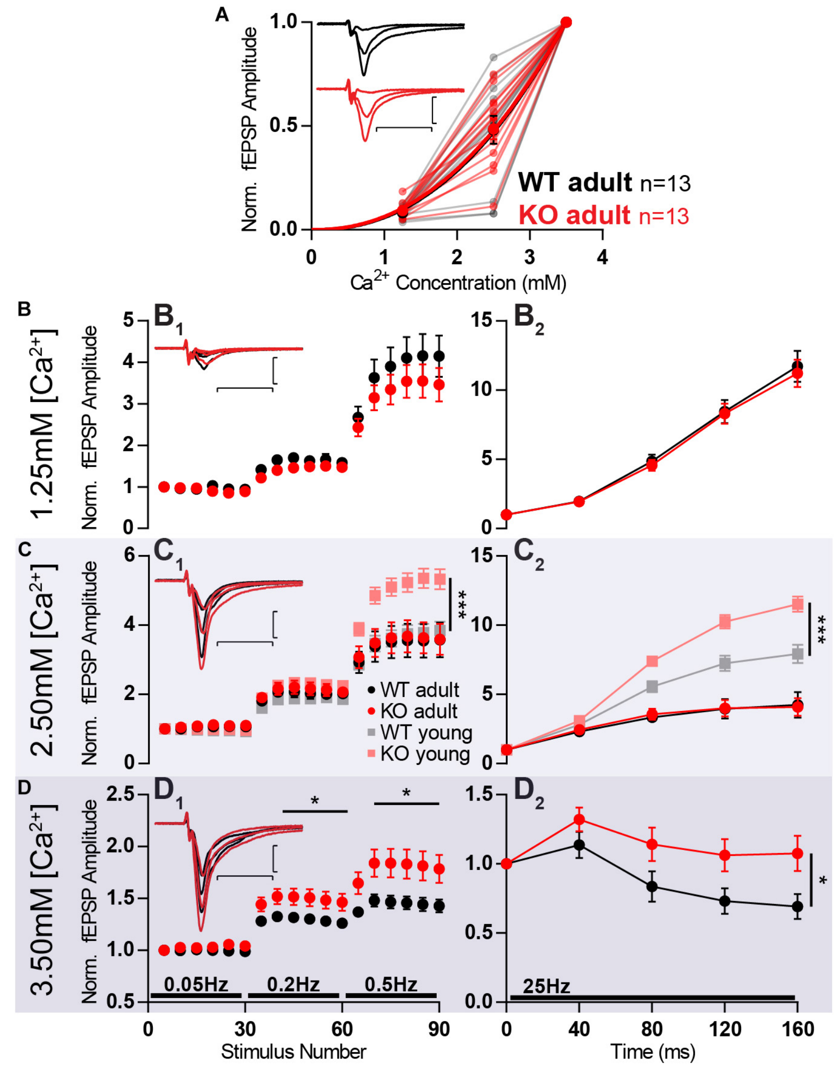

FIGURE 7 | Increased facilitation in KO is age- and calcium-dependent. MF of 8-week old animals KO (KO adult) has stronger facilitation than WT (WT adult) only in high extracellular calcium concentration. **(A)** Increasing calcium concentration leads to similar baseline responses in WT and KO. Responses were normalized to fEPSP amplitudes at 3.5 mM Ca^{2+}. **(B–D)** Short-term plasticity at different extracellular calcium concentrations. **(B_1)** Normalized responses to stimuli delivered at 0.05, 0.2, and 0.5 Hz at 1.25 mM extracellular calcium. **(B_2)** Normalized responses to a 25 Hz train of stimulation at 1.25 mM extracellular calcium. **(C_1)** Normalized responses to stimuli delivered at 0.05, 0.2, and 0.5 Hz at 2.5 mM extracellular calcium, in four different conditions: 8-week old WT (adult), 8-week old KO (adult), 3-week old WT (WT young), and 3-week old KO (KO young). The last two conditions are the same dataset as presented in **Figures 6A,B**. **(C_2)** Normalized responses to a 25 Hz train of stimulation at 2.5 mM extracellular calcium. **(D_1)** Normalized responses to stimuli delivered at 0.05, 0.2, and 0.5 Hz at 3.5 mM extracellular calcium. **(D_2)** Normalized responses to a 25 Hz train of stimulation at 3.5 mM extracellular calcium. **(B_1,C_1,D_1)** Each dot represents the average response to five consecutive stimuli. **(B–D)** Responses were normalized to the amplitude of the first fEPSP. (**Insets**) Representative traces from WT (*black*) and KO (*red*) hippocampi. Scale bars: vertical = 1 mV, horizontal = 10 ms. Error bars indicate SEM. WT adult n = 13; KO adult n = 13. *$p < 0.05$; ***$p < 0.001$.

happens over a wide range of frequencies (Salin et al., 1996), which we also observed in our experiments.

Different mechanisms have been proposed to explain the relationship between Ca^{2+} and facilitation at this synapse. First, the presence of calcium buffers coupled with a loose coupling between Ca^{2+} channels and Ca^{2+} sensors (Blatow et al., 2003; Vyleta and Jonas, 2014) could act in a way that repeated stimulation could saturate the buffers and allow for a stronger presence of available Ca^{2+} to act on the release sensor. Another proposed mechanism is the presence of a second Ca^{2+} sensor, a "facilitation sensor," with high affinity and slow kinetics, which would remain bound to calcium after the action potential-evoked calcium transient. In Jackman et al. (2016) proposed that this sensor is Synaptotagmin 7 as the KO of Synaptotagmin 7 shows a dramatic reduction on the degree of MF facilitation. Other mechanisms that could underlie facilitation at MF-CA3 synapse include distinct contribution from different Ca^{2+} channel types (Chamberland et al., 2017), modulation by adenosine receptors (Moore et al., 2003; Gundlfinger et al., 2007a; Klausnitzer and Manahan-Vaughan, 2008), by Kainate

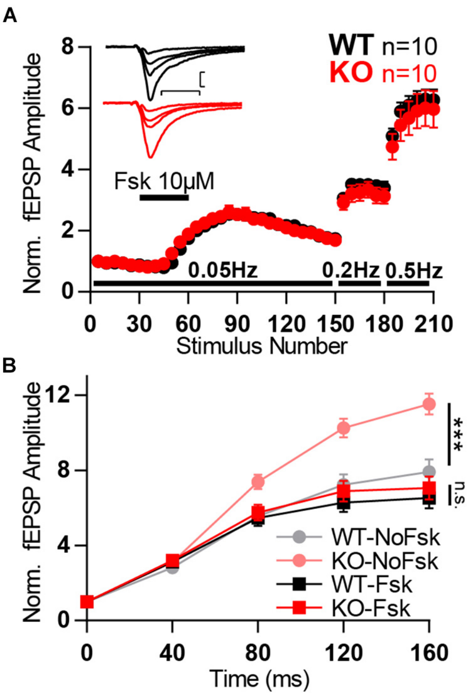

FIGURE 8 | Forskolin potentiation occlude KO boost in facilitation.
(A) Normalized MF fEPSP amplitudes during the time course of experiment in which forskolin (*fsk*, 10 μM) is applied for 10 min and frequency of stimulation is changed from 0.05 to 0.2 and further to 0.5 Hz. Each data point corresponds to the average response to five consecutive stimuli. (Inset) Representative traces from WT (*black*) and KO (*red*) hippocampi.
(B) Normalized MF responses to a 25 Hz train of stimulation in four different conditions: WT without forskolin application (WT-NoFsk), KO without forskolin application (KO-NoFsk), WT after forskolin potentiation (WT-Fsk), and KO after forskolin potentiation (KO-Fsk). The first two conditions are the same dataset as present in **Figure 6B**. Responses were normalized to the amplitude of the first response. Scale bars: vertical = 200 μV, horizontal = 10 ms; WT n = 10; KO n = 10. Error bars indicate SEM. n.s.: not significant; $^{***}p < 0.001$.

receptors (Lauri et al., 2001; Schmitz et al., 2001; Breustedt and Schmitz, 2004) often in connection with increased Ca^{2+} influx or Ca^{2+} release from internal stores (Kamiya et al., 2002; Lauri et al., 2003; Scott and Rusakov, 2006; Scott et al., 2008) and the CaM and/or adenylyl cyclase pathways (Salin et al., 1996; Wang et al., 2003; Rodríguez-Moreno and Sihra, 2004; Andrade-Talavera et al., 2012).

The mechanisms that affect facilitation in response to high-frequency stimulation and low-frequency stimulation (frequency facilitation) greatly overlap. It has been previously described that both phenomena act on residual calcium and occlude each other (Salin et al., 1996). As in Salin et al. (1996), our work shows that increase of frequency facilitation led to a reduction in paired-pulse facilitation (**Figure 6**), suggesting that both processes operate under a common mechanism. Admittedly, due to the long-lasting nature of frequency facilitation, and different modulation between the two time ranges (Gundlfinger et al., 2007b), the involvement of intermediary biochemical processes that are independent of residual Ca^{2+} have been suggested (Nicoll and Schmitz, 2005; Sihra and Rodríguez-Moreno, 2013) possibly by acting in the CaM and cAMP pathways (Salin et al., 1996; Wang et al., 2003; Rodríguez-Moreno and Sihra, 2004; Andrade-Talavera et al., 2012). Nevertheless, manipulations affecting frequency facilitation but not facilitation in the millisecond range still need to be performed to decisively show a mechanistic difference between the two different time scales.

In order to study how Mover is affecting facilitation and its calcium-dependency we have used different extracellular Ca^{2+} concentrations, which influence the Ca^{2+} influx into the synaptic terminal and changes release probability. The increase in Ca^{2+} was compensated by a decrease in extracellular Mg^{2+} in the opposite direction. This way, the concentration of divalent ions was kept constant. This minimizes the possible voltage shifts that could occur due to changes in surface charge screening. Nevertheless, we cannot rule out that shifts could have occurred since Ca^{2+} produces a stronger shift in surface potential than Mg^{2+} (Hille, 2001). Other mechanisms through which changing extracellular Ca^{2+} concentrations can lead to changes in excitability include its binding to voltage-gated channels, blocking channel pores, through a G-protein coupled receptor called calcium-sensing receptor (CaSR) and through a calcium- and voltage-dependent cation channel called calcium homeostasis modulator 1 (Armstrong and Cota, 1990, 1991; Santarelli et al., 2007; Ma et al., 2012; Jones and Smith, 2016). In every case increased Ca^{2+} concentration leads to decreased excitability. On the other hand, the decrease of Mg^{2+} can also lead to consequences in neuronal transmission. Most notably, the reduction of Mg^{2+} concentration would lead to a reduced block on NMDA receptors (Nowak et al., 1984). The activation of NMDA receptors by glutamate in this situation would lead to stronger EPSCs with a slower decay. While the aforementioned effects may occur in our approach, we applied changes in $Ca^{2+}$and Mg^{2+} concentrations equally to both WT and KO samples. This way, even though excitability and synaptic responses would be altered when the Ca^{2+}/Mg^{2+} ratio is changed they should be comparable between WT and KO and should not interfere with the analysis done here.

It is also important to note that CA3 pyramidal cells form an auto-associative network through associational recurrent axonal collaterals that target other CA3 pyramidal cells (Hablitz, 1984; Traub et al., 1993; Nicoll and Schmitz, 2005). Such organization can lead to the situation where the cell being recorded shows responses, not to a MF input, but from the synaptic release from another pyramidal cell, which was activated by the stimulation. Therefore, di- or poly-synaptic contamination, or even contamination from direct stimulation of association/commissural fibers is common in CA3 recordings. We took the following precautions to ensure monosynaptic MF-CA3 pyramidal cell responses. Firstly, recordings were succeeded by application of DCG-IV, which selectively blocks MF responses (Kamiya et al., 1996). Therefore, recordings in which responses did not reduce by 80% were excluded from the analysis. Secondly, in whole-cell recordings NBQX was applied to the bath so that only NMDA receptor responses would occur. Because NMDA receptors are blocked by Mg^{2+} at resting potential polysynaptic responses are unlikely to occur (Weisskopf and Nicoll, 1995; Nicoll and Schmitz, 2005). Furthermore, the use of 4 mM Ca^{2+}

and Mg^{2+} during whole-cell recordings further ensures pure monosynaptic responses due to three factors: increased block of NMDA receptors at resting membrane potential, reduced release probability and hyperpolarization of neurons due to surface charge screening (Nowak et al., 1984; Hille, 2001). Such strategies are commonly used (Salin et al., 1996; Kwon and Castillo, 2008a,b; Kaeser-Woo et al., 2013) to ensure absence of contamination in recordings and better quality of recordings.

Ca^{2+} Dependency of Mover Action

How does Mover interact with calcium signaling or the release machinery? The amino acid structure of Mover does not reveal any canonical calcium binding domain (Kremer et al., 2007). Here we observe an occlusion of the KO effect after activation of adenylyl cyclase by forskolin, which suggests that Mover and adenylyl cyclase – or its product, cAMP – act in the same pathway. Activation of adenylyl cyclase has been shown to increase neurotransmitter release in MF (Weisskopf et al., 1994; Tzounopoulos et al., 1998; Rodríguez-Moreno and Sihra, 2004). cAMP has been shown to influence release in MF through its direct targets Epac2 (exchange protein directly activated by cAMP) and protein kinase A (Weisskopf et al., 1994; Rodríguez-Moreno and Sihra, 2004). One proposed way through which synaptic activity increases cAMP levels is by the activation of adenylyl cyclases 1 and 8 by CaM (Villacres et al., 1998; Wang et al., 2003; Sihra and Rodríguez-Moreno, 2013). Mover could participate in this pathway via its known CaM binding property (Körber et al., 2015; Akula et al., 2019). Further experiments would be necessary to test this hypothesis.

The participation of Mover in a Ca^{2+}-sensing pathway is corroborated by the observation that Mover affects MF plasticity differently under different extracellular calcium concentrations (**Figure 7**). This differential response indicates that there is a calcium-dependency of Mover action: it only influenced release in higher calcium concentrations.

The Ca^{2+}-dynamics in MF also seem to change with age. The knockout of Mover also did not show an effect on short-term plasticity in older mice under the same experimental conditions as juvenile mice (**Figure 7**). When comparing 3- and 9-week old mice Mori-Kawakami et al. (2003) show reduced paired-pulse ratios and frequency-dependent facilitation in older mice. This was attributed to a lower availability of residual Ca^{2+}. This lower Ca^{2+} concentration, in addition to the calcium-dependency of the effect of Mover explains the smaller effect of the KO in older animals. It is also possible to assume that homeostatic plasticity could have played a stronger role in the older mice and, therefore, reduced the consequences of the absence of Mover. Nonetheless, the exact mechanism through which Mover acts to, most likely indirectly, sense intracellular Ca^{2+} levels and influence release will be the object of future studies.

DATA AVAILABILITY STATEMENT

The datasets generated for this study are available on request to the corresponding author.

ETHICS STATEMENT

The animal study was reviewed and approved by the Tierschutzkommission der Universitätsmedizin Göttingen.

AUTHOR CONTRIBUTIONS

JV performed the research, analyzed the data, designed the experiments, and wrote the manuscript. TD designed the experiments and wrote the manuscript.

FUNDING

This study was supported by the DFG Center for Nanoscale Microscopy and Molecular Physiology of the Brain (CNMPB, B1-1 to TD), as well as by the Excellence fellowship (DFG Grant GSC 226/1) provided by the Göttingen Graduate School for Neurosciences, Biophysics and Molecular Biosciences (GGNB to JV).

ACKNOWLEDGMENTS

We would like to thank Irmgard Weiß for expert technical assistance. We would also like to thank Thomas J. Younts and Yoav Ben-Simon for help with the electrophysiological recordings as well as Tobias Moser for kindly providing Cs-gluconate and many fruitful discussions. Some of the results presented here have been released as a Pre-Print at Viotti et al. (2019).

REFERENCES

Acuna, C., Liu, X., and Südhof, T. C. (2016). How to make an active zone: unexpected universal functional redundancy between RIMs and RIM-BPs. *Neuron* 91, 792–807. doi: 10.1016/j.neuron.2016.07.042

Ahmed, S., Wittenmayer, N., Kremer, T., Hoeber, J., Kiran Akula, A., Urlaub, H., et al. (2013). Mover is a homomeric phospho-protein present on synaptic vesicles. *PLoS One* 8:e63474. doi: 10.1371/journal.pone.0063474

Akula, A. K., Zhang, X., Viotti, J. S., Ebrecht, R., Reim, K., Wouters, F., et al. (2019). The Calmodulin binding region of the synaptic vesicle protein mover is required for homomeric interaction and presynaptic targeting. *Front. Mol. Neurosci.* 12:249. doi: 10.3389/fnmol.2019.00249

Andrade-Talavera, Y., Duque-Feria, P., Negrete-Díaz, J. V., Sihra, T. S., Flores, G., and Rodríguez-Moreno, A. (2012). Presynaptic kainate receptor-mediated facilitation of glutamate release involves Ca2+-calmodulin at mossy fiber-CA3 synapses. *J. Neurochem.* 122, 891–899. doi: 10.1111/j.1471-4159.2012.07844.x

Antonini, D., Dentice, M., Mahtani, P., De Rosa, L., Della Gatta, G., Mandinova, A., et al. (2008). Tprg, a gene predominantly expressed in skin, is a direct target of the transcription factor p63. *J. Invest. Dermatol.* 128, 1676–1685. doi: 10.1038/jid.2008.12

Armstrong, C. M., and Cota, G. (1990). Modification of sodium channel gating by lanthanum. Some effects that cannot be explained by surface charge theory. *J. Gen. Physiol.* 96, 1129–1140. doi: 10.1085/jgp.96.6.1129

Armstrong, C. M., and Cota, G. (1991). Calcium ion as a cofactor in Na channel gating. *Proc. Natl. Acad. Sci. U.S.A.* 88, 6528–6531. doi: 10.1073/pnas.88.15.6528

Augustin, I., Rosenmund, C., Südhof, T. C., and Brose, N. (1999). Munc13-1 is essential for fusion competence of glutamatergic synaptic vesicles. *Nature* 400, 457–461. doi: 10.1038/22768

Blatow, M., Caputi, A., Burnashev, N., Monyer, H., and Rozov, A. (2003). Ca2+ buffer saturation underlies paired pulse facilitation in calbindin-D28k-containing terminals. *Neuron* 38, 79–88. doi: 10.1016/s0896-6273(03)00196-x

Breustedt, J., Gundlfinger, A., Varoqueaux, F., Reim, K., Brose, N., and Schmitz, D. (2010). Munc13-2 differentially affects hippocampal synaptic transmission and plasticity. *Cereb. Cortex* 20, 1109–1120. doi: 10.1093/cercor/bhp170

Breustedt, J., and Schmitz, D. (2004). Assessing the role of GLUK5 and GLUK6 at hippocampal mossy fiber synapses. *J. Neurosci.* 24, 10093–10098. doi: 10.1523/jneurosci.3078-04.2004

Bruckner, J. J., Gratz, S. J., Slind, J. K., Geske, R. R., Cummings, A. M., Galindo, S. E., et al. (2012). Fife, a drosophila Piccolo-RIM homolog, promotes active zone organization and neurotransmitter release. *J. Neurosci.* 32, 17048–17058. doi: 10.1523/JNEUROSCI.3267-12.2012

Burré, J., Beckhaus, T., Corvey, C., Karas, M., Zimmermann, H., and Volknandt, W. (2006). Synaptic vesicle proteins under conditions of rest and activation: analysis by 2-D difference gel electrophoresis. *Electrophoresis* 27, 3488–3496. doi: 10.1002/elps.200500864

Butola, T., Wichmann, C., and Moser, T. (2017). Piccolo promotes vesicle replenishment at a fast central auditory synapse. *Front. Synaptic Neurosci.* 9:14. doi: 10.3389/fnsyn.2017.00014

Cases-Langhoff, C., Voss, B., Garner, A., Appeltauer, U., Takei, K., Kindler, S., et al. (1996). Piccolo, a novel 420 kDa protein associated with the presynaptic cytomatrix. *Eur. J. Cell Biol.* 69, 214–223.

Chamberland, S., Evstratova, A., and Tóth, K. (2017). Short-term facilitation at a detonator synapse requires the distinct contribution of multiple types of voltage-gated calcium channels. *J. Neurosci.* 37, 792–807. doi: 10.1523/JNEUROSCI.0159-17.2017

Englitz, B., Tolnai, S., Typlt, M., Jost, J., and Rübsamen, R. (2009). Reliability of synaptic transmission at the synapses of held *in vivo* under acoustic stimulation. *PLoS One* 4:e7014. doi: 10.1371/journal.pone.0007014

Fejtova, A., and Gundelfinger, E. D. (2006). Molecular organization and assembly of the presynaptic active zone of neurotransmitter release. *Results Probl. Cell Differ.* 43, 49–68. doi: 10.1007/400_012

Gundelfinger, E. D., Reissner, C., and Garner, C. C. (2016). Role of bassoon and piccolo in assembly and molecular organization of the active zone. *Front. Synaptic Neurosci.* 7:19. doi: 10.3389/fnsyn.2015.00019

Gundlfinger, A., Bischofberger, J., Johenning, F. W., Torvinen, M., Schmitz, D., and Breustedt, J. (2007a). Adenosine modulates transmission at the hippocampal mossy fibre synapse via direct inhibition of presynaptic calcium channels. *J. Physiol.* 582, 263–277. doi: 10.1113/jphysiol.2007.132613

Gundlfinger, A., Leibold, C., Gebert, K., Moisel, M., Schmitz, D., and Kempter, R. (2007b). Differential modulation of short-term synaptic dynamics by long-term potentiation at mouse hippocampal mossy fibre synapses. *J. Physiol.* 585, 853–865. doi: 10.1113/jphysiol.2007.143925

Hablitz, J. J. (1984). Picrotoxin-induced epileptiform activity in hippocampus: role of endogenous versus synaptic factors. *J. Neurophysiol.* 51, 1011–1127.

Hallermann, S., Fejtova, A., Schmidt, H., Weyhersmüller, A., Silver, R. A., Gundelfinger, E. D., et al. (2010). Bassoon speeds vesicle reloading at a central excitatory synapse. *Neuron* 68, 710–723. doi: 10.1016/j.neuron.2010.10.026

Hille, B. (2001). *Ion Channels of Excitable Membranes (Sinauer)*. Washington, DC: University Of Washington.

Imig, C., Min, S.-W., Krinner, S., Arancillo, M., Rosenmund, C., Südhof, T. C., et al. (2014). The morphological and molecular nature of synaptic vesicle priming at presynaptic active zones. *Neuron* 84, 416–431. doi: 10.1016/j.neuron.2014.10.009

Jackman, S. L., and Regehr, W. G. (2017). The mechanisms and functions of synaptic facilitation. *Neuron* 94, 447–464. doi: 10.1016/j.neuron.2017.02.047

Jackman, S. L., Turecek, J., Belinsky, J. E., and Regehr, W. G. (2016). The calcium sensor synaptotagmin 7 is required for synaptic facilitation. *Nature* 529, 88–91. doi: 10.1038/nature16507

Jones, B. L., and Smith, S. M. (2016). Calcium-sensing receptor: a key target for extracellular calcium signaling in neurons. *Front. Physiol.* 7:116. doi: 10.3389/fphys.2016.00116

Junge, H. J., Rhee, J.-S., Jahn, O., Varoqueaux, F., Spiess, J., Waxham, M. N., et al. (2004). Calmodulin and Munc13 Form a Ca2+ sensor/effector complex that controls short-term synaptic plasticity. *Cell* 118, 389–401.

Kaeser-Woo, Y. J., Younts, T. J., Yang, X., Zhou, P., Wu, D., Castillo, P. E., et al. (2013). Synaptotagmin-12 phosphorylation by cAMP-dependent protein kinase is essential for hippocampal mossy fiber LTP. *J. Neurosci.* 33, 9769–9780. doi: 10.1523/JNEUROSCI.5814-12.2013

Kamiya, H., Ozawa, S., and Manabe, T. (2002). Kainate receptor-dependent short-term plasticity of presynaptic ca2+ influx at the hippocampal mossy fiber synapses. *J. Neurosci.* 22, 9237–9243. doi: 10.1523/jneurosci.22-21-09237.2002

Kamiya, H., Shinozaki, H., and Yamamoto, C. (1996). Activation of metabotropic glutamate receptor type 2/3 suppresses transmission at rat hippocampal mossy fibre synapses. *J. Physiol.* 493, 447–455. doi: 10.1113/jphysiol.1996.sp021395

Klausnitzer, J., and Manahan-Vaughan, D. (2008). Frequency facilitation at mossy fiber-CA3 synapses of freely behaving rats is regulated by adenosine A1 receptors. *J. Neurosci.* 28, 4836–4840. doi: 10.1523/JNEUROSCI.3729-07.2008

Körber, C., Horstmann, H., Venkataramani, V., Herrmannsdörfer, F., Kremer, T., Kaiser, M., et al. (2015). Modulation of presynaptic release probability by the vertebrate-specific protein mover. *Neuron* 87, 521–533. doi: 10.1016/j.neuron.2015.07.001

Kremer, T., Kempf, C., Wittenmayer, N., Nawrotzki, R., Kuner, T., Kirsch, J., et al. (2007). Mover is a novel vertebrate-specific presynaptic protein with differential distribution at subsets of CNS synapses. *FEBS Lett.* 581, 4727–4733. doi: 10.1016/j.febslet.2007.08.070

Kwon, H.-B., and Castillo, P. E. (2008a). Long-term potentiation selectively expressed by nmda receptors at hippocampal mossy fiber synapses. *Neuron* 57, 108–120. doi: 10.1016/j.neuron.2007.11.024

Kwon, H.-B., and Castillo, P. E. (2008b). Role of glutamate autoreceptors at hippocampal mossy fiber synapses. *Neuron* 60, 1082–1094. doi: 10.1016/j.neuron.2008.10.045

Lauri, S. E., Bortolotto, Z. A., Nistico, R., Bleakman, D., Ornstein, P. L., Lodge, D., et al. (2003). A role for Ca2+ stores in kainate receptor-dependent synaptic facilitation and LTP at mossy fiber synapses in the hippocampus. *Neuron* 39, 327–341. doi: 10.1016/s0896-6273(03)00369-6

Lauri, S. E., Delany, C., Clarke, J. V. R., Bortolotto, Z. A., Ornstein, P. L., Isaac, T. R. J., et al. (2001). Synaptic activation of a presynaptic kainate receptor facilitates AMPA receptor-mediated synaptic transmission at hippocampal mossy fibre synapses. *Neuropharmacology* 41, 907–915. doi: 10.1016/s0028-3908(01)00152-6

Ma, Z., Siebert, A. P., Cheung, K.-H., Lee, R. J., Johnson, B., Cohen, A. S., et al. (2012). Calcium homeostasis modulator 1 (CALHM1) is the pore-forming subunit of an ion channel that mediates extracellular Ca2+ regulation of neuronal excitability. *Proc. Natl. Acad. Sci. US.A.* 109, E1963–E1971. doi: 10.1073/pnas.1204023109

Mendoza Schulz, A., Jing, Z., María Sánchez Caro, J., Wetzel, F., Dresbach, T., Strenzke, N., et al. (2014). Bassoon-disruption slows vesicle replenishment and induces homeostatic plasticity at a CNS synapse. *EMBO J.* 1–16.

Moore, K. A., Nicoll, R. A., and Schmitz, D. (2003). Adenosine gates synaptic plasticity at hippocampal mossy fiber synapses. *Proc. Natl. Acad. Sci. U.S.A.* 100, 14397–14402. doi: 10.1073/pnas.1835831100

Mori-Kawakami, F., Kobayashi, K., and Takahashi, T. (2003). Developmental decrease in synaptic facilitation at the mouse hippocampal mossy fibre synapse. *J. Physiol.* 553, 37–48. doi: 10.1113/jphysiol.2003.045948

Motulsky, H. J., and Christopoulos, A. (2003). *Fitting Models to Biological Data Using Linear and Nonlinear Regression*. San Diego, CA: GraphPad Software, Inc.

Mukherjee, K., Yang, X., Gerber, S. H., Kwon, H.-B., Ho, A., Castillo, P. E., et al. (2010). Piccolo and bassoon maintain synaptic vesicle clustering without directly participating in vesicle exocytosis. *Proc. Natl. Acad. Sci. USA* 107, 6504–6509. doi: 10.1073/pnas.1002307107

Nicoll, R. A., and Schmitz, D. (2005). Synaptic plasticity at hippocampal mossy fibre synapses. *Nat. Rev. Neurosci.* 6, 863–876. doi: 10.1038/nrn1786

Nowak, L., Bregestovski, P., Ascher, P., Herbet, A., and Prochiantz, A. (1984). Magnesium gates glutamate-activated channels in mouse central neurones. *Nature* 307, 462–465. doi: 10.1038/307462a0

Okerlund, N. D., Schneider, K., Leal-Ortiz, S., Montenegro-Venegas, C., Kim, S. A., Garner, L. C., et al. (2017). Bassoon controls presynaptic autophagy through Atg5. *Neuron* 93:897-913.e7. doi: 10.1016/j.neuron.2017.01.026

Parthier, D., Kuner, T., and Körber, C. (2018). The presynaptic scaffolding protein Piccolo organizes the readily releasable pool at the calyx of Held. *J. Physiol.* 596, 1485–1499. doi: 10.1113/JP274885

Regehr, W. G., Delaney, K. R., and Tank, D. W. (1994). The role of presynaptic calcium in short-term enhancement at the hippocampal mossy fiber synapse. *J. Neurosci.* 14, 523–537. doi: 10.1523/jneurosci.14-02-00523.1994

Rodríguez-Moreno, A., and Sihra, T. S. (2004). Presynaptic kainate receptor facilitation of glutamate release involves protein kinase a in the rat hippocampus. *J. Physiol.* 557, 733–745. doi: 10.1113/jphysiol.2004.065029

Rozov, A., and Burnashev, N. (1999). Polyamine-dependent facilitation of postsynaptic AMPA receptors counteracts paired-pulse depression. *Nature* 401, 594–598. doi: 10.1038/44151

Salin, P. A., Scanziani, M., Malenka, R. C., and Nicoll, R. A. (1996). Distinct short-term plasticity at two excitatory synapses in the hippocampus. *Proc. Natl. Acad. Sci. U.S.A.* 93, 13304–13309. doi: 10.1073/pnas.93.23.13304

Santarelli, V. P., Eastwood, A. L., Dougherty, D. A., Ahern, C. A., and Horn, R. (2007). Calcium block of single sodium channels: role of a pore-lining aromatic residue. *Biophys. J.* 93, 2341–2349. doi: 10.1529/biophysj.107.106856

Schmitz, D., Mellor, J., and Nicoll, R. A. (2001). Presynaptic kainate receptor mediation of frequency facilitation at hippocampal mossy fiber synapses. *Science* 291, 1972–1976. doi: 10.1126/science.1057105

Schoch, S., and Gundelfinger, E. D. (2006). Molecular organization of the presynaptic active zone. *Cell Tissue Res.* 326, 379–391. doi: 10.1007/s00441-006-0244-y

Scott, R., Lalic, T., Kullmann, D. M., Capogna, M., and Rusakov, D. A. (2008). Target-cell specificity of kainate autoreceptor and Ca2+-Store-dependent short-term plasticity at hippocampal mossy fiber synapses. *J. Neurosci.* 28, 13139–13149. doi: 10.1523/JNEUROSCI.2932-08.2008

Scott, R., and Rusakov, D. A. (2006). Main determinants of presynaptic Ca2+ dynamics at individual mossy fiber–CA3 pyramidal cell synapses. *J. Neurosci.* 26, 7071–7081. doi: 10.1523/jneurosci.0946-06.2006

Sihra, T. S., and Rodríguez-Moreno, A. (2013). Presynaptic kainate receptor-mediated bidirectional modulatory actions: mechanisms. *Neurochem. Int.* 62, 982–987. doi: 10.1016/j.neuint.2013.03.012

Südhof, T. C. (2012). The presynaptic active zone. *Neuron* 75, 11–25. doi: 10.1016/j.neuron.2012.06.012

Südhof, T. C. (2013). A molecular machine for neurotransmitter release: synaptotagmin and beyond. *Nat. Med.* 19, 1227–1231. doi: 10.1038/nm.3338

tom Dieck, S., Sanmartí-Vila, L., Langnaese, K., Richter, K., Kindler, S., Soyke, A., et al. (1998). Bassoon, a novel zinc-finger CAG/glutamine-repeat protein selectively localized at the active zone of presynaptic nerve terminals. *J. Cell Biol.* 142, 499–509. doi: 10.1083/jcb.142.2.499

Toth, K., Suares, G., Lawrence, J. J., Philips-Tansey, E., and McBain, C. J. (2000). Differential mechanisms of transmission at three types of mossy fiber synapse. *J. Neurosci.* 20, 8279–8289. doi: 10.1523/jneurosci.20-22-08279.2000

Traub, R. D., Miles, R., and Jefferys, J. G. (1993). Synaptic and intrinsic conductances shape picrotoxin-induced synchronized after-discharges in the guinea-pig hippocampal slice. *J. Physiol.* 461, 525–547. doi: 10.1113/jphysiol.1993.sp019527

Tzounopoulos, T., Janz, R., Südhof, T. C., Nicoll, R. A., and Malenka, R. C. (1998). A role for cAMP in long-term depression at hippocampal mossy fiber synapses. *Neuron* 21, 837–845. doi: 10.1016/s0896-6273(00)80599-1

Varoqueaux, F., Sigler, A., Rhee, J.-S., Brose, N., Enk, C., Reim, K., et al. (2002). Total arrest of spontaneous and evoked synaptic transmission but normal synaptogenesis in the absence of munc13-mediated vesicle priming. *Proc. Natl. Acad. Sci. U.S.A.* 99, 9037–9042. doi: 10.1073/pnas.122623799

Villacres, E. C., Wong, S. T., Chavkin, C., and Storm, D. R. (1998). Type I adenylyl cyclase mutant mice have impaired mossy fiber long-term potentiation. *J. Neurosci.* 18, 3186–3194. doi: 10.1523/jneurosci.18-09-03186.1998

Viotti, J. S., Ott, F. W., Schleicher, E. M., Wagner, J. M., Bouter, Y., Bayer, T. A., et al. (2019). *Increased Synaptic Facilitation and Exploratory Behavior in Mice Lacking the Presynaptic Protein Mover. BioRxiv*. [Preprint]. doi: 10.1101/560896

Vyleta, N. P., Borges-Merjane, C., and Jonas, P. (2016). Plasticity-dependent, full detonation at hippocampal mossy fiber-CA3 pyramidal neuron synapses. *Elife* 5, 355–405. doi: 10.7554/eLife.17977

Vyleta, N. P., and Jonas, P. (2014). Loose coupling between Ca2+ channels and release sensors at a plastic hippocampal synapse. *Science* 343, 665–670. doi: 10.1126/science.1244811

Waites, C. L., Leal-Ortiz, S. A., Okerlund, N., Dalke, H., Fejtova, A., Altrock, W. D., et al. (2013). Bassoon and Piccolo maintain synapse integrity by regulating protein ubiquitination and degradation. *EMBO J.* 32, 954–969. doi: 10.1038/emboj.2013.27

Wallrafen, R., and Dresbach, T. (2018). The presynaptic protein mover is differentially expressed across brain areas and synapse types. *Front. Neuroanat.* 12:58. doi: 10.3389/fnana.2018.00058

Wang, H., Pineda, V. V., Chan, G. C. K., Wong, S. T., Muglia, L. J., and Storm, D. R. (2003). Type 8 adenylyl cyclase is targeted to excitatory synapses and required for mossy fiber long-term potentiation. *J. Neurosci.* 23, 9710–9718. doi: 10.1523/jneurosci.23-30-09710.2003

Wang, X., Kibschull, M., Laue, M. M., Lichte, B., Petrasch-Parwez, E., and Kilimann, M. W. (1999). Aczonin, a 550-kD putative scaffolding protein of presynaptic active zones, shares homology regions with rim and bassoon and binds profilin. *J. Cell Biol.* 147, 151–162. doi: 10.1083/jcb.147.1.151

Weisskopf, M. G., Castillo, P. E., Zalutsky, R. A., and Nicoll, R. A. (1994). Mediation of hippocampal mossy fiber long-term potentiation by cyclic AMP. *Science* 265, 1878–1882. doi: 10.1126/science.7916482

Weisskopf, M. G., and Nicoll, R. A. (1995). Presynaptic changes during mossy fibre LTP revealed by NMDA receptor-mediated synaptic responses. *Nature* 376, 256–259. doi: 10.1038/376256a0

Zucker, R. S., and Regehr, W. G. (2002). Short-term synaptic plasticity. *Annu. Rev. Physiol.* 64, 355–405.

Conflict of Interest: The authors declare that the research was conducted in the absence of any commercial or financial relationships that could be construed as a potential conflict of interest.

frontiers in Synaptic Neuroscience

BRIEF RESEARCH REPORT
published: 10 January 2020
doi: 10.3389/fnsyn.2019.00037

Presynaptic Boutons That Contain Mitochondria Are More Stable

Robert M. Lees[†], *James D. Johnson*[†] *and Michael C. Ashby**

School of Physiology, Pharmacology, and Neuroscience, Faculty of Biomedical Sciences, University of Bristol, Bristol, United Kingdom

The addition and removal of presynaptic terminals reconfigures neuronal circuits of the mammalian neocortex, but little is known about how this presynaptic structural plasticity is controlled. Since mitochondria can regulate presynaptic function, we investigated whether the presence of axonal mitochondria relates to the structural plasticity of presynaptic boutons in mouse neocortex. We found that the overall density of axonal mitochondria did not appear to influence the loss and gain of boutons. However, positioning of mitochondria at individual presynaptic sites did relate to increased stability of those boutons. In line with this, synaptic localization of mitochondria increased as boutons aged and showed differing patterns of localization at *en passant* and *terminaux* boutons. These results suggest that mitochondria accumulate locally at boutons over time to increase bouton stability.

Keywords: presynaptic bouton, synaptic plasticity, *in vivo* 2-photon imaging, mitochondria, neocortex, synapse turnover

OPEN ACCESS

Edited by:
Joachim H. R. Lübke,
Jülich Research Centre, Germany

Reviewed by:
Seok-Kyu Kwon,
Korea Institute of Science and Technology (KIST), South Korea
Stefan Hallermann,
Leipzig University, Germany

****Correspondence:***
Michael C. Ashby
m.c.ashby@bristol.ac.uk

†Present address:
Robert M. Lees,
Department of Physiology, Anatomy, and Genetics, University of Oxford, Oxford, United Kingdom
James D. Johnson
John Edward Porter Neuroscience Research Center, National Institutes of Health, Bethesda, MD, United States

Received: *07 October 2019*
Accepted: *18 December 2019*
Published: *10 January 2020*

Citation:
Lees RM, Johnson JD and Ashby MC (2020) Presynaptic Boutons That Contain Mitochondria Are More Stable. Front. Synaptic Neurosci. 11:37. doi: 10.3389/fnsyn.2019.00037

INTRODUCTION

Individual cortical presynaptic terminals can be added and removed on axonal branches on a timescale ranging from days to years (De Paola et al., 2006; Grillo et al., 2013; Mostany et al., 2013; Qiao et al., 2015). Alterations in this presynaptic turnover are related to learning (Holtmaat and Caroni, 2016; Johnson et al., 2016; Ash et al., 2018) and disease (Jackson et al., 2017), showing their importance for the plasticity of neural circuits. However, little is known about cellular control of bouton structural plasticity, although it has been suggested that mitochondria may play a role (Smit-Rigter et al., 2016).

Mitochondria and synaptic efficacy are strongly linked. Ultrastructural features of efficacy (e.g., postsynaptic density size or number of docked vesicles) are positively correlated to presynaptic mitochondria (Kasthuri et al., 2015; Smith et al., 2016; Cserép et al., 2018), mitochondrially-derived ATP is required to sustain neurotransmission during elevated levels of stimulation (Hall et al., 2012; Rangaraju et al., 2014; Sobieski et al., 2017) and mitochondria modulate presynaptic release by sequestering cytosolic calcium or altering ATP concentrations (Sun et al., 2013; Kwon et al., 2016; Vaccaro et al., 2017; Lewis et al., 2018). However, mitochondria only localize to a subpopulation of boutons (Chang et al., 2006; Kang et al., 2008; Obashi and Okabe, 2013; Smit-Rigter et al., 2016; Vaccaro et al., 2017) and very little is known about whether the spatial distribution of mitochondria relative to presynaptic sites is related to bouton formation, longevity or removal (Smit-Rigter et al., 2016). To address this, we have used chronic, *in vivo* two-photon (2P) imaging to investigate the relationship between mitochondrial localization in axons and the structural plasticity of presynaptic boutons.

MATERIALS AND METHODS

Item	Supplier	Description	Code
AAV2/1-hSyn-EGFP-P2A-MTS-TagRFP-WPRE at 1–2 × 10^{13} GC ml^{-1}	Eli Lilly	Custom viral vector	
Cortex buffer		125 mM NaCl, 5 mM KCl, 10 mM Glucose, 10 mM HEPES, 2 mM $CaCl_2$, 2 mM $MgSO_4$ in dH_2O, pH 7.4	
Glass microcapillary	Harvard apparatus	Borosilicate, thin wall, without filament, Clark capillary glass	300035
Skull screw	Bilaney	0–80 UNF thread × 1/16 inch length	
Vetbond	Vet tech solutions	Surgical adhesive	IN004
Coverslip (cranial window)	Harvard Apparatus	CS-5R Coverslips, 0.15 mm (0.006 in), 5 mm diameter, pack of 100	640700
Stainless steel head bar		Custom-made, 10 × 3 × 1 mm with 2 × M2 holes centered 2 mm from each end	
Bone cement	DePuy	With gentamicin	
Hydrogel solution kit	Logos biosystems		C1310X
Electrophoretic tissue clearing solution	Logos biosystems		C13001
Mounting solution (cleared brain)	Logos biosystems	X-CLARITY mounting solution	C13101
Fluoromount-Gw/DAPI	Thermo Fisher Scientific		00-4959-52

Equipment

Item	Supplier	Description
Two-photon microscopy (*in vivo imaging)*	Scientifica	Custom-built with filter cube carousel and epifluorescence capabilities
Ti-Sapphire laser	Spectra-Physics	MaiTai Ti-Sapphire tuneable laser (680–1, 040 nm)
60× water-immersion objective	Olympus	For *in vivo* 2P imaging, 1.1 NA
X-CLARITY tissue clearing system	Logos Biosystems	
Two-photon microscopy (cleared brain imaging)	Leica	Leica SP8 AOBS laser-scanning microscope w/Leica DM6000 upright epifluorescence microscope
Ti-Sapphire laser	Spectra-Physics	MaiTai DeepSee Ti-Sapphire tuneable laser (680–1,300 nm)

Software

Software	Developer	Version	Description
ScanImage	Vidrio technologies	5.1	Two-photon microscope control
Micromanager	Open imaging	1.4	Camera control
ImageJ (FIJI package)	ImageJ Development Team	1.51a (2.0.0-rc-43)	Image processing and analysis
MATLAB	MathWorks	R2016a	Data processing and analysis
Prism	GraphPad	7	Graph making and basic statistical testing
G*Power	Universität Düsseldorf		Statistical power calculations
SPSS statistics	IBM	24	Statistical testing

Animal Husbandry

All procedures involving animals adhered to the Animals (Scientific Procedures) Act 1986 and Amendment Regulations 2012 as outlined in UK law and approved by the University of Bristol Animal Welfare and Ethics Review Board.

Adult (2.5 months old) C57Bl/6 male mice were used for all experiments, living on a 12-h light-dark cycle. Animals were housed individually to avoid loss of the cranial window implant due to fighting. Large (∼30 × 50 × 25 cm) cages were used and extra enrichment was provided for each cage, consisting of tunnels, shelters, wheels and foraging food to increase experience-dependent turnover of presynaptic terminals (Briones et al., 2004; Nithianantharajah et al., 2004; Landers et al., 2011).

Viral DNA Construct

The virus used for intracranial injection was a custom-made adeno-associated virus (AAV) of serotype 2/1 expressing a bi-cistronic vector (AAV2/1-hSYN-EGFP-P2A-MTS-TagRFP). The human synapsin promoter (hSYN) was used to limit expression to neuronal cells. Cytosolic enhanced green fluorescent protein (EGFP) was separated by a P2A peptide from mitochondrially-targeted tagRFP (red fluorescent protein, fused to amino acids 1–29 of Cox8a subunit of cytochrome oxidase), which localized to the inner mitochondrial membrane. The P2A peptide is a self-cleaving peptide of the 2A family from porcine teschovirus, which has a high cleaving efficiency (Kim et al., 2011). Additionally, Woodchuck Hepatitis Virus Posttranscriptional Regulatory Element was used to increase protein expression (Zufferey et al., 1999). The viral titer used for injections was in the range of 1–2 × 10^{13} particles ml^{-1} in cortex buffer (125 mM NaCl, 5 mM KCl, 10 mM Glucose, 10 mM HEPES, 2 mM $CaCl_2$, 2 mM $MgSO_4$ in dH_2O, pH 7.4).

Surgery

To reduce stress, animals were allowed at least 1 week to acclimatize to unfamiliar environments after relocation before the commencement of procedures. Intraperitoneal injections of Rimadyl (analgesic, 4 mg ml^{-1} kg^{-1}) and dexamethasone (anti-inflammatory, 0.5 mg ml^{-1} kg^{-1}) were given pre-operatively to reduce pain and inflammation. Aseptic technique was used to limit the possibility of infection, guidelines were followed as outlined by the Laboratory Animal Science Association[1]. The protocol described in Holtmaat et al. (2009) was followed for cranial window implantation, which is briefly described below with amendments.

Animals were anesthetized using gaseous isoflurane at 3–4% for induction and 1–2% to sustain anesthesia throughout surgery, carried by O_2. The top of the head was shaved and placed in a stereotaxic frame, and the scalp and periosteum were removed. The skull bone was kept moist throughout surgery with cortex buffer.

The intracranial viral injection site was measured +0.7 mm lateral (always to the right) and +1.0 mm anterior from Bregma, as these coordinates correspond to the primary/secondary motor cortex (Lein et al., 2007; Petreanu et al., 2012). A small (∼0.5 mm diameter) burr hole was made in the skull using a high-speed motorized hand drill. For viral injections, a glass capillary tube was pulled into a micropipette with a long, pointed tip and beveled on a whetstone to sharpen it further. The virus was injected intracranially using a Hamilton syringe and motorized pump at a rate of 100 nl/min. A volume of 300 nl was injected at depths of 300 μm (first) and 700 μm (second) from the pial surface to spread it across all cortical layers. The virus was allowed to spread for 3 min before moving the micropipette.

After viral injection, a screw (0–80 UNF thread, 1/16 inch length) was implanted in the left parietal skull bone to anchor the cranial window implant to the skull. Subsequently, a thin layer of VetBond^{TM} glue was spread across the skull, to the skin edges, avoiding the right parietal skull bone where the cranial window was to be implanted. A 3–4 mm diameter craniectomy was made using a motorized hand drill centered on +2.5 mm lateral and −1.8 mm anterior of Bregma. A 5 mm circular glass coverslip was then secured over the craniectomy on top of a small volume of cortex buffer using VetBond^{TM} glue.

Quick-drying bone cement (with gentamycin, DePuy) was used to apply a 1–2 mm thick layer of cement over the layer of VetBond^{TM} glue. Cement was spread just over the edge of the coverslip as well as up to the edges of the skin incision. A stainless-steel bar (10 × 3 × 1 mm; used for securing the head during *in vivo* imaging) was placed over the left hemisphere as close to the cranial window as possible while leaving enough space for microscope objective access.

Animals were left for ∼24 days before imaging to allow for any inflammation to clear under the window and to allow viral expression.

In vivo Imaging

For *in vivo* imaging, a customized Scientifica upright 2P microscope was used along with a motorized stage to aid precise movement in coordinate space for relocation of regions of interest (ROIs). Epifluorescence was used for low-resolution mapping of expression across the window to guide 2P imaging. Two MaiTai Ti-Sapphire tuneable lasers (tuneable from 680 to 1,040 nm, Spectra-Physics) were used and attenuation of laser power was controlled through either a Pockel's cell or half-wave plate. 2P excitation wavelengths for imaging were typically 920 nm (EGFP) and 1,040 nm (TagRFP). Laser lines were combined using a polarising beamsplitter cube in reverse, and combined power never exceeded 60 mW at the back focal plane of the objective. The acquisition was controlled by ScanImage software (Pologruto et al., 2003, version 5.1) and Micromanager software (Edelstein et al., 2014, version 1.4). Objective lenses used: 4× air 0.15 NA, 10× water-immersion 0.6 NA and 60× water-immersion 1.1 NA. Emission filter sets used for PMTs were BP 620/60 nm for TagRFP and BP 525/50 nm for EGFP. The stage was fitted with a micromanipulator for precise head fixation and rotation in every repeated imaging session using the implanted steel bar on the animal's head, increasing ROI relocation efficiency. During *in vivo* imaging, mice were anesthetized by gaseous isoflurane anesthetic (1–2% carried by O_2) and breathing was monitored to judge depth of anesthesia. Breathing was kept in the range of 80–100 beats per minute by eye.

For each mouse, a large blood vessel bifurcation was chosen using reflected light and set as the origin for recording coordinates of ROIs. 2P imaging was used to locate ROIs based on the following criteria: sparse labeling, to reduce background and contamination from crossing axons; distinctive axonal structures, for easy relocation; distance from other ROIs, to increase the diversity of sampling.

Z-stacks of 20–50 μm were acquired at each ROI with a step size of 1 μm (60×, 1.1 NA objective). Images were acquired with 3× frame averaging, 1 μs pixel dwell time at 1,024 × 1,024 pixels and a field of view of 76 × 76 μm, resulting in a final pixel size of 74 nm. Signal was matched between sessions by adjusting laser power because of differences in window quality between imaging sessions, which altered the signal-to-noise ratio. Up to seven ROIs were chosen per animal and each imaging session was kept between 1 and 2 h.

Axons were tracked for up to 35 days after the initial session, for a total of nine sessions (ethical limit) or until the cranial window was no longer optically clear due to bone regrowth or dural thickening. A small proportion of ROIs were first tracked at days one and two, rather than day zero of the imaging paradigm. Most ROIs and animals were tracked for the entire imaging time series.

Histology

Following the end of an imaging paradigm, mice were administered a dose of 70–100 μl of Euthatal (200 mg/ml sodium pentobarbital) intraperitoneally to achieve terminal anesthesia. When the animal was deeply anesthetized, exsanguination was performed, and the animal was transcardially perfused with 5–10 ml of 0.01 M PBS. This was followed by an infusion of 20–30 ml of 4% paraformaldehyde (PFA) in 0.01 M PBS. The brain was then dissected out and post-fixed in 4% PFA in 0.01 M PBS at 4°C.

---

[1] http://www.lasa.co.uk/wp-content/uploads/2017/04/Aseptic-surgery-final.pdf

Tissue Clearing

Tissue clearing was carried out by following the protocol described in Lee et al. (2016), which is briefly outlined below. The brain was post-fixed for 24 h in 4% PFA followed by overnight incubation in hydrogel solution (4% w/v acrylamide without bis-acrylamide, 1% w/v VA-044 initiator in 0.01 M PBS) at 4°C. Oxygen was removed from the solution by degasification using pure nitrogen bubbling through the solution (providing some agitation). Polymerization of the hydrogel was carried out at 37°C in a water bath for ∼3 h. The brain was then mounted inside the X-CLARITY electrophoresis chamber (Logos Biosystems) in electrophoretic tissue clearing solution (4% SDS and 200 mM boric acid). The X-CLARITY machine was used according to the manufacturer's instructions.

Tissue Sectioning

Histological sectioning was achieved using either a vibratome or freezing microtome. For vibratome sectioning, brains were embedded in 2% agarose (in distilled H_2O), trimmed to the region of interest and series of 50 μm-thick sections were cut in 0.01 M PBS on a vibratome. For freezing microtomy, brains were incubated in a 30% sucrose solution (w/v) for up to 1 week. The brains were then sectioned in optimal cutting temperature (OCT) solution. The sections were directly mounted on glass microscope slides with No. 1.5 coverslips using Fluoromount-G containing DAPI nuclear stain.

Imaging of Tissue Sections

Imaging of whole tissue sections was carried out on a widefield microscope (Leica DMI6000) with a mercury lamp and CCD camera (Leica DFC365FX monochrome) using Leica LAS X software. Filter sets were assigned for the following fluorophores: DAPI (Ex. 350/50 nm, 400 nm dichroic mirror, Em. BP 460/50 nm), EGFP (Ex.: 480/40 nm, 505 nm dichroic mirror, Em. BP 527/30 nm), TagRFP (Ex. 620/60,660 nm dichroic mirror, Em. BP 700/38). Objective lenses used: 5× dry 0.15 numerical aperture (NA) and 20× dry 0.4 NA. Brightfield and DAPI signal of coronal or sagittal tissue sections were compared to the Paxinos Mouse Brain Atlas (Franklin and Paxinos, 2008) or Allen Mouse Brain Atlas (Lein et al., 2007) as a reference to confirm the positions of viral injections and window sites.

Imaging of Cleared Tissue

The cleared brain was immersed in a small volume (5–10 ml) of mounting medium (X-CLARITY mounting solution) inside a 50 ml Falcon tube for at least 2 h before mounting. It was then placed in the center of a circular wall of Blu-tac inside the lid of a 35 mm dish to create a water-tight well. The well was filled partially with fresh X-CLARITY mounting medium and the chamber was sealed on top with a 35 mm coverslip pressed into the Blu-tac. The chamber was filled from a small inlet in the Blu-tac using a 200 μl pipette and the inlet was sealed by squeezing the Blu-tac back together.

Cleared tissue was imaged using a Leica SP8 AOBS confocal laser scanning microscope attached to a Leica DM6000 upright epifluorescence microscope with a Ti-Sapphire laser (MaiTai DeepSee; tuneable from 680 to 1,300 nm) and a fixed-wavelength 1,040 nm laser. Two-hybrid GaAsP detectors were used with a BP 525/50 nm filter for EGFP and BP 630/75 nm for TagRFP. Objectives lenses used: 10× water-immersion 0.3 NA and 25× water-immersion 0.95 NA. Large z-stack mosaic images (5 μm steps for ∼1 mm) were acquired using the tilescan function in Leica LAS X software. The laser intensity was attenuated at shallower imaging depths to maintain the signal-to-noise ratio. The images were then resliced to obtain the correct viewing angle.

Image Processing

In vivo images were processed using the FIJI package for ImageJ (Schindelin et al., 2012, version 2.0.0-rc-43/1.51a) and a custom ImageJ macro. The macro allowed for automated processing of images for each ROI, carrying out the following functions: (1) alignment of the EGFP signal within a single z-stack to correct drift and application of the transformation to the TagRFP channel using the MultiStackReg registration plugin; (2) matching of z-stack sizes between time-points by addition of blank slices; (3) alignment of z-stacks between time-points in the x- and y-axes using maximum z-projections and the MultiStackReg plugin; and (4) alignment of z-stacks in the z-axis using an edited version of the Correct 3D Drift plugin to only include the z-axis transformation. This resulted in a 5-dimensional (5D—XYZCT) stack of each ROI aligned to within 5 μm in x, y and z for both channels across all timepoints. For presentation in figures only, images were cropped and had brightness and contrast adjusted and a median filter (74 nm kernel) applied.

Data Quantification

Axonal segments were manually traced using the segmented line tool with spline as part of a custom ImageJ macro script. After tracing at each time point, a minimum volume that encompassed the axon across all the timepoints was cropped from the original 5D stack. Between 1 and 12 axonal segments were chosen from each ROI. Factors used to choose axonal segments were: good signal-to-noise (subjective measure by the analyst), few crossing axons and existence in all time-points.

Identification and indexing of presynaptic terminals and mitochondria were carried out manually on each cropped axonal segment using a custom ImageJ macro script and the multi-point tool. A gaussian blur (sigma = 2 pixels, 154 nm) was used to smooth the signal and presynaptic terminals were scored subjectively, using the local intensity profile as a guide (further information below). The position of each object (bouton or mitochondrion) was estimated from a point placed by the analyst.

Boutons were tracked across imaging sessions from the first timepoint they were identified. Boutons in separate timepoints were linked if they were in the same place relative to fiducial markers, including any crossing axons, kinked structure or other persistent boutons. Any bouton that was lost from the field of view for one timepoint (through a shift in alignment in the x- or y-axes) was excluded entirely. All boutons were scored blind to the mitochondrial signal.

En passant boutons (EPBs) were larger in volume than the axon backbone and therefore had higher intensity relative to the backbone due to increased numbers of fluorescent molecules (cytosolic EGFP). An EPB had to have contiguous pixels in the x-, y- and z-axes to ensure it was not the result of noise. The intensity profile of an EPB needed to include sharp edges (relatively steep curve either side of the peak) to exclude gentle changes in the axonal thickness. If the peak of an EPB was twice that of the local axon backbone (1.5 μm either side of the bouton) at any time point, the bouton was scored as being present. A bouton was scored as lost if it was below 1.3 times the local axon backbone. These criteria have been shown to be faithful indicators of synapse presence in correlative light and electron microscopy studies (Grillo et al., 2013; Song et al., 2016).

Terminaux boutons were scored as unilateral protrusions from the axon backbone with a bulbous appearance and sometimes consisted of a resolved thin neck that extended for less than 5 μm. Those extending for longer than 5 μm were considered to be axonal branches (Grillo et al., 2013).

A small proportion of boutons changed bouton type (*en passant* or *terminaux*) over the time series and so those boutons were classified based on their predominant type.

Mitochondria were identified as discrete objects that were 2× the global median background signal, with contiguous pixels in the x-, y- and z-axes and steep edges to their intensity profile. The axonal EGFP signal was used to verify that each mitochondrion was inside the axon only after it was scored.

Data Analysis

A priori power calculations were performed in G*Power software (Faul et al., 2007) to calculate the number of newly-formed boutons required to detect a 10% difference in survival between the two mitochondrial conditions (less than or greater than 1.5 μm from a bouton). This calculation resulted in an estimated sample size of 450 newly-formed boutons. The number of animals required to achieve this was estimated from pilot studies to be 10–15 animals. In this study, 21 animals were used, 15 were imaged and 12 produced high-quality data that was included (see exclusion criteria below).

The final dataset was obtained from three different batches of littermates. A total of 51 ROIs and 306 axons were tracked. The total number of mitochondria counted across all time-points was 11,264 along with 4,892 unique boutons. Mitochondria were not linked between timepoints because they lacked individuality due to their ability to move, fuse and split (Lewis et al., 2018).

Some data were excluded from the final dataset. Any ROI that was too dim for accurate axon tracing (subjectively based on analyst experience) within the first four time points was not tracked. Any axon where the signal-to-noise in a session was low enough that the scorer could not be confident in bouton scoring was removed. Data from one animal that had only two axons tracked was also removed.

The bouton dynamic fraction was calculated as the proportion of unique boutons on an axon that were either lost or gained. Specifically, the sum of gains and losses divided by the total number of unique boutons across the two time-points: (gained + lost)/(gained + $\text{total}_{\text{time1}}$).

Mitochondrion and Bouton Co-localization

Mitochondria were classified as being present at a bouton if the distance between their centroids (defined by points placed by the analyst) was less than or equal to 1.5 μm. A dichotomous variable (mitochondria present or not) was chosen for analyses rather than a continuous variable (distance from nearest mitochondrion) because the axonal segment was a small sample of the axonal arbor and the true distance to the nearest mitochondria from each bouton could not be accurately measured, especially for boutons at the edge of the field of view. The distance of 1.5 μm was biologically-relevant because a distance-dependent relationship with synaptic ultrastructure has been seen up to 3 μm away (edge of vesicle pool to edge of mitochondrion) using electron microscopy (Smith et al., 2016). Stronger effects on synaptic ultrastructure were seen with closer distances of mitochondria. The accuracy of the measured distance in our study was limited due to the resolution of light microscopy and accuracy of point placement by the analyst, therefore only one distance was chosen in the middle of the range (0–3 μm).

The Randomization of bouton or mitochondrion position was carried out in a similar fashion to Smit-Rigter et al. (2016). Axons were first plotted in two dimensions in MATLAB using interpolation from segmented line coordinates recorded in ImageJ. The length of the axon was then estimated using Euclidean distances and a line was created and split into segments of 74 nm (the original pixel size of the 2P images). The real positions of the objects of interest (mitochondria or boutons) were plotted to the closest segment of the axon based on where they were in the original image using nearest neighbor distance calculations. Either mitochondria or boutons were then removed and randomly re-plotted along the axon without being placed closer than 1 μm together. Intervals of at least 1 μm were chosen to attempt to match the resolution limit with which two objects could be resolved using the 2P microscope in this study. This was repeated 1,000 times for each axon and the range plotted.

Statistics

Statistics were calculated using MATLAB (release 2016a), GraphPad Prism 7 or SPSS (IBM). Statistical significance was set at $p < 0.05$. Confidence intervals for proportions were calculated using the formula for single samples (Newcombe, 1998). The z^*-value for a 95% coverage of a gaussian distribution is 1.96. Therefore, the formula is as follows:

$$\hat{p} \pm z^* \sqrt{\frac{\hat{p}(1-\hat{p})}{n}}$$

where prop1 is the proportion, z^* is 1.96 and N is the number of samples in the population. Errors are given as 95% confidence intervals for proportions and standard deviation for all other data, unless otherwise stated.

For repeated measures statistical tests, group sizes were matched by only including axons present in all relevant time-points for the particular test. To avoid pseudo-replication, samples were not pooled together across time from repeated measures.

A Gaussian mixture model was used to calculate posterior probabilities of axons being in EPB-rich or TB-rich groups based on EPB and TB densities. An assumed number of two Gaussian components were defined by the analyst. Axons that fell under the threshold of 0.7 probability for both groups were not assigned a group.

Kaplan-Meier curves were created for survival analysis, based on time-to-event data. For bouton survival, this was the time from first observation until the bouton was no longer observed. Boutons that were no longer observed due to reasons other than loss were classed as 'censored' for the analysis.

RESULTS

To monitor presynaptic bouton structure alongside axonal mitochondria, we transduced neurons of the mouse primary and secondary motor cortex (M1 and M2) with an AAV that co-expressed cytosolic EGFP and mitochondrially-targeted (MTS)-TagRFP (**Figure 1A**). There was a substantial projection from the motor cortex made up of long-range axons that ramify in the ipsilateral somatosensory cortex (**Figure 1B**; Veinante and Deschênes, 2003; Petreanu et al., 2009; Mao et al., 2011; Oswald et al., 2013). Imaging of intact cleared brains showed that these axons travel over distances of more than 3 mm *via* cortical layers 5/6 or, to a lesser extent, superficially within layer 1 (**Supplementary Figures S1, S2**). By placing a cranial window over the primary somatosensory cortex (S1), we imaged segments of these long-range axons within layer 1 using *in vivo* 2P microscopy. Mitochondria, putative EPBs and *terminaux* boutons (TBs) were clearly identified as increases in fluorescence intensity along the local axon backbone (**Figure 1C**, see "Materials and Methods" section). We tracked structural synaptic plasticity of individual boutons by repeated imaging of the same axons at daily and weekly intervals over a total of up to 35 days (**Figure 1D**; $n = 12$ animals, 306 axons). Visual inspection (**Figure 1C**) and statistical analysis based on the density of EPBs and TBs along each axon (**Figure 1E**) indicated that axons were mostly either EPB-rich or TB-rich. As this is the first characterization of boutons in this axonal pathway, we compared the density and turnover of boutons in individual axonal branches. While there was a higher density of boutons in TB-rich axons, no differences were found in bouton turnover between EPB-rich and TB-rich axons (**Supplementary Figure S3**).

As mitochondria can support presynaptic function, we assessed whether the numerical density of boutons and mitochondria are correlated in axons (population mean overtime was 1.09 ± 0.41, 1 SD, and 0.69 ± 0.23 per 10 μm, respectively; **Figure 2A**). For individual axonal segments (median length of 75 μm, **Supplementary Figure S4**), there was a strong correlation between the densities of mitochondria and putative boutons (mean over time; Pearson's correlation, $R^2 = 0.50$, $p = 1.16 \times 10^{-20}$; **Figure 2B**). This suggested that the formation and/or elimination of boutons may relate to the mitochondrial population. To assess this, we compared the fraction of dynamic boutons (proportion lost *and* gained divided by the total number of unique boutons) across daily and weekly intervals to the mean mitochondrial density between the two time-points (**Figure 2C**, **Supplementary Table S1**). Bouton dynamics were not significantly correlated to mitochondrial density in axonal segments at daily or weekly intervals ($R_s = 0.005$, Spearman's correlation, $p = 0.944$; **Figure 2C**, **Supplementary Table S1**). Similarly, there was no apparent correlation between bouton dynamics and mitochondrion-to-bouton ratios ($R_s = 0.024$, Spearman's correlation, $p = 0.733$; **Figure 2C**, **Supplementary Table S1**), indicating that the overall availability of mitochondria along a stretch of axon is not related to the degree of structural plasticity occurring there.

As the overall density of axonal mitochondria was related to bouton density, but not to bouton dynamics, we assessed if there was instead a more local relationship between individual boutons and mitochondria near them. Based on previous studies and effective resolution limits of our imaging, we chose 1.5 μm as a biologically relevant distance to presynaptic terminals Smith et al., 2016; Smit-Rigter et al., 2016; see "Materials and Methods" section). Whereas most mitochondria (65%) were found within 1.5 μm of presynaptic terminals (centroid-to-centroid distance; **Figure 3A**), only a minority of the total pool of putative boutons (44%) had mitochondria closer than 1.5 μm (**Figure 3B**). This local organization did not occur by chance, as randomizing or mirroring positions of either mitochondria or boutons along the axon backbone resulted in greater distances between them (**Figures 3A–C**). To determine if the structure of boutons affected the ability of mitochondria to localize there, we divided the bouton population into EPBs and TBs. There was a higher likelihood of mitochondria at EPBs (45 ± 3%, 95% CI) than TBs (measured from TB head, 27 ± 3%; Chi-squared test, $p < 0.0001$; **Figures 3D–F**). It is possible that mitochondria reside near TBs, but do not traverse their neck region. Therefore, we estimated the location of the base of TBs by re-plotting them to where they joined the axon backbone (**Figure 3G**). The probability of mitochondria at the base of TBs was higher (42 ± 3%) than at the head, and not different from that of EPBs (data from day 0; Chi-squared test, $p = 0.188$; **Figures 3F,G**).

Given that mitochondria have been implicated in the control of presynaptic function, we hypothesized that mitochondrial presence may relate to bouton maturity. To test this hypothesis, we separated boutons by age (*new* or *pre-existing*; **Figure 4A**). New boutons were formed between daily imaging sessions (<24 h old), whereas pre-existing boutons were present before imaging began (mixed ages). Some pre-existing boutons would have been formed in the previous day and should have been classed as new boutons, but we estimated this to be <10% of the total population as this was the rate of daily bouton formation (**Supplementary Figure S5**). Pre-existing boutons were more likely than newly-formed boutons to have a resident mitochondrion (proportion with mitochondria on the first day tracked, *pre-existing* 38 ± 2%, *new* 32 ± 4%, 95% CI, Chi-squared test, $p = 0.0024$; **Figure 4B**). However, new boutons were still more likely to have mitochondria nearby than predicted by chance (17 ± 3%, 95% CI, Chi-squared test, $p < 0.0001$), as were pre-existing boutons (17 ± 2%, Chi-squared test, $p < 0.0001$; **Figure 4B**). Further to this, the likelihood of mitochondrial presence at long-lived boutons

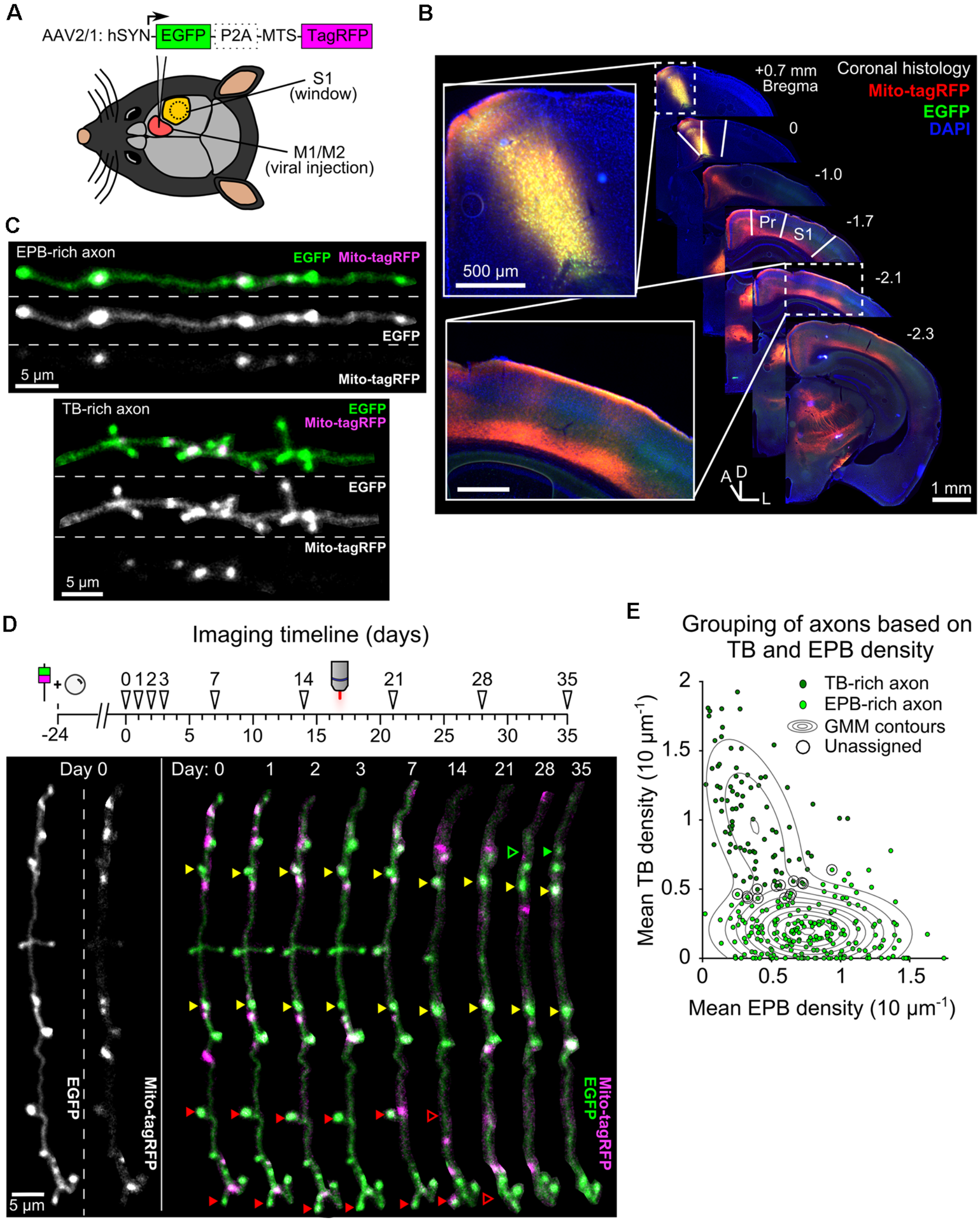

FIGURE 1 | Tracking bouton plasticity and mitochondrial positioning in axons of motor cortex neurons. **(A)** Adeno-associated virus (AAV) expressing cytosolic EGFP and a mitochondrial targeting sequence (MTS) conjugated to TagRFP was injected into M1/M2 and a glass cranial window was implanted over S1. **(B)** A series of coronal brain slices showing the viral injection site across the M1/M2 border (inset, top) and the axonal projection site at S1 under the cranial window (inset, bottom). Only the ipsilateral half of the brain sections are shown. Pr = parietal cortex, D = dorsal, L = lateral, A = anterior. **(C)** Cropped two-photon (2P) images from *in vivo* imaging show axons with high EPB density (EPB-rich) or high TB density (TB-rich). **(D)** (top) Imaging timeline for tracking bouton structural plasticity bouton loss and gain. Viral injection and cranial window implantation were performed 24 days prior to initial 2P imaging. Arrowheads indicate imaging time-points. (bottom) Structure and mitochondrial localization in a single cropped axon over 35 days imaged using *in vivo* 2P microscopy. Some boutons are labeled with arrowheads to show examples of stable (yellow), lost (red) or gained (green) boutons. **(E)** Gaussian mixture modeling (GMM) was used to determine two potential populations (*EPB-rich* and *TB-rich* axons) that result in the observed sample distribution of axonal EPB and TB densities (mean across time). Axons that had posterior probabilities below 70% were not assigned to a group (*circled*; see "Materials and Methods" section). Contour lines indicate the slope of the GMM distribution.

(those that survived the entire imaging period from the start) rose over time (*new* boutons 28 ± 12% to 43 ± 13%, *pre-existing* 46 ± 4% to 52 ± 4%, Cochran's Q test, *new*, $p = 0.235$, *pre-existing*, $p < 0.0005$; **Figure 4C**). This was not the case with randomized mitochondrial positions, suggesting it is not a chance phenomenon (*pre-existing* 15 ± 3% to 18 ± 3%, *new*

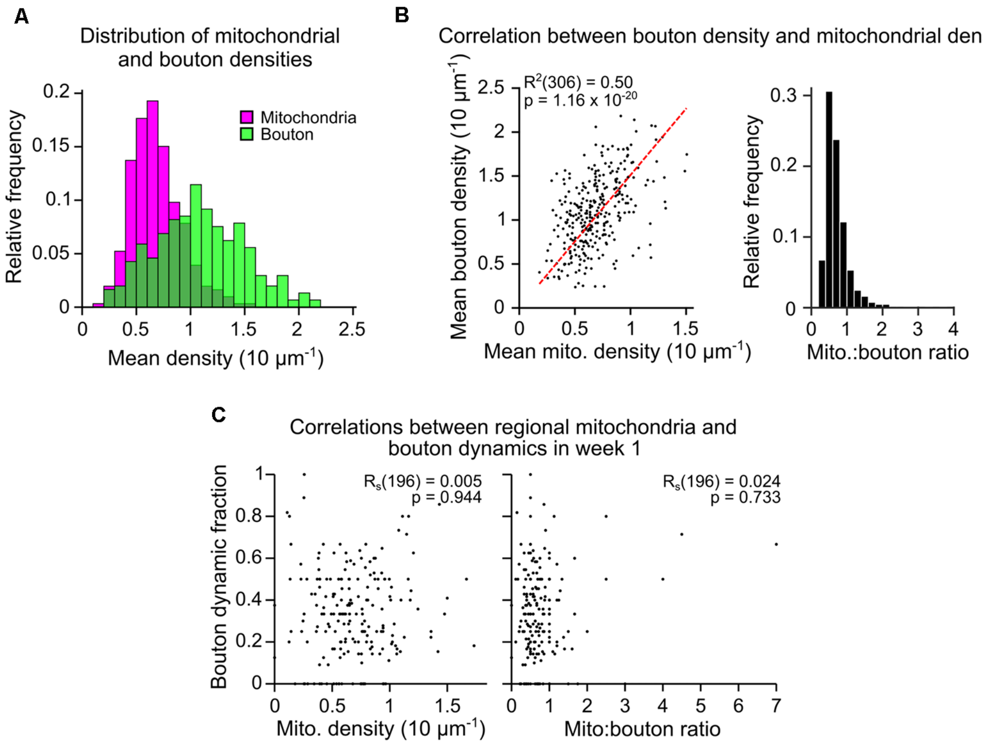

FIGURE 2 | Mitochondrial density along an axonal segment is correlated to bouton density but not bouton dynamics. **(A)** Mitochondrial and bouton density distributions for all axons (mean across time, $n = 306$ axons). **(B)** (left) Bouton and mitochondrial densities for each axon were strongly correlated (mean across time; R^2 = Pearson's correlation, $n = 306$). *Red dashed line* = linear regression. (right) Histogram showing the distribution of mitochondrion-to-bouton ratios for all axons (median = 0.65, approximately two mitochondria to every three boutons). **(C)** Example correlations between the fraction of boutons on each axon that were dynamic (lost or gained; *bouton dynamic fraction*) and either: (left) the number of mitochondria relative to the number of boutons (mito:bouton ratio), or (right) mitochondrial density. Results from the first weekly interval (between days 7 and 14) are shown ($n = 196$ axons over all weekly intervals, R_S = Spearman's rank correlation, see **Supplementary Table S1**).

13 ± 9% to 22 ± 11%, Cochran's Q test, *new*, $p = 0.578$, *pre-existing*, $p = 0.134$). It was also not due to a general trend towards increased synaptic localization of mitochondria over time, as this was stable across the imaging paradigm (**Supplementary Figure S6**). These data show that the longer a bouton survives, the more likely it is to have a mitochondrion nearby.

It has been shown that newly-formed cortical boutons tend to be lost more quickly than pre-existing boutons (Qiao et al., 2015; Ash et al., 2018). Here, we show this is also true for boutons on long-range axons of motor cortical neurons, in which less than 30% of new boutons survived more than 1 week compared to ∼70% survival for pre-existing boutons (median survival: *new*, 4 days, *pre-existing*, 35 days, Log-rank test, $p < 0.0001$; **Figure 4D**). Interestingly—despite their differing structures—TBs and EPBs show similar survival within these groups (**Figures 4E,F**), with only a small difference in median survival between new EPBs and TBs (*new EPB*, 4 days, *new TB*, 6 days, *pre-existing EPB* and *TB*, 35 days, Log-rank test, *new*, $p = 0.0006$, *pre-existing*, $p = 0.154$; **Figure 4F**). This aligns with the similarity in overall bouton turnover rates between EPB-rich and TB-rich axons (**Supplementary Figure S3**).

To determine if mitochondria relate to the stability of individual boutons locally, we assessed the survival of boutons with and without mitochondria. For new synaptic boutons, the chance of being removed was only slightly reduced if mitochondria were present (*without mitochondria* 45 ± 6% chance of being removed, *with mitochondria* 36 ± 8%; Fisher's Exact test, $p = 0.031$; **Figure 4G**). As localization of mitochondria at TBs and EPBs appeared to be different, we assessed the impact of having resident mitochondria on the survival of the two bouton types separately. This stabilizing effect on new boutons appeared to be mediated by influence on EPBs, which were less likely to be lost if they had a mitochondrion, whereas we did not detect any mitochondrial influence on TB survival, albeit with lower n numbers (**Figure 4G**; Fisher's Exact test—EPBs, $p = 0.031$; TBs, $p = 0.784$). The effect was much more pronounced for older, pre-existing boutons, in which having mitochondria decreased the probability of subsequent removal by ∼60% (*without mitochondria* 17 ± 2%, *with mitochondria* 7 ± 2%; Chi-squared, $p < 0.0005$; **Figure 4H**). This relationship between mitochondrial proximity and enhanced bouton survival was consistent across time for pre-existing boutons (**Supplementary Figure S7**). Again, we assessed whether the stabilization of boutons was dependent on bouton type. Even more strongly than in new boutons, mitochondrial presence was strongly

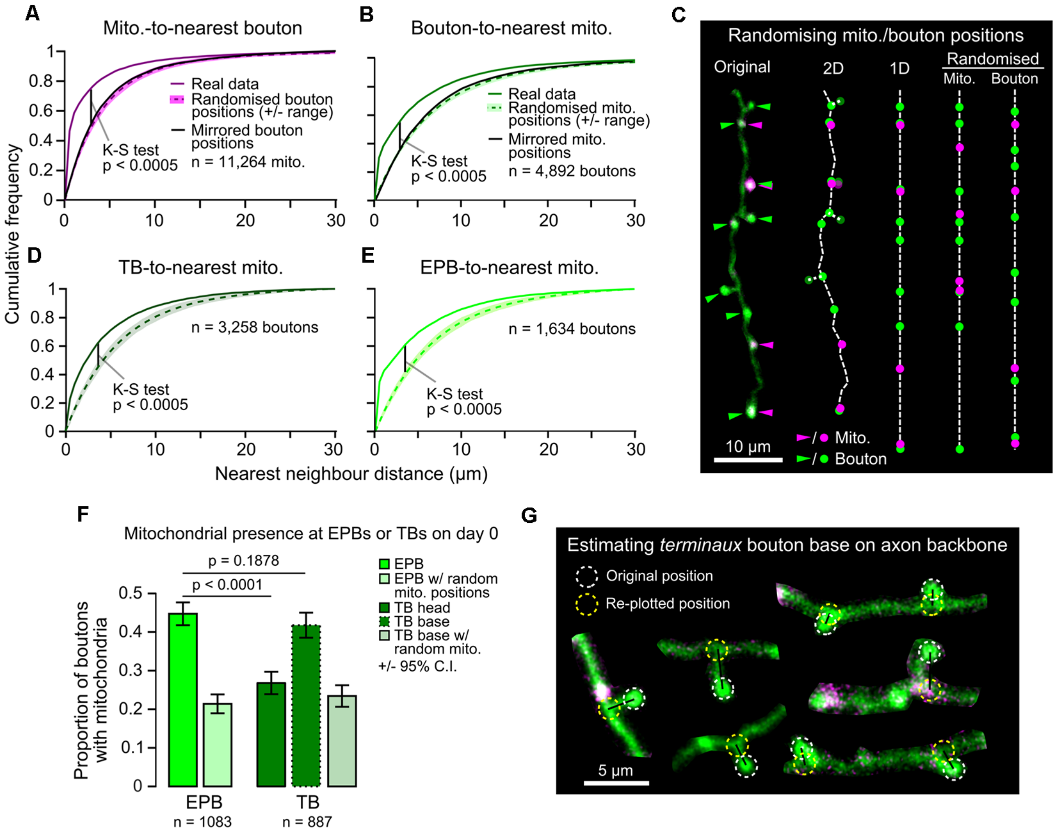

FIGURE 3 | Mitochondria are positioned more closely to *en passant* boutons (EPBs) than *terminaux* boutons (TBs). **(A)** The distribution of distances between each mitochondrion and its nearest bouton was plotted against the results from 1,000 rounds of randomized positioning of boutons for comparison to chance levels. Median ± range (*shaded area*). Kolmogorov–Smirnov (*K–S*) test between real data and the median of randomized positioning. As a further control, the real bouton positions were mirrored along the axon backbone to maintain the inter-bouton distances (*black line*) resulting in a similar distribution to the randomized positioning. **(B)** Same as in **(A)**, but for boutons and their nearest mitochondrion compared to results from randomized/mirrored positioning of mitochondria. **(C)** Illustration of the routine for randomizing positions. The original image was manually traced and a 2D skeleton interpolated from the segmented line trace. TBs were approximately placed at the nearest point on the axon backbone (their base) for randomizing in 1D. The 2D skeleton was then straightened to 1D and either mitochondria were randomly positioned alongside real bouton positions or vice versa. **(D,E)** Same as in **(B)**, but for TBs only (**D**; using TB base position, see **G**) or EPBs only **(E)**. **(F)** A greater proportion of EPBs have mitochondria within a biologically relevant distance (1.5 μm, see "Materials and Methods" section) than TBs (day 0 data; Chi-squared test). When mitochondrial localization was considered from the TB base instead of the head the difference was lost (Chi-squared test). Error bars ± 95% CI. **(G)** Estimated location of TB bases was achieved by finding the nearest neighbor point on the axon backbone that was closest to the TB head and re-plotting the TB to that position. 2P images were cropped for easier visualization.

related to decreased loss of pre-existing EPBs, but not of TBs (**Figure 4H**; Fisher's Exact test—EPBs, $p < 0.0005$; TBs, $p = 0.506$). Overall, these results suggest that the immediate survival of new boutons is weakly related to local mitochondrial presence, but this relationship becomes stronger and more consistent as boutons age.

DISCUSSION

It has long been reported that many, but not all, presynaptic release sites have mitochondria in close proximity to them (Gray, 1959; Shepherd and Harris, 1998; Chang et al., 2006; Kang et al., 2008; Obashi and Okabe, 2013; Smit-Rigter et al., 2016; Vaccaro et al., 2017). We found that axonal mitochondria in motor-somatosensory projection neurons are also preferentially associated with a subpopulation of synaptic boutons (**Figures 3, 4B,C**), suggesting bouton-specific recruitment and/or anchoring mechanisms (Kang et al., 2008; Courchet et al., 2013). The fact that mitochondria can modulate synaptic function suggests that having a resident mitochondrion may also relate to the activity-dependent plasticity of the synapse. Here, we have shown that there is indeed an association between mitochondrial positioning at presynaptic terminals and their structural longevity. As with other axons (De Paola et al., 2006; Qiao et al., 2015; Ash et al., 2018; Morimoto et al., 2018), we found that these motor-somatosensory axons exhibit structural plasticity driven by the turnover of a minority of their synaptic boutons (**Figures 4D–F**). Newly-formed boutons are more likely to possess mitochondria within their first 24 h (our smallest imaging interval) than by chance (**Figure 4B**), suggesting a link between synaptic and mitochondrial function even in the early stages of the synaptic lifecycle. Long-lasting

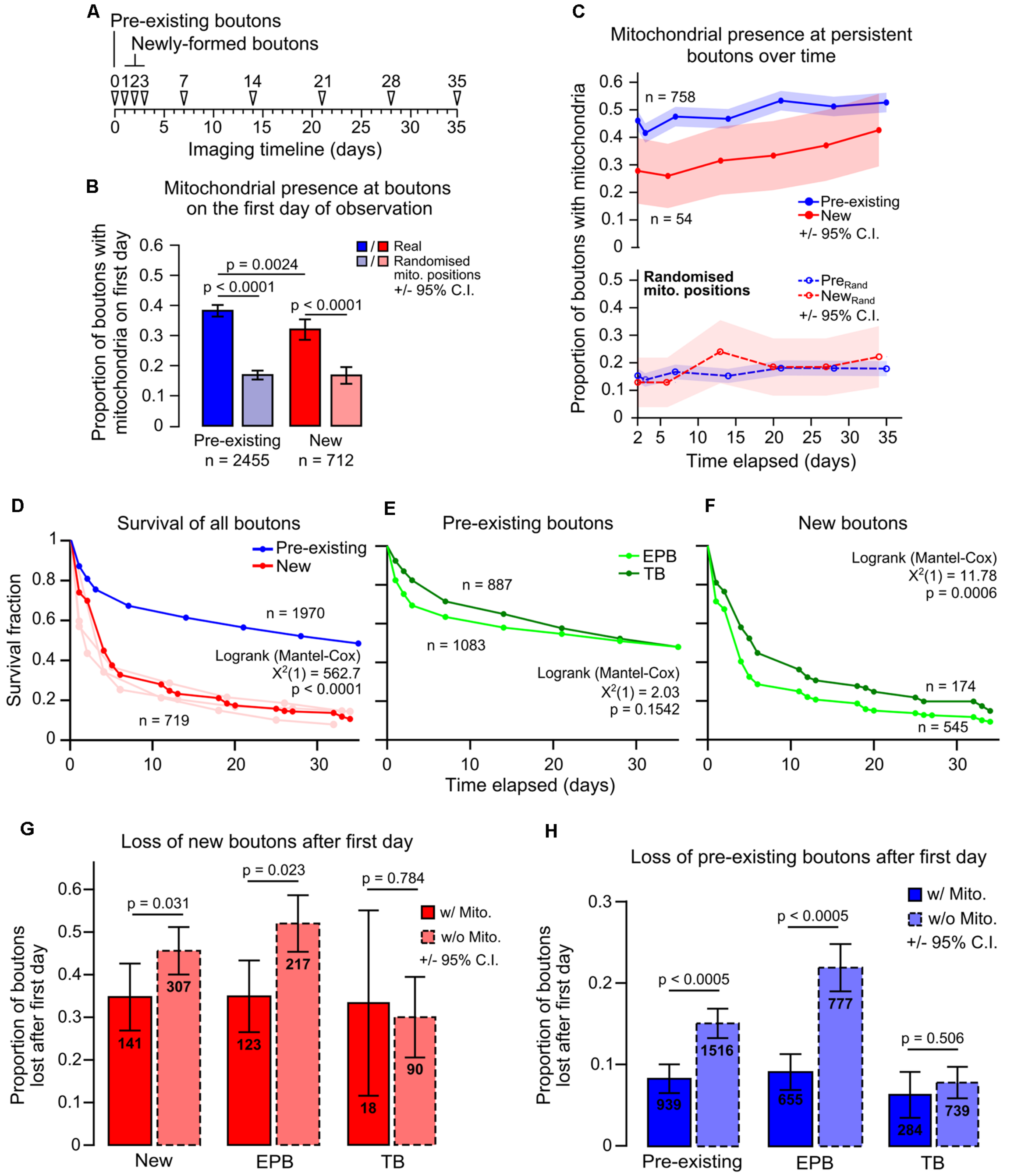

FIGURE 4 | Mitochondrial presence at individual boutons is positively related to bouton age and longevity. **(A)** Timeline indicating the classification of pre-existing boutons (first identified on day 0) and newly-formed boutons (first identified on days 1, 2 or 3). **(B)** Pre-existing boutons were more likely to have mitochondria (<1.5 μm) than newly-formed boutons (Chi-squared test). Newly-formed boutons had more mitochondria present than with randomized positioning of mitochondria, as did pre-existing boutons (Chi-squared test). Error bars ± 95% CI. **(C)** Boutons that persisted in every time point after day 2 (after all newly-formed boutons were identified) had their mitochondrial localization tracked. Pre-existing boutons showed a significant increase in mitochondrial presence (Cochran's Q test: $\chi^2_{(6)} = 51.359$, $p < 0.0005$). New boutons also showed an increase; however, this was not statistically significant (Cochran's Q test: $\chi^2_{(5)} = 6.81$, $p = 0.235$). When mitochondrial positions were randomized, both new and pre-existing boutons did not show significant increases in mitochondrial localization (Cochran's Q test: New, $\chi^2_{(5)} = 3.807$, $p = 0.578$; pre-existing, $\chi^2_{(6)} = 9.787$, $p = 0.134$). Shaded areas are ± 95% CI. **(D)** Survival of boutons was measured as the time until bouton loss. Pre-existing boutons were significantly more stable than new boutons (Log-rank test). The new bouton population was pooled from day 1–3 (light red lines). **(E,F)** Of the pre-existing population, TB and EPB survival was similar **(E)**, however, there was a small significant decrease in survival for new EPBs compared to TBs (**F**; Log-rank test). **(G)** The proportion of new boutons with or without mitochondria that were lost after their first day. There was a significant decrease in bouton loss when mitochondria were present at new boutons (Fisher's exact test). This relationship was due to the population of EPBs and not TBs. **(H)** Similarly, pre-existing EPBs with mitochondria were half as likely to be lost when compared to those without mitochondria (Fisher's exact test). Error bars ± 95% CI.

boutons are even more likely to have resident mitochondria (**Figures 4B,C**) and this decreases the chance of those boutons being removed by half (**Figure 4H**). This results in a persisting population of synaptic boutons that are more likely to contain mitochondria. As such, it seems likely that mitochondrial recruitment links to some synaptic function that promotes synaptic longevity (Rangaraju et al., 2019). This aligns with the previous finding that, in local axons within the visual cortex, boutons without mitochondria are more likely to be lost over a 4-day period (Smit-Rigter et al., 2016). Presynaptic mitochondria can modulate short-term plasticity of neurotransmitter release *via* their sequestration and slow release of calcium (Billups and Forsythe, 2002; Sun et al., 2013; Kwon et al., 2016). Also, presynaptic release probability does correlate with overall synaptic strength and vesicle pool size suggesting that there may be a link between mitochondrial influence on presynaptic release and the likelihood of a synapse becoming stronger and/or more stable (Monday et al., 2018). However, it remains unknown whether mitochondria directly influence long-term plasticity of synaptic function, as recently shown within dendrites (Smith et al., 2016; Divakaruni et al., 2018), or are simply recruited by alterations in synaptic activity to support ongoing presynaptic function (Vaccaro et al., 2017).

Our data suggest that any link between mitochondria and plasticity is local to neighboring synapses. This is because, although the density of mitochondria along different axonal branches varied considerably, it did not correlate with rates of bouton plasticity at the branch level (**Figure 2**). In contrast, the close proximity of mitochondria (within 1.5 μm) did relate to individual bouton stability (**Figure 4**). Mitochondria can be highly dynamic, undergoing rapid rounds of fusion and fission alongside axonal trafficking (Lewis et al., 2018), making it difficult to identify individual mitochondria over long periods of time with low imaging frequency. However, it has been reported that, despite the overall axonal positioning of mitochondria being unstable, there are more likely to be mitochondria stably retained near boutons than non-synaptic locations (Smit-Rigter et al., 2016). In this study, we found that the spatial arrangement of mitochondria and synaptic boutons depends on bouton type as mitochondria were generally located closer to EPBs than to TBs (**Figure 3**). This may be because physical access to the bouton head is restricted by the neck of TBs or could reflect functional differences between bouton types. Indeed, the difference in proximity was mirrored by the fact that local mitochondria were strongly linked to the survival of EPBs but not TBs. Interestingly, reported alterations in the stability of EPBs associated with aging might hint at parallel changes in synapse-mitochondrial coupling in the aged brain (Grillo et al., 2013). There is no information on potentially different mechanisms linking mitochondria to presynaptic function or plasticity in TBs vs. EPBs. Perhaps the longer distance between active zone and mitochondria in TB alters the way in which mitochondria can influence local signals, such as Ca^{2+}, that may be crucial for plasticity. Potentially divergent plasticity mechanisms at TBs and EPBs highlights the need for further investigation of the underexplored differences between different axonal bouton types.

DATA AVAILABILITY STATEMENT

The datasets generated for this study are available on request to the corresponding author.

ETHICS STATEMENT

All studies involving animals adhered to the Animals (Scientific Procedures) Act 1986 and Amendment Regulations 2012 as outlined in UK law and approved by the University of Bristol Animal Welfare and Ethics Review Board.

AUTHOR CONTRIBUTIONS

RL, JJ, and MA designed, developed and carried out the experiments and analysis. RL and MA wrote the manuscript.

FUNDING

RL was funded by a Wellcome Trust Ph.D. studentship (105386). JJ was funded by a Biotechnology and Biological Sciences Research Council (BBSRC)-CASE Ph.D. studentship (1370828). Equipment used in MA's laboratory was partially funded by the Medical Research Council (MR/J013188/1) and FP7 People:EUFP17 Marie Curie Actions (PCIG10-GA-2011-303680).

ACKNOWLEDGMENTS

We thank the Wolfson Bioimaging Facility for their support and expertise and MRC funding of a preclinical *in vivo* functional imaging platform for translational regenerative medicine. We thank Lilly UK for the gift of the AAV used in this study. This manuscript has been released as a preprint in BioRxiv (Lees et al., 2019).

SUPPLEMENTARY MATERIAL

The Supplementary Material for this article can be found online at: https://www.frontiersin.org/articles/10.3389/fnsyn.2019.00037/full#supplementary-material.

REFERENCES

Ash, R. T., Fahey, P. G., Park, J., Zoghbi, H. Y., and Smirnakis, S. M. (2018). Increased axonal bouton stability during learning in the mouse model of MECP2 duplication syndrome. *eNeuro* 5:ENEURO.0056-17.2018. doi: 10.1523/eneuro.0056-17.2018

Billups, B., and Forsythe, I. D. (2002). Presynaptic mitochondrial calcium sequestration influences transmission at mammalian central synapses. *J. Neurosci.* 22, 5840–5847.

Briones, T. L., Klintsova, A. Y., and Greenough, W. T. (2004). Stability of synaptic plasticity in the adult rat visual cortex induced by complex environment exposure. *Brain Res.* 1018, 130–135. doi: 10.1016/j.brainres.2004.06.001

Chang, D. T. W., Honick, A. S., and Reynolds, I. J. (2006). Mitochondrial trafficking to synapses in cultured primary cortical neurons. *J. Neurosci.* 26, 7035–7045. doi: 10.1523/jneurosci.1012-06.2006

Courchet, J., Lewis, T. L., Lee, S., Courchet, V., Liou, D.-Y., Aizawa, S., et al. (2013). Terminal axon branching is regulated by the LKB1-NUAK1 kinase pathway *via* presynaptic mitochondrial capture. *Cell* 153, 1510–1525. doi: 10.1016/j.cell.2013.05.021

Cserép, C., Pósfai, B., Schwarcz, A. D., and Dénes, Á. (2018). Mitochondrial ultrastructure is coupled to synaptic performance at axonal release sites. *eNeuro* 5:ENEURO.0390-17.2018. doi: 10.1523/eneuro.0390-17.2018

De Paola, V., Holtmaat, A., Knott, G., Song, S., Wilbrecht, L., Caroni, P., et al. (2006). Cell type-specific structural plasticity of axonal branches and boutons in the adult neocortex. *Neuron* 49, 861–875. doi: 10.1016/j.neuron.2006.02.017

Divakaruni, S. S., Dyke, A. M. V., Chandra, R., LeGates, T. A., Contreras, M., Dharmasri, P. A., et al. (2018). Long-term potentiation requires a rapid burst of dendritic mitochondrial fission during induction. *Neuron* 100, 860.e7–875.e7. doi: 10.1016/j.neuron.2018.09.025

Edelstein, A. D., Tsuchida, M. A., Amodaj, N., Pinkard, H., Vale, R. D., and Stuurman, N. (2014). Advanced methods of microscope control using µManager software. *J. Biol. Methods* 1:e10. doi: 10.14440/jbm.2014.36

Faul, F., Erdfelder, E., Lang, A.-G., and Buchner, A. (2007). G*Power 3: a flexible statistical power analysis program for the social, behavioral and biomedical sciences. *Behav. Res. Methods* 39, 175–191. doi: 10.3758/bf03193146

Franklin, K., and Paxinos, G. (2008). *The Mouse Brain in Stereotaxic Coordinates.* San Diego, CA: Academic Press.

Gray, E. G. (1959). Axo-somatic and axo-dendritic synapses of the cerebral cortex: an electron microscope study. *J. Anat.* 93, 420–433.

Grillo, F. W., Song, S., Teles-Grilo Ruivo, L. M., Huang, L., Gao, G., Knott, G. W., et al. (2013). Increased axonal bouton dynamics in the aging mouse cortex. *Proc. Natl. Acad. Sci. U S A* 110, E1514–E1523. doi: 10.1073/pnas.1218731110

Hall, C. N., Klein-Flügge, M. C., Howarth, C., and Attwell, D. (2012). Oxidative phosphorylation, not glycolysis, powers pre- and postsynaptic mechanisms underlying brain information processing. *J. Neurosci.* 32, 8940–8951. doi: 10.1523/jneurosci.0026-12.2012

Holtmaat, A., and Caroni, P. (2016). Functional and structural underpinnings of neuronal assembly formation in learning. *Nat. Neurosci.* 19, 1553–1562. doi: 10.1038/nn.4418

Holtmaat, A., Bonhoeffer, T., Chow, D. K., Chuckowree, J., Paola, V. D., Hofer, S. B., et al. (2009). Long-term, high-resolution imaging in the mouse neocortex through a chronic cranial window. *Nat. Protoc.* 4, 1128–1144. doi: 10.1038/nprot.2009.89

Jackson, J. S., Witton, J., Johnson, J. D., Ahmed, Z., Ward, M., Randall, A. D., et al. (2017). Altered synapse stability in the early stages of tauopathy. *Cell Rep.* 18, 3063–3068. doi: 10.1016/j.celrep.2017.03.013

Johnson, C. M., Peckler, H., Tai, L.-H., and Wilbrecht, L. (2016). Rule learning enhances structural plasticity of long-range axons in frontal cortex. *Nat. Commun.* 7:10785. doi: 10.1038/ncomms10785

Kang, J.-S., Tian, J.-H., Pan, P.-Y., Zald, P., Li, C., Deng, C., et al. (2008). Docking of axonal mitochondria by syntaphilin controls their mobility and affects short-term facilitation. *Cell* 132, 137–148. doi: 10.1016/j.cell.2007.11.024

Kasthuri, N., Hayworth, K. J., Berger, D. R., Schalek, R. L., Conchello, J. A., Knowles-Barley, S., et al. (2015). Saturated reconstruction of a volume of neocortex. *Cell* 162, 648–661. doi: 10.1016/j.cell.2015.06.054

Kim, J. H., Lee, S.-R., Li, L.-H., Park, H.-J., Park, J.-H., Lee, K. Y., et al. (2011). High cleavage efficiency of a 2A peptide derived from porcine teschovirus-1 in human cell lines, zebrafish and mice. *PLoS One* 6:e18556. doi: 10.1371/journal.pone.0018556

Kwon, S.-K., Iii, R. S., Lewis, T. L., Hirabayashi, Y., Maximov, A., and Polleux, F. (2016). LKB1 regulates mitochondria-dependent presynaptic calcium clearance and neurotransmitter release properties at excitatory synapses along cortical axons. *PLoS Biol.* 14:e1002516. doi: 10.1371/journal.pbio.1002516

Landers, M. S., Knott, G. W., Lipp, H. P., Poletaeva, I., and Welker, E. (2011). Synapse formation in adult barrel cortex following naturalistic environmental enrichment. *Neuroscience* 199, 143–152. doi: 10.1016/j.neuroscience.2011.10.040

Lee, E., Choi, J., Jo, Y., Kim, J. Y., Jang, Y. J., Lee, H. M., et al. (2016). ACT-PRESTO: rapid and consistent tissue clearing and labeling method for 3-dimensional (3D) imaging. *Sci. Rep.* 6:18631. doi: 10.1038/srep18631

Lees, R. M., Johnson, J. D., and Ashby, M. C. (2019). Presynaptic boutons that contain mitochondria are more stable. *BioRxiv [Preprint].* doi: 10.1101/580530

Lein, E. S., Hawrylycz, M. J., Ao, N., Ayres, M., Bensinger, A., Bernard, A., et al. (2007). Genome-wide atlas of gene expression in the adult mouse brain. *Nature* 445, 168–176. doi: 10.1038/nature05453

Lewis, T. L., Kwon, S.-K., Lee, A., Shaw, R., and Polleux, F. (2018). MFF-dependent mitochondrial fission regulates presynaptic release and axon branching by limiting axonal mitochondria size. *Nat. Commun.* 9:5008. doi: 10.1038/s41467-018-07416-2

Mao, T., Kusefoglu, D., Hooks, B. M., Huber, D., Petreanu, L., and Svoboda, K. (2011). Long-range neuronal circuits underlying the interaction between sensory and motor cortex. *Neuron* 72, 111–123. doi: 10.1016/j.neuron.2011.07.029

Monday, H. R., Younts, T. J., and Castillo, P. E. (2018). Long-term plasticity of neurotransmitter release: emerging mechanisms and contributions to brain function and disease. *Ann. Rev. Neurosci.* 41, 299–322. doi: 10.1146/annurev-neuro-080317-062155

Morimoto, M. M., Tanaka, S., Mizutani, S., Urata, S., Kobayashi, K., and Okabe, S. (2018). *In vivo* observation of structural changes in neocortical catecholaminergic projections in response to drugs of abuse. *eNeuro* 5:ENEURO.0071-17.2018. doi: 10.1523/eneuro.0071-17.2018

Mostany, R., Anstey, J. E., Crump, K. L., Maco, B., Knott, G., and Portera-Cailliau, C. (2013). Altered synaptic dynamics during normal brain aging. *J. Neurosci.* 33, 4094–4104. doi: 10.1523/JNEUROSCI.4825-12.2013

Newcombe, R. G. (1998). Two-sided confidence intervals for the single proportion: comparison of seven methods. *Stat. Med.* 17, 857–872. doi: 10.1002/(sici)1097-0258(19980430)17:8<857::aid-sim777>3.0.co;2-e

Nithianantharajah, J., Levis, H., and Murphy, M. (2004). Environmental enrichment results in cortical and subcortical changes in levels of synaptophysin and PSD-95 proteins. *Neurobiol. Learn. Mem.* 81, 200–210. doi: 10.1016/j.nlm.2004.02.002

Obashi, K., and Okabe, S. (2013). Regulation of mitochondrial dynamics and distribution by synapse position and neuronal activity in the axon. *Eur. J. Neurosci.* 38, 2350–2363. doi: 10.1111/ejn.12263

Oswald, M. J., Tantirigama, M. L. S., Sonntag, I., Hughes, S. M., and Empson, R. M. (2013). Diversity of layer 5 projection neurons in the mouse motor cortex. *Front. Cell. Neurosci.* 7:174. doi: 10.3389/fncel.2013.00174

Petreanu, L., Gutnisky, D. A., Huber, D., Xu, N., O'Connor, D. H., Tian, L., et al. (2012). Activity in motor-sensory projections reveals distributed coding in somatosensation. *Nature* 489, 299–303. doi: 10.1038/nature11321

Petreanu, L., Mao, T., Sternson, S. M., and Svoboda, K. (2009). The subcellular organization of neocortical excitatory connections. *Nature* 457, 1142–1145. doi: 10.1038/nature07709

Pologruto, T. A., Sabatini, B. L., and Svoboda, K. (2003). ScanImage: flexible software for operating laser scanning microscopes. *Biomed. Eng. Online* 2:13. doi: 10.1186/1475-925X-2-13

Qiao, Q., Ma, L., Li, W., Tsai, J.-W., Yang, G., and Gan, W.-B. (2015). Long-term stability of axonal boutons in the mouse barrel cortex. *Dev. Neurobiol.* 76, 252–261. doi: 10.1002/dneu.22311

Rangaraju, V., Calloway, N., and Ryan, T. A. (2014). Activity-driven local ATP synthesis is required for synaptic function. *Cell* 156, 825–835. doi: 10.1016/j.cell.2013.12.042

Rangaraju, V., Lauterbach, M., and Schuman, E. M. (2019). Spatially stable mitochondrial compartments fuel local translation during plasticity. *Cell* 176, 73.e15–84.e15. doi: 10.1016/j.cell.2018.12.013

Schindelin, J., Arganda-Carreras, I., Frise, E., Kaynig, V., Longair, M., Pietzsch, T., et al. (2012). Fiji: an open-source platform for biological-image analysis. *Nat. Methods* 9, 676–682. doi: 10.1038/nmeth.2019

Shepherd, G. M. G., and Harris, K. M. (1998). Three-dimensional structure and composition of CA3→CA1 axons in rat hippocampal slices: implications for presynaptic connectivity and compartmentalization. *J. Neurosci.* 18, 8300–8310. doi: 10.1523/jneurosci.18-20-08300.1998

Smith, H. L., Bourne, J. N., Cao, G., Chirillo, M. A., Ostroff, L. E., Watson, D. J., et al. (2016). Mitochondrial support of persistent presynaptic vesicle mobilization with age-dependent synaptic growth after LTP. *Elife* 5:e15275. doi: 10.7554/eLife.15275

Smit-Rigter, L., Rajendran, R., Silva, C. A. P., Spierenburg, L., Groeneweg, F., Ruimschotel, E. M., et al. (2016). Mitochondrial dynamics in visual cortex are limited *in vivo* and not affected by axonal structural plasticity. *Curr. Biol.* 26, 2609–2616. doi: 10.1016/j.cub.2016.07.033

Sobieski, C., Fitzpatrick, M. J., and Mennerick, S. J. (2017). Differential presynaptic ATP supply for basal and high-demand transmission. *J. Neurosci.* 37, 1888–1899. doi: 10.1523/jneurosci.2712-16.2017

Song, S., Grillo, F. W., Xi, J., Ferretti, V., Gao, G., and De Paola, V. (2016). EPBscore: a novel method for computer-assisted analysis of axonal structure and dynamics. *Neuroinformatics* 14, 121–127. doi: 10.1007/s12021-015-9274-5

Sun, T., Qiao, H., Pan, P.-Y., Chen, Y., and Sheng, Z.-H. (2013). Motile axonal mitochondria contribute to the variability of presynaptic strength. *Cell Rep.* 4, 413–419. doi: 10.1016/j.celrep.2013.06.040

Vaccaro, V., Devine, M. J., Higgs, N. F., and Kittler, J. T. (2017). Miro1-dependent mitochondrial positioning drives the rescaling of presynaptic Ca^{2+} signals during homeostatic plasticity. *EMBO Rep.* 18, 231–240. doi: 10.15252/embr.201642710

Veinante, P., and Deschênes, M. (2003). Single-cell study of motor cortex projections to the barrel field in rats. *J. Comp. Neurol.* 464, 98–103. doi: 10.1002/cne.10769

Zufferey, R., Donello, J. E., Trono, D., and Hope, T. J. (1999). Woodchuck hepatitis virus posttranscriptional regulatory element enhances expression of transgenes delivered by retroviral vectors. *J. Virol.* 73, 2886–2892.

Conflict of Interest: The authors declare that the research was conducted in the absence of any commercial or financial relationships that could be construed as a potential conflict of interest.

frontiers in Synaptic Neuroscience

ORIGINAL RESEARCH
published: 10 March 2020
doi: 10.3389/fnsyn.2020.00009

Modeling the Shape of Synaptic Spines by Their Actin Dynamics

Mayte Bonilla-Quintana [1]*, Florentin Wörgötter [1,2], Christian Tetzlaff [1,2] and Michael Fauth [1]

[1] Department for Computational Neuroscience, Third Institute of Physics-Biophysics, Georg-August-University, Göttingen, Germany, [2] Bernstein Center for Computational Neuroscience, Georg-August-University, Göttingen, Germany

Dendritic spines are the morphological basis of excitatory synapses in the cortex and their size and shape correlates with functional synaptic properties. Recent experiments show that spines exhibit large shape fluctuations that are not related to activity-dependent plasticity but nonetheless might influence memory storage at their synapses. To investigate the determinants of such spontaneous fluctuations, we propose a mathematical model for the dynamics of the spine shape and analyze it in 2D—related to experimental microscopic imagery—and in 3D. We show that the spine shape is governed by a local imbalance between membrane tension and the expansive force from actin bundles that originates from discrete actin polymerization foci. Experiments have shown that only few such polymerization foci co-exist at any time in a spine, each having limited life time. The model shows that the momentarily existing set of such foci pushes the membrane along certain directions until foci are replaced and other directions may now be affected. We explore these relations in depth and use our model to predict shape and temporal characteristics of spines from the different biophysical parameters involved in actin polymerization. Approximating the model by a single recursive equation we finally demonstrate that the temporal evolution of the number of active foci is sufficient to predict the size of the model-spines. Thus, our model provides the first platform to study the relation between molecular and morphological properties of the spine with a high degree of biophysical detail.

Keywords: dendritic spines, actin, simulations, model, spontaneous shape change

Edited by:
Richard Naud,
University of Ottawa, Canada

Reviewed by:
Nicolas Doyon,
Quebec Mental Health Institute (IUSMQ), Canada
Pirta Elina Hotulainen,
Minerva Foundation Institute for Medical Research, Finland

****Correspondence:***
Mayte Bonilla-Quintana
mayte.bonilla-quintana@phys.uni-goettingen.de

Received: *15 December 2019*
Accepted: *24 February 2020*
Published: *10 March 2020*

Citation:
Bonilla-Quintana M, Wörgötter F, Tetzlaff C and Fauth M (2020) Modeling the Shape of Synaptic Spines by Their Actin Dynamics. Front. Synaptic Neurosci. 12:9. doi: 10.3389/fnsyn.2020.00009

1. INTRODUCTION

Dendritic spines are small protrusions from neural dendrites, which form the post-synaptic part of most excitatory synapses in the cortex (Yuste, 2010). One of the central paradigms of neuroscience is that synapses store memories by changing their transmission efficacies during learning (Martin et al., 2000) and it has been shown that synaptic transmission efficacy correlates with size and shape of the spines. This has been mostly studied using the volume of the spine head (Matsuzaki et al., 2001, 2004; Zhou et al., 2004; Hotulainen and Hoogenraad, 2010, more details in Fauth and Tetzlaff, 2016) providing evidence for a link between spine-morphological and synaptic-functional properties. However, it recently became clear that most of the dynamic properties of changing spine volumes emerge from spontaneous spine specific processes that are not determined by the activity of the pre- or post-synaptic neuron (Dunaevsky et al., 1999; Yasumatsu et al., 2008; Dvorkin and Ziv, 2016). As such spontaneous fluctuations could affect memory functions due to the above described link (Mongillo et al., 2017), a thorough understanding of their characteristics and underlying processes is necessary. Experiments imaging the shape of dendritic spines can provide snapshots at distinct time points, but mathematical models are needed to bridge between these time points and to understand shape fluctuations and their properties. However, so far only phenomenological models have been proposed (Yasumatsu et al., 2008; Loewenstein et al., 2011; Statman et al., 2014; Hartmann et al., 2015) that describe fluctuations coarsely on a timescale of days. Here, we take a different approach by modeling the fast actin dynamics underlying shape fluctuations. This approach also allows us to explore the influence of the molecular and mechanical processes involved and to make predictions on the fluctuations when their properties vary.

The spine shape is determined by its cytoskeleton, the main component of which is actin. Actin is a globular protein (G-actin), which can assemble into filamentous polymers (F-actin). These polymers undergo a continuous treadmilling process (**Figure 1A**; see e.g., Pollard et al., 2000; Mogilner and Edelstein-Keshet, 2002; Bennett et al., 2011 for details): G-actin with bound ATP is added preferentially to the barbed (+) ends of the filament (see for example added monomer marked with P in **Figure 1A**), while at the pointed (−) end older actin monomers of the filament are mostly depolymerized. Thus, actin filaments are polar structures with one end growing more rapidly than the other. This asymmetry between barbed and pointed end is further strengthened when the ATP bound at actin filaments hydrolyzes to ADP, which promotes disassembling of the pointed ends by severing proteins, such as cofilin (D in **Figure 1A**), when the pointed end is in an uncapped state (U in **Figure 1A**). Following this, the disassembled cofilin-ADP-actin dissociates to cofilin and an ADP-actin monomere and finally, profilin catalyzes the exchange of ADP to ATP and the resulting ATP-actin is again available for the polymerization process at the barbed end (omitted in **Figure 1A**). Additional to this treadmilling process, complexes, such as Arp2/3 can induce branching of a filament whose two daughter-filaments have uncapped barbed ends (B in **Figure 1A**) and capped minus ends. Moreover, barbed ends can become unable to polymerize G-actin due to capping proteins (C in **Figure 1A**).

Although the treadmilling process in dendritic spines occurs at different velocities, two distinctive pools of F-actin can be identified (Honkura et al., 2008): The static pool, which has a slow treadmilling velocity and is localized at the base of the spine head whilst the dynamic pool treadmills faster and is found at the tip of the spine head. Honkura et al. (2008) suggest that these pools have different functions: the static pool gives stability to the base of the spine, while the dynamic pool causes spine expansion due to the higher rate of actin polymerization resulting from

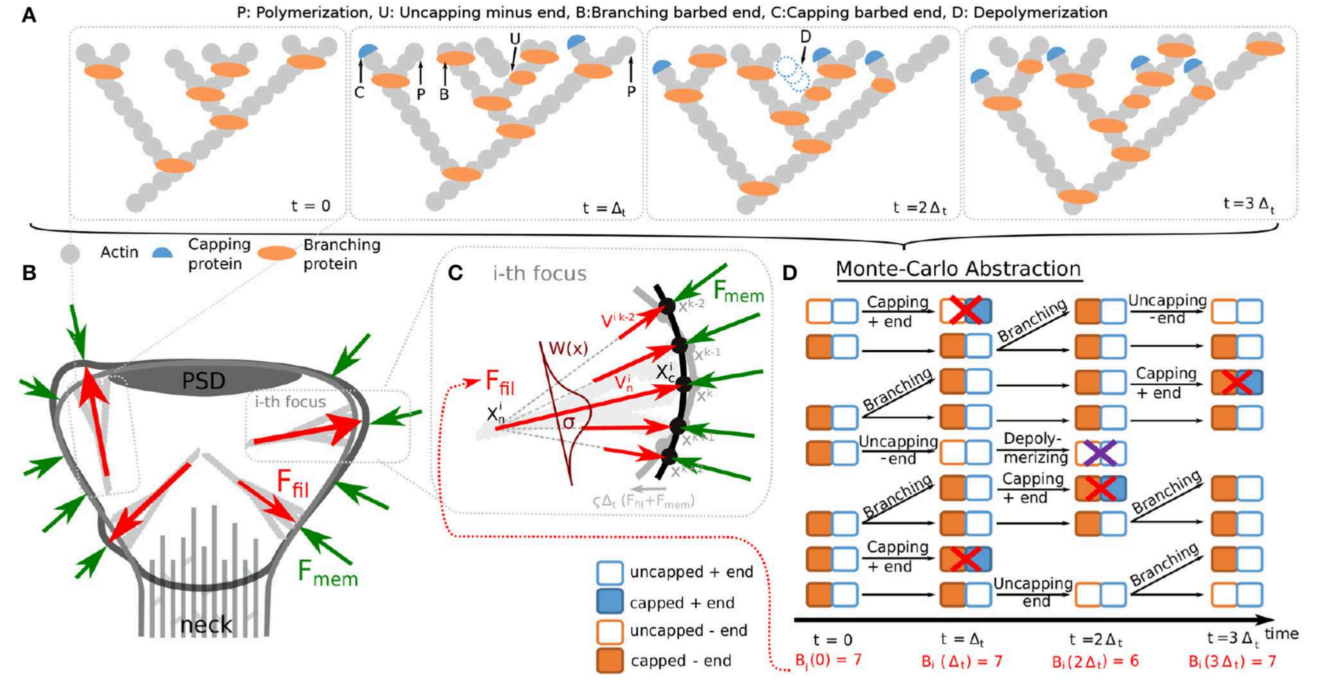

FIGURE 1 | Components of the proposed spine fluctuation model. **(A)** Schematic picture of actin filaments in a polymerization foci at successive time-points. Additional to polymerization of new actin monomers at the barbed ends, other events can occur in actin filaments, such as: branching the barbed ends by inserting branching protein Arp2/3, capping barbed ends with capping proteins, uncapping minus end and depolymerizing uncapped minus ends. These events are indicated by an arrow and the corresponding first letter (see glossary above the panels). **(B)** Our model for spine fluctuation assumes that the shape of the membrane is determined by the membrane forces $\mathbf{F}_{mem}$ resisting bending and stretching and the forces generated by actin polymerization $\mathbf{F}_{fil}$ at a few foci. **(C)** Actin filaments at the foci are considered to extent laterally to the membrane. Hence, force is proportional to the number of barbed ends at the focus and attenuated by a spatial kernel $W(x)$. The membrane is simulated by a discrete mesh (here depicted by dots) that moves every time-step proportional to imbalance of the acting forces (black membrane → gray membrane). **(D)** The dynamics of actin in each focus are abstracted to a Monte Carlo model describing the state of the barbed and pointed ends of any filament. We depict these state representations for the time course shown in **(A)**. During simulations, the transitions between different states happen according to the processes described in **(A)** with defined rates. See main text for details.

the fast treadmilling velocity. Therefore, in this paper, we will focus on the dynamic pool. Interestingly, the fast treadmilling in this pool is not occurring uniformly distributed over the whole spine, but at discrete foci of actin polymerization (Frost et al., 2010). There are usually only a handful of those foci in one spine, which are well-separated from each other and can be identified by their increased polymerization rate. Because polymerization has been identified as the molecular mechanism responsible for spine shape fluctuations (Fischer et al., 1998), it can be assumed that these foci generate the main expansive force that underlies shape fluctuations, which are usually inhomogeneous and asymmetric. Although the role of actin in synaptogenesis and synaptic function has been thoroughly described (Cingolani and Goda, 2008; Hotulainen et al., 2009; Korobova and Svitkina, 2010; Basu and Lamprecht, 2018; Borovac et al., 2018), the exact role of actin spontaneous protrusions is still unknown, albeit found in the living mouse brain (Berning et al., 2012) and across different neuron types (Dunaevsky et al., 1999).

Mathematical models that link actin activity to such asymmetric spine fluctuations are, however, missing so far. Although models of the actin treadmilling process have been derived (Mogilner and Edelstein-Keshet, 2002) and adapted to the conditions in the dendritic spine (Bennett et al., 2011), they have not been connected to spine shape. To evaluate how shape is influenced by actin dynamics, one has to consider not only the forces created by the filaments, but also the counteracting forces from the lipid membrane that encloses the spine. Such models for force generation by actin filaments (Mogilner and Oster, 1996) and their interaction with the membrane have been derived and successfully applied to the movement of bacteria, cell motility (Mogilner and Oster, 2003; Rubinstein et al., 2009; Craig et al., 2015; for a review see Mogilner, 2006), and to explain dendritic spine maturation (Miermans et al., 2017). Yet, most of these models describe the dynamics of the cell shape based on density descriptions of the actin filaments or assume a homogeneous distribution of F-actin. However, considering the comparably small numbers of filaments within the spine (compare Korobova and Svitkina, 2010), a density description is not applicable. The homogeneity assumption, in turn, entails very regular and symmetric spine shapes, which are not observed in experiment (e.g., Fischer et al., 1998) and also are not consistent with the existence of actin polymerization foci.

Here, we present a model that considers heterogeneous actin dynamics caused by foci of actin polymerization. We use the forces generated by their treadmilling activity together with the counteracting forces from the membrane and the membrane-mediated coupling to other foci to derive a model of spine membrane shape fluctuations in 2D. Moreover, we extend the model to 3D to have a more realistic description of the spine and show that shape fluctuations behave similarly to those in 2D, suggesting that the 2D model can be used as a computationally more efficient surrogate. We show that the properties of spine fluctuations are strongly influenced by the dynamics of filament assembly constituting the determinants of the force generation by actin. The central finding of this study is that spine shape fluctuations can be fully explained by the effect that the small number of polymerization foci leads to a discretization of the outwards pushing-force direction, while their limited life time determines the temporal properties of these fluctuations. Thus, we can also show that spine area evolution can be predicted by the number of polymerization foci. Thus, this model provides the required biophysically detailed basis for future investigations of spine shape changes induced by synaptic plasticity.

2. MATERIALS AND METHODS

2.1. Model

Based on the findings of Frost et al. (2010), we assume that the spine shape is determined by a small number of distinct foci of actin polymerization (gray filaments in **Figure 1B**), for which the processes of treadmilling, branching, and capping of the filaments are modeled individually (see section 2.1.2). As a consequence, each focus can have multiple barbed ends generating forces that push the membrane outward (see section 2.1.4, red arrows in **Figures 1B,C**). These forces concur with the inward directed forces generated by the membrane's resistance against deformation (see section 2.1.5, green arrows in **Figures 1B,C**). If these forces are locally unbalanced, the membrane moves giving rise to shape fluctuations (transition from black to gray membrane shape in **Figure 1C**). To simulate this interaction of membrane shape and forces, we use discrete time-steps and the finite elements method. In particular, the membrane is represented by a mesh of points (or vertices) for which geometrical properties, forces, and movements are calculated (see **Supplementary Material**).

2.1.1. Membrane Mesh Initialization and Morphological Constraints

As stated above, we represent the membrane enclosing the spine by a mesh of vertices $k \in \{1, 2, ...n_{vertices}\}$ described by their (two-dimensional) position vectors $\mathbf{x}^k = (x^k, y^k)$, $1 \leq k \leq n$. Upon initialization, a polygonal approximation for a circle with radius r_s and centered at the origin of the x-y plane is created. As in this study we focus on the shape fluctuations of mature spines, we implement two major morphological constraints:

On the one hand, the spine neck of mature spines typically contains heavily interlinked actin bundles which are rather stable and have a much slower treadmilling velocity than those in the spine tips (Okamoto et al., 2004). Along this line, the spine neck width is largely stable on the here considered timescale of hours (Tønnesen et al., 2014). Therefore, we fix the location of mesh-points at the neck throughout the whole simulation. We establish those fixed mesh points during the mesh initialization by selecting all points $\mathbf{x} = (x, y)$ with $y \leq h_{neck}$ and fixing them to (x, h_{neck}). Here we define h_{neck} as the value of y where $x = r_{neck}$ and $y < 0$.

On the other hand, the movement of the post-synaptic density (PSD) is constrained as it is heavily interlinked with the presynaptic site. Also, the PSD size on unstimulated spines is conserved over the timescale of hours (Meyer et al., 2014). Therefore, we fix the mesh-points (x, y) with $y \geq h_{PSD}$ to (x, h_{PSD}), where h_{PSD} is the value of y where $x = r_{PSD}$ and $y > 0$. Hence, the resulting initial shape resembles a flat disk. A schematic depiction of this process is given in **Figure S1**. Note that because the number of synaptic receptors is correlated with PSD size, the assumption of fixed PSD size implies no change in synaptic current.

2.1.2. Actin Dynamics at Individual Foci

We adapt the stochastic model proposed by Bennett et al. (2011) for F-actin dynamics of the actin dynamic pool in the spine head. Because we are concerned about the spontaneous spine shape fluctuations, we only simulate the treadmilling process of Bennett et al. (2011) in which G-actin is polymerized at the uncapped barbed ends in every time-step of length Δ_t. In addition, the following processes can occur at each actin filament:

- Uncapped barbed ends branch by including an Arp2/3 molecule and give rise to a new filament with a probability $\Delta_t \gamma_{branch}(t)$.
- Uncapped barbed ends are capped by a capping protein with a probability $\Delta_t \gamma_{cap}$. Because polymerization is not possible when a barbed end is capped, such barbed end does not generate force. As uncapping occurs very seldom, these filaments are eliminated from the simulation.
- Capped minus ends are uncapped with a probability $\Delta_t \gamma_{uncap}$.
- Uncapped minus ends are severed with a probability $\Delta_t \gamma_{sever}$, which leads to the removal of the respective filament.

Note that these events are necessary so that the length and concentration of F-actin are within a biologically plausible range. Otherwise, filaments will grow and live indefinitely. In Bennett et al. (2011), the branching rate for a filament $\gamma_{branch}(t)$ depends on the total number of barbed ends $B(t)$ in the spine at time t, $\gamma_{branch}(t) = \hat{\gamma}_{branch}(t)/B(t)$. However, in our model we assume that there are discrete foci of actin polymerization. Hence, we adapt the branching rate to be proportional to the local number of barbed ends B^i at each focus i, thus $\gamma^i_{branch}(t) = \hat{\gamma}_{branch}(t)/B^i(t)$.

Moreover, actin dynamics in our model are embedded in a 2D membrane that approximates the dendritic spine morphology instead of one straight line used by Bennett et al. (2011) in which the barbed ends at the membrane branch freely at a rate $\hat{\gamma}_{branch}(t)$ proportional to a constant treadmilling velocity $v_T(t)$. However, the cell membrane imposes a resistance to filament assembly and thus, decreases this rate: if the membrane resistance is high, then the filament will be less likely to branch. In our model, this membrane resistance depends on the local spine geometry. Hence, following Mogilner and Edelstein-Keshet (2002) we assume that the branching rate depends on the treadmilling velocity $v_T(t) = \phi k_{on} \delta a$ where δ is the length of an actin monomer, k_{on} the barbed end monomer assembly rate, and a the concentration profilin-ATP-actin available for polymerization. As we are not modeling plasticity related changes in this study, we can consider a as a constant (see **Supplementary Material**). This free polymerization velocity is attenuated due to a counteracting membrane force according to the Brownian ratchet theory (Mogilner and Oster, 1996; Footer et al., 2007), which takes into account the absolute temperature T, the Boltzmann's constant k_B and the force $\mathbf{F}^i_{mem}(t)$ working against polymerization which is generated by the membrane at the ith focus center. Thus, the branching probability at each focus is given by

$$\gamma^i_{branch}(t) = \phi k_{on} \delta a \exp\left(-\frac{||\mathbf{F}^i_{mem}(t)||\delta}{k_B T B^i(t)}\right) \frac{1}{B^i(t)}. \qquad (1)$$

Note that this membrane-force-dependency of the branching rate generates a feedback between the number of barbed ends and membrane shape.

In this study, we are not interested in the geometrical configuration of the actin filaments but rather in the amount of force generated by actin polymerization. Therefore, we characterize F-actin by the states (capped/uncapped) of its barbed end (normally uncapped) and pointed end (normally capped or bound to a Arp2/3 complex) instead of explicitly simulate each filament and how it grows in space as in Bennett et al. (2011). Such filament states change when a branching, capping or severing event occur in the model described above, i.e., when a random number drawn for this filament falls below the indicated probability. We iterate through all filaments with uncapped barbed ends within the active actin polymerization foci and the above processes in the indicated order. Afterwards, the remaining uncapped barbed ends in each polymerization focus i are counted and their number B^i is used to calculate the expansive force exerted by that focus (see section 2.1.4). **Figure 1D** shows an exemplary temporal evolution of the active filaments in one of the polymerization foci, where all of these processes occur. The rate values are stated in **Table 1**.

2.1.3. Foci Generation and Removal

Note that the activity of a focus is determined by its uncapped barbed ends, which can only emerge from other uncapped barbed ends due to branching; hence, foci naturally become inactive and removed as soon as they have no uncapped barbed ends left. Therefore, mechanisms for generation of new foci are necessary. Frost et al. (2010) observed that the discrete actin polymerization foci locate mostly at the spine tip but also through out the spine. The majority of their F-actin is shorter than 200 nm and reaches a peak density within 300 nm of the PSD center. Moreover, Frost et al. (2010) noted that the dynamics of F-actin at these foci must be regulated near the membrane due that the branching protein Arp2/3 concentrates within 100 nm of the spine membrane whilst the filament severing protein cofilin concentrates within 200 nm of the membrane. Furthermore, data from Rácz and Weinberg (2008) show that Arp2/3 complex is mainly distributed in a doughnut-shaped domain within the spine that could represent a zone where F-actin branches and generates the forces necessary for membrane protrusion. Taken all together, we assume that actin polymerization foci must initiate near to the membrane and PSD so that filaments conserve their small size and co-locate with the branching proteins.

Therefore, in our model the nucleation of a new actin polymerization focus i is implemented in two steps: First, a two dimensional nucleation position denoted by a vector $\mathbf{X}^i_n$ (see **Figure 1C**) is selected in the following way: To simultaneously account for the above geometrical restrictions and the asymmetrical form of the spine head, we generate a set of 1,000 uniformly distributed candidate points inside the spine.

TABLE 1 | Model parameter values.

Symbol	Unit	Definition	Value	References
Δ_t	s	Length of the time-step	1/8	Frost et al., 2010 (fitted as in Mogilner and Edelstein-Keshet, 2002)
δ_s	μm	Target length of and edge	0.03	Fitted for numerical accuracy (see text)
r_s	μm	Initial spine radius	0.5	Tønnesen et al., 2014; Miermans et al., 2017
r_{neck}	μm	Neck radius	0.0995	Tønnesen et al., 2014; Miermans et al., 2017
r_{PSD}	μm	PSD radius	0.3571	Meyer et al., 2014
n_{f_0}	1	Initial number of nucleation points	4	Frost et al., 2010
γ_{cap}	s^{-1}	Barbed-end capping rate	1	Bennett et al., 2011
γ_{uncap}	s^{-1}	Uncapping rate for—ends	1/30	Bennett et al., 2011
γ_{sever}	s^{-1}	Depolymerization/Severing rate of—ends	1	Bennett et al., 2011
γ_f	s^{-1}	Nucleation rate of new actin focus of activity	0.1	Basu and Lamprecht, 2018, see text
a	μM	Concentration of profilin-ATP-actin at steady state	3.8	Bennett et al., 2011, see **Supplementary Material**
ϕ	μm^{-2}	Proportionality constant	75	–
k_{on}	$\mu M^{-1}s^{-1}$	Barbed-end monomer assembly rate constant	11.6	Mogilner and Edelstein-Keshet, 2002
δ	μm	Length of an actin monomer	0.0022	Mogilner and Edelstein-Keshet, 2002
k_BT	pNμm	Thermal energy	0.0041	Mogilner and Edelstein-Keshet, 2002
P	pNμm^{-2}	Difference between internal and external pressure	85.7143	Young-Laplace law see Deserno, 2015
τ	pNμm^{-1}	Surface tension	15	Pontes et al., 2013
κ	pNμm	Bending modulus	0.18	Pontes et al., 2013
α	pN	Strength of filament influence	3.8	Miermans et al., 2017
σ	1	Extend of filament influence	0.3	–
ζ	$\mu m^2 s^{-1} pN^{-1}$	Strength of force update	0.002	–
λ	μm	Nucleation distance parameter	0.025	–

From this candidate set, we remove all points that are not within a distance of 0.1μm from the membrane and that are within 0.1μm from the PSD. Then, one of the remaining n_{cand} points j is selected with probability $p_j = e^{-d_j/\lambda}\left(\sum_{l=1}^{n_{cand}} e^{-d_l/\lambda}\right)^{-1}$, which depends on its distance from the PSD d_j via a scale parameter λ. For $\lambda \to 0^+$ nucleation near to the PSD is favored whereas for $\lambda \to \infty$ the distance to the PSD has no influence.

Second, the primary nucleation direction is randomly selected as the vector pointing from $\mathbf{X}_n^i$ to one of the membrane points that are within 0.1μm. The position of the selected membrane vertex k is referred to as the center of the focus $\mathbf{X}_c^i := \mathbf{x}^k$. As the foci are relatively short-lived, we assume that this direction does not change over the lifetime of the focus.

2.1.4. Actin-Generated Force

As in Mogilner and Oster (2003), we take the propulsive force generated by actin polymerization to be proportional to the number of uncapped barbed ends within each focus. Here, such force is assumed to be acting at the center of an actin polymerization focus $\mathbf{X}_c^i$ and to extend laterally to the nearby vertices. When a branching event occurs, a new filament extends at an angle of 70° from the branched filament. Here, instead of explicitly modeling each filament, as in Bennett et al. (2011), we assume that a continuously changing amount of short-lived filaments with uncapped barbed ends at each focus generates a force that distributes symmetrically. Hence, the force contributions can be summed into a Gaussian Kernel around the focus center, given by

$$W(x) = \frac{\alpha}{\sigma\sqrt{2\pi}} e^{-\frac{x^2}{2\sigma^2}}, \tag{2}$$

with an amplitude α and standard deviation σ. Then, the resulting force vector at the vertex k (located at $\mathbf{x}^k$) is proportional to the number of barbed ends in the focus and is given by

$$\mathbf{F}_{fil}(\mathbf{x}^k) = \sum_{i \in 1,2,..n_f} W(||\mathbf{x}^k - \mathbf{X}_c^i||)B^i(t)\mathbf{V}^{i,k}, \tag{3}$$

with n_f being the number of currently active actin foci with B barbed ends and $\mathbf{V}^{i,k} = \frac{\mathbf{x}^k - \mathbf{X}_n^i}{||\mathbf{x}^k - \mathbf{X}_n^i||}$ the normalized direction vector of the force from focus i. In this way, the force exerted by actin is spatially extended proportionally to the number of barbed ends at each focus.

2.1.5. Membrane Force

Biological lipid membranes, such as the one confining the spine head, are composed of single molecules that self-assemble into stable fluid films of macroscopic lateral scales with lateral dimensions greatly exceeding their thickness (Deserno, 2015). Therefore, modeling approaches consider the membranes as two-dimensional elastic continuum (Guckenberger and Gekle, 2017) (described by a manifold Γ) in which any deviation of the equilibrium shape increases the membrane energy and induces response forces that return the membrane to its equilibrium

(Krüger, 2012). Generally, the bending contributions to this energy are described by the Helfrich free energy (Helfrich, 1973), for which constrains of size and total surface conservation are often added. Hence, the membrane energy is given by

$$\mathcal{E}_{mem} = P\Omega + \tau S + 2\kappa \int_{\Gamma} H^2 \mathrm{d}s \tag{4}$$

where the membrane's physical properties are characterized by the difference between internal and external pressure P, the line tension (or surface tension in 3D) τ, and the bending modulus κ. Ω is the area enclosed by the membrane (or volume in 3D), S is the boundary length (or surface area) and H is the mean curvature. The membrane force vector $\mathbf{F}_{mem}(\mathbf{x}^k)$ at vertex k is given by

$$\mathbf{F}_{mem}(\mathbf{x}^k) = -\frac{\partial \mathcal{E}_{mem}}{\partial \mathbf{x}^k}. \tag{5}$$

On our discrete mesh, the geometrical properties Ω, S, and H, and hence, the resulting force can be approximated for each vertex by taking its next neighbors in the mesh into account (see **Supplementary Material**). Note, however, that the approximations of the geometrical properties are only valid when the mesh is dense enough. Therefore, when the vertices move too far apart from each other, we refine our mesh (remeshing, see section 2.2).

Together with the fixed spine neck and PSD vertices, the membrane force gives rise to a characteristic "resting shape," to which the spine converges in the absence of other forces to minimize area, length and curvature (see e.g., **Figure 4A** for resting shapes resulting for different PSD-sizes).

2.1.6. Membrane Movement

In the presence of both actin and membrane generated forces, the spine shape is determined by a balance between them. If the forces are unbalanced at one of the mesh vertices, they will generate a movement of that vertex and deformation of the membrane. For simplicity, we assume that the motion of the vertex k is proportional to the net force with a proportionality constant ζ. Thus, the displacement of vertex k in time is given by

$$\frac{\mathrm{d}\mathbf{x}^k}{\mathrm{d}t} = \varsigma \left(\mathbf{F}_{mem}(\mathbf{x}^k) + \mathbf{F}_{fil}(\mathbf{x}^k) \right). \tag{6}$$

This equation is implemented in discrete time-steps using a classical Runge-Kutta algorithm, in which we keep $\mathbf{F}^k_{fil}$ constant during the whole calculation step. However, the interaction between neighboring membrane points can still give rise to diverging oscillations. Therefore, if the membrane displacement in a single time-step exceeds a certain displacement tolerance ($d_{tol} = 0.0001\mu$m), we split this time-step in two intervals and calculate the displacement of all membrane vertices in each of them until the displacement is smaller than the tolerance.

2.2. Simulation

2.2.1. Individual Foci

First, a single actin polymerization focus is simulated using the Monte Carlo model (section 2.1.2) with fixed $||\mathbf{F}_{mem}||$ in Equation (1). The focus is initialized with different numbers of barbed ends (between 1 and 20) and simulated until all barbed ends have vanished. Hereby, the number of barbed ends in each time-step as well as the lifetime of the focus are tracked. In order to compare the outcomes of these simulations with theoretical expectations, we investigate the dynamics of the barbed ends in a deterministic framework where we take B as a continuous quantity. For this, we derive the rate equations assuming that a focus has B filaments with barbed ends that classify into two types according to the state of its minus end. Here, m_c denotes the filaments with capped and m_u filaments with uncapped minus end, and the deterministic dynamics of B in a focus is given by

$$\begin{aligned}
\frac{\mathrm{d}m_u}{\mathrm{d}t} &= \gamma_{uncap} m_c - \gamma_{sever} m_u - \gamma_{cap} m_u, \\
\frac{\mathrm{d}m_c}{\mathrm{d}t} &= \hat{\gamma}_{branch}(t) - \gamma_{uncap} m_c - \gamma_{cap} m_c, \\
B &= m_u + m_c.
\end{aligned} \tag{7}$$

As $\hat{\gamma}_{branch}(t)$ in turn depends on B, these equations are highly non-linear and have been solved for their stationary state numerically. Note that the steady state of such deterministic system should match the mean value of our stochastic simulations.

2.2.2. 2D Model

Simulations are performed in MATLAB on a desktop computer. **Table 1** contains the parameters used in the simulations, unless stated otherwise. We first initialize the mesh by tracing a circle with equidistant vertices of δ_s, then the vertices of PSD (neck) are fixed as described in section 2.1.1. Subsequently, we simulate an initialization period in which the mesh points $\mathbf{x}^k$ move considering only the force generated by the membrane (see **Figure S1**). In such simulation, the force generated by the membrane is computed for each vertex (following to the calculations given in the **Supplementary Material**). Then the vertices move according to Equation (6), except those belonging to the PSD or neck that we fixed when generating the initial shape. During this initialization period the spine shape shrinks until it reaches a stable configuration, which we refer to as the resting shape.

As discussed above, the finite elements approximations of the geometrical properties are only valid when the mesh is dense enough. If the vertices move too far apart from each other these properties are lost, and therefore, the mesh has to be redefined. Thus, we perform remeshing at each time-step by calculating recursively the distance between two neighboring vertices and remove one if the distance between them is below $d_{min} = (3/5)\delta_s$ or add a new vertex in between if the distance is above $d_{max} = (4/3)\delta_s$. Hence, for a mesh with vertices $\{\mathbf{x}^1, \ldots, \mathbf{x}^k, \mathbf{x}^{k+1}, \ldots, \mathbf{x}^{n_{vertices}}\}$, if $\left\| \mathbf{x}^k, \mathbf{x}^{k+1} \right\| > d_{max}$ then $\mathbf{x}^{new} = (\mathbf{x}^k + \mathbf{x}^{k+1})/2$ and the new mesh is given by $\{\mathbf{x}^1, \ldots, \mathbf{x}^k, \mathbf{x}^{new}, \mathbf{x}^{k+1}, \ldots, \mathbf{x}^{n_{vertices}}\}$. Note that the order of the mesh persists despite the addition or deletion of vertices that changes the size of the mesh $n_{vertices}$.

After finding the resting shape configuration of the dendritic spine, we include actin dynamics and forces in the simulation (sections 2.1.2 and 2.1.4). For this, initially, n_{f0} actin polymerization foci are inserted as described in section 2.1.3 and the generation of new foci is enabled. Note, that the indicated simulation times start after the initialization phase. During the simulations (**Figure 3**) we track the spine shape by saving the mesh regularly as well as the spine area, which is recorded every time-step. To assess the influence of different model parameters (**Figures 4–10**), we perform one 90 min simulation for each parameter value and determine the mean, standard deviation and auto-correlation function of the spine area fluctuations. Moreover, we evaluate the distribution over the assumed values of the number of foci and barbed ends and the mean lifetime of polymerization foci. We then perform fifteen 15-min-simulations with different initial polymerization foci to obtain statistics for different initial conditions, estimate their uncertainty, and test whether values vary significantly.

2.2.3. 3D Model

Simulations in 3D are performed as in 2D, albeit with some changes in the analytical calculations for the membrane force. For example, the curvature calculation of a vertex in 2D only considers that and the next adjacent vertices, whilst in 3D this calculation is a function of the six neighbors of that vertex (see **Supplementary Material** for more details). Therefore, simulations in 3D are more complex.

In the 3D case, the mesh is initialized using the MATLAB function icosphere.m (Ward, 2015) which generates a unit geodesic sphere that we multiply by r_s. Additionally, in 3D the mesh has to be isotropic and conserve the number of neighbors of each vertex at each time-step to maintain the geometrical properties of the finite elements approximation. Thus, remeshing is implemented using the MATLAB function remeshing.m (Helf, 2015), that is based on OpenMesh (Botsch et al., 2002; Computer Graphics Group, 2018). The target edge length is set to δ_s and three iterations are performed each time. To compare the 3D shapes with the 2D simulations we do a two-dimensional projection of the three-dimensional mesh. For this, we project all points to the x-z-plane and trace a boundary around the projected points using the MATLAB function boundary.m. Likewise, we project to the y-z-plane to compare the two 2D projections of the same spine.

3. RESULTS

3.1. Individual Polymerization Foci Have Finite Lifetime Depending on the Membrane Force

In order to understand the highly non-linear interaction between actin dynamics and membrane force, we first simulated the model for a single actin polymerization focus with a constant counteracting membrane force $\mathbf{F}_{mem}$ in Equation (1). We then tracked the time course of the number of barbed ends in our Monte-Carlo model (**Figure 2A**). During these simulations the number of barbed ends changes on the scale of 100 ms, meaning that there is a fast turnover of barbed end, which justifies our assumption of force kernel (section 2.1.4). Moreover, the number of barbed ends fluctuates around a mean value (dashed lines in

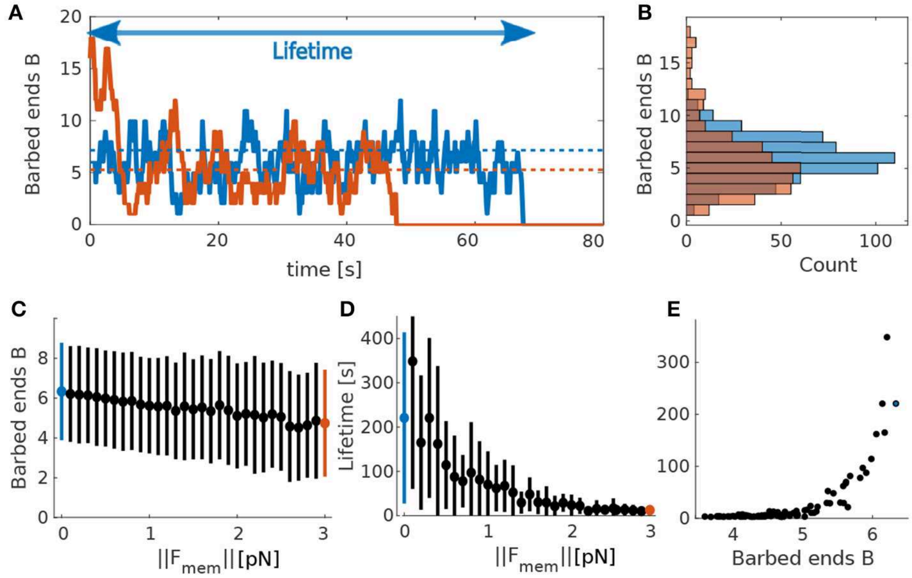

FIGURE 2 | Actin polymerization focus. **(A)** Evolution of barbed ends over time at a single actin polymerization focus. Blue solid line corresponds to $||\mathbf{F}_{mem}|| = 0$pN and orange solid line to $||\mathbf{F}_{mem}|| = 3$pN. Dotted lines indicate theoretical mean values calculated using the deterministic model for barbed ends in Equation 7. Colors correspond to the different values of $||\mathbf{F}_{mem}||$. Arrow indicates the lifetime of the focus corresponding to the blue curve. **(B)** Occurrence frequency (x-axis) of each number of barbed ends (y-axis) over all time-steps (of length Δ_t) in **(A)**. Colors as in **(A)**. **(C)** Mean and standard deviations of mean number of barbed ends B over 50 simulations each for different values of $||\mathbf{F}_{mem}||$. **(D)** Same for focus lifetimes. Blue and red dots mark the force values used in **(A,B)**. **(E)** Mean lifetime over mean number of barbed ends for 50 simulations varying force values.

Figure 2A) on a timescale of seconds. This mean value depends on the counteracting force: If $\mathbf{F}_{mem}$ increases, the mean number of barbed ends decreases (blue and orange dashed lines in **Figures 2A–C**). Importantly, the foci have non-zero probability to transit to $B = 0$. At that point no barbed end can be generated by branching anymore and the focus is dynamically dead. As a result all foci have limited lifetime. We also tracked this lifetime at different counteracting forces and find that it decreases when increasing the force (see **Figure 2D**). We finally evaluated the relation between the mean number of foci and the lifetime for varying forces and find that foci with more barbed ends live longer (**Figure 2E**), as expected from the above reasoning.

The dependency of the mean number of barbed ends (**Figure 2C**) and the lifetime of a focus (**Figure 2D**) on the membrane force can be explained by the fact that increasing $\mathbf{F}_{mem}$ decreases the branching rate (see Equation 1). Accordingly, the mean number of barbed ends is smaller and the distribution is shifted toward smaller numbers of B (**Figures 2B,C**). This increases the probability of being at $B = 1$, and, in turn, the probability to reach zero barbed ends. Consequently, the lifetime of these actin polymerization foci decreases when increasing the counteracting force. This relation between membrane force and focus lifetime indicates that the spine shape, which determines the membrane force, influences magnitude and the temporal properties of the shape fluctuations.

3.2. Shape-Fluctuations of the Spine

In the next step, we studied the interplay between the membrane and actin forces. For this, we simulated the full model with multiple actin polymerization foci distributed within a spine head (**Figures 3A,B**). We initialized the model with four of such foci that push the spine membrane outward. However, as the lifetimes of foci (**Figures 3C,G**) are much shorter than the lifetime of spines, which can persist over months (Holtmaat et al., 2005), we introduced a focus creation mechanism (i.e., nucleation of new actin polymerization foci, see section 2.1.3) where new foci are created at the beginning of each time-step at a rate γ_f. As it is not clear from experimental data where such nucleations happen, we also introduced a distance parameter λ which allows us to scale continuously between focus nucleation everywhere within the spine and nucleation close to the PSD. The influence of these parameters on the emerging shape fluctuations will be investigated in detail later (see section 3.3.5). Without this nucleation mechanism, all foci quickly reach zero barbed ends (in <9 s in **Figure 3G**) and the spine returns to the resting shape (gray line in **Figure 3B**). Moreover, spine area fluctuations also cease (gray line in **Figure 3D**).

Figures 3A,B (blue line) show the resulting shape dynamics of the spine in our model. The proposed nucleation mechanism together with the short lifetimes of individual foci allows the spine to have different asymmetric shapes over time, which are qualitative similar to the experiments (Fischer et al., 1998). Note that during the depicted time interval, several foci have died out and several others have been nucleated (**Figure 3E**). Moreover, the mean number of barbed ends at these foci is continuously fluctuating (**Figure 3F**). In general, we observed that spine area increases when several foci are active at the same time or when a focus is long-lived (**Figures 3D,E**). Thus, shape and area fluctuations of a spine are the result of the transiently active foci working against the membrane. In particular, they are generated by the stochasticity of the molecular dynamics of actin filament assembly, which eventually leads to the die-out of foci. Therefore, it can be expected that the molecular dynamics as well as the mechanics through which they interact with the membrane will have a major impact on the emerging fluctuations.

3.3. Influence of Model Parameters

In order to better understand how spine size fluctuations are affected by the dynamics of actin and the interplay between forces generated by actin polymerization foci and spine membrane, we investigated the effect of varying multiple model parameters. For this, we used the parameters in **Table 1** and increased or decreased the value of one selected parameter at a time.

3.3.1. Size of the Post-synaptic Density

Experimental studies show that there is a strong correlation between spine volume and PSD size (Arellano et al., 2007; Meyer et al., 2014). Therefore, we tested if this correlation holds in the presence of spontaneous fluctuations by changing the size of the PSD (r_{PSD}, see section 2.1.1), which affected the size, and thus, also the area of the resting spine shape. For example, when the radius of the PSD was enlarged to $r_{PSD} = 0.4330$, the distance between PSD and neck was also affected, which altered the resting shape of the spine (**Figures 4A,C**, black line). Accordingly, the mean spine area, evaluated over 90 min simulations of individual spines, increased with the PSD size (**Figure 4G**, pale bars). To test whether this tendency is significant, we performed a Welch-test comparing the mean spine areas in fifteen 15 min simulations for each PSD size (**Figure 4G**, full colored bars). We found that the small PSD size (set to $r_{PSD} = 0.2179$) gives rise to significantly smaller mean areas.

Figures 4D,F shows that area fluctuations behave differently when the PSD size varies. To quantitatively describe such fluctuations, we used the standard deviation and autocorrelation functions. A small standard deviation indicates that spine area fluctuations tend to be close to the mean, whilst high values indicate larger area fluctuations. The autocorrelation function shows the area correlation with itself at different time points. Therefore, if the autocorrelation function decays fast, then the area fluctuation is correlated to itself only for a short time, indicating that the area fluctuations occur more rapidly. Thus, the area standard deviation accounts for the size of area fluctuations and the slope of the autocorrelation function for their speed. Using these functions, we find that the medium PSD-size spine from the 90 min simulation shows a smaller area standard deviation than the 90 min simulations of spines with different PSD-size (**Figure 4H**, pale bars), multiple simulations show that the area standard deviations are similar. We found that the area of spines with large PSD-size is temporally longer correlated to itself, indicating that the fluctuations occur more slowly (**Figure 4I**). One reason for this might be that the membrane forces typically decrease for larger spines such that the decay back to the rest shape happens more slowly. Interestingly, the autocorrelation for spines with medium PSD size decays even

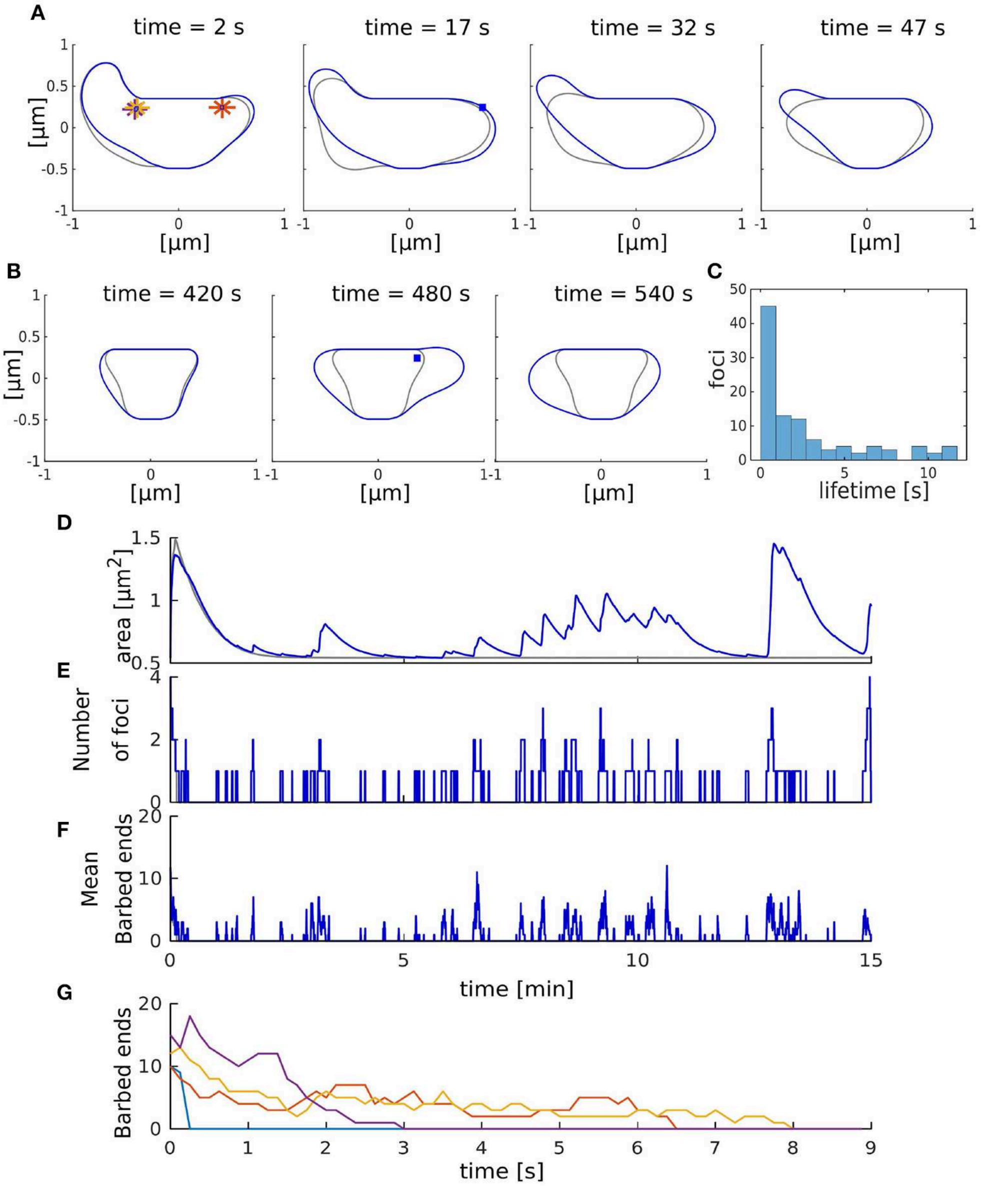

FIGURE 3 | Shape fluctuations of the spine. **(A)** Snapshots of the spine head shape with (blue line) and without (gray line) nucleation of new actin polymerization focus taken every 15 s. Asterisk correspond to the initial nucleation positions $\mathbf{X}_n$ and blue squares indicate nucleation positions of the active foci at the indicated time. **(B)** Same as **(A)** but taken every 60 s. **(C)** Occurrence frequency of foci lifetime over all time-steps (of length Δ_t) in the simulation with nucleation. **(D–F)** Evolution of the spine area **(D)**, number of foci **(E)**, and mean number of barbed ends **(F)** over time. Gray and blue lines represent the simulation without and with nucleation of new foci, respectively. **(G)** Evolution of the number of barbed ends in each actin focus (color-coded) in the simulation without nucleation of new foci.

faster than that for small PSD size. This may be due to the fact that the actin polymerization foci in spines with smaller PSD tend to last longer (**Figure 4L**). Taken all together, the correlation between the spine and PSD size find in experiments hold in our model with spontaneous shape fluctuations. Interestingly, the size of these fluctuations was similar despite PSD size due that the number and lifetime of the actin polymerization foci were not significantly affected by the PSD size.

The 90 min simulation of the spine with a large PSD-size also exhibits a period (between min 60 and 70) where the spine area fluctuations cease (blue bar in **Figure 4F**, spine shapes in **Figure 4C.II**). Although new foci are nucleated during this period, changes in spine shape are minor because new foci randomly nucleate nearby each other (locations marked by circles in **Figure 4C.II**). Moreover, the curvature near these foci is large, such that the force generated by the membrane is higher decreasing the branching rate; and hence, the lifetime of those foci.

3.3.2. Branching Rate Amplitude ϕ

The branching rate of actin polymerization foci γ_{branch} in Equation (1) is scaled by an amplitude ϕ. Three simulations with

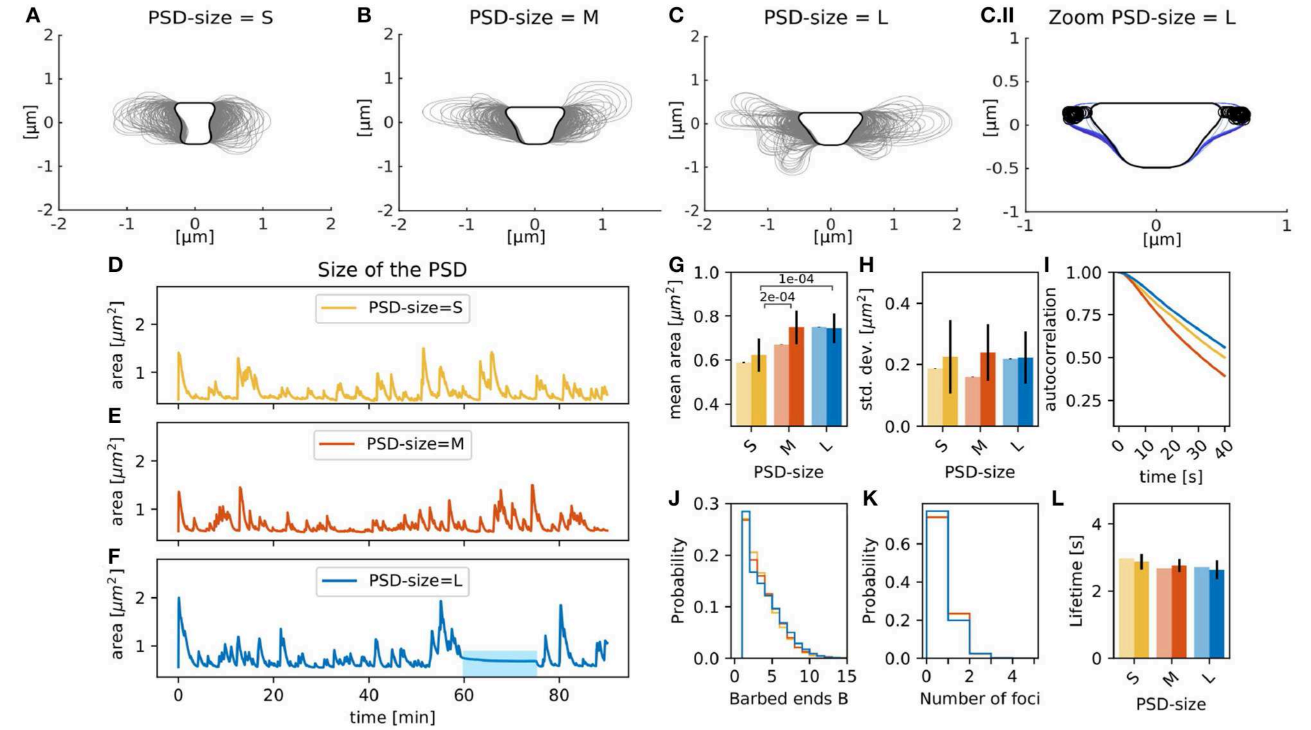

FIGURE 4 | Spines with varying PSD size. Spine shapes (gray lines, plotted every 15 s) over 90 min of simulation for **(A)** small, **(B)** medium, and **(C)** large sized PSDs. Black line corresponds to the resting shape. **(C.II)** Shapes of the large PSD-size spine between min 60 and 70 (color-coded from dark to light blue). Black open circles correspond to the nucleation points. **(D–F)** Evolution of the spine area over time. **(G)** Temporal mean over area in 90 min simulation (pale bars, errors are standard deviations over 50 bootstraps) and average of temporal means over fifteen 15 min simulations (saturated color, errors are standard deviations of the mean) over different PSD sizes. The *p*-value for significant Welch-tests is indicated. **(H)** Same as **(G)** but for standard deviation of the area fluctuations. **(I)** Autocorrelation functions for the area fluctuations in the 90 min simulations. **(J)** Histogram of the mean number of barbed ends at the polymerization foci at each time-step of the 90 min simulation. **(K)** Histogram of the active actin polymerization foci. **(L)** Mean lifetime of a focus, color-coded as in **(G)**.

different values of ϕ over 90 min, as well as the fifteen 15 min repetitions with different initial conditions, show that an increase of ϕ enlarges the mean spine head area significantly (compare orange and blue bars in **Figure 5D**, *p*-value for significant Welch-tests indicated). The 90 min simulations (**Figures 5A,B**) show that a decrease of ϕ induces a small decrease in spine mean area (light bars in **Figure 5D**). However, the fifteen 15 min simulation show a larger decrease (full bars in **Figure 5D**). This relation between the mean area and ϕ can be explained by the fact that spines with a larger value of ϕ also have more barbed ends at the actin polymerization foci (**Figure 5G**). Due to this increased number of barbed ends, the polymerization foci of those spines tend to last longer (**Figure 5I**). As a consequence, there are more actin polymerization foci in spines with a larger branching rate amplitude (**Figure 5H**), which push the membrane outwards and increase the area. A similar picture emerges for the magnitude of the fluctuations measured by the standard deviation (**Figure 5E**) of the area as well as for the timescale of the autocorrelation decay (**Figure 5F**). Especially for large values of ϕ we observe a significantly larger standard deviation (**Figure 5E**) and a slower autocorrelation decay (**Figure 5F**). This fits well with the idea that the polymerization foci are more long lived; and therefore, push the membrane outward for longer times leading to larger area deviations. We conclude that an increase of ϕ enlarges the mean, the standard deviation and the autocorrelation decay timescale of the spine area fluctuations due to an increase of the lifetime of actin polymerization foci. However, a decrease in ϕ by the same magnitude does not affect the spine area to the same degree, which highlights that the underlying processes are subject to non-linear interactions.

3.3.3. Lateral Extent of Actin Filament σ

Besides the number of barbed ends at the actin polymerization foci, the actin generated forces and the resulting deformations of the membrane are also determined by the lateral spatial extent of actin filaments (σ in Equation 2). When the lateral extent is small, the width of the bump pushing the membrane forward generated by the focus is narrow. The shape of this bump has a direct effect on the geometrical properties of the spine membrane around the focus. For example, a narrow protrusion has a greater curvature, which produces an increase in $||\mathbf{F}_{mem}||$ working against this deformation. This entails a decrease in the branching rate as well as in the mean number of barbed ends (**Figure 6G**) and leads to less active foci with a shorter lifetime (**Figures 6H,I**). This shorter lifetime implies that foci push the membrane for shorter time such that the variations in the spine area become smaller (**Figure 6E**) and decay faster (**Figure 6F**).

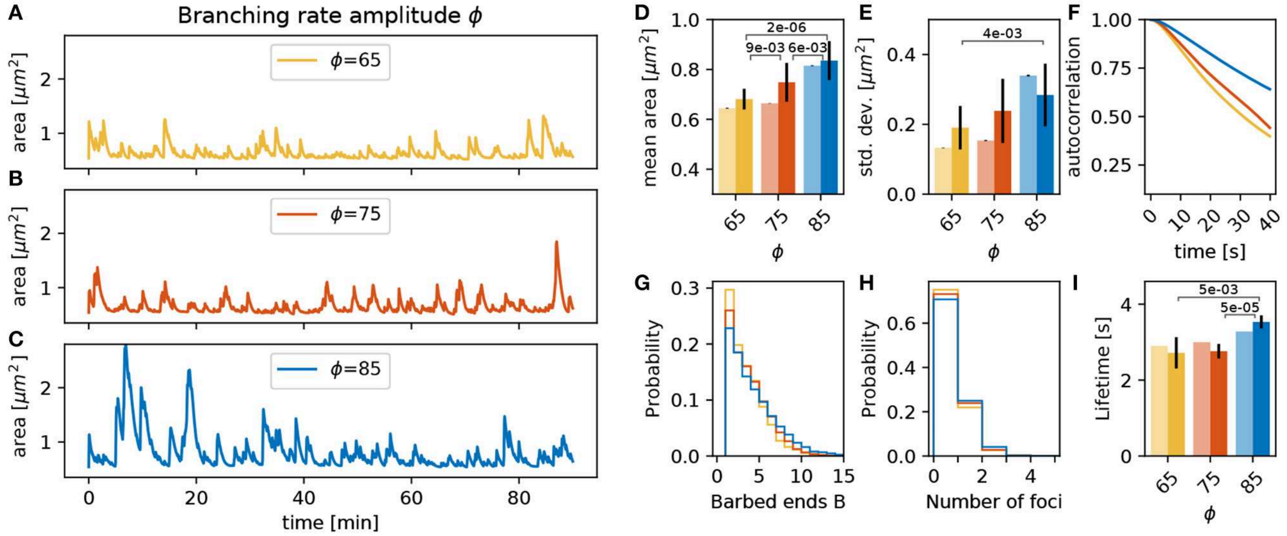

FIGURE 5 | Varying the branching rate amplitude ϕ. **(A–C)** Evolution of the spine head area over time for different values of ϕ: **(A)** $\phi = 65$, **(B)** $\phi = 75$, and **(C)** $\phi = 85$. **(D)** Temporal mean of the spine head area. Light bars correspond to values from single 90 min simulations (standard deviations obtained from 50-fold bootstrap). Full colored bars and errors correspond to the mean and standard deviation over fifteen 15 min simulations. The p-value for significant Welch-tests is indicated. **(E)** Standard deviation of the spine head area over time. **(F)** Autocorrelation functions for the area fluctuations in the 90 min simulations. **(G)** Relative frequency of the mean number of barbed ends per focus over all simulation time-steps from **(A–C)**. **(H)** Relative frequency of the number of actin polymerization foci. **(I)** Mean lifetime of a focus.

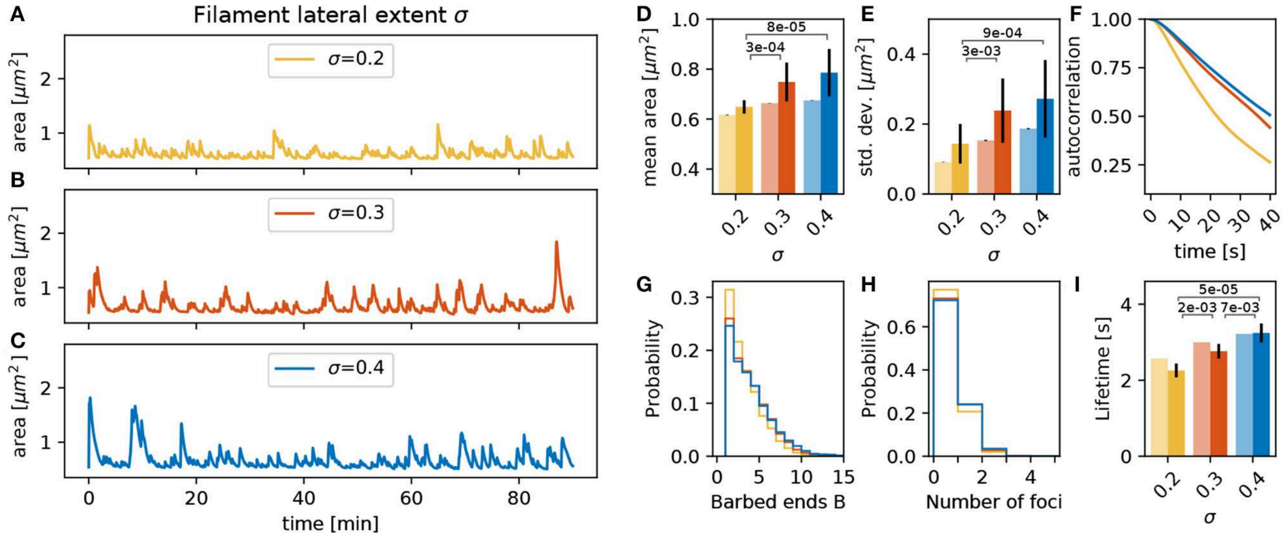

FIGURE 6 | Varying the filament lateral extent σ. **(A–C)** Evolution of the spine head area over time for different values of σ: **(A)** $\sigma = 0.2$, **(B)** $\sigma = 0.3$, and **(C)** $\sigma = 0.4$. **(D)** Temporal mean of the spine head area. Light bars correspond to values from single 90 min simulations (standard deviations obtained from 50-fold bootstrap). Full colored bars and errors correspond to the mean and standard deviation over fifteen 15 min simulations. The p-value for significant Welch-tests is indicated. **(E)** Standard deviation of the spine head area over time. **(F)** Autocorrelation functions for the area fluctuations in the 90 min simulations. **(G)** Relative frequency of the mean number of barbed ends per focus over all simulation time-steps in **(A–C)**. **(H)** Relative frequency of the number of actin polymerization foci. **(I)** Mean lifetime of a focus.

3.3.4. Movement Speed ζ

The conversion factor between force imbalance and movement ζ can be expected to have a strong influence on the magnitude of spine shape change per time-step. Judging from the dynamics shown in **Figures 7A–C**, the area fluctuations also seem to be much faster when increasing ζ. However, this is mostly due to an increase in the amplitude of the fluctuations (**Figure 7E**) whereas the timescale of the autocorrelation decay remains relatively constant. Note that an increase of ζ enhances spine fluctuation extent, and it also affects the membrane geometrical properties, the membrane force and, hence, the barbed end branching rate. This leads to less barbed ends (**Figure 7G**) and a reduction of the

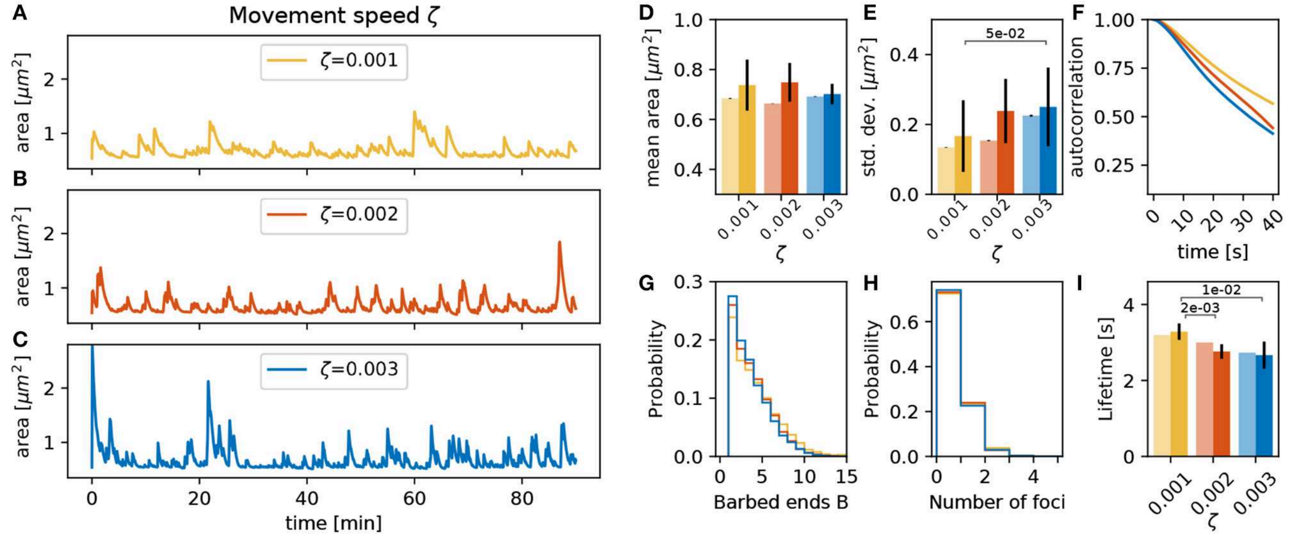

FIGURE 7 | Varying the movement speed ζ. **(A–C)** Evolution of the spine head area over time for different values of ζ: **(A)** $\zeta = 0.001$, **(B)** $\zeta = 0.002$, and **(C)** $\zeta = 0.003$. **(D)** Temporal mean of the spine head area. Light bars correspond to values from single 90 min simulations (standard deviations obtained from 50-fold bootstrap). Full colored bars and errors correspond to the mean and standard deviation over fifteen 15 min simulations. **(E)** Standard deviation of the spine head area over time. The *p*-value for significant Welch-tests is indicated. **(F)** Autocorrelation functions for the area fluctuations in the 90 min simulations. **(G)** Relative frequency of the mean number of barbed ends per focus over all simulation time-steps in **(A–C)**. **(H)** Relative frequency of the number of actin polymerization foci. **(I)** Mean lifetime of a focus.

foci lifetime (**Figure 7I**). Still, in sum, spines with different values of ζ have similar mean area over time (**Figure 7D**).

3.3.5. Nucleation Rate γ_f and Location λ

Additionally to the parameters that influence force generation and translation to movement, the parameters of the nucleation mechanism proposed in section 3.2 can have a strong influence. First, we vary the nucleation rate γ_f at an intermediate value of the PSD distance scaling parameter λ. As expected, an increase in γ_f raises the number of actin polymerization foci and the spine area over time (**Figure 8H**). This leads to a significant increase in the mean area and a trend toward increasing standard deviations (**Figures 8D,E**). Although these foci have slightly shorter lifetimes (**Figure 8I**), the decay of the autocorrelation remains at the same timescale (**Figure 8F**). The main reason for the reduction of foci lifetime is the feedback between the number of barbed ends and the branching rate in Equation (1). If B increases then γ_{branch} decreases ensuring a limited number of barbed ends at the actin polymerization foci.

The location for the polymerization of new foci depends on the distance from the PSD scaled by parameter λ, as stated in section 2.1.3. For larger values of λ, the nucleation points are more likely to be located far from the PSD and the spine mean area is larger due an increase in the lifetime of the actin foci (**Figures 9E–I**). We speculate that this can be explained by the fact that for small λ all foci nucleate close to the PSD. Hence, all foci push outward the same small fraction of the membrane, which thereby assumes a strong curvature. This, in turn, leads to a strong counteracting force and hence a shorter lifetime of the foci.

In conclusion, we find that geometrical constraints as well as parameters related to actin filament assembly, force generation and focus nucleation have a strong influence on the emerging fluctuation. We summarized the most prominent effects in **Table 2**.

3.3.6. Influence of Parameter Variation on Spine Area

After evaluating the influence of individual parameters, we investigated whether there are general relations between the evaluated quantities that are preserved over all these variations. To investigate this, we used the fifteen 15 min simulations for each parameter variation and plotted the values of mean area, focus lifetime and mean number of foci for each of these individual simulations against each other. On the one hand, we find that spines with greater mean area over time, have larger mean foci lifetimes (**Figure 10A**). However, spines with smaller mean area can also have long-lasting foci when the force generated by the membrane is not affecting the branching rate strongly. For example, when the focus nucleation rate γ_f is high or the movement speed ζ is small. On the other hand, there is a positive correlation between the mean number of actin polymerization foci and spine mean area (**Figure 10B**), which has also been found in experimental data from Frost et al. (2010). These results imply that the macroscopic spine area fluctuation is heavily relying on the stochastic dynamics of the actin polymerization foci and filament dynamics therein.

3.4. Correlation of the Number of Foci and Spine Area Fluctuations

Although the spine shape is determined by a complex interplay between forces emerging from actin activity and the geometrical

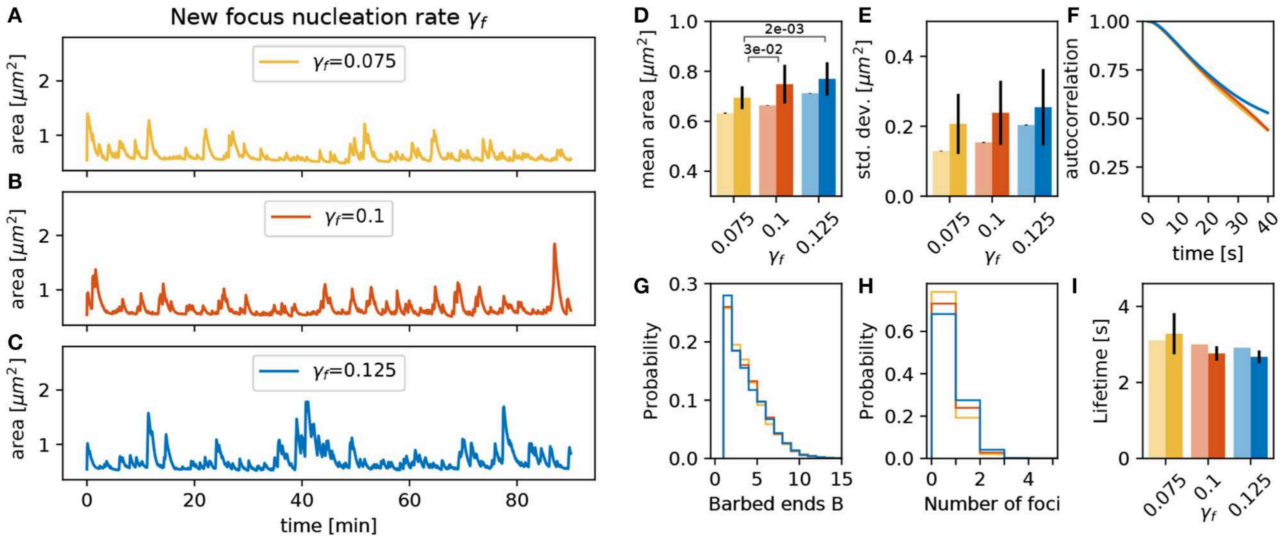

FIGURE 8 | Varying the focus nucleation rate γ_f. **(A–C)** Evolution of the spine head area over time for different values of γ_f: **(A)** $\gamma_f = 0.075$, **(B)** $\gamma_f = 0.100$, and **(C)** $\gamma_f = 0.125$. **(D)** Temporal mean of the spine head area. Light bars correspond to values from single 90 min simulations (standard deviations obtained from 50-fold bootstrap). Full colored bars and errors correspond to the mean and standard deviation over fifteen 15 min simulations. The *p*-value for significant Welch-tests is indicated. **(E)** Standard deviation of the spine head area over time. **(F)** Autocorrelation functions for the area fluctuations in the 90 min simulations. **(G)** Relative frequency of the mean number of barbed ends per focus over all simulation time-steps in **(A–C)**. **(H)** Relative frequency of the number of actin polymerization foci. **(I)** Mean lifetime of a focus.

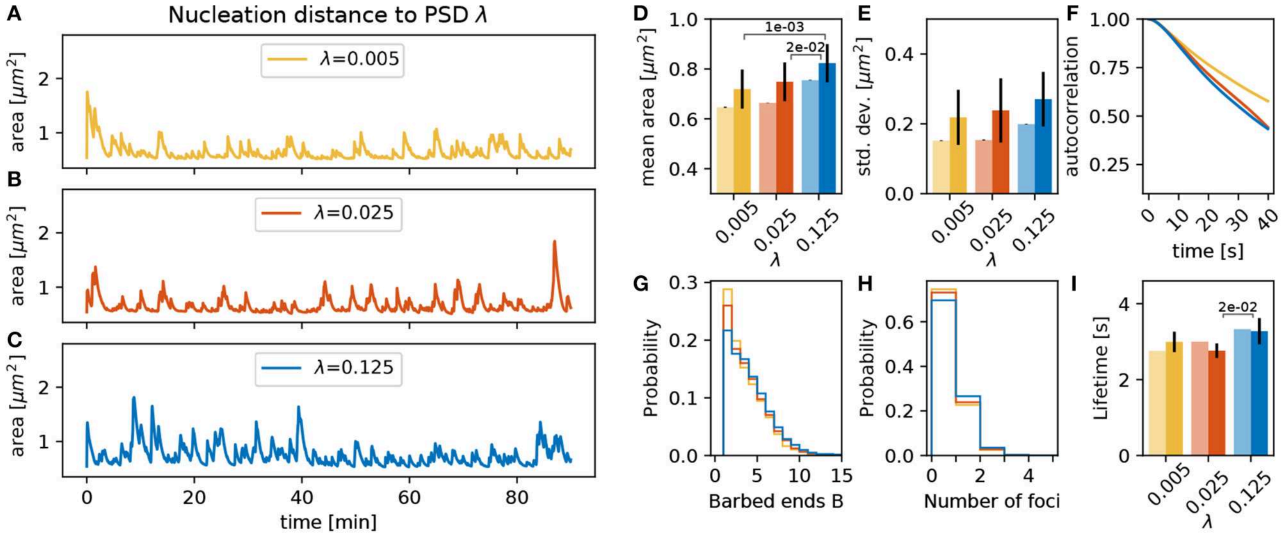

FIGURE 9 | Varying the nucleation distance parameter λ. **(A–C)** Evolution of the spine head area over time for different values of λ: **(A)** $\lambda = 0.005$, **(B)** $\lambda = 0.025$, and **(C)** $\lambda = 0.125$. **(D)** Temporal mean of the spine head area. Light bars correspond to values from single 90 min simulations (standard deviations obtained from 50-fold bootstrap). Full colored bars and errors correspond to the mean and standard deviation over fifteen 15 min simulations. **(E)** Standard deviation of the spine head area over time. The *p*-value for significant Welch-tests is indicated. **(F)** Autocorrelation functions for the area fluctuations in the 90 min simulations. **(G)** Relative frequency of the mean number of barbed ends per focus over all simulation time-steps in **(A–C)**. **(H)** Relative frequency of the number of actin polymerization foci. **(I)** Mean lifetime of a focus.

properties of the membrane, the above described correlations indicate that there is a strong link between spine area and its polymerization foci. Therefore, we investigated whether the number of polymerization foci at each time-step can be used to predict not only the mean but also the time-course of the spine head size, which is commonly measured in experiments. As the expanding force in our model comes from the actin foci, we first tested whether there is a relationship between number of actin polymerization foci and the spine head area. To quantify this, we tracked the area and the number of foci throughout a 90 min simulation of a spine (**Figure 11A**) and evaluated the correlation between these quantities. We found a significant correlation, but with a very small correlation coefficient (**Figure 11B**). When examining the time courses in **Figure 11A**, we see that when there is no focus the area shrinks to a state close to the resting shape area and a slight increase in area when the number of foci increases. Hence, we investigated the relationship between the actin foci and spine area changes Δarea (**Figure 11C**) and found that there is indeed a significant correlation with a high correlation coefficient between these quantities. Thus, we constructed a simple model that predicts the area of a spine using only the number of foci at a given time-step. Apart from the area change being proportional to the number of foci, we also included mean retrieval that drives the area back to the area of the Helfrich resting shape A_s. In particular, the estimator $\overline{A}$ for the spine area A at each time-step t_j is recursively calculated by the following model

$$\overline{A}(t_j) = \overline{A}(t_{j-1}) - \Phi\left(\overline{A}(t_{j-1}) - A_s\right) + mn_f(t_j) + b, \tag{8}$$

where the term $mn_f(t_j) + b$ accounts for the change of area that scales linearly with the number of actin polymerization foci n_f at time t_j and Φ represents a decay rate to the resting area A_s, which we extracted from our simulations. The model parameters m, b and Φ from Equation (8) and the initial area $\overline{A}(t_0)$ were fitted using the fit.m function in MATLAB with the non-linear least square method and the area trace of **Figure 11A** from min 1 to 60 (**Figure 11D**, fit results: root mean square error (RMSE) = 0.0562, $\overline{A}(t_0) = 0.7507, m = 0.002734, b = -0.0004135, \Phi = 0.002734$). Hereby, the obtained values for b and m are close to a linear fit to the relation between the number of foci and the change of the area (orange line in **Figure 11C**; $\Delta\text{area} = m'n_f + b'$, with $m' = 0.00197$ and $b' = -0.000570$). Also, and $\overline{A}(t_0)$ is close to the actual starting value $A(t_0) = 0.7239$. Given that our area estimator is recursive and could accumulate errors over time, $\overline{A}$ performs well, even for a time interval that it was not fitted to (**Figure 11D** from min 60 to 90, RMSE = 0.0652). Moreover, it performed well when applied to a different simulation with the same parameters (**Figure 11F**, RMSE = 0.0822). Note that the estimator error increases in periods with large areas (**Figures 11E,G**), which may be due to the fact that the relation between foci and the change in area may be non-linear (compare **Figure 11C**). Nevertheless, we deduce that area fluctuations can be predicted very well from the number of actin polymerization foci. Because the fitted model performed well with different simulations, we can conclude that the behavior of the spine area over time is similar regardless of the stochasticity of the model. Thus, already such a relatively simple model gives a good description of the area dynamics. This again underlines a strong link between the microscopic stochastic dynamics at the actin polymerization foci and the macroscopic area fluctuations. Note, however, that this simple model cannot be used as a surrogate for the complete model proposed in this paper, as it relies on knowledge about the number of foci, which is, in turn, only obtainable by stimulating the full non-linear interaction between actin and membrane geometry.

TABLE 2 | Summary table.

Increase in	Mean area	Standard deviation	Foci lifetime
PSD-size	⇑	–	–
Branching rate amplitude ϕ	⇑	⇑	⇑
Lateral extent of F-actin σ	⇑	⇑	⇑
Movement speed ζ	–	⇑	⇓
Nucleation rate γ_f	⇑	↑	↓
Nucleation location λ	⇑	↑	–

Here ↑ (↓) denotes a tendency to increase (decrease) the mean area, standard deviation of the area or foci lifetime whilst ⇑ (⇓) indicates a significant increase (decrease).

3.5. Model Extension to 3D

So far we have only considered spine shapes in 2D, but in order to verify if the dynamics of actin polymerization foci influence spine

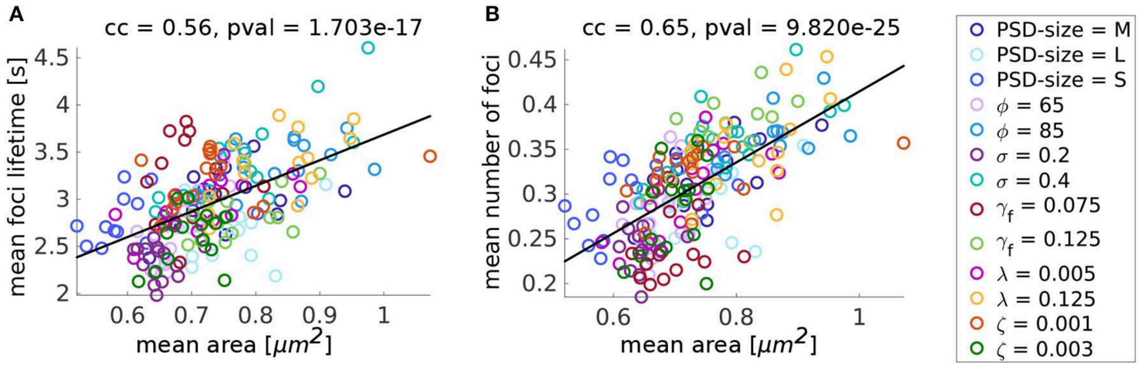

FIGURE 10 | Summary of the parameter variation simulations. **(A)** Mean focus lifetime over mean spine area for different parameter variations. Each dot represents one simulation with a parameter variation corresponding to its color. Standard values of the parameters are reported in **Table 1**. For every variation of a parameter 15 simulations of 15 min were performed. cc denotes the linear correlation coefficient and pval is the *p*-value for testing the hypothesis of no correlation against the alternative hypothesis of a non-zero correlation, using Pearson's Linear correlation coefficient. **(B)** Same for mean number of foci over mean area.

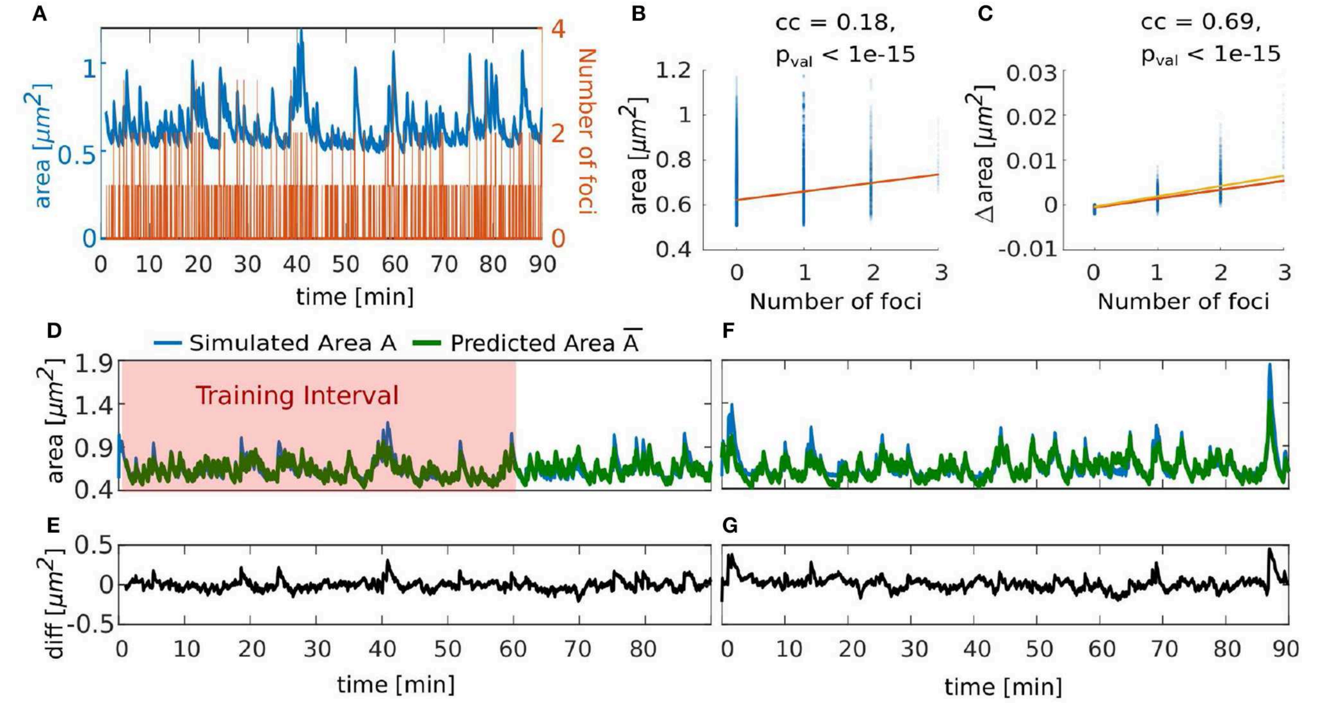

FIGURE 11 | Temporal evolution of spine area can be predicted by number of actin polymerization foci. **(A)** Evolution of number of actin polymerization foci (orange line) and spine area (blue line). **(B)** Spine area over the number of actin polymerization foci for each time-step of the simulation. Color saturation indicates overlay of data points; darker regions contain more data observations. Orange line is a linear fit to the data, cc denotes the linear correlation coefficient and pval is the *p*-value for testing the hypothesis of no correlation against the alternative hypothesis of a non-zero correlation, using Pearson's Linear Correlation Coefficient. **(C)** Same for the difference in spine area over the number of actin polymerization foci. Yellow line is a linear function using the parameters fitted to Equation (8) in **(D)**. **(D)** Simulated area (blue line) and its approximation by estimator $\overline{A}$ (green line, Equation 8) over time. Red shaded zone depicts the training data set for fitting the estimator parameters. **(E)** Difference between simulated and predicted area in **(D)**. **(F)** Simulated area (blue line) corresponding to the plot in **Figure 5B** and its approximation (green line) over time. **(G)** Difference between the simulated and predicted area in **(F)**.

shape fluctuations in real three-dimensional spines in a similar way, we extended our model to 3D. In this extended model, actin dynamics are preserved but the membrane mesh, all positions and forces are adapted to 3D (see **Supplementary Material**). Note that the calculation of geometrical properties in 3D is more complex, as more neighboring vertices must be considered. Furthermore, the 3D mesh contains far more vertices than the 2D mesh. Thus, the 3D simulations are computationally expensive and rigorous statistical analysis, as conducted for the 2D model above, is not feasible.

However, we wanted to check whether the qualitative behavior of the 3D and the 2D simulation are comparable. For this, we assumed that the 3D spine shape is observed as in a microscope and projected to a two-dimensional plane. Hereby, we performed projections from multiple sides, in particular to the y-z- and the x-z-plane (**Figures 12B–C,G–H**, respectively). Deformations in the 3D model where the acting forces are not in the projection plane will appear to be effectively slowed down in 2D projections. To compensate for this, the movement speed of the 2D model has been slowed down by adjusting the movement speed ζ. Moreover, multiple foci in the 3D model may be projected onto the same 2D bump such that it appears as if the foci are more long-lived. To compensate for this, an adjustment in the branching rate amplitude ϕ allows the 2D model to have more barbed ends such that the foci last longer. After adjusting the parameters for these geometrical properties, 3D simulations exhibit qualitatively similar fluctuations to 2D simulations. Hence, we assume that the parameter dependencies and relations between molecular and geometric dynamics discussed above apply similarly to the three-dimensional model.

4. DISCUSSION

We proposed a model for dendritic spine shape fluctuations based on actin polymerization foci. We used the model to simulate the dynamics of a single focus as well as the interaction of multiple foci within a spine in 2D and 3D and analyzed the resulting fluctuations of the spine head size. We find that the fluctuations from the projected 3D model are similar to the area fluctuations from the 2D model. Variations of the model parameters revealed that the properties of the molecular processes and mechanics have strong influence on the emergent shape fluctuations. Along these lines, we showed that the changes of the spine head size could be very well-predicted from only knowing how many foci were active over time. Importantly, we showed that the lifetime and hence, the number of foci result from the highly non-linear interactions between actin

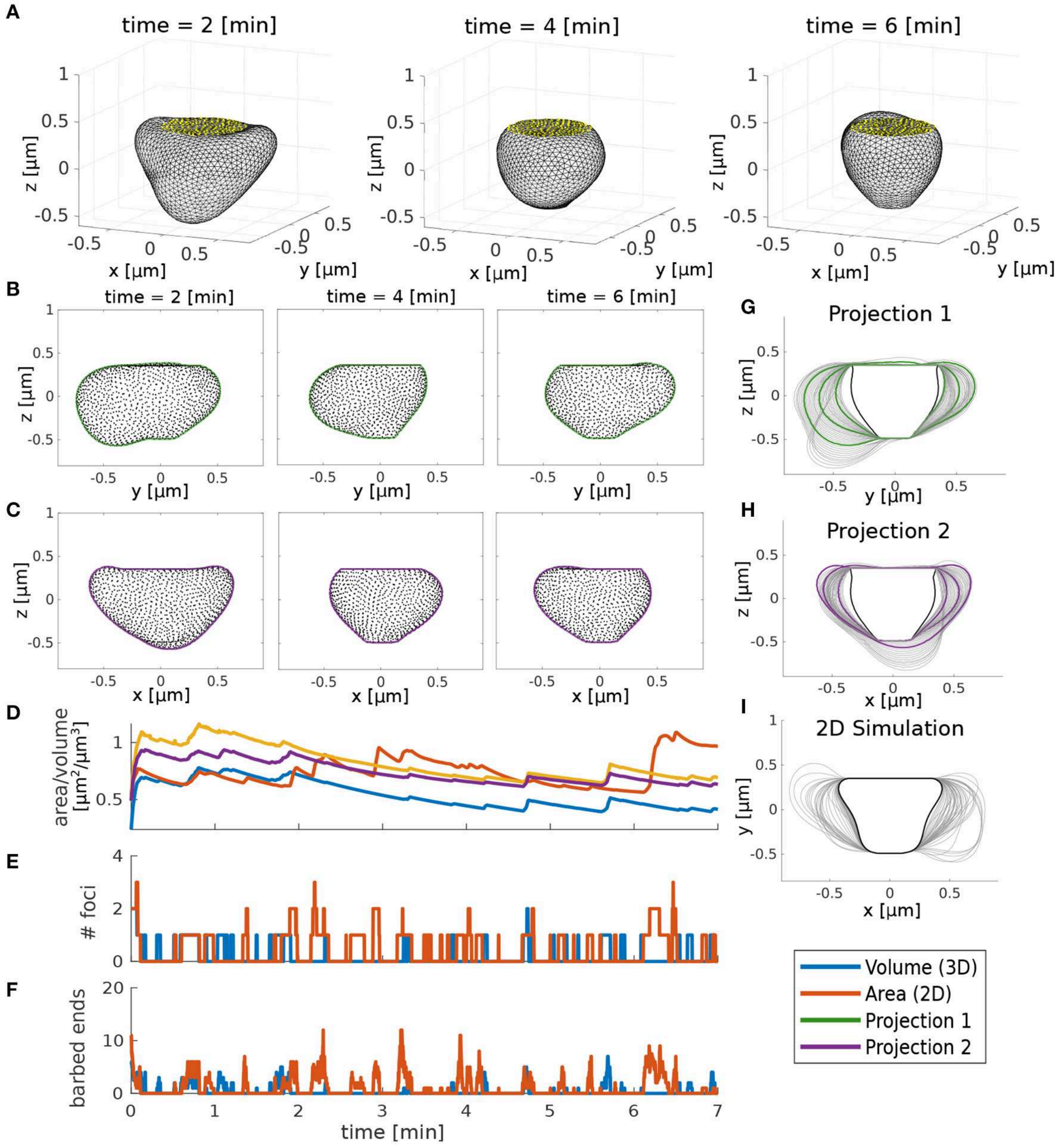

FIGURE 12 | Comparison between 3D and 2D model. **(A)** 3D simulation snapshots at different time points. Yellow dots indicate the PSD. **(B,C)** Projection of the 3D simulation to two 2D views. Black dots are the corresponding 3D vertices and lines are a fitted boundary around these points. **(D)** Time evolution of volume (3D simulation) and area (2D simulation and 2D projections). **(E)** Number of actin foci during the 2D/3D simulation. **(F)** Mean number of barbed ends. **(G,H)** Spine shapes emerging from the 2D projections of the 3D model in time intervals of 10 s. Black lines represent the initial shape and green and purple lines correspond to the snapshots in **(B,C)**, respectively. **(I)** Spine shapes emerging from 2D simulation of the model. Parameters for 3D and 2D simulations are in **Table 1** except that in 3D $\delta_s = 0.06$, $\zeta = 0.004$, and $\phi = 30$, and in 2D $\zeta = 0.0015$.

and membrane forces revealing the importance of embedding actin dynamics on a realistic membrane. Thus, our model provides a platform to study the relation between molecular and morphological properties of the spine.

The proposed model is, to our knowledge, the first to reproduce the rapid asymmetric shape fluctuations observed in experiments. Although the functional role of these fluctuations is an open question, there is the hypothesis that the dynamic actin pool generating the fluctuations is necessary to maintain the spine volume by a dynamic equilibrium (Honkura et al., 2008), and that the dynamic F-actin distribution in the discrete polymerization foci optimizes the spine reaction to plasticity-related events (Frost et al., 2010). In the future, the here presented model can be extended to test this hypothesis.

In our model the asymmetric shape fluctuations result from local imbalances between forces generated by membrane deformation and forces generated by the active actin polymerization foci. Strikingly, these foci have a limited lifetime due to the stochastic nature of the actin filament dynamics. Thereby, the stochasticity of actin dynamics is also transferred onto the spine shape and size, which is evidenced by the fact that the number of active foci can predict the spine area (**Figures 10**, **11**). Our model shows that the focus lifetime is inversely proportional to the force generated by the spine membrane (**Figure 2**), which is caused by a feedback between this force and the branching rate. This mechanism, thus, couples geometric properties and molecular dynamics, and links the dynamics of multiple foci via the membrane. Moreover, it exhibits that spine size can be maintained by the dynamic actin pool, as proposed by Honkura et al. (2008), while allowing large shape changes seen in Fischer et al. (1998).

Due to the limited lifetime of the actin polymerization foci, we proposed a nucleation that mechanism stochastically generates foci at different locations in the spine. The generation rate and the initial location of these new foci have a great impact on the evolution of spine area over time. For example, an increase of the nucleation rate causes increases of the mean spine area and its standard deviation (**Figure 8**). Interestingly, foci generated with fast nucleation rate also tend to have a shorter lifetime evidencing a saturating mechanism or self-regulation (compare Statman et al., 2014). Moreover, we used our model to test the influence of the nucleation location of these foci. Experimentally, it has been observed that actin foci are mainly located at the tip of the spine (Honkura et al., 2008; Frost et al., 2010) and the branching protein Arp2/3 is mainly located in a doughnut-shaped zone around the PSD (Rácz and Weinberg, 2008). Such a constraint on the nucleation location of polymerization foci has a strong impact on the shape fluctuations of our model-spines (**Figure 9**): When foci nucleate closer to the PSD, they tend to last for shorter time intervals such that the mean number of foci is smaller which, in turn, reduces the mean area of the spine. This demonstrates that changes in the polymerization activity can be caused only by differences in geometry without changing any reaction rates.

Furthermore, we observed that, despite the change of shape, the spine area always fluctuates around a mean value, in agreement with experimentally observed spine fluctuations on short timescales (Fischer et al., 1998). This mean value, as well as the magnitude and timescale of the fluctuations are affected by various model parameters. For example, there is a strong influence of the PSD-size on the mean spine area (**Figure 4**) which is in line with the experimentally observed correlation between these quantities (Boyer et al., 1998; Arellano et al., 2007). Similarly, reducing the branching rate in our model by decreasing ϕ leads to a decrease in the mean and standard deviation of spine area (**Figure 5**), which is in line with findings that the branching factor Arp2/3 is necessary for spine enlargement and maintenance of spine morphology (Kim et al., 2013). Furthermore, an increase of the movement speed parameter ζ leads to a increase in spine area standard deviation (**Figure 7**), which has been similarly observed experiments that artificially decreased the density of the extra-cellular matrix in visual cortex (De Vivo et al., 2013). Overall, these results indicate that the mean spine size as well as the magnitude and timescale of spine shape fluctuations are regulated by the properties of the underlying molecular processes (e.g., reaction rates, force generation). Therefore, our model can represent a broad variety of different fluctuation characteristics as observed in experiments through different parameterizations. Moreover, our model agrees with experimental observations that spine size changes, which are not just fluctuations but, instead, affect the mean spine size over longer periods of time or lead to spine loss, result from processes different from actin polymerization (Fischer et al., 1998). Such processes have a longer timescale than that used in this study and may involve the induction of LTP or LTD that can affect the dynamics of actin polymerization. For example, alterations that affect actin-binding proteins change the mean spine size and the spine density (Fortin et al., 2012). Interestingly, this can lead to spine abnormalities that are present in brain-related disorders, such as Alzheimer's disease (Lin and Webb, 2009; Bellot et al., 2014), where memory storage is heavily affected. Thus, it appears that processes that alter the production or function of actin-related proteins, which lead to prominent changes of the spines, can interfere with memory, while spontaneous shape fluctuations presented in this study may aid memory storage by maintaining the spines's typical characteristics.

In conclusion, our model can serve as a basis to investigate the relation between microscopic properties like molecular dynamics, membrane geometry and emerging properties as spine volume fluctuations. As such, it can be extended into various directions: On the one hand, the shape fluctuations may influence the model parameters, such as PSD size, molecule concentrations and reaction rates on longer timescales. Hence, the mean area around which the spine fluctuates as well as other fluctuation characteristics could be continuously adapted giving rise to a slower feedback-loop (compare Yasumatsu et al., 2008 and Statman et al., 2014). On the other hand, so far, the proposed model only considers spines at basal neuronal activity. However, in the future, it can be extended to include induction of activity-dependent plasticity (LTP/LTD) by modeling the changes in actin treadmilling process during plasticity (compare Bennett et al., 2011).

DATA AVAILABILITY STATEMENT

The code for 2D and 3D simulations is available from GitHub (https://github.com/MayteBQ/Dendritic-Spine-Simulation). Any additional data or code will be made available by the authors, without undue reservation, to any qualified researcher.

AUTHOR CONTRIBUTIONS

MB-Q, FW, CT, and MF contributed to the study concept and edited the paper. MB-Q developed the model and performed the simulations. MB-Q and MF analyzed the results and wrote the original draft.

FUNDING

This research was funded by the German Science Foundation through the Collaborative Research Center SFB-1286 (Project C3).

ACKNOWLEDGMENTS

We thank the members of the SFB-1286 for fruitful discussions. A previous version of this manuscript has been released as a Pre-Print at Bonilla-Quintana et al. (2019).

SUPPLEMENTARY MATERIAL

The Supplementary Material for this article can be found online at: https://www.frontiersin.org/articles/10.3389/fnsyn.2020.00009/full#supplementary-material

REFERENCES

Arellano, J., Benavides-Piccione, R., DeFelipe, J., and Yuste, R. (2007). Ultrastructure of dendritic spines: correlation between synaptic and spine morphologies. *Front. Neurosci.* 1:10. doi: 10.3389/neuro.01.1.1.010.2007

Basu, S., and Lamprecht, R. (2018). The role of actin cytoskeleton in dendritic spines in the maintenance of long-term memory. *Front. Mol. Neurosci*. 11:143. doi: 10.3389/fnmol.2018.00143

Bellot, A., Guivernau, B., Tajes, M., Bosch-Morato, M., Valls-Comamala, V., and Munoz, F. J. (2014). The structure and function of actin cytoskeleton in mature glutamatergic dendritic spines. *Brain Res*. 1573, 1–16. doi: 10.1016/j.brainres.2014.05.024

Bennett, M. R., Farnell, L., and Gibson, W. G. (2011). A model of nmda receptor control of f-actin treadmilling in synaptic spines and their growth. *Bull. Math. Biol*. 73, 2109–2131. doi: 10.1007/s11538-010-9614-4

Berning, S., Willig, K. I., Steffens, H., Dibaj, P., and Hell, S. W. (2012). Nanoscopy in a living mouse brain. Science 335, 551–551. doi: 10.1126/science.1215369

Bonilla-Quintana, M., Wörgötter, F., Tetzlaff, C., and Fauth, M. (2019). Modeling the shape of synaptic spines by their actin dynamics. *bioRxiv*. doi: 10.1101/817932

Borovac, J., Bosch, M., and Okamoto, K. (2018). Regulation of actin dynamics during structural plasticity of dendritic spines: Signaling messengers and actin-binding proteins. *Mol. Cell. Neurosci*. 91, 122–130. doi: 10.1016/j.mcn.2018.07.001

Botsch, M., Steinberg, S., Bischoff, S., and Kobbelt, L. (2002). *Openmesh–A Generic and Efficient Polygon Mesh Data Structure*. Darmstadt: OpenSG Symposium.

Boyer, C., Schikorski, T., and Stevens, C. F. (1998). Comparison of hippocampal dendritic spines in culture and in brain. *J. Neurosci*. 18, 5294–5300. doi: 10.1523/JNEUROSCI.18-14-05294.1998

Cingolani, L. A., and Goda, Y. (2008). Actin in action: the interplay between the actin cytoskeleton and synaptic efficacy. *Nat. Rev. Neurosci*. 9:344. doi: 10.1038/nrn2373

Computer Graphics Group, R. A. (2018). *Openmesh 7.1*. Available online at: https://www.openmesh.org (accessed November 20, 2018).

Craig, E. M., Stricker, J., Gardel, M., and Mogilner, A. (2015). Model for adhesion clutch explains biphasic relationship between actin flow and traction at the cell leading edge. *Phys. Biol*. 12:035002. doi: 10.1088/1478-3975/12/3/035002

De Vivo, L., Landi, S., Panniello, M., Baroncelli, L., Chierzi, S., Mariotti, L., et al. (2013). Extracellular matrix inhibits structural and functional plasticity of dendritic spines in the adult visual cortex. *Nat. Commun*. 4:1484. doi: 10.1038/ncomms2491

Deserno, M. (2015). Fluid lipid membranes: From differential geometry to curvature stresses. *Chem. Phys. Lipids* 185, 11–45. doi: 10.1016/j.chemphyslip.2014.05.001

Dunaevsky, A., Tashiro, A., Majewska, A., Mason, C., and Yuste, R. (1999). Developmental regulation of spine motility in the mammalian central nervous system. *Proc. Natl. Acad. Sci. U. S. A*. 96, 13438–13443. doi: 10.1073/pnas.96.23.13438

Dvorkin, R., and Ziv, N. E. (2016). Relative contributions of specific activity histories and spontaneous processes to size remodeling of glutamatergic synapses. *PLoS Biol*. 14:e1002572. doi: 10.1371/journal.pbio.1002572

Fauth, M., and Tetzlaff, C. (2016). Opposing effects of neuronal activity on structural plasticity. *Front. Neuroanat*. 10:75. doi: 10.3389/fnana.2016.00075

Fischer, M., Kaech, S., Knutti, D., and Matus, A. (1998). Rapid actin-based plasticity in dendritic spines. *Neuron* 20, 847–854. doi: 10.1016/S0896-6273(00)80467-5

Footer, M. J., Kerssemakers, J. W., Theriot, J. A., and Dogterom, M. (2007). Direct measurement of force generation by actin filament polymerization using an optical trap. *Proc. Natl. Acad. Sci. U. S. A*. 104, 2181–2186. doi: 10.1073/pnas.0607052104

Fortin, D. A., Srivastava, T., and Soderling, T. R. (2012). Structural modulation of dendritic spines during synaptic plasticity. *Neuroscientist* 18, 326–341. doi: 10.1177/1073858411407206

Frost, N. A., Shroff, H., Kong, H., Betzig, E., and Blanpied, T. A. (2010). Single-molecule discrimination of discrete perisynaptic and distributed sites of actin filament assembly within dendritic spines. *Neuron* 67, 86–99. doi: 10.1016/j.neuron.2010.05.026

Guckenberger, A., and Gekle, S. (2017). Theory and algorithms to compute Helfrich bending forces: a review. *J. Phys. Condens. Matter* 29:203001. doi: 10.1088/1361-648X/aa6313

Hartmann, C., Miner, D. C., and Triesch, J. (2015). Precise synaptic efficacy alignment suggests potentiation dominated learning. *Front. Neural Circuits* 9:90. doi: 10.3389/fncir.2015.00090

Helf, C. (2015). *Matlab Isotropic Remesher*. GitHub, Inc. Available online at: https://github.com/christopherhelf/isotropicremeshing/blob/master/README.md (accessed November 20, 2018).

Helfrich, W. (1973). Elastic properties of lipid bilayers: theory and possible experiments. *Z. Naturforsch. C* 28, 693–703. doi: 10.1515/znc-1973-11-1209

Holtmaat, A. J. G. D., Trachtenberg, J. T., Wilbrecht, L., Shepherd, G. M., Zhang, X., Knott, G. W., et al. (2005). Transient and persistent dendritic spines in the neocortex *in vivo*. *Neuron* 45, 279–291. doi: 10.1016/j.neuron.2005.01.003

Honkura, N., Matsuzaki, M., Noguchi, J., Ellis-Davies, G. C., and Kasai, H. (2008). The subspine organization of actin fibers regulates the structure and plasticity of dendritic spines. *Neuron* 57, 719–729. doi: 10.1016/j.neuron.2008.01.013

Hotulainen, P., and Hoogenraad, C. C. (2010). Actin in dendritic spines: connecting dynamics to function. *J. Cell Biol*. 89, 619–629. doi: 10.1083/jcb.201003008

Hotulainen, P., Llano, O., Smirnov, S., Tanhuanpää, K., Faix, J., Rivera, C., et al. (2009). Defining mechanisms of actin polymerization and depolymerization during dendritic spine morphogenesis. *J. Cell Biol*. 185, 323–339. doi: 10.1083/jcb.200809046

Kim, I. H., Racz, B., Wang, H., Burianek, L., Weinberg, R., Yasuda, R., et al. (2013). Disruption of Arp2/3 results in asymmetric structural plasticity of dendritic spines and progressive synaptic and behavioral abnormalities. *J. Neurosci*. 33, 6081–6092. doi: 10.1523/JNEUROSCI.0035-13.2013

Korobova, F., and Svitkina, T. (2010). Molecular architecture of synaptic actin cytoskeleton in hippocampal neurons reveals a mechanism of dendritic spine morphogenesis. *Mol. Biol. Cell* 21, 165–176. doi: 10.1091/mbc.e09-07-0596

Krüger, H. (2012). *Computer Simulation Study of Collective Phenomena in Dense Suspensions of Red Blood Cells Under Shear*. Wiesbaden: Springer Science & Business Media.

Lin, W.-H., and Webb, D. J. (2009). Actin and actin-binding proteins: masters of dendritic spine formation, morphology, and function. *Open Neurosci. J*. 3:54. doi: 10.2174/1874082000903020054

Loewenstein, Y., Kuras, A., and Rumpel, S. (2011). Multiplicative dynamics underlie the emergence of the log-normal distribution of spine sizes in the neocortex *in vivo*. *J. Neurosci*. 31, 9481–9488. doi: 10.1523/JNEUROSCI.6130-10.2011

Martin, S. J., Grimwood, P. D., and Morris, R. G. (2000). Synaptic plasticity and memory: an evaluation of the hypothesis. *Annu. Rev. Neurosci*. 23, 649–711. doi: 10.1146/annurev.neuro.23.1.649

Matsuzaki, M., Ellis-Davies, G. C., Nemoto, T., Miyashita, Y., Iino, M., and Kasai, H. (2001). Dendritic spine geometry is critical for AMPA receptor expression in hippocampal CA1 pyramidal neurons. *Nat. Neurosci*. 4, 1086–1092. doi: 10.1038/nn736

Matsuzaki, M., Honkura, N., Ellis-Davies, G. C. R., and Kasai, H. (2004). Structural basis of long-term potentiation in single dendritic spines. *Nature* 429, 761–766. doi: 10.1038/nature02617

Meyer, D., Bonhoeffer, T., and Scheuss, V. (2014). Balance and stability of synaptic structures during synaptic plasticity. *Neuron* 82, 430–443. doi: 10.1016/j.neuron.2014.02.031

Miermans, C., Kusters, R., Hoogenraad, C., and Storm, C. (2017). Biophysical model of the role of actin remodeling on dendritic spine morphology. *PLoS ONE* 12:e0170113. doi: 10.1371/journal.pone.0170113

Mogilner, A. (2006). On the edge: modeling protrusion. *Curr. Opin. Cell Biol.* 18, 32–39. doi: 10.1016/j.ceb.2005.11.001

Mogilner, A., and Edelstein-Keshet, L. (2002). Regulation of actin dynamics in rapidly moving cells: a quantitative analysis. *Biophys. J.* 83, 1237–1258. doi: 10.1016/S0006-3495(02)73897-6

Mogilner, A., and Oster, G. (1996). Cell motility driven by actin polymerization. *Biophys. J.* 71, 3030–3045. doi: 10.1016/S0006-3495(96)79496-1

Mogilner, A., and Oster, G. (2003). Force generation by actin polymerization II: the elastic ratchet and tethered filaments. *Biophys. J.* 84, 1591–1605. doi: 10.1016/S0006-3495(03)74969-8

Mongillo, G., Rumpel, S., and Loewenstein, Y. (2017). Intrinsic volatility of synaptic connections — a challenge to the synaptic trace theory of memory. *Curr. Opin. Neurobiol.* 46, 7–13. doi: 10.1016/j.conb.2017.06.006

Okamoto, K.-I., Nagai, T., Miyawaki, A., and Hayashi, Y. (2004). Rapid and persistent modulation of actin dynamics regulates postsynaptic reorganization underlying bidirectional plasticity. *Nat. Neurosci.* 7:1104. doi: 10.1038/nn1311

Pollard, T. D., Blanchoin, L., and Mullins, R. D. (2000). Molecular mechanisms controlling actin filament dynamics in nonmuscle cells. *Annu. Rev. Biophys. Biomol. Struct.* 29, 545–576. doi: 10.1146/annurev.biophys.29.1.545

Pontes, B., Ayala, Y., Fonseca, A. C. C., Romão, L. F., Amaral, R. F., Salgado, L. T., et al. (2013). Membrane elastic properties and cell function. *PLoS ONE* 8:e67708. doi: 10.1371/journal.pone.0067708

Rácz, B., and Weinberg, R. J. (2008). Organization of the Arp2/3 complex in hippocampal spines. *J. Neurosci.* 28, 5654–5659. doi: 10.1523/JNEUROSCI.0756-08.2008

Rubinstein, B., Fournier, M. F., Jacobson, K., Verkhovsky, A. B., and Mogilner, A. (2009). Actin-myosin viscoelastic flow in the keratocyte lamellipod. *Biophys. J.* 97, 1853–1863. doi: 10.1016/j.bpj.2009.07.020

Statman, A., Kaufman, M., Minerbi, A., Ziv, N. E., and Brenner, N. (2014). Synaptic size dynamics as an effectively stochastic process. *PLoS Comput. Biol.* 10:e1003846. doi: 10.1371/journal.pcbi.1003846

Tønnesen, J., Katona, G., Rózsa, B., and Nägerl, U. V. (2014). Spine neck plasticity regulates compartmentalization of synapses. *Nat. Neurosci.* 17:678. doi: 10.1038/nn.3682

Ward, W. O. (2015). Icosphere. MATLAB Central File Exchange. Available online at: https://de.mathworks.com/matlabcentral/fileexchange/50105-icosphere (accessed September 19, 2018).

Yasumatsu, N., Matsuzaki, M., Miyazaki, T., Noguchi, J., and Kasai, H. (2008). Principles of long-term dynamics of dendritic spines. *J. Neurosci.* 28, 13592–13608. doi: 10.1523/JNEUROSCI.0603-08.2008

Yuste, R. (2010). *Dendritic Spines*. Cambridge, MA: MIT Press.

Zhou, Q., Homma, K. J., and Ming Poo, M. (2004). Shrinkage of dendritic spines associated with long-term depression of hippocampal synapses. *Neuron* 44, 749–757. doi: 10.1016/j.neuron.2004.11.011

Conflict of Interest: The authors declare that the research was conducted in the absence of any commercial or financial relationships that could be construed as a potential conflict of interest.

frontiers
in Synaptic Neuroscience

REVIEW
published: 11 August 2020
doi: 10.3389/fnsyn.2020.00032

The Decade of Super-Resolution Microscopy of the Presynapse

Georgii Nosov[1,2], **Martin Kahms**[1] **and Jurgen Klingauf**[1]*

[1] Institute of Medical Physics and Biophysics, University of Münster, Münster, Germany, [2] CIM-IMPRS Graduate Program in Münster, Münster, Germany

The presynaptic compartment of the chemical synapse is a small, yet extremely complex structure. Considering its size, most methods of optical microscopy are not able to resolve its nanoarchitecture and dynamics. Thus, its ultrastructure could only be studied by electron microscopy. In the last decade, new methods of optical superresolution microscopy have emerged allowing the study of cellular structures and processes at the nanometer scale. While this is a welcome addition to the experimental arsenal, it has necessitated careful analysis and interpretation to ensure the data obtained remains artifact-free. In this article we review the application of nanoscopic techniques to the study of the synapse and the progress made over the last decade with a particular focus on the presynapse. We find to our surprise that progress has been limited, calling for imaging techniques and probes that allow dense labeling, multiplexing, longer imaging times, higher temporal resolution, while at least maintaining the spatial resolution achieved thus far.

Keywords: presynapse, active zone, exo-endocytosis, nanoscopy, CLEM

OPEN ACCESS

Edited by:
Shelley Halpain,
University of California, San Diego,
United States

Reviewed by:
Craig Curtis Garner,
Charité – Universitätsmedizin Berlin,
Germany
Ling-Gang Wu,
National Institute of Neurological
Disorders and Stroke (NINDS),
United States

Correspondence:
Jurgen Klingauf
klingauf@uni-muenster.de

Received: *27 September 2019*
Accepted: *21 July 2020*
Published: *11 August 2020*

Citation:
Nosov G, Kahms M and Klingauf J (2020) The Decade of Super-Resolution Microscopy of the Presynapse.
Front. Synaptic Neurosci. 12:32.
doi: 10.3389/fnsyn.2020.00032

INTRODUCTION

The classical chemical synapse in the central nervous system (CNS) of vertebrates is a discontinuous structure consisting of a presynapse formed by the signal transducing neuron and a postsynapse formed by the receiving neuron. The existence of the synapse was originally put forward by Ramón y Cajal (1904), but the first direct observation and most of our current knowledge about the structure of this intercellular contact site has been derived from electron microscopy (EM) (for review see, e.g., Siksou et al., 2009; Harris and Weinberg, 2012). The two halves of the synapse are separated by a synaptic cleft with a width of approximately 15–20 nm (De Robertis and Bennett, 1955; Palay and Palade, 1955) and the presynaptic swelling or bouton is densely filled with granular structures designated as synaptic vesicles (SVs). The discovery of SVs occurred in parallel with establishment of the quantal hypothesis of neurotransmitter (NT) release (Del Castillo and Katz, 1954) and it was only later that SVs were unambiguously identified as subcellular compartments releasing discrete packages of NT ("quanta") upon fusion with the plasma membrane (PM) (De Robertis et al., 1963; Heuser and Reese, 1973).

The advent of nanoscopic light microscopy techniques more than a decade ago, held the particular promise that nanometer resolution in combination with highly efficient protein labeling strategies, either by immunostaining or genetically encoded fluorescent proteins will greatly increase our understanding of the presynaptic nano-architecture and protein networks far beyond the electron-microscopic picture. Thus, in combination with live cell experiments, nanoscopic light microscopy should contribute to a better understanding of fundamental presynaptic processes such as SV release, compensatory endocytosis and cargo sorting. After briefly summarizing the previous results made by EM, we ascertain the advances in our understanding of the presynaptic nano-architecture driven by the application of nanoscopic techniques.

THE SYNAPSE IN THE ELECTRON MICROSCOPIC PICTURE

The classical chemical synapse in the vertebrate CNS has a size of 0.5 to 2 μm and can harbor between 100 and 400 SVs in boutons of hippocampal pyramidal neurons. In contrast, large mossy fiber boutons of dentate gyrus granular cells in the hippocampus contain up to several thousand SVs (Schikorski and Stevens, 1997; Rollenhagen et al., 2007). In most mature synapses SVs exhibit a low size variation with a typical diameter of 40–50 nm (De Robertis and Bennett, 1955; Harris and Sultan, 1995). A small pool of SVs is docked at the presynaptic PM at the active zone (AZ), a spatially defined region where SV fusion and NT release occur (Couteaux and Pecot-Dechavassine, 1970; Heuser et al., 1979). Docked SVs are associated with a dense amorphous material, termed the cytomatrix of the presynaptic active zone (CAZ) (Pfenninger et al., 1972; Harlow et al., 2001). In the postsynapse, a submembrane layer of electron-dense material can be distinguished, the so-called postsynaptic density (PSD) (Palay, 1958; Gulley and Reese, 1981). Based on the observation that SVs in the presynapse tend to cluster opposite to the PSD, it is common sense today that the PSD constitutes a postsynaptic cytoskeleton involved in organizing postsynaptic receptor localization face to face to the presynaptic AZ. The size of the average presynaptic AZ, estimated by the size of the PSD is 200–400 nm in diameter (Cohen and Siekevitz, 1978).

Besides such common features, EM also revealed a remarkable diversity in synaptic ultrastructure both between different organisms and between neuronal types (**Figure 1**). Synapses at the neuromuscular junction (NMJ) vary noticeably between species but display common structural features, such as their large size compared to CNS synapses (30 μm in mice). NMJs are also notable for their complex internal structure including hundreds of individual regularly distributed AZs with a mean inter-AZ spacing of about 1 μm (Rowley et al., 2007). In vertebrates, the synaptic cleft of the NMJ contains the basal lamina and evidently, the width of the cleft is much larger compared to CNS synapses (de Harven and Coërs, 1959). In the NMJ of *Drosophila* larvae (**Figure 1D**), CAZ proteins form specialized electron-dense projections, the so called T-bars (Prokop and Meinertzhagen, 2006).

Large specialized hippocampal mossy fiber boutons in the mammalian CNS (**Figure 1F**) contain more than a few ten AZs and contact multiple postsynaptic partners (Rollenhagen et al., 2007). Another type of specialized synapses comprises ribbon synapses of the visual and auditory system of vertebrates (**Figure 1C**). Their distinguishing feature is the presence of large rod-shaped structures in the presynaptic terminal. These structures are joined by dozens of SVs (Sjoestrand, 1958). It is believed that these ribbons facilitate fusion of SVs with the presynaptic membrane either by an active mechanism that shuttles SVs downward toward docking/release sites (conveyor belt model) or by compound fusion of SVs allowing multivesicular release and thus, extremely high release rates (safety belt hypothesis) (Parsons and Sterling, 2003; Matthews and Sterling, 2008). Remarkably, presynaptic filamentous structures that partially resemble those of ribbons also exist in the cytomatrix of hippocampal boutons (Siksou et al., 2007).

In classical EM chemical fixation methods are applied, such as aldehyde and/or osmium fixation. Fixation is typically followed by dehydration, embedding in a suitable resin, slicing and heavy metal staining (Hayat, 2000). Large structures can be reconstructed in 3D by manual serial sectioning (Stevens et al., 1980), automated serial block face imaging (Denk and Horstmann, 2004) or by focused ion beam (FIB) milling in combination with scanning electron microscopy (SEM) (Knott et al., 2008). For the 3D reconstruction of fine structures, electron tomography (ET) with axial resolution well below slice thickness can be utilized (Perkins et al., 2015).

However, chemical fixation may alter the synaptic ultrastructure by inducing protein polymerization and tissue shrinkage. For example, EM tomography in frog NMJ revealed intricate scaffold structures forming a highly ordered network. The macromolecular assemblies could be sorted according to their shape into distinct classes such as beams, pegs or booms (Harlow et al., 2001, 2013). Nonetheless, the dense projections observed in these chemically fixed synapses might at least partially stem from condensation and collapse of filamentous structures by cross-linking during chemical fixation. In recent years, physical fixation methods have become widespread, and these methods allow overcoming most of the artifacts inherent in chemical fixation.

High-pressure freezing (HPF) followed by freeze-substitution preserves the synaptic ultrastructure significantly better and avoids distortions of the cellular morphology induced by slow chemical fixation (Studer et al., 2001; Rostaing et al., 2006). In addition, it allows rapid vitrification within a few tens of milliseconds even for thicker specimens. HPF in combination with ET of rat hippocampal slices uncovered that SVs are surrounded by a dense network of filaments that link SVs together. Furthermore, longer filaments were observed that directly link SVs to the AZ (Siksou et al., 2007). Nevertheless, HPF is also not artifact-free since ice-crystal formation, high pressure-induced shearing and collapse of air-filled spaces can deform the tissue.

In freeze fracturing, samples are also rapidly frozen and then broken up in the vacuum. A carbon-platinum replica is prepared from the fractured sample surface that can be analyzed by EM (Moor and Mühlethaler, 1963; Bullivant and Ames, 1966). Since PMs can be split into half-membrane leaflets, this method is very well suited for membrane studies. In addition, epitopes of membrane proteins are partially preserved for immune-gold labeling after SDS replica cleaning (Fujimoto, 1995; Masugi-Tokita et al., 2007). This method contributed to the further

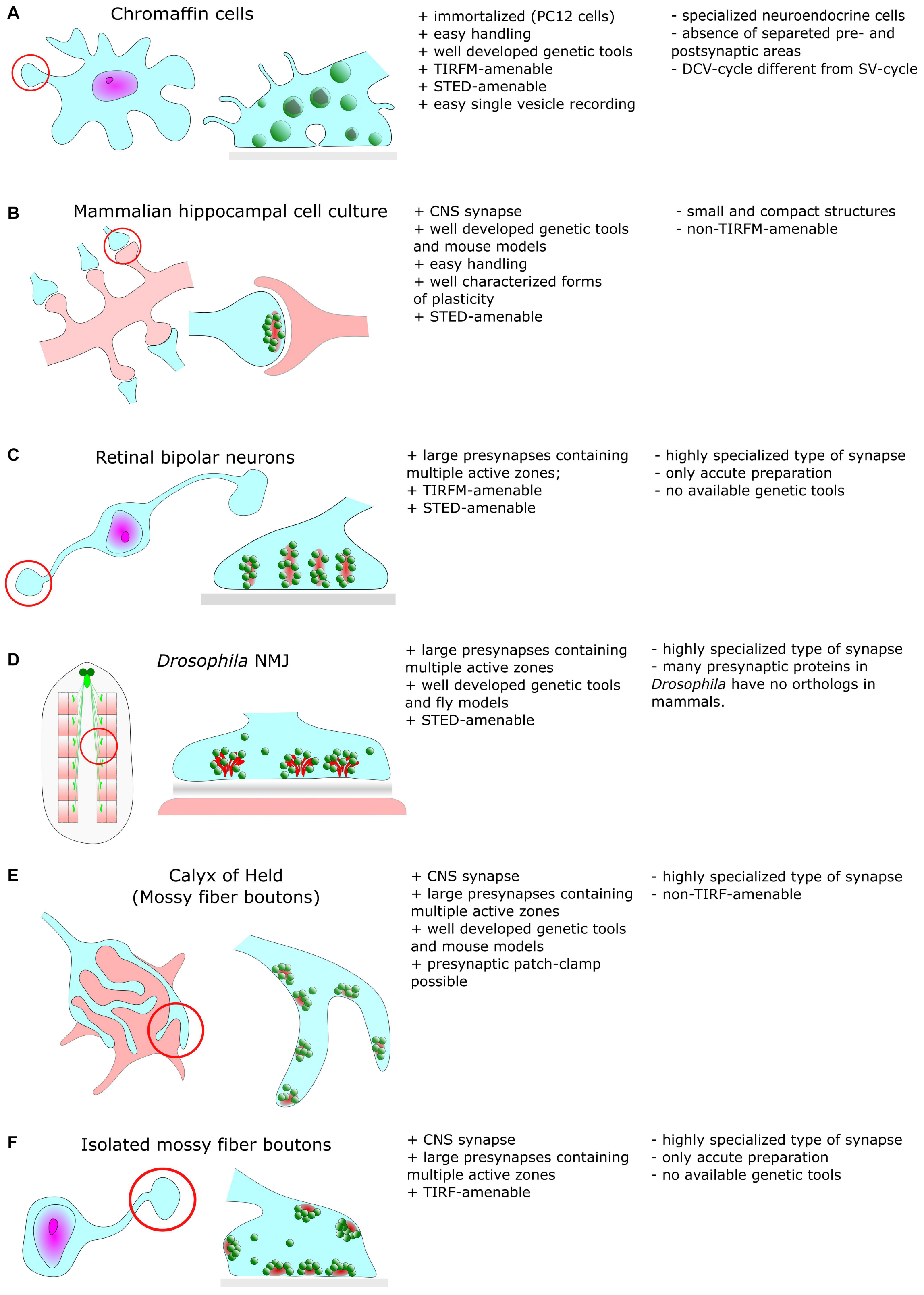

A Chromaffin cells

+ immortalized (PC12 cells)
+ easy handling
+ well developed genetic tools
+ TIRFM-amenable
+ STED-amenable
+ easy single vesicle recording

- specialized neuroendocrine cells
- absence of separeted pre- and postsynaptic areas
- DCV-cycle different from SV-cycle

B Mammalian hippocampal cell culture

+ CNS synapse
+ well developed genetic tools and mouse models
+ easy handling
+ well characterized forms of plasticity
+ STED-amenable

- small and compact structures
- non-TIRFM-amenable

C Retinal bipolar neurons

+ large presynapses containing multiple active zones;
+ TIRFM-amenable
+ STED-amenable

- highly specialized type of synapse
- only accute preparation
- no available genetic tools

D *Drosophila* NMJ

+ large presynapses containing multiple active zones
+ well developed genetic tools and fly models
+ STED-amenable

- highly specialized type of synapse
- many presynaptic proteins in *Drosophila* have no orthologs in mammals.

E Calyx of Held (Mossy fiber boutons)

+ CNS synapse
+ large presynapses containing multiple active zones
+ well developed genetic tools and mouse models
+ presynaptic patch-clamp possible

- highly specialized type of synapse
- non-TIRF-amenable

F Isolated mossy fiber boutons

+ CNS synapse
+ large presynapses containing multiple active zones
+ TIRF-amenable

- highly specialized type of synapse
- only accute preparation
- no available genetic tools

FIGURE 1 | Common cellular model systems for studying synaptic structure and function with super-resolution methods include **(A)** Chromaffin cells **(B)** Hippocampal cell culture **(C)** Retinal biopolar neurons **(D)** *Drosophila* neuromuscular junction **(E)** Calyx of Held **(F)** Isolated mossy fiber boutons. However, all these model systems have their advantages and disadvantages, which we briefly discuss in this figure.

characterization of presynaptic SV recycling (Heuser et al., 1979; Heuser and Reese, 1981). However, as with HPF, freeze fracturing necessitates rapid cooling and some biological samples require treatment with a cryo-protectant to minimize ice crystal damage.

Cryo-electron tomography (cryo-ET) in conjunction with cryo-fixation techniques and relative mild sample preparation also aims to overcome some of the above mentioned limitations and allows reconstruction of molecular assemblies under more native conditions (Lucić et al., 2005). This technique is discussed in more detail in a later section.

Though for all EM techniques the preservation of biological structures in a state as native as possible is a crucial and vividly discussed issue, EM in principle resolves fine structures well and in conjunction with correlative approaches, like electrophysiology and genetic modification of synapses by gene ablation, EM gave a wealth of information on the structural organization of synapses. Yet, labeling of specific proteins to unravel the exact molecular assembly of proteins remains challenging in EM. Pre- or post-embedding protein labeling using gold-conjugated antibodies usually results in low labeling densities. A notable exception is the giant reticulospinal axons in lamprey. These axons can be cut along their longitudinal axis providing access for antibodies to target the sites of SV recycling (Evergren et al., 2004).

Genetically encoded tags suitable for EM, like the singlet oxygen generator miniSOG (Shu et al., 2011) or the peroxidase APEX (Martell et al., 2012) are still far from being used routinely since the experimental conditions for the generation of precipitate resolvable by EM have to be carefully adjusted. Thus, we are still lacking tools in EM akin to fluorescent proteins in cell biology and light microscopy.

SUB-DIFFRACTION MICROSCOPY: BEARING FRUIT AFTER A DECADE OF IMPLEMENTATION

A wide range of fluorescence microscopy techniques using different physical principles to overcome the diffraction limit has emerged during the last two decades (for review see, e.g., Sahl et al., 2017; Schermelleh et al., 2019) and consequently, these techniques found their way into neuroscience (Tønnesen and Nägerl, 2013; Igarashi et al., 2018). Among these super-resolution (SR) concepts, stimulated emission depletion (STED) and stochastic optical reconstruction microscopy (STORM) or photoactivated localization microscopy (PALM) are the most commonly used techniques and have been rewarded with the Noble Prize for Chemistry in 2014. Here, we briefly describe the main principles underlying these techniques (**Table 1**).

In STED microscopy, the effective excitation volume is shrunk by overlaying the excitation spot with a doughnut-shaped red-shifted depletion laser that de-excites molecules in the periphery of the excitation spot. By these means, a resolution of 40 nm and below can be achieved (Hell and Wichmann, 1994; Klar et al., 2000).

In STORM or PALM, stochastic switching of photoactivatable (PA) or switchable fluorophores is employed to visualize single emitters. Subsequently, the intensity profiles of single emitters are fit by, e.g., a 2D Gaussian function to determine the exact localization of these molecules. After repeatedly imaging different subsets of fluorescent molecules, a high-resolution image is reconstructed by summing up the single molecule coordinates. Depending on the number of detected photons per molecule, a localization precision down to 10 nm is feasible (Betzig et al., 2006; Hess et al., 2006; Bates et al., 2007) allowing to separate, e.g., pre- and postsynaptic compartments with fluorescence light microscopy (**Figure 2**).

Other concepts in SR microscopy are structured illumination microscopy (SIM) and lattice light sheet microscopy (LLSM). In SIM, the sample is illuminated with a periodic excitation pattern. By these means, high-resolution information is shifted into the resolvable regime and can be extracted by linear image processing to obtain a final image with twofold increased resolution (Gustafsson, 2000). Resolution in SIM can be even further improved by using nonlinear structured illumination patterns (Gustafsson, 2005). LLSM is a specialized version of ultramicroscopy in which light sheets are created by 2D optical lattices. This illumination mode enables high spatiotemporal resolution and low phototoxicity for live cell imaging. Furthermore, LLSM can be operated in different modes allowing either high-speed 3D imaging down to the single molecule level or spatial resolution beyond the diffraction limit (Chen et al., 2014).

A further SR approach that was recently introduced is MINFLUX. Like in STED microscopy, the exact position of individual molecules is determined with a doughnut-shaped laser beam. However, the doughnut is not used to deplete but to excite fluorescence, and emitter positions are probed with the local intensity minimum of the doughnut. This way, the absolute photon number for precise emitter localization is minimized (Balzarotti et al., 2017).

While at first the application of these techniques was reserved for a few expert laboratories, the commercial availability of these instruments today also enables the non-advanced user to perform SR microscopy. Here, we briefly summarize some of the key applications in the neuronal field.

Time-lapse STED microscopy has been successfully employed to visualize plasticity-dependent morphological changes of YFP-positive dendritic spines in hippocampal organotypical slices with a resolution of $\sim$ 70 nm (Nägerl et al., 2008) and the distribution and dynamics of actin within spines could be resolved at a resolution of 60–80 nm in (Urban et al., 2011).

The distances between synaptic proteins and even individual epitopes of single proteins in fixed brain slices and cultured neurons were determined using 3D STORM (Dani et al., 2010; Herrmannsdörfer et al., 2017; Lagache et al., 2018). These studies revealed, e.g., that the large AZ proteins Bassoon and Piccolo are organized in an extended and oriented manner forming the CAZ together with other presynaptic proteins.

PALM in combination with single particle tracking (sptPALM) was used in live cells to analyze the distribution and mobility of individual synaptic proteins such as Syntaxin1A (Bademosi et al., 2017), voltage gated Ca^{2+} channels (VGCCs)

TABLE 1 | Comparison of different super-resolution methods.

Super-resolution method	**SIM**	**STED**	**Single molecule localization microscopy**		
			STORM	**PALM/sptPALM**	**DNA-PAINT**
Illumination/ Detection	Wide-field/TIRF	Scanning confocal	Wide-field/TIRF	Wide-field/TIRF	TIRF/ spinning disk confocal
Lateral resolution	∼100 nm (linear) ∼60 nm (non-linear)	40–70 nm	10–30 nm	10–30 nm	10–30 nm
Axial resolution	300 nm (3D SIM)	Down to 40 nm (iso-STED)	∼20 nm (astigmatism) ∼10 nm (interference)	∼20 nm (astigmatism) ∼10 nm (interference)	∼100 nm (TIRF) ∼80 nm (astigmatism)
Acquisition time	Seconds	Seconds	Minutes	ms-seconds (sptPALM) minutes (PALM)	Minutes-hours
Dyes	Conventional	Dyes suitable for efficient stimulated emission	Photoswitchable dyes	Photo-activatable fluorescent proteins	Dye-conjugated oligonucleotides
Live cell imaging	Yes	Yes	No	Yes	Very limited
Number of frames for single SR-image	9–15 frames	1 frame	Several thousand frames	Several thousand frames	Several thousand frames
Post-processing	Yes (reconstruction in reciprocal space)	No	Yes (emitter localization)	Yes (emitter localization)	Yes (emitter localization)

(Schneider et al., 2015; Heck et al., 2019) and postsynaptic AMPA receptors (Hoze et al., 2012; Nair et al., 2013). The results show, e.g., that physical interactions with a large number of PM surface binding sites rather than molecular crowding is responsible for the high density of AMPA receptors at the postsynapse (Hoze et al., 2012).

However, one of the most surprising observations in this context is certainly the discovery of periodic Actin cytoskeleton rings by STORM and STED microscopy (Xu et al., 2013; D'Este et al., 2015). Here it was shown that Actin and Spectrin form alternating ring-like structures with a periodicity of 180–190 nm to stabilize the dendritic and axonal PM.

The application of SR techniques to the presynapse comes along with several challenges. Synapses are usually small structures with a high density of supramolecular complexes. The orientation in space of CNS synapses in culture or slices is random, complicating reconstruction of synaptic structures by simple averaging approaches unless 3D imaging is performed. In addition, the differentiation of pre- and postsynaptic structures is hampered by the small width of the synaptic cleft. Therefore, many structural reconstructions of protein distributions have been performed on large and highly specialized synapses such as the NMJ of *Drosophila* larvae (**Figure 1D**).

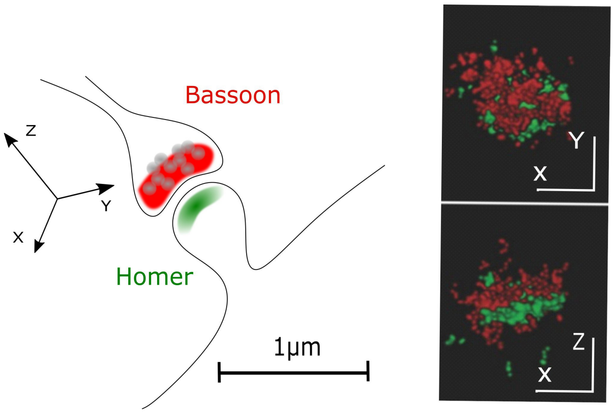

FIGURE 2 | Pre- and postsynaptic compartments resolved with STORM microscopy. A classical CNS synapse and STORM reconstruction of primary hippocampal neurons stained for presynaptic (Bassoon, red) and postsynaptic (Homer, green) markers (adapted from Boening et al., 2017; Copyright (2017) Wiley. Used with permission).

THE PRESYNAPTIC COMPARTMENT AND SV RECYCLING

Excitatory synapses of cultured hippocampal neurons have a diameter of 600–800 nm and are densely filled with SVs of 40 nm size (Schikorski and Stevens, 1997). A combination of genetic perturbation, electrophysiology, EM and fluorescence microscopy culminated in the current model of NT release (Lisman et al., 2007). First, membrane docked SVs fuse with the presynaptic PM by Ca^{2+}-triggered exocytosis. Subsequently, exocytosed SV membranes and proteins are resorted and recycled by triggered compensatory endocytosis, followed by refilling of newly formed SVs with NTs. The hallmark of presynaptic SV recycling is the tight coupling of exo- and endocytosis in space and time, which is necessary to sustain high release rates. Therefore, processes like exocytosis, release site clearance, re-sorting of SV components post fusion and endocytosis have to occur in a highly coordinated manner. A complex set of proteins is required to organize the SV release and retrieval machinery and they are a natural target for SR microscopy to elucidate their molecular organization and dynamics at the presynapse to finally address the following questions: (1) Are there defined SV fusion sites? (2) How tight are release sites and VGCCs coupled in space? (3) Are there defined endocytic sites? (4) What is the mechanism responsible for tight temporal and spatial coupling of exo- and endocytosis? (5) What is the fate of SV proteins at the presynaptic PM after SV fusion? (6) Are presynaptic release sites and postsynaptic NT receptors spatially correlated across the synaptic cleft?

AZ ARCHITECTURE AND ORGANIZATION OF SV RELEASE SITES

Synaptic vesicles fuse with the presynaptic PM at the AZ (Heuser et al., 1979). In order to elucidate the molecular organization of the underlying release sites, it is essential to understand the molecular assembly and relative position of CAZ-proteins, VGCCs, SNARE proteins and other release factors. STED microscopy has been intensively used in the NMJ of *Drosophila* larvae to unravel the molecular scaffold responsible for AZ organization (**Figure 3**). These presynaptic terminals contain several AZs and the protein Bruchpilot (BRP) was observed in doughnut-shaped structures centered at these AZs (Kittel et al., 2006). AZs of a BRP mutant displayed loss of T-bars, reduced clustering of VGCCs and depressed evoked SV release. Thus, BRP was one of the first scaffolding proteins identified as being responsible for AZ integrity by establishing a close proximity between docked SVs and VGCCs. Later on, other CAZ proteins such as Rab3-interacting molecule (RIM), RIM-binding protein (RIM-BP) and Fife were identified to play major roles in correct AZ formation and thus, NT release (Liu et al., 2011; Graf et al., 2012; Bruckner et al., 2017). A recent two-color STED microscopy study in *Drosophila* NMJ uncovered yet another protein, the priming factor Unc13A, as essential for stable release site generation (Reddy-Alla et al., 2017).

The mammalian CAST/ELKs proteins are orthologs of BRP and deletion of CAST/ELKs, similar to deletion of BRP in *Drosophila*, led to impairment of the AZ ultrastructure in mouse retinal ribbon synapses (Hagiwara et al., 2018). In contrast, loss of CAST/ELKs hardly affected AZ integrity in cultured hippocampal neurons. Here, only minor effects on readily releasable pool (RRP) size and Ca^{2+} influx were observed (Liu et al., 2014; Held et al., 2016).

In mammalian neurons, the large scaffolding proteins Bassoon and Piccolo are integral parts of the CAZ (**Figure 3**). Dual-color STED microscopy in mouse NMJ disclosed non-overlapping punctuate patterns for these presynaptic scaffolding proteins, and it was found that the Bassoon puncta co-localized with P/Q type VGCCs (Nishimune et al., 2016), in agreement with the earlier finding that Bassoon localizes P/Q type VGCCs to the AZ in hippocampal cultures (Davydova et al., 2014). Furthermore, loss of Bassoon impairs recruitment of SVs to release sites in mossy fiber synapses (Hallermann et al., 2010). However, despite the aforementioned phenotypes, loss of function studies for Piccolo and Bassoon have not been shown to affect the AZ ultrastructure in CNS synapses (for review see Gundelfinger et al., 2015) pointing to functional redundancy of CAZ proteins in these synapses. The situation is different for vertebrate sensory synapses. In mice hair cells, STED microscopy upon genetic disruption of Bassoon revealed a lack of ribbons and a reduced number of VGCCs at the AZ (Frank et al., 2010). Deletion of Piccolino, a Piccolo splice variant specifically expressed in sensory ribbon synapses, compromised the synaptic ribbon ultrastructure (Regus-Leidig et al., 2014).

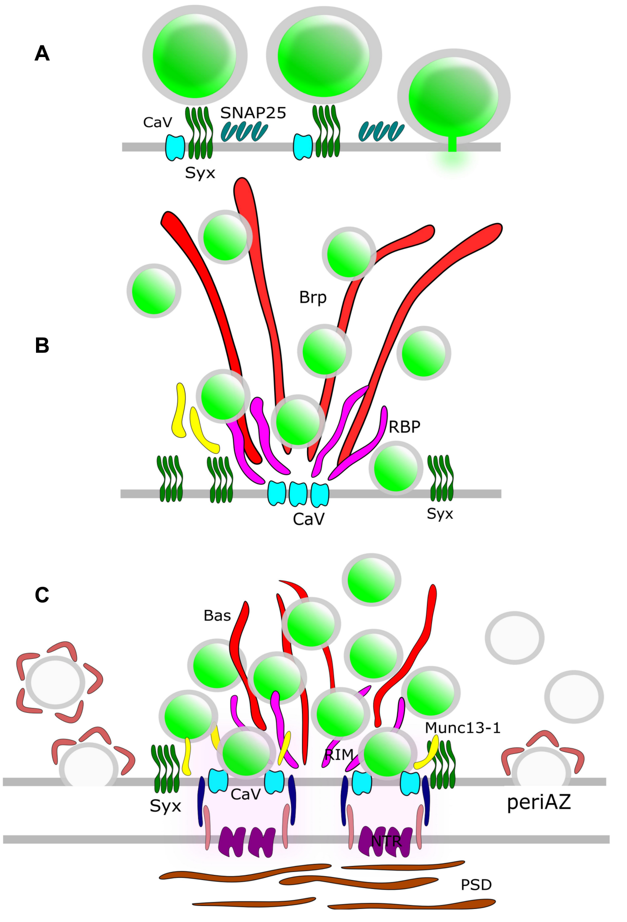

FIGURE 3 | AZ Nano-architecture in common synapse models as suggested by SR microscopy. **(A)** Rat neuroendocrine cells. SR microscopy revealed syntaxin clusters (Syx) potentially serve as docking sites for dense-core vesicles in neuroendocrine cells. Vesicle fusion causes disassembly of the Syx nanoclusters. SNAP25 also form clusters at the plasma membrane; nevertheless, these clusters do not overlap with Syx. **(B)** Drosophila NMJ. The large T-bar forming proteins Bruchpilot (BRP) and Rim-binding protein (RBP) are positioned with their *N*-terminus and *C*-terminus, respectively, close to Ca^{2+}-channel clusters (CaV). Syx clusters are situated in the active zone near Brp and RBP. **(C)** Mammalian CNS synapse. The large filamentous protein Bassoon (Bas) faces the AZ with its *C*-terminus. Munc13-1, CaV, and Syx clusters are positioned close to the SV release sites. The postsynaptic neurotransmitter receptors (NTRs) are aligned with SV fusion sites in a columnar manner via synaptic cell adhesion molecules (SCAMs). Compensatory endocytosis of SVs occurs in a spatially distinct region of the presynapse, the peri-active zone. Here, a surface fraction of SV proteins, the readily retrievable pool (RRetP), is pre-assembled.

Isoforms of Munc13, the mammalian homolog of Unc13, have also been implicated in organizing SV release sites. Munc13-3 regulates density and localization of VGCCs at the AZ (Kusch et al., 2018). However, the role of Munc13 isoforms in presynaptic VGCC recruitment is still disputed. A direct interaction of, e.g., Munc13-1 and VGCCs has been shown (Calloway et al., 2015) but attributed to control of VGCC function rather than recruitment. 3D STORM revealed that Munc13-1 molecules form multiple supramolecular clusters that serve as independent SV release sites by recruiting Syntaxin1A, one of the target SNARE proteins (t-SNARE) in the presynaptic PM (Sakamoto et al., 2018). In this way, Munc13-1 provides platforms for open Syntaxin1A molecules to generate activated SNARE complexes (Rizo, 2018) that facilitate bridging of PM and SVs.

Not surprisingly, Syntaxin1A has emerged as another candidate for organizing the SV fusion machinery. Much of the investigation into this protein has focused on its tendency to cluster at the PM, triggered by the interaction with PIP2 (Milovanovic et al., 2016). Early evidence from neuroendocrine PC12 cells showed the granule fusion sites are "premarked" with Syntaxin1A clusters (Knowles et al., 2010) and L-type VGCCs expressed in HEK cells exhibit strong co-localization with Syntaxin1A clusters (Bar-On et al., 2012; Sajman et al., 2017). The role of Syntaxin1A clusters as release site organizers is challenged by the lack of overlap with clusters of SNAP25, its t-SNARE partner, in PC12 cells (Bar-On et al., 2012) (**Figure 3**). Moreover, a significant pool of extrasynaptic t-SNARE-proteins exists that is recruited to the presynapse during stimulation (Maidorn et al., 2019). Furthermore, an increase in Syntaxin1A trapping was observed after treatment with the widely used anesthetic propofol (Bademosi et al., 2018). However, propofol-induced clustering of Syntaxin1A is associated with impaired neurotransmission, which lends itself to the conclusion that clustered Syntaxin1A is excluded from the SV fusion process. Thus, the exact function of these t-SNARE clusters in organizing release sites remains open to debate.

In a recent study using live hippocampal neurons, single SV fusion events were detected using the pH-sensitive fluorescent protein pHluorin fused to the vesicular glutamate transporter vGlut (Maschi and Klyachko, 2017). The individual fusion events were spatially mapped with a precision of ~30 nm and the results show that mammalian CNS synapses indeed display a dozen of stable SV release sites per bouton. Moreover, the spatial pattern of these fusion sites changed in an activity-dependent manner.

To summarize, presynapses harbor distinct SV fusion sites that are defined by a complex interplay between CAZ proteins, VGCCs, Munc13 and t-SNARES and significant contributions from SR microscopy has helped shed to more light on AZ architecture and organization of SV release sites.

THE MECHANISM OF SV EXOCYTOSIS

Exocytosis of SVs is mediated by SNARE-proteins that drive fusion of the SV membrane with the presynaptic PM. However, the exact mechanism of SNARE-mediated membrane fusion is still under debate. Different models have been proposed and one of these involves priming of docked SVs into a stable hemifused intermediate, in which the inner leaflet of the PM is already fused with the outer leaflet of the SV membrane before cargo release (Kweon et al., 2017). ET has been utilized to reconstruct high-resolution images of docked SVs in different preparations like frog NMJ (Jung, 2019), mice photoreceptors (Zampighi et al., 2011) and thin sections of rat brain (Zampighi et al., 2006). In these studies, hemifused structures at SV/PM contact sites could be frequently observed. However, the results depend heavily on image processing and interpretation and have not been accepted in the field as a strong evidence for a stable hemifused primed state for SVs. In addition, these attempts are limited by the fact that a real population of hemifused SVs might simply be lost during chemical fixation.

Recently, evidence supporting the fusion-through-hemifusion model was reported for fusion of dense core vesicles (DCVs) in live bovine chromaffin cells (Zhao et al., 2016). The authors analyzed the reorganization of the inner PM leaflet lipid PtdIns(4,5)P_2 before and during DCV fusion using 3D STED microscopy. They could observe hemifused Ω-shaped structures seconds before fusion pore opening with the transition to full fusion or fission depending on a completion between fusion and a Ca^{2+}/Dynamin mediated fission mechanism.

Furthermore, STED microscopy enabled the observation of dynamic fusion pore behaviors in neuroendocrine cells (Shin et al., 2018). The results showed a surprisingly large pore size range with varying rates for expansion, constriction and closure (kiss-and-run), critically determining cargo release. The same study found constriction to be mediated by Ca^{2+}/Dynamin while expansion was driven by Actin-dependent membrane tension. However, these studies were only possible on bovine chromaffin cells with large secretory granules (up to 400–500 nm in diameter). And while chromaffin cells share essentially the same core exocytosis machinery with neurons, AZ specializations are missing (Neher, 2018). At presynaptic AZs, proteins like, e.g., Rim and RimBP are implicated in docking and priming and confer extra speed and an extra layer of control for exocytosis. But interestingly, similar Ω-shaped profiles can be induced in Lamprey synapses by electrical stimulation after treatment with Actin-depolymerizing drugs (Wen et al., 2016), suggesting that Actin-induced merging of Ω-shaped release intermediates also occurs in neurons.

SPATIAL COUPLING OF Ca^{2+}CHANNELS AND RELEASE SITES

Synaptic vesicles fusion is tightly coupled to the entry of Ca^{2+} ions into the presynapse. Ca^{2+} influx upon opening of VGCCs triggers SV priming and fusion with the presynaptic PM. Precise timing of transmitter release relative to the arrival of an action potential requires a certain proximity between VGCCs and docked SVs. Typically, presynaptic VGCCs organize into distinct clusters (Kittel et al., 2006; Holderith et al., 2012; Nishimune et al., 2016) and using immuno-gold labeling of SDS-treated freeze fracture replicas, it was found that the number of VGCC clusters matches the number of presynaptic SV docking sites (Miki et al., 2017). However, classical experiments with Ca^{2+} chelators like BAPTA and EGTA have shown that the spatial coupling of Ca^{2+} entry points and Ca^{2+} sensors varies, ranging from 10 to 30 nm in some types of cortical glutamatergic and GABAergic synapses (Bucurenciu et al., 2008; Schmidt et al., 2013) to 100 nm in the mature Calyx of Held (Borst and Sakmann, 1996). Using STED microscopy in *Drosophila* NMJ it has been found, that the topology of docked SVs and VGCCs can be regulated by isoform specific interactions between Unc13 and scaffold proteins like Syd-1, Liprin-α, BRP, and Rim-BP (Böhme et al., 2016). In cerebellar preparations weak synapses exhibited three-fold more VGCCs than strong synapses, but with a five-fold longer coupling distance pointing toward a diverse arrangement of SV/VGCCs even in CNS synapses (Rebola et al., 2019).

The picture of VGGC coupling was further enhanced by using sptPALM on live hippocampal neurons (Schneider et al., 2015). Here it was shown that around 60% of VGCCs are mobile while confined to the presynaptic PM. These data suggest that the fractions of mobile and immobile channels are transient within the AZ and that an interplay between channel density, mobility and Ca^{2+} influx supports Ca^{2+} domain co-operativity to control release probability.

PRESYNAPTIC ENDOCYTIC SITES AND COUPLING OF EXO-ENDOCYTOSIS

Synaptic vesicle exo- and endocytosis in the presynapse are temporally coupled but spatially segregated in different PM domains (Wienisch and Klingauf, 2006). Compensatory endocytosis occurs in the peri-AZ (Roos and Kelly, 1999; Teng et al., 1999), and preformed endocytic patches organized around the AZ could be visualized by iso-STED microscopy (Hua et al., 2011). The main pathway for SV retrieval at the peri-AZ under moderate stimulation conditions was considered to be Clathrin-dependent (Heuser and Reese, 1973; Granseth et al., 2006). However, optogenetics in combination with ultrafast freezing followed by EM analysis revealed that after a single stimulus SVs fuse in the AZ and are directly retrieved by a Clathrin-independent mechanism at the AZ periphery within 50–100 ms (Watanabe et al., 2013). EM, however, only provides snapshots of the presynaptic ultrastructure and in order to finally resolve the mechanism of compensatory endocytosis, it is essential to perform high-resolution live-cell imaging and visualize single SV recycling. Video-rate (28 frames/s) STED microscopy already enabled mapping of the movement and mobility of single SVs in live presynaptic boutons (Westphal et al., 2008). Furthermore, spatially highly resolved tracking of single endocytosed SVs has been performed (Joensuu et al., 2016). Nevertheless, these attempts have not yet brought novel insights into the SV retrieval mechanism.

In addition, the mechanism that tightly couples exo-endocytosis in time is controversial and could not finally be resolved with the help of SR microscopy. It has been reported that Ca^{2+} modulates the time course of endocytosis (Sankaranarayanan and Ryan, 2001; Wu et al., 2009; Leitz and Kavalali, 2011). While in the calyx of Held a Ca^{2+}/Calmodulin-dependent mechanism was found to highly stimulate and to initiate all modes of endocytosis (Wu et al., 2009), in hippocampal cultures Ca^{2+} inhibits endocytosis for single APs (Leitz and Kavalali, 2011). However, in most studies Ca^{2+} stimulates endocytosis (Sankaranarayanan and Ryan, 2001; Wu et al., 2009; Wu and Wu, 2014). The exact molecular mechanism how Ca^{2+} can couple SV fusion and retrieval remains elusive, but Calmodulin and myosin light chain kinase are strong candidates (Wu et al., 2009; Yue and Xu, 2014). Recently it has been shown that endocytosis is also triggered upon Ca^{2+}-independent exocytosis suggesting that compensatory endocytosis might also be initiated by biophysical changes induced by addition of the SV membrane to the presynaptic PM (Orlando et al., 2019). But this finding does not rule out an important role of Ca^{2+} in compensatory endocytosis.

THE FATE OF SV PROTEINS AT THE PRESYNAPTIC PM AFTER SV FUSION

Synaptic vesicle function relies on a distinct set of proteins present in a defined stoichiometry. The molecular sorting mechanisms for individual SV components during exo-endocytosis, however, remain largely unresolved. In one scenario, SV constituents remain clustered upon fusion and diffuse as a raft-like patch to the peri-AZ, preventing the need for re-sorting prior to endocytosis. Indeed, it was shown using live cell STED microscopy that Synaptotagmin1 remains clustered after SV exocytosis (Willig et al., 2006). In contrast, other reports claim rapid dispersion of SV proteins by diffusion upon exocytosis (Wienisch and Klingauf, 2006; Funahashi et al., 2018) and re-sorting and clustering into patches at the peri-AZ (Hua et al., 2011). In this context the exact role of adaptor proteins like, e.g., AP2, Stonin2 and AP180 in productive cargo clustering at endocytic sites is still not fully understood since knockdown or knockout in neurons often resulted in only minor inhibition of SV retrieval (for review see Gauthier-Kemper et al., 2015). The precise sorting of SV constituents for retrieval is a complex process involving self-assembly and several layers of adaptor protein interactions. Thus, the picture remains far from being complete.

TRANS-CELLULAR NANO-ALIGNMENT BETWEEN PRESYNAPTIC AND POSTSYNAPTIC COMPARTMENTS

While on the presynaptic PM stable SV release sites exist at which SVs fuse and release their NT content, the postsynaptic PM harbors the NT receptors that bind NTs. SR microscopy revealed that postsynaptic receptors and scaffolding proteins are organized in clusters of 70–80 nm size (MacGillavry et al., 2013; Nair et al., 2013). Based on these observations the hypothesis was established that PM nanodomains involved in neurotransmission in pre- and postsynaptic membranes are aligned on both sides of the synaptic cleft (**Figure 3**). Indeed, a trans-synaptic alignment of RIM1 and PSD95 nanoclusters was visualized by 3D STORM in cultured hippocampal neurons (Tang et al., 2016). In inhibitory synapses, postsynaptic $GABA_A$ receptors are strongly associated with presynaptic RIM clusters (Crosby et al., 2019). According to this model, RIM nanoclusters define SV release sites that align opposite to postsynaptic receptor-scaffold ensembles within tens of nanometers creating a functional unit across the synaptic cleft.

Recently, trans-synaptic nano-alignment was also observed in the mammalian NMJ (York and Zheng, 2017).

Clustered patterns are also described for several synaptic cell adhesion molecules (SCAMs) including postsynaptic LRRTM2 and presynaptic Neurexin1β, while postsynaptic Neuroligin1 is dispersed in dendritic spines (Chamma et al., 2016). In addition, Neurexin1 nanodomains are dynamically regulated by the matrix metalloproteases ADAM-10. Blocking ADAM-10 mediated Neurexin1 cleavage leads to an increase in cluster size (Trotter et al., 2019). These SCAM clusters are likely to be involved in the trans-synaptic alignment as, e.g., expression of truncated Neuroligin1 disrupts trans-synaptic alignment causing mislocalization of SV fusion sites away from AMPAR clusters (Haas et al., 2018).

RECONSTRUCTION OF THE CELLULAR ULTRASTRUCTURE BY LOCALIZATION MICROSCOPY

For the analysis of protein distributions, localization microscopy techniques (STORM and PALM) feature a unique advantage as these pointillist methods provide single molecule coordinates allowing for comprehensive cluster analysis. Cluster formation at pre- and postsynaptic membranes has been described for CAZ proteins, SNARE proteins, SCAMs and NT receptors. Similar protein clusters were observed not only in neurons but also in neuroendocrine cells (Bar-On et al., 2012). Moreover, the advent of localization microscopy prompted a surge of publications reporting clusters of PM and PM-associated proteins in almost every cell type (Aaron et al., 2012; Itano et al., 2014; Lima et al., 2018) underlining the theory, that nano-clustering of PM proteins is an integral part of the hierarchical organization at the PM (Garcia-Parajo et al., 2014). These results have come to be viewed more critically because the protein clusters observed might be at least partially based on artifacts resulting from poor sample preparation or of inappropriate imaging conditions and reconstruction algorithms (Burgert et al., 2015; Culley et al., 2018).

Aggregate-forming labels and low labeling densities result in apparent protein clusters, which hardly reflect the underlying protein distribution (**Figure 4**). In addition, artificial clustering can be induced by the interaction of cell membranes with the polymer coating on the cover slide (Santos et al., 2018) or by sample preparation, e.g., during chemical fixation (Whelan and Bell, 2015). Thus, the development of improved labeling strategies is crucial to elucidate structure and function of sub-synaptic compartments.

High labeling densities carries its own risks since, in combination with inappropriate photo-switching rates, it can lead to overlapping single fluorophore signatures (Burgert et al., 2015). This introduces artificial sharpening during data analysis and thus, false protein clusters. This can be overcome with the judicious application of experimental and analytical tools such as variation of labeling density (Baumgart et al., 2016), temporal band pass filtering using Haar wavelet kernels (Marsh et al., 2018) or compressed sensing (Zhu et al., 2012).

Thus, the interpretation of localization microscopy data is a non-trivial task. The localization precision for single molecules scales with the inverse of the square root of the number of detected photons (Thompson et al., 2002) and benchmark studies have been performed to compare different software packages in terms of filtering and fitting algorithms for optimized data analysis (Sage et al., 2015). Nevertheless, the resolution in reconstructed images depends on both, the localization uncertainty and density of fluorescent labels, and several approaches have been proposed to estimate the true resolution in reconstructed images based, e.g., on estimation theory (Fitzgerald et al., 2012) or Fourier ring correlation (Nieuwenhuizen et al., 2013).

Once the single molecule coordinates have been accurately determined, cluster analysis can be applied. For this purpose, several standardized quantitative methods have been proposed. The most widespread methods to distinguish a clustered from a random distribution are nearest neighbor and pair correlation analysis (Sengupta et al., 2011; Rajappa et al., 2016; Sajman et al., 2017). Unfortunately, these methods are susceptible to the level of single molecule background and cluster shape (Lagache et al., 2013). It is possible to detect false clustering caused by stochastic local density increases for proteins mostly uniformly present in the PM (Baumgart et al., 2016). Recently, more advanced methods for cluster analysis have been introduced. These methods avoid artifacts caused by the geometry of the cell surface, the level of protein labeling and multiple blinks of fluorophores (Itano et al., 2014; Dinic et al., 2015). Bayesian statistical analysis of localization data, e.g., significantly increases the chance to find real protein clusters (Rubin-Delanchy et al., 2015; Griffié et al., 2016). However, the most promising methods for cluster analysis are Voronoi tessellation and Delaunay triangulation (Levet et al., 2015; Alán et al., 2016; Andronov et al., 2016; Boening et al., 2017). These methods are only minimally sensitive to the background signals, and are applicable for detecting clusters of various shape (**Figure 4**).

In addition, PALM exploits the possibility to count the number of individual molecules (Specht et al., 2013). In contrast to small organic fluorophores used in STORM, PA proteins emit a limited number of photons after activation before they irreversibly photobleach. However, most of the PA proteins display a blinking behavior, which may cause an over counting of the molecules in the sample. But knowing the time between multiple appearances of a fluorophore, one can convert the number of detections into the number of molecules (Lee et al., 2012; Nino et al., 2017). Nevertheless, it should be borne in mind that the labeled protein is often expressed in addition to the endogenous protein and thus, the number of molecules in a cluster can be easily over- or underestimated.

MOBILITY ANALYSIS BY SINGLE TRACKING AND sptPALM

The era of SR microscopy started with the advent of single molecule imaging and tracking techniques (Schmidt et al., 1996; Dickson et al., 1997; Schütz et al., 2000;

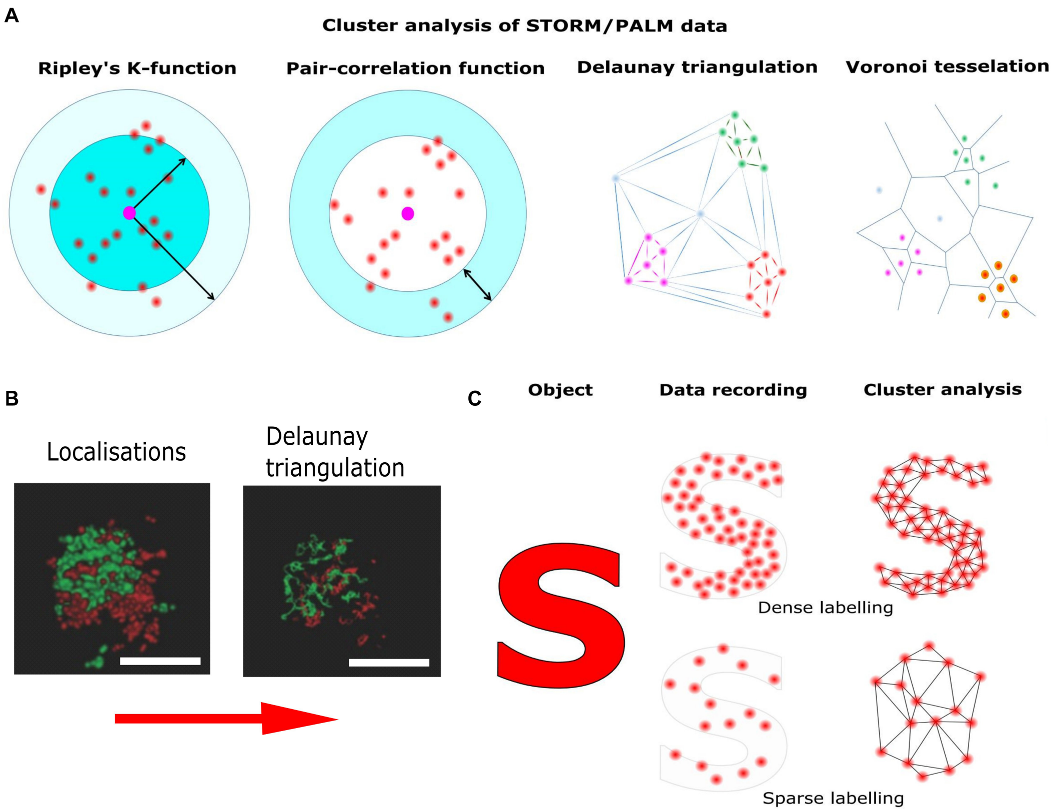

FIGURE 4 | Pointillist localization microscopy and the sparse labeling problem. Localization microscopy techniques base on the precise localization of single emitters followed by image reconstruction using the single molecule coordinates. **(A)** Different methods of cluster analysis for the interpretation of STORM/PALM data. Ripley's K function describes the molecular density as a function of an area of interest around a reference particle. The radial distribution function (also known as pair correlation function) describes density variations as a function of distance from a reference particle. Delaunay triangulation is a triangulation method such, that no point is inside the circumcircle of any triangle in the triangulation. Delaunay triangulation maximizes the minimum angle of all the angles of the triangles in the triangulation. Cluster distributions can be extracted by deleting edges longer than individually set thresholds. Voronoi tessellation splits the area into convex polygons such that each polygon contains one seed (molecule coordinate). The polygon areas consist of all points that are closer to their generating seed than to any other. Based on individually set thresholds (e.g., molecular density) image segmentation based on the Voronoi diagram results in cluster distributions**. (B)** STORM reconstruction of a hippocampal synapse stained for presynaptic (Bassoon, red) and postsynaptic (Homer, green) markers and Delaunay triangulation built on these localization (adapted from Boening et al., 2017; Copyright (2017) Wiley. Used with permission). **(C)** Though in principle the localization of single emitters can be as precise as 10 nm, the overall resolution is also determined by labeling density. Thus, if the labeling density is not high enough, relevant information is missing and cellular structures are falsely reconstructed.

Triller and Choquet, 2008; Kusumi et al., 2014). The evolution of these techniques and the fluorescent probes used, from sparse antibody or quantum dot labeling to sptPALM using photo-convertible fluorescent proteins is well documented in a number of studies analyzing localization and mobility of postsynaptic AMPA receptors (Tardin et al., 2003; Opazo et al., 2010; Nair et al., 2013). Tracking the motion of individual protein molecules provides information, which can be used for quantification of molecular mobility (Manley et al., 2008). However, localization precision can be compromised by motion blur, i.e., fast diffusing molecules spread out their emitted photons over multiple pixels. Furthermore, high particle densities can lead to tracking errors when molecules are falsely connected into trajectories. Technical and analytical solutions have been provided that overcome these biases like stroboscobic illumination (Elf et al., 2007) or data analysis using sophisticated kinetic frameworks (Hansen et al., 2018).

sptPALM revealed, that synaptic molecules like VGCCs, Syntaxin1A and AMPA receptors and are highly mobile and usually exhibit only transient trapping in nanodomains (Bademosi et al., 2017; Lee et al., 2017). The relevance of this mobility becomes increasingly clear since it was recently shown that transient confinement of VGCCs shapes presynaptic short term plasticity (Heck et al., 2019) and that AMPA receptor surface diffusion is required for postsynaptic long term potentiation (Penn et al., 2017).

However, in order to gain insights into molecular motion from single molecule trajectories, adequate physical models are needed (Masson et al., 2014; Holcman et al., 2015). Diffusing molecules in the PM often exhibit non-Brownian motion due to interaction with other molecules in the PM, cytoskeletal elements or adaptor proteins (Weigel et al., 2011; Metzler et al., 2016). Hidden Markov chain modeling (HMM) has been applied to distinguish diffusional states with different diffusion coefficients in sptPALM data sets (Persson et al., 2013; Slator and Burroughs, 2018). This kind of analysis not only provides a quantitative description of different diffusion modalities but also an estimate of transition probabilities between them. Such an approach allows different diffusive states to be characterized for Syntaxin1A at the presynaptic PM of *Drosophila* NMJ (Bademosi et al., 2017) and for single SVs which were labeled with internalized fluorescent Vamp2 in hippocampal boutons (Joensuu et al., 2016).

A comprehensive analysis of diffusional properties of proteins in the cell is essential for understanding the molecular underpinnings of cellular processes. However, we cannot measure the diffusion of any protein molecule without the addition of a molecular tag. While fusion of the protein of interest with a fluorescent protein has mostly only a minor effect on mobility (the diffusion coefficient scales (hydrodynamic radius)$^{-1}$ or (molecular mass)$^{-3}$ for spherical molecules according to Stokes's law) fluorescent proteins may induce artificial dimerization, as reported for EGFP (Snapp et al., 2003). In the PM where the local concentration of PM proteins can be very high due to crowding, dimerization may have a significant impact on protein mobility. It was, e.g., shown that mEos2 causes artificial clustering of PM proteins in the cell (Zhang et al., 2012), putting the diffusion coefficients measured for Syntaxin1A with mEos2 (Bademosi et al., 2017) or anti-EGFPF antibodies (Wang et al., 2014) under debate. Therefore, the use of fluorescent proteins with highly reduced dimerization properties such as Dendra2 or mEos3.2 is preferable for cluster analysis and diffusion coefficient estimation.

DISCUSSION

What is the status after more than a decade of SR microscopy? At first glance, the wealth of data is impressive. With the help of SR microscopy the architecture of the AZ could be described in more detail, SV fusion sites could be mapped and a trans-synaptic alignment between presynaptic SV fusion sites and postsynaptic NT receptors could be observed. Moreover, due to the applicability of SR microscopy to living cells, it was possible to analyze the single molecule dynamics of presynaptic membrane proteins. On closer examination, however, it is noticeable that structural reconstruction in the range 100–200 nm works well, such as in the case of the periodicity of actin filaments of 190 nm, the width of spine necks or the localization of BRP in doughnut-shaped structures of 190 nm length. However, the fundamental resolution of the corresponding techniques is significantly higher and can be as good as 20–40 nm. Structural reconstructions in this resolution range usually produce an analysis-dependent dot pattern, the meaning of which is subject to an individual interpretation. The outcome strongly depends on the algorithms and thresholds used. The mean cluster size of Syntaxin1A in the PM of PC12 cells, e.g., has been estimated to be around 90 nm by STORM but to be around 60 nm by STED (Sieber et al., 2007; Bar-On et al., 2012). Thus, meticulous acquisition and analysis is required. Fortunately, the toolbox for data acquisition and evaluation is constantly growing, which helps to increase the reliability of SR microscopy data interpretation.

However, in SR microscopy we now face a problem, which has been discussed analogously in EM since years: What is the best labeling procedure to analyze the cellular ultrastructure in a state as native as possible? It has become increasingly obvious that immuno-labeling is subject to a sparse labeling problem, not as strongly as in immuno-gold EM, but in dense protein assemblies like CAZ and PSD this is a severe limitation. Despite this, STORM studies persist in utilizing classic standard labeling methods like immunostaining using primary and secondary antibodies. In principle, promising alternatives are already available such as the use of nanobodies (Ries et al., 2012; Seitz and Rizzoli, 2019) or RNA-based aptamers (Gomes de Castro et al., 2017). Nevertheless, the available labeling strategies are the limiting factor to exploit the full resolution capability of SR microscopy right now.

For other issues like multiplexing, i.e., imaging several proteins of interest, minimizing photon count (and thus photodamaging), and the problem of thick specimens promising solutions have been developed. Most of the variations of STORM, PALM, and STED techniques are not applicable to the use of more than two different fluorescent markers. Recently, DNA-PAINT was introduced which is theoretically unlimited with respect to the number of probes being analyzed (Jungmann et al., 2010; Agasti et al., 2017). Thus, DNA-PAINT appears advantageous for multiplexing and multi-channel reconstruction. However, DNA-PAINT can be best applied in conjunction with total internal refection microscopy (TIRFM), since then the background due to freely diffusing labeled DNA strands is low compared to the signal of bound labeled DNA. Thus, to decipher molecular events in presynaptic boutons with this technique a TIRFM-amenable presynaptic preparation is desirable. Some modifications of dSTORM, such as the recently invented MadSTORM (Yi et al., 2016) are also applicable for multiplexing.

For minimizing the number of detected photons needed for localization and thus avoiding photobleaching as well as photodamage, the recently introduced MINFLUX concept is one of the most promising developments with regard to driving the field forward (Balzarotti et al., 2017). Recently, the postsynaptic protein PSD-95 was imaged with 3D resolution of 2–3 nm in hippocampal cultures using MINFLUX (Gwosch et al., 2020).

For imaging of whole cells and thicker specimens like, e.g., slice preparations, light sheet-based methods, in particular LLSM, will be of great importance in the future since these methods allow imaging with strongly reduced phototoxicity (Dodt et al., 2007; Chen et al., 2014). Bessel lightsheet microscopy has recently successfully combined with imaging of spontaneous blinking fluorophores to obtain an imaging speed of 2.7×10^4 μm^3 s^{-1} with a lateral resolution of 75 nm (Lu et al., 2019).

Strong limitations for the application of SR methods *in vivo* are high levels of autofluorescence and tissue photodamage, in particular for the green/yellow spectral range (König, 2000; Berning et al., 2012). To overcome these limitations, far red-emitting fluorescent proteins have been employed in STED microscopy (Wegner et al., 2017). However, red-emitting fluorescent proteins display low photostability and quantum yield compared to their shorter wavelengths analogs. Nevertheless, the quality of the *in vivo* SR imaging could be increased by using red and far-red emitting organic fluorophores linked to the protein of interest via click-chemistry (Masch et al., 2018). Here the authors succeeded in recognizing PSD95 domains labeled with the far-red emitting fluorophore SiR in live mouse brain using HaloTag based labeling.

For sptPALM, it will become more relevant to circumvent overexpression of tagged proteins and observe localization and mobility of the endogenous population of proteins. A toolbox for targeted genomic integration of fluorescent tags via CRISPR mediated knock-in in neurons has recently been published (Willems et al., 2019). Additionally, the MINFLUX concept also appears to be an encouraging approach for single molecule tracking since the spatiotemporal resolution can be greatly improved (Eilers et al., 2018).

But despite the enormous achievements of EM and constant improvements in the field of SR fluorescent microscopy, as well as long-term biochemical and electrophysiological studies, many questions regarding synaptic structure and function remain unresolved. The fine structure of the presynaptic AZ and the distribution and function of CAZ-proteins is still not fully understood. The importance of molecular clusters, like e.g., observed for t-SNAREs, remains enigmatic. In addition, the dynamics and molecular mechanisms of exo-endocytosis coupling, compensatory endocytosis and cargo sorting prior to endocytosis are still only incompletely described.

In summary, we conclude that SR microscopy on the one hand did deliver important insights into presynaptic molecular mechanisms and the underlying ultrastructure, on the other hand, SR microscopy could not fully hold its promise. However, the limitations are mostly not the microscopy techniques themselves but lie in sample preparation and labeling strategies. Thus, the development of artifact-free methods for labeling and analysis is still paramount with urgent imperative to the solution of the sparse labeling problem.

What could be the avenues for future structural research? In CNS synapses, however, to date EM has been only combined with immuno-gold labeling to introduce protein-specific contrast. For instance, the regularly spaced cone shaped structures frequently observed in EM at the presynaptic PM (also referred to as dense projections), could be positively correlated with the abundance of the scaffold proteins Piccolo and Bassoon (Limbach et al., 2011). Nevertheless, these probes were chemically fixed, which might introduce artifacts, and immune-gold labeling is in general poor because of steric hindrance (typically 10 nm gold particles are used).

Therefore, correlative light and electron microscopy (CLEM) seems to be a favorable way to go. Here, high-resolution light microscopy provides specific protein distributions while EM unravels the underlying cellular structures. Thus, CLEM mitigates the sparse labeling problem, as structural information is not solely extracted from light microscopy data. This approach has been successfully employed to show that endocytic proteins distribute into distinct spatial zones in relation to the edge of the clathrin lattice in non-neuronal cells using SEM on unroofed cells (Sochacki et al., 2017).

In terms of structure conservation, cryo-ET conjunction with cryo-fixation techniques appears to be superior among EM techniques. Indeed, using cryo-ET on isolated synaptosomes, the dense projections seen in chemically fixed samples (Harlow et al., 2001) could no longer be observed. Instead, numerous small filamentous tethers that link docked SVs to the presynaptic PM could be resolved and it appears that Rim1α plays a critical role in correct tether formation (Fernández-Busnadiego et al., 2013). Recently, an experimental pipeline for CLEM that combines cryo-ET with cryo-fluorescence microscopy has been published (Tao et al., 2018). Here, intact excitatory and inhibitory synapses could be distinguished in hippocampal culture, and their organelles and macromolecules could be visualized close to the native state.

In addition, cryogenic techniques were successfully applied to localization microscopy (Li et al., 2015; Weisenburger et al., 2017). It was shown that fluorophores under cryogenic conditions are much more photostable allowing the collection of more than 10^6 photons, thus providing down to Ångstrom resolution. Therefore, correlation of cryogenic localization microscopy with cryogenic EM tomography appears to be a promising approach. Recently a platform for correlative 3D imaging of entirely frozen cells using cryo-SR fluorescence microscopy and cryo-FIB EM has been published (Hoffman et al., 2020). However, at the moment such correlative approaches are reserved for a few expert labs and need to be optimized for routine use.

In summary, we conclude that high-resolution microscopy on its own has not fully lived up to its promises, and that we still need to rely on EM. This is likely to remain the case until correlative methods come to full fruition and the development of a “GFP” for EM, i.e., a reliable protein-specific tag for EM, remains elusive.

AUTHOR CONTRIBUTIONS

GN, MK, and JK wrote the manuscript. All authors contributed to the article and approved the submitted version.

FUNDING

The work was supported by grants from the DFG (CRC 944, CRC 1348, and EXC 1003, Cells in Motion Cluster of Excellence, Münster, Germany).

REFERENCES

Aaron, J. S., Carson, B. D., and Timlin, J. A. (2012). Characterization of differential Toll-like receptor responses below the optical diffraction limit. *Small* 8, 3041–3049. doi: 10.1002/smll.201200106

Agasti, S. S., Wang, Y., Schueder, F., Sukumar, A., Jungmann, R., and Yin, P. (2017). DNA-barcoded labeling probes for highly multiplexed exchange-PAINT imaging. *Chem. Sci.* 8, 3080–3091. doi: 10.1039/c6sc05420j

Alán, L., Špaèek, T., and Ježek, P. (2016). Delaunay algorithm and principal component analysis for 3D visualization of mitochondrial DNA nucleoids by biplane FPALM/dSTORM. *Eur. Biophys. J.* 45, 443–461. doi: 10.1007/s00249-016-1114-5

Andronov, L., Orlov, I., Lutz, Y., Vonesch, J.-L., and Klaholz, B. P. (2016). ClusterViSu, a method for clustering of protein complexes by Voronoi tessellation in super-resolution microscopy. *Sci. Rep.* 6:24084. doi: 10.1038/srep24084

Bademosi, A. T., Lauwers, E., Padmanabhan, P., Odierna, L., Chai, Y. J., Papadopulos, A., et al. (2017). In vivo single-molecule imaging of syntaxin1A reveals polyphosphoinositide- and activity-dependent trapping in presynaptic nanoclusters. *Nat. Commun.* 8:13660. doi: 10.1038/ncomms13660

Bademosi, A. T., Steeves, J., Karunanithi, S., Zalucki, O. H., Gormal, R. S., Liu, S., et al. (2018). Trapping of syntaxin1a in presynaptic nanoclusters by a clinically relevant general anesthetic. *Cell Rep.* 22, 427–440. doi: 10.1016/j.celrep.2017.12.054

Balzarotti, F., Eilers, Y., Gwosch, K. C., Gynnå, A. H., Westphal, V., Stefani, F. D., et al. (2017). Nanometer resolution imaging and tracking of fluorescent molecules with minimal photon fluxes. *Science* 355, 606–612. doi: 10.1126/science.aak9913

Bar-On, D., Wolter, S., van de Linde, S., Heilemann, M., Nudelman, G., Nachliel, E., et al. (2012). Super-resolution imaging reveals the internal architecture of nano-sized syntaxin clusters. *J. Biol. Chem.* 287, 27158–27167. doi: 10.1074/jbc.M112.353250

Bates, M., Huang, B., Dempsey, G. T., and Zhuang, X. (2007). Multicolor super-resolution imaging with photo-switchable fluorescent probes. *Science* 317, 1749–1753. doi: 10.1126/science.1146598

Baumgart, F., Arnold, A. M., Leskovar, K., Staszek, K., Fölser, M., Weghuber, J., et al. (2016). Varying label density allows artifact-free analysis of membrane-protein nanoclusters. *Nat. Methods* 13, 661–664. doi: 10.1038/nmeth.3897

Berning, S., Willig, K. I., Steffens, H., Dibaj, P., and Hell, S. W. (2012). Nanoscopy in a living mouse brain. *Science* 335:551. doi: 10.1126/science.1215369

Betzig, E., Patterson, G. H., Sougrat, R., Lindwasser, O. W., Olenych, S., Bonifacino, J. S., et al. (2006). Imaging intracellular fluorescent proteins at nanometer resolution. *Science* 313, 1642–1645. doi: 10.1126/science.1127344

Boening, D., Gauthier-Kemper, A., Gmeiner, B., and Klingauf, J. (2017). Cluster recognition by delaunay triangulation of synaptic proteins in 3D. *Adv. Biosyst.* 1:1700091. doi: 10.1002/adbi.201700091

Böhme, M. A., Beis, C., Reddy-Alla, S., Reynolds, E., Mampell, M. M., Grasskamp, A. T., et al. (2016). Active zone scaffolds differentially accumulate Unc13 isoforms to tune Ca(2+) channel-vesicle coupling. *Nat. Neurosci.* 19, 1311–1320. doi: 10.1038/nn.4364

Borst, J. G., and Sakmann, B. (1996). Calcium influx and transmitter release in a fast CNS synapse. *Nature* 383, 431–434. doi: 10.1038/383431a0

Bruckner, J. J., Zhan, H., Gratz, S. J., Rao, M., Ukken, F., Zilberg, G., et al. (2017). Fife organizes synaptic vesicles and calcium channels for high-probability neurotransmitter release. *J. Cell Biol.* 216, 231–246. doi: 10.1083/jcb.201601098

Bucurenciu, I., Kulik, A., Schwaller, B., Frotscher, M., and Jonas, P. (2008). Nanodomain coupling between Ca2+ channels and Ca2+ sensors promotes fast and efficient transmitter release at a cortical GABAergic synapse. *Neuron* 57, 536–545. doi: 10.1016/j.neuron.2007.12.026

Bullivant, S., and Ames, A. (1966). A simple freeze-fracture replication method for electron microscopy. *J. Cell Biol.* 29, 435–447. doi: 10.1083/jcb.29.3.435

Burgert, A., Letschert, S., Doose, S., and Sauer, M. (2015). Artifacts in single-molecule localization microscopy. *Histochem. Cell Biol.* 144, 123–131. doi: 10.1007/s00418-015-1340-4

Calloway, N., Gouzer, G., Xue, M., and Ryan, T. A. (2015). The active-zone protein Munc13 controls the use-dependence of presynaptic voltage-gated calcium channels. *eLife* 4:e07728. doi: 10.7554/eLife.07728

Chamma, I., Levet, F., Sibarita, J.-B., Sainlos, M., and Thoumine, O. (2016). Nanoscale organization of synaptic adhesion proteins revealed by single-molecule localization microscopy. *Neurophotonics* 3:41810. doi: 10.1117/1.NPh.3.4.041810

Chen, B.-C., Legant, W. R., Wang, K., Shao, L., Milkie, D. E., Davidson, M. W., et al. (2014). Lattice light sheet microscopy: imaging molecules to embryos at high spatiotemporal resolution. *Science* 346:1257998. doi: 10.1126/science.1257998

Cohen, R. S., and Siekevitz, P. (1978). Form of the postsynaptic density. a serial section study. *J. Cell Biol.* 78, 36–46. doi: 10.1083/jcb.78.1.36

Couteaux, R., and Pecot-Dechavassine, M. (1970). Vesicules synaptiques et poches au niveau des "zones actives" de la junction neuromusculaire. *C. R. Acad. Sci. Ser. D* 271, 2346–2349.

Crosby, K. C., Gookin, S. E., Garcia, J. D., Hahm, K. M., Dell'Acqua, M. L., and Smith, K. R. (2019). Nanoscale subsynaptic domains underlie the organization of the inhibitory synapse. *Cell Rep.* 26, 3284.e3–3297.e3. doi: 10.1016/j.celrep.2019.02.070

Culley, S., Albrecht, D., Jacobs, C., Pereira, P. M., Leterrier, C., Mercer, J., et al. (2018). Quantitative mapping and minimization of super-resolution optical imaging artifacts. *Nat. Methods* 15, 263–266. doi: 10.1038/nmeth.4605

Dani, A., Huang, B., Bergan, J., Dulac, C., and Zhuang, X. (2010). Superresolution imaging of chemical synapses in the brain. *Neuron* 68, 843–856. doi: 10.1016/j.neuron.2010.11.021

Davydova, D., Marini, C., King, C., Klueva, J., Bischof, F., Romorini, S., et al. (2014). Bassoon specifically controls presynaptic P/Q-type Ca(2+) channels via RIM-binding protein. *Neuron* 82, 181–194. doi: 10.1016/j.neuron.2014.02.012

de Harven, E., and Coërs, C. (1959). Electron microscope study of the human neuromuscular junction. *J. Biophys. Biochem. Cytol.* 6, 7–10. doi: 10.1083/jcb.6.1.7

De Robertis, E., Rodriguez de Lores Arnaiz, G., Salganicoff, L., Pellegrino de Ilraldi, I., and Zieher, L. M. (1963). Isolation of synaptic vesicles and structural organization of the acetycholine system within brain nerve endings. *J. Neurochem.* 10, 225–235. doi: 10.1111/j.1471-4159.1963.tb05038.x

De Robertis, E. D. P., and Bennett, H. S. (1955). SOME features of the submicroscopic morphology of synapses in frog and earthworm. *J. Biophys. Biochem. Cytol.* 1, 47–58. doi: 10.1083/jcb.1.1.47

Del Castillo, J., and Katz, B. (1954). Quantal components of the end-plate potential. *J. Physiol.* 124, 560–573. doi: 10.1113/jphysiol.1954.sp005129

Denk, W., and Horstmann, H. (2004). Serial block-face scanning electron microscopy to reconstruct three-dimensional tissue nanostructure. *PLoS Biol.* 2:e329. doi: 10.1371/journal.pbio.0020329

D'Este, E., Kamin, D., Göttfert, F., El-Hady, A., and Hell, S. W. (2015). STED nanoscopy reveals the ubiquity of subcortical cytoskeleton periodicity in living neurons. *Cell Rep.* 10, 1246–1251. doi: 10.1016/j.celrep.2015.02.007

Dickson, R. M., Cubitt, A. B., Tsien, R. Y., and Moerner, W. E. (1997). On/off blinking and switching behaviour of single molecules of green fluorescent protein. *Nature* 388, 355–358. doi: 10.1038/41048

Dinic, J., Riehl, A., Adler, J., and Parmryd, I. (2015). The T cell receptor resides in ordered plasma membrane nanodomains that aggregate upon patching of the receptor. *Sci. Rep.* 5:10082. doi: 10.1038/srep10082

Dodt, H.-U., Leischner, U., Schierloh, A., Jährling, N., Mauch, C. P., Deininger, K., et al. (2007). Ultramicroscopy: three-dimensional visualization of neuronal networks in the whole mouse brain. *Nat. Methods* 4, 331–336. doi: 10.1038/nmeth1036

Eilers, Y., Ta, H., Gwosch, K. C., Balzarotti, F., and Hell, S. W. (2018). MINFLUX monitors rapid molecular jumps with superior spatiotemporal resolution. *Proc. Natl. Acad. Sci. U.S.A.* 115, 6117–6122. doi: 10.1073/pnas.1801672115

Elf, J., Li, G.-W., and Xie, X. S. (2007). Probing transcription factor dynamics at the single-molecule level in a living cell. *Science* 316, 1191–1194. doi: 10.1126/science.1141967

Evergren, E., Tomilin, N., Vasylieva, E., Sergeeva, V., Bloom, O., Gad, H., et al. (2004). A pre-embedding immunogold approach for detection of synaptic endocytic proteins in situ. *J. Neurosci. Methods* 135, 169–174. doi: 10.1016/j.jneumeth.2003.12.010

Fernández-Busnadiego, R., Asano, S., Oprisoreanu, A.-M., Sakata, E., Doengi, M., Kochovski, Z., et al. (2013). Cryo-electron tomography reveals a critical role of RIM1α in synaptic vesicle tethering. *J. Cell Biol.* 201, 725–740. doi: 10.1083/jcb.201206063

Fitzgerald, J. E., Lu, J., and Schnitzer, M. J. (2012). Estimation theoretic measure of resolution for stochastic localization microscopy. *Phys. Rev. Lett.* 109:48102.

Frank, T., Rutherford, M. A., Strenzke, N., Neef, A., Pangršiè, T., Khimich, D., et al. (2010). Bassoon and the synaptic ribbon organize Ca2+ channels and vesicles to add release sites and promote refilling. *Neuron* 68, 724–738. doi: 10.1016/j.neuron.2010.10.027

Fujimoto, K. (1995). Freeze-fracture replica electron microscopy combined with SDS digestion for cytochemical labeling of integral membrane proteins. Application to the immunogold labeling of intercellular junctional complexes. *J. Cell Sci.* 108(Pt 11), 3443–3449.

Funahashi, J., Tanaka, H., and Hirano, T. (2018). Visualization of synchronous or asynchronous release of single synaptic vesicle in active-zone-like membrane formed on neuroligin-coated glass surface. *Front. Cell. Neurosci.* 12:140. doi: 10.3389/fncel.2018.00140

Garcia-Parajo, M. F., Cambi, A., Torreno-Pina, J. A., Thompson, N., and Jacobson, K. (2014). Nanoclustering as a dominant feature of plasma membrane organization. *J. Cell Sci.* 127, 4995–5005. doi: 10.1242/jcs.146340

Gauthier-Kemper, A., Kahms, M., and Klingauf, J. (2015). Restoring synaptic vesicles during compensatory endocytosis. *Essays Biochem.* 57, 121–134. doi: 10.1042/bse0570121

Gomes de Castro, M. A., Höbartner, C., and Opazo, F. (2017). Aptamers provide superior stainings of cellular receptors studied under super-resolution microscopy. *PLoS One* 12:e0173050. doi: 10.1371/journal.pone.0173050

Graf, E. R., Valakh, V., Wright, C. M., Wu, C., Liu, Z., Zhang, Y. Q., et al. (2012). RIM promotes calcium channel accumulation at active zones of the Drosophila neuromuscular junction. *J. Neurosci.* 32, 16586–16596. doi: 10.1523/JNEUROSCI.0965-12.2012

Granseth, B., Odermatt, B., Royle, S. J., and Lagnado, L. (2006). Clathrin-mediated endocytosis is the dominant mechanism of vesicle retrieval at hippocampal synapses. *Neuron* 51, 773–786. doi: 10.1016/j.neuron.2006.08.029

Griffié, J., Shannon, M., Bromley, C. L., Boelen, L., Burn, G. L., Williamson, D. J., et al. (2016). A Bayesian cluster analysis method for single-molecule localization microscopy data. *Nat. Protoc.* 11, 2499–2514. doi: 10.1038/nprot.2016.149

Gulley, R. L., and Reese, T. S. (1981). Cytoskeletal organization at the postsynaptic complex. *J. Cell Biol.* 91, 298–302. doi: 10.1083/jcb.91.1.298

Gundelfinger, E. D., Reissner, C., and Garner, C. C. (2015). Role of bassoon and piccolo in assembly and molecular organization of the active zone. *Front. Syn. Neurosci.* 7:19. doi: 10.3389/fnsyn.2015.00019

Gustafsson, M. G. (2000). Surpassing the lateral resolution limit by a factor of two using structured illumination microscopy. *J. Microsc.* 198, 82–87. doi: 10.1046/j.1365-2818.2000.00710.x

Gustafsson, M. G. L. (2005). Nonlinear structured-illumination microscopy: wide-field fluorescence imaging with theoretically unlimited resolution. *Proc. Natl. Acad. Sci. U.S.A.* 102, 13081–13086. doi: 10.1073/pnas.0406877102

Gwosch, K. C., Pape, J. K., Balzarotti, F., Hoess, P., Ellenberg, J., Ries, J., et al. (2020). MINFLUX nanoscopy delivers 3D multicolor nanometer resolution in cells. *Nat. Methods* 17, 217–224. doi: 10.1038/s41592-019-0688-0

Haas, K. T., Compans, B., Letellier, M., Bartol, T. M., Grillo-Bosch, D., Sejnowski, T. J., et al. (2018). Pre-post synaptic alignment through neuroligin-1 tunes synaptic transmission efficiency. *eLife* 7:e31755. doi: 10.7554/eLife.31755

Hagiwara, A., Kitahara, Y., Grabner, C. P., Vogl, C., Abe, M., Kitta, R., et al. (2018). Cytomatrix proteins CAST and ELKS regulate retinal photoreceptor development and maintenance. *J. Cell Biol.* 217, 3993–4006. doi: 10.1083/jcb.201704076

Hallermann, S., Fejtova, A., Schmidt, H., Weyhersmüller, A., Silver, R. A., Gundelfinger, E. D., et al. (2010). Bassoon speeds vesicle reloading at a central excitatory synapse. *Neuron* 68, 710–723. doi: 10.1016/j.neuron.2010.10.026

Hansen, A. S., Woringer, M., Grimm, J. B., Lavis, L. D., Tjian, R., and Darzacq, X. (2018). Robust model-based analysis of single-particle tracking experiments with Spot-On. *eLife* 7:e33125. doi: 10.7554/eLife.33125

Harlow, M. L., Ress, D., Stoschek, A., Marshall, R. M., and McMahan, U. J. (2001). The architecture of active zone material at the frog's neuromuscular junction. *Nature* 409, 479–484. doi: 10.1038/35054000

Harlow, M. L., Szule, J. A., Xu, J., Jung, J. H., Marshall, R. M., and McMahan, U. J. (2013). Alignment of synaptic vesicle macromolecules with the macromolecules in active zone material that direct vesicle docking. *PLoS One* 8:e0069410. doi: 10.1371/journal.pone.0069410

Harris, K. M., and Sultan, P. (1995). Variation in the number, location and size of synaptic vesicles provides an anatomical basis for the nonuniform probability of release at hippocampal CA1 synapses. *Neuropharmacology* 34, 1387–1395. doi: 10.1016/0028-3908(95)00142-s

Harris, K. M., and Weinberg, R. J. (2012). Ultrastructure of synapses in the mammalian brain. *Cold Spring Harb. Perspect. Biol.* 4:a005587. doi: 10.1101/cshperspect.a005587

Hayat, M. A. (ed.) (2000). *Principles and Techniques of Electron Microscopy: Biological Applications*. Cambridge, MA: Cambridge University Press.

Heck, J., Parutto, P., Ciuraszkiewicz, A., Bikbaev, A., Freund, R., Mitlöhner, J., et al. (2019). Transient confinement of CaV2.1 *Ca2*(-channel splice variants shapes synaptic short-term plasticity. *Neuron* 103, 66.e12–79.e12. doi: 10.1016/j.neuron.2019.04.030

Held, R. G., Liu, C., and Kaeser, P. S. (2016). ELKS controls the pool of readily releasable vesicles at excitatory synapses through its N-terminal coiled-coil domains. *eLife* 5:e14862. doi: 10.7554/eLife.14862

Hell, S. W., and Wichmann, J. (1994). Breaking the diffraction resolution limit by stimulated emission: stimulated-emission-depletion fluorescence microscopy. *Opt. Lett.* 19, 780–782.

Herrmannsdörfer, F., Flottmann, B., Nanguneri, S., Venkataramani, V., Horstmann, H., Kuner, T., et al. (2017). 3D d STORM imaging of fixed brain tissue. *Methods Mol. Biol.* 1538, 169–184. doi: 10.1007/978-1-4939-6688-2_13

Hess, S. T., Girirajan, T. P. K., and Mason, M. D. (2006). Ultra-high resolution imaging by fluorescence photoactivation localization microscopy. *Biophys. J.* 91, 4258–4272. doi: 10.1529/biophysj.106.091116

Heuser, J. E., and Reese, T. S. (1973). Evidence for recycling of synaptic vesicle membrane during transmitter release at the frog neuromuscular junction. *J. Cell Biol.* 57, 315–344. doi: 10.1083/jcb.57.2.315

Heuser, J. E., and Reese, T. S. (1981). Structural changes after transmitter release at the frog neuromuscular junction. *J. Cell Biol.* 88, 564–580. doi: 10.1083/jcb.88.3.564

Heuser, J. E., Reese, T. S., Dennis, M. J., Jan, Y., Jan, L., and Evans, L. (1979). Synaptic vesicle exocytosis captured by quick freezing and correlated with quantal transmitter release. *J. Cell Biol.* 81, 275–300. doi: 10.1083/jcb.81.2.275

Hoffman, D. P., Shtengel, G., Xu, C. S., Campbell, K. R., Freeman, M., Wang, L., et al. (2020). Correlative three-dimensional super-resolution and block-face electron microscopy of whole vitreously frozen cells. *Science* 367:eaaz5357. doi: 10.1126/science.aaz5357

Holcman, D., Hoze, N., and Schuss, Z. (2015). Analysis and interpretation of superresolution single-particle trajectories. *Biophys. J.* 109, 1761–1771. doi: 10.1016/j.bpj.2015.09.003

Holderith, N., Lorincz, A., Katona, G., Rózsa, B., Kulik, A., Watanabe, M., et al. (2012). Release probability of hippocampal glutamatergic terminals scales with the size of the active zone. *Nat. Neurosci.* 15, 988–997. doi: 10.1038/nn.3137

Hoze, N., Nair, D., Hosy, E., Sieben, C., Manley, S., Herrmann, A., et al. (2012). Heterogeneity of AMPA receptor trafficking and molecular interactions revealed by superresolution analysis of live cell imaging. *Proc. Natl. Acad. Sci. U.S.A.* 109, 17052–17057. doi: 10.1073/pnas.1204589109

Hua, Y., Sinha, R., Thiel, C. S., Schmidt, R., Hüve, J., Martens, H., et al. (2011). A readily retrievable pool of synaptic vesicles. *Nat. Neurosci.* 14, 833–839. doi: 10.1038/nn.2838

Igarashi, M., Nozumi, M., Wu, L.-G., Cella Zanacchi, F., Katona, I., Barna, L., et al. (2018). New observations in neuroscience using superresolution microscopy. *J. Neurosci.* 38, 9459–9467. doi: 10.1523/JNEUROSCI.1678-18.2018

Itano, M. S., Graus, M. S., Pehlke, C., Wester, M. J., Liu, P., Lidke, K. A., et al. (2014). Super-resolution imaging of C-type lectin spatial rearrangement within the dendritic cell plasma membrane at fungal microbe contact sites. *Front. Phys.* 2:46. doi: 10.3389/fphy.2014.00046

Joensuu, M., Padmanabhan, P., Durisic, N., Bademosi, A. T. D., Cooper-Williams, E., Morrow, I. C., et al. (2016). Subdiffractional tracking of internalized molecules reveals heterogeneous motion states of synaptic vesicles. *J. Cell Biol.* 215, 277–292. doi: 10.1083/jcb.201604001

Jung, J. H. (2019). Synaptic vesicles having large contact areas with the presynaptic membrane are preferentially hemifused at active zones of frog neuromuscular junctions fixed during synaptic activity. *Int. J. Mol. Sci.* 20:2692. doi: 10.3390/ijms20112692

Jungmann, R., Steinhauer, C., Scheible, M., Kuzyk, A., Tinnefeld, P., and Simmel, F. C. (2010). Single-molecule kinetics and super-resolution microscopy by fluorescence imaging of transient binding on DNA origami. *Nano Lett.* 10, 4756–4761. doi: 10.1021/nl103427w

Kittel, R. J., Wichmann, C., Rasse, T. M., Fouquet, W., Schmidt, M., Schmid, A., et al. (2006). Bruchpilot promotes active zone assembly, Ca2(channel clustering, and vesicle release. *Science* 312, 1051–1054. doi: 10.1126/science.1126308

Klar, T. A., Jakobs, S., Dyba, M., Egner, A., and Hell, S. W. (2000). Fluorescence microscopy with diffraction resolution barrier broken by stimulated emission. *Proc. Natl. Acad. Sci. U.S.A.* 97, 8206–8210. doi: 10.1073/pnas.97.15.8206

Knott, G., Marchman, H., Wall, D., and Lich, B. (2008). Serial section scanning electron microscopy of adult brain tissue using focused ion beam milling. *J. Neurosci.* 28, 2959–2964. doi: 10.1523/JNEUROSCI.3189-07.2008

Knowles, M. K., Barg, S., Wan, L., Midorikawa, M., Chen, X., and Almers, W. (2010). Single secretory granules of live cells recruit syntaxin-1 and synaptosomal associated protein 25 (SNAP-25) in large copy numbers. *Proc. Natl. Acad. Sci. U.S.A.* 107, 20810–20815. doi: 10.1073/pnas.1014840107

König, K. (2000). Multiphoton microscopy in life sciences. *J. Microsc.* 200, 83–104. doi: 10.1046/j.1365-2818.2000.00738.x

Kusch, V., Bornschein, G., Loreth, D., Bank, J., Jordan, J., Baur, D., et al. (2018). Munc13-3 is required for the developmental localization of Ca2(channels to active zones and the nanopositioning of Cav2.1 near release sensors. *Cell Rep.* 22, 1965–1973. doi: 10.1016/j.celrep.2018.02.010

Kusumi, A., Tsunoyama, T. A., Hirosawa, K. M., Kasai, R. S., and Fujiwara, T. K. (2014). Tracking single molecules at work in living cells. *Nat. Chem. Biol.* 10, 524–532. doi: 10.1038/nchembio.1558

Kweon, D.-H., Kong, B., and Shin, Y.-K. (2017). Hemifusion in synaptic vesicle cycle. *Front. Mol. Neurosci.* 10:65. doi: 10.3389/fnmol.2017.00065

Lagache, T., Grassart, A., Dallongeville, S., Faklaris, O., Sauvonnet, N., Dufour, A., et al. (2018). Mapping molecular assemblies with fluorescence microscopy and object-based spatial statistics. *Nat. Commun.* 9:698. doi: 10.1038/s41467-018-03053-x

Lagache, T., Lang, G., Sauvonnet, N., and Olivo-Marin, J.-C. (2013). Analysis of the spatial organization of molecules with robust statistics. *PLoS One* 8:e0080914. doi: 10.1371/journal.pone.0080914

Lee, S. H., Jin, C., Cai, E., Ge, P., Ishitsuka, Y., Teng, K. W., et al. (2017). Super-resolution imaging of synaptic and Extra-synaptic AMPA receptors with different-sized fluorescent probes. *eLife* 6:e27744. doi: 10.7554/eLife.27744

Lee, S.-H., Shin, J. Y., Lee, A., and Bustamante, C. (2012). Counting single photoactivatable fluorescent molecules by photoactivated localization microscopy (PALM). *Proc. Natl. Acad. Sci. U.S.A.* 109, 17436–17441. doi: 10.1073/pnas.1215175109

Leitz, J., and Kavalali, E. T. (2011). Ca2+ influx slows single synaptic vesicle endocytosis. *J. Neurosci.* 31, 16318–16326. doi: 10.1523/JNEUROSCI.3358-11.2011

Levet, F., Hosy, E., Kechkar, A., Butler, C., Beghin, A., Choquet, D., et al. (2015). SR-Tesseler: a method to segment and quantify localization-based super-resolution microscopy data. *Nat. Methods* 12, 1065–1071. doi: 10.1038/nmeth.3579

Li, W., Stein, S. C., Gregor, I., and Enderlein, J. (2015). Ultra-stable and versatile widefield cryo-fluorescence microscope for single-molecule localization with sub-nanometer accuracy. *Opt. Express* 23, 3770–3783. doi: 10.1364/OE.23.003770

Lima, A. M., Wegner, S. V., Martins Cavaco, A. C., Estevão-Costa, M. I., Sanz-Soler, R., Niland, S., et al. (2018). The spatial molecular pattern of integrin recognition sites and their immobilization to colloidal nanobeads determine α2β1 integrin-dependent platelet activation. *Biomaterials* 167, 107–120. doi: 10.1016/j.biomaterials.2018.03.028

Limbach, C., Laue, M. M., Wang, X., Hu, B., Thiede, N., Hultqvist, G., et al. (2011). Molecular in situ topology of Aczonin/Piccolo and associated proteins at the mammalian neurotransmitter release site. *Proc. Natl. Acad. Sci. U.S.A.* 108, E392–E401. doi: 10.1073/pnas.1101707108

Lisman, J. E., Raghavachari, S., and Tsien, R. W. (2007). The sequence of events that underlie quantal transmission at central glutamatergic synapses. *Nat. Rev. Neurosci.* 8, 597–609. doi: 10.1038/nrn2191

Liu, C., Bickford, L. S., Held, R. G., Nyitrai, H., Südhof, T. C., and Kaeser, P. S. (2014). The active zone protein family ELKS supports Ca2+ influx at nerve terminals of inhibitory hippocampal neurons. *J. Neurosci.* 34, 12289–12303. doi: 10.1523/JNEUROSCI.0999-14.2014

Liu, K. S. Y., Siebert, M., Mertel, S., Knoche, E., Wegener, S., Wichmann, C., et al. (2011). RIM-binding protein, a central part of the active zone, is essential for neurotransmitter release. *Science* 334, 1565–1569. doi: 10.1126/science.1212991

Lu, C.-H., Tang, W.-C., Liu, Y.-T., Chang, S.-W., Wu, F. C. M., Chen, C.-Y., et al. (2019). Lightsheet localization microscopy enables fast, large-scale, and three-dimensional super-resolution imaging. *Commun. Biol.* 2:177. doi: 10.1038/s42003-019-0403-9

Lucić, V., Förster, F., and Baumeister, W. (2005). Structural studies by electron tomography: from cells to molecules. *Annu. Rev. Biochem.* 74, 833–865. doi: 10.1146/annurev.biochem.73.011303.074112

MacGillavry, H. D., Song, Y., Raghavachari, S., and Blanpied, T. A. (2013). Nanoscale scaffolding domains within the postsynaptic density concentrate synaptic AMPA receptors. *Neuron* 78, 615–622. doi: 10.1016/j.neuron.2013.03.009

Maidorn, M., Olichon, A., Rizzoli, S. O., and Opazo, F. (2019). Nanobodies reveal an extra-synaptic population of SNAP-25 and Syntaxin 1A in hippocampal neurons. *mAbs* 11, 305–321. doi: 10.1080/19420862.2018.1551675

Manley, S., Gillette, J. M., Patterson, G. H., Shroff, H., Hess, H. F., Betzig, E., et al. (2008). High-density mapping of single-molecule trajectories with photoactivated localization microscopy. *Nat. Methods* 5, 155–157. doi: 10.1038/nmeth.1176

Marsh, R. J., Pfisterer, K., Bennett, P., Hirvonen, L. M., Gautel, M., Jones, G. E., et al. (2018). Artifact-free high-density localization microscopy analysis. *Nat. Methods* 15, 689–692. doi: 10.1038/s41592-018-0072-5

Martell, J. D., Deerinck, T. J., Sancak, Y., Poulos, T. L., Mootha, V. K., Sosinsky, G. E., et al. (2012). Engineered ascorbate peroxidase as a genetically-encoded reporter for electron microscopy. *Nat. Biotechnol.* 30, 1143–1148. doi: 10.1038/nbt.2375

Masch, J.-M., Steffens, H., Fischer, J., Engelhardt, J., Hubrich, J., Keller-Findeisen, J., et al. (2018). Robust nanoscopy of a synaptic protein in living mice by organic-fluorophore labeling. *Proc. Natl. Acad. Sci. U.S.A.* 115, E8047–E8056. doi: 10.1073/pnas.1807104115

Maschi, D., and Klyachko, V. A. (2017). Spatiotemporal regulation of synaptic vesicle fusion sites in central synapses. *Neuron* 94, 65.e3–73.e3. doi: 10.1016/j.neuron.2017.03.006

Masson, J.-B., Dionne, P., Salvatico, C., Renner, M., Specht, C. G., Triller, A., et al. (2014). Mapping the energy and diffusion landscapes of membrane proteins at the cell surface using high-density single-molecule imaging and Bayesian inference: application to the multiscale dynamics of glycine receptors in the neuronal membrane. *Biophys. J.* 106, 74–83. doi: 10.1016/j.bpj.2013.10.027

Masugi-Tokita, M., Tarusawa, E., Watanabe, M., Molnár, E., Fujimoto, K., and Shigemoto, R. (2007). Number and density of AMPA receptors in individual synapses in the rat cerebellum as revealed by SDS-digested freeze-fracture replica labeling. *J. Neurosci.* 27, 2135–2144. doi: 10.1523/JNEUROSCI.2861-06.2007

Matthews, G., and Sterling, P. (2008). Evidence that vesicles undergo compound fusion on the synaptic ribbon. *J. Neurosci.* 28, 5403–5411. doi: 10.1523/JNEUROSCI.0935-08.2008

Metzler, R., Jeon, J.-H., and Cherstvy, A. G. (2016). Non-Brownian diffusion in lipid membranes: experiments and simulations. *Biochim. Biophys. Acta* 1858, 2451–2467. doi: 10.1016/j.bbamem.2016.01.022

Miki, T., Kaufmann, W. A., Malagon, G., Gomez, L., Tabuchi, K., Watanabe, M., et al. (2017). Numbers of presynaptic Ca2+ channel clusters match those of functionally defined vesicular docking sites in single central synapses. *Proc. Natl. Acad. Sci. U.S.A.* 114, E5246–E5255. doi: 10.1073/pnas.1704470114

Milovanovic, D., Platen, M., Junius, M., Diederichsen, U., Schaap, I. A. T., Honigmann, A., et al. (2016). Calcium promotes the formation of syntaxin 1 mesoscale domains through phosphatidylinositol 4,5-bisphosphate. *J. Biol. Chem.* 291, 7868–7876. doi: 10.1074/jbc.M116.716225

Moor, H., and Mühlethaler, K. (1963). Fine structure in frozen-etched yeast cells. *J. Cell Biol.* 17, 609–628. doi: 10.1083/jcb.17.3.609

Nägerl, U. V., Willig, K. I., Hein, B., Hell, S. W., and Bonhoeffer, T. (2008). Live-cell imaging of dendritic spines by STED microscopy. *Proc. Natl. Acad. Sci. U.S.A.* 105, 18982–18987. doi: 10.1073/pnas.0810028105

Nair, D., Hosy, E., Petersen, J. D., Constals, A., Giannone, G., Choquet, D., et al. (2013). Super-resolution imaging reveals that AMPA receptors inside synapses are dynamically organized in nanodomains regulated by PSD95. *J. Neurosci.* 33, 13204–13224. doi: 10.1523/JNEUROSCI.2381-12.2013

Neher, E. (2018). Neurosecretion: what can we learn from chromaffin cells. *Pflugers Arch.* 470, 7–11. doi: 10.1007/s00424-017-2051-6

Nieuwenhuizen, R. P. J., Lidke, K. A., Bates, M., Puig, D. L., Grünwald, D., Stallinga, S., et al. (2013). Measuring image resolution in optical nanoscopy. *Nat. Methods* 10, 557–562. doi: 10.1038/nmeth.2448

Nino, D., Rafiei, N., Wang, Y., Zilman, A., and Milstein, J. N. (2017). Molecular counting with localization microscopy: a bayesian estimate based on fluorophore statistics. *Biophys. J.* 112, 1777–1785. doi: 10.1016/j.bpj.2017.03.020

Nishimune, H., Badawi, Y., Mori, S., and Shigemoto, K. (2016). Dual-color STED microscopy reveals a sandwich structure of Bassoon and Piccolo in active zones of adult and aged mice. *Sci. Rep.* 6:27935. doi: 10.1038/srep27935

Opazo, P., Labrecque, S., Tigaret, C. M., Frouin, A., Wiseman, P. W., et al. (2010). CaMKII triggers the diffusional trapping of surface AMPARs through phosphorylation of stargazin. *Neuron* 67, 239–252. doi: 10.1016/j.neuron.2010.06.007

Orlando, M., Schmitz, D., Rosenmund, C., and Herman, M. A. (2019). Calcium-independent exo-endocytosis coupling at small central synapses. *Cell Rep.* 29, 3767.e3–3774.e3. doi: 10.1016/j.celrep.2019.11.060

Palay, S. L. (1958). The morphology of synapses in the central nervous system. *Exp. Cell Res.* 14, 275–293.

Palay, S. L., and Palade, G. E. (1955). The fine structure of neurons. *J. Biophys. Biochem. Cytol.* 1, 69–88.

Parsons, T. D., and Sterling, P. (2003). Synaptic ribbon. Conveyor belt or safety belt? *Neuron* 37, 379–382.

Penn, A. C., Zhang, C. L., Georges, F., Royer, L., Breillat, C., Hosy, E., et al. (2017). Hippocampal LTP and contextual learning require surface diffusion of AMPA receptors. *Nature* 549, 384–388. doi: 10.1038/nature23658

Perkins, G. A., Jackson, D. R., and Spirou, G. A. (2015). Resolving presynaptic structure by electron tomography. *Synapse* 69, 268–282. doi: 10.1002/syn.21813

Persson, F., Lindén, M., Unoson, C., and Elf, J. (2013). Extracting intracellular diffusive states and transition rates from single-molecule tracking data. *Nat. Methods* 10, 265–269. doi: 10.1038/nmeth.2367

Pfenninger, K., Akert, K., Moor, H., and Sandri, C. (1972). The fine structure of freeze-fractured presynaptic membranes. *J. Neurocytol.* 1, 129–149. doi: 10.1007/bf01099180

Prokop, A., and Meinertzhagen, I. A. (2006). Development and structure of synaptic contacts in *Drosophila*. *Semin. Cell Dev. Biol.* 17, 20–30. doi: 10.1016/j.semcdb.2005.11.010

Rajappa, R., Gauthier-Kemper, A., Böning, D., Hüve, J., and Klingauf, J. (2016). Synaptophysin 1 clears synaptobrevin 2 from the presynaptic active zone to prevent short-term depression. *Cell Rep.* 14, 1369–1381. doi: 10.1016/j.celrep.2016.01.031

Ramón y Cajal, S. (1904). *Texture of the Nervous System of Man and the Vertebrates*. Wien: Springer.

Rebola, N., Reva, M., Kirizs, T., Szoboszlay, M., Lõrincz, A., Moneron, G., et al. (2019). Distinct nanoscale calcium channel and synaptic vesicle topographies contribute to the diversity of synaptic function. *Neuron* 104, 693.e9–710.e9. doi: 10.1016/j.neuron.2019.08.014

Reddy-Alla, S., Böhme, M. A., Reynolds, E., Beis, C., Grasskamp, A. T., Mampell, M. M., et al. (2017). Stable positioning of Unc13 restricts synaptic vesicle fusion to defined release sites to promote synchronous neurotransmission. *Neuron* 95, 1350.e12–1364.e12. doi: 10.1016/j.neuron.2017.08.016

Regus-Leidig, H., Fuchs, M., Löhner, M., Leist, S. R., Leal-Ortiz, S., Chiodo, V. A., et al. (2014). In vivo knockdown of Piccolino disrupts presynaptic ribbon morphology in mouse photoreceptor synapses. *Front. Cell. Neurosci.* 8:259. doi: 10.3389/fncel.2014.00259

Ries, J., Kaplan, C., Platonova, E., Eghlidi, H., and Ewers, H. (2012). A simple, versatile method for GFP-based super-resolution microscopy via nanobodies. *Nat. Methods* 9, 582–584. doi: 10.1038/nmeth.1991

Rizo, J. (2018). Mechanism of neurotransmitter release coming into focus. *Protein Sci.* 27, 1364–1391. doi: 10.1002/pro.3445

Rollenhagen, A., Sätzler, K., Rodríguez, E. P., Jonas, P., Frotscher, M., and Lübke, J. H. R. (2007). Structural determinants of transmission at large hippocampal mossy fiber synapses. *J. Neurosci.* 27, 10434–10444. doi: 10.1523/JNEUROSCI.1946-07.2007

Roos, J., and Kelly, R. B. (1999). The endocytic machinery in nerve terminals surrounds sites of exocytosis. *Curr. Biol.* 9, 1411–1414. doi: 10.1016/s0960-9822(00)80087-1

Rostaing, P., Real, E., Siksou, L., Lechaire, J.-P., Boudier, T., Boeckers, T. M., et al. (2006). Analysis of synaptic ultrastructure without fixative using high-pressure freezing and tomography. *Eur. J. Neurosci.* 24, 3463–3474. doi: 10.1111/j.1460-9568.2006.05234.x

Rowley, K. L., Mantilla, C. B., Ermilov, L. G., and Sieck, G. C. (2007). Synaptic vesicle distribution and release at rat diaphragm neuromuscular junctions. *J. Neurophysiol.* 98, 478–487. doi: 10.1152/jn.00251.2006

Rubin-Delanchy, P., Burn, G. L., Griffié, J., Williamson, D. J., Heard, N. A., Cope, A. P., et al. (2015). Bayesian cluster identification in single-molecule localization microscopy data. *Nat. Methods* 12, 1072–1076. doi: 10.1038/nmeth.3612

Sage, D., Kirshner, H., Pengo, T., Stuurman, N., Min, J., Manley, S., et al. (2015). Quantitative evaluation of software packages for single-molecule localization microscopy. *Nat. Methods* 12, 717–724. doi: 10.1038/nmeth.3442

Sahl, S. J., Hell, S. W., and Jakobs, S. (2017). Fluorescence nanoscopy in cell biology. *Nat. Rev. Mol. Cell Biol.* 18, 685–701. doi: 10.1038/nrm.2017.71

Sajman, J., Trus, M., Atlas, D., and Sherman, E. (2017). The L-type Voltage-Gated Calcium Channel co-localizes with Syntaxin 1A in nano-clusters at the plasma membrane. *Sci. Rep.* 7:11350. doi: 10.1038/s41598-017-10588-4

Sakamoto, H., Ariyoshi, T., Kimpara, N., Sugao, K., Taiko, I., Takikawa, K., et al. (2018). Synaptic weight set by Munc13-1 supramolecular assemblies. *Nat. Neurosci.* 21, 41–49. doi: 10.1038/s41593-017-0041-9

Sankaranarayanan, S., and Ryan, T. A. (2001). Calcium accelerates endocytosis of vSNAREs at hippocampal synapses. *Nat. Neurosci.* 4, 129–136. doi: 10.1038/83949

Santos, A. M., Ponjavic, A., Fritzsche, M., Fernandes, R. A., La Serna, J. B. D., Wilcock, M. J., et al. (2018). Capturing resting T cells: the perils of PLL. *Nat. Immunol.* 19, 203–205. doi: 10.1038/s41590-018-0048-8

Schermelleh, L., Ferrand, A., Huser, T., Eggeling, C., Sauer, M., Biehlmaier, O., et al. (2019). Super-resolution microscopy demystified. *Nat. Cell Biol.* 21, 72–84. doi: 10.1038/s41556-018-0251-8

Schikorski, T., and Stevens, C. F. (1997). Quantitative ultrastructural analysis of hippocampal excitatory synapses. *J. Neurosci.* 17, 5858–5867. doi: 10.1523/jneurosci.17-15-05858.1997

Schmidt, H., Brachtendorf, S., Arendt, O., Hallermann, S., Ishiyama, S., Bornschein, G., et al. (2013). Nanodomain coupling at an excitatory cortical synapse. *Curr. Biol.* 23, 244–249. doi: 10.1016/j.cub.2012.12.007

Schmidt, T., Schütz, G. J., Baumgartner, W., Gruber, H. J., and Schindler, H. (1996). Imaging of single molecule diffusion. *Proc. Natl. Acad. Sci. U.S.A.* 93, 2926–2929.

Schneider, R., Hosy, E., Kohl, J., Klueva, J., Choquet, D., Thomas, U., et al. (2015). Mobility of calcium channels in the presynaptic membrane. *Neuron* 86, 672–679. doi: 10.1016/j.neuron.2015.03.050

Schütz, G. J., Kada, G., Pastushenko, V. P., and Schindler, H. (2000). Properties of lipid microdomains in a muscle cell membrane visualized by single molecule microscopy. *EMBO J.* 19, 892–901. doi: 10.1093/emboj/19.5.892

Seitz, K. J., and Rizzoli, S. O. (2019). GFP nanobodies reveal recently-exocytosed pHluorin molecules. *Sci. Rep.* 9:7773. doi: 10.1038/s41598-019-44262-8

Sengupta, P., Jovanovic-Talisman, T., Skoko, D., Renz, M., Veatch, S. L., and Lippincott-Schwartz, J. (2011). Probing protein heterogeneity in the plasma membrane using PALM and pair correlation analysis. *Nat. Methods* 8, 969–975. doi: 10.1038/nmeth.1704

Shin, W., Ge, L., Arpino, G., Villarreal, S. A., Hamid, E., Liu, H., et al. (2018). Visualization of membrane pore in live cells reveals a dynamic-pore theory governing fusion and endocytosis. *Cell* 173, 934.e12–945.e12. doi: 10.1016/j.cell.2018.02.062

Shu, X., Lev-Ram, V., Deerinck, T. J., Qi, Y., Ramko, E. B., Davidson, M. W., et al. (2011). A genetically encoded tag for correlated light and electron microscopy of intact cells, tissues, and organisms. *PLoS Biol.* 9:e1001041. doi: 10.1371/journal.pbio.1001041

Sieber, J. J., Willig, K. I., Kutzner, C., Gerding-Reimers, C., Harke, B., Donnert, G., et al. (2007). Anatomy and dynamics of a supramolecular membrane protein cluster. *Science* 317, 1072–1076. doi: 10.1126/science.1141727

Siksou, L., Rostaing, P., Lechaire, J.-P., Boudier, T., Ohtsuka, T., Fejtová, A., et al. (2007). Three-dimensional architecture of presynaptic terminal cytomatrix. *J. Neurosci.* 27, 6868–6877. doi: 10.1523/JNEUROSCI.1773-07.2007

Siksou, L., Triller, A., and Marty, S. (2009). An emerging view of presynaptic structure from electron microscopic studies. *J. Neurochem.* 108, 1336–1342. doi: 10.1111/j.1471-4159.2009.05888.x

Sjoestrand, F. S. (1958). Ultrastructure of retinal rod synapses of the guinea pig eye as revealed by three-dimensional reconstructions from serial sections. *J. Ultrastructure Res.* 2, 122–170. doi: 10.1016/s0022-5320(58)90050-9

Slator, P. J., and Burroughs, N. J. (2018). A hidden markov model for detecting confinement in single-particle tracking trajectories. *Biophys. J.* 115, 1741–1754. doi: 10.1016/j.bpj.2018.09.005

Snapp, E. L., Hegde, R. S., Francolini, M., Lombardo, F., Colombo, S., Pedrazzini, E., et al. (2003). Formation of stacked ER cisternae by low affinity protein interactions. *J. Cell Biol.* 163, 257–269. doi: 10.1083/jcb.200306020

Sochacki, K. A., Dickey, A. M., Strub, M.-P., and Taraska, J. W. (2017). Endocytic proteins are partitioned at the edge of the clathrin lattice in mammalian cells. *Nat. Cell Biol.* 19, 352–361. doi: 10.1038/ncb3498

Specht, C. G., Izeddin, I., Rodriguez, P. C., El Beheiry, M., Rostaing, P., Darzacq, X., et al. (2013). Quantitative nanoscopy of inhibitory synapses: counting gephyrin molecules and receptor binding sites. *Neuron* 79, 308–321. doi: 10.1016/j.neuron.2013.05.013

Stevens, J. K., Davis, T. L., Friedman, N., and Sterling, P. (1980). A systematic approach to reconstructing microcircuitry by electron microscopy of serial sections. *Brain Res.* 2, 265–293. doi: 10.1016/0165-0173(80)90010-7

Studer, D., Graber, W., Al-Amoudi, A., and Eggli, P. (2001). A new approach for cryofixation by high-pressure freezing. *J. Microsc.* 203, 285–294. doi: 10.1046/j.1365-2818.2001.00919.x

Tang, A.-H., Chen, H., Li, T. P., Metzbower, S. R., MacGillavry, H. D., and Blanpied, T. A. (2016). A transsynaptic nanocolumn aligns neurotransmitter release to receptors. *Nature* 536, 210–214. doi: 10.1038/nature19058

Tao, C.-L., Liu, Y.-T., Sun, R., Zhang, B., Qi, L., Shivakoti, S., et al. (2018). Differentiation and characterization of excitatory and inhibitory synapses by cryo-electron tomography and correlative microscopy. *J. Neurosci.* 38, 1493–1510. doi: 10.1523/JNEUROSCI.1548-17.2017

Tardin, C., Cognet, L., Bats, C., Lounis, B., and Choquet, D. (2003). Direct imaging of lateral movements of AMPA receptors inside synapses. *EMBO J.* 22, 4656–4665. doi: 10.1093/emboj/cdg463

Teng, H., Cole, J. C., Roberts, R. L., and Wilkinson, R. S. (1999). Endocytic active zones: hot spots for endocytosis in vertebrate neuromuscular terminals. *J. Neurosci.* 19, 4855–4866. doi: 10.1523/jneurosci.19-12-04855.1999

Thompson, R. E., Larson, D. R., and Webb, W. W. (2002). Precise nanometer localization analysis for individual fluorescent probes. *Biophys. J.* 82, 2775–2783. doi: 10.1016/s0006-3495(02)75618-x

Tønnesen, J., and Nägerl, U. V. (2013). Superresolution imaging for neuroscience. *Exp. Neurol.* 242, 33–40. doi: 10.1016/j.expneurol.2012.10.004

Triller, A., and Choquet, D. (2008). New concepts in synaptic biology derived from single-molecule imaging. *Neuron* 59, 359–374. doi: 10.1016/j.neuron.2008.06.022

Trotter, J. H., Hao, J., Maxeiner, S., Tsetsenis, T., Liu, Z., Zhuang, X., et al. (2019). Synaptic neurexin-1 assembles into dynamically regulated active zone nanoclusters. *J. Cell Biol.* 218, 2677–2698. doi: 10.1083/jcb.201812076

Urban, N. T., Willig, K. I., Hell, S. W., and Nägerl, U. V. (2011). STED nanoscopy of actin dynamics in synapses deep inside living brain slices. *Biophys. J.* 101, 1277–1284. doi: 10.1016/j.bpj.2011.07.027

Wang, S., Moffitt, J. R., Dempsey, G. T., Xie, X. S., and Zhuang, X. (2014). Characterization and development of photoactivatable fluorescent proteins for single-molecule–based superresolution imaging. *Proc. Natl. Acad. Sci. U.S.A.* 111, 8452–8457. doi: 10.1073/pnas.1406593111

Watanabe, S., Rost, B. R., Camacho-Pérez, M., Davis, M. W., Söhl-Kielczynski, B., Rosenmund, C., et al. (2013). Ultrafast endocytosis at mouse hippocampal synapses. *Nature* 504, 242–247. doi: 10.1038/nature12809

Wegner, W., Ilgen, P., Gregor, C., van Dort, J., Mott, A. C., Steffens, H., et al. (2017). In vivo mouse and live cell STED microscopy of neuronal actin plasticity using far-red emitting fluorescent proteins. *Sci. Rep.* 7:11781. doi: 10.1038/s41598-017-11827-4

Weigel, A. V., Simon, B., Tamkun, M. M., and Krapf, D. (2011). Ergodic and nonergodic processes coexist in the plasma membrane as observed by single-molecule tracking. *Proc. Natl. Acad. Sci. U.S.A.* 108, 6438–6443. doi: 10.1073/pnas.1016325108

Weisenburger, S., Boening, D., Schomburg, B., Giller, K., Becker, S., Griesinger, C., et al. (2017). Cryogenic optical localization provides 3D protein structure data with Angstrom resolution. *Nat. Methods* 14, 141–144. doi: 10.1038/nmeth.4141

Wen, P. J., Grenklo, S., Arpino, G., Tan, X., Liao, H.-S., Heureaux, J., et al. (2016). Actin dynamics provides membrane tension to merge fusing vesicles into the plasma membrane. *Nat. Commun.* 7:12604. doi: 10.1038/ncomms12604

Westphal, V., Rizzoli, S. O., Lauterbach, M. A., Kamin, D., Jahn, R., and Hell, S. W. (2008). Video-rate far-field optical nanoscopy dissects synaptic vesicle movement. *Science* 320, 246–249. doi: 10.1126/science.1154228

Whelan, D. R., and Bell, T. D. M. (2015). Image artifacts in single molecule localization microscopy: why optimization of sample preparation protocols matters. *Sci. Rep.* 5:7924. doi: 10.1038/srep07924

Wienisch, M., and Klingauf, J. (2006). Vesicular proteins exocytosed and subsequently retrieved by compensatory endocytosis are nonidentical. *Nat. Neurosci.* 9, 1019–1027. doi: 10.1038/nn1739

Willems, J., de Jong, A. P. H., Scheefhals, N., and Mac Gillavry, H. D. (2019). ORANGE: a CRISPR/Cas9-based genome editing toolbox for epitope tagging of endogenous proteins in neurons. *BioRxiv* [Preprint]. doi: 10.1101/700187

Willig, K. I., Rizzoli, S. O., Westphal, V., Jahn, R., and Hell, S. W. (2006). STED microscopy reveals that synaptotagmin remains clustered after synaptic vesicle exocytosis. *Nature* 440, 935–939. doi: 10.1038/nature04592

Wu, X.-S., McNeil, B. D., Xu, J., Fan, J., Xue, L., Melicoff, E., et al. (2009). Ca2+ and calmodulin initiate all forms of endocytosis during depolarization at a nerve terminal. *Nat. Neurosci.* 12, 1003–1010. doi: 10.1038/nn.2355

Wu, X.-S., and Wu, L.-G. (2014). The yin and yang of calcium effects on synaptic vesicle endocytosis. *J. Neurosci.* 34, 2652–2659. doi: 10.1523/JNEUROSCI.3582-13.2014

Xu, K., Zhong, G., and Zhuang, X. (2013). Actin, spectrin and associated proteins form a periodic cytoskeletal structure in axons. *Science* 339, 452–456. doi: 10.1126/science.1232251

Yi, J., Manna, A., Barr, V. A., Hong, J., Neuman, K. C., and Samelson, L. E. (2016). madSTORM: a superresolution technique for large-scale multiplexing at single-molecule accuracy. *Mol. Biol. Cell* 27, 3591–3600. doi: 10.1091/mbc.E16-05-0330

York, A. L., and Zheng, J. Q. (2017). Super-resolution microscopy reveals a nanoscale organization of acetylcholine receptors for trans-synaptic alignment at neuromuscular synapses. *eNeuro* 4:ENEURO.0232-17.2017. doi: 10.1523/ENEURO.0232-17.2017

Yue, H.-Y., and Xu, J. (2014). Myosin light chain kinase accelerates vesicle endocytosis at the calyx of held synapse. *J. Neurosci.* 34, 295–304. doi: 10.1523/JNEUROSCI.3744-13.2014

Zampighi, G. A., Schietroma, C., Zampighi, L. M., Woodruff, M., Wright, E. M., and Brecha, N. C. (2011). Conical tomography of a ribbon synapse: structural evidence for vesicle fusion. *PLoS One* 6:e0016944. doi: 10.1371/journal.pone.0016944

Zampighi, G. A., Zampighi, L. M., Fain, N., Lanzavecchia, S., Simon, S. A., and Wright, E. M. (2006). Conical electron tomography of a chemical synapse: vesicles docked to the active zone are hemi-fused. *Biophys. J.* 91, 2910–2918. doi: 10.1529/biophysj.106.084814

Zhang, M., Chang, H., Zhang, Y., Yu, J., Wu, L., Ji, W., et al. (2012). Rational design of true monomeric and bright photoactivatable fluorescent proteins. *Nat. Methods* 9, 727–729. doi: 10.1038/nmeth.2021

Zhao, W.-D., Hamid, E., Shin, W., Wen, P. J., Krystofiak, E. S., Villarreal, S. A., et al. (2016). Hemi-fused structure mediates and controls fusion and fission in live cells. *Nature* 534, 548–552. doi: 10.1038/nature18598

Zhu, L., Zhang, W., Elnatan, D., and Huang, B. (2012). Faster STORM using compressed sensing. *Nat. Methods* 9, 721–723. doi: 10.1038/nmeth.1978

Conflict of Interest: The authors declare that the research was conducted in the absence of any commercial or financial relationships that could be construed as a potential conflict of interest.

frontiers
in Synaptic Neuroscience

ORIGINAL RESEARCH
published: 18 August 2020
doi: 10.3389/fnsyn.2020.00037

Reducing Glutamate Uptake in Rat Hippocampal Slices Enhances Astrocytic Membrane Depolarization While Down-Regulating CA3–CA1 Synaptic Response

*Ipsit Srivastava, Erika Vazquez-Juarez and Maria Lindskog**

Division of Neurogeriatrics, Center for Alzheimer Research, Department of Neurobiology, Care Sciences and Society, Karolinska Institutet, Solna, Sweden

The majority of synaptic activity in the brain consists of glutamatergic transmission, and there are numerous mechanisms, both intra- and inter-cellular that regulate this excitatory synaptic activity. Importantly, uptake of glutamate plays an important role and a reduced level of astrocytic glutamate transporters affect the normally balanced neurotransmission and is observed in many mental disorders. However, reduced glutamate uptake affects many different synaptic mechanisms in the astrocyte as well as in the neuron, and the effects are challenging to delineate. Combining electrophysiological recordings from neurons and astrocytes as well as extracellular glutamate recordings in rat hippocampal slices, we confirmed previous work showing that synaptic stimulation induces a long-lasting depolarization of the astrocytic membrane that is dependent on inward-rectifier potassium channels. We further showed that when glutamate transporters are blocked, this astrocytic depolarization is greatly enhanced although synaptic responses are reduced. We propose that increasing the levels of synaptic glutamate through blocking glutamate transporters reduces the AMPA-mediated synaptic response while the NMDA receptor current increases, contributing to a rise in extracellular K^+ leading to enhanced astrocytic depolarization.

Keywords: EAAT-1, EAAT-2, GLAST, GLT-1, synapse, currents, adaptation

Edited by:
Jean-Claude Lacaille,
Université de Montréal, Canada

Reviewed by:
Kumamoto Eiichi,
Saga University, Japan
Marco Martina,
Northwestern University,
United States

****Correspondence:***
Maria Lindskog
mia.lindskog@ki.se

Received: *26 March 2020*
Accepted: *30 July 2020*
Published: *18 August 2020*

Citation:
Srivastava I, Vazquez-Juarez E and Lindskog M (2020) Reducing Glutamate Uptake in Rat Hippocampal Slices Enhances Astrocytic Membrane Depolarization While Down-Regulating CA3–CA1 Synaptic Response.
Front. Synaptic Neurosci. 12:37.
doi: 10.3389/fnsyn.2020.00037

INTRODUCTION

Glutamate uptake is a key component in the regulation of excitatory synaptic strength. In the central nervous system the astrocytic excitatory amino acid transporters 1 and 2 (EAAT-1 and -2) are responsible for the majority of glutamate uptake (Bergles and Jahr, 1998), and the neuronal transporters EAAT 3–5 contribute to a lesser extent (Rose et al., 2018). Glutamate transporters are crucial for proper neuronal functioning (Anderson and Swanson, 2000; Rose et al., 2017). Interestingly, a reduction in the expression of these transporters is seen in neurodegenerative as well as psychiatric disorders (Gomez-Galan et al., 2013, 2016; Spangaro et al., 2014; Chung et al., 2015; Garcia-Esparcia et al., 2018) and glutamate transporters have been suggested as targets for new pharmacological treatments of mental disorders (Jensen et al., 2015). A reduction in glutamate uptake leads to increased extracellular glutamate and activation of extrasynaptic NMDA receptors as well as presynaptic metabotropic glutamate receptors (Potier et al., 2010), increasing postsynaptic excitation (Tong and Jahr, 1994; Arnth-Jensen et al., 2002) and eventually to excitotoxicity. However, with increased knowledge about the very tight synapse-astrocyte interaction, it is becoming clear that a pathological increase in glutamate affects the neuronal activity in more complex ways than by inducing excessive increase in activity and excitotoxicity (Goncalves-Ribeiro et al., 2019).

In addition to glutamate uptake, astrocytes regulate synaptic activity through release of gliotransmitters (Araque et al., 2014), potassium buffering (Orkand, 1980; Sibille et al., 2014), regulation of extracellular fluid circulation (Iliff et al., 2012) etc. Vice-versa, the astrocytes themselves can be regulated by a plethora of mechanisms, including pressure (Bowman et al., 1992), metabolism (Bélanger et al., 2011), inflammatory signals (Habbas et al., 2015) and, most importantly for their integral role in neural circuits, by neuronal activity (Martin et al., 2015; Adamsky et al., 2018; Covelo and Araque, 2018). Indeed, the close functional and anatomical interaction between perisynaptic astrocytic processes and the synaptic structure, often referred to as the tripartite synapse, is fundamental for a balanced network activity (Araque et al., 1999; Santello et al., 2019).

A prerequisite for the close astrocyte-synapse interaction is that astrocytes can sense neuronal activities. Several mechanisms have been proposed, including metabotropic glutamate receptors (Panatier et al., 2011), metabolic signals (Choi et al., 2012), and extracellular potassium concentration (Bellot-Saez et al., 2017). A considerable attention has been given to intracellular Ca^{2+} signal in astrocytes (Khakh and McCarthy, 2015; Bazargani and Attwell, 2016) whereas much less is known about a change in membrane potential could act as a signal transduction mechanism. Compared to neurons, astrocytes are electrically passive and do not seem to express voltage sensitive channels to any large extent (Steinhauser et al., 1992; Verkhratsky and Nedergaard, 2018). Their low resting membrane potential (approximately −80 mV) and low input resistance are largely determined by the high number of potassium channels (Ransom and Goldring, 1973; Djukic et al., 2007; Dallerac et al., 2013; Hwang et al., 2014). Although astrocytes have been shown to depolarize in response to synaptic response (Zhang et al., 2003; Pannasch et al., 2012) as well as to direct application of glutamate and GABA (Kettenmann and Schachner, 1985) we still lack an understanding of the electric response of astrocytes in normal or pathological conditions.

In this work, we examine the effect of astrocyte membrane potential, mimicking the pathological state of reduced glutamate uptake where the levels of extrasynaptic glutamate is increased by blocking glutamate transporters. We confirm that evoked synaptic activity in the Schaffer collaterals, axons projecting from the CA3 area to the CA1 area of the hippocampus, leads to a distinct, slow depolarization mediated by an increase in extracellular K^{+}, and that this depolarization is significantly increased in conditions of increased extracellular glutamate. Interestingly, this response is not a linear readout of the synaptic signal, since an inhibition of glutamate transporters leads to a decrease in the synaptic response concomitant to the increase in astrocytic membrane depolarization. Instead the slow astrocytic membrane depolarization is dependent on an increase in NMDA receptor activation.

MATERIALS AND METHODS

Animals and Husbandry

All experiments were performed using male Sprague Dawley rats (Charles River Laboratories) aged 21–29 days for patch clamp recordings or 6–8 weeks for field recordings. The animals were housed at the Karolinska Institutet animal facility at 12:12 light/dark cycle and kept and used according to local and national regulation. Experiments were performed with the ethical permit granted by the Animal Ethics Committee at the County Administrative Board (Norra Stockholms Djurförsöksetiska Nämnd, approval N13/15).

Slice Preparation

Rats were deeply anesthetized with isoflurane, decapitated and the brain was quickly removed. For field recordings the brain was placed in ice-cold standard artificial CSF (aCSF) containing in mM: 130 NaCl, 3.5 KCl, 1.25 NaH2PO4, 24 NaHCO3, 10 glucose, 2 CaCl2, and 1 MgCl2 (pH 7.3–7.4, 310–330 mOsm), bubbled with carbogen gas (5% CO_2, 95% O_2). Hippocampal horizontal slices (400 μm thick) were prepared using a Leica VT1200S vibratome (Leica Microsystems). Immediately after slicing, sections were transferred into an interphase incubation chamber filled with standard aCSF (in mM: 130 NaCl, 3.5 KCl, 1.25 NaH2PO4, 24 NaHCO3, 10 glucose, 2 CaCl2, and 1.3 MgCl2). The chamber was held at 34°C during the slicing and was subsequently allowed to cool down at room temperature. For patch clamp recordings 300 μm slices were prepared in the same way, with dissection solution containing (in mM): 250 sucrose, 2.5 KCl, 1.4 NaH_2PO_4, 26 $NaHCO_3$, 10 glucose, 1 $CaCl_2$, and 4 $MgCl_2$ (310–330 mOsm). The recovery and recording was done in the same standard aCSF solution as above.

Patch-Clamp Recordings

After a recovery period of at least 1 h, slices were transferred to a submerged recording chamber with perfusion rate 2–3 ml per min with aCSF at 32 ± 1°C, bubbled with carbogen. Picrotoxin (50 μM, Tocris Biosciences) was added to the recording solution to omit effects of inhibitory input. Ag/AgCl electrode was used with borosilicate glass pipettes with a tip resistance of 5–7 MOhm for patching astrocytes, and 4–5 MOhm for neurons. The glass pipettes were filled with a solution containing (in mM): 110 K-gluconate, 10 KCl, 4 Mg-ATP, 10 Na_2-phosphocreatine, 0.3 Na-GTP, 10 4-(2-hydroxyethyl)piperzine-1-ethanesulfonic acid (HEPES) and 0.2 ethylene glycol tetraacetic acid (EGTA) (pH 7.2–7.4; 270–290 mOsm). Neurons were identified by shape and localization in the pyramidal cell layer, astrocytes were identified by shape and localization in the stratum radiatum. Astrocyte identity was confirmed by a hyperpolarized membrane potential (−75 to −85 mV) and no voltage dependent currents (see **Figures 1A–C**). Voltage response to an injected current pulse was monitored to ensure the quality of the recording throughout the experiment and data was included only for stable values (<20% variation). Synaptic responses were evoked by electrical stimulation of the Schaffer collaterals (SC) using a bipolar concentric electrode and stimulation intensity to evoke 50–60% of the maximal response was used. A single stimulation pulse was given and the postsynaptic response was averaged over 5 sweeps. Data acquisition was done using Multiclamp 700B amplifier and Clampex 10.0 (Molecular Devices), digitized with Digidata 1440A (Molecular Devices). Glutamate transporter currents were recorded in astrocytes voltage clamped at −80 mV in the presence of NBQX (10 μM) and DL-APV (50 μM) in response to increasing Schaffer collateral stimulation using a bipolar electrode. For neuronal recordings, all neurons were voltage clamped at −65 mV. Traces were analyzed in the pClamp or Minianalysis software (Synaptosoft, United States).

Field Recordings

After a recovery period of 2 h, slices were transferred to a submerged recording chamber with perfusion rate of 2–3 ml per min with standard aCSF at 32 ± 1°C, bubbled with carbogen gas. Field excitatory postsynaptic potentials (fEPSPs) were evoked at 0.1 Hz by electrical stimulation of the Schaffer collaterals (SC) using a bipolar concentric electrode coupled to an isolated stimulator. Stimulation intensity to evoke 50–60% of the maximal response were used. Responses were recorded in the CA1 using an Ag/AgCl electrode coupled to an amplifier (EXT-02, npi), digitized (Digidata, Molecular Devices, United States) and monitored with the pClamp software (Molecular devices). Traces were analyzed in the pClamp software. A 20 min stable fEPSP baseline was recorded before the slices were perfused with specific drugs (see below). The size of the responses was measured by determining the slope of the linear rising phase of the fEPSP (between 10 and 80% before reaching the peak amplitude). Experiments were normalized to their individual baseline periods. The effect of each specific drug was determined by comparing a 5 min average of the normalized fEPSP slope after treatment (minutes 16–20) to the averaged fEPSP slope of baseline recording (30 sweeps, respectively).

Glutamate Recordings

R1 ceramic-based microelectrode arrays (MEAs; The Center for Microelectrode Technology, University of Kentucky) containing four vertical-aligned recording sites were used to monitor glutamate concentration in hippocampal slices. The glutamate-sensitive site of the MEA, was coated with glutamate oxidase (0.1 unit/μL; G4001-01, US Biological, United States), BSA (0.8%), and glutaraldehyde (0.1%). An adjacent site, used as a sentinel detector for background noise and non-specific signals, was only coated with BSA and glutaraldehyde. Coated MEAs were allowed to dry for 48 h at room temperature and then electroplated with a size-exclusion *m*-phenylene diamine layer. Prior to every experiment, MEAs were calibrated using a potential of 0.7 V versus an Ag/AgCl reference electrode. Briefly, calibration was performed in PBS solution (0.05 M, 40 ml, pH 7.4, 37°C). After stabilization of the baseline signal, Ascorbic Acid (250 μM), L-Glutamate (3 μM × 20 μM), Dopamine (2 μM), and H_2O_2 (8.8 μM) were sequentially added to the calibration beaker. Amperometric signals were acquired at 10 Hz using a FAST-16 mkIV electrochemical recording system (Quanteon LLC, United States) and analyzed off-line. The final concentration of glutamate in the slice was calculated by subtracting the signal recorded by the sentinel to that of the glutamate-sensitive site.

Drugs

The following (concentrations of) drugs were delivered through the recording aCSF solution: $GABA_A$ receptor antagonist: Picrotoxin, PTX (50 μM), AMPA receptor antagonist NBQX (1, 2,3,4-Tetrahydro-6-nitro-2,3-dioxo-benzo[f]quinoxaline-7-sulfonamide hydrate; 10 μM), NMDA receptor antagonist DL-AP5 (DL-2-Amino-5-phosphonopentanoic acid; 25 μM), EAAT blocker DL-TBOA (DL-threo-beta-Hydroxyaspartic acid; 50 μM), Group II mGluR antagonist LY341495 were from Tocris Bioscience (United Kingdom). Barium chloride, $BaCl_2$ (100 μM) and NMDA antagonist MK-801 [(5S,10R)-(+)-5-Methyl-10,11-dihydro-5H-dibenzo[a,d]cyclohepten-5,10-imine; 10 μM] were from Sigma-Aldrich (United States). Both DL-AP5 and MK-801 completely blocks NMDA receptors under these conditions and are considered equivalent.

Statistics

Unless otherwise noted, data is presented as average value ± SEM. Statistical analysis was done using the GraphPad software and assuming normal distribution. Statistical significance is analyzed with Student *t*-test when two groups are compared or with ANOVA followed by Tukey's multiple comparison for comparing values before and after treatment in the same cell or Bonferroni's multiple comparison to compare unpaired values from different cells or slices.

RESULTS

Synaptic Activation Generates a Slow Depolarization of Astrocytes

Patch-clamp recordings from astrocytes in the stratum radiatum revealed an average resting membrane potential (RMP) of −77.33 ± 0.43 mV (*n* = 18; **Figure 1A**). The cells did not respond with action potentials at depolarizing voltage pulses up to +40 mV (**Figure 1B**) and showed a linear I–V curve (**Figure 1C**). Synaptic activity triggered by stimulation of Schaffer collaterals generated a fast membrane potential response (**Figure 1D**) with an average peak amplitude of 0.49 ± 0.05 mV (**Figure 1E**) and decay time of 2.11 ± 0.25 ms (*n* = 18; **Figure 1F**). This fast response has previously been described and is a reflection of the field EPSP that can be measured in the astrocyte due to the low membrane resistance (Henneberger and Rusakov, 2012) and is present in all our astrocytic recordings when the Schaffer collateral is stimulated. In addition, we identified a long-lasting depolarization of the astrocytic membrane in response to collateral stimulation (**Figure 1G**) with a decay time of 1.51 ± 0.93 s and an average peak amplitude of 0.92 ± 0.10 mV (*n* = 18; **Figures 1H,I**). Since astrocytic membrane potential is largely set by potassium, we examined the role of K^+ channels in

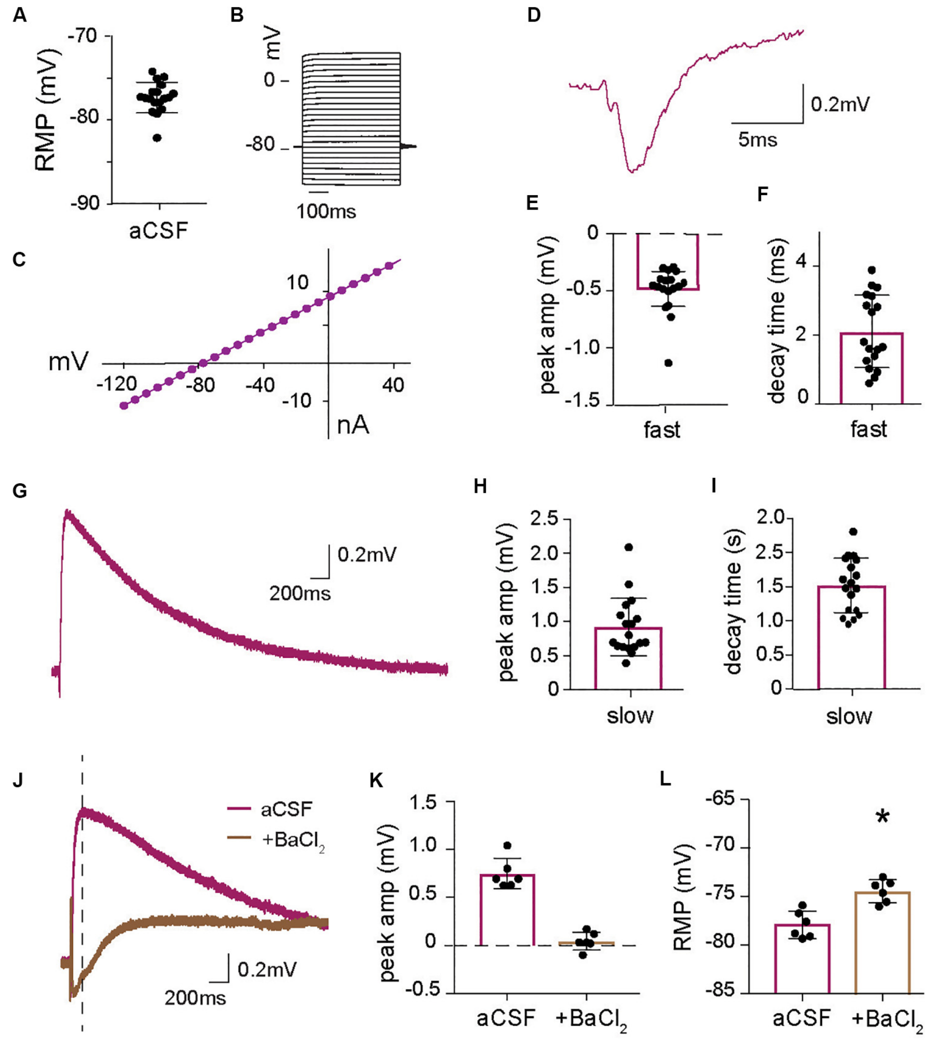

FIGURE 1 | Astrocytic long lasting depolarization induced by increase in extracellular K^+ at synaptic activity. **(A)** Baseline resting membrane potential (RMP) of all astrocytes recorded in current clamp for this paper ($n = 18$). **(B)** Voltage steps protocol and **(C)** I–V curve of a representative astrocyte showing a linear relationship between current and voltage confirming astrocyte identity. **(D)** Representative trace of the fast astrocytic response to synaptic stimulation with **(E)** mean peak amplitude and **(F)** mean decay time ($n = 18$, including cells also analyzed in **Figures 3**, **5**). **(G)** Representative trace of the long-lasting astrocytic depolarization in response to synaptic activity and quantification of **(H)** peak amplitude and **(I)** decay time ($n = 18$). **(J)** Representative trace of the long-lasting astrocytic depolarization in the absence and presence of barium chloride, $BaCl_2$ (100 μM), purple and brown, respectively, with the baseline adjusted. $BaCl_2$ application significantly reduces the **(K)** peak amplitude (time of measurement indicated by line in **J**) of the astrocytic long-lasting depolarization ($p < 0.01$, $n = 6$). **(L)** $BaCl_2$ application depolarizes the astrocyte resting membrane potential (RMP) ($p < 0.01$, $n = 6$). Electrical stimulation artifact removed from displayed traces for clarity. *Denotes statistical significance.

this response by blocking them with 100 μM $BaCl_2$. As expected, $BaCl_2$ resulted in a significantly depolarized astrocytic resting membrane potential compared to baseline (-74.36 ± 0.48 mV with $BaCl_2$ versus -77.83 ± 0.57 mV before, $p < 0.01$, $n = 6$; **Figure 1L**). To investigate the effect of blocking of potassium channels on the slow depolarization evoked by synaptic activity the change in potential compared to the baseline was measured and showed that $BaCl_2$ completely blocked the depolarization (0.04 ± 0.04 mV, compared to 0.74 ± 0.06 mV in control; $p < 0.01$, $n = 6$; **Figures 1J,K**). These results suggest that astrocytes respond to synaptic activity with a slow depolarization mediated by an increase in extracellular K^+ triggered by synaptic activity. The recordings display a biphasic response to $BaCl_2$, with a slow depolarization appearing about 0.5 s after stimulation. Although we did not explore this effect, it indicates that blocking K^+ channels affects many cellular processes, including the Na^+/K^+-ATPase, that can affect the membrane potential.

Astrocytic Response to Glutamate Transporter Blocking

Glutamate transporters are critical for regulating synaptic strength, and they are highly relevant target for the treatment of many mental disorder. When glutamate is released through

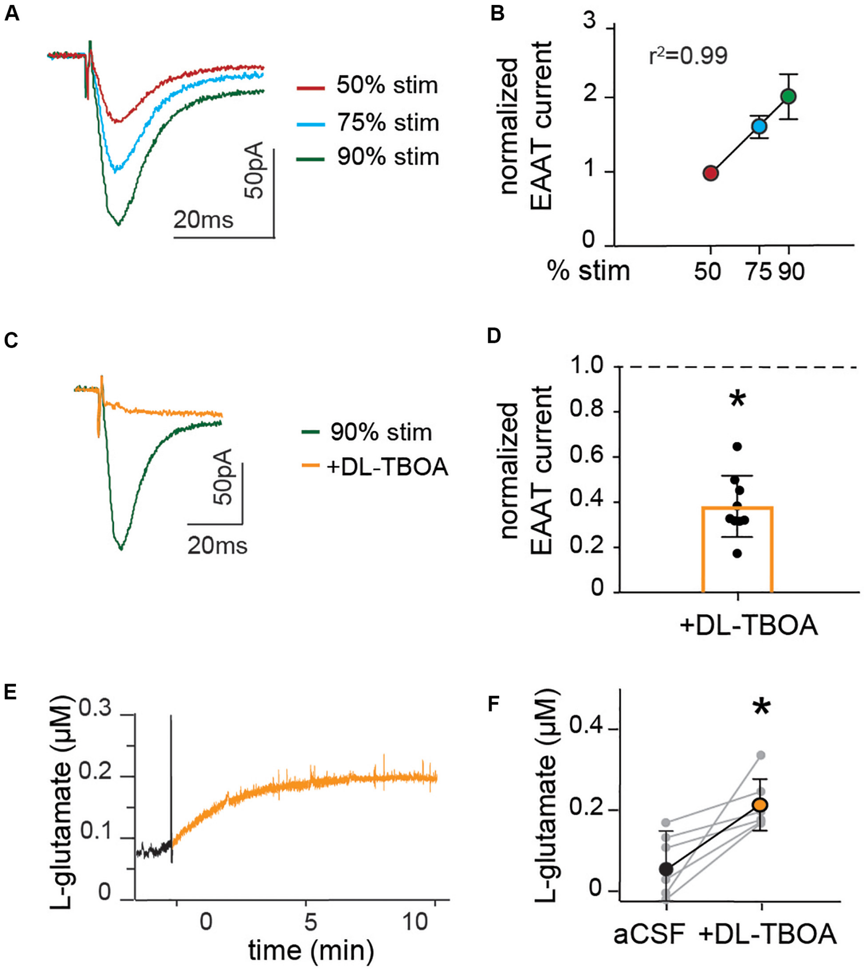

FIGURE 2 | Astrocytic glutamate transporter currents increase linearly with synaptic stimulation and blocking glutamate transporters doubles baseline extracellular levels of glutamate. **(A)** Representative trace of EAAT current measured in the presence of NBQX and AP5, at schaffer collateral stimulation corresponding to 50% (red), 75% (blue), and 90% (green) of maximal stimulation strength. **(B)** Peak amplitude of EAAT current normalized to the amplitude at 50%, showing that glutamate transporter currents increase linearly with increase in stimulation strength. **(C)** Representative recordings of EAAT current in the presence of EAAT blocker DL-TBOA (50 µM). **(D)** Average glutamate transporter currents normalized to current before the application of EAAT blocker are significantly reduced in the presence of DL-TBOA ($p < 0.01$, $n = 9$). Enzyme coated microelectrode were used for recording of glutamate concentration. **(E)** Representative figure showing L-glutamate recordings under baseline conditions (black) and after application of DL-TBOA (50 µM; orange). **(F)** Glutamate concentrations before and 15 min after DL-TBOA (50 µM) application shown for each slice, the averages are significantly different ($p < 0.05$, $n = 6$). Electrical stimulation artifact removed from displayed traces for clarity. *Denotes statistical significance.

presynaptic stimulation of Schaffer collaterals, a glutamate transporter mediated inward current that can be recorded in patch-clamped astrocytes in the presence of AMPA and NMDA receptor inhibitors NBQX (10 µM) and AP5 (25 µM). In fEPSP recordings, with synaptic release triggered by Schaffer collateral stimulation, we identified the stimulation triggering 50, 75, and 90% of maximal fEPSP response. This stimulation generated a linear increase of glutamate transporter currents ($r^2 = 0.99$, slope = 0.03, $n = 10$; **Figures 2A,B**), suggesting that under basal conditions, the main determinant of glutamate transporter activity is extracellular glutamate concentrations. The current's identity was confirmed by applying the glutamate transporter blocker DL-TBOA (50 µM) that reduced the fast component of the current (peak amplitude 0.38 ± 0.04 of control, $p < 0.01$, $n = 9$; **Figures 2C,D**), leaving a slow residual current previously described as potassium mediated (Cheung et al., 2015).

We further assessed the effect of glutamate transporter blocking on the levels of ambient glutamate. Extracellular glutamate concentrations were recorded in slices using an enzyme-coated microelectrode coupled to amperometric detection and DL-TBOA was applied to the slice to block astrocytic as well as neuronal glutamate transporters. The amount of glutamate measured increased gradually after DL-TBOA bath perfusion (**Figure 2E**), reaching a significant twofold increase from 61 ± 4 to 220 ± 3 nM ($p < 0.05$, $n = 6$, **Figure 2F**) 15 min after application of DL-TBOA.

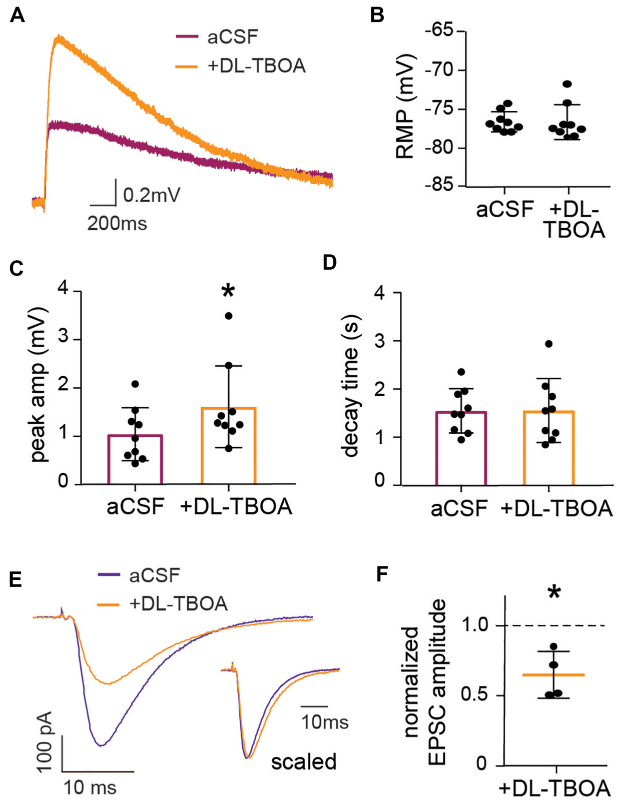

FIGURE 3 | EAAT blocking enhances astrocytic membrane depolarization while reducing neuronal evoked EPSC. **(A)** Representative trace showing astrocytic long-lasting depolarization under control conditions (purple) and 2 min after DL-TBOA application (orange). **(C)** DL-TBOA significantly increases the peak amplitude of the long-lasting depolarization ($p < 0.01$, $n = 9$, where 6 out of 9 cells are the same as in **Figure 5**) with no significant changes in the **(D)** decay time and **(B)** resting membrane potential (RMP). Voltage-clamp recordings from individual neurons held at −65 mV during stimulation of Schaffer collateral under control conditions and in the presence of glutamate transporter blocker DL-TBOA. **(E)** Representative trace of evoked EPSC before (blue) and 2 min after DL-TBOA application (orange), insert shows traces with amplitude scaled. **(F)** Peak amplitude of evoked EPSC normalized to before application of DL-TBOA for each cell, the average amplitude is significantly reduced in presence of DL-TBOA compared to before ($p < 0.05$, $n = 4$). Electrical stimulation artifact removed from displayed traces for clarity. *Denotes statistical significance.

Astrocytic and Neuronal Response to Acute Blocking of Glutamate Transporters

To investigate the response of astrocytes to reduced glutamate uptake, we recorded membrane potential changes in patched astrocytes in response to Schaffer collateral stimulation in the absence or presence of DL-TBOA (50 µM) to block the glutamate transporters. DL-TBOA application significantly increased the average peak amplitude of astrocytic depolarization from 1.04 ± 0.18 mV to 1.61 ± 0.28 mV ($p < 0.01$, $n = 9$; **Figures 3A,C**) without modifying the decay time (1.55 ± 0.22 s in the presence of DL-TBOA compared to 1.55 ± 0.15 s at baseline, $n = 9$; **Figure 3D**). DL-TBOA had no significant effect on the RMP (−76.6 ± 0.43 mV before DL-TBOA compared to −76.6 ± 0.75 mV after treatment, $n = 9$; **Figure 3B**). A possible explanation for the increased astrocytic depolarization after glutamate transporter inactivation is that the increase in extracellular glutamate (**Figure 2**) leads to increased neuronal activity, thus enhancing the synaptically evoked depolarization. To confirm this, we recorded the evoked EPSC from CA1 neurons in response to Schaffer collateral stimulation. To our surprise, blocking glutamate transporters with DL-TBOA reduced the evoked EPSC peak amplitude significantly to 0.65 ± 0.08 of control ($p < 0.05$, $n = 4$; **Figures 3E,F**). When the recordings were scaled to the same amplitude (**Figure 3E**, inset) a slight and not significant increase of the decay time was observed, from 12.72 ± 1.5 ms at baseline to 14.6 ± 1.0 ms in the presence of DL-TBOA ($p = 0.14$, $n = 4$).

Blocking Glutamate Transporters Induces a NMDA Mediated Reduction of EPSP Amplitude

To understand the effect of glutamate transporter blocking on the overall synaptic activity, we turned to extracellular recordings of evoked field EPSPs (fEPSP) at Schaffer collateral-CA1 pyramidal cell synapses. Again, DL-TBOA (50 µM) treatment reduced the normalized fEPSP to 0.67 ± 0.04 ($n = 5$; **Figures 4A,B**) of baseline as measured by the slope of the response. This decrease was significantly different from control slices in which the normalized fEPSP remained at 0.98 ± 0.03 ($p < 0.05$; $n = 5$) of baseline at the same timepoint after mock change of perfusion solution. Adding glutamate (1 mM) to the perfused aCSF induced a similar reduction in fEPSP response as DL-TBOA (0.53 ± 0.06 of baseline, $p < 0.01$, $n = 4$; **Figures 4A,B**), confirming that DL-TBOA indeed mediated the synaptic adaptation through elevating the levels of extracellular glutamate. LY341495 to inhibit presynaptic metabotropic glutamate receptors and MK-801 to block NMDA receptors were then used to understand how the decreased synaptic response was mediated. In the presence of 200 nM LY341495 (Losonczy et al., 2003) the evoked fEPSP was still significantly decreased after DL-TBOA treatment (0.72 ± 0.07 of baseline, $p < 0.05$, $n = 4$; **Figures 4C,D**), however, in the presence of MK-801 (10 µM) the recorded response remained unaltered from baseline level both in the presence of DL-TBOA (0.98 ± 0.05, $n = 4$) and 1 mM glutamate (0.86 ± 0.07, $n = 4$, **Figures 4E,F**). MK-801 alone did not change the fEPSP slope (1.01 ± 0.06, $n = 3$). This result suggests that the observed reduction in synaptic strength after blocking glutamate transporters is the result of an active homeostatic response to increased extracellular levels of glutamate orchestrated by the NMDA receptor activation and is in line with previous work showing that glutamate overload can induce an NMDA receptor mediated AMPA receptor removal from the synapse (Siddoway et al., 2014).

A Switch in AMPA/NMDA Activity After Glutamate Transporter Blocking

The fact that astrocytic depolarization is increased, whereas synaptic activity is reduced to less than half when glutamate

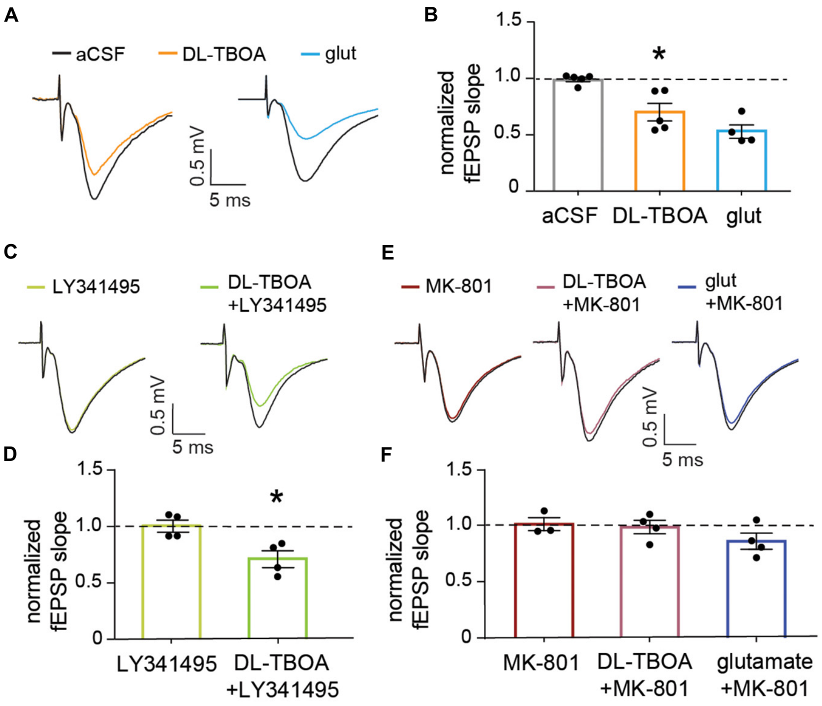

FIGURE 4 | EAAT blocking or exogenous glutamate reduce the evoked synaptic population response in an NMDA receptor-dependent manner. **(A)** Representative traces showing baseline field EPSPs evoked by electrical stimulation of Schaffer collateral and recorded in the striatum radiatum of the CA1 (black traces) and 15 min after 50 μM DL-TBOA or 1 mM glutamate application (orange and blue traces, respectively). **(B)** The fEPSP reduction induced by DL-TBOA and 1 mM glutamate was significantly different when compared to control experiments measured at the same time point after a mock change of perfusion solution ($p < 0.05$, $n = 5$ for DL-TBOA and $p < 0.01$, $n = 5$ for 1 mM glutamate). **(C)** Representative traces showing baseline fEPSP responses (black traces) and 15 min after 10 μM LY341495 alone or combined with DL-TBOA. **(D)** Inhibition of mGlu receptors with LY341495 did not modify either the fEPSP response ($n = 4$) or the significant reduction in amplitude induced by DL-TBOA ($n = 4$). **(E)** Representative traces showing fEPSP responses at baseline (black traces) and 15 min after 10 μM MK-801 alone or combined with 50 μM DL-TBOA or 1 mM glutamate. **(F)** Blocking NMDA receptors fully prevent the reduction in the fEPSP response induced by 50 μM DL-TBOA ($n = 4$) or 1 mM glutamate ($n = 4$). *Denotes statistical significance.

transporters are blocked, shows that the slow astrocytic membrane depolarization is not a linear readout of synaptic potentials. However, NMDA receptors, as well as AMPA receptors are permeable to K^+, and an increase in NMDA receptor activation results in an increase of extracellular K^+ (Shih et al., 2013). Indeed, application of the NMDA receptor inhibitor AP5 completely reversed the increase in synaptically evoked membrane depolarization induced by DL-TBOA from 1.50 ± 0.20 mV in the presence of DL-TBOA to 0.78 ± 0.07 mV when AP5 was added to the slice ($p < 0.05$ compared to DL-TBOA), which was not significantly different from the astrocytic depolarization in response to synaptic activity before the drugs were added; (0.99 ± 0.17 mV, $n = 6$; **Figures 5A,B**). Again, there was no difference in decay time (control 1.49 ± 0.17 s, DL-TBOA 1.39 ± 0.21 s, DL-TBOA + AP5 1.2 ± 0.15 s, $n = 6$; **Figure 5C**). Blocking the NMDA receptor alone did not change the astrocytic RMP (control −77.96 ± 1.48 mV, AP5 −78.21 ± 1.89 mV; **Figure 5F**). Interestingly, AP5 application alone, in the absence of DL-TBOA did not have any effect on the stimulation induced astrocytic membrane depolarization (peak amplitude control 0.77 ± 0.16 mV, in the presence of AP5 0.74 ± 0.12 mV, $n = 4$; **Figures 5D,E**) suggesting that the NMDA receptors are only activated enough to affect astrocytic membrane potential when glutamate transporters are blocked and extracellular glutamate is increased.

The slight shift in decay time observed in the neuronal EPSC after DL-TBOA application (**Figure 3E**) suggested that NMDA currents may be increased in this condition, however, this effect was masked by the fast AMPA response. Indeed, by recording the evoked EPSC of pyramidal neurons in the CA1 in presence of AMPA receptor blocker NBQX to isolate the NMDA current, we confirmed that blocking glutamate transporters does indeed lead to an increase in NMDA currents in neurons. In contrast to the effect on the AMPA mediated current (**Figures 3E,F**), DL-TBOA application significantly increased the peak amplitude of evoked EPSC to 1.52 ± 0.09 of control ($p < 0.01$, $n = 6$; **Figures 5G,H**).

DISCUSSION

In this work, we show that astrocytes in the hippocampus depolarize upon synaptic stimulation. The slow time course and the fact that the depolarization can be blocked by $BaCl_2$ indicate that the depolarization is mediated by rises in extracellular potassium (Ballanyi et al., 1987; Meeks and Mennerick, 2007), a finding consistent with K^+ currents recorded under similar

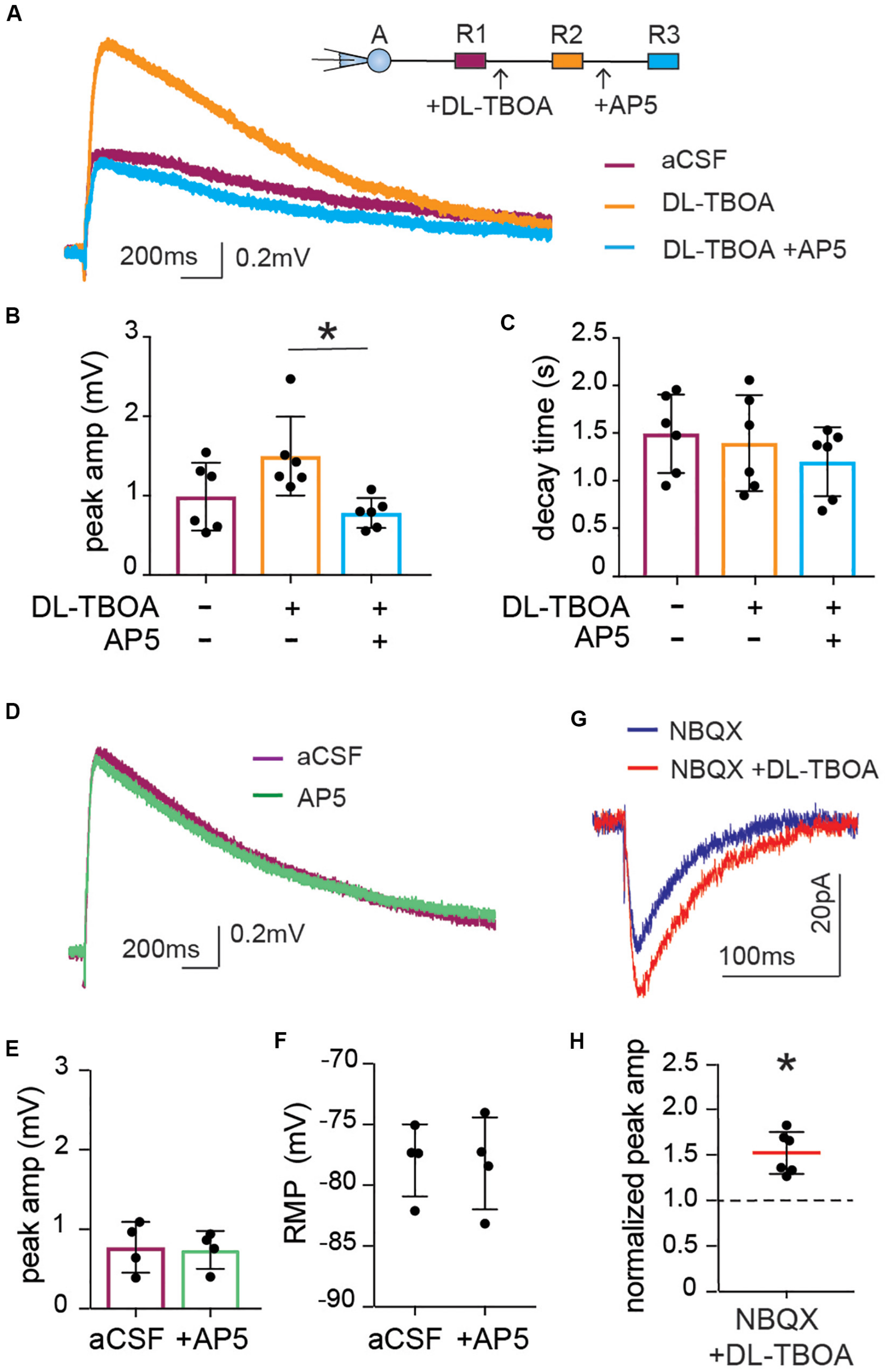

FIGURE 5 | Enhanced astrocytic depolarization after glutamate transporter blocking is dependent on increase in NMDA receptor activity. **(A)** Representative trace of astrocytic depolarization at baseline (purple), after DL-TBOA application (orange) and in the presence of DL-TBOA as well as NMDA receptor inhibitor AP5 (blue). **(B)** The significant increase in peak amplitude of astrocytic depolarization in the presence of DL-TBOA (50 μM) was completely inhibited when AP5 (25 μM) was added along with DL-TBOA (*n* = 6), **(C)** with no difference in decay time in any of the three conditions. **(D)** Representative trace showing the synaptically induced astrocytic depolarization before and after application of AP5 (25 μM, green). **(E)** AP5 does not significantly change peak amplitude or **(F)** resting membrane potential (*n* = 4). Neuronal NMDA responses were recorded as evoked EPSC in patch-clamped neurons by stimulation of Schaffer collateral in the presence of the AMPA receptor antagonist NBQX. **(G)** Representative trace of NMDA component of EPSC recorded before (blue) and after DL-TBOA application (red). **(H)** DL-TBOA significantly increased the average peak amplitude of the synaptically evoked NMDA current ($p < 0.01$; *n* = 6). Electrical stimulation artifact removed from displayed traces for clarity. *Denotes statistical significance.

conditions (Sibille et al., 2014). Interestingly, the depolarization is not a linear read-out of the synaptic EPSC. When we block glutamate transporters, the astrocytic depolarization is increased, whereas the postsynaptic neuronal response, as recorded either as a single cell EPSC (**Figures 3E,F**) or a field EPSP (**Figures 4A,B**), is decreased. We also show that the increased astrocytic depolarization after blocking glutamate transporters is mediated by NMDA receptors. Taken together, our results reinforce the close interaction and finely tuned relationship between neurons and astrocytes at the synapse. We propose that a reduced glutamate uptake by the astrocytes induces a rearrangement of the synapse with a down regulation of synaptic AMPA receptor response but an increase in extrasynaptic NMDA receptor activation, leading to an increase in extracellular potassium that is sensed by the astrocyte through an increased membrane depolarization. This interaction is compatible with previous work, using the method of intrinsic optical signal (Woo et al., 2019).

The importance of astrocytes to buffer extracellular K^+ is well described (Kofuji and Newman, 2004), but our work shows that K^+ can also be a signal, in contrast to what have been proposed in an *in silico* model (Savtchenko et al., 2018). Barium sensitive potassium channels are well-known to set the resting membrane potential of astrocytes (Olsen and Sontheimer, 2008). Since potassium currents are the main effectors of the slow depolarization, our data suggests that in conditions of high glutamate (in our case when glutamate transporters are blocked), the activation of presumably extrasynaptic NMDA receptors generates currents that substantially contribute to extracellular potassium levels (Lackington and Orrego, 1986; Shih et al., 2013) and enhances the synaptically induced astrocytic membrane depolarization. An alternative explanation would be that the increased activation of NMDA receptors causes a depolarization of the postsynaptic cell, leading to an increased neuronal firing. However, the time course of the astrocytic depolarization is constant under control and DL-TBOA application, and only the peak amplitude is affected. This makes it unlikely that the effect is due to increased neuronal firing, since this would have led to multiple peaks, or a shift in decay time due to potassium build up after each action potential.

The interdependence of neuronal and astrocytic responses and the fast adaptation of the responses impose particular challenges to study them and to specifically pinpoint the localization of specific mechanisms. Our results do not, for example, allow us to rule out that part of the increase in astrocytic depolarization after DL-TBOA is due to NMDA receptors expressed on the astrocytes. The existence of NMDA receptors on astrocytes is controversial (Dzamba et al., 2013), recordings of NMDA currents in pure astrocytic cell cultures show that astrocytes have the capability to express NMDA receptors (Kettenmann et al., 1984), but whether this is true *in vivo* is less certain and difficult to tease out due to the interdependency of the synaptic and astrocytic events. Recent single-cell sequencing data show that astrocytes express very low levels of NMDA mRNA (Skowronska et al., 2019) and their functional role is unclear. The slow time course and consistent decay-time in our experiments and the fact that neuronal NMDA currents are increased in the presence of DL-TBOA, are compatible with the hypothesis that increased astrocytic membrane potential is mediated through a rise in extracellular K^+ through increased activation of neuronal NMDA receptors. The possibility that the depolarization is mediated by extracellular K^+ originating from an increase in action potentials (triggered by NMDA receptor induced depolarization of the postsynaptic neuron), seems less likely based on the constant time course of the depolarization in the absence and presence of DL-TBOA. Our model of explanation is also compatible with previously published work where astrocytic currents were recorded upon NMDA receptor activation (Schipke et al., 2001). On the other hand, work from acutely isolated astrocytes does point to the presence of functional NMDA receptors on astrocytes (Lalo et al., 2006). In our experiments, the NMDA receptor inhibitor AP5 does not have any effect in the absence of DL-TBOA suggesting that extrasynaptic NMDA receptors are involved, activated only when the blockade of glutamate transporters causes an overflow of glutamate beyond the synaptic cleft.

Although astrocytic membrane depolarization is an understudied phenomenon, there is now accumulating evidence that membrane depolarization in astrocytes is functionally relevant. It has been shown that depolarization of cortical astrocytes can increase intracellular Ca^{2+} (Wu et al., 2015) and glutamate transporter currents are affected by changes in astrocyte membrane potential (Tanui et al., 2016; Lebedeva et al., 2018). Interestingly, the fast decrease in the amplitude of the fast neuronal postsynaptic potential in response to high levels of extracellular glutamate can be an adaptation to prevent runaway excitation. In contrast, the astrocytic response to increases in extracellular glutamate, measured as the membrane depolarization, is enhanced. Thus, the signal transduction through astrocytic membrane potential can be especially important at situations with high levels of glutamate and can potentially induce adaptation of the network within a longer timeframe, consistent with the idea that astrocytes are important to sustain a balanced neuronal network activity over time.

DATA AVAILABILITY STATEMENT

The raw data supporting the conclusions of this article will be made available by the authors, without undue reservation, to any qualified researcher.

ETHICS STATEMENT

The animal study was reviewed and approved by Stockholms Norra Försöksdjursetiska nämnd.

AUTHOR CONTRIBUTIONS

IS and ML conceived and designed the work together with EV-J. EV-J and IS performed the experiments. All authors contributed in analysis and interpretation of the data as well as writing the manuscript.

FUNDING

We acknowledge the following funding sources: The Brain & Behavior Research Foundation (NARSAD Independent Investigator grant to ML), The Swedish Research Council, and The Swedish Brain Foundation.

ACKNOWLEDGMENTS

The authors thank Julia Van Adrichem for valuable input to the study and help with preparation of the manuscript.

REFERENCES

Adamsky, A., Kol, A., Kreisel, T., Doron, A., Ozeri-Engelhard, N., Melcer, T., et al. (2018). Astrocytic activation generates de novo neuronal potentiation and memory enhancement. *Cell* 174, 59.e–71.e. doi: 10.1016/j.cell.2018.05.002

Anderson, C. M., and Swanson, R. A. (2000). Astrocyte glutamate transport: review of properties, regulation, and physiological functions. *Glia* 32, 1–14. doi: 10.1002/1098-1136(200010)32:1<1::AID-GLIA10<3.0.CO;2-W

Araque, A., Carmignoto, G., Haydon, P. G., Oliet, S. H., Robitaille, R., and Volterra, A. (2014). Gliotransmitters travel in time and space. *Neuron* 81, 728–739. doi: 10.1016/j.neuron.2014.02.007

Araque, A., Parpura, V., Sanzgiri, R. P., and Haydon, P. G. (1999). Tripartite synapses: glia, the unacknowledged partner. *Trends Neurosci.* 22, 208–215. doi: 10.1016/S0166-2236(98)01349-6

Arnth-Jensen, N., Jabaudon, D., and Scanziani, M. (2002). Cooperation between independent hippocampal synapses is controlled by glutamate uptake. *Nat. Neurosci.* 5, 325–331. doi: 10.1038/nn825

Ballanyi, K., Grafe, P., and ten Bruggencate, G. (1987). Ion activities and potassium uptake mechanisms of glial cells in guinea-pig olfactory cortex slices. *J. Physiol.* 382, 159–174. doi: 10.1113/jphysiol.1987.sp016361

Bazargani, N., and Attwell, D. (2016). Astrocyte calcium signaling: the third wave. *Nat. Neurosci.* 19, 182–189. doi: 10.1038/nn.4201

Bélanger, M., Allaman, I., and Magistretti, P. J. (2011). Brain energy metabolism: focus on astrocyte-neuron metabolic cooperation. *Cell Metabo.* 14, 724–738. doi: 10.1016/j.cmet.2011.08.016

Bellot-Saez, A., Kekesi, O., Morley, J. W., and Buskila, Y. (2017). Astrocytic modulation of neuronal excitability through K(+) spatial buffering. *Neurosci. Biobehav. Rev.* 77, 87–97. doi: 10.1016/j.neubiorev.2017.03.002

Bergles, D. E., and Jahr, C. E. (1998). Glial Contribution to Glutamate Uptake at Schaffer Collateral–Commissural Synapses in the Hippocampus. *J. Neurosci.* 18, 7709–7716. doi: 10.1523/jneurosci.18-19-07709.1998

Bowman, C. L., Ding, J. P., Sachs, F., and Sokabe, M. (1992). Mechanotransducing ion channels in astrocytes. *Brain Res.* 584, 272–286. doi: 10.1016/0006-8993(92)90906-p

Cheung, G., Sibille, J., Zapata, J., and Rouach, N. (2015). Activity-Dependent Plasticity of Astroglial Potassium and Glutamate Clearance. *Neural Plast.* 2015:109106. doi: 10.1155/2015/109106

Choi, H. B., Gordon, G. R. J., Zhou, N., Tai, C., Rungta, R. L., Martinez, J., et al. (2012). Metabolic communication between astrocytes and neurons via bicarbonate-responsive soluble adenylyl cyclase. *Neuron* 75, 1094–1104. doi: 10.1016/j.neuron.2012.08.032

Chung, W.-S., Welsh, C. A., Barres, B. A., and Stevens, B. (2015). Do glia drive synaptic and cognitive impairment in disease? *Nat. Neurosci.* 18:1539. doi: 10.1038/nn.4142

Covelo, A., and Araque, A. (2018). Neuronal activity determines distinct gliotransmitter release from a single astrocyte. *eLife* 7:e32237. doi: 10.7554/eLife.32237

Dallerac, G., Chever, O., and Rouach, N. (2013). How do astrocytes shape synaptic transmission? Insights from electrophysiology. *Front. Cell Neurosci.* 7:159. doi: 10.3389/fncel.2013.00159

Djukic, B., Casper, K. B., Philpot, B. D., Chin, L. S., and McCarthy, K. D. (2007). Conditional knock-out of Kir4.1 leads to glial membrane depolarization, inhibition of potassium and glutamate uptake, and enhanced short-term synaptic potentiation. *J. Neurosci.* 27, 11354–11365. doi: 10.1523/JNEUROSCI.0723-07.2007

Dzamba, D., Honsa, P., and Anderova, M. (2013). NMDA receptors in glial cells: pending questions. *Curr. Neuropharmacol.* 11, 250–262. doi: 10.2174/1570159x11311030002

Garcia-Esparcia, P., Diaz-Lucena, D., Ainciburu, M., Torrejón-Escribano, B., Carmona, M., Llorens, F., et al. (2018). Glutamate Transporter GLT1 Expression in Alzheimer Disease and Dementia With Lewy Bodies. *Front. Aging Neurosci.* 10:122. doi: 10.3389/fnagi.2018.00122

Gomez-Galan, M., De Bundel, D., Van Eeckhaut, A., Smolders, I., and Lindskog, M. (2013). Dysfunctional astrocytic regulation of glutamate transmission in a rat model of depression. *Mol. Psychiatry* 18, 582–594. doi: 10.1038/mp.2012.10

Gomez-Galan, M., Femenia, T., Aberg, E., Graae, L., Van Eeckhaut, A., Smolders, I., et al. (2016). Running Opposes the Effects of Social Isolation on Synaptic Plasticity and Transmission in a Rat Model of Depression. *PLoS One* 11:e0165071. doi: 10.1371/journal.pone.0165071

Goncalves-Ribeiro, J., Pina, C. C., Sebastiao, A. M., and Vaz, S. H. (2019). Glutamate Transporters in Hippocampal LTD/LTP: not just prevention of excitotoxicity. *Front. Cell Neurosci.* 13:357. doi: 10.3389/fncel.2019.00357

Habbas, S., Santello, M., Becker, D., Stubbe, H., Zappia, G., Liaudet, N., et al. (2015). Neuroinflammatory TNFα Impairs Memory via Astrocyte Signaling. *Cell* 163, 1730–1741. doi: 10.1016/j.cell.2015.11.023

Henneberger, C., and Rusakov, D. A. (2012). Monitoring local synaptic activity with astrocytic patch pipettes. *Nat. Protoc.* 7, 2171–2179. doi: 10.1038/nprot.2012.140

Hwang, E. M., Kim, E., Yarishkin, O., Woo, D. H., Han, K. S., Park, N., et al. (2014). A disulphide-linked heterodimer of TWIK-1 and TREK-1 mediates passive conductance in astrocytes. *Nat. Commun.* 5:3227. doi: 10.1038/ncomms4227

Iliff, J. J., Wang, M., Liao, Y., Plogg, B. A., Peng, W., Gundersen, G. A., et al. (2012). A paravascular pathway facilitates CSF flow through the brain parenchyma and the clearance of interstitial solutes, including amyloid beta. *Sci. Transl. Med.* 4, 147ra111. doi: 10.1126/scitranslmed.3003748

Jensen, A. A., Fahlke, C., Bjorn-Yoshimoto, W. E., and Bunch, L. (2015). Excitatory amino acid transporters: recent insights into molecular mechanisms, novel modes of modulation and new therapeutic possibilities. *Curr. Opin. Pharmacol.* 20, 116–123. doi: 10.1016/j.coph.2014.10.008

Kettenmann, H., Backus, K. H., and Schachner, M. (1984). Aspartate, glutamate and gamma-aminobutyric acid depolarize cultured astrocytes. *Neurosci. Lett.* 52, 25–29. doi: 10.1016/0304-3940(84)90345-8

Kettenmann, H., and Schachner, M. (1985). Pharmacological properties of gamma-aminobutyric acid-, glutamate-, and aspartate-induced depolarizations in cultured astrocytes. *J. Neurosci.* 5, 3295–3301. doi: 10.1523/jneurosci.05-12-03295.1985

Khakh, B. S., and McCarthy, K. D. (2015). Astrocyte calcium signaling: from observations to functions and the challenges therein. *Cold Spring Harb. Perspect. Biol.* 7:a020404. doi: 10.1101/cshperspect.a020404

Kofuji, P., and Newman, E. A. (2004). Potassium buffering in the central nervous system. *Neuroscience* 129, 1045–1056. doi: 10.1016/j.neuroscience.2004.06.008

Lackington, I., and Orrego, F. (1986). Continuous measurement of net potassium movements in rat brain cortex suspensions. Effects of glutamate, veratridine, creatine and other substances. *Brain Res.* 378, 390–393. doi: 10.1016/0006-8993(86)90943-1

Lalo, U., Pankratov, Y., Kirchhoff, F., North, R. A., and Verkhratsky, A. (2006). NMDA Receptors Mediate Neuron-to-Glia Signaling in Mouse Cortical Astrocytes. *J. Neurosci.* 26, 2673–2683. doi: 10.1523/jneurosci.4689-05.2006

Lebedeva, A., Plata, A., Nosova, O., Tyurikova, O., and Semyanov, A. (2018). Activity-dependent changes in transporter and potassium currents in hippocampal astrocytes. *Brain Res. Bull.* 136, 37–43. doi: 10.1016/j.brainresbull.2017.08.015

Losonczy, A., Somogyi, P., and Nusser, Z. (2003). Reduction of excitatory postsynaptic responses by persistently active metabotropic glutamate receptors in the hippocampus. *J. Neurophysiol.* 89, 1910–1919. doi: 10.1152/jn.00842.2002

Martin, R., Bajo-Graneras, R., Moratalla, R., Perea, G., and Araque, A. (2015). Circuit-specific signaling in astrocyte-neuron networks in basal ganglia pathways. *Science* 349, 730–734. doi: 10.1126/science.aaa7945

Meeks, J. P., and Mennerick, S. (2007). Astrocyte membrane responses and potassium accumulation during neuronal activity. *Hippocampus* 17, 1100–1108. doi: 10.1002/hipo.20344

Olsen, M. L., and Sontheimer, H. (2008). Functional implications for Kir4.1 channels in glial biology: from K+ buffering to cell differentiation. *J. Neurochem.* 107, 589–601. doi: 10.1111/j.1471-4159.2008.05615.x

Orkand, R. K. (1980). Extracellular potassium accumulation in the nervous system. *Fed Proc.* 39, 1515–1518.

Panatier, A., Vallee, J., Haber, M., Murai, K. K., Lacaille, J. C., and Robitaille, R. (2011). Astrocytes are endogenous regulators of basal transmission at central synapses. *Cell* 146, 785–798. doi: 10.1016/j.cell.2011.07.022

Pannasch, U., Sibille, J., and Rouach, N. (2012). Dual electrophysiological recordings of synaptically-evoked astroglial and neuronal responses in acute hippocampal slices. *J. Vis. Exp.* 69:e4418. doi: 10.3791/4418

Potier, B., Billard, J. M., Riviere, S., Sinet, P. M., Denis, I., Champeil-Potokar, G., et al. (2010). Reduction in glutamate uptake is associated with extrasynaptic NMDA and metabotropic glutamate receptor activation at the hippocampal CA1 synapse of aged rats. *Aging Cell* 9, 722–735. doi: 10.1111/j.1474-9726.2010.00593.x

Ransom, B. R., and Goldring, S. (1973). Ionic determinants of membrane potential of cells presumed to be glia in cerebral cortex of cat. *J. Neurophysiol.* 36, 855–868. doi: 10.1152/jn.1973.36.5.855

Rose, C. R., Felix, L., Zeug, A., Dietrich, D., Reiner, A., and Henneberger, C. (2017). Astroglial Glutamate Signaling and Uptake in the Hippocampus. *Front. Mol. Neurosci.* 10:451. doi: 10.3389/fnmol.2017.00451

Rose, C. R., Ziemens, D., Untiet, V., and Fahlke, C. (2018). Molecular and cellular physiology of sodium-dependent glutamate transporters. *Brain Res. Bull.* 136, 3–16. doi: 10.1016/j.brainresbull.2016.12.013

Santello, M., Toni, N., and Volterra, A. (2019). Astrocyte function from information processing to cognition and cognitive impairment. *Nat. Neurosci.* 22, 154–166. doi: 10.1038/s41593-018-0325-8

Savtchenko, L. P., Bard, L., Jensen, T. P., Reynolds, J. P., Kraev, I., Medvedev, N., et al. (2018). Disentangling astroglial physiology with a realistic cell model in silico. *Nat. Commun.* 9:3554. doi: 10.1038/s41467-018-05896-w

Schipke, C. G., Ohlemeyer, C., Matyash, M., Nolte, C., Kettenmann, H., and Kirchhoff, F. (2001). Astrocytes of the mouse neocortex express functional N-methyl-D-aspartate receptors. *FASEB J.* 15, 1270–1272. doi: 10.1096/fj.00-0439fje

Shih, P. Y., Savtchenko, L. P., Kamasawa, N., Dembitskaya, Y., McHugh, T. J., Rusakov, D. A., et al. (2013). Retrograde synaptic signaling mediated by K+ efflux through postsynaptic NMDA receptors. *Cell Rep.* 5, 941–951. doi: 10.1016/j.celrep.2013.10.026

Sibille, J., Pannasch, U., and Rouach, N. (2014). Astroglial potassium clearance contributes to short-term plasticity of synaptically evoked currents at the tripartite synapse. *J. Physiol.* 592(Pt 1), 87–102. doi: 10.1113/jphysiol.2013.261735

Siddoway, B., Hou, H., and Xia, H. (2014). Molecular mechanisms of homeostatic synaptic downscaling. *Neuropharmacology* 78, 38–44. doi: 10.1016/j.neuropharm.2013.07.009

Skowronska, K., Obara-Michlewska, M., Zielinska, M., and Albrecht, J. (2019). NMDA Receptors in Astrocytes: in Search for Roles in Neurotransmission and Astrocytic Homeostasis. *Int. J. Mol. Sci.* 20:309. doi: 10.3390/ijms20020309

Spangaro, M., Bosia, M., Zanoletti, A., Bechi, M., Mariachiara, B., Pirovano, A., et al. (2014). Exploring effects of EAAT polymorphisms on cognitive functions in schizophrenia. *Pharmacogenomics* 15, 925–932. doi: 10.2217/pgs.14.42

Steinhauser, C., Berger, T., Frotscher, M., and Kettenmann, H. (1992). Heterogeneity in the Membrane Current Pattern of Identified Glial Cells in the Hippocampal Slice. *Eur. J. Neurosci.* 4, 472–484. doi: 10.1111/j.1460-9568.1992.tb00897.x

Tanui, R., Tao, Z., Silverstein, N., Kanner, B., and Grewer, C. (2016). Electrogenic Steps Associated with Substrate Binding to the Neuronal Glutamate Transporter EAAC1. *J. Biol. Chem.* 291, 11852–11864. doi: 10.1074/jbc.M116.722470

Tong, G., and Jahr, C. E. (1994). Block of glutamate transporters potentiates postsynaptic excitation. *Neuron* 13, 1195–1203. doi: 10.1016/0896-6273(94)90057-4

Verkhratsky, A., and Nedergaard, M. (2018). Physiology of Astroglia. *Physiol. Rev.* 98, 239–389. doi: 10.1152/physrev.00042.2016

Woo, J., Han, Y. E., Koh, W., Won, J., Park, M. G., An, H., et al. (2019). Pharmacological dissection of intrinsic optical signal reveals a functional coupling between synaptic activity and astrocytic volume transient. *Exp. Neurobiol.* 28, 30–42. doi: 10.5607/en.2019.28.1.30

Wu, K. C., Kuo, C. S., Chao, C. C., Huang, C. C., Tu, Y. K., Chan, P., et al. (2015). Role of voltage-gated K(+) channels in regulating Ca(2+) entry in rat cortical astrocytes. *J. Physiol. Sci.* 65, 171–177. doi: 10.1007/s12576-015-0356-9

Zhang, J.-M., Wang, H.-K., Ye, C.-Q., Ge, W., Chen, Y., Jiang, Z.-L., et al. (2003). ATP Released by Astrocytes Mediates Glutamatergic Activity-Dependent Heterosynaptic Suppression. *Neuron* 40, 971–982. doi: 10.1016/S0896-6273(03)00717-7

Conflict of Interest: The authors declare that the research was conducted in the absence of any commercial or financial relationships that could be construed as a potential conflict of interest.